Universidade de Lisboa
Faculdade de Ciências
(Departamento de Química e Bioquímica)

EXPLORING THE CHEMICAL PROPERTIES OF ELEMENTARY ACTINIDE SPECIES IN THE GAS PHASE

Ana Filipa Folgado de Lucena

Tese orientada por Doutor Joaquim Marçalo (C^2TN-IST),
Doutor John K. Gibson (LBNL) e Doutor João Paulo Leal (FCUL, C^2TN-IST),
Documento especialmente elaborado para a obtenção do grau de
Doutor em Química, especialidade Química-Física

2015

The work presented in this thesis was performed at Grupo de Química dos Elementos-*f*, Centro de Ciências e Tecnologias Nucleares, Instituto Superior Técnico, Universidade de Lisboa (C^2TN/IST), and also at Glenn T. Seaborg Center, Chemical Sciences Division, Lawrence Berkeley National Laboratory (LBNL) and Laboratory of Ligand-Actinide Interactions (LILA) at Comissariat à l'Energie Atomique et aux Energies Alternatives (CEA), with financial support from the Fundação para a Ciência e a Tecnologia (SFRH/BD/70475/2010).

To my husband and my daughter

To my mother

Acknowledgments

There are a great number of people that have contributed, directly or indirectly, to the completion of this thesis and without whom this journey would be much harder, if not, impossible.

First of all, I would like to express my sincere gratitude to my thesis supervisors:
Dr. Joaquim Marçalo, who generously suggested and invited me to go through this Ph.D., and has always motivated and supported me with his knowledge and competence. Although he is a very busy researcher, he always arranged time to explain and to make me aware of several important aspects, with a remarkable memory, sometimes better than mine! Thank you for leading me into the world of the gas-phase ion chemistry and to continuously challenging me, making me progress and grow as a scientist.
Dr. John K. Gibson, for hosting me at the Lawrence Berkeley National Laboratory with enormous sympathy, for his supervision with the actinides experiments, for all the scientific discussions together with Dr. Joaquim Marçalo, and the prompt corrections and email answers.
Dr. João Paulo Leal for accepting to supervise my work and being always available for any corrections and suggestions, and for being the link with the University, helping me with all the bureaucratic issues.

I would also like to acknowledge the Foundation for Science and Technology (FCT) for my personal doctoral grant (SFRH/BD/70475/2010) and to *Centro de Ciências e Tecnologias Nucleares, Instituto Superior Técnico, Universidade de Lisboa* (C^2TN/IST) for hosting and providing me the necessary conditions to develop my work. A special thanks to all the co-authors of the works described in this thesis. It would have never been possible to accomplish the reported results and conclusions if it wasn't your important contribution.

A special thanks to Dr. Maria Michelini for the theoretical computations and for such kindness and sympathy during my stay in Berkeley.
To Dr. Yu Gong, for guiding me with all the actinide ESI-MS experiments at LBNL and through all the necessary procedures to work under a radiological environment, more specifically with the radiologic glove box. Also, thank you for the hints and tips about Berkeley and San Francisco, for showing me the criminal map of Oakland and for understanding that a left-handed woman doesn't bring bad luck!
I want also to acknowledge the LILA Lab, at CEA France, specially Dr. Laurence Berthon and Mrs. Nicole Zorz for guiding me with the americium experiments. Also, I want to thank Mathieu Audras and Sarah Mostapha for the companionship at the office/lab and during my stay in France.
I would like also to acknowledge Dr. M. Conceição Oliveira and Mrs. Ana Dias, for the collaboration and all the ESI-MS experiments performed at CQE-IST.

To *Grupo de Química dos Elementos-f* at C^2TN-IST, in particular to Dr. Leonor Maria, for the scientific discussions, for all the suggestions regarding my thesis and for motivating me during all these years; it was a pleasure to work with you. To Dr. José Carretas, who collaborated in most of the experiments of my work, showing up always in a good mood, always "*moralizado*". To Adelaide Cruz, for helping me at the lab and sharing the office with me during all these years, spreading laughs and happiness everywhere. To my co-workers and friends - "as meninas" Cybelle

Soares, Marina Soares, Joana Vitorino, Vânia Sousa, Ana Ferreira and Ana Moura, thank you for sharing all the good and bad moments of this journey, for listening and advising me. A special thanks also to the former grantholders and my dearest friends Célia Lourenço and Elsa Mora, who were present since the very beginning of this journey. To Dr. Joaquim Branco, Dr. Teresa Gasche, Dr. Maria Augusta Antunes, Dr. Bernardo Monteiro and Dr. Cláudia Pereira, for the important comments and discussions at every group meeting.

To all my QA friends from the *Faculdade de Ciências e Tecnologia*, who directly or indirectly made my days better, specially, Catarina Custódio (a minha Pucca), Vanessa Nascimento, Ricardo Barata, Sofia Martins, Raquel Teixeira, Joana Pais, Patrique Nunes, Cristina Oliveira, Bárbara Chagas, Ricardo Melo, António Barata, Leonardo Mendes, Vitor Silva, André Costa, most of you great scientists, thank you all for the friendship, the days spent at *Dona Teresa* and at the S*ala de convívio* playing endless *sueca*, the nights out, all the weird geek discussions, all the laughs and the support in every moment of my life, that greatly contributed for who I am today.
To my new friends in Italy, le ragazze: Suzanne, Sylvia, Kaat, Manuela, Carolina, Vera, Heidi, Amelia, Nami and Mrs. Giuliana Potts (insegnante di italiano), per le ottime pause pranzo ogni martedì. È stato sicuramente il giorno più bello della settimana! Un bacione a tutti voi!

I would like to acknowledge also the ones that have always supported me in the background: *my family*, *aos Lopes e Mendes, queridas manas Inês e Andreia, fofinhos Margarida e Miguel e Avó Alice; à minha avózinha Lia, aos meus tios Sú, Cadi e Lívia e primos AlexDaTuga e Catas. À minha querida mãe, pelo seu amor incondicional e achar que eu sou "a maior", e, por último, um agradecimento mais que especial ao meu melhor amigo, companheiro, marido e pai, João, e à nossa bebé Filipa, vocês são a base da pirâmide – obrigada por tudo.*

Por último, dedico a tese em memória do meu Pai, que sempre me incentivou a progredir e que ficaria certamente orgulhoso de me ver atingir tamanha conquista.

Exploring the chemical properties of elementary actinide species in the gas phase

Abstract

Gas-phase ion chemistry studies were conducted to search for new elementary actinide (An) species and reactions and to enhance the fundamental understanding of these elements. In the gas phase, with the absence of external perturbations (solvents), physical and chemical properties of elementary actinide species were better studied and relationships between electronic structure, reactivity and energetics established. The role of the 5*f* electrons and the covalency in these heavy elements were important aspects examined. Most of the studies were performed in parallel with theoretical calculations (through international collaborations), which were essential for complementing the understanding of actinide chemistry. The studies were performed with the use of mass spectrometry techniques, namely Laser Ionization Fourier Transform Ion Cyclotron Resonance (LI-FT-ICR-MS) and Electrospray Ionization Quadrupole Ion Trap (ESI-QIT-MS). The use of these ion traps were very effective for the ion/molecule reaction studies, enabling to perform complex sequences of ion manipulation and obtaining kinetic and mechanistic information. New actinide species and processes were identified, with the actinyl ions, $AnO_2^{+/2+}$, being the highlight of the work: oxo-exchange with water and methanol; addition reactions of water and oxygen to actinyl ions, with a focus in the formation of superoxide uranyl(VI) ions from uranyl(V); synthesis of sulfur "analogues" of actinyls from reactions of $An^{+/2+}$ ions with COS; determination of the effective charge density of U in uranyl(VI), comparable to that of the late trivalent lanthanides, from the dissociation of bimetallic clusters; evaluation of III/IV redox stabilities of lanthanides and actinides by measurement of hydrolysis rates for $MO(NO_3)_3^-$ species; and coordination studies of biologically relevant ligands, amino acids in particular, that allowed establishing trends of relative stabilities/affinities towards the actinyl ions.

Keywords Gas-phase ion chemistry, FT-ICR-MS, ESI-QIT-MS, Actinyl ions, Ion/molecule reactions, Collision-induced dissociation, 5*f* electrons.

Estudo das propriedades químicas de espécies elementares de actinídeos em fase gasosa

Resumo

Foram efetuados estudos de química de iões em fase gasosa com o objetivo de obter novas espécies e reações de actinídeos (An) e ampliar o conhecimento destes elementos a nível fundamental. Devido à ausência de fatores externos na fase gasosa, nomeadamente solventes, é possível realizar estudos mais precisos das propriedades físicas e químicas de espécies com actinídeos e estabelecer relações entre reatividade, energética e estrutura eletrónica. O papel dos eletrões 5*f* e a covalência neste tipo de elementos foram dois aspetos importantes abordados. A parte experimental foi realizada em simultâneo com cálculos teóricos, através de colaborações internacionais, que foram essenciais uma vez que permitiram complementar o conhecimento da química dos actinídeos. Recorreu-se ao uso de técnicas de espectrometria de massa, Ionização Laser/Ressonância Ciclotrónica de Iões com Transformada de Fourier (LI-FT-ICR-MS) e Ionização por Eletronebulização/Trapa de Iões Quadrupolar (ESI-QIT-MS). As trapas de iões utilizadas foram bastante vantajosas no estudo de reações ião/molécula, permitindo realizar sequências complexas de manipulação de iões e estudos cinéticos e mecanísticos. Foram identificadas novas espécies e processos envolvendo actinídeos, em que os iões actinilos foram o alvo principal do estudo: oxo-permuta com água e metanol; adição de água e oxigénio molecular a iões actinilos, em que a formação de iões superóxidos de uranilo(VI) partindo de uranilo(V) foi relevante; síntese de espécies análogas de actinilos com enxofre, partido de reações de iões $An^{+/2+}$ com COS; determinação da carga efetiva do U no uranilo(VI), a qual se verificou ser comparável à dos iões lantanídeos trivalentes, através da dissociação de agregados bimetálicos; avaliação de estabilidades redox dos estados III/IV de lantanídeos e actinídeos estimadas através de reações de hidrólise de espécies $MO(NO_3)_3^-$; e estudos de coordenação de ligandos aminoácidos com iões actinilos, onde ordens de estabilidade/afinidade foram estimadas.

Palavras-chave Química de iões em fase gasosa, FT-ICR-MS, ESI-QIT-MS, iões actinilos, reações ião/molécula, dissociação induzida por colisão, eletrões 5*f*.

Structure of the thesis

The present thesis is divided into five chapters. The main body of the thesis is based on five papers published in international journals. All are identified in the first page of each sub-chapter as well as the author's identification and contributions. Other preliminary results are also presented in the Chapters II.4 and IV. The contents of each chapter are summarized below:

Chapter I describes general concepts and fundamentals about the *f* elements and gas-phase chemistry, and is a general introduction to the thesis. The following chapters are based on the experimental work and presented as adapted versions of the published paper or as first drafts of manuscripts with unpublished work.

In ***Chapter II***, fundamental properties of the actinide ions were explored, as for instance, elementary gas-phase reactions (oxo-exchange, hydration and oxidation) and also the synthesis of new actinide polysulfide cations as potential uranyl analogues. The latter topic is presented as preliminary results.

Fragmentation and reactivity of lanthanide and actinide species were studied in detail in ***Chapter III***, in particular fragmentation of rare earth, lanthanide and uranyl bimetallic clusters in order to estimate the charge density of uranyl(VI), and the synthesis of lanthanide and actinide oxide nitrate complexes for which the obtained hydrolysis rates relate to the intrinsic stability of the M^{IV} oxidation states.

The last aspect studied with the actinide elements described in ***Chapter IV*** was the basic interactions of actinides with molecules of biological relevance, namely amino acids. The effects of the presence of different binding sites were examined as well as the relative gas-phase affinities of these amino acids towards actinyl ions, $AnO_2^{+/2+}$ (uranyl, neptunyl and plutonyl), with a focus on uranyl. The few existent theoretical calculations on actinyl-aa coordination were useful for elucidation of the most favorable structures of some of the species formed by ESI-MS and CID. This chapter is a first draft of a manuscript.

The last chapter, ***Chapter V***, contains the general conclusions and final remarks regarding the overall work carried out under the scope of this thesis.

List of publications

The PhD work described in this thesis resulted in the publications listed below.

INTERNATIONAL REFEREED JOURNALS

1. **Lucena AF**, Lourenço C, Michelini MC, Rutkowski P, Carretas J, Zorz N, Berthon L, Dias A, Oliveira MC, Gibson JK, Marçalo J, Synthesis and Hydrolysis of Gas-Phase Lanthanide and Actinide Oxide Nitrate Complexes: A Correspondence to Trivalent Metal Ion Redox Potentials and Ionization Energies, **Phys. Chem. Chem. Phys., 2015**, 17, 9942 -9950, DOI: 10.1039/C5CP00515A.

2. **Lucena AF**, Carretas J, Marçalo J, Michelini M, Gong Y, Gibson JK, Gas-phase Reactions of Molecular Oxygen with Uranyl(V) Anionic Complexes – Synthesis and Characterization of New Superoxides of Uranyl(VI), **J. Phys. Chem. A, 2015**, 119 (15), 3628–3635, DOI: 10.1021/acs.jpca.5b01445.

3. **Lucena AF**, Carretas J, Marçalo J, Michelini M, Rutkowski P, Gibson JK, Dissociation of Gas-Phase Bimetallic Clusters as a Probe of Charge Densities: The Effective Charge of Uranyl, **J. Phys. Chem. A**, **2014**, 118 (11), 2159–2166, DOI: 10.1021/jp500946y.

4. **Lucena AF**, Samuel O, Zhao J, Marçalo J, Schreckenbach G, Gibson JK, Oxo-Exchange of Gas-Phase Uranyl, Neptunyl and Plutonyl with Water and Methanol, **Inorg. Chem**., **2014**, 53 (4), 2163–2170, DOI: 10.1021/ic402824k.

5. Rios D, Michelini MC, **Lucena AF**, Marçalo J, Gibson JK, On the Origins of Faster Oxo-Exchange for Uranyl(V) versus Plutonyl(V), **J. Am. Chem. Soc.**, **2012**, 134 (37), 15488-15496, DOI: 10.1021/ja305800q.

6. Rios D, Michelini MC, **Lucena AF**, Marçalo J, Bray TH, Gibson JK, Gas-Phase Uranyl, Neptunyl, and Plutonyl: Hydration and Oxidation Studied by Experiment and Theory, **Inorg. Chem., 2012**, 51, 6603–6614, DOI: 10.1021/ic3001625.

COMMUNICATIONS IN CONFERENCES

Oral presentations

1. **Lucena AF**, Exploring the chemical differences between trivalent lanthanides and actinides by mass spectrometry, ACTiNET-I3 plenary meeting, 23-24 Jan 2013, Avignon, France.

2. **Lucena AF**, Rios D, Michelini MC, Marçalo J, Gibson JK, Gas-Phase Reactions of Actinyl Ions with $H_2{}^{18}O$: Investigating Oxygen Exchange by Experiment and Theory, Pu Futures, 15-20 July 2012, Cambridge, UK.

3. Gibson JK, Rios D, Gong Y, Lucena AF, Marçalo J, Michelini MC, Inorganic and Organometallic Actinide Chemistry Studied by Tandem Mass Spectrometry, , SciX 2012 - 39th Annual Meeting of FACSS, October 2012, Kansas City, Missouri (EUA).

4. Gibson JK, Marçalo J, Michelini MC, Rios D, Lucena AF, Rutkowski PX, Actinide Chemistry from a Gas-Phase Perspective, 243rd ACS National Meeting & Exposition, March 2012, San Diego, California (EUA).

5. **Lucena AF**, Pereira CCL, Marsden C, Gibson JK, Marçalo J, Actinide polysulfides in the gas phase, European f-element network – COST CM1006, 1-4 April 2012, Salou, Spain.

6. Gibson JK, Rios D, Rutkowski PX, Marçalo J, Lucena AF, Lourenço C, Carretas JM, Michelini MC, Synthetic Actinide Chemistry in the Gas Phase, 2012 MRS Spring Meeting & Exhibit, April 2012, São Francisco, California (EUA).

7. Marçalo J, Lucena AF, Lourenço C, Monteiro B, Maria L, Carretas JM, Rutkowski PX, Gibson JK, Mass Spectrometry of Rare Earths—From Compound Characterization to Fundamental Gas-Phase Properties, XXIV. Terrae Rarae 2011, October 2011, Karlsruhe (Germany).

Poster Communications

1. J. Marçalo, Lucena AF, Carretas JM, Maria L, Michelini MC, Gong Y, Gibson JK, Exploring the Gas-Phase Chemistry of Uranyl: New Complexes with Superoxide and Amino Acid Ligands, XXIV Encontro Nacional da SPQ, July 2015, Coimbra, Portugal.

2. Lucena AF, Marçalo J, Gibson JK, Oxo-Exchange of Actinide Oxides and Hydroxides with Water in the Gas Phase, European f-element network (EUFEN4), April 2015, Lisbon, Portugal.

3. Lucena AF, Carretas JM, Marçalo J, Michelini M, Rutkowski P, Gibson JK, The Effective Charge of Uranyl in the gas phase, SPQ 10th Inorganic Chemistry Conference, April 2014, Costa da Caparica, Portugal.

4. Lucena AF, Maria L, Gong Y, Gibson JK, Marçalo J, Formation and Competitive Dissociation of Uranyl-Amino Acid Complexes in the Gas Phase, European f-element network (EUFEN3), April 2014, Nuremberg, Germany.

5. Lucena AF, Samuel O, Zhao J, Marçalo J, Schreckenbach G, Gibson JK, Oxo-Exchange of Uranyl, Neptunyl and Plutonyl with Water and Methanol in the Gas Phase, European f-element network (EUFEN3), April 2014, Nuremberg, Germany.

6. Lucena AF, Carretas JM, Michelini MC, Rutkowski PX, Gibson JK, Marçalo J, Probing the Effective Charge Density of Uranyl, UO_2^{2+}, in the Gas Phase, EUFEN3 - Meeting of COST Action CM1006: European f-Element Network, April 2014, Nuremberg, Germany.

7. Lucena AF, Maria L, Gong Y, Gibson JK, Marçalo J, Formation and Dissociation of Uranyl-, Neptunyl- and Plutonyl-Glycine-Complexes in the Gas Phase, European f-element network (EUFEN2), April 2013, Dublin, Ireland.

8. Lucena AF, Carretas J, Gong Y, Michelini MC, Gibson JK, Marçalo J, Oxygen Addition Reactions of Uranyl(V) Complexes in the Gas Phase, European f-element network (EUFEN2), April 2013, Dublin, Ireland.

9. Rios D, Michelini MC, Lucena AF, Marçalo J, Gibson JK, Advancing Organoactinyl Chemistry by In-Situ Ligand Synthesis in the Gas-Phase, Symposium honoring the 100th birthday of Glenn T. Seaborg, April 2012, Berkeley, California (EUA).

10. Lucena AF, Lourenço C, Carretas J, Rutkowski P, Michelini MC, Zorz N, Berthon L, Gibson JK, Marçalo J, III/IV Oxidation stability of lanthanide and actinides in the gas phase, European f-element network – COST CM1006, 1-4 April 2012, Salou, Spain.

11. Pereira CCL, Lucena AF, Marsden C, Marçalo J, Gibson JK, Thorium and uranium polysulfides in the gas phase, 3-6 Jun 2011, XXII Encontro Nacional da Sociedade Portuguesa de Química, Braga, Portugal.

12. Lucena AF, Carretas J, Marçalo J, Rutkowski P, Gibson JK, Questioning the Effective Charge of Uranyl, UO_2^{2+}, by ESI/QITMS, XXII Encontro Nacional da Sociedade Portuguesa de Química, Braga, 3-6 Jun 2011, Portugal.

13. Lucena AF, Pereira CCL, Marsden C, Gonçalves AP, Marçalo J, Gibson JK, Andrews L, Sulfuretos e carbonetos de tório em fase gasosa, 1º Encontro dos alunos de doutoramento do DQB-FCUL, 1 Jun 2011, FCUL, Lisboa, Portugal.

Table of contents

List of abbreviations and acronyms

A	
aa	Amino acid
$(aa-H)^-$	Deprotonated amino acid
$(aa-2H)^{2-}$	Doubly deprotonated amino acid
ADO	Average Dipole Orientation
An	Actinide
An-aa	Actinyl-amino acid species
APCI	Atmospheric pressure chemical ionization
API	Atmospheric Pressure Ionization
B	
BDE	Bond Dissociation Energy
B3LYP	Becke three-parameter Lee-Yang-Parr exchange-correlation functional
C	
CAD	Collisionally Activated Dissociation
CASPT2	Complete Active Space With Second-Order Perturbation Theory
CASSCF	Complete Active Space-Self Consistent Field
CID	Collision-Induced Dissociation
CI	Chemical Ionization
D	
DFT	Density-Functional Theory
DNA	Deoxyribonucleic Acid
E	
ECD	Electron Capture Detector
EI	Electron Ionization
ES	Electrospray
ESI-MS	Electrospray Ionization Mass Spectrometry
F	
FAB	Fast Atom Bombardment
FI	Field Ionization
FT-ICR-MS	Fourier Transform Ion Cyclotron Resonance Mass Spectrometry
FT-OT	Fourier Transform Orbitrap
G	
GGA	Generalized Gradient Approximations
GS	Ground State
I	
ICP-MS	Inductively Coupled Plasma Mass Spectrometry
IE	Ionization Energy
IE4	Fourth Ionization Energy
IT	Ion Trap

IM	ion/molecule reaction
IP	Ionization Potential
IR	Infrared
IRMPD	Infrared Multiphoton Dissociation
IS	Ionization Spectroscopy
L	
LA	Laser ablation
LD	Laser Desorption
LDI	Laser Desorption Ionization
LIT	Linear Ion Trap
Ln	Lanthanide
M	
MALDI	Matrix-Assisted Laser Desorption Ionization
M-aa	Metal-amino acid bond
mM	millimolar (concentration unit)
MS^n	Multiple stage mass spectrometry
MW	Molecular Weight
m/z	Mass-to-charge ratio
N	
NMR	Nuclear Magnetic Resonance
NPA	Natural Population Analysis
NR	No reaction
P	
PBE	Hybrid functional theory
PES	Potential Energy Surface
PEP	Potential Energy Profile
Q	
QIT	Quadrupole Ion Trap
QIT-MS	Quadrupole Ion Trap Mass Spectrometry
QTAIM	Quantum Theory of Atoms in Molecules
QqQ	Triple Quadrupole Spectrometer
R	
RASPT2	Multiconfigurational Second-Order Perturbation Theory Restricted Active Space
RF	Radio Frequency
S	
SI	International system of units
SIMS	Secondary Ion Mass Spectrometry
SWIFT	Stored waveform inverse Fourier Transform
T	
TOF-MS	Time of flight mass spectrometry
Z	
Z	Formal metal ion charge state

List of figures

CHAPTER I. Introduction and background

CHAPTER II. Fundamental aspects of actinyl chemistry

II.1 Oxo-exchange of actinyl(V) and actinyl(VI) with water and methanol

Supporting Information

II.2 Gas-phase uranyl, neptunyl and plutonyl: Hydration and oxidation

Supporting Information

CHAPTER IV. Coordination of actinyl ions with amino acids in the gas phase

List of tables

II.2 Gas-phase uranyl, neptunyl and plutonyl: Hydration and oxidation

II.4 Exploring the nature of actinide polysulfide ions

CHAPTER III. Lanthanide and actinide cluster fragmentation and chemistry

CHAPTER IV. Coordination of actinyl ions with amino acids in the gas phase

Chapter I

Introduction and background

Chapter II.
Fundamental aspects of actinyl chemistry

Chapter III.
Lanthanide and actinide cluster fragmentation and chemistry

Chapter IV.
Coordination of actinyl ions with amino acids in the gas phase

Chapter V.
Conclusions and final remarks

Chapter I. Introduction and background

I.1. f-Element chemistry: an overview

I.1.1. Lanthanides and actinides

The f-block elements consist of two series of transition elements: the lanthanides (Ln) and the actinides (An). The corresponding 4f and 5f orbitals of these elements play a central role in determining their properties.

In the lanthanide series (La-Lu), the +3 oxidation state is the most common; which allows observing the effect in their size and nuclear charge across the series. They are usually described as rare earth elements, a term which is rather misleading as many of the lanthanides are quite abundant in nature. Scandium and yttrium, d-block elements, also show strong chemical similarities to the lanthanides, so that the chemistry of these elements is also often considered in conjunction with that of the lanthanide series.

On the other hand, the chemistry of the actinides (Ac-Lr) is much more complex due to the wide range of possible oxidation states. All actinides are radioactive which leads to special care when handling and studying these elements.[1]

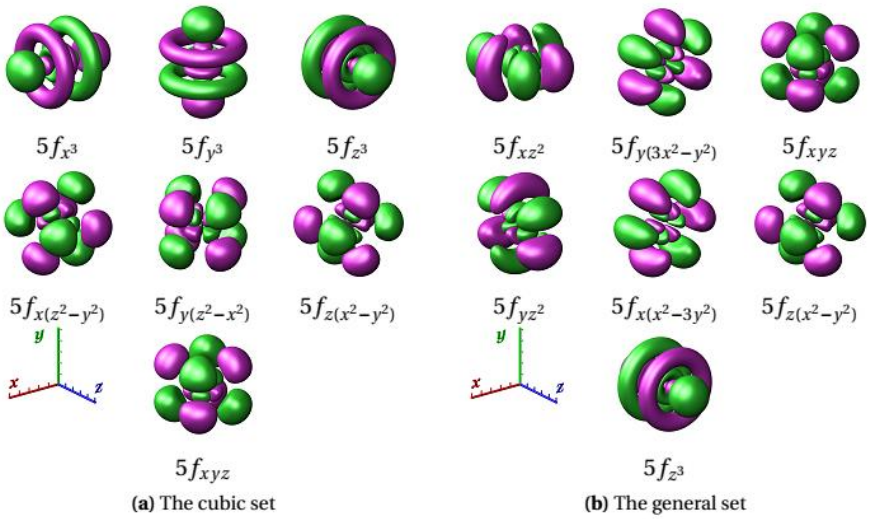

Figure I.1 The two common ways of representing 5*f*-orbitals: the cubic set, and the general set. Green represents the positive phase surface, and purple the negative phase surface. (Adapted from Kirker I.[2])

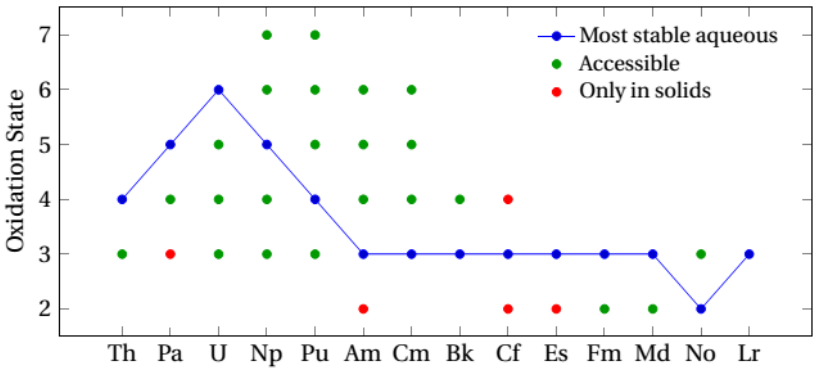

Figure I.2 Accessible oxidation states for the actinides. (Adapted from Kirker I.[2])

Most of the actinide elements (those heavier than uranium) were first discovered by synthetic methods with bombardment of heavy atoms with neutrons in nuclear reactors or with other particles in accelerators. Bonding in actinides derives mainly from the 5*f*, 6*d* and 7*s* orbitals. There is no unique way of representing the f orbitals (Figure I.1). One of the most common sets of *f* orbitals, the cubic set, is appropriate for molecules in which the x, y, and z axes are symmetry related.

The early actinides from protactinium (Pa) to americium (Am) can show more than one available oxidation state while the later actinides are more like the lanthanides since their chemistry is dominated by An^{3+} ions (Figure I.2).[3,4] The widely studied actinide, uranium, is known to be able to form more covalent bonds using both the 5f and 6d orbitals in bonding where a lanthanide would, in most cases, bond essentially ionically. Lanthanides are assumed to be strongly ionic, due to the behavior of the 4f orbital set which is highly contracted thus spatially confined to a region that makes them largely unavailable for bonding[3], and thus the majority of chemistry involves hard ionic bonding, with Ln^{3+} and Ln^{2+} ions, though cerium also has the 4+ oxidation state available.[3,5]

The 4f and 5f orbitals of the lanthanides and actinides respectively, are gradually filled (Table I.1). In the lanthanide series, the 5d subshell of lanthanum (La) is lower in energy than the 4f, and consequently it has a $[Xe]6s^25d^1$ configuration. As more protons are added to the nucleus, the 4f orbitals contract rapidly and become more stable than the 5d, so that Ce has the electron configuration $[Xe]6s^25d^14f^1$ and the trend continues with Pr having the arrangement $[Xe]6s^24f^3$. The 5s and 5p orbitals penetrate the 4f subshell and are not shielded from increasing nuclear charge, and hence because of the increasing effective nuclear charge, Z_{eff}, they contract as the atomic number increases – a phenomenon known as the *lanthanide contraction*, in which a decrease in ionic radius from La^{3+} (116 pm) to Lu^{3+} (97.7 pm) occur.

Table I.1 Electronic structure and ionic radii of lanthanides and actinides.[1]

Lanthanides			Actinides			
Element	Valence shell[a]	Ionic radius[b] (pm)	Element	Valence shell[c]	Ionic radius[b] (pm)	
	M^0	M^{3+}		M^0	M^{3+}	M^{4+}
La	$4f^05d^16s^2$	116	Ac	$5f^06d^17s^2$	*112*	—
Ce	$4f^15d^16s^2$	114.3	Th	$5f^06d^27s^2$	—	105
Pr	$4f^35d^06s^2$	112.6	Pa	$5f^26d^17s^2$	*104*	101
Nd	$4f^45d^06s^2$	110.9	U	$5f^36d^17s^2$	*102.5*	100
Pm	$4f^55d^06s^2$	109.3	Np[d]	$5f^46d^17s^2$	*101*	98
Sm	$4f^65d^06s^2$	107.9	Pu	$5f^66d^07s^2$	*100*	96
Eu	$4f^75d^06s^2$	106.6	Am	$5f^76d^07s^2$	*97.5*	95
Gd	$4f^75d^16s^2$	105.3	Cm	$5f^76d^17s^2$	*97*	95
Tb	$4f^95d^06s^2$	104	Bk	$5f^86d^17s^2$	*96*	93
Dy	$4f^{10}5d^06s^2$	102.7	Cf	$5f^{10}6d^07s^2$	*95*	92
Ho	$4f^{11}5d^06s^2$	101.5	Es	$5f^{11}6d^07s^2$	–	–
Er	$4f^{12}5d^06s^2$	100.4	Fm	$5f^{12}6d^07s^2$	–	–
Tm	$4f^{13}5d^06s^2$	99.4	Md	$5f^{13}6d^07s^2$	–	–
Yb	$4f^{14}5d^06s^2$	98.5	No	$5f^{14}6d^07s^2$	–	–
Lu	$4f^{14}5d^16s^2$	97.7	Lr	$5f^{14}6d^17s^2$	–	–

[a]Valence shell for $[Xe]4f^n5d^y6s^z6p^0$.
[b]Effective ionic radii (pm) for coordination number 8 or, if *italic*, 6 (from Shannon[1]). Crystal radii are ca. 14 pm larger for cations and ca. 14 pm smaller for anions.
[c]Valence shell for $[Rn]5f^n6d^y7s^z7p^0$.
[d]Also cited as $5f^56d^07s^2$.

Table I.2 Effective ionic radii for metal ions.[1]

M^{3+}	*r* (pm)	M^{4+}	*r* (pm)	M^{3+}	*r* (pm)	M^{4+}	*r* (pm)
Sc^{3+}	74.5	Ti^{4+}	60.5	V^{3+}	64	Ni^{4+}	48
Y^{3+}	90	Zr^{4+}	72	Nb^{3+}	72	Pd^{4+}	61.5
La^{3+}	103	Hf^{4+}	71	Ta^{3+}	72	Pt^{4+}	62.5

This has also an important effect on the radii of the third-row d-block elements, as it compensates for the size effect of filling the 5*p* and 6s subshells between cadmium and hafnium (Table I.2).
Early in the actinide series, electrons in the 6d orbitals are also lower in energy than the 5f orbitals, and so the 6*d* orbitals are filled before 5*f*. The 5*f* orbitals are starting to be filled at protactinium (Pa), and except for curium, the 6d orbitals are not occupied again. The 5*f* orbitals are not as effectively shielded by the filled 6*s* and 6*p* subshells as the 4*f* orbitals of the lanthanides are and thus are more perturbed in bonding.

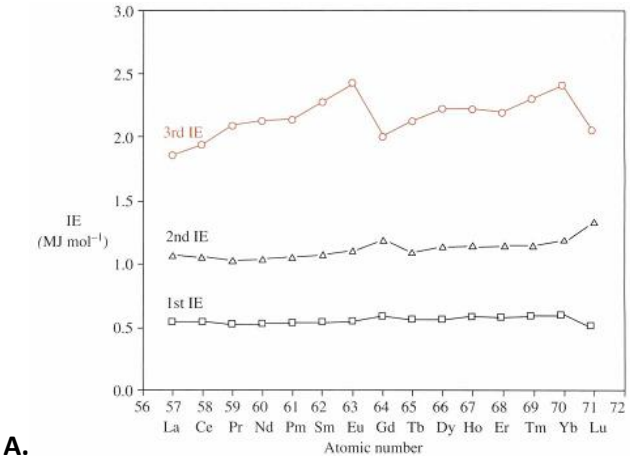

A.

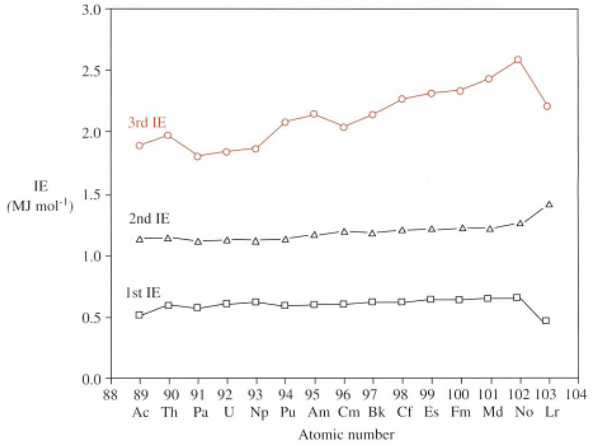

B.

Figure I.3 Variation of the ionization energy (IE) with the atomic number for A. lanthanides B. actinides.[1]

The first and second ionization energies (IE) of the lanthanides and actinides show little variation with atomic number (Figure I.3), but the third IE is more irregular in both cases. In the lanthanides series, the third IE does increase strongly to Eu^{2+}, where the $4f^7$ configuration is reached. There is a decrease in the IE after Eu^{2+} until Yb^{2+} when it increases again on approaching the $4f^{14}$ configuration. For the actinides, however, due to the similarity in energies between the 6*d* and 5*f* subshells, the behavior of the third IEs is more complex than for the lanthanides mainly due to the relativistic effects that result in a contraction of the 7*s* and 7*p* orbitals and an expansion and destabilization of the 6*d* and 5*f* orbitals. As a consequence, the actinide valence shell 6*d* and 5*f* electrons are easier to ionize.

I.1.2. Covalency in the f-block

In 1945 Seaborg probed the strong similarity in chemical behavior of the trivalent 4*f* lanthanides and the heavy 5*f* actinide elements[6,7]. This allowed the identification of heavier elements, transplutonium actinides[8], by accurate prediction of the chemical properties of undiscovered elements. Since that time, there has been considerable controversy and much debate about the degree of covalency in metal–ligand bonds of the 4*f* and 5*f* elements.[7,9-12]

As mentioned above, the lighter actinide elements have many characteristics in common with d-block elements (multiple oxidation states, possible covalent bonding) while the heavier actinides resemble the lanthanides since they also have a strong ionic nature of the bonds and similar ionic radii of the trivalent 4*f* and 5*f* cations.

The 5*d* orbitals of the lanthanide Ln^{3+} ions are empty and electrons in the core-like 4*f* orbitals are unable to enter into covalent bonding to any significant extent. Thus, although the sum of the first, second and third *IE*s is lower for the lanthanides than for the early d-block elements, oxidation state +3 is the maximum which can normally be attained, because the bonding is predominantly ionic in character.

The actinides are of special interest because two sets of atomic orbitals, the 5*f* and 6*d*, are very close in energy and both are capable of contributing to bonding. The early actinide elements can have variable oxidation state behavior rather like the early d-block elements, despite the sums of their first, second and third *IE*s being very similar to those of the lanthanides. The relativistic effects lead to the 6d and 5f orbitals being similar in energy and less core-like than the corresponding lanthanide valence shell orbitals. This allows some covalent contribution to bonding and hence higher oxidation states become accessible. By the middle of the actinide series the 6*d* and 5*f* orbitals are sufficiently contracted by the increasing Z_{eff} that both start to behave more as core electron shells, and the behavior of the elements becomes like that of the lanthanide series, with oxidation state +3 becoming the most stable for Am and beyond, with exception of No (+2).

In nuclear industry, covalency also plays an important role since there is an urgent need for efficient methods to separate trivalent actinides from trivalent lanthanides[13] which are a major problem in nuclear waste management. Ln(III) and An(III) cations with hard donor ligands are practically indistinguishable since they are both hard cations of identical charge and similar ionic radii.[14] These similarities make the chemical separation of Am(III) and Cm(III) (minor products of the neutron irradiation of U or Pu) from the light lanthanides (abundant products of U or Pu fission) a difficult problem to overcome. Some well-known separation processes have been tested:

PUREX, TRUEX, DIAMEX, among others.[15] Ligands containing soft-donor atoms such as N and S, have showed a slight preference for the heavier trivalent actinides over the trivalent lanthanides[10,13,15-17] possibly reflecting a slight enhancement of covalency in actinide metal-ligand bonds.[18,19]

Although there has been much discussion whether *s*, *p*, *d* and *f* orbitals are contributors to covalent bonding in various *f*-element complexes, this is still a subject of continuing scientific investigation and debate.[13]

I.2. Gas-phase ion chemistry

Gas phase ion chemistry is a broad field constantly developing with many applications, which embraces several branches of chemistry and physics. Organometallic chemistry largely focused on methane/hydrocarbon activation and reaction mechanisms[20-22], gas-phase catalysis[23,24] or the chemistry of multiply-charged metal cations[25,26] are a few examples reported in this field. New approaches for obtaining kinetic and thermochemical information and to reach new insights into the mechanisms of ion/molecule reactions under a wide variety of experimental conditions and methodologies are available. The information obtained is of major importance in formulating reasonable reaction mechanisms, in the determination of product ion structures and to obtain information on the intrinsic reactivity of ions in the absence of solvent or solid-state neighbors, important external perturbations characteristic of the condensed phases. In the gas phase, reactive intermediates and other chemically exotic species can be generated and studied.[27,28] Most of the research in this area uses mass spectrometric analysis, which allows a controlled manipulation of reactants and products and brings a wide number of advantages such as information on metal-ion complexation and the precise examination at a molecular level of the importance of selected ligands, solvent molecules and counter ions. Thermodynamic parameters that include standard enthalpies of formation and bond dissociation energies of ligated species, as well as electron affinities, ionization energies and proton affinities of neutral molecules can be determined.[29]

Progress on the mechanistic aspect is already extensively advanced by the availability of structural information on the reactants, products and reaction intermediates. Nevertheless, there is a continued need for more detailed reaction studies at the fundamental level. The joint effort developed so far between experiment and theory in gas-phase ion chemistry has greatly facilitated the understanding in this area.[30] Theoretical methods play an important role in the elucidation of gas-phase ion reactivity and experimental studies may help to validate the theoretical methodologies used.

I.2.1 Gas-phase ion chemistry of the f-elements

Several fundamental aspects of *f*-element chemistry have been extensively explored due to their distinctive electronic structures and chemical properties. Initial studies on lanthanide elements were performed by Schilling and Beauchamp[31] who revealed marked variations in the reactivities of different Ln ions, this in contrast to the mostly common similarity of the condensed-phase organolanthanide properties exhibited across the series, with the trivalent oxidation state

prevalent under most conditions. Gas-phase reactions of lanthanide cations Ln^+ (Ln = La-Lu, except Pm) with several linear, branched and cyclic alkanes, cyclopropane, and alkenes were reported in the early 1990s.[31,32] FT-ICR-MS was used to study the relative reactivity of the Ln^+ ions in relation to the C-H and C-C bond activation of hydrocarbons. Later in 2008, Marçalo et al. analyzed the gas-phase reactivity of the doubly-charged lanthanide cations, Ln^{2+} (Ln = La-Lu, except Pm), with alkanes (methane, ethane, propane, n-butane) and alkenes (ethene, propene, 1-butene). They observed that the only lanthanide cations capable of activating the hydrocarbons to form doubly-charged organometallic ions were La^{2+}, Ce^{2+}, Gd^{2+}, and Tb^{2+}.[33]

In relation to the actinides, organoactinide chemistry became a topic of interest[34-37] motivated by the role of relativistic effects and 5*f* bonding and the apparent intermediate character of the actinides between the covalent d-block transition metals and ionic lanthanides. Initial gas-phase organoactinide studies of U^+ [38] and Th^+ [39] were focused essentially on the activation of small hydrocarbons. It was found that the Th^+ ion activates small hydrocarbons with increasing efficiency as the number of carbon atoms increase. FT-ICR-MS and ion beam mass spectrometry were the primary techniques for studying hydrocarbon activation by metal ions.[40] Studies were later extended to several of the highly radioactive elements of the actinide series, from Np through Cf and allowed establishing an order of reactivity.[36,41-43] Santos et al. reported several other studies with monopositive and dipositive actinide ions, An^+ and An^{2+}, as well as actinide monoxides AnO^+ (An = Th, Pa, U, Np, Pu, Am and Cm) with alkanes, CH_4, C_2H_6, C_3H_8, *n*-C_4H_{10}, and alkenes, C_2H_4, C_3H_6, 1-C_4H_8.[44-47] The authors confirmed the importance of the 5f electrons for the reactivity of the actinide ions with these hydrocarbons. A scale of relative reactivity was reported following the order $Th^+ > Pa^+ > U^+ > Np^+ > Cm^+ > Pu^+ > Am^+$. Reactions of doubly-charged actinide cations, An^{2+}, with hydrocarbons provided a means to further explore the relationships between actinide electronic configurations and organometallic bond activation. In the case of the monoxides, only ThO^+, PaO^+ and UO^+ were reactive, with PaO^+ being the most reactive. Again, these results emphasized the active role of the 5f electrons in the oxidative insertion and provided information about the nature of activation processes and the inherent electronic structures of actinides.

Besides studies with small hydrocarbons there is a wide variety of other organic molecules as for instance the arenes[48], polyaromatic hydrocarbons (PAHs)[49], small nitriles[50], alcohols and thiols[51] as well as biologically relevant molecules (amino acids and peptides).[52,53] Most of these gas-phase actinide ion chemistry studies have been comprehensively reviewed over the years.[29,35]

I.2.2 Actinyl ions

Actinyl ions, $AnO_2^{+/2+}$, were comprehensively evaluated in 1992.[9] At the time, the most discussed actinide compounds were uranyl, UO_2^{2+}, and neptunyl, NpO_2^{2+}, and optical spectroscopy methods were the main source for obtaining experimental data. After that time, other techniques such as X-ray spectroscopy were also used to enhance the understanding of the nature of the An-O bonds. The actinyl ions exhibit unusually strong covalent bonds which has a profound influence on their chemistry. Their actinide-oxygen bonds are short, strong, and collinear which makes them chemically robust species.

Uranium (U) is known to form stable linear dioxocations in oxidation states above 4+. It is chemically very stable in the hexavalent oxidation state and the corresponding dioxocation UO_2^{2+}, the uranyl ion, is the most common stable form of uranium in contact with water and atmospheric oxygen. The uranyl ion is usually not observed in an uncomplexed state but is usually bound to coordinating ligands which are, in general, oxygen or halogens in inorganic complexes and nitrogen, sulfur, and even carbon in organic complexes.[54,55]

In aqueous chemistry, monopositive dioxo ions, UO_2^+, NpO_2^+, PuO_2^+, and AmO_2^+ are quite important actinide ions and all have also been prepared as bare gas-phase ions and their properties explored.[41,56-58] However, the dipositive actinyl ions, AnO_2^{2+}, are of greater importance in the chemistry of U, Np, Pu, and Am since they are hexavalent actinide species of varying stability found also in solution and with different and more complex behavior which have been studied extensively.[56,59,60]

For a better understanding of the nature of these oxo-actinide species, it is important to obtain information of the bare species/ions without perturbations caused by coordination as is usually present in the condensed phases.

The electronic structure of these elements have been unraveled by the use of a variety of measurements and by spectroscopy, which together with theoretical calculations, established the composition and role of the valence orbitals.[61] In Figure I.4 is represented an energy level scheme for the molecular orbitals (MOs) with particular relevance to An-O bonding. Actinide ions have two primary valence shells, 5*f* and 6d. Both can form σ and π bonds to oxygen. The four highest filled MOs, 3 σ_g, 3 σ_u, 1π_g, and 2π_u, centered on the oxygen atoms, participate in bonding and suggest a formal U-O bond order of three. Another important contribution to the bonding arises from the pseudo-core 6p shell, which is important in determining the linearity of the ions.[9,61]

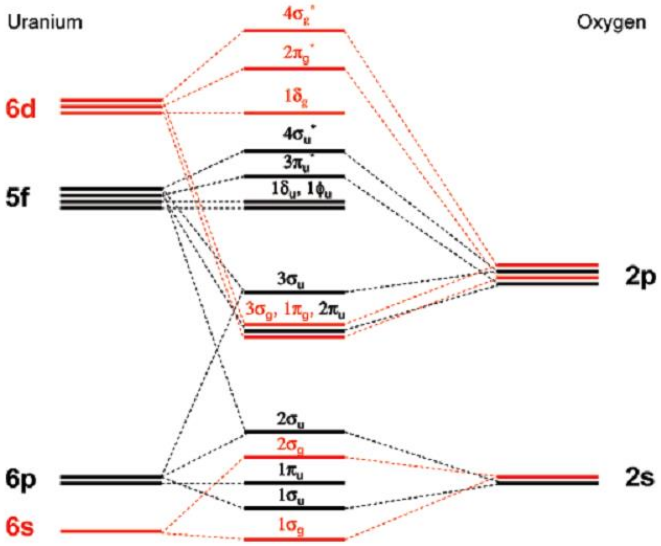

Figure I.4 Schematic energies of actinyl valence orbitals. (Reproduced from Denning R.[61])

Despite the abundant information available on uranyl ions in solution and in the solid state, basic thermochemical data for isolated uranyl ions, unperturbed by the presence of counterions and bulk effects, was still scarce at that time. The first gas-phase synthesis of the bare uranyl ion, UO_2^{2+}, was carried out in 1996 by Cornehl et al.[62] under FT-ICR-MS conditions by ion/molecule reactions of laser-generated of U^{2+} with various oxygen donors as shown in Figure I.5.

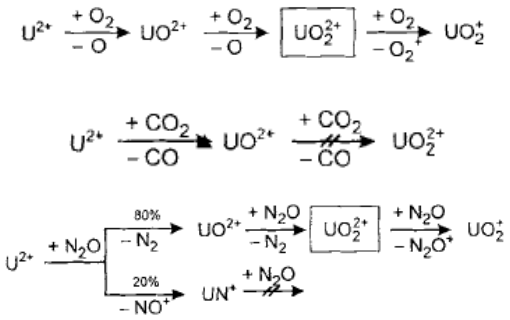

Figure I.5 Gas-phase synthesis of uranyl ion, UO_2^{2+}, by ion/molecule reactions of U^{2+} with 1. Molecular oxygen, 2. Carbon dioxide, 3. Nitrous oxide.

The authors predicted the stability of the bare UO_2^{2+} and the second ionization energy of the dioxide, IE[UO_2^+], based on the exothermicity of oxidation and electron-transfer reactions. They also outlined fundamental important issues regarding the intrinsic stabilities of gas-phase actinyl dipositive ions when compared to the condensed phase where stabilization is affected by interactions with solvent or other coordinating molecules or counterions.[60]

I.2.3 Theoretical studies in actinide gas-phase ion chemistry: concepts and practical applications

This section attempts to give a brief overview of the theoretical and computational basic concepts and developments and the various techniques required to model electronic structure nowadays. Not only was it important for the presented studies (through international collaborations) to complement the experimental observations but also to give a general idea about gas-phase ion chemistry, including specific methods required for modelling heavy atoms that have increased the understanding of the electronic structure and several properties of rare or even apparently "*impossible*" or "exotic" species which sometimes are not accessible experimentally.

Computational chemistry has become a useful way to investigate materials that are too difficult to find or handle (especially in the case of the actinide elements). In some areas, of which gas-phase ion chemistry is most prominent,[63] quantum chemistry can provide results with high accuracy and with the freedom to consider rare species and configurations which are hardly accessible for experimental observation. Quantum chemistry theory is based on the study of practical solutions to the Schrödinger equation. It allows electronic structure determinations, geometry optimizations, frequency calculations, transition structures, electron and charge distributions, potential energy surfaces (PES), rate constants for chemical reactions (kinetics), thermodynamic calculations - enthalpies of reactions, energy of activation, and other key parameters.[30,64]

An important aspect of computational actinide chemistry lies in its ability to complement experimental studies and, in some cases, guide them. The application of modern electronic structure methodologies to actinide systems remains one of the great challenges in quantum chemistry due to their complexity with respect to the calculation of ground- and excited-state energies, bonding descriptions, and molecular properties. The difficulties in creating, isolating, and handling many of the elements provide an opportunity for computational chemistry to be an important partner in developing an understanding of the chemistry of these elements. The significance of computational studies towards a better understanding of actinide chemistry is being recognized, and the relevant studies cover a wide range of issues. A variety of methods are used in electronic structure calculations on actinide molecules. Some of these methods and their historical development are outlined in the review by Pepper and Bursten (1991).[34]

Density Functional Theory (DFT) studies dominated the work in the past ten years, which is not surprising concerning the efficiency and accuracy of DFT methods in predicting the geometry and

energy of the ground state of molecular systems.[64,65] Amongst the variants in the hierarchy of DFT, local density approximation (LDA) is mostly seen in the study of solid state physics, while for molecular systems in gas and condensed phases, generalized gradient approximations (GGA)/hybrid-GGA and meta-GGA are confirmed to be better choices. Specifically, GGA functionals in general are able to give comparable results on geometry with hybrid functionals, while the latter show better performance in describing the thermochemistry of molecular systems, but with a bit more computational cost.[66] Nevertheless, the theoretical study of actinides still remains a challenging task, given the large number of electrons to be included in the calculations, the dense manifold of low-lying states, and the need to include relativistic effects. Because of the large number of electrons which must be correlated, the methods must, at least approximately, be both size-consistent and size-extensive, and the dynamical and non-dynamical electronic correlation must be treated in a balanced way.

Some practical applications

Topics such as the role of the 5f orbitals, geometry and electronic structure (study of the An-O bond in oxo and oxide species, actinide–carbide complexes, metal-metal bonds), chemical reactions (hydration, ligand exchange, disproportionation, oxidation and reduction, among others), and also applications in nuclear energy have been studied extensively by experiment and theory. A few examples are given below.

The uranyl ion and related species

As mentioned before, the U(VI) uranyl ion, UO_2^{2+}, is by far the most studied of the actinyl ions[67-70], and the electronic structure of this isolated species has been the subject of numerous theoretical studies.[71-75] Although relativistic quantum chemical methodology continued to grow from the 1960s through the 1980s, there was still surprisingly little agreement among quantum chemists concerning the 5*f* contributions to and the energetic ordering of the highest occupied orbitals in UO_2^{2+}. The electronic structural origins of the nearly invariably linear geometry of the UO_2^{2+} ion have been the focus of many theoretical studies, especially given that isoelectronic ThO_2 and the analogous transition metal ion MoO_2^{2+} typically exhibit bent geometries. The issue was first addressed on the basis of extended Hückel calculations by Tatsumi and Hoffmann[76] in 1980. The factors include the relative admixture of 5f(σ_u) vs 6d as the ion bends, the role of the filled 'outer core' U 6*p* shell, and the relative contributions of covalent and ionic bonding. RECP calculations at the Hartree–Fock level by Wadt correctly predicted bent ThO_2 and linear UO_2^{2+} but disagreed in the interpretation of the role of U 6p orbitals.[77] Dyall in 1999 carried out Dirac–

Hartree–Fock calculations on ThO_2, PaO_2^+, and UO_2^{2+} and has analyzed in detail the role of the actinide 6*p*, 6*d*, and 5*f* orbitals across the series on the basis of the more sophisticated results.[78] He observed that the energy of the 6d orbitals remain roughly unchanged across this region of the actinide series whereas the 5*f* orbitals drop in energy and becoming more radially contracted. For Th, the 5*f* orbitals lie above the 6d and it is favorable to bend and use *f*–d hybrids in the bonding, while for U the lower energy of the 5*f* orbitals favors linearity. In Figure I.6, the energy of the orbitals as a function of bending is shown. The highest-energy spinor, which corresponds to the σ_u orbital, increases in energy with bending for UO_2^{2+} but decreases for ThO_2.

The synthesis of uranyl analogues, where oxygen is replaced by another main-group element, is an ongoing goal.[79-81] Recently, Pereira *et al* reported a gas-phase study on the reaction of atomic uranium cations, U^+ and U^{2+} with the sulfur-atom donor COS to produce several monopositive and dipositive uranium sulfide species containing up to four sulfur atoms.[82] Sequential abstraction of two sulfur atoms by U^{2+} resulted in the bare gas-phase US_2^{2+} ion. DFT computations indicated that the ground-state structure of US_2^{2+} is a triangular isomer, with the linear thiouranyl structure 171 kJ mol^{-1} higher in energy. The higher energy of the thiouranyl isomer of US_2^{2+} is consistent with the prediction by Denning that the uranyl-type moiety should be limited to the first short period of elements, including carbon, nitrogen, and oxygen.[61]

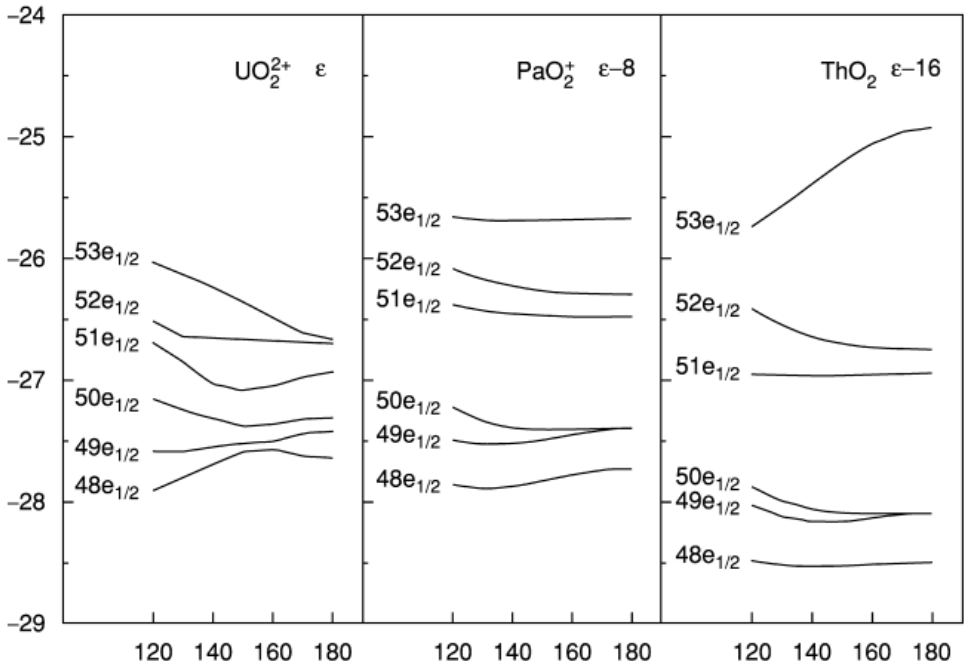

Figure I.6 Valence spinor energies (*eV*) as a function of bending angle (degrees) for ThO_2, PaO_2^+ and UO_2^{2+} from relativistic calculations at M-O = 1.9 Å.[64]

Ionization energies and bonding

In 2010 Infante I. *et al* determined theoretically the first and second ionization energies of actinide monoxides (AnO) and dioxides (AnO_2) for An = Th, Pa, U, Np, Pu, Am, and Cm, by multiconfigurational quantum chemical methods (complete active space (CAS) SCF method followed by multiconfigurational second order perturbation theory (CASPT2); scalar relativistic effects were included using the Douglas-Kroll-Hess Hamiltonian) and compared with available experimental values.[83] The trend along the series was analyzed in terms of the electronic configurations of the various species. Only the *IE* of AnO_2, Th (*IE*1) and Pa (*IE*2) did not fit the trend well. This could be explained in terms of the electronic configurations of the dioxides. The ionization energies and the ground and excited states of neutral and cationic PuO and PuO_2 have also been previously studied with the SO-CASSCF/SO-CASPT2 method and were predicted to be 6.17 eV for PuO, 14.36 eV for PuO^+, 6.20 eV for PuO_2 [84], which are in agreement with the experimental values of 6.1±0.2 eV for PuO,[58,85] 13.7±0.8 eV for PuO^+,[60] and 7.03±0.12 eV [41] or 6.6 eV [86-88] for PuO_2. The ground state of PuO is dominated by two electronic states $^7\Pi$ and $^7\Sigma$, and the former is characterized by two electronic configurations $7s^15f^1{}_\pi5f^2{}_\vartheta5f^2{}_\phi$ and $7s^15f^1{}_\sigma5f^1{}_\vartheta5f^1{}_\pi5f^2{}_\phi$. For the ionization of PuO, first the electron in the 7*s* orbital is lost (giving PuO^+), followed by the loss of the electron in the 5*f* orbital. A refinement of *IE* of PuO_2 has been obtained with the recently developed method for electronic excited states, the multiconfigurational second-order perturbation theory restricted active space (RASPT2) method.[87,89]

The bonding interaction between actinides and chalcogen elements has also been investigated both theoretically and experimentally. As an example, the geometry and electronic structure of the complexes $M[N(EPH_2)_2]_3$ (M = La, U, Pu; E = O, S, Se, Te)[11,90] were calculated by DFT and proved to be consistent with experimental values. The calculated natural charge analysis indicated that the M–E bond becomes less ionic in the order O > S > S > Te, with larger decrease for U and smallest for La. Also, they performed natural and Mulliken overlap populations determinations which suggested an increase in M–E covalency as group 16 is descended, and also in the order La < Pu < U for a given chalcogen. They stated that this increased covalency down group 16 arises from increased metal d (and s) participation in the bonding, while that from La to Pu and U stems from larger 5f orbital involvement compared with 4f.

In summary, the few examples given show the variety of applications in actinide chemistry that has been comprehensively studied in the last decade by experiment and in theory.[66,91] Continued improvements in the theory and implementation will ensure progress, advancing toward the ultimate goal of theory achieving full partnership with experiment as both an explanatory and predictive methodology.

I.3. Mass spectrometry and gas-phase ion chemistry

Mass spectrometry (MS) is the science that studies ions and molecules in the gas phase separating them according to their mass-to-charge ratio (*m/z*). It is an analytical technique that measures with precision the molecular masses of individual compounds and atoms by converting them into charged ions. Due to its very high sensitivity and low detection limits, the analysis of very small sample volumes is possible. Mass spectrometry provides qualitative and quantitative information of an analyte, structure specificity and sensitivity and it allows the study of reaction dynamics and chemistry of ions. In gas-phase ion chemistry, most of the research uses mass spectrometric analysis which enables studying the kinetics of reactions and provides data on physical and thermodynamic parameters such as ionization energy, appearance energy, enthalpy of a reaction, proton and ion affinities, and to verify molecular orbital calculations-based theoretical predictions. Thus, mass spectrometry is a very versatile and comprehensive analytical and physical chemistry technique in use nowadays. Figure I.7 shows a schematic representation of how mass spectrometry in general works from the introduction of the sample to the ion formation and separation until the detection and data processing. Some examples of ionization sources and mass analyzers are given.

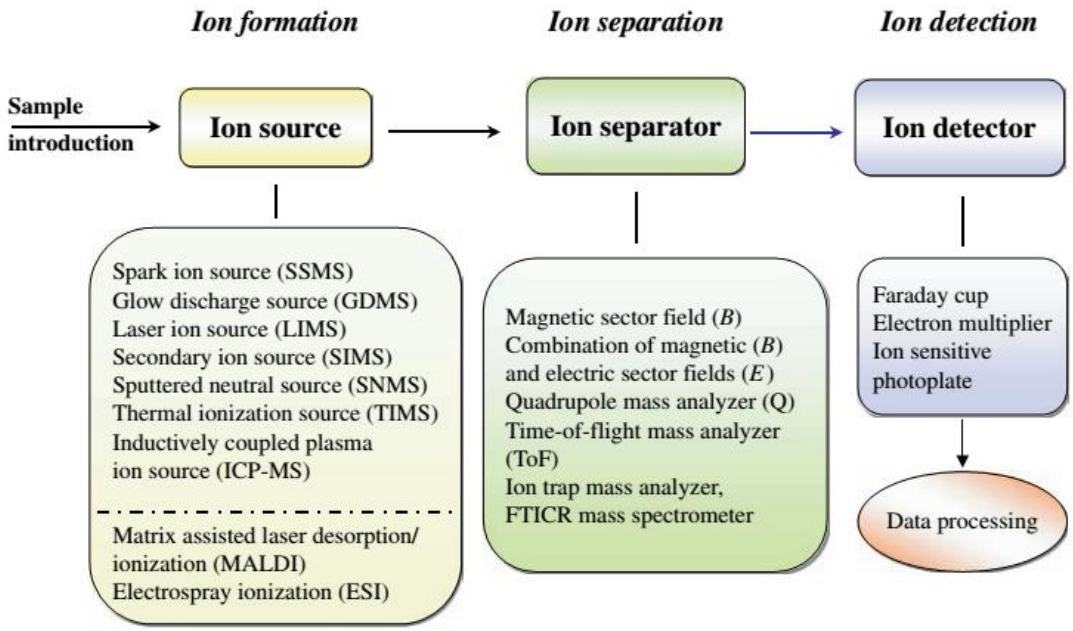

Figure I.7 Basic diagram of mass spectrometry: generation of ions from compounds in sample, introduction into the ion source, separation by their *m/z* ratio and detection.[92]

In the 1960s, mass spectrometry had become a standard analytical tool in the analysis of organic compounds. Its applications to biological fields were practically nonexistent, primarily due to the lack of suitable ionization techniques for sensitive and nonvolatile compounds. Over the last two decades, that situation has changed and several developments in softer modes of ionization have allowed the production of ions from compounds of large molecular mass and compounds of biological relevance. These methods include fast atom bombardment[93] (FAB) in 1981, electrospray ionization[94] (ESI) in 1984–1988, and matrix-assisted laser desorption/ionization[95] (MALDI) in 1988. The last two methods have extended the upper mass range beyond 100 kilodaltons (kDa) and had an enormous impact on the use of mass spectrometry in diverse fields of biology and chemistry. Along with these developments, several innovations in mass analyzer technology, such as the introduction of high field and superfast magnets and improvements in the TOF and Fourier transform ion cyclotron resonance (FT-ICR-MS) analysis concepts, have also improved the sensitivity and upper mass range amenable to mass spectrometry. Moreover, new atmospheric pressure sources[96-99] were developed, existing analyzers were improved and new hybrid instruments were realized by new combinations of analyzers. The current decade has seen the introduction of two new types of ion traps, the quadrupole linear ion trap (LIT) and the orbitrap (OT), for mass spectrometric analysis.

In this thesis, the gas-phase ion chemistry of *f*-elements was studied with the use of two types of ion sources and two types of mass analyzers: Electrospray Ionization (ESI) and Laser Desorption Ionization (LDI), and Quadrupole Ion Trap (QIT) and Fourier Transform Ion Cyclotron Resonance (FT-ICR), described in section 3.1 and section 3.2, respectively.

I.3.1 Ionization sources

In mass spectrometry, one of the most important and crucial steps is the ionization of the analyte of any class of compounds. A successful mass spectrometric experiment essentially depends on the approach used to convert neutral compounds into gas-phase ionic species. The ion source is an essential component of all mass spectrometers where the ionization of a gaseous, liquid or solid sample takes place. In inorganic mass spectrometry, several ion sources, based on different evaporation and ionization processes have been employed for a variety of different application fields. Several ionization techniques have become available over the years, but none has universal appeal. An example of different types of ionizations, atomic and molecular, is represented in Table I.4. The choice of a particular method depends essentially on the nature of the sample and type

of information wanted. Some methods require sample molecules to be present in the ion source as gas-phase species, whereas others can accommodate condensed-phase samples.

Table I.3 Modes of ionization.[100]

	Molecular Ionization		
Atomic Ionization	Sample Phase	Mode	Pressure[a]
Thermal ionization	Gas phase	Electron ionization	HV
Spark source		Chemical ionization (CI)	IV
Glow discharge		Photoionization (PI)	HV
Inductively coupled plasma		Field ionization	HV
Resonance ionization		Metastable atom bombardment	HV
	Solution phase	Thermospray	LV
		Atmospheric-pressure CI	AP
		Atmospheric-pressure PI	AP
		Electrospray	AP
	Solid phase	Plasma desorption	HV
		Field desorption	HV
		Secondary-ion MS	HV
		Fast atom bombardment	HV
		Matrix-assisted laser desorption	HV

[a] HV, high vacuum; IV, intermediate vacuum; LV, low vacuum; AP, atmospheric pressure.

In the ion sources, the analyzed samples are ionized prior to analysis in the mass spectrometer. The ions are produced mainly by ionization of a neutral molecule in the gas phase through electron ejection, electron capture, protonation, deprotonation, adduct formation or by the transfer of a charged species from a condensed phase to the gas phase. Ion production often requires gas-phase ion/molecule reactions. The main processes in the ion source of a mass spectrometer are the evaporation of solid samples or desolvation and vaporization of liquids, atomization of gaseous compounds and ionization of atoms and molecules. The internal energy transferred during the ionization process and the physico-chemical properties of the analyte that can be ionized are also important considerations.

In all types of ion sources, during the ionization process singly- and multiply-charged atomic ions, as well as polyatomic or cluster ions, with different ion intensities are formed. Some ionization techniques are very energetic and cause extensive fragmentation while others are softer and only produce ions of the molecular species. Electron ionization (EI), chemical ionization (CI) and field ionization (FI) are only suitable for gas-phase ionization and thus their use is limited to compounds sufficiently volatile and thermally stable. However, a large number of compounds are thermally labile or do not have sufficient vapor pressure. Molecules of these compounds must be directly extracted from the condensed to the gas phase. These direct ion sources fall under two types: liquid-phase ion sources and solid-state ion sources. In liquid-phase ion sources like electrospray

(ESI), atmospheric pressure chemical ionization (APCI) and atmospheric pressure photoionization (API) sources, the analyte is in solution. The solution is introduced, by nebulization, as droplets into the source where ions are produced at atmospheric pressure and focused into the mass spectrometer through vacuum pumping stages. In solid-state ion sources, the analyte is in a non-volatile deposit. It is obtained by various preparation methods which frequently involve the introduction of a matrix that can be either a solid or a viscous fluid. This deposit is then irradiated by energetic particles or photons that desorb ions near the surface of the deposit. These ions can be extracted by an electric field and focused towards the analyzer. Matrix-assisted laser desorption (MALDI), secondary ion mass spectrometry (SIMS), plasma desorption and field desorption sources all use this strategy to produce ions. Fast atom bombardment (FAB) uses a non-volatile liquid matrix.

I.3.1.1 Electrospray ionization

The first electrospray ionization experiments were carried out by Malcolm Dole and his co-workers in the late 1960s.[92,101] The authors discovered the phenomenon of the generation of multiply charged molecule ions during electrospray ionization and successfully introduced a polystyrene polymer (average MW = 51,000 Da) into the gas phase as a charged species.[102] Dole used a very dilute solution of the analyte and then nebulized it into extremely small droplets, to obtain many droplets that contained only one analyte molecule. Evaporation of the droplets led to a transfer of the analyte molecules into the gas phase. Subsequent work by Fenn and co-workers[94,103] confirmed and continued Dole's approach by demonstrating that ESI-MS could be used very effectively for analysis of peptides and proteins with molecular mass *m* which could be much higher than *m/z* 1500 daltons.[104] Fenn was latter on recognized for his contributions by the award of the 2002 Nobel Prize for Chemistry.[105] This soft ionization technique in combination with mass spectrometry is today used as one of the commonly employed soft ionization techniques for the investigation of large biomolecules and many other analytes.[92] The remarkable growth in popularity of this technique is representative of its powerful abilities to investigate species in solution even in very low concentrations and in complex mixtures.[106]

The electrospray is a process which involves the creation of a fine aerosol of highly charged micro droplets in a strong electric field. The sample is passed through a highly charged capillary with a voltage, V_c, typically in the range of 2-5 kV in which the solution is distorted into a

Taylor cone*, producing a fine spray of highly charged droplets that evaporate due to the presence of the electric field with the aid of a stream of nitrogen, a process called nebulization. Because the spray capillary tip is very thin, the electric field E_c at the capillary tip is very high ($E_c \approx 100$ V/m).

The value of the field at the capillary tip can be estimated with the approximate relationship:

$$E_c = \frac{2V_c}{r_c \ln(\frac{4d}{r_c})} \quad (1.1)$$

where V_c is the applied potential, r_c the capillary outer radius, and d the distance from the capillary tip to the planar counter electrode.

The imposed field, E_c, will also partially penetrate the liquid at the capillary tip. When the capillary is the positive electrode (positive ion mode) some positive ions will drift toward the liquid surface and some negative ions will drift away from it until the imposed field inside the liquid is removed by charge redistribution. The accumulated positive charge at the surface leads to its destabilization since the positive ions are drawn down-field but cannot escape from the liquid. The surface is then drawn down-field in such a way that a liquid cone is formed.

Under these conditions, the droplets break down and, while moving inside the source, their size is continuously being reduced. The charge density on the shrinking droplets builds up until surface tension is balanced by the Coulombic repulsion. This process is called the Rayleigh limit,[108,109] and the number, z_R, of elementary charges e is given by

$$z_R = \frac{8\pi}{e}\sqrt{\varepsilon_0 \gamma R^3} \quad (1.2)$$

where R is the droplet radius, ε_0 is the vacuum permittivity, and γ is the surface tension. Droplets at the Rayleigh limit produce even smaller and highly charged offspring droplets via jet fission. Repeated evaporation/fission events ultimately yield the final generation of ESI droplets with radii of a few nanometers. Gaseous analyte ions that are detected by MS are produced from these highly charged nanodroplets.[105,110-112]

* The Taylor cone was named after Sir Geofrey Ingram Taylor in 1964 before the appearance of the electrospray technique. He was one of the first to investigate the conditions under which a stable liquid cone can be observed in spray processes from which a jet of charged particles emanates above a threshold voltage.[107]

There are two possible mechanisms for the production of gas-phase ions in electrospray: the charge residue model (CRM) proposed by Dole et al.[101] and the ion evaporation model (IEM) proposed by Iribarne and Thomson who worked with small ionic analytes such as Na^+ and Cl^- (Figure I.8).[113,114] The IEM typically prevails for relatively small ions (m/z < 3300)[115,116] whereas the CRM is more applicable for larger large globular species such as natively folded proteins.[117]

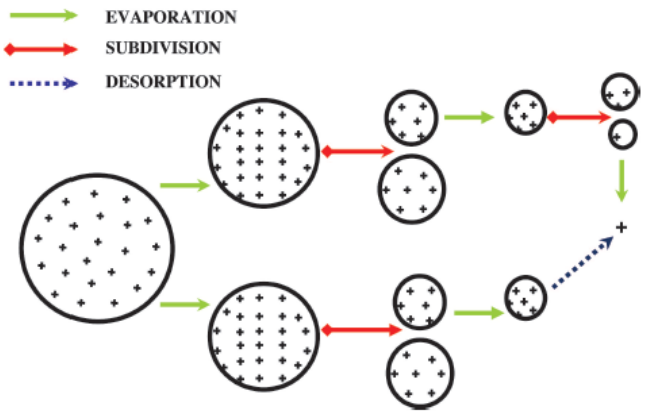

Figure I.8 A schematic representation of the possible pathways for ion formation from a charged liquid droplet. The upper and the lower parts of the diagram illustrate the ion formation mechanisms depicted in the CRM of Dole *et al.* and the IEM of Iribarne and Thomson, respectively. (Adapted from Fenn B.[112])

Dole's idea[†] of how solute ions are formed was that the offspring droplets resulting from a first Rayleigh Instability would continue to evaporate solvent so that they too would undergo a Rayleigh Instability and disrupt. If the original solution was sufficiently dilute, a sequence of such evaporation–disruption episodes would ultimately produce droplets so small that each would contain only one solute molecule. As the last of the solvent evaporated from the ultimate droplet the remaining solute molecules would retain some of the droplet charge and thus become a free gas-phase ion. This process is known as the charged residue model (CRM) for ES ion formation. CRM comes from the observation that ESI of globular proteins produces ions with a composition close to $[M + z_R\ H]^{zR+}$, where z_R is the Rayleigh charge of protein-sized water droplets. The IEM later proposed by Iribarne and Thomson is based on the fact that the electric field emanating from a Rayleigh-charged nanodroplet (with R < 10 nm) is sufficiently high to cause the ejection of small solvated ions from the droplet surface.[105,109,118]

The experimental results involved measurements of the relative abundance of the ions produced by ESI of solutions containing NaCl as the only solute. The authors found that there was a large

[†] "*I got this idea from learning about the electrospraying of paint on to automobile bodies while working as a consultant for a paint company in Chicago"* – Dole M.

number of ion aggregates of the type $[(NaCl)_n(Na)_m]^{m+}$ the abundance of which decreased rapidly as *n* decreases. However, the lowest mass ion in that series, Na^+ (*n* = 0 and *m* = 1), and the hydrated species $Na(H_2O)^{k+}$ (*k* = 1-3) had the highest abundances.[113,114] This observation led the authors to conclude that while large aggregate ions are probably due to a charged residue mechanism (CRM) type process, the abundant Na^+ and Na^+ hydrates must be formed through a different mechanism where sodium ions escape directly from the droplet's surface.[110] The applicability of one of the two theories to account for the generation of gas phase ions is yet not well established and at which stage it takes place, considering the size and the charge of the droplets.

The electrospray ion source is at very high pressure (atmospheric) with respect to the very low pressure that is required for ion separation by a mass analyzer, so the interface between the two involve a series of skimmer cones (acting as small orifices) between the various differentially pumped regions (Figure I.9). The ions are drawn into the spectrometer proper through the skimmer cones. A voltage can be applied (the cone voltage), which will accelerate the ions relative to the neutral gas molecules. This leads to energetic ion/neutral collisions and fragmentation due to what is termed collision induced dissociation (CID). The remaining bath gas is pumped away in stages (in order to attain the high vacuum necessary for separation of the ions) and the ions are focused through a lensing system into the mass analyzer.[106]

Because ESI-MS is a very sensitive method, very low concentrations, 10^{-7} to 10^{-3} mol/L (M), of analyte can be used. Although methanol, acetonitrile or mixtures of acetonitrile-water and methanol-water are often used as solvents, other solvents such as toluene (that have a very low solubility for electrolytes) can also be used.

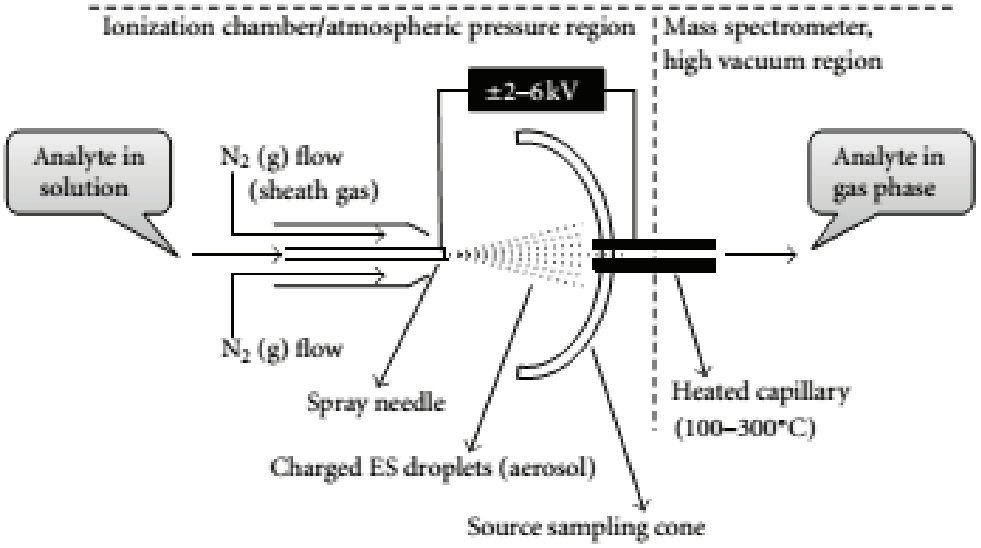

Figure I.9 A schematic representation of the ESI-ion source.[106]

I.3.1.2. Laser desorption ionization/Laser ablation

Lasers in general are used in mass spectrometry for sample volatilization by laser desorption and sample ionization, atomization, and excitation. Any samples with known light absorptivity can be analyzed by laser ablation (LA) and ionization to provide elemental information. They are suitable for the production of intact gas-phase species from non-volatile, polar, high molecular weight, and thermally labile substances. The technique of laser sampling has many advantages, e.g. little sample size requirement and little or no sample preparation, low risk of reagent or solution waste, the avoidable introduction of contamination, and high spatial (lateral and in-depth) resolution. The power density deposited on the spot area can easily be controlled by adjustment of laser parameters (e.g., pulse duration, wavelength and energy) in comparison with other ionization sources. In combination with the proper detection system, it is an attractive technique for the elemental composition analysis of various samples through various spectroscopic methods. Some disadvantages of direct laser desorption ionization are a strong matrix effect, and the inability for the operator to control the sample volatilization and ionization processes independently. In 1988, Karas and Hillenkamp developed the Matrix-Assisted Laser Desorption Ionization method for the production of parent ions from large and very large non-volatile molecules.[95] This method was originally developed from LDI with the idea to add to the analyte a chemical matrix that strongly absorbs the wavelength of the desorption laser and promote efficient desorption of the fragile analyte molecules. MALDI has become a very successful method for soft ionization and is widely used for obtaining large ions in the gas phase such as biomolecules (DNA, proteins, peptides, sugars) and large organic molecules (polymers, dendrimers) which tend to be fragile and fragment when ionized by more conventional ionization methods.

Laser desorption (LD) and laser ablation are two laser–matter interaction regimes to be considered. LD results in emission of ions, atoms, and molecules without any substantial disturbance in the surrounding surface. LA implies a large scale disruption of surface and near-surface geometrical and electronic structure. LD and LA have to be viewed as the extremes of a continuum, which ranges from the emission of isolated neutrals or ions in the case of LD to the massive removal of material resulting from the collective effects of multiple photons irradiating the same spatial locale in the case of LA.

LA relies on the formation of a plume of ejected species, which follows the laws of plasma and gas dynamics, and produces a large number of ionized species. Collisions of ions with neutrals occurring in the gas-phase plume after LA lead to ion/molecule condensation reactions. On the

other hand, ions and neutrals possess a significant amount of energy, which can result in dissociation reactions. Laser desorption ionization (LDI) and LA experiments are generally conducted on the same instruments since in both cases, ions are generated by laser irradiation of the sample surface. In LA experiments, the amounts of matter expelled from the surface are definitely greater than are observed under LDI conditions. Usually, LA refers to removing material with a pulsed laser, but it is possible to ablate material with a continuous wave laser beam if the laser intensity is high enough. LA is used in a widespread range of applications, including as a sampling procedure for the elementary chemical analysis of materials. Many analytical techniques makes use of LA such as LA Ion Mobility Spectrometry, Resonant LA, LA-Atomic Fluorescence Spectrometry and LA-Microwave Induced Plasma-Atomic Emission Spectrometry; among them the most popular ones are probably the LA Inductively Coupled Plasma (LA-ICP) techniques and the Laser Induced Breakdown Spectroscopy (LIBS).

LDI is more commonly used for the analysis of inorganic non-volatile solid materials.[119-121] The technique uses one single laser source (pulsed or CW) to perform desorption and ionization in a single step. A laser beam is focused directly on the solid sample usually deposited on a direct inlet probe. LDIMS was first used as an analogous technique to other methods for direct ion production such as Secondary Ion Mass Spectrometry (SIMS), Fast Atom Bombardment (FAB), or Plasma Desorption Mass Spectrometry (PDMS). In 1978, the group of Kistemaker published impressive LDIMS data of complex organic and bio-organic thermally labile substances such as sucrose (*m/z*= 342) and digitonin (*m/z* = 1228), setting a high mass record at this time with the latter substance.[122] LDIMS has been widely used with a variety of lasers (pulsed and CW CO_2 lasers, pulsed ruby, Nd glass, Nd:YAG, and N_2 lasers), and with quadrupole, time-of-flight (TOF), FT-ICR and sector mass analyzers. Mass range and mass resolution of LDIMS instruments are essentially determined by the type of mass analyzer used.[123] The sensitivity is given by the product of the ionization efficiency and the instrument throughput. At very high laser power densities, the ionization efficiency can approach 100%, but this condition also causes extensive analyte fragmentation, broad ion energy distributions, and the presence of multiply charged species. For inorganic analysis using LDI/LA-FT-ICR, the ionization step is usually performed using a Nd-YAG laser. The diameter of the laser beam on the sample can be adjusted by means of the internal lens and an external adjustable telescope from 5 to several hundred micrometers, which corresponds to a power density ranging from 10^6 to $4x10^{10}$ $W.cm^{-2}$. An example of the experimental sequence used for these analyses is as follows:[124]

- Ions are formed by laser ablation in the source cell. During the ionization event, the conductance limit plate between the two cells and the source trap plate is fixed at a

trapping potential (of typically 2 V or at a lower potential in some particular cases, down to 0.25 V).

- A variable delay period follows, typically close to 1 min, during which ion/molecule reactions can occur.
- Ions are then excited by a frequency excitation chirp and the resulting image current is detected, amplified, digitized, apodized and Fourier-transformed to produce a mass spectrum.

For practical applications, sensitivities in the pmol/cm^2 range have been reported for organic LDIMS.[125] Also, laser microprobe FT-ICR-MS, developed by Carre et al[124] has led to several further experiments in gas-phase ion chemistry. As an example, LA-FT-ICR-MS of UO_3 or $(NH_4)_2U_2O_7$ allowed the formation of gas-phase molecular uranium oxide anions with compositions ranging from $[UO_n]^-$, with n =2-4, to $[U_{14}O_n]^-$, with n=32-35 by using a Nd:YAG laser (1064 nm) with an average focused power density of ca. 200 MW cm^{-2}. Single or multiple pulses on the same or on fresh spots yielded similar results.[126] Also, several negatively charged metal chalcogenide clusters, namely, sulfides[127,128] and oxides,[129-133] have been also generated by LDI/LA and studied by FT-ICR-MS. Furthermore, uranyl analogues, $IrUO^+$, have too been prepared by direct LDI of a U/Ir alloy, and by oxidation of UIr^+ with N_2O and C_2H_4O. Properties of the formed bimetallic ions have been studied and they demonstrate direct actinide–transition metal bonding, and support the concept of "autogenic isolobality".[134]

I.3.2 Mass analyzers

Since the early twentieth century, when mass spectrometry was being established, many methods have been applied to the sorting of gas-phase ions according to their *m/z*.[106,135] A mass analyzer is a key component of the mass spectrometer. Each mass analyzer has its own special characteristics and applications and its own benefits and limitations (Table I.4). The separation of ions according to their *m/z* can be based on different principles. All mass analyzers use static or dynamic electric and magnetic fields that can be applied alone or in a combined way. Most of the basic differences between the various common types of mass analyzer are in the method in which such fields are used to achieve separation. Up to now, there are several types of mass analyzers that can be used for the separation of ions in mass spectrometry: time-of-flight (TOF), sector, quadrupole (Q), quadrupole ion traps (QIT), Fourier transform ion cyclotron resonance (FT-ICR) and the most recent mass analyzer, orbitrap (OT).

Table I.4 Types of analyzers used in mass spectrometry.[136]

Type of analyzer	Symbol	Principle of separation
Electric sector	E or ESA	Kinetic energy
Magnetic sector	B	Momentum
Quadrupole	Q	*m/z* (trajectory stability)
Ion trap	IT	*m/z* (resonance frequency)
Time-of-flight	TOF	Velocity (flight time)
Fourier transform ion cyclotron resonance	FT-ICR	*m/z* (resonance frequency)
Fourier transform orbitrap	FT-OT	*m/z* (resonance frequency)

TOF analyzers separate ions by time without the use of an electric field. The ions are accelerated and thus, separated according to their kinetic energy and velocity. Lower mass ions will obtain a greater velocity than higher mass ions and will pass through the drift region in a shorter amount of time than heavier ions, resulting in the separation of ions according to their *m/z*. As the length of the drift region is known, ion velocities can be determined by measuring the time they take to reach the detector. TOF has allowed ionization methods other than MALDI, most notably electrospray ionization, to benefit from the strong performance characteristics of TOF mass analysis. These types of mass analyzers have higher levels of abundance sensitivity when compared to ion trapping devices. Of particular importance is the mass range of TOF mass analyzers. Mass ranges of 2000 kDa have been demonstrated in a cryodetection MALDI-TOF instrument[137], and in practice, mass ranges of > 70000 can be readily achieved using commercial instrumentation. In combination, these performance characteristics make TOF mass analysis an attractive option for many polymer studies.

In the magnetic and electrostatic sector analyzers there is a magnetic/electric field involved the ion separation. In the sector analyzers, ions leaving the ion source are accelerated to a high velocity. As moving charges enter a magnetic field, the ion is deflected to a circular motion of a unique radius in a direction perpendicular to the applied magnetic field. Ions experience two equal forces: magnetic and centripetal force. Electrostatic sector analyzer disperse ions according to their kinetic energy-to-charge ratios, while also providing the same type of direction focusing as magnetic sectors (Figure I.10 A and I.10 B).

Quadrupoles and quadrupole ion traps use an electric field for the separation of the ions according to their *m/z*. FTICR is an ion trap that uses a high magnetic field and the ions have a cyclotron motion and the frequency of this motion can be related to their *m/z* (Figure I.10 C). The resultant time-domain signals of ion motion are converted into frequency domain signals via a Fourier transform, which leads to the generation of a mass spectrum. Due to the very low pressure which

is possible to achieve within the FT-ICR cell, the cyclotron motion can be held for many cycles, reducing the uncertainty of the frequency measurements and thereby allowing *m/z* to be determined with great accuracy.[135]

Orbitraps were first described in the year 2000 by Makarov.[138,139] They represent the most recently developed form of mass analyzer in usage. Orbitraps are a new type of mass analyzer which performs their trapping functions in the absence of magnetic or radiofrequency (RF) fields and instead uses an electrostatic field. The potential distribution of the field is a combination of quadrupole and logarithmic potentials. In the absence of any magnetic or RF fields, ion stability is achieved only due to ions orbiting around an axial electrode (Figure I.10 D).

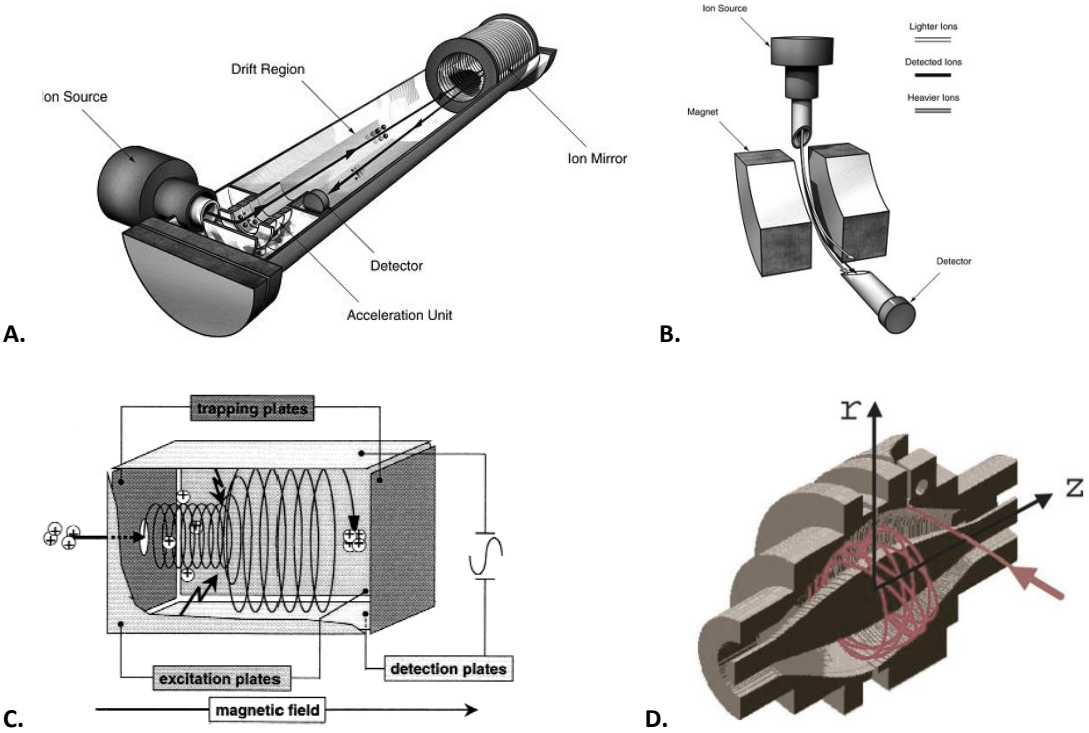

Figure I.10 A. Basic components of a TOF mass analysis system featuring an ion mirror, and the means by which it achieves *m/z*-based ion separation. **B.** Basic components of a magnetic sector mass analyzer system.[135] ; **C.** Scheme of a FT-ICR analyzer cell. The cyclotron motion and the excitation process is shown schematically.[140] **D.** Orbitrap mass analyzer: ions are injected into the Orbitrap at the point indicated by the red arrow. The ions are injected with a velocity perpendicular to the long axis of the Orbitrap (the z-axis).[141]

Below in this section the basic operating principles of Quadrupole Ion Traps and Fourier Transform Ion Cyclotron Resonance and their performance characteristics will be described in more detail.

I.3.2.1 Quadrupole ion trap

In the 1950s, Wolfgang Paul and coworkers[142,143] introduced the quadrupole ion trap analyzer in order to trap ions in a 3D quadrupole radio frequency electric field, a discovery for which in 1989 Paul was awarded a Nobel Prize for Physics. The basic theory of operation of quadrupole devices was enunciated almost 100 years before the QIT was invented by Paul and Steinwedel.[144] The QIT is a device which functions both as ion storage and as a mass spectrometer of a considerable mass range and variable mass resolution at a pressure of approximately 1 *m*Torr of helium buffer gas. As storage device, in which gaseous ions can be confined for a period of time, the ion trap acts as an electric field test-tube for the confinement of gaseous ions, either positively or negatively charged, in the absence of solvent. The confinement of gaseous ions in such a system allows the study of gas-phase ion chemistry and the elucidation of ion structures by the use of repeated stages of mass selection known as tandem mass spectrometry. With the introduction of new methods by which ions can be formed in the gas phase, the range of applications of the quadrupole ion trap became very wide. [145]

Brief overview of the QIT structure and working principle

The QIT itself consists essentially of three shaped electrodes. Two of the three electrodes are nearly identical and have a hyperboloidal geometry. They resemble small inverted saucers which are called end-cap electrodes. One end-cap electrode has a single small central hole through which ions can be gated periodically and the other has several small holes also centrally arranged and through which ions pass to a detector. The third electrode is also of hyperboloidal geometry and is called the ring electrode which is positioned symmetrically between the two end-cap electrodes. The geometries of the electrodes are defined so as to produce an ideal quadrupole potential distribution that will produce the necessary trapping field for the confinement of ions. A schematic representation of the 3D quadrupole model is shown in Figure I.11.[106,144,145]

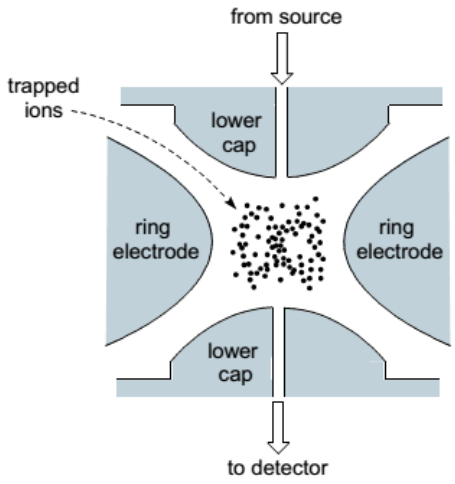

Figure I.11 Schematic representation of a quadrupole ion trap. (Reproduced from Henderson, W. and McIndoe, J. S.)[106]

The working principle of the quadrupole ion trap is based on creating stable trajectories for ions of a certain *m/z* or *m/z* range while removing unwanted ions by colliding them with the walls, or by axial ejection from the trap due to their unstable trajectories. Ions enter the source through the end cap, and by applying a combination of voltages to the ring and capping electrodes, the ions can be trapped in a complex three-dimensional orbit. The stability of the oscillating ions in the trap is determined by *m/z*, the RF (radio frequency) and voltage supplied to the ring electrode. By changing the frequency of the RF generator, which excites the ion oscillation in the ion trap, ions with different masses are destabilized step by step. They then leave the ion trap and are detected. The mass spectrum of the ions ejected from the ion trap (and separated according to their *m/z*) is obtained by scanning the RF voltage. Another procedure for ejecting ions from the ion trap is known as the mass selective instability mode whereby a second rf voltage (lower in frequency than that of the ring electrode) is supplied to the end caps. When the rf voltage is scanned on the ring electrode, causing mass selective instability, ions are sequentially brought into resonance with the rf of the end caps. This behavior results in an increase in translation energy of the trapped ions with defined *m/z* and the ions are ejected from the ion trap in a well-defined manner.[146] Cooks et al. reported developments in new geometries of quadrupole ion traps and trap arrays[147] including various linear and rectilinear ion traps, the simplest form being a rectilinear ion trap geometry made from four flat electrodes.[106] In spite of the significant reduction in instrumental size, in comparison to quadrupole, sector field and Fourier transform mass spectrometers, ion trap mass analyzers also permit mass spectrometric measurements of large organic compounds such as proteins and biomolecules (with masses ~100 000 Da) at high mass resolution and low detection limit. In addition, using a suitable collision gas in the ion trap, the

isobaric interference problems in mass spectrometry can be solved by collision induced dissociation. The possibilities of applying ion traps are limited by restricted quantification possibilities and low dynamic range. Over the last few decades, QIT mass analyzers together with soft ionization techniques, such as electrospray ionization or MALDI, have developed into a sensitive and versatile analytical tool for identifying different types of molecules, especially for biomolecular analysis.

I.3.2.2 Fourier transform ion cyclotron resonance

The ion cyclotron resonance (ICR) theory was developed in 1932 by Ernest O. Lawrence (Nobel Prize in Physics in 1951) and Stanley M. Livingston.[148,149] In 1951 the principle of ion cyclotron resonance was first incorporated into a mass spectrometer, called the omegatron, by Sommer and co-workers, who successfully applied the concept of cyclotron resonance to determine the charge-to-mass ratio of the proton.[150-153] Since then, FT-ICR-MS has had tremendous growth for the analysis of a wide variety of compounds.

The FT-ICR mass spectrometer has four key components: a superconducting magnet with a strong magnetic field that can vary from 3 T to 20 T, the analyzer cell or ICR cell placed in the center of the strong magnetic field where the ions are stored, analyzed and detected, an ultra-high vacuum system and a sophisticated data system. The analyzer cell can take on different geometries but generally consists of a front and back trapping electrode, two opposite excitation electrodes and two opposite detection electrodes, as indicated in Figure I.12.
The analyzer cell is a low pressure (10^{-10} mbar) Penning trap[‡] in which ions can be stored for extended periods of time. The timescale of the experiment is one of the first distinctions of FT-ICR-MS, and is extensively used to study ion/molecule reactions, conformational changes in molecules, the dissociation of very large molecules with a large number of degrees of freedom, and many more processes that require both gas-phase ions and relatively long time to complete.[154]

[‡] The Penning Trap was named after F. M. Penning by Hans Georg Dehmelt who was awarded with the Nobel Prize in Physics in 1989 for developing the first trap.

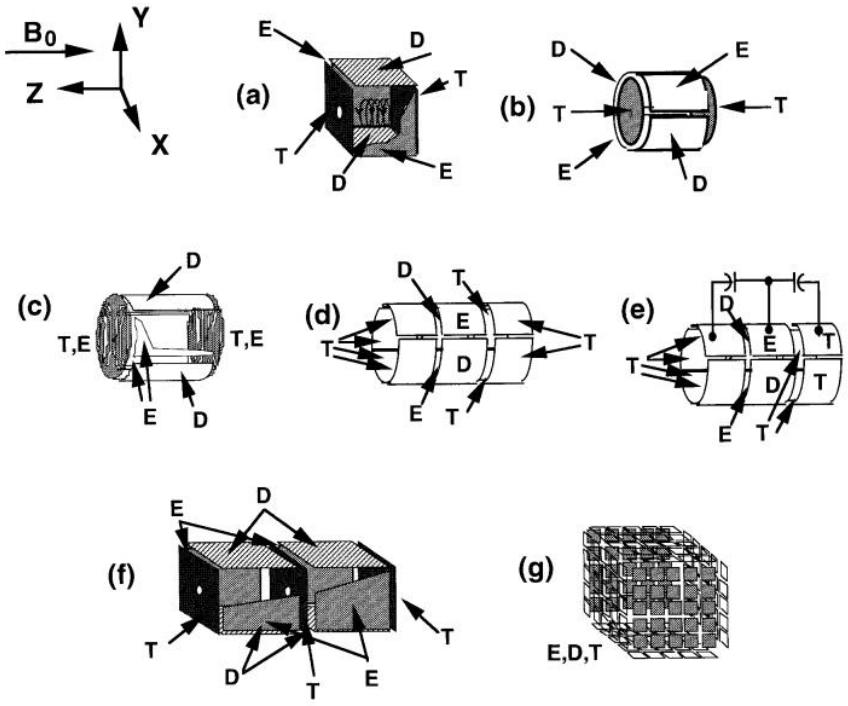

Figure I.12 ICR ion trap configurations. E=excitation; D=detection; T=end cap ("trapping"). (a) cubic; (b) cylindrical; (c) end caps segmented to linearize excitation potential ("infinity" trap); (d) and (e) open-ended; (f) dual; and (g) "matrix-shimmed".[155]

Fundamental aspects of FT-ICR are summarized below:[154,155]

- Ion cyclotron frequency, radius, velocity and energy, as a function of ion mass, ion charge and magnetic field strength, follow directly from the motion of an ion in a spatially uniform static magnetic field (eq. 1.3).

$$Force = mass\ x\ aceleration = m\frac{dv}{dt} = q\boldsymbol{v}\ x\ \boldsymbol{B} \quad (1.3)$$

  in which *m*, *q*, and *v* are ionic mass, charge, and velocity, and the vector cross product term means that the direction of the magnetic component of the Lorentz force is perpendicular to the plane determined by *v* and *B*.

- If the ion maintains constant speed (i.e. no collisions), then the magnetic field bends the ion path into a circle of radius *r*, the cyclotron motion (Figure I.13).

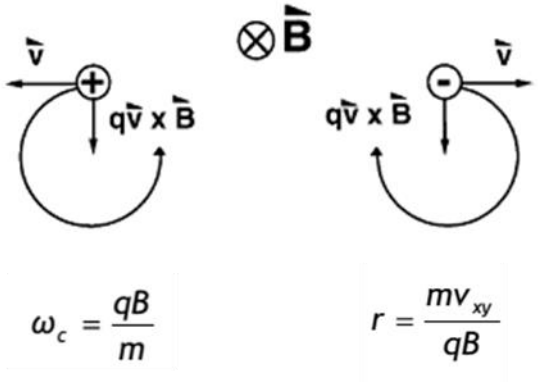

Figure I.13 Ion cyclotron motion; ω_c is the angular cyclotron frequency, and r is the ion cyclotron radius. (Adapted from Reference 155).

- Ion cyclotron motion becomes coherent by the application of a spatially uniform RF electric field (excitation) at the same frequency as the ion cyclotron frequency. The ICR signal results from induction of an oscillating "image" charge on two conductive infinitely extended opposed parallel electrodes. A frequency-domain spectrum is obtained by Fourier transformation of the digitized ICR signal (Figure I.14).

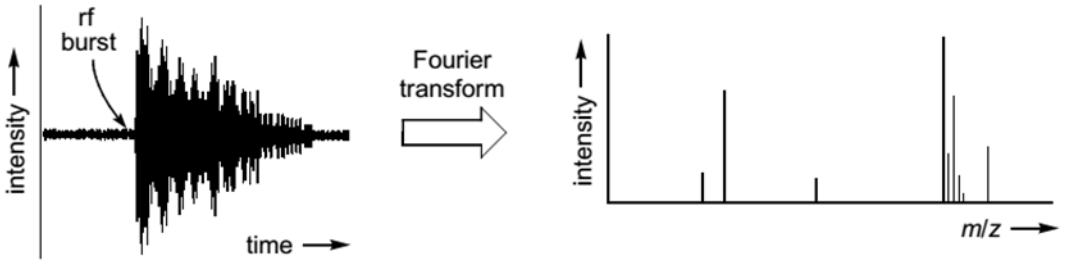

Figure I.14 An rf burst accelerates the ions, generating a transient ion image current signal (left). The signal is digitalized, stored in the computer and a Fourier transform is applied to the data to convert the information into a mass spectrum (right).[106]

- Confinement of ions by application of a three-dimensional axial quadrupolar dc electric field shifts the ion cyclotron frequency, whereas excitation and detection remain essentially linear, but with a reduced proportionality constant (Figure I.15).

- Collisions broaden the ICR signal in a simple way, and actually make it possible to cool and compress an ion packet for improved detection.

- Although FT-ICR-MS has been coupled to many types of ion sources, most ion sources work best outside the magnet. Thus, several methods have been developed to guide the externally generated ions into the ion trap inside a high-field magnet.

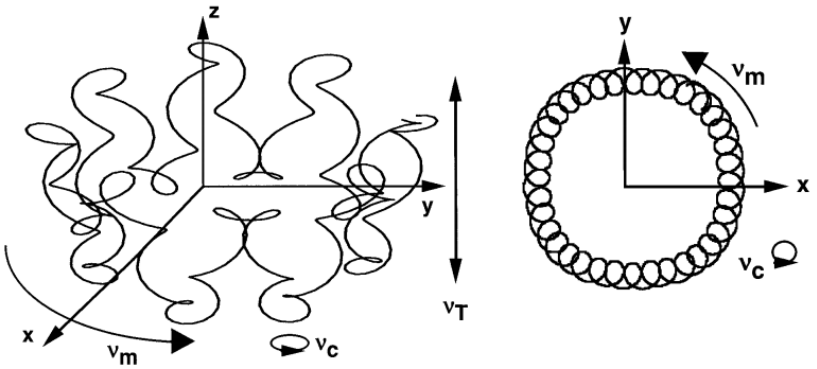

Figure I.15 Schematic representation of the three natural motions of an ion confined in an ICR cell (m-magnetron rotation; c-cyclotron rotation; T-trapping oscillation).[155]

- The above features may be combined in various experimental "event sequences" to perform tandem-in-time mass spectrometry (MS/MS or MS^n). In most regular mass spectrometers, after ion formation the ions are accelerated forming a focused beam and selected according to their *m/z* after passing through distinct fields, electric or magnetic. The ion/molecule collisions take place in a separated division and the ultimate stage is ion detection. In the FT-ICR-MS, all experimental steps occur in the same space, the ICR cell. An FT-ICR mass spectrometer combines high resolution, high mass-accuracy, non-destructive multichannel detection, long ion-observation times, the possibility of performing gas-phase reactions on trapped ions, and, perhaps most importantly, tools for structural analysis of large biomolecules.

The FT-ICR-MS is a complete ion laboratory by itself.[154] The nature of an FT-ICR-MS experiment implies that the different analytical steps are separated in time. A typical sequence of events for a tandem mass FT-ICR-MS experiment is shown in Figure I.16. A usual ICR experiment consists of four time-spread events: quenching, ion formation/injection, excitation, and detection. All of these functions are performed in the ICR cell, which consists of three pairs of opposing plates; each pair performs a distinct function: trapping, excitation, or detection of ions (Figure I.17). The total duration of a tandem FT-ICR-MS experiment in which no collision gas is used is approximately 1 s.[154]

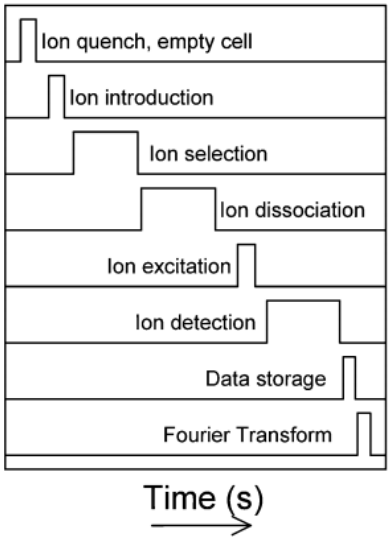

Figure I.16 FT-ICR-MS sequence showing the order of the different time-separated process steps.[154]

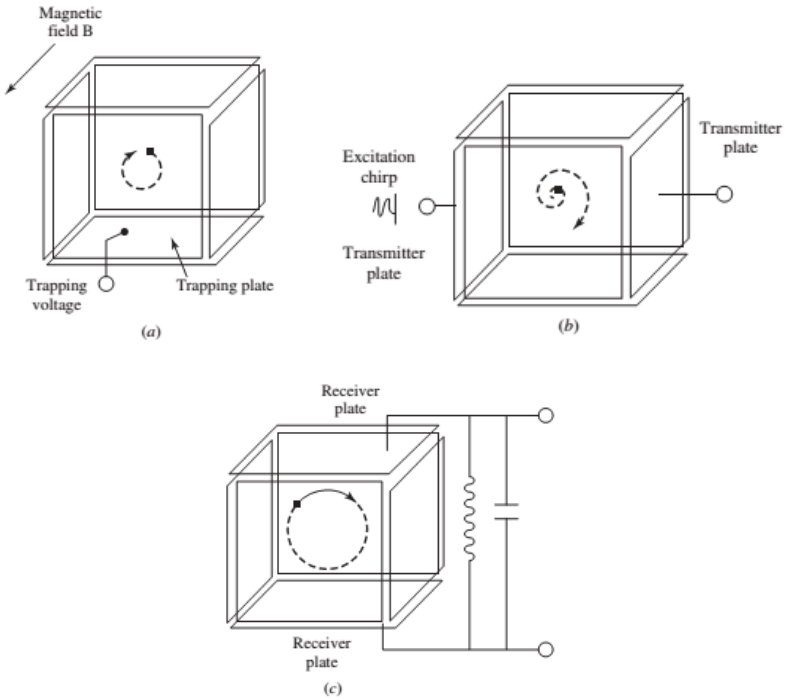

Figure I.17 Schematic representation of the operation of FT-ICR/MS. The mass analysis involves three steps: (a) ion formation and storage; (b) excitation of the trapped ions by an external broad-frequency range pulse; (c) detection of the ions by measuring their image current.[154]

I.3.3 Collision-induced dissociation (CID)

Collision-induced dissociation, or sometimes also mentioned as collision-activated decomposition (CAD) became very important in mass spectrometry, since the beginning of soft ionization techniques such as fast atom bombardment[156], electrospray ionization[157,158], and matrix-assisted laser desorption/ionization[159]. The ability to obtain practically intact molecular ions for many classes of compound was enormously useful but the ability to obtain structural information through characteristic fragmentation patterns was therefore lost.

CID occurs when some of the translational energy of an accelerated ion is converted into internal energy upon collision with a residual gas – a process designated as collision endothermicity, *q*. CID leads to an increase of the internal energy that can induce decomposition (fragmentation) of the ions and can be employed to increase the number of precursor ions that fragment and also the number of fragmentation pathways.

The CID process is a two-step mechanism, where the excitation of the precursors and their fragmentations are separated in time since the activation time for fast-moving ions is generally orders of magnitude faster than the dissociation time. The first step is very fast (10^{-14} to 10^{-16} s) where a collision between an ion and a neutral target results in an increase in the internal energy of the ion. This extra energy is redistributed amongst its vibrational modes (3*N* - 6 for an ion with N non-linear atoms) – this can be seen as an ergodic ion activation mode. The second step is much slower in which there is unimolecular decomposition of the excited ion to generate product ions and neutral fragments. Because the first step is much faster than the second, large ions are more difficult to fragment as they have more vibrational modes in which to deposit the extra energy. Therefore, the dissociation products that are observed result from a series of competitive and consecutive reactions and the fragmentation pathways depend on the amount of energy deposited and not on the method of ion activation used. As the energy is distributed with an equal probability among all of the internal modes of the ion, this leads preferentially to cleavage sites at the weakest bonds. For the same reason, molecules with more atoms will need more energy, or more time, to dissociate.

The total available energy for the transfer of kinetic energy to internal energy is called relative energy (E_{com}) and depends on the collision partners' masses (Eq. 1.4).

$$E_{com} = (\frac{N}{m_p+N})E_{lab} \quad \textbf{(1.4)}$$

E_{lab} is the ion's kinetic energy and N and m_p represent the masses for the neutral target and precursor ion, respectively. The CID process is highly dependent on the relative masses of the two species. E_{com} represents the maximum amount of energy that can be converted into internal energy of the precursor ion. This energy, increases with the target's mass, allowing more of the ion's kinetic energy to be converted into internal energy. Also, E_{com} decreases as a function of $1/m_p$, meaning that larger precursor ions have less internal energy available for fragmentation through the collision process.[160]

As explained above, activation of the selected ions occurs by collision(s) with neutral gas molecules in a collision cell. This experiment can be done at high collision energies (range of keV), usually using tandem sector and time-of-flight instruments, or at low energies (1- 100 eV), more commonly observed in triple quadrupoles (QqQ) and trapping devices, such as quadrupole ion traps and Fourier-transform ion cyclotron resonance instruments.

One of the main inconveniences of CID is the limitation of the energy transferred to an ion and thus the limitation of its degree of fragmentation. With large ions, the energy is distributed on a greater number of bonds and thus the result is a slower reaction rate of the fragmentation. To minimize those issues, several other ion activation methods that have become progressively useful for specific applications (Table I.5).[161]

Table I.5 Different ion activation processes.

Method	Energy range	Type of instrument
Collision-induced dissociation (CID)	Low	QqQ, IT, QqTOF, QqLIT, FT-ICR
	High	Tandem TOF, sectors
Surface-induced dissociation (SID)	Low	Hybrid (BqQ), QqQ, IT, FT-ICR
	High	Tandem TOD, RETOF
Electron-capture dissociation (ECD)	Low	FT-ICR
Infrared multiphoton dissociation (IRMPD)	Low	IT, FT-ICR
Blackbody infrared radiative dissociation (BIRD)	Low	IT, FT-ICR

SID is very similar to CID, but allows increased control for energy deposition and can lead to increased fragmentation, especially for large ions with high dissociation thresholds. ECD is a unique technique for the observation of non-ergodic dissociation behavior of multiply charged

cations and exhibits distinct fragmentation mechanisms. IRMPD works with IR radiation, usually by the use of low-power continuous-wave CO_2 lasers, in order to cause fragmentation of ions in trapping instruments, and BIRD can thermally activate ions in FT-ICR instruments. It allows the determination of activation energies and Arrhenius constants for dissociation reactions, and can ultimately assist in the elucidation of specific fragmentation mechanisms. These activation techniques can be used separately or in combination to yield very interesting and comprehensive results. Nevertheless, CID still remains the most common ion activation technique employed nowadays.[162-164]

I.3.4 Ion/molecule reactions

Ion/molecule (IM) reactions provide information on the secondary structure of ions, often under the conditions of thermal equilibrium, contrasting with collision-induced dissociation, which probes the primary structure during collisional activation. Also, ion/molecule reactions can provide key information on intrinsic factors that determine gas-phase ion structures.[165] In the gas phase, the physical and chemical properties of ionic species can be studied in the absence of solvent and other disturbing factors present in condensed phases, solution or solid. The effect of solvation creates an energetic barrier difficult to overcome in any ion/molecule reaction in solution. As a consequence, exothermic ion/molecule reactions in the gas phase are often observed to be barrierless and occur with high efficiencies. However, as for any exothermic process, increasing the amount of energy available will decrease the probability of the reaction.[166,167]

When a reactant gas is introduced into a collision cell, ion/molecule collisions usually lead to the observation of gas-phase reactions. The evolution of these reactions can be followed as a function of time, and equilibrium can be observed, leading to an easy determination of kinetic and thermodynamic parameters. Tandem-in-time instruments (QIT or FT-ICR-MS) are the most used for observation of ion/molecule reactions. In tandem-in-space instruments (e.g. TOF-MS), the time allowed for reaction is short and can be varied over only a limited range. Also, the achievement of very low collision energies that promote exothermic ion/molecule reactions is more difficult.[92]

The substitution reaction shown below is a good example to correlate energy characteristics of both the gas-phase and aqueous solution phase. The correspondent diagram of energy is displayed in Figure I.18.

$$Cl^- + CH_3Br \rightarrow CH_3Cl + Br^-$$

As in the condensed phase molecules are strongly solvated, it is necessary to remove the solvation sphere in order to form the activated complex, a process which requires a lot of energy. In the gas phase the opposite occurs since there is no solvent, the ion interaction with the molecule is therefore exothermic, which leads to the formation of an ion–molecule complex. Some activation energy thus becomes necessary in order to obtain the activated complex. This activation energy is generally lower than the energy produced by the first step. Therefore, in solution the reaction rate is dependent of the amount of energy used to destroy the solvation sphere, which results in much slower rates than in the gas phase.

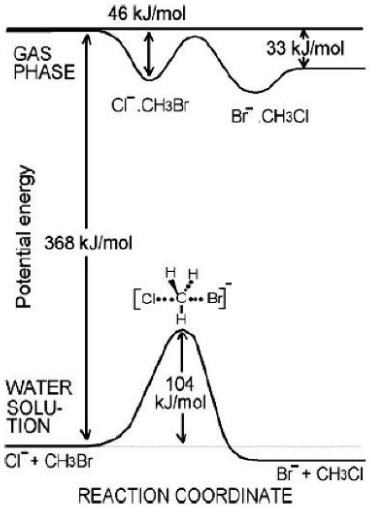

Figure I.18 Potential energy diagram for a substitution reaction in the gas phase and in solution in water.[168]

The first IM reaction was reported by Dempster in 1916.[169] He suggested that the H_3^+ ion was formed by the reaction

$$H^+ + H_2 \rightarrow H_3^+$$

This proposal was consistent with his observation that the abundance of H_3^+ decreased significantly with decreasing pressure as required for a two-body process. Later in 1928, Hogness and Harkness reported the analogous reactions,

$$I_2^+ + I_2 \rightarrow I_3^+ + I$$
$$I_2^- + I_2 \rightarrow I_3^- + I$$

as well as the electron transfer processes

$$I^+ + I_2 \rightarrow I_2^+ + I$$
$$I^- + I_2 \rightarrow I_2^- + I$$

I.3.4.1 Types of ion/molecule reactions [136,170]

The generic ion/molecule reaction shown below includes several categories or types of processes that transform the reacting species. These possibilities are summarized in Table I.6.

$$A^+ + B \rightarrow C^+ + D$$

The most abundant types of reactions known are *charge transfer*. This is a gas-phase reaction between an ion and a neutral species in which the charge of the ion is transferred to the neutral molecule. *Proton transfer* reactions are known to produce a cation or an anion and are the most often observed ion/molecule reaction in sources that allow collisions. The general rule is that the proton affinity of the proton acceptor (neutral or anion) has to be higher than the proton affinity of the donor (cation or neutral). If there is a difference in proton affinity such that the reaction is exergonic, the transfer generally occur for nearly each collision (as discussed below). In *association or clustering* reactions, dimer ions such as $(M+M+H)^+$ or of higher order $(nM+H)^+$ are often observed. The proton can be replaced by another cation. Heterodimers of the general formula $(M+M'+H)^+$, or with a metal cation or of higher order, are also observed. The corresponding ions are also observed in negative ion mode. The formation of these aggregates in the gas phase causes a diminution of entropy. Furthermore, if the partners have similar basicities or affinities for the cation, the cluster is generally more stable. Otherwise it dissociates, one of the partners taking the proton, or the cation, according to the relative stabilities. This is why associations of two or more identical molecules are observed more often or at higher abundances. Indeed, they have the same affinities. Aggregates are not so common in the negative ion mode, because the presence of the negative charge causes an expansion of the electronic shell, thus reducing the electric field around the negatively charged ion which reduces the interactions between the partners. In *adduct formation*, an ion is formed by direct combination of a neutral molecule and an 'ionizing' ion other than the proton. All of these types of IM reactions have been extensively reported.

Table I.6 Types of ion/molecule reactions.

Equation	Type of ion/molecule reactions
$A^+ + B \rightarrow B^+ + A$	Charge transfer
$AH^+ + B \rightarrow BH^+ + A$	Proton transfer
$A^+ + BH \rightarrow AH^+ + B$	Hydrogen atom transfer
$A^+ + BH \rightarrow B^+ + AH$	Hydride (H^-) atom transfer
$A^+ + BO \rightarrow AO^+ + B$	Oxidation reaction
$A^+ + B \rightarrow AB^+$	Association or clustering
$A^+ + B \rightarrow (A+B)^+$	Adduct formation

I.3.4.2 Reaction thermochemistry[170,171]

Thermochemistry refers to the energy balance in a reaction process. It is the study of the energy and heat associated with chemical reactions and physical transformations. It focuses essentially on the system's energy exchange with its surroundings. Ion thermochemistry is of great practical importance to mass spectrometry. A variety of mass spectrometry and ion spectroscopy techniques have been developed to measure ion thermochemical quantities. Ion source intensities and fragmentation patterns in mass spectra are related to ion energetics. Measurements on isolated ions give information about the intrinsic behavior of the species in the absence of solvent effects. Comparison with the behavior of the same ions in the condensed phase shows how solvent influences reactivity. Ion/molecule reaction equilibrium measurements can provide very accurate ion thermochemistry values.

Ion thermochemical parameters are usually determined by means of differences in molar enthalpies (ΔH) or molar Gibbs energies (ΔG) between products and reactants of a specific reaction. These are related by the standard thermodynamic relationships:

$$\Delta H = \Delta U + \Delta(pV) \text{ and } \Delta G = \Delta H - T\Delta S$$

ΔU is the variation of the internal energy (SI unit: joule, J), p is the pressure of the system (SI unit: pascal, Pa), V the molar volume (SI unit: m^3), T temperature (SI unit: kelvin, K), and ΔS the variation of the molar entropy (SI unit: J/K). The unit of measurement for enthalpy and Gibbs energy in the International System of Units (SI) is the joule, J.

Gibbs energies of reaction are commonly obtained from equilibrium constant measurements using the following equation:

$$\Delta G_T^\circ = -RTlnK_T \qquad \textbf{(1.5)}$$

At 0 K, $\Delta_r H_0 = \Delta_r U_0 = \Delta_r G_0$ for any gas-phase reaction.

Enthalpy (*H*) is a state property which incorporates many thermodynamic parameters of a system such as temperature, pressure and composition, among others. It is the heat effect defined as the sum of the internal energy of the system plus the expansion work performed on the surroundings for a constant pressure process. The reaction enthalpy, $\Delta H_{r,T}$, is the difference between the sums of the gas phase heats of formation, $\Delta H_{f,T}$, of the reactants and products at the temperature *T*.

Considering the bimolecular reaction:

$A^+ + B \rightarrow C^+ + D$

The change of enthalpy is given by:

$$\Delta H_r = \Delta H_f(C^+) + \Delta H_f(D) - \Delta H_f(A^+) - \Delta H_f(B) \qquad \textbf{(1.6)}$$

According to the First Law of thermodynamics, which states that the internal energy of an isolated system is constant, when the enthalpy is negative, the reaction is exothermic and can proceed and is often fast, and when positive it is endothermic. An exothermic reaction releases energy to the environment and, thus, is thermodynamically allowed. An endothermic reaction absorbs energy from the environment and is thermodynamically disallowed since energy must be supplied as heat so the reaction can occur.
The reaction energy is given by the free Gibbs energy:

$$\Delta G_r = \Delta H_r - T\Delta S_r \qquad \textbf{(1.7)}$$

The entropy term in gas-phase bimolecular processes under low pressure conditions is negligible.[172, 173]

Other important ion thermochemical parameters[174] we can extract from an ion/molecule reaction include:

Ionization energy or enthalpy (IE) (or also termed ionization potential, IP) - refers to the removal of an electron from a neutral species.

Electron affinity (EA) - The analogous energy required to remove an electron from an anion.

Vertical ionization energy (VIE) or vertical detachment energy (VDE) – is defined as the energy difference between the lower charge state and the potential energy surface of the upper charge state at the equilibrium geometry of the lower state.

Proton affinity (PA) – Is defined as the negative of the enthalpy change in the gas phase reaction between a proton and the chemical species concerned, usually an electrically neutral species to give the conjugate acid of that species. Formally, the relationship between the enthalpy of formation of MH^+ and its neutral counterpart, M, is defined in terms of a quantity called the proton affinity, PA. This the negative of the enthalpy change of the hypothetical protonation reaction:

$$M + H^+ \rightarrow MH^+ \qquad \Delta H_{rxn} = -PA$$

$$\Delta_f H;(MH^+) = \Delta_f H°(M) + \Delta_f H;(H^+) - PA$$

PA is a quantity defined at 298 K. The Gibbs energy change associated with the protonation reaction is called the *gas phase basicity*, GB, of molecule M.

Bond dissociation enthalpy (BDE) - applies to a fragmentation process where it is known that a specific bond is cleaved. BDE usually refers to neutral species AB at 298 K. The corresponding 0 K bond dissociation energy $D_0(AB) = \Delta_D H_0$, refers here to the dissociation of a molecule in its ground electronic, vibrational, and rotational state to form the ground states of the products (regardless of whether an adiabatic potential energy surface connects those products). Above 0 K, AB bond dissociation enthalpies are related to bond dissociation energies by $\Delta_D H_T(A\text{-}B) = \Delta_D U_T(A\text{-}B) + RT$. Reactions leading to polyatomic products generally release the enthalpy of reaction into internal degrees of freedom (chemical bond vibrations and molecular rotations).

If an exothermic small particle transfer reaction occurs, it usually occurs with high probability (i.e. close to the collision rate) and is relatively fast. Usually this is because such processes do not generally exhibit an activation energy barrier due to the relatively strong ion-induced dipole electrostatic interaction. Hence, thermochemistry provides a high degree of specificity for ion/molecule reactions.

Theoretical calculations using ab initio molecular orbital theory or density functional theory have become extremely important as a complement for the interpretation on experimental ion chemistry data.

I.3.4.3 Reaction rate determination[44,166,169,171]

In the gas phase, kinetic studies allow examining the evolution of an ion/molecule system during a certain reaction time and it is expressed by means of reaction rate in molecule.cm^{-3}.s^{-1}. Using a mass spectrometer (FT-ICR-MS for example) for this purpose, many multiple collisions can occur and therefore only the kinetics of the disappearance of ions can be measured. The ions can interact with neutral molecules and form new ions, so it becomes complex to quantify the ions formed.

In 2nd order reactions with the exemplified equation below

$A^+ + B \rightarrow$ products

The rate equation is given by:

$$\text{Rate} = k[A^+][B] \quad \textbf{(1.8)}$$

It involves two reactants, the ion A^+ and the neutral molecule B, which are two unlike species. Since in ion/molecule reactions, the concentration of the ion is usually much lower than the neutral molecule ($[A^+] << [B]$), it follows **pseudo-first order kinetics**. Therefore it is assumed that the concentration of B remains constant during the reaction because its consumption is so small that the change in concentration is negligible regardless the number of neutral molecules involved.

Thus, the disappearance of the reactant ion is given by

$$-\frac{d[A^+]}{dt} = k[A^+][B] \qquad \textbf{(1.9a)}$$

From which, as explained above, the equation is as follows:

$$-\frac{d[A^+]}{dt} = k'[A^+] \qquad \textbf{(1.9b)}$$

Where k' = k*d*[B]

The reaction is then a pseudo-first order reaction which can be expressed in a logarithmic form

$$\ln[A^+]_t = -k't + \ln[A^+]_0 \qquad \textbf{(1.10)}$$

and can be represented in a plot of ln[A^+] versus time, where the reaction rate, *k'*, is obtained from the slope.

I.3.4.4 Reaction efficiency

Depending on the type of ion/neutral interactions present, the rate constants *k* that can be obtained are normally compared with theoretical collisional rate constants, k_{COL}, of Langevin, average dipole orientation (ADO), or Su and Chesnavich models, which are briefly summarized below.[175] A reaction efficiency k/k_{COL} can then be defined, representing the fraction of ion/neutral collisions which are effective in the formation of reaction products.

Theory proposed by Langevin[166]

According to the Langevin approach, the ion is considered as a point charge and all its interactions are predetermined by the polarizability, α, of the molecule. Langevin defined the reaction efficiency as the probability of reaction upon each interaction of the reagents, i.e., the ratio of the reaction cross section to the collision cross section, $\sigma_{rxn}/\sigma_{col}$. The collision cross section is controlled by the long-range interaction potential between the reactants, whereas the reaction cross section depends on the details of the potential energy surface once the reactants are close enough to interact chemically. For all molecules, an important component of the strength of the long-range interaction with ions is the ion-induced dipole potential (V),

$$V(r) = -\frac{\alpha q^2}{8\pi\varepsilon_0 r^4} \qquad \textbf{(1.11)}$$

where α is the polarizability volume of the molecule (in units of m^3; $\alpha=4\pi\varepsilon_0\alpha_v$), q is the charge on the ion (1.60219×10^{-19} Coulomb), ε_0 is the permittivity of vacuum ($8{,}85418 \times 10^{-12}$ $m^3\,kg^{-1}\,s^4\,A^2$), and r is the distance between the centers of mass of the reactants.

LGS (Langevin–Gioumousis–Stevenson) refers to the recognition of Langevin, Gioumousis and Stevenson, who first developed a model for the collision cross section and recognized that it was a useful upper limit to the probability of ion/molecule reactions. When the neutral reactant has a dipole moment, there is a strong directionality to the ion/molecule interaction. If the dipole were always favorably oriented towards the ion, then the interaction potential has an additional term:

$$V(r) = -q\mu_D/(4\pi\varepsilon_0)r^2 \qquad \textbf{(1.12)}$$

where μ_D is the permanent dipole moment such that the collision probability increases substantially. Nevertheless, in real collisions, the dipole moment is rotating and the strength of the interaction depends on the relative rates of rotation and the speed at which the reactants approach one another. Overall there is still an enhancement in the collision probability compared with a molecule with no dipole. A cross section can be converted to a rate constant simply by multiplying by the velocity v:

$$k_{LGS}(E) = v\sigma(E) = q\left(\frac{\pi\alpha}{\varepsilon_0\mu}\right)^{1/2} \qquad \textbf{(1.13)}$$

To convert to units of cm^3 $molecule^{-1}$ s^{-1}:

$$k_{\mathrm{LGS}} = \left(\frac{q}{2\varepsilon_0}\right)\sqrt{\left(\frac{4\pi\varepsilon_0\alpha}{\mu}\right)}\mathrm{x}10^{-6} \qquad \textbf{(1.14)}$$

Therefore, the Langevin theory is suitable to reaction rate constants of simple ion/molecule reactions of low energies but the rates for polar ion/molecule reactions are underestimated and other theories were developed.

Average dipole orientation theory (ADO)[176]

The first ion-polar molecule collision theory that could be generally applied was the average dipole orientation (ADO) theory of Su and Bowers. This theory used statistical methods to calculate the average orientation of the polar molecule in the ion field and then a Langevin approach to calculate the rate constant. The ADO theory was shown to predict accurately the dipole dependence of charge transfer, proton transfer and momentum transfer collisions, and to predict accurately absolute proton transfer rate constants. The ADO theory does not always accurately predict the absolute magnitude of charge transfers and momentum transfer rate constants even though it does predict their dipole dependence.

The major assumption in the original formulation of ADO theory is that there is no net angular momentum transfer between the rotating molecule and the ion/molecule orbital motion. While this assumption is quite good at large ion/molecule separations it becomes less valid as the separation decreases toward the capture limit. Using the same approach in Langevin theory and the Maxwell-Boltzmann distribution of relative velocities, the ion collision rate is given by

$$k_{\mathrm{L}} = \frac{2\pi q}{\sqrt{\mu}}\left[\sqrt{\mathrm{a}} + \mu_{\mathrm{D}}\sqrt{\frac{2}{\pi k_{\mathrm{B}} T}}\right] \qquad \textbf{(1.15)}$$

where k_B is the Boltzmann constant and T is the absolute temperature.

Su and Bowers added to this equation a C component with values between 0 and 1 to represent the dipole hindrance and thus k_{ADO} converted to cm^3 $molecule^{-1}$ s^{-1} is given by:

$$k_{\mathrm{ADO}} = \frac{q}{2\varepsilon_0\sqrt{\mu}}\left[\sqrt{4\pi\varepsilon_0 \mathrm{a}} + \mathrm{C}\mu_{\mathrm{D}}\sqrt{\frac{2}{\pi k_{\mathrm{B}} T}}\right]10^{-6} \qquad \textbf{(1.16)}$$

Su and Chesnavich ion-polar molecule collision theory[177,178]

In 1980, Chesnavich, Su, and Bowers reported a new ion/molecule transition state theory study on thermal energy of ion-polar molecule capture collisions. They assumed the ion as a point charge, the polar molecule as a two-dimensional rigid rotor, and assumed a new interaction potential.

They showed that the ratio of $k_{COL}(T)$ in comparison with the Langevin capture rate constant k_L depends only on two reduced parameters T_R and I^* ($T_R = 2\alpha k_B T/\mu_D^2$ and $I^* = \mu_D I/\alpha q\mu$).

$$\frac{k_{\mathrm{COL}}(T)}{k_{\mathrm{L}}} = K_{\mathrm{COL}}(T_R, I^*) \qquad \textbf{(1.17)}$$

However, K_{COL} seems to be insensitive to I^* at low values of I^*. As I^* increases, K_{COL} enters a region near the adiabatic limit. Several calculations were performed in order to obtain a most viable K_{COL} formula, reported in more detail by Su, Chesnavich and Bowers.

In the following chapters, this last approach was the one used in all reaction efficiency determinations.

References

(1) Jones, C. J., *d- and f- block chemistry*, University of Birmingham, Wiley Interscience Royal Society of Chemistry, Bristol, **2002**.

(2) Kirker, I., Computational study of covalency and complexation in actinides using static and dynamic simulation and topological density analysis, Ph.D. Thesis, Department of Chemistry, University College London, **2013**.

(3) Kaltsoyannis, N.; Scott, P., *The f elements*; Oxford Chemistry Primers, Oxford University Press Inc, **1999**; Vol. 76.

(4) Neidig, M. L.; Clark, D. L.; Martin, R. L., Covalency in f-element complexes, *Coordination Chemistry Reviews* **2013**, *257*, 394.

(5) Kerridge, A.; Coates, R.; Kaltsoyannis, N., Is cerocene really a Ce(III) compound? All-electron spin-orbit coupled CASPT2 calculations on M(η_8-C_8H_8)$_2$ (M = Th, Pa, Ce), *Journal of Physical Chemistry A* **2009**, *113*, 2896.

(6) Seaborg, G. T., Place in periodic system and electronic structure of the heaviest elements, *Nucleonics* **1949**, *5*, 16.

(7) Choppin, G. R., Covalency in f-element bonds, *Journal of Alloys and Compounds* **2002**, *344*, 55.

(8) Ghiorso, A.; Harvey, B. G.; Choppin, G. R.; Thompson, S. G.; Seaborg, G. T., New element mendelevium, atomic number 101, *Physical Review* **1955**, *98*, 1518.

(9) Denning, R. G., Electronic structure and bonding in actinyl ions, *Structure and Bonding* **1992**, *79*, 215.

(10) Gaunt, A. J.; Reilly, S. D.; Enriquez, A. E.; Scott, B. L.; Ibers, J. A.; Sekar, P.; Ingram, K. I. M.; Kaltsoyannis, N.; Neu, M. P., Experimental and theoretical comparison of actinide and lanthanide bonding in $M[N(EPR_2)_2]_3$ complexes (M = U, Pu, La, Ce; E = S, Se, Te; R = Ph, iPr, H), *Inorganic Chemistry* **2008**, *47*, 29.

(11) Ingram, K. I. M.; Tassell, M. J.; Gaunt, A. J.; Kaltsoyannis, N., Covalency in the f element-chalcogen bond. Computational studies of $M[N(EPR_2)_2]_3$ (M = La, Ce, Pr, Pm, Eu, U, Np, Pu, Am, Cm; E = O, S, Se, Te; R = H, (i)Pr, Ph), *Inorganic Chemistry* **2008**, *47*, 7824.

(12) Raymond, K. N.; Wellman, D. L.; Sgarlata, C.; Hill, A. P., Curvature of the lanthanide contraction: An explanation, *Comptes Rendus Chimie* **2010**, *13*, 849.

(13) Jensen, M. P.; Bond, A. H., Comparison of covalency in the complexes of trivalent actinide and lanthanide cations, *Journal of the American Chemical Society* **2002**, *124*, 9870.

(14) Choppin, G. R., Comparison of the solution chemistry of the actinides and lanthanides, *Journal of the Less-Common Metals* **1983**, *93*, 323.

(15) Nash, K. L.; Madic, C.; Mathur, J. N., *The chemistry of the actinide and transactinide elements*; Springer, Berlin, **2006**; Vol. 4.

(16) Mehdoui, T.; Berthet, J. C.; Thuery, P.; Ephritikhine, M., Lanthanide(III)/actinide(III) differentiation in coordination of azine molecules to tris(cyclopentadienyl) complexes of cerium and uranium, *Dalton Transactions* **2004**, 579.

(17) Prodan, I. D.; Scuseria, G. E.; Martin, R. L., Covalency in the actinide dioxides: Systematic study of the electronic properties using screened hybrid density functional theory, *Physical Review B* **2007**, *76* (3), 033101.

(18) Nash, K. L., A review of the basic chemistry and recent developments in trivalent f-elements separations, *Solvent Extraction and Ion Exchange* **1993**, *11*, 729.

(19) Drew, M. G. B.; Iveson, P. B.; Hudson, M. J.; Liljenzin, J. O.; Spjuth, L.; Cordier, P. V.; Enarsson, A.; Hill, C.; Madic, C., Separation of americium(III) from europium(III) with tridentate heterocyclic nitrogen ligands and crystallographic studies of complexes formed by 2,2 ': 6 ',2-terpyridine with the lanthanides, *Journal of the Chemical Society-Dalton Transactions* **2000**, 821.

(20) Schwarz, H., Chemistry with methane: Concepts rather than recipes, *Angewandte Chemie-International Edition* **2011**, *50*, 10096.

(21) Roithova, J.; Schroeder, D., Selective activation of alkanes by gas-phase metal ions, *Chemical Reviews* **2010**, *110*, 1170.

(22) Schroeder, D.; Schwarz, H., Gas-phase activation of methane by ligated transition-metal cations, *Proceedings of the National Academy of Sciences of the United States of America* **2008**, *105*, 18114.

(23) Bohme, D. K.; Schwarz, H., Gas-phase catalysis by atomic and cluster metal ions: The ultimate single-site catalysts, *Angewandte Chemie-International Edition* **2005**, *44*, 2336.

(24) Schlangen, M.; Schwarz, H., Effects of ligands, cluster size, and charge state in gas-phase catalysis: A happy marriage of experimental and computational studies, *Catalysis Letters* **2012**, *142*, 1265.

(25) Roithova, J.; Schroeder, D., Bimolecular reactions of molecular dications: reactivity paradigms and bond-forming processes, *Physical Chemistry Chemical Physics* **2007**, *9*, 2341.

(26) Stace, A. J., Metal ion solvation in the gas phase: The quest for higher oxidation states, *Journal of Physical Chemistry A* **2002**, *106*, 7993.

(27) Freiser, B. S., Gas-phase metal ion chemistry, *Journal of Mass Spectrometry* **1996**, *31*, 703.

(28) Adams, N. G.; Babcock, L. M., *Advances in Gas Phase Ion Chemistry*; Adams, N. G.; Babcock, L. M., Eds., Elsvier, Jai Press Inc., The Netherlands, **1996**, vol. 4.

(29) Marçalo, J.; Gibson, J. K., Gas-phase ion chemistry of rare earths and actinides, In *Handbook on the Physics and Chemistry of Rare Earths (Including Actinides),* J.-C. G. Bünzli, V. K. Pecharsky, Eds., Elsevier, Amsterdam, The Netherlands, **2014***,* Vol. 45, Cap. 263, pp. 1–110.

(30) Mercero, J. M.; Matxain, J. M.; Lopez, X.; York, D. M.; Largo, A.; Eriksson, L. A.; Ugalde, J. M., Theoretical methods that help understanding the structure and reactivity of gas phase ions, *International Journal of Mass Spectrometry* **2005**, *240*, 37.

(31) Schilling, J. B.; Beauchamp, J. L., Hydrocarbon activation by gas-phase lanthanide cations - Interaction of Pr^+, Eu^+, and Gd^+ with small alkanes, cycloalkanes and alkenes *Journal of the American Chemical Society* **1988**, *110*, 15.

(32) Cornehl, H. H.; Heinemann, C.; Schroeder, D.; Schwarz, H., Gas-phase reactivity of lanthanide cations with hydrocarbons, *Organometallics* **1995**, *14*, 992.

(33) Marçalo, J.; Santos, M.; Pires de Matos, A.; Gibson, J. K.; Haire, R. G., Gas-phase reactions of doubly charged lanthanide cations with alkanes and alkenes. Trends in metal(2+) reactivity, *Journal of Physical Chemistry A* **2008**, *112*, 12647.

(34) Pepper, M.; Bursten, B. E., The Electronic-structure of actinide-containing molecules - A challenge to applied quantum chemistry, *Chemical Reviews* **1991**, *91*, 719.

(35) Gibson, J. K., Gas-phase chemistry of actinide ions: probing the distinctive character of the 5f elements, *International Journal of Mass Spectrometry* **2002**, *214*, 1.

(36) Gibson, J. K.; Marçalo, J., New developments in gas-phase actinide ion chemistry, *Coordination Chemistry Reviews* **2006**, *250*, 776.

(37) Heaven, M.C.; Gibson, J.K.; Marçalo, J. Molecular spectroscopy and reactions of actinides in the gas phase and cryogenic matrices, In *The chemistry of the actinide and transactinide elements*; Morss, L. R., Edelstein, N. M., Fuger, J., Eds., Springer, Dordrecht, The Netherlands, **2011**, Vol. 6, Chap. 38, pp. 4079-4156.

(38) Heinemann, C.; Cornehl, H. H.; Schwarz, H., Hydrocarbon activation by bare uranium cations - Formation of a cationic ranium-benzene complex from 3 ethylene units, *Journal of Organometallic Chemistry* **1995**, *501*, 201.

(39) Marçalo, J.; Leal, J. P.; Pires de Matos, A., Gas phase actinide ion chemistry: Activation of alkanes and alkenes by thorium cations, *International Journal of Mass Spectrometry and Ion Processes* **1996**, *157*, 265.

(40) Sunderlin, L. S.; Armentrout, P. B., Periodic trends in chemical reactivity - reactions of Sc^+, Y^+, La^+ and Lu^+ with methane and ethane, *Journal of the American Chemical Society* **1989**, *111*, 3845.

(41) Santos, M.; Marçalo, J.; Pires de Matos, A.; Gibson, J. K.; Haire, R. G., Gas-phase oxidation reactions of neptunium and plutonium ions investigated via Fourier Transform Ion Cyclotron Resonance Mass Spectrometry, *Journal of Physical Chemistry A* **2002**, *106*, 7190.

(42) Gibson, J. K.; Haire, R. G., Einsteinium chemistry in the gas phase: exploring the divalent character of heavy actinides, *Radiochimica Acta* **2003**, *91*, 441.

(43) Gibson, J. K.; Haire, R. G., Gas-phase chemistry of bare and oxo-ligated protactinium ions: A contribution to a systematic understanding of actinide chemistry, *Inorganic Chemistry* **2002**, *41*, 5897.

(44) Santos, M., Estudos de química de actinídeos por espectrometria de massa, Ph.D. thesis, Universidade de Lisboa, **2008**.

(45) Di Santo, E.; Santos, M.; Michelini, M. C.; Marçalo, J.; Russo, N.; Gibson, J. K., Gas-phase reactions of the bare Th^{2+} and U^{2+} ions with small alkanes, CH_4, C_2H_6, and C_3H_8: Experimental and theoretical study of elementary organoactinide chemistry, *Journal of the American Chemical Society* **2011**, *133*, 1955.

(46) Marçalo, J.; Santos, M.; Gibson, J. K., Gas-phase reactions of doubly charged actinide cations with alkanes and alkenes-probing the chemical activity of 5f electrons from Th to Cm, *Physical Chemistry Chemical Physics* **2011**, *13*, 18322.

(47) Marçalo, J.; Santos, M.; Gibson, J. K., Gas-phase reactions of doubly charged actinide cations with alkanes and alkenes-probing the chemical activity of 5f electrons from Th to Cm (vol 13, pg 18322, 2011), *Physical Chemistry Chemical Physics* **2012**, *14*, 16775.

(48) Marçalo, J.; Leal, J. P.; Pires de Matos, A.; Marshall, A. G., Gas-phase actinide ion chemistry: FT-ICR/MS study of the reactions of thorium and uranium metal and oxide ions with arenes, *Organometallics* **1997**, *16*, 4581.

(49) Kazazic, S.; Kazazic, S. P.; Klasinc, L.; Rolman, M.; Srzic, D., Gas phase ligation of U^+. Comparison of pyrene, phenanthridine and phenanthrene as ligands, *Croatica Chemica Acta* **2006**, *79*, 125.

(50) Gibson, J. K., Actinide gas-phase chemistry: Reactions of An(+) and AnO(+) An = Th, U, Np, Pu, Am with nitriles and butylamine, *Inorganic Chemistry* **1999**, *38*, 165.

(51) Gibson, J. K., Gas-phase transuranium chemistry: Reactions of actinide ions with alcohols and thiols, *Journal of Mass Spectrometry* **1999**, *34*, 1166.

(52) Huang, H.; Chaudhary, S.; Van Horn, J. D., Uranyl-peptide interactions in carbonate solution with DAHK and derivatives, *Inorganic Chemistry* **2005**, *44*, 813.

(53) Kemp, T. J.; Read, P. A., Fast atom bombardment studies of amino acid and peptide complexes of the uranyl ion: Ligand attachment, dissociation and fragmentation, *Inorganica Chimica Acta* **1996**, *241*, 105.

(54) Giesting P., Uranyl complexes with organic ligands. Classification, crystal structures and applications, Ph.D. thesis, University of Notre Dame, **2006**.

(55) Spezia, R.; Siboulet, B.; Abadie, S.; Vuilleumier, R.; Vitorge, P., Stability and instability of the isoelectronic UO_2^{2+} and PaO_2^{+} actinyl oxo-cations in aqueous solution from density functional theory based molecular dynamics, *Journal of Physical Chemistry B* **2011**, *115*, 3560.

(56) Nevitt, M. V.; Brodsky, M. B.; The metalic state, in *The chemistry of the actinide elements*, 2nd ed.; Eds. Katz J.J.; Seaborg G.T.; Morss L.R., Chapman & Hall, London, **1986**, vol.2, p 1388.

(57) Armentrout, P. B.; Beauchamp, J. L., Collision-induced dissociation of UO^{+} and UO_2^{+}, *Chemical Physics* **1980**, *50*, 21.

(58) Santos, M.; Marçalo, J.; Leal, J. P.; Pires de Matos, A.; Gibson, J. K.; Haire, R. G., FT-ICR-MS study of the gas-phase thermochemistry of americium oxides, *International Journal of Mass Spectrometry* **2003**, *228*, 457.

(59) Morss, L. R.; Edelstein, N. M.; Fuger, J. *The Chemistry of the Actinide and Transactinide Elements*; 4th ed.; Springer, **2010**; Vol. 1-6.

(60) Gibson, J. K.; Haire, R. G.; Santos, M.; Marçalo, J.; Pires de Matos, A., Oxidation studies of dipositive actinide ions, An^{2+} (An = Th, U, Np, Pu, Am) in the gas phase: Synthesis and characterization of the isolated uranyl, neptunyl, and plutonyl ions UO_2^{2+} (g), NpO_2^{2+} (g), and PuO_2^{2+} (g), *Journal of Physical Chemistry A* **2005**, *109*, 2768.

(61) Denning, R. G., Electronic structure and bonding in actinyl ions and their analogs, *Journal of Physical Chemistry A* **2007**, *111*, 4125.

(62) Cornehl, H. H.; Heinemann, C.; Marçalo, J.; Pires de Matos, A.; Schwarz, H., The ''bare'' uranyl(2+) ion, UO_2^{2+}, *Angewandte Chemie-International Edition in English* **1996**, *35*, 891.

(63) Hase, W. L.; Koch, W., Foreword - Gas phase ion chemistry: A fruitful playground for the interplay between experiment and theory, *International Journal of Mass Spectrometry* **2000**, *201*, IX.

(64) Kaltsoyannis, N.; Hay, P. J.; Li, J.; Blaudeau, J. P.; Bursten, B. E., Theoretical studies of the electronic structure of compounds of the actinide elements, in *The Chemistry of the Actinide and Transactinide Elements,* Morss L. R., Edelstein N. M., Fuger J., Eds., Springer, The Netherlands, **2006**, p 1893, vol. 3.

(65) Alcami, M.; Mo, O.; Yanez, M., Computational chemistry: A useful (sometimes mandatory) tool in mass spectrometry studies, *Mass Spectrometry Reviews* **2001**, *20*, 195.

(66) Wang, D.; van Gunsteren, W. F.; Chai, Z., Recent advances in computational actinoid chemistry, *Chemical Society Reviews* **2012**, *41*, 5836.

(67) Fortier, S.; Hayton, T. W., Oxo ligand functionalization in the uranyl ion (UO_2^{2+}), *Coordination Chemistry Reviews* **2010**, *254*, 197.

(68) Arnold, P. L.; Love, J. B.; Patel, D., Pentavalent uranyl complexes, *Coordination Chemistry Reviews* **2009**, *253*, 1973.

(69) Van Horn, J. D.; Huang, H., Uranium(VI) bio-coordination chemistry from biochemical, solution and protein structural data, *Coordination Chemistry Reviews* **2006**, *250*, 765.

(70) Szabo, Z.; Toraishi, T.; Vallet, V.; Grenthe, I., Solution coordination chemistry of actinides: Thermodynamics, structure and reaction mechanisms, *Coordination Chemistry Reviews* **2006**, *250*, 784.

(71) Vats, B. G.; Kannan, S.; Pius, I. C.; Noronha, D. M.; Maity, D. K.; Drew, M. G. B., Synthetic, structural, extraction and theoretical studies of uranyl nitrate dithio-diglycolamide compounds, *Polyhedron* **2014**, *75*, 81.

(72) Xu, C.; Su, J.; Xu, X.; Li, J., Theoretical studies on the complexation of uranyl with typical carboxylate and amidoximate ligands, *Science China-Chemistry* **2013**, *56*, 1525.

(73) Gong, Y.; Hu, H. S.; Rao, L.; Li, J.; Gibson, J. K., Experimental and theoretical studies on the fragmentation of gas-phase uranyl-, neptunyl-, and plutonyl-diglycolamide complexes, *Journal of Physical Chemistry A* **2013**, *117*, 10544.

(74) Das, D.; Kannan, S.; Maity, D. K.; Drew, M. G. B., Steric effects on uranyl complexation: Synthetic, structural, and theoretical studies of carbamoyl pyrazole compounds of the uranyl (VI) Ion, *Inorganic Chemistry* **2012**, *51*, 4869.

(75) Majumdar, D.; Balasubramanian, K., Theoretical studies on the nature of uranyl-silicate, uranyl-phosphate and uranyl-arsenate interactions in the model $H_2UO_2SiO_4$ center dot $3H_2O$, HUO_2PO_4 center dot $3H_2O$, and HUO_2AsO_4 center dot $3H_2O$ molecules, *Chemical Physics Letters* **2004**, *397*, 26.

(76) Tatsumi, K.; Hoffmann, R., Bent cis d^0 MoO_2^{2+} vs linear trans d^0f^0 UO_2^{2+} - A significant role for non-valence 6p orbitals in uranyl, *Inorganic Chemistry* **1980**, *19*, 2656.

(77) Wadt, W. R., Why UO_2^{2+} is linear and isoelectronic and ThO_2 is bent, *Journal of the American Chemical Society* **1981**, *103*, 6053.

(78) Dyall, K. G., The role of the 6p orbital in the bending of the actinyls, *Abstracts of Papers of the American Chemical Society* **1999**, *217*, U12.

(79) La Pierre, H. S.; Meyer, K., Uranium-ligand multiple bonding in uranyl analogues, $L=U=L^{(n+)}$, and the inverse trans influence, *Inorganic Chemistry* **2013**, *52*, 529.

(80) Hayton, T. W.; Boncella, J. M.; Scott, B. L.; Batista, E. R.; Hay, P. J., Synthesis and reactivity of the imido analogues of the uranyl ion, *Journal of the American Chemical Society* **2006**, *128*, 10549.

(81) Kaltsoyannis, N., Computational study of analogues of the uranyl ion containing the -N=U=N- unit: Density functional theory calculations on UO_2^{2+}, UON^+, UN_2, $UO(NPH_3)^{3+}$, $U(NPH_3)_2^{4+}$, $UCl_4\{NPR_3\}_2$ (R = H, Me), and $UOCl_4\{NP(C_6H_5)_3\}^-$, *Inorganic Chemistry* **2000**, *39*, 6009.

(82) Pereira, C. C. L.; Michelini, M. C.; Marçalo, J.; Gong, Y.; Gibson, J. K., Synthesis and poperties of uranium sulfide cations. An evaluation of the stability of thiouranyl, $\{S=U=S\}^{2+}$, *Inorganic Chemistry* **2013**, *52*, 14162.

(83) Infante, I.; Kovacs, A.; La Macchia, G.; Shahi, A. R. M.; Gibson, J. K.; Gagliardi, L., Ionization energies for the actinide mono- and dioxides series, from Th to Cm: Theory versus experiment, *Journal of Physical Chemistry A* **2010**, *114*, 6007.

(84) La Macchia, G.; Infante, I.; Raab, J.; Gibson, J. K.; Gagliardi, L., A theoretical study of the ground state and lowest excited states of $PuO^{0/+/+2}$ and $PuO_2^{0/+/+2}$, *Physical Chemistry Chemical Physics* **2008**, *10*, 7278.

(85) Gibson, J. K.; Haire, R. G.; Marçalo, J.; Santos, M.; Pires de Matos, A.; Leal, J. P., Determination of the ionization energy of NpO_2 and comparative ionization energies of actinide oxides, *Journal of Nuclear Materials* **2005**, *344*, 24.

(86) Capone, F.; Colle, J. Y.; Hiernaut, J. P.; Ronchi, C., Controversy on the first ionization potential of PuO_2 (nearly) settled by new experimental evidence, *Journal of Physical Chemistry A* **2005**, *109*, 12054.

(87) Malmqvist, P. A.; Pierloot, K.; Shahi, A. R. M.; Cramer, C. J.; Gagliardi, L., The restricted active space followed by second-order perturbation theory method: Theory and application to the study of CuO_2 and Cu_2O_2 systems, *Journal of Chemical Physics* **2008**, *128*.

(88) Gibson, J. K.; Santos, M.; Marçalo, J.; Leal, J. P.; Pires de Matos, A.; Haire, R. G., Comment on "Controversy on the first ionization potential of PuO_2 (Nearly) settled by new experimental evidence", *Journal of Physical Chemistry A* **2006**, *110*, 4131.

(89) Shahi, A. R. M.; Cramer, C. J.; Gagliardi, L., Second-order perturbation theory with complete and restricted active space reference functions applied to oligomeric unsaturated hydrocarbons, *Physical Chemistry Chemical Physics* **2009**, *11*, 10964.

(90) Ingram, K. I. M.; Kaltsoyannis, N.; Gaunt, A. J.; Neu, M. P., Covalency in the f-element-chalcogen bond computational studies of $M[N(EPH_2)_2]_3$ (M = La, U, Pu; E = O, S, Se, Te), *Journal of Alloys and Compounds* **2007**, *444*, 369.

(91) Friesner, R. A., Ab initio quantum chemistry: Methodology and applications, *Proceedings of the National Academy of Sciences of the United States of America* **2005**, *102*, 6648.

(92) Becker, J. S. *Inorganic mass spectrometry. Principles and applications.*; John Wiley & Sons Ltd, England, **2007**.

(93) Barber, M.; Bordoli, R. S.; Sedgwick, R. D.; Tyler, A. N., Fast atom bombardment of solids (FAB) - a new ion-source for mass spectrometry, *Journal of the Chemical Society-Chemical Communications* **1981**, 325.

(94) Fenn, J. B.; Mann, M.; Meng, C. K.; Wong, S. F.; Whitehouse, C. M., Electrospray ionization for mass spectrometry of large biomolecules, *Science* **1989**, *246*, 64.

(95) Karas, M.; Hillenkamp, F., Laser desorption ionization of proteins with molecular masses exceeding 1000 Daltons, *Analytical Chemistry* **1988**, *60*, 2299.

(96) Laiko, V. V.; Baldwin, M. A.; Burlingame, A. L., Atmospheric pressure matrix assisted laser desorption/ionization mass spectrometry, *Analytical Chemistry* **2000**, *72*, 652.

(97) Robb, D. B.; Covey, T. R.; Bruins, A. P., Atmospheric pressure photoionisation: An ionization method for liquid chromatography-mass spectrometry, *Analytical Chemistry* **2000**, *72*, 3653.

(98) Takats, Z.; Wiseman, J. M.; Gologan, B.; Cooks, R. G., Mass spectrometry sampling under ambient conditions with desorption electrospray ionization, *Science* **2004**, *306*, 471.

(99) Cody, R. B.; Laramee, J. A.; Durst, H. D., Versatile new ion source for the analysis of materials in open air under ambient conditions, *Analytical Chemistry* **2005**, *77*, 2297.

(100) Dass, C., Modes of ionization, in *Fundamentals of contemporary mass spectrometry*; Desiderio D. M.; Nibbering N. M., Eds.; John Wiley & Sons ed., Canada, **2007**, chapter 2, 15.

(101) Dole, M.; Mack, L. L.; Hines, R. L., Molecular beams of macroions, *Journal of Chemical Physics* **1968**, *49*, 2240.

(102) El-Aneed, A.; Cohen, A.; Banoub, J., Mass spectrometry, review of the basics: electrospray, MALDI, and commonly used mass analyzers, *Applied Spectroscopy Reviews* **2009**, *44*, 210.

(103) Fenn, J. B.; Mann, M.; Meng, C. K.; Wong, S. F.; Whitehouse, C. M., Electrospray ionization principles and practice, *Mass Spectrometry Reviews* **1990**, *9*, 37.

(104) Cole, R. B., *Electrospray and MALDI mass spectrometry. Fundamentals, instrumentation, practicalities, and biological applications*; 2nd ed.; John Wiley & Sons, New Jersey, **2010**.

(105) Fenn, J. B., Electrospray wings for molecular elephants (Nobel lecture), *Angewandte Chemie-International Edition* **2003**, *42*, 3871.

(106) Henderson, W.; McIndoe, J. S., *Mass spectrometry of inorganic, coordination and organometalic compounds. Tools, techniques, tips.*; John Wiley & Sons, Ltd., Ed. Chichester, **2005**.

(107) Taylor, G., Disintegration of water drops in electric field, *Proceedings of the Royal Society of London Series a-Mathematical and Physical Sciences* **1964**, *280*.

(108) Last, I.; Levy, Y.; Jortner, J., Beyond the Rayleigh instability limit for multicharged finite systems: From fission to Coulomb explosion, *Proceedings of the National Academy of Sciences of the United States of America* **2002**, *99*, 9107.

(109) Konermann, L.; Ahadi, E.; Rodriguez, A. D.; Vahidi, S., Unraveling the mechanism of electrospray ionization, *Analytical Chemistry* **2013**, *85*, 2.

(110) Kebarle, P.; Verkerk, U. H., Electrospray: from ions in solution to ions in the gas phase, what we know now, *Mass Spectrometry Reviews* **2009**, *28*, 898.

(111) Cech, N. B.; Enke, C. G., Practical implications of some recent studies in electrospray ionization fundamentals, *Mass Spectrometry Reviews* **2001**, *20*, 362.

(112) Nguyen, S.; Fenn, J. B., Gas-phase ions of solute species from charged droplets of solutions, *Proceedings of the National Academy of Sciences of the United States of America* **2007**, *104*, 1111.

(113) Thomson, B. A.; Iribarne, J. V., Field-induced ion evaporation from liquid surfaces at atmospheric pressure, *Journal of Chemical Physics* **1979**, *71*, 4451.

(114) Iribarne, J. V.; Thomson, B. A., Evaporation of small ions from charged droplets, *Journal of Chemical Physics* **1976**, *64*, 2287.

(115) Gamero-Castano, M.; de la Mora, J. F., Direct measurement of ion evaporation kinetics from electrified liquid surfaces, *Journal of Chemical Physics* **2000**, *113*, 815.

(116) Gamero-Castano, M.; de la Mora, J. F., Kinetics of small ion evaporation from the charge and mass distribution of multiply charged clusters in electrosprays, *Journal of Mass Spectrometry* **2000**, *35*, 790.

(117) de la Mora, J. F., Electrospray ionization of large multiply charged species proceeds via Dole's charged residue mechanism, *Analytica Chimica Acta* **2000**, *406*, 93.

(118) Rohner, T. C.; Lion, N.; Girault, H. H., Electrochemical and theoretical aspects of electrospray ionisation, *Physical Chemistry Chemical Physics* **2004**, *6*, 3056.

(119) Freiser, B. S., Investigation of reaction of metal-ions and their clusters in the gas-phase by laser ionization Fourier Transform Mass Spectrometry, *Talanta* **1985**, *32*, 697.

(120) Zenobi, R., Modern laser mass spectrometry, *Fresenius Journal of Analytical Chemistry* **1994**, *348*, 506.

(121) Busch, K. L., Desorption ionization mass spectrometry, *Journal of Mass Spectrometry* **1995**, *30*, 233.

(122) Posthumus, M. A.; Kistemaker, P. G.; Meuzelaar, H. L. C.; Tennoeverdebrauw, M. C., Laser desorption mass spectrometry of polar non-volatile bio-organic molecules, *Analytical Chemistry* **1978**, *50*, 985.

(123) Conzemius, R. J.; Capellen, J. M., A review of the application to solids of the laser ion-source in mass spectrometry, *International Journal of Mass Spectrometry and Ion Processes* **1980**, *34*, 197.

(124) Carre, V.; Aubriet, F.; Scheepers, P. T.; Krier, G.; Muller, J. F., Potential of laser ablation and laser desorption mass spectrometry to characterize organic and inorganic environmental pollutants on dust particles, *Rapid Communications in Mass Spectrometry* **2005**, *19*, 871.

(125) Hardin, E. D.; Vestal, M. L., Laser ionization mass spectrometry of non-volatile samples, *Analytical Chemistry* **1981**, *53*, 1492.

(126) Marçalo, J.; Santos, M.; Pires de Matos, A.; Gibson, J. K., Molecular uranates: Laser synthesis of uranium oxide anions in the gas phase, *Inorganic Chemistry* **2009**, *48*, 5055.

(127) Dance, I. G.; Fisher, K. J.; Willett, G. D., Molecular manganese sulfide clusters formed by laser ablation, *Journal of the Chemical Society-Dalton Transactions* **1997**, 2557.

(128) Fisher, K.; Dance, I.; Willett, G.; Yi, M. N., Gas-phase metal sulfide cluster anions, *Journal of the Chemical Society-Dalton Transactions* **1996**, 709.

(129) Yi, M. N.; Fisher, K. J.; Dance, I. G., The generation of gaseous $Co_xO_y^-$ clusters and their reactions with alcohols: formation of homoleptic cobalt alkoxides $Co_4(OR)_8$, *International Journal of Mass Spectrometry* **2002**, *216*, 155.

(130) Aubriet, F.; Muller, J. F., About the atypical behavior of CrO_3, MoO_3, and WO_3 during their UV laser ablation/ionization, *Journal of Physical Chemistry A* **2002**, *106*, 6053.

(131) Aubriet, F.; Poleunis, C.; Muller, J. F.; Bertrand, P., Laser ablation and secondary ion mass spectrometry of inorganic transition-metal compounds. Part I: comparison between static ToF-SIMS and LA-FTICRMS, *Journal of Mass Spectrometry* **2006**, *41*, 527.

(132) Aubriet, F.; Muller, J.-F., Laser ablation mass spectrometry of inorganic transition metal compounds. Additional knowledge for the understanding of ion formation, *Journal of the American Society for Mass Spectrometry* **2008**, *19*, 488.

(133) Aubriet, F.; Maunit, B.; Muller, J. F., Speciation of chromium compounds by laser ablation/ionization mass spectrometry and a study of matrix effects, *International Journal of Mass Spectrometry* **2001**, *209*, 5.

(134) Santos, M.; Marçalo, J.; Pires de Matos, A.; Gibson, J. K.; Haire, R. G., Actinide-transition metal heteronuclear ions and their oxides: $\{IrUO\}^+$ as an analogue to uranyl, *European Journal of Inorganic Chemistry* **2006**, 3346.

(135) Hart-Smith, G.; Blanksby, S. J., Mass spectrometry, in *Polymer chemistry*; Barner-Kowollik, C., Gruendling, T., Falkenhagen, J., Weidner, S., Eds.; Wiley-VCH Verlag GmbH & Co. KGaA, **2012**, p 5.

(136) Hoffmann, E. d.; Strooban, V., *Mass spectrometry, principles and applications*; 3rd ed.; John Wiley & Sons Ltd, Chichester, **2007**.

(137) Aksenov, A. A.; Bier, M. E., The analysis of polystyrene and polystyrene aggregates into the mega Dalton mass range by cryodetection MALDI-TOF-MS, *Journal of the American Society for Mass Spectrometry* **2008**, *19*, 219.

(138) Makarov, A., Electrostatic axially harmonic orbital trapping: A high-performance technique of mass analysis, *Analytical Chemistry* **2000**, *72*, 1156.

(139) Hardman, M.; Makarov, A. A., Interfacing the orbitrap mass analyzer to an electrospray ion source, *Analytical Chemistry* **2003**, *75*, 1699.

(140) Schmid, D. G.; Grosche, P.; Bandel, H.; Jung, G., FTICR-Mass spectrometry for high-resolution analysis in combinatorial chemistry, *Biotechnology and Bioengineering* **2000**, *71*, 149.

(141) Hu, Q. Z.; Noll, R. J.; Li, H. Y.; Makarov, A.; Hardman, M.; Cooks, R. G., The Orbitrap: a new mass spectrometer, *Journal of Mass Spectrometry* **2005**, *40*, 430.

(142) Paul, W.; Steinwedel, H., Ein neues massenspektrometer ohne magnetfeld, *Zeitschrift Fur Naturforschung Section a-a Journal of Physical Sciences* **1953**, *8*, 448.

(143) Paul, W., Electromagnetic traps for charged and neutral particles, *Angewandte Chemie-International Edition in English* **1990**, *29*, 739.

(144) March, R. E. Quadrupole ion trap mass spectrometer; in *Encyclopedia of Analytical Chemistry*, Meyers, R. A., Ed., John Wiley & Sons Ltd, **2000**.

(145) March, R. E., An introduction to quadrupole ion trap mass spectrometry, *Journal of Mass Spectrometry* **1997**, *32*, 351.

(146) OConnor G.; Eavens, E. H., *Inductively coupled plasma mass spectrometry*, Sheffield Academy Press, **2000**; Vol. 138.

(147) Cooks, G.; Ouyang, Z.; Gao, L.; Fico, M.; Chappell, W., Ion traps and quadrupoles, *in 17th International Mass Spectrometry Conference*, Czech Republic, **2006**.

(148) Lawrence, E. Q.; Livingston, M. S., The production of high speed light ions without the use of high voltages, *Physical Review* **1932**, *40*, 19.

(149) Comisarow, M. B.; Marshall, A. G., The early development of Fourier transform ion cyclotron resonance (FT-ICR) spectroscopy, *Journal of Mass Spectrometry* **1996**, *31*, 581.

(150) Sommer, H.; Thomas, H. A.; Hipple, J. A., The measurment of E/M by cyclotron resonance, *Physical Review* **1951**, *82*, 697.

(151) Marshall, A. G.; Comisarow, M. B.; Parisod, G., Theory of fourier-transform ion-cyclotron resonance mass spectrometry - III.1 Relaxation and spectral line shape in FTICR spectroscopy, *Journal of Chemical Physics* **1979**, *71*, 4434.

(152) Comisarow M. B.; Marshall, A. G., Fourier-transform ion-cyclotron resonance spectroscopy, *Chemical Physics Letters* **1974**, *25*, 282.

(153) Madeira, P., A mass spectrometry study of compounds with environmental and biological interest, Ph.D. thesis, Faculdade de Ciências da Universidade de Lisboa, **2010**.

(154) Heeren, R. M. A.; Kleinnijenhuis, A. J.; McDonnell, L. A.; Mize, T. H., A mini-review of mass spectrometry using high-performance FTICR-MS methods, *Analytical and Bioanalytical Chemistry* **2004**, *378*, 1048.

(155) Marshall, A. G.; Hendrickson, C. L.; Jackson, G. S., Fourier transform ion cyclotron resonance mass spectrometry: A primer, *Mass Spectrometry Reviews* **1998**, *17*, 1.

(156) Barber, M.; Bordoli, R. S.; Elliott, G. J.; Sedgwick, R. D.; Tyler, A. N., Fast atom bombardment mass spectrometry, *Analytical Chemistry* **1982**, *54*, A645.

(157) Yamashita, M.; Fenn, J. B., Electrospray ion source - another variation on the free-jet theme, *Journal of Physical Chemistry* **1984**, *88*, 4451.

(158) Yamashita, M.; Fenn, J. B., Negative ion production with the electrospray ion source, *Journal of Physical Chemistry* **1984**, *88*, 4671.

(159) Karas, M.; Bachmann, D.; Bahr, U.; Hillenkamp, F., Matrix-assisted ultraviolet-laser desorption of nonvolatile compounds, *International Journal of Mass Spectrometry and Ion Processes* **1987**, *78*, 53.

(160) Busch, K.L.; Glish, G.L.; McLuckey, S. A., *Mass spectrometry: Techniques and applications of tandem mass spectrometry*; VCH, New York, **1989**.

(161) Sleno, L.; Volmer, D. A., Ion activation methods for tandem mass spectrometry, *Journal of Mass Spectrometry* **2004**, *39*, 1091.

(162) McLuckey, S. A., Principles of collisional activation in analytical mass spectrometry, *Journal of the American Society for Mass Spectrometry* **1992**, *3*, 599.

(163) Jennings, K. R., The changing impact of the collision-induced decomposition of ions on mass spectrometry, *International Journal of Mass Spectrometry* **2000**, *200*, 479.

(164) Shukla, A. K.; Futrell, J. H., Tandem mass spectrometry: dissociation of ions by collisional activation, *Journal of Mass Spectrometry* **2000**, *35*, 1069.

(165) Green, M. K.; Lebrilla, C. B., Ion-molecule reactions as probes of gas-phase structures of peptides and proteins, *Mass Spectrom. Rev.* **1997**, *16*, 53.

(166) Armentrout, P. B., Fundamentals of ion-molecule chemistry, *Journal of Analytical Atomic Spectrometry* **2004**, *19*, 571.

(167) Marçalo, J.; Pires de Matos, A., Organolanthanide chemistry in the gas phase, *Journal of Organometallic Chemistry* **2002**, *647*, 216.

(168) McIver, R. T., Chemical reactions without solvation, *Scientific American* **1980**, *243*, 186.

(169) Hamill, W. H., Ion-molecule reactions, *Journal of Chemical Education* **1959**, *36*, 346.

(170) Tanner, S. D.; Baranov, V. I.; Bandura, D. R., Reaction cells and collision cells for ICP-MS: a tutorial review, *Spectrochimica Acta Part B-Atomic Spectroscopy* **2002**, *57*, 1361.

(171) Ervin, K. M., Experimental techniques in gas-phase ion thermochemistry, *Chemical Reviews* **2001**, *101*, 391.

(172) Irikura, K. K. The ionization energy of CF_3: When does entropy matter in gas-phase reactions?, *Journal of the American Chemical Society* **1999**, 121, 7689.

(173) Ferguson, E. E.; Miller, T. M.; Viggiano, A. A. The reaction $HCl^+ + CF_4 \rightarrow HCF_4^+ + Cl$: Implications for the heat of formation of CF_3^+, *Journal of Chemical Physics* **2003**, 118, 2130.

(174) Linstrom J., and Mallard W.G., Eds., NIST Chemistry WebBook, NIST Standard Reference Database Number 69, National Institute of Standards and Technology, Gaithersburg MD, 20899, http://webbook.nist.gov, (retrieved May 19, 2015).

(175) Su, T.; Bowers, M.T.; Classical ion-molecule collision theory, M. T. Bowers, Ed., in Gas phase ion chemistry, Academic Press: New York, **1979**; Vol. 1, Chap. 3.

(176) Su, T.; Su, E. C. F.; Bowers, M. T., Ion-polar molecule collisions - conservation of angular momentum in average dipole orientation theory - AADO theory *Journal of Chemical Physics* **1978**, *69*, 2243.

(177) Su, T.; Chesnavich, W. J., Parametrization of the ion-polar molecule collision rate-constant by trajectory calculations, *Journal of Chemical Physics* **1982**, *76*, 5183.

(178) Chesnavich, W. J.; Su, T.; Bowers, M. T., Collisions in a non-central field - Variational and trajectory investigation of ion-dipole capture, *Journal of Chemical Physics* **1980**, *72*, 2641.

Chapter I

Introduction and background

Chapter II.

Fundamental aspects of actinyl chemistry

Chapter III.

Lanthanide and actinide cluster fragmentation and chemistry

Chapter IV.

Coordination of actinyl ions with amino acids in the gas phase

Chapter V.

Conclusions and final remarks

Chapter II.

Fundamental aspects of actinyl chemistry

II.1.Oxo-exchange of actinyl(V) and actinyl(VI) with water and methanol (II1)

II.2.Gas-phase uranyl, neptunyl and plutonyl: Hydration and oxidation (II2)

II.3.Gas-phase reactions of molecular oxygen with uranyl(V) anionic complexes: Synthesis and characterization of new superoxides of uranyl(VI) (II3)

II.4.Exploring the nature of actinide polysulfide ions (II4)

II.1 Oxo-exchange of gas-phase uranyl, neptunyl, and plutonyl with water and methanol

The content here described is based on the following publication:

***Lucena AF**, Odoh S, Zhao J, Marçalo J, Schreckenbach G, Gibson JK, Oxo-Exchange of Gas-Phase Uranyl, Neptunyl and Plutonyl with Water and Methanol., **Inorg. Chem.**, **2014**, 53 (4), 2163–2170. DOI: 10.1021/ic402824k*

I contributed with the experimental work and all the data retrieved from the mass spectra analysis. The theoretical calculations were carried out by Dr. Samuel Odoh, Mr. Jing Zhao and Dr. Georg Schreckenbach.

Abstract

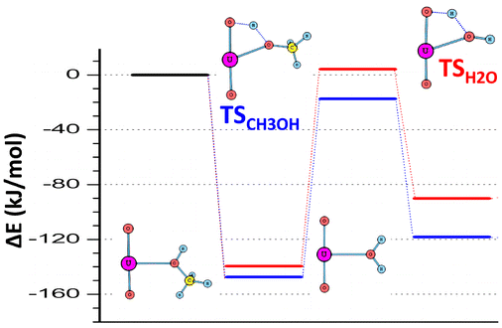

A challenge in actinide chemistry is activation of the strong bonds in the actinyl ions, AnO_2^+ and AnO_2^{2+}, where An = U, Np or Pu. Actinyl activation in oxo-exchange with water in solution is well established but the exchange mechanisms are unknown. Gas-phase actinyl oxo-exchange is a means to probe these processes in detail for simple systems, which are amenable to computational modeling. Gas-phase exchange reactions of UO_2^+, NpO_2^+, PuO_2^+ and UO_2^{2+} with water and methanol were studied by experiment and density functional theory (DFT); reported for the first time are experimental results for UO_2^{2+} and for methanol exchange, as well as exchange rate constants. Key findings are faster exchange of UO_2^{2+} versus UO_2^+ and faster exchange with methanol versus water; faster exchange of UO_2^+ versus PuO_2^+ was quantified. Computed potential energy profiles (PEPs) are in accord with the observed kinetics, validating the utility of DFT to model these exchange processes. The seemingly enigmatic result of faster exchange for uranyl, which has the strongest oxo-bonds, may reflect reduced covalency in uranyl as compared with plutonyl.

II.1.1. Introduction

The actinyl ions, AnO_2^+ and AnO_2^{2+}, are important solution species for An = U, Np and Pu, with UO_2^{2+} being a particularly prevalent species in the chemistry of uranium.[1] The An-O_{yl} bonds in these actinyls are strong, with bond dissociation energies, $D[OAn^{2+}\text{-}O]$, ranging from 403 kJ/mol for PuO_2^{2+} to 529 kJ/mol for UO_2^{2+}; the $D[OAn^{+}\text{-}O]$ bond energies are even greater.[2] Activation of the strong actinyl bonds is a challenge in synthetic actinide chemistry, with a particular focus having been on functionalization or cleavage of the U-O_{yl} bond in the UO_2^{2+} moiety,[3,4] such as has been accomplished in the conversion of UO_2^{2+} to $UO(O\text{-}tert\text{-butyl})_4$,[5] and the coordination of the O_{yl} by highly electrophilic Li.[6]

A special case of O_{yl} activation is oxo-exchange with an O-atom donor, principally with water as in Eqn. 1.

$$[AnO_2]^{+/2+} + H_2O^* \rightarrow [AnOO^*]^{+/2+} + H_2O \qquad (1)$$

In Eqn. 1 there is no net change in the chemical composition of the actinyl moiety but the exchange of O-atoms necessarily proceeds through a mechanism that disrupts the initial $[OAn{=}O]^{+/2+}$ moiety to result in the $[OAn{=}O^*]^{+/2+}$ product.[a] The first studies of oxo-exchange by Gordon and Taube in 1961 were performed by reaction between UO_2^{2+} and $H_2{}^{18}O$, followed by precipitation and gravimetric analysis.[7,8] These studies revealed that the rate of oxo-exchange depends on both the H^+ and UO_2^+ concentrations. The proton-dependence suggested a mechanism involving $UO_2(OH)^{2+}$, and the uranyl(V)-dependence indicated that UO_2^+ exchanges more rapidly than UO_2^{2+}. Oxo-exchange in solution can be more directly monitored using isotopic labeling in $H_2{}^{17}O$ and monitoring changes in the ^{17}O NMR spectra.[9,10] The rate of O_{yl}-exchange was determined for UO_2^{2+} by Rabideau under acidic conditions using ^{17}O NMR,[11] with the results in accord with those of Gordon and Taube. These studies revealed that the half-life for uranyl(VI) oxo-exchange under acidic conditions was on the order of ca. 10^4 hours, in accord with strong U-O bonds resistant to disruption. Clark et al. studied uranyl(VI) oxo-exchange under highly alkaline conditions and determined an exchange rate of 45 s^{-1},[12] which is several orders of magnitude faster than under acidic conditions and supports the role of hydroxides as key species for enabling facile exchange. Although a rate for direct comparison with uranyl(VI) was not obtained, Clark et al. demonstrated that neptunyl(VI) oxo-exchange was adequately fast that it was complete within two hours;[13] this is much faster than determined by Rabideau for neptunyl(VI) and plutonyl(VI) under acidic conditions.[14,15] Exchange studies for the pentavalent AnO_2^+ ions have revealed that the exchange rate of UO_2^+ is significantly faster than the exchange rates for NpO_2^+ and PuO_2^+,[7,14,15] a result in apparent discord with the stronger bonds in uranyl.

In recent years a number of theoretical studies have attempted to explain the observed exchange behavior of uranyl,[16-26] most of which invoke monomeric or polymeric hydroxide species comprising one or more uranyl moieties. Although several of these theoretical evaluations are substantiated by experimental observations, such as for example ^{17}O NMR magnetization transfer,[20] there is no detailed experimental information to directly confirm any of the proposed mechanisms. Given that it is not yet practical to reliably deduce molecular scale transformations involved in oxo-exchange in solution, we have undertaken to confront the issue in the rarified environment of the gas phase for bare $AnO_2^{+/2+}$ ions. In an initial report on this topic, the comparative exchange rates of UO_2^+, NpO_2^+ and PuO_2^+ with $H_2{}^{18}O$ in the gas phase were reported and rationalized by computed potential energy profiles.[27] In the present work we extend the experimental measurements to UO_2^{2+}, which can be compared with those for UO_2^+. Also reported here are the first quantitative values for the gas-phase oxo-exchange rate constants. Potential energy profiles (PEPs) computed by DFT are reported for all of the studied oxo-exchange processes. Furthermore, experimental studies of oxo-exchange with $CH_3{}^{18}OH$ were performed for comparison with the results for $H_2{}^{18}O$, and to further assess the reliability of the computational modeling to understand exchange mechanisms and efficiencies.

It had previously been proposed that the seemingly enigmatic more facile oxo-activation in exchange of uranyl(V) versus plutonyl(V) with water was a manifestation of greater covalency upon proceeding across the series of actinyls.[27] Although it is known that the actinyls exhibit substantial covalent bonding,[28-30] there is less consensus as to whether covalency in actinide bonds with ligands increases across the actinide series, particularly as the meaning of "covalency" is not necessarily well defined.[31-35] The issue of actinide covalency and its variation across the actinyl series is evaluated in this work by bonding analyses of the AnO_2^+ and AnO_2^{2+} species, with consideration as to the significance of the conventional concept of covalency for the particular case of the 5f actinides, as has been discussed by Kaltsoyannis.[35]

[a]In Eqn. 1, and throughout this paper, "O" represents the dominant (99.8%) naturally occurring ^{16}O isotope; O^* represents ^{17}O or ^{18}O, depending on the experimental method used to study oxo-exchange. The experiments reported here were performed using O-atom donors isotopically enriched in ^{18}O, as specified in the following sections.

II.1.2. Experimental procedures

The experimental approach has been described previously.[36-38] The actinide dioxide monopositive cations, AnO_2^+ where An = U, Np or Pu, were produced by laser desorption ionization (LDI) of solid alloys of Pt containing a few atom percent of the actinide.[37] There was sufficient oxygen contamination in the alloys that the AnO_2^+ ions were produced by LDI. The UO_2^{2+} reactant ion was prepared by oxidation of U^{2+} produced by LDI, using N_2O pulsed into the ICR cell, as described previously.[36] Bimolecular gas-phase reactions of isotopically labeled $H_2{}^{18}O$ and $CH_3{}^{18}O$ with actinyl cations were studied by Fourier transform ion cyclotron resonance mass spectrometry. Pseudo first-order reaction kinetics for oxo-exchange were determined by isolating and cooling the oxide ions, and measuring the time-dependence of the decay of reactant ions and in-growth of product ions. For comparative purposes, in addition to absolute rate constants, reaction efficiencies are reported as k/k_{COL}, where k_{COL} is the collisional rate constant derived from the modified variational transition-state/classical trajectory theory developed by Su and Chesnavich.[39]

II.1.3. Computational details

The scalar relativistic DFT calculations were performed with the NWChem[40] and ADF software suites.[41] The geometry optimizations, transition state searches and vibrational frequency analyses were carried out with the NWChem code. In these calculations, we employed the scalar relativistic Stuttgart small-core effective core potential[42-44] for the actinide atoms. The triple-ζ polarized (TZVP) basis sets of Godbout *et al*. were used for the oxygen and hydrogen atoms.[45] The B3LYP density functional was used in these calculations.[46,47] The combination of these pseudopotential and basis sets with this functional (labeled as B3LYP/TZVP level) has been shown to give accurate predictions of the properties and reaction energies of actinide complexes.[21,48-54] The geometry optimizations were performed without symmetry restrictions and were followed by vibrational frequency analysis to determine the local minima or saddle point natures of the optimized structures. The reported reaction energies were obtained by combining the electronic energies with the zero-point vibrational energy corrections.

The Mulliken charge and the binding energy analyses were carried out with the ADF code. The geometries obtained at the B3LYP/TZVP level were used in these calculations. The scalar Zeroth Order Regular Approximation (ZORA)[55,56] was used in conjunction with Slater Type Orbitals (STOs) of TZ2P quality. The decomposition of the binding energies was carried out with the Extended Transition State method.[57,58 59]

The calculations on the open-shell actinyl complexes were carried out with unrestricted wavefunctions. The ground electronic states of these species were all found to be of high-spin

character: U^{5+}: f^1, Np^{6+}: f^1, Np^{5+}: f^2, Pu^{6+}: f^2 and Pu^{5+}: f^3. The correct occupations of the 5f orbitals were obtained by swapping the unpaired electrons between various combinations of occupied and unoccupied orbitals.

II.1.4. Results and discussion

II.1.4.1 Experimental oxo-exchange reaction kinetics

The studied actinyl oxo-exchange reactions are given by Eqns. (2) – (5), where An = U, Np or Pu.

$$AnO_2^+ + H_2{}^{18}O \rightarrow AnO^{18}O^+ + H_2O \quad (2)$$

$$UO_2^{2+} + H_2{}^{18}O \rightarrow UO^{18}O^{2+} + H_2O \quad (3a)$$

$$UO_2^{2+} + H_2{}^{18}O \rightarrow UO^{18}O^+ + H_2O^+ \quad (3b)$$

$$AnO_2^+ + CH_3{}^{18}OH \rightarrow AnO^{18}O^+ + CH_3OH \quad (4)$$

$$UO_2^{2+} + CH_3{}^{18}OH \rightarrow UO^{18}O^+ + CH_3OH^+ \quad (5)$$

The measured pseudo-first order exchange rate constants, k, and efficiencies relative to the collisional rate constants, k/k_{COL}, are given in Table II.1.1 for oxo-exchange with water and in Table II.1.2 for oxo-exchange with methanol. A representative kinetics plot is shown in Figure II.1.1 for the reaction of UO_2^{2+} with $CH_3{}^{18}OH$, for which the three observed products are $UO^{18}O^+$ (oxo-exchange Eqn. 5; 15%), $UO^{18}OH^+$ ($^{18}OH^-$-transfer; 35%) and UO_2^+ (electron-transfer; 50%). Qualitative results previously reported for Eqn. 2 are in accord with the measured rate constants for the AnO^+ given in Table II.1.1.[27] Oxo-exchange was observed for UO_2^+ and UO_2^{2+} with both water and methanol; partial or complete electron-transfer from the neutral ligand to UO_2^{2+} occurred concomitant with oxo-exchange. The NpO_2^+ and PuO_2^+ ions did not exhibit oxo-exchange with either water or methanol to within the experimental detection limit of ~0.002% efficiency. Although hydrates were not observed, all three of the $AnO_2(CH_3{}^{18}OH)$ adducts were produced inefficiently ($k/k_{COL} \approx 0.001$); the appearance of methanol adducts, but not hydrates, is attributed to the greater capability of CH_3OH to dissipate coordination energy as compared with the smaller H_2O ligand.[60] Collision induced dissociation (CID) of the three $AnO_2(CH_3{}^{18}OH)^+$ resulted in

exclusively elimination of $CH_3{}^{18}OH$, confirming that oxo-exchange had not occurred in the adducts to produce $AnO^{18}O(CH_3OH)^+$.

The reaction of UO_2^{2+} with $H_2{}^{18}O$ resulted in three products, $UO^{18}O^{2+}$ (+ H_2O; Eqn. 3a; 35%), $UO^{18}O^+$ (+ H_2O^+; Eqn. 3b; 20%) and UO_2^+ (+ $H_2{}^{18}O^+$; 45%). The net oxo-exchange rate constant is given by the sum of those for Eqns. 3a and 3b.

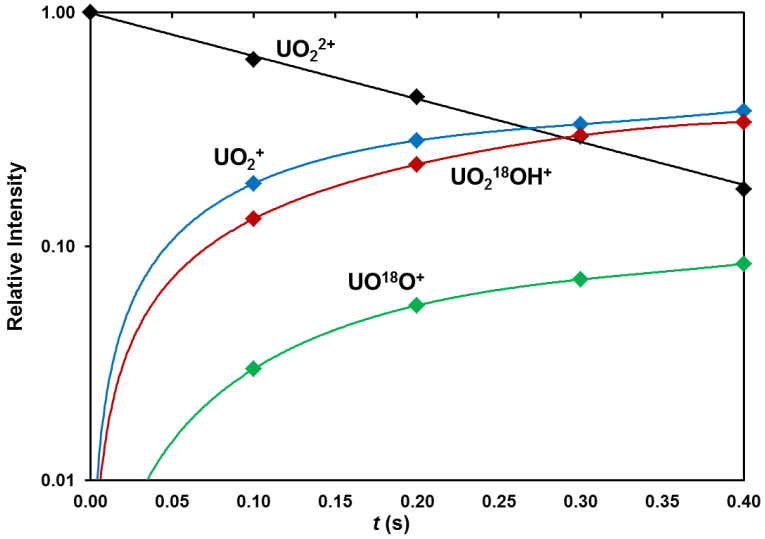

Figure II.1.1 Pseudo-first order kinetics plot for the reaction of UO_2^{2+} with $CH_3{}^{18}O$. The ingrowth of the three bimolecular reaction products, UO_2^+, $UO_2{}^{18}OH^+$ and $UO^{18}O^+$, results in the overall pseudo-first order linear decay of the semi-logaritmic plot of the decay of UO_2^{2+} vs. reaction time that provides a net rate constant $k = 1.350 \times 10^{-9}$ cm^3 molecule^{-1} s^{-1}. The partial rate constant for charge-transfer oxo-exchange to produce $UO^{18}O^+$ is $k = 0.203 \times 10^{-9}$ cm^3 molecule^{-1} s^{-1}.

Oxo-exchange of UO_2^{2+} with methanol was exclusively accompanied by electron-transfer from CH_3OH to produce $UO^{18}O^+$ (Eqn. 5). The occurrence of electron-transfer to all of the $UO^{18}O^{2+}$ oxo-exchange product with methanol but to only 20% of the oxo-exchange product with water reflects the higher ionization energy of water: IE[H_2O] = 12.6 eV; IE[CH_3OH] = 10.9 eV.[61] As discussed below, the oxo-exchange kinetics for UO_2^{2+} are determined by processes that occur in the dipositive uranyl species; charge-separation by electron transfer from the neutral O-atom donor occurs after exchange has occurred, during elimination of the water or methanol molecule from the exchange product, and therefore does not affect the observed exchange kinetics. Oxo-exchange of UO_2^+ is inefficient, 0.02% with water and 0.04% with methanol; oxo-exchange of UO_2^{2+} is significantly more efficient, 3.9% with water and 6.0% with methanol. The following key comparisons of oxo-exchange efficiencies (k/k_{COL}) are evident from the results in Tables II.1.1 and II.1.2:

• The oxo-exchange efficiencies of UO_2^+ and UO_2^{2+} with $CH_3{}^{18}O$ are greater than with $H_2{}^{18}O$ by a factor of 1.5-2.

• For both $H_2{}^{18}O$ and $CH_3{}^{18}OH$, the oxo-exchange efficiencies with UO_2^+ are more than 10 times greater than with NpO_2^+ or PuO_2^+.

• For both $H_2{}^{18}O$ and $CH_3{}^{18}OH$, the oxo-exchange efficiencies with UO_2^{2+} are more than 100 times greater than with UO_2^+.

Table II.1.1 Experimental results for actinyl oxo-exchange with $H_2{}^{18}O$.[a]

	k	k_{COL}	k/k_{COL}
UO_2^+ / Eqn. 2	0.00046	2.220	0.00021
NpO_2^+ / Eqn. 2	<0.00003	2.220	<0.00002
PuO_2^+ / Eqn. 2	<0.00003	2.219	<0.00002
UO_2^{2+} / Eqns. 3a and 3b[b]	0.171	4.439	0.039

[a]Rate constants, k and k_{COL} in units of 10^{-9} cm^3 molecule^{-1} s^{-1}, and reaction efficiencies, k/k_{COL}, for the oxo-exchange reactions given by Eqns. 2, 3 and 4.

[b]The exchange reactions accounted for 55% of the products. The product distribution was: 35% $UO^{18}O^{2+}$ (Eqn. 4a), 20% $UO^{18}O^+$ (Eqn. 4b), and 45% UO_2^+ (electron-transfer to $H_2{}^{18}O$). The reported k and k/k_{COL} are for the exchange reactions only; the total rate constant for exchange and charge-transfer is $k = 0.311\times10^{-9}$ cm^3 molecule^{-1} s^{-1}.

Table II.1.2 Experimental results for actinyl oxo-exchange with $CH_3{}^{18}OH$.[a]

	k	k_{COL}	k/k_{COL}
UO_2^+ / Eqn. 4	0.00070 (0.00106)[b]	1.694	0.00042 (0.00062)[b]
NpO_2^+ / Eqn. 4	<0.00003 (0.00176)[b]	1.695	<0.00002 (0.00104)[b]
PuO_2^+ / Eqn. 4	<0.00003 (0.00173)[b]	1.693	<0.00002 (0.00102)[b]
UO_2^{2+} / Eqn. 5 [c]	0.203	3.388	0.060

[a]Rate constants, k and k_{COL} in units of 10^{-9} cm3 molecule^{-1} s-1, and reaction efficiencies, k/k_{COL}, for the oxo-exchange reactions given by Eqns. 4 and 5.

[b]Inefficient formation of adducts, $AnO_2(CH_3{}^{18}OH)^+$, was observed with k and k/k_{COL} as given in parentheses.

[c]The values for k and k/k_{COL} are for oxo-exchange with charge separation according to Eqn. 5, which accounted for only 15% of the products of the reaction of $UO_2^{2+} + CH_3{}^{18}OH$. The other products were $UO_2(^{18}OH)^+$ (35%) and UO_2^+ (50%).

II.1.4.2 Potential energy profiles: Relationships to observed oxo-exchange kinetics

To understand the underlying basis for the observed k/k_{COL} differences between water and methanol, between the three AnO_2^+ (An = U, Np, Pu), and between UO_2^{2+} and UO_2^+, PEPs were computed for the pertinent exchange reactions, as discussed below.

Water versus methanol

The calculated PEPs for exchange of UO_2^+ with water and methanol are shown in Figure II.1.2, with the structures of reactants **1**, transition states **3** and **5**, and intermediates **2**, **4** and **6** shown in Figure II.1.3, and the energetics of reactions involving species **1-4** given in Tables II.1.3-II.1.5. In the initial reaction, **1-2**, the water or methanol ligand is coordinated to uranyl. This is followed by H-atom transfer from the ligand to the uranyl axial group, resulting in the formation of equatorial hydroxo or methoxy ligands (**2-4**), Figure II.1.3. The **2-4** reaction has the largest transition barrier **3** and is thus presumed to be the rate determining step, Figure II.1.2. Intermediate **4** then undergoes rearrangement reactions that lead to second intermediate **6**, which has an axial methoxy ligand in the reaction with methanol, and has interchanged the axial and equatorial hydroxo groups in the reaction with water. The rearrangement reactions **4-6** generally have very small transition state barriers. The oxo-exchange process is completed by the elimination of H_2O or CH_3OH from the association complex **2** to produce the reactant uranyl ion **1** in which an O atom has been replaced by an ^{18}O atom, $UO^{18}O^+$. As the only difference between the reactants and products is exchange of ^{16}O and ^{18}O atoms, the reactions are essentially thermoneutral.

The efficiency of a reaction under the near-thermal conditions of the experiments should correlate with the energy of the highest energy species along the PEP, which is **3** for the oxo-exchange

reactions: the farther below the reactant energies ($E[\mathbf{1}] \equiv 0$) the highest transition state lies, the more facile the reaction should be. The transition state **3** in Figure II.1.2 for the UO_2^+/water reaction lies slightly above the reactant asymptote, at 4.2 kJ/mol (Table II.1.5). This energy is within the computational uncertainty; furthermore, at 300 K the translational energy is ~4 kJ/mol and the reactants possess additional internal energy that may be available to surmount such minor barriers. It is thus reasonable that this oxo-exchange reaction proceeds albeit very inefficiently (k/k_{COL} = 0.00021). For the UO_2^+/methanol reaction, transition state **3** is ~22 kJ/mol lower than that for the water reaction and 17.5 kJ/mol below the reactants **1** (Figure 2, Table II.1.5). It is thus predicted that oxo-exchange of UO_2^+ with methanol should occur more efficiently than with water. The experimental result is that exchange with methanol occurs twice as efficiently as with water (Tables II.1.1 and II.1.2).

The conversion of the association complexes **2** to intermediates **4** results from cleaving an O-H bond in water or methanol to create a hydroxyl O-H bond. The comparative energetics of the **2-3-4** reactions should reflect the ease with which the O_{yl} can be functionalized by hydrogen atoms from water or methanol. The ease of H-atom transfer is given by the bond dissociation energies: D[HO-H] = 499 kJ/mol and D[CH_3O-H] = 436 kJ/mol.[61] These energies suggest that more facile transfer of an H-atom from methanol versus water should result in an energetically more favorable **2-4** transformation for the former, as indicated by both the computed PEPs and the measured reaction kinetics. The greater association energies **1-2** of actinyl ions with methanol versus water lower the energies of the entire PEPs for methanol, further contributing to a lowering of the height of transition state **3** relative to the reactant energies.

Uranyl(V), neptunyl(V) and plutonyl(V)

For NpO_2^+ and PuO_2^+, the PEPs and the structures of **1-6** are similar to those for UO_2^+ shown in Figures II.1.2 and II.1.3. For the oxo-exchange reactions of NpO_2^+ with water, and of PuO_2^+ with both water and methanol, the computed transition state **3** lies above the reactant energies (Table II.1.5) such that it is predicted that the reactions should not occur; these reactions are not observed to within the detection limit of $k/k_{COL} < 0.00002$. However, the transition state **3** for the NpO_2^+/methanol oxo-exchange reaction lies 12.4 kJ/mol below the reactant energies such that it is predicted that this reaction should occur; however, it was not observed to within the detection limit. This last example reveals that computed static PEPs cannot necessarily accurately predict all the details of dynamic processes such as oxo-exchange. It is feasible that the computed energy of transition state **3** for NpO_2^+/methanol could be in error, and/or that dynamic factors not considered in these computations preclude the reaction from occurring to within the detection

limit. An implication of the apparent failure of the computed PEP to predict the non-observation of the NpO_2^+/methanol oxo-exchange reaction is that the primary utility of static PEPs is for comparisons of general trends in reactivities, not for quantitative predictions of dynamic reaction rates. From the barrier heights **3** of the PEPs it is predicted that NpO_2^+ should generally be less susceptible than UO_2^+ towards oxo-exchange, in accord with the experimental results.

Table II.1.3 Energies (kJ/mol) obtained for the complex formation reactions (**1-2**) in the gas-phase.

	Water	Methanol	Ethanol	*i*-Propanol	*t*-Butanol
UO_2^+	-139.5	-147.4	-162.9	-166.0	-165.0
NpO_2^+	-139.6	-159.6	-180.3	-187.3	-186.6
PuO_2^+	-139.8	-157.9	-168.5	-175.2	-173.9
UO_2^{2+}	-279.8	-344.0	-381.3		

Table II.1.4 Energies (kJ/mol) obtained for the oxo-protonation (**2**-**4** reactions) of the axial oxo-atoms by the acidic protons of water and several alcohols.

	Water	Methanol	Ethanol	Propan-2-ol	t-Butanol
UO_2^+	49.4	29.2	32.9	34.2	30.2
NpO_2^+	73.1	63.6	79.2	81.7	78.2
PuO_2^+	114.5	102.7	114.0	110.8	106.4
UO_2^{2+}	92.7	76.5			

Table II.1.5. Transition state barriers heights (**3)** of the **2-4** reaction. The energies (kJ/mol) of **3** relative to the reactant asymptote, $AnO_2^{2+/+}$ + ROH, where R = H, CH_3, CH_3CH_2, $(CH_3)_2CH$ and $(CH_3)_3C$, are given in parenthesis.

	Water	Methanol	Ethanol	*i*-Propanol	*t*-Butanol
UO_2^+	143.7 (4.2)	129.9 (-17.5)	133.6 (-23.9)	138.3 (-27.8)	132.5 (-32.5)
NpO_2^+	147.4 (7.8)	147.2 (-12.4)	162.4 (-18.3)	164.1 (-23.2)	160.6 (-26.0)
PuO_2^+	177.2 (37.4)	173.7 (15.9)	181.5 (13.4)	180.8 (5.7)	176.6 (2.7)
UO_2^{2+}	227.9 (-51.9)	205.4 (-138.5)			

Monopositive uranyl versus dipositive uranyl

In the case of UO_2^{2+}, the oxo-exchange PEPs and structures of **1-6** are similar to those for UO_2^+. However, as is apparent from the PEPs shown in Figure II.1.4 for the reactions of UO_2^{2+} with water and methanol, the energies of the intermediates **2** and **4**, and the transition states **3** are very different from those for UO_2^+ (Figure II.1.2). For both water and methanol the transition state barrier heights for the **2**-**4** reaction are substantially greater for UO_2^{2+} (228 and 205 kJ/mol, Table II.1.5) than for UO_2^+ (144 and 130 kJ/mol). The greater reactivity of the UO_2^{2+} is attributed to the much more favorable initial association energy of dipositive versus monopositive uranyl, by 140 kJ/mol with water and by 197 kJ/mol with methanol, to produce intermediate **2**. Due to the greater association energies for the dipositive ions, the entire PEPs are shifted down. As a result, for UO_2^{2+} the transition states **3** lie well below the reactant energies, by 52 kJ/mol for water and by 139 kJ/mol for methanol, this despite that the **2-3** barriers are larger than for UO_2^+ (Figure II.1.4). It was previously predicted that oxo-exchange with water should be more efficient for UO_2^{2+} than UO_2^+ in the gas phase,[27] which has now been experimentally confirmed.

The PEPs in Figures II.1.2 and II.1.4 can be used to predict relative oxo-exchange rates of UO_2^+ and UO_2^{2+} with water and methanol in solution under conditions where the mechanism involves the species shown in Figure II.1.2, i.e., under acidic conditions. Perturbations to the energetics will be introduced by interactions with solvent species, but the general character of the PEPs should be similar in gas phase and solution. A significant difference is that the initial state in the gas phase reaction corresponds to the separated ion and neutral ligand whereas the initial state in solution corresponds to an ion that is already fully solvated. Accordingly, the energy provided by the association reaction **1-2** is absent in solution; the solution PEPs can be approximated as starting at the association intermediate **2** such that the **2-3** energy barrier heights provide a prediction of comparative oxo-exchange rates in solution. From the values in Table II.1.5 it is apparent that the **2-3** barrier heights are substantially greater for UO_2^{2+} than UO_2^+, by 84 kJ/mol with water and by 76 kJ/mol with methanol. Whereas gas-phase exchange is predicted and observed to proceed more efficiently for UO_2^{2+} with both water and methanol, the prediction is that solution exchange should be more efficient for UO_2^+ with both, as has been demonstrated in the case of water;[8] uranyl/methanol exchange in solution has not yet been reported.

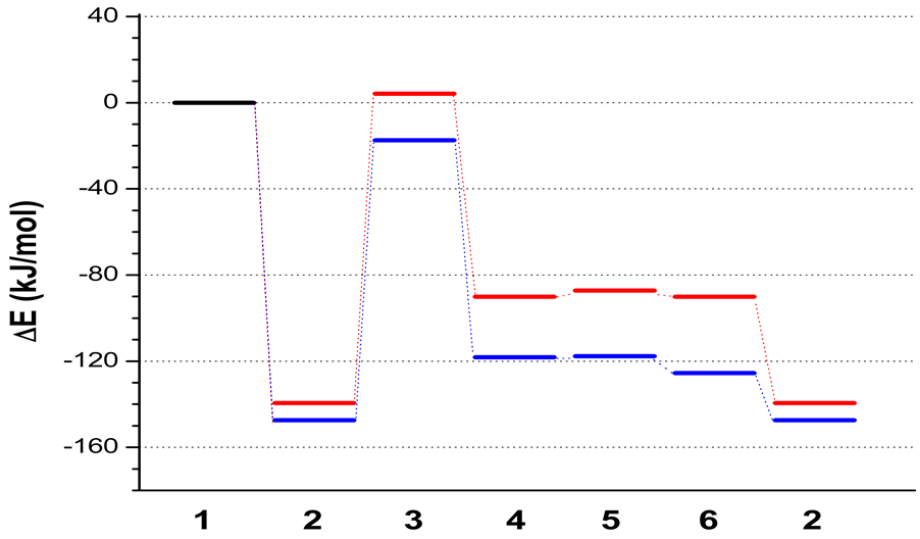

Figure II.1.2. Potential energy profiles for the oxo-exchange reactions of UO_2^+ with water (red) and methanol (blue). The energies are relative to the reactant asymptotes. The PEPs are similar for NpO_2^+ and PuO_2^+ although with substantially different energies. The structures of the species are shown in Figure II.1.3. The energies for **1-2** and **2-4** are in Tables II.1.3 and II.1.4, respectively. The transition state barrier heights (**3**) of the **2-4** reactions, as well as the energy of **3** relative to the reactant asymptote, are provided in Table II.1.5.

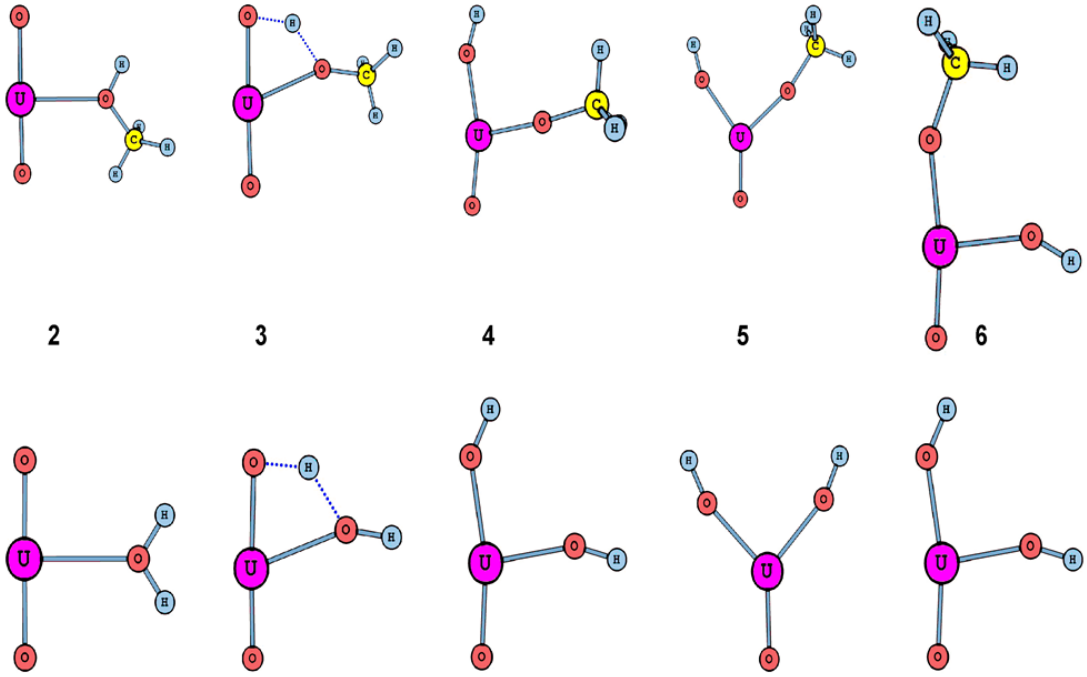

Figure II.1.3. Structures of the species found in the potential energy profiles for oxo-exchange between UO_2^+ and methanol (top) or water (bottom). The structures are essentially the same for those for the reactions of NpO_2^+, PuO_2^+ and UO_2^{2+}. Structure **1** in the PEPs corresponds to separated UO_2^{2+} and CH_3OH or H_2O.

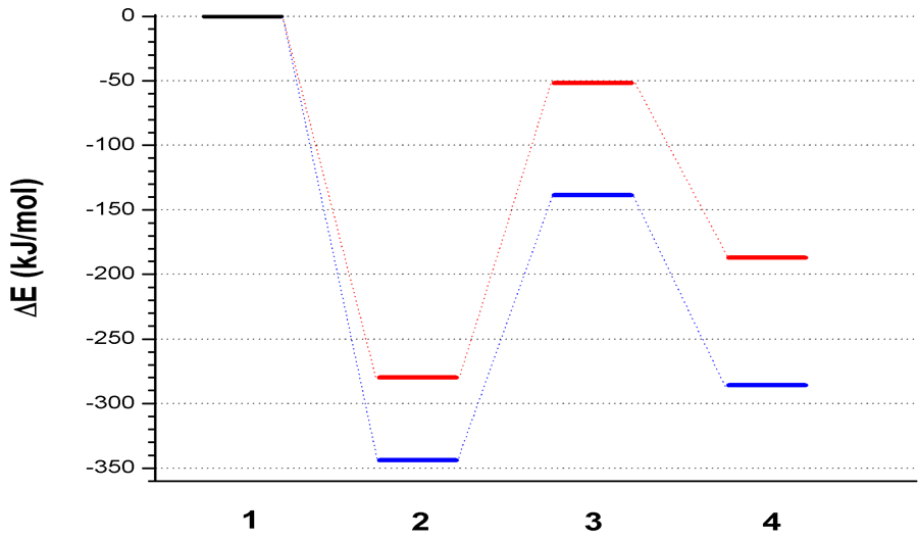

Figure II.1.4. Section of the potential energy profiles for the oxo-exchange reactions of UO_2^{2+} with water (red) and methanol (blue). The energies are relative to the reactant asymptotes. The energies for **1-2** and **2-4** are in Tables II.1.3 and II.1.4, respectively. The transition state barrier heights (**3**) of the **2-4** reactions, as well as the energy of **3** relative to the reactant asymptote, are in Table II.1.5. The structures of the species are essentially the same as for the UO_2^+ reactions, shown in Figure II.1.3.

II.1.4.3 Comparative PEPs for water, methanol and larger alcohols

Reaction energetics were computed for the reactions of AnO_2^+ (An = U, Np, Pu) and UO_2^{2+} with ethanol (EtOH), *i*-propanol (*i*-PrOH), and *t*-butanol (*t*-BuOH); the results are included in Tables II.1.3-II.1.5. The **1-2** association reactions are more exothermic for methanol versus water, and become increasingly exothermic as the size of the alcohol increases, Table II.13. The following gas-phase basicities of the neutral O-atom donors (kJ/mol), derived from proton affinities, provide an indication of the ability to bind to a positively charged metal center:[62]

H_2O / 660 < MeOH / 724 < EtOH / 746 < *i*-PrOH / 763 < *t*-BuOH / 772

The association energies between the actinyl cations and the O-atom donors generally correlate with these gas-phase basicities. The computed association energies for *i*-PrOH and *t*-BuOH for a given AnO_2^+ are nearly the same; although the basicity of *t*-BuOH is greater than that of *i*-PrOH, the difference is only 9 kJ/mol. The transition state **3** barrier heights relative to the reactant energies decrease from water to MeOH and continue to decrease as the size of the alcohol increases, an effect that can be largely attributed to the increasing **1-2** association energies and resulting lowering of the entire PEPs.

***NOTE** (not in the publication): A questionable assumption was made in evaluating the PEPs for the alcohol exchange reactions that should be noted here. Referring to Figures II.1.2 and II.1.3, it is*

*apparent that the PEP is symmetrical with respect to transition state **5** in the case of exchange with water such that the reverse reaction in which exchange occurs is provided by the computed PEP. However, this is not the case for exchange with alcohols where the first transition state **3** corresponds to transfer of a hydrogen atom to an O_{yl} while the transition state **3'**, not shown in the PEP, corresponds to transfer of a CH_3 group, or a larger alkyl group for the larger alcohols, from an O_{yl}. The transition states **3'** were not computed for the alcohol exchange reactions, with the implicit assumption that the barrier introduced by transition state **3** is rate determining. To more completely evaluate the comparative rates and barriers it is necessary to compute the transition states **3'** for the alcohol exchange reactions; these transition states may well be above transition state **3** and thus be rate determining. The additional computations are planned, and will be reported later.*

II.1.4.4 The possible role of covalency in actinyl exchange

It was previously postulated that the more facile oxo-exchange with water of UO_2^+ versus NpO_2^+ and PuO_2^+ could be attributed to increasing covalency across the actinyl series.[27] The rationale was that formation of intermediate **4** requires disruption of the An=O bond to produce two ionic An-OH bonds. The barrier to this process should not necessarily reflect the intrinsic An=O bond energy, but rather the covalent component of the bonding that is disrupted, which evidently increases from UO_2^+ to PuO_2^+. The same effect has now been revealed in the experimental results and the PEPs for exchange of the actinyl(V) ions with methanol. We here provide bonding analyses to evaluate covalency in the actinyls.

The axial An-O_{yl} bonds in the $AnO_2(CH_3OH)^+$ complexes **2** are calculated to be about 1.767, 1.757 and 1.739 Å long for the uranyl, neptunyl and plutonyl species, respectively. A similar contraction is obtained for the bare AnO_2^+ species (Table II.1.6), as well as for the $AnO_2(H_2O)^+$ complexes. These values are consistent with the actinide contraction and do not reveal any variation in bonding across the series.[63]

To evaluate the degree of covalency in the actinyls, we analyzed the binding energies of the $(O^{2-})_2$ to the An^{5+} and An^{6+} centers in AnO_2^+ and AnO_2^{2+}, with the results presented in Table II.1.6. The total binding energies increase from uranyl to neptunyl to plutonyl for both the +1 and +2 actinyls. It should be remarked that these intrinsic binding energies do not correspond to measured bond dissociation energies to neutral O and $An^{+/2+}$, which contrastingly *decrease* from $UO_2^{+/2+}$ to $NpO_2^{+/2+}$ to $PuO_2^{+/2+}$.[2] The computed orbital interaction energies of the $AnO_2^{+/2+}$ as $(O^{2-})_2$-An^{5+} and $(O^{2-})_2$-An^{6+} provide an indication of the transfer of electron density, which is evidently greatest for plutonyl in both the actinyl(V) and actinyl(VI) series. Experimental bond energies for the actinyls

correspond to the reactions: $An^{+/2+} + 2O \rightarrow AnO_2^{+/2+}$. Bond energy decomposition analysis[57-59] with An^{2+} and atomic oxygen fragments indicate orbital interaction energies of -4386, -4172 and -4903 kJ/mol for UO_2^{2+}, NpO_2^{2+} and PuO_2^{2+}, respectively (Table S2). For the analogous pentavalent AnO_2^+, the orbital interaction energies when An^+ is the considered fragment are calculated as -5003, -4299 and -4228 kJ/mol respectively. This alternative analysis to that presented in Table 6 suggests a *decrease* in covalency from UO_2^+ to PuO_2^+. It is apparent that these binding energy decompositions do not provide a clear indication of the extent of covalency.

The calculated Mulliken charges for the AnO_2^+ and AnO_2^{2+} complexes (Table II.1.7) may suggest increasing covalency across the actinyl series: the electron density at the axial oxygen atoms is largest for uranyl and smallest for plutonyl. The implication from this analysis is that the plutonyl complexes have the highest overlap (most covalent) of the 5f/6d orbitals with the atomic 2p orbitals of the axial oxygen atoms. In accord with this interpretation is the trend in the calculated Mayer bond orders[64,65] of the axial bonds: $Pu\text{-}O_{yl} > Np\text{-}O_{yl} > U\text{-}O_{yl}$ (Table II.1.8). However, the Mayer bond orders increase by only 0.03 from $UO_2^{+/2+}$ to $PuO_2^{+/2+}$, which is too small a change to clearly indicate an increase in covalency.

Analysis of the An-O bonds in the actinyl moieties with the atoms in molecules (AIM) approach[66,67] shows little difference in the Laplacian of the electron density obtained at the bond critical points between the actinide and oxygen atoms of the AnO_2^{2+} and AnO_2^+ species (Figure S2).

However, Prodan et al. have proposed that covalency increases across the series of actinide dioxides due to a 5f-O2p orbital energy degeneracy, not due to the conventional concept of covalency as an increase in charge density between atoms.[31] Kaltsoyannis has discussed this non-traditional concept of covalency in the particular context of organoactinide complexes, with caution that "care must be taken when using quantum chemistry to assess metal-ligand covalency in this part of the periodic table."[35] We concur with this assessment. In summary, the computed orbital interaction energies seem to provide conflicting indications of covalency, the Mulliken charges may indicate an increase in covalency from uranyl to plutonyl, and the small changes in the Mayer bond orders are essentially inconclusive regarding a change in covalency from uranyl to plutonyl. However, the experimental results and computed PEPs are consistent with such an increase in covalency, as has been discussed previously.[27] The increase in the **2**-**3**-**4** energy in the PEPs from uranyl to plutonyl is clearly manifested in the experimental results. Conversion of **2** to **4** disrupts the An=O bond to produce two less directional and more ionic An-OR bonds (R = H or CH_3). Despite that $D[OU\text{-}O]^+ = 741\pm14$ kJ/mol is larger than $D[OPu\text{-}O]^+ = 509\pm38$ kJ/mol,[2] the **2**-**4** barrier for UO_2^+ (144 kJ/mol) is lower than for PuO_2^+ (177 kJ/mol)—greater resistance of the weaker $[OPu\text{-}O]^+$ towards disruption is consistent with greater directionality, in this case linearity,

and thus covalency. The present results do not establish the postulated increase in covalency from uranyl to plutonyl, but are at least consistent with it.

Table II.1.6. Calculated lengths and strengths (kJ/mol) of the An-O_{yl} bonds. The latter is defined as the $(O^{2-})_2$-An^{5+} and $(O^{2-})_2$-An^{6+} binding energies for the pentavalent and hexavalent species respectively.

	An-O_{yl} (Å)	**Pauli Repulsion Interaction Energy**	**Electrostatic Interaction Energy**	**Orbital Interaction Energy**	**Total**
UO_2^+	1.760	6714	-16770	-5451	-15507
NpO_2^+	1.741	6827	-16977	-5930	-16080
PuO_2^+	1.723	6932	-17165	-6307	-16540
UO_2^{2+}	1.701	7645	-20279	-7473	-20107
NpO_2^{2+}	1.697	7814	-20302	-8216	-20704
PuO_2^{2+}	1.683	7858	-20467	-8843	-21452

Table II.1.7. Calculated Mulliken atomic charges on the actinide atoms of AnO_2^+, $AnO_2(H_2O)^+$ and $AnO_2(CH_3OH)^+$. The charges on the axial oxygen atoms are given in parenthesis.

	Pentavalent			**Hexavalent**	
	AnO_2^+	$AnO_2(H_2O)^+$	$AnO_2(CH_3OH)^+$	AnO_2^{2+}	$AnO_2(CH_3OH)^{2+}$
U	2.10 (-0.55)	2.03 (-0.58)	2.03 (-0.60)	2.72 (-0.36)	2.55 (-0.44)
Np	2.01 (-0.51)	1.96 (-0.55)	1.96 (-0.56)	2.60 (-0.30)	[a]
Pu	1.97 (-0.48)	1.94 (-0.53)	1.93 (-0.54)	2.53 (-0.26)	2.36 (-0.37)

[a] Value not computed.

Table II.1.8. Calculated Mayer bond orders of the An-O_{yl} bonds of the $AnO_2^{2+/+}$, $AnO_2(H_2O)^+$ and $AnO_2(CH_3OH)^{2+/+}$ species.

	Pentavalent			**Hexavalent**	
	AnO_2^+	$AnO_2(H_2O)^+$	$AnO_2(CH_3OH)^+$	AnO_2^{2+}	$AnO_2(CH_3OH)^{2+}$
U	2.15	2.11	2.10	2.29	2.21
Np	2.18	2.14	2.12	2.31	2.22
Pu	2.18	2.15	2.13	2.32	2.23

II.1.5. Conclusions

It had previously been demonstrated that oxo-exchange reactions of actinyls in the gas phase could illuminate mechanisms in solution, specifically under acidic conditions where hydrolysis is suppressed and the dominant species are AnO_2^+ and/or AnO_2^{2+}.[27] The comparative gas-phase oxo-exchange rates previously reported for UO_2^+, NpO_2^+ and PuO_2^+ with H_2O have now been quantified with the pseudo-first order rate constant for UO_2^+, and limits for NpO_2^+ and PuO_2^+. It was previously predicted that gas-phase exchange with UO_2^{2+} should be faster than with UO_2^+. In the present work it was demonstrated that exchange with UO_2^{2+} is at least 100 times faster than with UO_2^+, validating the prediction.

Oxo-exchange of UO_2^+, NpO_2^+, PuO_2^+ and UO_2^{2+} with methanol was studied in the present work. The PEPs for exchange with water and methanol were computed, revealing similar mechanisms. The largest barrier on the reaction pathways is to the first intermediate bis-hydroxy or hydroxy-methoxy species produced by transfer of an H-atom from a coordinated water or methanol molecule to an actinyl oxo-group. These barrier heights are lower for methanol versus water, an effect attributed primarily to cleavage of the weaker CH_3O-H bond as compared with the HO-H bond. The measured rate constants reveal faster exchange with methanol versus water, in accord with the computed PEPs, and providing validation of the DFT methodology.

Gas-phase results can be used to predict comparative exchange rates in solution. A crucial difference between gas and solution is that the association energies between actinyl ions available to enable the reactions in gas phase are absent in solution. Gas-phase kinetics of bimolecular reactions are related to the energy of the highest barrier relative to the energies of the reactants: for barriers significantly above the reactant energies, the reaction should not proceed; for barriers significantly below the reactant energies, the reaction should proceed; for reactions with barriers close to the reactant energies (e.g. within ca. 10 kJ/mol), predictions are less reliable. In solution phase it is the absolute height of the barrier that predicts relative kinetics. Thus it is predicted that for water, gas-phase exchange should be more efficient with UO_2^+ than with UO_2^{2+}, whereas the opposite relative rates are predicted in solution; these comparative kinetics have now been demonstrated. It is predicted that UO_2^+ and UO_2^{2+} should exchange more efficiently with methanol than water in both gas and solution phases; this has been demonstrated in gas phase; actinyl/methanol exchange in solution has yet to be studied.

The experimental result and DFT prediction that oxo-exchange should be decreasingly efficient from UO_2^+ to PuO_2^+ can be taken to suggest greater covalency of the actinyl bonds upon proceeding across the actinyl series. Although analysis of actinyl binding energies was

inconclusive in evaluating covalency, the computed Mulliken atomic charges are in accord with a covalency increase across the actinyl series. Further analysis is needed to clarify this covalency issue.[35]

Acknowledgements

This work was supported by Fundação para a Ciência e a Tecnologia/Portugal (PhD grant SFRH/BD/70475/2010 to A.F.L.), by the Natural Sciences and Engineering Research Council of Canada (NSERC, G.S.), and by the U.S. Department of Energy, Office of Science, Office of Basic Energy Sciences, Division of Chemical Sciences, Geosciences and Biosciences, Heavy Element Chemistry Program at LBNL under Contract Number DE-AC02-05CH11231 (J.K.G.).

References

(1) Morss, L. R.; Edelstein, N. M.; Fuger, J. The chemistry of the actinide and transactinide elements; Springer, Dordrecht, **2006**.

(2) Marçalo, J.; Gibson, J. K., Gas-phase energetics of actinide oxides: an assessment of neutral and cationic monoxides and dioxides from thorium to curium, *Journal of Physical Chemistry A* **2009**, 113, 12599.

(3) Fortier, S.; Hayton, T. W., Oxo ligand functionalization in the uranyl ion (UO_2^{2+}), *Coordination Chemistry Reviews* **2010**, 254, 197.

(4) Baker, R. J., New reactivity of the uranyl(VI) ion, *Chemistry - A European Journal* **2012**, 18, 16258.

(5) Burns, C. J.; Sattelberger, A. P., Uranium(VI)-oxo-alkoxide cluster synthesis via ligand redistribution, *Inorganic Chemistry* **1988**, 27, 3692.

(6) Arnold, P. L.; Pecharman, A. F.; Hollis, E.; Yahia, A.; Maron, L.; Parsons, S.; Love, J. B., Uranyl oxo activation and functionalization by metal cation coordination, *Nature Chemistry* **2010**, 2, 1056.

(7) Gordon, G.; Taube, H., The exchange reaction between uranyl ion and water in perchloric acid solution, *Journal of Inorganic Nuclear Chemistry* **1961**, 19, 189.

(8) Gordon, G.; Taube, H., The Uranium(V)-catalysed exchange reaction between uranyl ion and water in perchloric acid solution, *Journal of Inorganic Nuclear Chemistry* **1961**, 16, 272.

(9) Rabideau, S. W.; Hecht, H. G., Oxygen-17 NMR Linewidths as influenced by proton exchange in water, *The Journal of Chemical Physics* **1967**, 47, 544.

(10) Jurisson, S. S.; Murmann, R. K., Oxygen exchange on ReO_4^- and TcO_4^- by O-17-NMR, *Inorganic Chemistry* **1999**, 38, 3919.

(11) Rabideau, S. W., Oxygen-17 Nuclear magnetic resonance in uranyl ion, *Journal of Physical Chemistry* **1967**, 71, 2747.

(12) Clark, D. L.; Conradson, S. D.; Donohoe, R. J.; Keogh, D. W.; Morris, D. E.; Palmer, P. D.; Rogers, R. D.; Tait, C. D., Chemical speciation of the uranyl ion under highly alkaline conditions. Synthesis, structures, and oxo ligand exchange dynamics, *Inorganic Chemistry* **1999**, 38, 1456.

(13) Clark, D. L.; Conradson, S. D.; Donohoe, R. J.; Gordon, P. L.; Keogh, D. W.; Palmer, P. D.; Scott, B. L.; Tait, C. D., Chemical speciation of neptunium(VI) under strongly alkaline conditions. Structure, composition, and oxo ligand exchange, *Inorganic Chemistry* **2013**, 52, 3547.

(14) Rabideau, S. W., Oxygen exchange reactions of NpO_2^{+2} and NpO_2^+ with water, *Journal of Physical Chemistry* **1963**, 67, 2655.

(15) Masters, B. J.; Rabideau, S. W., Exchange of plutonyl and solvent water oxygen, *Inorganic Chemistry* **1963**, 2, 1.

(16) Tsushima, S., "yl"-Oxygen exchange in uranyl(VI) Ion: A mechanism involving $(UO_2)_2$(mu-OH)$_2^{2+}$ via U-O-yl-U bridge formation, *Inorganic Chemistry* **2012**, 51, 1434.

(17) Wang, D. Q.; van Gunsteren, W. F.; Chai, Z. F., Recent advances in computational actinoid chemistry, *Chemical Society Reviews* **2012**, 41, 5836.

(18) Bühl, M.; Wipff, G., Insights into uranyl chemistry from molecular dynamics simulations, *Chemphyschem* **2011**, 12, 3095.

(19) Bühl, M.; Schreckenbach, G., Oxygen exchange in uranyl hydroxide via two "nonclassical" ions, *Inorganic Chemistry* **2010**, 49, 3821.

(20) Szabo, Z.; Grenthe, I., On the mechanism of oxygen exchange between uranyl(VI) oxygen and water in strongly alkaline solution as studied by O-17 NMR magnetization transfer, *Inorganic Chemistry* **2010**, 49, 4928.

(21) Schreckenbach, G.; Shamov, G. A., Theoretical actinide molecular science, *Accounts of Chemical Research* **2010**, 43, 19.

(22) Real, F.; Vallet, V.; Wahlgren, U.; Grenthe, I., Ab initio study of the mechanism for photoinduced yl-oxygen exchange in uranyl(VI) in acidic aqueous solution*, Journal of the American Chemical Society* **2008**, 130, 11742.

(23) Shamov, G. A.; Schreckenbach, G., Theoretical study of the oxygen exchange in uranyl hydroxide. An old riddle solved? *Journal of the American Chemical Society* **2008**, 130, 13735.

(24) Szabo, Z.; Grenthe, I., Reactivity of the "yl"-bond in Uranyl(VI) complexes. 1. Rates and mechanisms for the exchange between the trans-dioxo oxygen atoms in $(UO2)_2(OH)_2^{2+}$ and mononuclear $UO_2(OH)_n^{2-n}$ complexes with solvent water, *Inorganic Chemistry* **2007**, 46, 9372.

(25) Wahlin, P.; Danilo, C.; Vallet, V.; Real, F.; Flament, J. P.; Wahlgren, U., An investigation of the accuracy of different DFT functionals on the water exchange reaction in hydrated uranyl(VI) in the ground state and the first excited state, *Journal of Chemical Theory Computation* **2008**, 4, 569.

(26) Schreckenbach, G.; Hay, P. J.; Martin, R. L., Theoretical study of stable trans and cis isomers in $[UO2(OH)_4]^{2-}$ using relativistic density functional theory, *Inorganic Chemistry* **1998**, 37, 4442.

(27) Rios, D.; Michelini, M. C.; Lucena, A. F.; Marçalo, J.; Gibson, J. K., On the origins of faster oxo exchange for uranyl(V) versus plutonyl(V), *Journal of the American Chemical Society* **2012**, 134, 15488.

(28) Glueckauf, E.; Mckay, H. A. C., Possible f-shell covalency in the actinide elements, *Nature* **1950**, 166, 605.

(29) Denning, R. G., Electronic structure and bonding in actinyl ions and their analogs, *Journal of Physical Chemistry A* **2007**, 111, 4125.

(30) Neidig, M. L.; Clark, D. L.; Martin, R. L., Covalency in f-element complexes, *Coordination Chemistry Reviews* **2013**, 257, 394.

(31) Prodan, I. D.; Scuseria, G. E.; Martin, R. L., Covalency in the actinide dioxides: Systematic study of the electronic properties using screened hybrid density functional theory, *Physical Review B* **2007**, 76.

(32) Ingram, K. I. M.; Tassell, M. J.; Gaunt, A. J.; Kaltsoyannis, N., Covalency in the f element-chalcogen bond. Computational studies of $M[N(EPR)_2)_2]_3$ (M = La, Ce, Pr, Pm, Eu, U, Np, Pu, Am, Cm; E = O, S, Se, Te; R = H, (i)Pr, Ph), *Inorganic Chemistry* **2008**, 47, 7824.

(33) Tassell, M. J.; Kaltsoyannis, N., Covalency in $AnCp_4$ (An = Th-Cm): a comparison of molecular orbital, natural population and atoms-in-molecules analyses, *Dalton Transactions* **2010**, 39, 6719.

(34) Kirker, I.; Kaltsoyannis, N., Does covalency really increase across the 5f series? A comparison of molecular orbital, natural population, spin and electron density analyses of $AnCp_3$ (An = Th-Cm; Cp = η^5-C_5H_5), *Dalton Transactions* **2011**, 40, 124.

(35) Kaltsoyannis, N., Does covalency increase or decrease across the actinide series? Implications for minor actinide partitioning, *Inorganic Chemistry* **2013**, 52, 3407.

(36) Gibson, J. K.; Haire, R. G.; Santos, M.; Marçalo, J.; Pires de Matos, A., Oxidation studies of dipositive actinide ions, An^{2+} (An = Th, U, Np, Pu, Am) in the gas phase: Synthesis and characterization of the isolated uranyl, neptunyl, and plutonyl ions UO_2^{2+} (g), NpO_2^{2+} (g), and PuO_2^{2+} (g), *Journal of Physical Chemistry A* **2005**, 109, 2768.

(37) Santos, M.; Marçalo, J.; Pires de Matos, A.; Gibson, J. K.; Haire, R. G., Gas-phase oxidation reactions of neptunium and plutonium ions investigated via Fourier Transform Ion Cyclotron Resonance Mass Spectrometry, *Journal of Physical Chemistry A* **2002**, 106, 7190.

(38) Marçalo, J.; Santos, M.; Pires de Matos, A.; Gibson, J. K., Molecular uranates: Laser synthesis of uranium oxide anions in the gas phase, *Inorganic Chemistry* **2009**, 48, 5055.

(39) Su, T.; Chesnavich, W. J., Parametrization of the ion-polar molecule collision rate-constant by trajectory calculations, *The Journal of Chemical Physics* **1982**, 76, 5183.

(40) Valiev, M.; Bylaska, E. J.; Govind, N.; Kowalski, K.; Straatsma, T. P.; Van Dam, H. J. J.; Wang, D.; Nieplocha, J.; Apra, E.; Windus, T. L.; de Jong, W., NWChem: A comprehensive and

scalable open-source solution for large scale molecular simulations, *Computer Physics Communications* **2010**, 181, 1477.

(41) te Velde, G.; Bickelhaupt, F. M.; van Gisbergen, S. J. A.; Fonseca Guerra, C.; Baerends, E. J.; Snijders, J. G.; Ziegler, T., Chemistry with ADF, *Journal of Computational Chemistry* **2001**, 22, 931.

(42) Bergner, A.; Dolg, M.; Küchle, W.; Stoll, H.; Preuss, H., AB-initio energy-adjusted pseudopotentials for elements of groups 13-17, *Molecular Physics* **1993**, 80, 1431.

(43) Küchle, W.; Dolg, M.; Stoll, H.; Preuss, H., Ab initio pseudopotentials for Hg through RN .1. Parameter sets and atomic calculations, *Molecular Physics* **1991**, 74, 1245.

(44) Küchle, W.; Dolg, M.; Stoll, H.; Preuss, H., Energy-adjusted pseudopotentials for the actinides – parameter sets and test calculations for thorium monoxide, *The Journal of Chemical Physics* **1994**, 100, 7535.

(45) Godbout, N.; Salahub, D. R.; Andzelm, J.; Wimmer, E., Optimization of Gaussian-type basis-sets for local spin-density functional calculations. 1. Boron through neon, optimization technique and validation, *Canadian Journal of Chemistry* **1992**, 70, 560.

(46) Becke, A. D., Density-functional thermochemistry. III. The role of exact exchange, *The Journal of Chemical Physics* **1993**, 98, 5648.

(47) Stephens, P. J.; Devlin, F. J.; Chabalowski, C. F.; Frisch, M. J., Ab-Initio calculation of vibrational absorption and circular-dichroism spectra using density-functional force-fields, *Journal of Physical Chemistry* **1994**, 98, 11623.

(48) de Jong, W. A.; Apra, E.; Windus, T. L.; Nichols, J. A.; Harrison, R. J.; Gutowski, K. E.; Dixon, D. A., Complexation of the carbonate, nitrate, and acetate anions with the uranyl dication: Density functional studies with relativistic effective core potentials, *Journal of Physical Chemistry A* **2005**, 109, 11568.

(49) de Jong, W. A.; Harrison, R. J.; Nichols, J. A.; Dixon, D. A., Fully relativistic correlated benchmark results for uranyl and a critical look at relativistic effective core potentials for uranium, *Theoretical Chemistry Accounts* **2001**, 107, 22.

(50) Odoh, S. O.; Schreckenbach, G., Performance of relativistic effective core potentials in DFT calculations on actinide compounds, *Journal of Physical Chemistry A* **2010**, 114, 1957.

(51) Odoh, S. O.; Schreckenbach, G., Theoretical study of the structural properties of plutonium(IV) and (VI) complexes, *Journal of Physical Chemistry A* **2011**, 115, 14110.

(52) Odoh, S. O.; Walker, S. M.; Meier, M.; Stetefeld, J.; Schreckenbach, G., QM and QM/MM studies of uranyl fluorides in the gas and aqueous phases and in the hydrophobic cavities of tetrabrachion, *Inorganic Chemistry* **2011**, 50, 3141.

(53) Shamov, G. A.; Schreckenbach, G., Density functional studies of actinyl aquo complexes studied using small-core effective core potentials and a scalar four-component relativistic method, *Journal of Physical Chemistry A* **2005**, 109, 10961.

(54) Shamov, G. A.; Schreckenbach, G.; Vo, T. N., A comparative relativistic DFT and ab initio study on the structure and thermodynamics of the oxofluorides of uranium(IV), (V) and (VI), *Chemistry – A European Journal* **2007**, 13, 4932.

(55) van Lenthe, E.; Baerends, E. J.; Snijders, J. G., Relativistic regular 2-component hamiltonians, *The Journal of Chemical Physics* **1993**, 99, 4597.

(56) van Lenthe, E.; Ehlers, A.; Baerends, E. J., Geometry optimizations in the zero order regular approximation for relativistic effects, *The Journal of Chemical Physics* **1999**, 110, 8943.

(57) Mitoraj, M. P.; Michalak, A.; Ziegler, T., A combined charge and energy decomposition scheme for bond analysis, *Journal of Chemical Theory and Computation* **2009**, 5, 962.

(58) Mitoraj, M. P.; Michalak, A.; Ziegler, T., On the nature of the agostic bond between metal centers and beta-hydrogen atoms in alkyl complexes. An analysis based on the extended transition state method and the natural orbitals for chemical valence scheme (ETS-NOCV), *Organometallics* **2009**, 28, 3727.

(59) Ziegler, T.; Rauk, A., Calculation of bonding energies by Hartree-Fock Slater method .1. Transition-State Method, *Theoretical Chemistry Accounts* **1977**, 46, 1.

(60) Rutkowski, P. X.; Michelini, M. C.; Bray, T. H.; Russo, N.; Marçalo, J.; Gibson, J. K., Hydration of gas-phase ytterbium ion complexes studied by experiment and theory, *Theoretical Chemistry Accounts* **2011**, 129, 575.

(61) Lias, S. G.; Bartmess, J. E.; Liebmann, J. F.; Holmes, J. L.; Levin, R. D.; Mallard, W. G. Gas-phase ion and neutral thermochemistry; American Institute of Physics, New York, **1988**.

(62) Hunter, E. P.; Lias, S. G. In NIST Chemistry WebBook, NIST Standard Reference Database Number 69; Linstron, P. J., Mallard, W. G., Eds.; National Institute of Standards and Technology: Gaithersburg, MD.

(63) Wang, S. A.; Villa, E. M.; Diwu, J. A.; Alekseev, E. V.; Depmeier, W.; Albrecht-Schmitt, T. E., Role of anions and reaction conditions in the preparation of uranium(VI), neptunium(VI), and plutonium(VI) borates, *Inorganic Chemistry* **2011**, 50, 2527.

(64) Mayer, I., Bond order and valence – relations to mulliken population analysis, *International Journal of Quantum Chemistry* **1984**, 26, 151.

(65) Mayer, I., Bond orders and valences from ab initio wave-functions, *International Journal of Quantum Chemistry* **1986**, 29, 477.

(66) Rodriguez, J. I.; Bader, R. F. W.; Ayers, P. W.; Michel, C.; Gotz, A. W.; Bo, C., A high performance grid-based algorithm for computing QTAIM properties, *Chemical Physics Letters* **2009**, 472, 149.

(67) Rodriguez, J. I.; Koster, A. M.; Ayers, P. W.; Santos-Valle, A.; Vela, A.; Merino, G., An efficient grid-based scheme to compute QTAIM atomic properties without explicit calculation of zero-flux surfaces, *Journal Computational Chemistry* **2009**, 30, 1082.

Supporting Information

Experimental Details

The experimental approach has been described previously.[1-4]. A summary of the methods, and details specific to the present work, is included here. The experiments were performed in a Finnigan FT/MS 2001-DT FTICR mass spectrometer, equipped with a 3 Tesla superconducting magnet, interfaced with a Spectra-Physics Quanta-Ray GCR-11 Nd:YAG laser operated at the fundamental wavelength (1064 nm), and controlled by a Finnigan Venus Odyssey data system.

The ions were produced by LDI from the solids probe of the spectrometer. All ion manipulations and analyses were performed in the source cell of the dual cell instrument. Isolation of ions was achieved using single frequency, frequency sweep, or SWIFT excitation[5]. Secondary and tertiary reactions after initial product formation were studied by imposing an initial reaction period and then isolating and studying sequential products by MS^n.

Isotopically substituted methanol, $CH_3{}^{18}OH$, or water, $H_2{}^{18}O$, was introduced into the spectrometer as supplied after degassing, through a leak valve, to pressures in the range of (1-3) x 10^{-7} Torr. The isotopic purities were specified by the vendor (Aldrich) as 95% $CH3{}^{18}OH$ and 97% $H_2{}^{18}O$, which were confirmed in situ by electron ionization (EI) mass spectra; EI confirmation of the reagents in use was frequently

performed during the experiments. The neutral reagent pressures were measured with a Bayard-Alpert type ionization gauge and calibrated using standard reactions of methane[6] and acetone[7] ions, a procedure that provides pressures in the ICR cell. The gauge readings were corrected for the relative sensitivities of the reagent.[8]. The background in the mass spectrometer mainly consisted of water and air, with base pressures of (1-2) x 10^{-8} Torr, which is about one order of magnitude lower than the reagent pressure. Nonetheless, care was taken to minimize the potential interference of reactions with residual water and oxygen in the ICR cell. This was accomplished by using long pumping periods after the solids probe was inserted into the high-vacuum chamber but before introducing the reagents. The measurements were furthermore verified by comparisons with reactions that occurred under background conditions, which were found to be insignificant. The reactant ions were thermalized by collisions with argon, which was introduced into the spectrometer through pulsed valves to pressures of ~10^{-5} Torr, or through a leak valve to a constant pressure in the range of (1-5) x 10^{-6} Torr. For these typical experimental conditions, about 100 ion-argon collisions per second should occur. Collisional cooling as performed in the present study is usually sufficient to remove any excess translational and rovibrational energy. Indications that effective thermalization had been achieved were provided by the reproducibility of the reaction kinetics for different collisional cooling periods or collision gas pressures and from the linearity of the semilog plots of normalized reactant ion intensities versus time (see below). Ions produced by LDI generally have excess kinetic energies and can also be formed in electronically excited states. For an exothermic reaction, ions with excess translational energies will have lower rate constants, which is clearly apparent in the kinetics plots exhibiting initial smaller slopes that persist until the hyperthermal ion population dissipates its energy. The presence of electronically excited ions cannot however be as easily discerned. Although the presence of electronically excited state ions cannot be ruled out, several previous studies involving actinide ions under the conditions employed in this work indicated that thermal ground-state chemistry was dominant[1,3]

Rate constants, *k*, were determined from the pseudo-first-order decay of the relative signals of the reactant ions as a function of time at constant neutral pressures. Because the steady-state concentration of the neutral reagent was much larger than that of the reactant ions, pseudo-first order kinetics were exhibited, whereby the ion A+ reacting with the neutral molecule B was depleted according to the rate law: d[A+]/dt=-*k*[A+][B]. Each decay was followed until the relative intensity of the reacting ion had reached less than 10% of its initial intensity. Along with the absolute rate constants, and for comparative purposes, reaction efficiencies are reported as *k*/*k*COL, where the *k*COL is the collisional rate constant derived from the modified variational transition-state/classical trajectory theory developed by Su and Chesnavich.[9] Collisional rate constants were calculated using the experimental molecular polarizabilities and dipole moments of CH3OH and H_2O .[10] The variations in the dipole moments, as well as the electronic parameters for the ^{18}O-substituted isotopologues, are assumed to be insignificant, as has been reported for D-substituted isotopologues.[11] The main source of uncertainty in the absolute rate constants is the pressure measurement, and we usually assign to them errors up to ±50%. Relative rate constants for different reactions are estimated to be accurate to ±20%, while typical precisions for replicate measurements of the same reaction are ±10%.

References

(1) Marçalo, J.; Santos, M.; Pires de Matos, A.; Gibson, J. K. *Inorg Chem* **2009**, *48*, 5055
(2) Gibson, J. K.; Haire, R. G.; Santos, M.; Marçalo, J.; Pires de Matos, A. *J Phys Chem A* **2005**, *109*, 2768.
(3) Santos, M.; Marçalo, J.; Pires de Matos, A.; Gibson, J. K.; Haire, R. G. *J Phys Chem A* **2002**, *106*, 7190-7194.
(4) Marçalo, J.; Santos, M.; Pires de Matos, A.; Gibson, J. K.; Haire, R. G. *J Phys Chem A* **2008**, *112*, 12647-12656.
(5) Guan, S.; Marshall, A. G. *Int. J. Mass Spectrom. Ion Processes* **1996**, *157-158*, 5-37.
(6) Bruce, J. E.; Eyler, J. R. *J. Am. Soc. Mass Spectrom.* **1992**, *3*, 727-733.
(7) Yi, L.; Ridge, D. P.; Munson, B. *Organic Mass Spectrom.* **1991**, *26*, 550-558.
(8) Bartmess, J. E.; Georgiadis, R. M. *Vacuum* **1983**, *33*, 149-153.
(9) Su, T.; Chesnavich, W. J. *J. Chem. Phys.* **1982**, *76*, 5183-5185.
(10) Lide, D. R. *CRC Handbook of Chemistry and Physics*; 75th Ed ed.; CRC Press: Boca Raton, FL, 1994.
(11) Ivanov, E. V.; Abrosimov, V. K. *Russian Chemical Bulletin, International Edition* **2005**, *54*, 1987-1988.

Table S1. Calculated lengths and strengths (kJ/mol) of the equatorial U-O bonds in $[UO_2(H_2O)]^+$ and $[UO_2(CH_3OH)]^+$.

	U-O (Å)	Pauli Repulsion Interaction Energy	Electrostatic Interaction Energy	Orbital Interaction Energy	Total
$[UO_2(H_2O)]^+$	2.471	140	-191	-212	-263
$[UO_2(CH_3OH)]^+$	2.403	192	-233	-249	-290

Table S2. Calculated and experimental strengths (kJ/mol) of the An-O_{yl} bonds, defined as the $(O)_2$-An^+ and $(O)_2$-An^{2+} binding energies for the pentavalent and hexavalent species, respectively.

	Pauli Repulsion Interaction Energy	Electrostatic Interaction Energy	Orbital Interaction Energy	Preparation Energy	Calculated Total Energy	Experimental Total Energy[a]
Pentavalent						
UO_2^+	4206	-1808	-5003	-203	-1757	-1515±19
NpO_2^+	3897	-1858	-4299	-141	-1671	-1370±24
PuO_2^+	3962	-1847	-4228	-119	-1615	-1160±42
Hexavalent						
UO_2^{2+}	4275	-1925	-4386	495	-1541	-1235±51
NpO_2^{2+}	4161	-1897	-4172	638	-1270	-1028±28
PuO_2^{2+}	4335	-1804	-4903	1514	-857	-842±107

[a]From J. Marçalo and J. K. Gibson, *J. Phys. Chem. A* **2009**,*113*, 12599-12606.

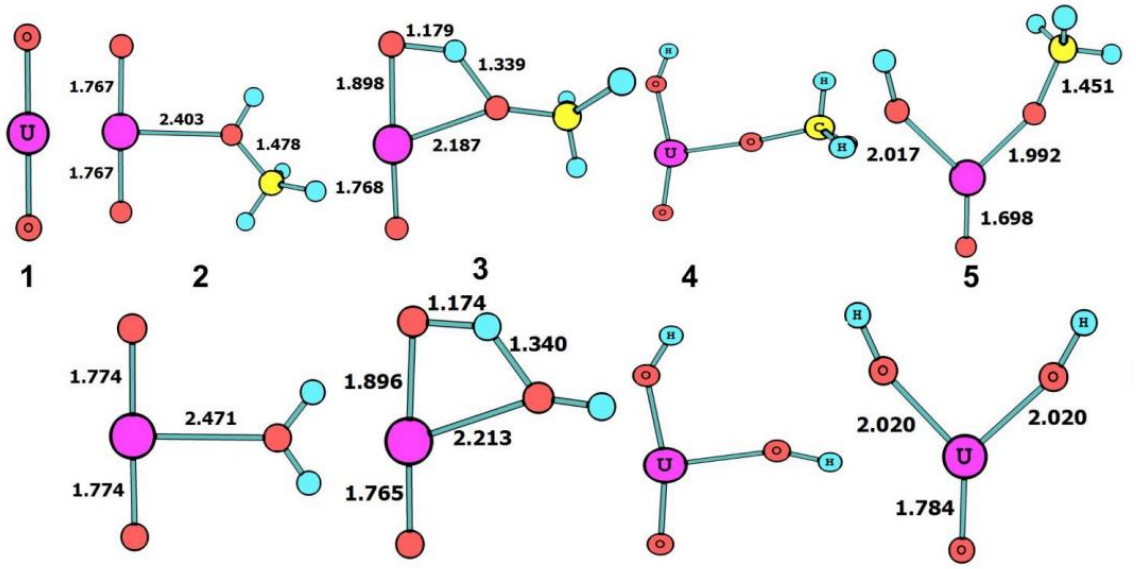

Figure S1. Structures of the species 2, 3 and 5 on the potential energy profile for the reactions of UO_2^+ with methanol (top) and water (bottom).

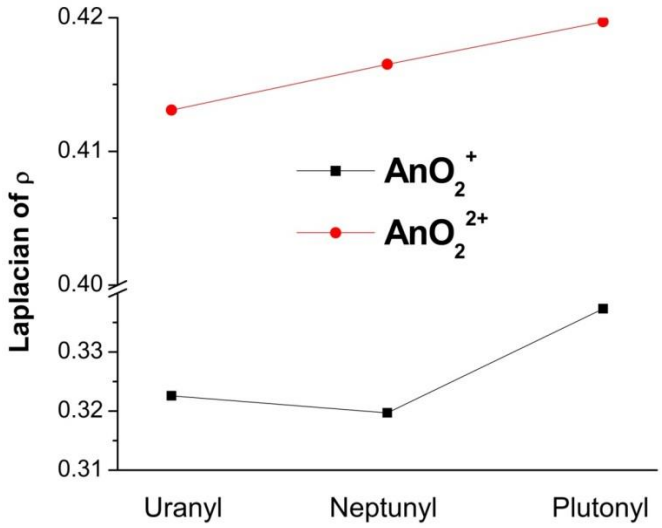

Figure S2. Calculated Laplacian of the electron density at the An-O bond critical points obtained from with the Atoms in Molecules approach.

Cartesian Coordinates of Species found on the PEPs

REACTANTS (#1)

NpO_2^{2+}

1 Np	93.0000	-0.00003333	0.00014319	0.00001088
2 O	8.0000	0.16367191	0.16993325	-1.68084228
3 O	8.0000	-0.16385909	-0.16912894	1.68090308

NpO_2^{+}

1 Np	93.0000	-0.00003809	0.00016709	0.00000601
2 O	8.0000	0.16787615	0.17427109	-1.72396733
3 O	8.0000	-0.16805857	-0.17349069	1.72403301

PuO_2^{2+}

1 Pu	94.0000	-0.00006204	0.00026603	0.00002117
2 O	8.0000	0.16233787	0.16847746	-1.66701043
3 O	8.0000	-0.16249690	-0.16779357	1.66706113

PuO_2^{+}

1 Pu	94.0000	-0.00005760	0.00024880	0.00001634
2 O	8.0000	0.16616442	0.17244965	-1.70630618
3 O	8.0000	-0.16632789	-0.17174853	1.70636170

UO_2^{2+}

1 U	92.0000	-0.00001280	0.00006079	-0.00000664
2 O	8.0000	0.16398103	0.17030354	-1.68410882
3 O	8.0000	-0.16418816	-0.16941931	1.68418696

UO_2^{+}

1 U	92.0000	-0.00002283	0.00010461	-0.00000469
2 O	8.0000	0.16975146	0.17625002	-1.74328544
3 O	8.0000	-0.16994856	-0.17540962	1.74336163

Water

1 O	8.0000	0.00000000	0.00000000	-0.11114741
2 H	1.0000	0.00000000	0.76714748	0.47280380
3 H	1.0000	0.00000000	-0.76714748	0.47280380

Methanol

1 O	8.0000	0.17458057	0.57430708	-0.45605578
2 H	1.0000	-0.20350204	1.34710037	-0.02149768
3 C	6.0000	0.02809956	-0.55600459	0.40389701
4 H	1.0000	-1.02373087	-0.78216383	0.61288667
5 H	1.0000	0.46545286	-1.40588053	-0.11962188
6 H	1.0000	0.55909992	-0.42373106	1.35345899

URANYL COMPLEXES WITH WATER AND METHANOL (#2)

UO_2^{2+}.water

1 U	92.0000	0.03491122	-0.14751603	-0.00906051
2 O	8.0000	0.20246831	0.02359654	-1.70607000
3 O	8.0000	-0.13546791	-0.30224628	1.68923080
4 O	8.0000	-0.51237307	2.11021820	0.14614585
5 H	1.0000	-0.57371157	2.74852884	-0.59857188
6 H	1.0000	-0.72358875	2.60720162	0.96722605

UO_2^{+}.water

1 U	92.0000	0.05197189	-0.21429591	-0.01488364
2 O	8.0000	0.22260610	-0.03641792	-1.77199090
3 O	8.0000	-0.12612250	-0.36482546	1.74405002

4 O	8.0000	-0.52899153	2.18125757	0.15143584
5 H	1.0000	-0.58637378	2.80978660	-0.58575296
6 H	1.0000	-0.74085194	2.66427800	0.96604197

UO_2^{2+}.methanol

1 U	92.0000	0.09492129	-0.33743083	-0.10316837
2 O	8.0000	0.26281295	-0.15551064	-1.80374087
3 O	8.0000	-0.07339584	-0.51643450	1.59795434
4 O	8.0000	-0.44842587	1.85509304	0.06227791
5 H	1.0000	-0.48302043	2.40027283	-0.75160864
6 C	6.0000	-0.79623593	2.77268692	1.24663301
7 H	1.0000	-1.79423845	3.15789782	1.04875765
8 H	1.0000	-0.76303614	2.14638945	2.13293175
9 H	1.0000	-0.03585530	3.55061300	1.25936855

UO_2^{+}.methanol

1 U	92.0000	0.10733550	-0.40453115	-0.10745184
2 O	8.0000	0.27569559	-0.21835467	-1.85700054
3 O	8.0000	-0.06809257	-0.55981826	1.64348001
4 O	8.0000	-0.45725732	1.92429126	0.06589015
5 H	1.0000	-0.48227160	2.45081660	-0.74855782
6 C	6.0000	-0.79620928	2.78125258	1.22119426
7 H	1.0000	-1.80041680	3.17670459	1.08223141
8 H	1.0000	-0.75287816	2.14160005	2.09774385
9 H	1.0000	-0.06237909	3.58161607	1.29187584

TRANSITION STATE COMPLEXES (#3)

UO_2^{2+}.water

1 U	92.0000	0.04533387	-0.15001151	-0.00331165
2 O	8.0000	-0.09072104	0.28503221	-1.76939294
3 O	8.0000	0.13588642	-0.43462430	1.68409274
4 O	8.0000	-0.61296443	1.83039045	-0.16981820
5 H	1.0000	-0.45659394	1.38363630	-1.48875502
6 H	1.0000	-0.89597504	2.67727581	0.24775242

UO_2^{+}.water

1 U	92.0000	0.06268363	-0.18717837	0.03485145
2 O	8.0000	-0.10445247	0.32415468	-1.78302500
3 O	8.0000	0.19311919	-0.58799196	1.74914194
4 O	8.0000	-0.63666790	1.89836577	-0.20456131
5 H	1.0000	-0.46100024	1.38533611	-1.43003132
6 H	1.0000	-0.92068888	2.75900429	0.13297783

UO_2^{2+}.methanol

1 U	92.0000	0.10775485	-0.34653106	-0.03809826
2 O	8.0000	-0.02641582	0.08695378	-1.81330459
3 O	8.0000	0.19837715	-0.64347293	1.65411337
4 O	8.0000	-0.53194399	1.61698111	-0.14717495
5 H	1.0000	-0.38317640	1.17796946	-1.46296972
6 C	6.0000	-0.96913407	2.95233802	0.38097019
7 H	1.0000	-1.96933071	3.12149249	-0.02026863
8 H	1.0000	-0.95707702	2.89419823	1.46714106
9 H	1.0000	-0.25479682	3.67841461	-0.00950331

UO_2^{+}.water

1 U	92.0000	0.13070409	-0.39691940	0.00316808
2 O	8.0000	-0.04763432	0.12648265	-1.81212272
3 O	8.0000	0.27770352	-0.83091280	1.71101605
4 O	8.0000	-0.55143442	1.67316827	-0.18254187
5 H	1.0000	-0.39379552	1.18308543	-1.41899658

6 C	6.0000	-0.97219393	2.95998167	0.33686339
7 H	1.0000	-1.96966484	3.17922689	-0.04261447
8 H	1.0000	-0.98395629	2.92175365	1.42544475
9 H	1.0000	-0.27026713	3.72001706	-0.00486229

#4 COMPLEXES

UO_2^{2+}.water

1 U	92.0000	0.04105406	-0.09801681	-0.00844019
2 O	8.0000	-0.61057335	0.21622007	-1.76643766
3 O	8.0000	0.73440980	-0.70674591	1.44606665
4 O	8.0000	-0.55004624	1.64882595	0.62233370
5 H	1.0000	-1.02992827	0.63403722	-2.56628690
6 H	1.0000	-0.80501620	2.50312361	1.04880043

UO_2^{+}.water

1 U	92.0000	0.05934216	-0.13250146	0.00148444
2 O	8.0000	-0.59872333	0.11884175	-1.86800156
3 O	8.0000	0.75728152	-0.70185456	1.52368164
4 O	8.0000	-0.61117802	1.70337129	0.49695303
5 H	1.0000	-1.04968668	0.74939171	-2.45735660
6 H	1.0000	-0.77713586	2.46019539	1.07927508

UO_2^{2+}.methanol

1 U	92.0000	0.06179059	-0.24873153	-0.13181455
2 O	8.0000	-0.54421977	-0.05668022	-1.94135200
3 O	8.0000	0.72989017	-0.79127644	1.36917705
4 O	8.0000	-0.56061542	1.50955955	0.38446795
5 H	1.0000	-0.93014145	0.27202456	-2.79189781
6 C	6.0000	-1.00505822	2.83422062	0.88017099
7 H	1.0000	-1.49703098	3.33289070	0.04410555
8 H	1.0000	-1.69030239	2.64210430	1.70667599
9 H	1.0000	-0.10720020	3.36192778	1.20450729

UO_2^{+}.methanol

1 U	92.0000	0.13125441	-0.32410600	-0.04614682
2 O	8.0000	-0.57573709	-0.01350356	-1.91482677
3 O	8.0000	0.90926054	-1.11567832	1.35038127
4 O	8.0000	-0.51759517	1.49561594	0.50176974
5 H	1.0000	-1.03218687	0.58936045	-2.52573769
6 C	6.0000	-1.02259365	2.81456252	0.78545580
7 H	1.0000	-1.43784956	3.24483438	-0.12656699
8 H	1.0000	-1.79603262	2.73447426	1.54873984
9 H	1.0000	-0.20140764	3.43047964	1.15097207

II.2. Gas-phase uranyl, neptunyl and plutonyl: Hydration and oxidation studied by experiment and theory

This sub-chapter is based on the following publication:

*Rios D, Michelini MC, **Lucena AF**, Marçalo J, Bray TH, Gibson JK, Gas-Phase Uranyl, Neptunyl, and Plutonyl: Hydration and Oxidation Studied by Experiment and Theory, **Inorg. Chem., 2012**, 51 (12), 6603–6614, DOI: 10.1021/ic3001625*

I contributioned with the experiments performed at C2TN-IST with uranyl nitrate solutions. The results obtained provided confirmation of the data obtained at LBNL, particularly the hydration rates, and also allowed to identify additional reactions and obtain additional rates. Dr. Daniel Rios and Dr. Travis H. Bray were responsible for the experimental studies at LBNL and Dr. Maria C. Michelini for all the theoretical computations.

Abstract

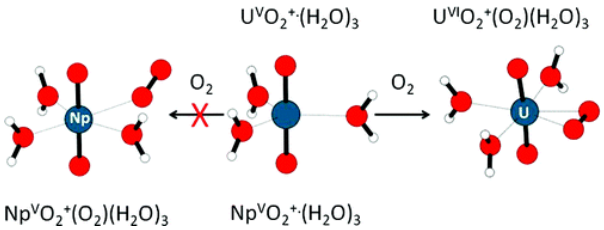

The following monopositive actinyl ions were produced by electrospray ionization of aqueous solutions of $An^{VI}O_2(ClO_4)_2$ (An = U, Np, Pu): $U^{V}O_2^+$, $Np^{V}O_2^+$, $Pu^{V}O_2^+$, $U^{VI}O_2(OH)^+$ and $Pu^{VI}O_2(OH)^+$; abundances of the actinyl ions reflect the relative stabilities of the An(VI) and An(V) oxidation states. Gas-phase reactions with water in an ion trap revealed that water-addition terminates at $AnO_2^+\cdot(H_2O)_4$ (An = U, Np, Pu) and $AnO_2(OH)^+\cdot(H_2O)_3$ (An = U, Pu), each with four equatorial ligands. These terminal hydrates evidently correspond to the maximum inner-sphere water coordination in the gas phase, as substantiated by density functional theory (DFT) computations of the hydrate structures and energetics. Measured hydration rates for the $AnO_2(OH)^+$ were substantially faster than for the AnO_2^+, reflecting additional vibrational degrees of freedom in the hydroxide ions for stabilization of hot adducts. Di-oxygen addition resulted in $UO_2^+(O_2)(H_2O)_n$ (n = 2, 3), whereas O_2 addition was not observed for NpO_2^+ or PuO_2^+ hydrates. DFT suggests that two-electron three centered bonds form between UO_2^+ and O_2, but not between NpO_2^+ and O_2. As formation of the UO_2^+-O_2 bonds formally corresponds to oxidation of U(V) to U(VI), the absence of this bonding with NpO_2^+ can be considered a manifestation of the lower relative stability of Np(VI).

II.2.1. Introduction

The preponderance of actinide chemistry occurs in the presence of water, commonly in aqueous solutions. The distinctive linear monopositive and dipositive actinyl ions, $\{O=An=O\}^{+,2+}$, are particularly important species in much of the solution chemistry of uranium, neptunium and plutonium.[1,2] Addition of water to actinyl ions in the gas phase, as described here, presents the most elementary basis to understand the fundamental phenomenon of hydration absent perturbations introduced in condensed phases. Among the key properties in the gas phase which can be experimentally determined are kinetics for water addition and the terminal extent of inner-sphere hydration. Previous experimental studies of gas-phase hydration of UO_2^+ and $UO_2(OH)^+$ have determined kinetics of water addition, and the maximum number of added water ligands.[3,4] In that work, it was found that UO_2^+ and $UO_2(OH)^+$ add up to four and three water molecules, respectively, resulting in a uranyl coordination number of four. Although aqueous $U^VO_2^+$ is generally unstable towards disproportionation into U^{IV} and $U^{VI}O_2^{2+}$ according to Equation (1)[5] there is evidence that the solution hydration characteristics of UO_2^+, NpO_2^+ and PuO_2^+ are generally similar, with an (average) inner-sphere hydration number of five.[6]

$$2UO_2^+ + 4H^+ \rightarrow U^{4+} + UO_2^{2+} + 2H_2O \qquad (1)$$

The inner-sphere hydration number of the aqueous dipositive AnO_2^{2+} ions (An = U, Np, Pu) has also been determined to be approximately five,[6,7] with the caveat that in solution inner-sphere coordination is not static, and there is likely a dynamic equilibrium between four and five inner-sphere waters.[8] Considering recent computational results of Bühl et al.,[9] it can be surmised that water coordination of cationic metal centers is enhanced in solution by electron donation from second-shell water molecules, which effectively renders the inner sphere water molecules as better Lewis bases. A result is that inner-sphere hydration in the gas-phase should generally be less than that in solution, evidently by one water ligand in the case of UO_2^+. Despite that hydration in the gas phase predictably does not directly reveal that in solution, it can provide important insights, including variations across the actinide series as well as differences due to changes in ligation and oxidation state.

As a crucial complement to gas-phase experimental studies in which no direct structural information is obtained, the structures and energetics of relatively simple gas-phase hydrates can generally be reliably computed by density functional theory (DFT). A number of theoretical studies on the hydration of actinyl ions have been performed in the last decade.[10-29] As remarked above, the majority of the experimental studies indicate that the dominant coordination number for early

AnO_2^{2+} in aqueous solution is five;[8,30-32] consequently, most theoretical effort has been directed towards penta-aquo complexes. Hydration of UO_2^{2+} is by far the most studied case. A critical review of theoretical studies of actinide chemistry in the gas-phase and in solution has been presented by Vallet et. al.[24] Most theory studies concluded that five-coordination is the most favorable structure for the uranyl (VI) complexes in water, although some have suggested that five- and six-coordination are equally preferred.[18] From detailed computations of the equatorial coordination number of UO_2^{2+} it is clear that the calculated coordination number is highly sensitive to several factors, including whether the computations are performed in the gas-phase or in solution, the accuracy of the gas-phase calculation, the solvation method, the inclusion of first/second solvation shells, and the inclusion of entropy effects.[20,21] Several previous theoretical studies report actinyl (V) and actinyl (VI) hydroxide gas-phase water complexes, including some of the cations studied in this work.[11,12,19,25-28,33]

Of particular interest in actinide chemistry, specifically actinyl chemistry, is the identification and comprehension of variations across the series, as from UO_2^+ to NpO_2^+ to PuO_2^+. An important result found in the course of the hydration studies reported here was the observation of O_2-addition to uranyl hydrates as a significant reaction pathway; these O_2 addition reactions were not observed for the corresponding neptunyl or plutonyl species. Gas-phase addition of O_2 to $UO_2^+\cdot(acetone)_{2,3}$ complexes has been reported;[34] a subsequent DFT study[35] characterized the $UO_2^+(O_2)(acetone)_{2,3}$ species as superoxo complexes, essentially with oxidation of U(V) to U(VI). Superoxo complexes were also produced by addition of O_2 to uranyl(V) coordinated by acetone and water, as well as by dimethylsulfoxide and water.[36] These gas-phase results were particularly intriguing as Bakac and Espenson[37] had earlier proposed $U^{VI}O_2^+(O_2^{\cdot-})$ as an intermediate in copper-catalyzed oxidation of $U^VO_2^+$ to $U^{VI}O_2^{2+}$ in aqueous solution. Notably, $UO_2^+(O_2)(H_2O)_n$ complexes were evidently not previously observed in a gas phase study of the hydration of UO_2^+, despite the reported presence of ~$2x10^{-7}$ Torr O_2, this being a sufficient oxygen concentration to oxidize $UO(OH)^+$ to $UO_2(OH)^+$.[3] More recently, the superoxo cation complexes $UO_2^+(\eta^2\text{-}O_2)$ and $UO_2^+(\eta^2\text{-}O_2)(\eta^1\text{-}O_2)$ have been produced and characterized by IR spectroscopy and DFT.[38] The present results for reactions of actinyl(V) hydrates with oxygen serve to further illuminate the important issue of the formation of actinyl(VI) superoxides, particularly in the presence of water ligands.

The main goal of the DFT computations performed here was to provide insights into the experimental results. Accordingly, attention was focused on the sequential water-addition reactions of $AnO_2^+\cdot(H_2O)_n$ and $AnO_2OH^+\cdot(H_2O)_{n-1}$ (An = U, Np and Pu, with n = 0–5) ions in the gas phase. The addition of O_2 to bare and hydrated UO_2^+ and NpO_2^+ ions was also studied by DFT to

illuminate the nature of the observed uranyl hydrate-dioxygen adducts, as well as the underlying basis for the absence of such species in the case of neptunyl.

II.2.2. Experimental section

The following stock acid solutions at Lawrence Berkeley National Laboratory (LBNL) were diluted to prepare the 180 µM actinyl solutions used for electrospray ionization (ESI): 177 mM $U^{VI}O_2(ClO_4)_2$ at pH = 0.6, 0.83 mM $Np^{VI}O_2(ClO_4)_2$ at pH = 1.6, and 0.70 mM $Pu^{VI}O_2(ClO_4)_2$ at pH = 1.6. The 180 µM uranyl solution had a measured pH = 3.9, reasonably close to the value of ~3.6 expected based on the ~1000x dilution of the stock solution; NaOH was added to the 180 µM neptunyl and plutonyl solutions to obtain pH ≈ 4. To confirm that the ESI mass spectra were not sensitive to pH, solutions for all three actinyls were prepared with pH ≈ 2 by addition of $HClO_4$, and with pH ≈ 6 by addition of NaOH. The actinide isotopes (>99%) were U-238 (α-decay half-life = 4 x 10^9 y), Np-237 (α-decay half-life = 2 x 10^6 y) and Pu-242 (α-decay half-life = 4 x 10^5 y). All handling of these hazardous radionuclides was in a containment glove box in a radiological laboratory. The ESI mass spectrometry experiments were performed using an Agilent 6340 quadrupole ion trap mass spectrometer (QIT/MS) with MS^n collision induced dissociation (CID) capabilities. A feature of the instrument is that ions in the trap can undergo ion-molecule reactions by applying a variable reaction delay time of up to 10 s; as no excitation is applied, observed reactions occur at the trap temperature of ~300 K.[39] The source region of the QIT/MS is inside of a radiological-containment glove box, as described in detail elsewhere.[40] In high resolution mode, the instrument has a detection range of 50 – 2200 m/z and a resolution of ~0.25 m/z. Mass spectra were recorded in the positive ion accumulation and detection mode. Most spectra were taken with the following instrumental parameters: solution flow rate, 60 µl.hr^{-1}; nebulizer gas pressure, 15 psi; capillary voltage and current, -4500 V, 14.648 nA; end plate voltage offset and current, -4500 V, 37.5 nA; dry gas flow rate, 5 l.min^{-1}; dry gas temperature, 325 °C; capillary exit, 141.7 V; skimmer, 26.3 V; octopole 1 and 2 DC, 13.75 V and 2.13 V; octopole RF amplitude, 58.3 Vpp; lens 1 and 2, -4.8 V and -65.5 V; trap drive, 216.8. High-purity nitrogen gas for nebulization and drying in the ion transfer capillary was supplied from the boil-off of a liquid nitrogen Dewar. As has been discussed elsewhere, the background water pressure in the ion trap is estimated as ~10^{-6} Torr;[41] reproducibility of hydration rates confirms that the background water pressure in the trap remains constant to within <5%. The helium buffer gas pressure in the trap is constant at ~10^{-4} Torr. The ion trap has been modified to allow for the introduction of reagent gases through a leak valve, including additional water in the present study.[40]

To provide confirmation of the uranyl results, particularly the hydration rates, and to obtain additional rates and reactions, independent uranyl studies were carried out at Instituto Tecnológico e Nuclear (ITN). The QIT/MS instrument at ITN is a Bruker HCT, which is very similar to the Agilent 6340 at LBNL, with comparable helium and water pressures in both ion traps; the results also suggest comparable O_2 pressures in both traps. Most spectra were taken with the following instrumental parameters: solution flow rate, 150 µl hr^{-1}; nebulizer gas pressure, 8 psi; capillary voltage, -4000 V; end plate voltage offset, -500 V; dry gas flow rate, 4 l/min; dry gas temperature, 250 ^{o}C; capillary exit, 128.5 V; skimmer, 40 V; octopole 1 and 2 DC, 12 V and 1.70 V; octopole RF amplitude, 187.1 Vpp; lens 1 and 2, -5 V and -60 V; trap drive, 216.8. Solution used for electrospray ionization: 100 µM solution of $U^{VI}O_2(NO_3)_2$ in H_2O/EtOH (1:10); pH ≈ 6. Comparative hydration kinetics suggest that the water pressure is slightly greater in the ITN trap, which may be due to the use of a nitrogen generator, rather than the boil-off from liquid nitrogen, as the source for the ESI nebulizing and drying gas. The high capacity ion traps in both the Agilent instrument at LBNL and the Bruker instrument at ITN were manufactured and calibrated by Bruker, and both thus operate at essentially the same He bath gas pressure, which allows for reliable relative kinetics comparisons to be obtained for hydration reactions which involve third-body collisional cooling.

II.2.3. Computational details

All quantum chemical calculations were performed within the framework of DFT using the B3LYP[42,43] hybrid functional and the Stuttgart small–core relativistic effective core potential (RECP) and associated basis sets for the actinide atoms.[44] The Stuttgart small–core RECP, so–called SDD pseudopotential, replaces the 60 electrons in the inner shells 1 through 4, leaving the explicit treatment of the n = 5 shell (5s 5p 5d and 5f), and also the 6s, 6p, 6d and 7s valence electrons. The choice of this level of theory (referred to as B3LYP/SDD) was based on the good performance found for similar calculations performed on the hydration of dipositive and monopositive actinyl and hydroxoactinyl ions.[19-21,25,26,28,45] The 6-311++G(d,p) basis sets were employed for the rest of the atoms.[46-48] These calculations were carried out with Gaussian09 package.[49] Ultrafine (99,590) pruned grids for numerical integration were employed in all the computations.

The sequential hydration reactions were analyzed for six cations, namely, AnO_2^+ and $AnO_2(OH)^+$ for An = U, Np and Pu. The geometry of the bare and hydrated cations, one to five water molecules for AnO_2^+ and one to four for $AnO_2(OH)^+$, was optimized without any symmetry restrictions. The lowest-energy structure is reported for each cation, along with some relevant high-energy structures. For each optimized stationary point, analytical frequencies were calculated to confirm

that the optimized structure was a local minimum on the potential energy surface of the system, and to evaluate the zero-point vibrational energy (ZPVE) corrections to the electronic energies. All the reported hydration energies include the ZPVE correction at 0 K (ΔE^0). The counterpoise correction was calculated to correct reaction energies for basis sets superposition errors.[50] In addition to the ΔE^0 values, the Gibbs free energy at 298 K is reported for each of the studied reactions. The accuracy of the ΔG^{298} values is necessarily somewhat limited by the use of the harmonic oscillator approximation to treat nuclear motion. Spin–orbit effects were not treated explicitly in this study. Spin–orbit effects are expected to be especially important for most of the cations studied here, as they exhibit open–shell ground states. However, these contributions have been shown to remain invariant with the addition of water molecules, and therefore are not expected to significantly affect the sequential hydration energies.[25]

In order to confirm that the used level of theory correctly identifies the lowest–energy spin state of the systems, two or more spin states were considered for each of the bare cations studied here. Exploratory calculations on the first and second hydrates of all the studied cations were performed in order to establish whether the addition of coordinating water molecules could change the lowest energy spin state of the ions. In all cases it was found that the lowest energy spin state of the hydrates is the same of the corresponding bare cations. Therefore, only the lowest-energy spin states of the bare cations were considered when studying the successive hydrates, namely, doublet spin state for UO_2^+, triplet for NpO_2^+, quartet for PuO_2^+, singlet for UO_2OH^+, doublet for NpO_2OH^+ and triplet for PuO_2OH^+. Calculations were carried out using spin–unrestricted methods. No appreciable spin contamination was found in any of these species.

The geometrical and energetic properties of the di-oxygen complexes $UO_2^+(O_2)(H_2O)_n$ and $NpO_2^+(O_2)(H_2O)_n$ for n=0-3, were performed at the same level of theory (B3LYP/SDD), and the energetics associated with the O_2 addition to the different hydrates is reported. It was considered that computations for these two systems would suffice to understand the distinctive nature of uranyl; accordingly, computations were not performed for $PuO_2^+(O_2)(H_2O)$. Two possible di-oxygen coordination modes were considered, i.e. end-on (η^1) and side-on (η^2). The doublet and quartet spin states were considered in the case of $UO_2^+(O_2)(H_2O)_n$ and the singlet, triplet and quintet states for the corresponding neptunyl cations. The broken-symmetry (BS) approach[51-54] was used to investigate the geometrical and energetic properties of the (open-shell) singlet η^1-$NpO_2^+(O_2)(H_2O)_n$ cation.

The charge distribution was analyzed using Natural Population Analysis (NPA)[55] as implemented in Gaussian09 package (NBO version 3.1).

II.2.4. Results and discussion

Whereas the neptunyl and plutonyl experiments were all performed at LBNL, uranyl experiments were performed at both LBNL and ITN, with essentially the same results. Obtaining duplicate results for uranyl was particularly important for the comparative hydration kinetics presented below in view of a significant discrepancy between the results obtained in this work and those reported previously.[3]

II.2.4.1 ESI-MS of uranyl, neptunyl and plutonyl

ESI of aqueous solutions of $An^{VI}O_2(ClO_4)_2$ (An = U, Np, Pu) generates both pentavalent and hexavalent monopositive gas-phase actinyl ions: $U^{V}O_2^+$, $Np^{V}O_2^+$, $Pu^{V}O_2^+$, $U^{VI}O_2(OH)^+$, and $Pu^{VI}O_2(OH)^+$; similar ESI mass spectra were obtained over a pH range from ~2 to ~6. Hydrates of dipositive AnO_2^{2+} did not appear in the ESI mass spectra; all three dipositive AnO_2^{2+} (An = U, Np, Pu) had previously been transferred from solution to gas in complexes with strong Lewis base ligands such as dimethylformamide (DMF) in the gaseous $AnO_2^{2+}\cdot(DMF)_4$ complex ions.[56] Evidently, ligands which are better electron donors than water are required to effectively stabilize dipositive actinyls from solution to the gas phase under our experimental conditions.

The primary disparity among the actinyls apparent in the ESI mass spectra is the appearance of substantial $U^{VI}O_2(OH)^+$ (~60% relative to UO_2^+), minor $Pu^{VI}O_2(OH)^+$ (~5% relative to PuO_2^+), and no detectable $Np^{VI}O_2(OH)^+$ (to an estimated detection limit of <3% relative to NpO_2^+). The overwhelmingly dominant process in ESI of $Np^{VI}O_2^{2+}$ and $Pu^{VI}O_2^{2+}$ is charge and oxidation state reduction to $An^{V}O_2^+$. In contrast, a significant product from ESI of $U^{VI}O_2^{2+}$ is $U^{VI}O_2(OH)^+$, in which charge-reduction has occurred but the hexavalent oxidation state is retained by hydrolysis to produce the hydroxide. ESI from a predominantly D_2O (>99%) solution resulted in almost exclusively $UO_2(OH)^+$ rather than $UO_2(OD)^+$; this result does not reveal whether hydrolysis occurs by reaction with background H_2O in the gas phase, or rather whether $UO_2(OD)^+$ is produced during ESI and subsequently undergoes gas-phase hydroxyl-exchange with background H_2O. Hay et al.[13] have computed that the gas-phase hydrolysis of UO_2^{2+} to $UO_2(OH)^+$ ($+H_3O^+$) is thermodynamically favorable, but the kinetics for this process are unknown. Regardless of the mechanism of hydroxide formation, the relative abundances, $U^{VI}O_2(OH)^+ >> Pu^{VI}O_2(OH)^+ > Np^{VI}O_2(OH)^+$ (the last of these was not observed), are consistent with the relative stabilities of the hexavalent actinide oxidation states, as indicted by the standard reduction potentials for $An^{VI}O_2^{2+} \rightarrow An^{V}O_2^+$: 0.09V for UO_2^{2+} << 0.94 V for PuO_2^{2+} < 1.16 V for NpO_2^{2+}.[57]

II.2.4.2 Hydration of AnO_2^+ (An = U, Np, Pu)

The AnO_2^+ ions were isolated and exposed to water present at a constant but indeterminate (~10^{-6} Torr) pressure in the ion trap.[41] Third body collisions with the helium buffer gas serve to collisionally cool nascent hydrates, as has been demonstrated previously by a nearly linear dependence of hydration rates on helium pressure.[41] Because measured hydration rates under these conditions are highly dependent on third-body collisions, it is not valid to report pseudo-first-order rate constants for hydration; these rates would be negligible in the absence of a high-pressure of cooling gas, ~10^{-4} Torr helium in the present experiments. However, it is appropriate to report relative hydration rates obtained under comparable conditions of both water pressure and helium pressure.

Representative hydration results are shown in Figure II.2.1 as mass spectra acquired for isolated UO_2^+, NpO_2^+ and PuO_2^+ after reaction with background gases in the trap for 10 s, the maximum accessible reaction time using the "block voltage scan delay" option in the QIT/MS software. It is apparent in Figure II.2.1 that hydration of all three AnO_2^+ terminates at the tetrahydrate, $AnO_2^+\cdot(H_2O)_4$. Additional water vapor was added to the trap through a leak valve; increasing the water pressure by approximately a factor of two accordingly increased the yields of the $AnO_2^+\cdot(H_2O)_4$ hydrate ions but resulted in no detectable pentahydrates, $AnO_2^+\cdot(H_2O)_5$. Previous hydration studies of ligated monopositive metal ions under these same experimental conditions led to the conclusion that the terminal observed hydrates correspond to the maximum extent of inner-sphere hydration in the gas-phase complexes; addition of second sphere water molecules is not observed under these conditions.[41]

Other features evident in Figure II.2.1 include the appearance of uranyl oxygen adducts, and differences between the rates of hydration among the three AnO_2^+ ions. These aspects are discussed below.

The most relevant optimized parameters of the ground–state (GS) $AnO_2^+\cdot(H_2O)_n$ (An = U, Np and Pu, n = 0–5) structures and some relevant higher-energy isomers are presented in Table II.2.1. In the chemical formulas of the hydrates, water molecules in the second solvation shell are shown in italics. In the discussion, tables and figures, O_{yl} is used to designate an axial actinyl oxygen atom, and O_w is used to designate an oxygen atom in an equatorial water ligand. The geometrical structures of $AnO_2^+\cdot(H_2O)_4$*(H_2O)* GS and the $AnO_2^+\cdot(H_2O)_5$ higher-energy isomer are shown in Figure II.2.2. For all three AnO_2^+ cations, the addition of water induces a lengthening of actinyl bond length, by ca. 0.04 Å from n=0 to n=5. The actinyl–water distance increases in going from $AnO_2^+\cdot(H_2O)$ to $AnO_2^+\cdot(H_2O)_4$ by between 0.06 and 0.09 Å, depending on the actinide. At the level of theory used in this work, the lowest-energy pentahydrates are obtained when the fifth water

molecule is placed in the second coordination shell, forming hydrogen bonds with two water molecules from the first coordination shell, designated as $AnO_2^+\cdot(H_2O)_4$*(H₂O)*, as shown in Figure II.2.2. These isomers, however, are followed very close in energy by the corresponding inner-sphere pentacoordinate isomers, $AnO_2^+\cdot(H_2O)_5$ (Fig. II.2.2).

As shown in Table II.2.1, for the series of complexes $AnO_2^+\cdot(H_2O)_n$ (n=0–4), the actinyl bond lengths show a slight contraction (ca. 0.03 Å) as one progresses along the series, from U to Pu. This trend is in agreement with previous theoretical,[13,20,21,24,28] and experimental,[30,58] studies that show a slight decrease in the An–O_{yl} bond length across the actinide series, together with a decrease in symmetric and antisymmetric O=An=O stretching frequencies.[13,58] Recent experimental studies have confirmed that the An–O bond strength diminishes across the series,[59] which is the expected trend basing on the decrease of the stretching frequency. The actinyl bond, therefore, becomes both shorter and weaker along the series.

According to experimental estimations, the effective metal charge of the actinyl (VI) cations in aqueous solutions diminishes in going from U to Pu.[60] Our calculations show the same trend in the case of actinyl (V) ions (Table S1). In particular, the computed NPA values for the tetrahydrates diminish from 1.70 for $UO_2^+\cdot(H_2O)_4$ to 1.45 for $PuO_2^+\cdot(H_2O)_4$. The computed NPA value for $NpO_2^+\cdot(H_2O)_4$ (1.59) is lower than the experimental effective charge on Np in NpO_2^+ in aqueous phase, 2.2±0.1,[60] which was obtained using a modified Born equation and stability constants. The actinide natural charges and orbital populations of the three bare cations are included as Supporting Information (Table S2).

The computed reaction energies at 0 K and Gibbs free energies at 298 K for all the sequential hydration reactions are summarized in Table II.2.2. The sequential hydration energies are in all cases exothermic and show a monotonic decrease in magnitude with an increase in the number of coordinated water molecules. The hydration energies change from -134 kJ.mol^{-1} for the formation of the first hydrate, $UO_2^+\cdot(H_2O)$, to -83 kJ.mol^{-1} for the formation of the tetrahydrate, $UO_2^+\cdot(H_2O)_4$. The first two hydration energies are practically identical for all the three studied cations (UO_2^+, NpO_2^+ and PuO_2^+), whereas there is a slight, but systematic, decrease in the magnitudes of the hydration energies (up to 9 kJ.mol^{-1}) in going from uranium to plutonium, for the addition of the third and fourth water molecules. The variations in the computed hydration energies are in all cases consistent with the decrease of the effective charge on the metal center (Supporting Information, Tables S1 and S2).

The ground-state pentahydrates are obtained when the fifth water molecule is placed in the second coordination shell, $AnO_2^+\cdot(H_2O)_4$*(H₂O)*, with an exothermicity of almost 50 kJ.mol^{-1}. The $AnO_2^+\cdot(H_2O)_5$ isomers with five inner-sphere water molecules were calculated to be very close in

energy to the GS structures (i.e., within 11 kJ.mol^{-1}). Calculations show, therefore, that the additions of a fifth water molecule to the $AnO_2^+\cdot(H_2O)_4$ complexes are exothermic. However, the computed ΔG^{298} values are considerable less favorable due to the unfavorable entropy of association (Table II2.2). In particular, the fifth hydration is practically ergoneutral ($\Delta G \sim 0$). Moreover, due to differences in the entropy of reaction, the ΔG^{298} of formation of the pentacoordinated $AnO_2^+\cdot(H_2O)_5$ and tetracoordinated $AnO_2^+\cdot(H_2O)_4$*(H₂O)* isomers are essentially the same. A complete table including ΔH^{298} and ΔS^{298} values for all the reported reactions is in the Supporting Information (Table S3). In a previous study, we have discussed whether the exothermicity, ΔH^{298}, or the exoergicity, ΔG^{298}, should be considered for the conditions used in the experiments performed here.[41] It was concluded that under the conditions used here—specifically a pressure of ~10^{-4} Torr—third-body collisions are crucial to stabilize the hydration products, and the Gibbs free energy changes are accordingly more relevant than hydration energies or enthalpies.[41] The absence of pentahydrates in the experiments is in accord with the computed free energies for addition of the fifth water molecule. Although it is not functional to define an equilibrium constant for reactions corresponding to association of water to cations present at very low and unknown concentrations, it can be inferred that under the low-pressure conditions of these experiments—i.e., ~10^{-6} Torr H_2O—the hydration free energy must be adequately negative to provide a sufficiently favorable effective "equilibrium constant" for hydration to be observed. It should be noted that as the free energies are nearly the same for addition of the fifth water in the inner-sphere or outer sphere, the experimental results—i.e., termination at the tetrahydrate—do not directly distinguish between inner-sphere and outer-sphere coordination, but do demonstrate that the maximum inner-sphere coordination is by four water molecules in the gas phase.

In summary, our computations indicate that at the present level of theory the tetracoordinated isomer, $AnO_2^+\cdot(H_2O)_4$*(H₂O),* is slightly favored energetically. The calculated Gibbs free energy of hydration for both the tetra- and pentacoordinated isomers is essentially the same. The key point of the computational results in relation to the experiments performed here is that the calculated Gibbs free energy of formation for the pentahydrated actinyl (V) cations, both tetra- and pentacoordinated, is essentially unfavorable at low water pressures such as ~10^{-6} Torr employed in the experiments; the DFT results effectively explain the absence of pentahydrates.

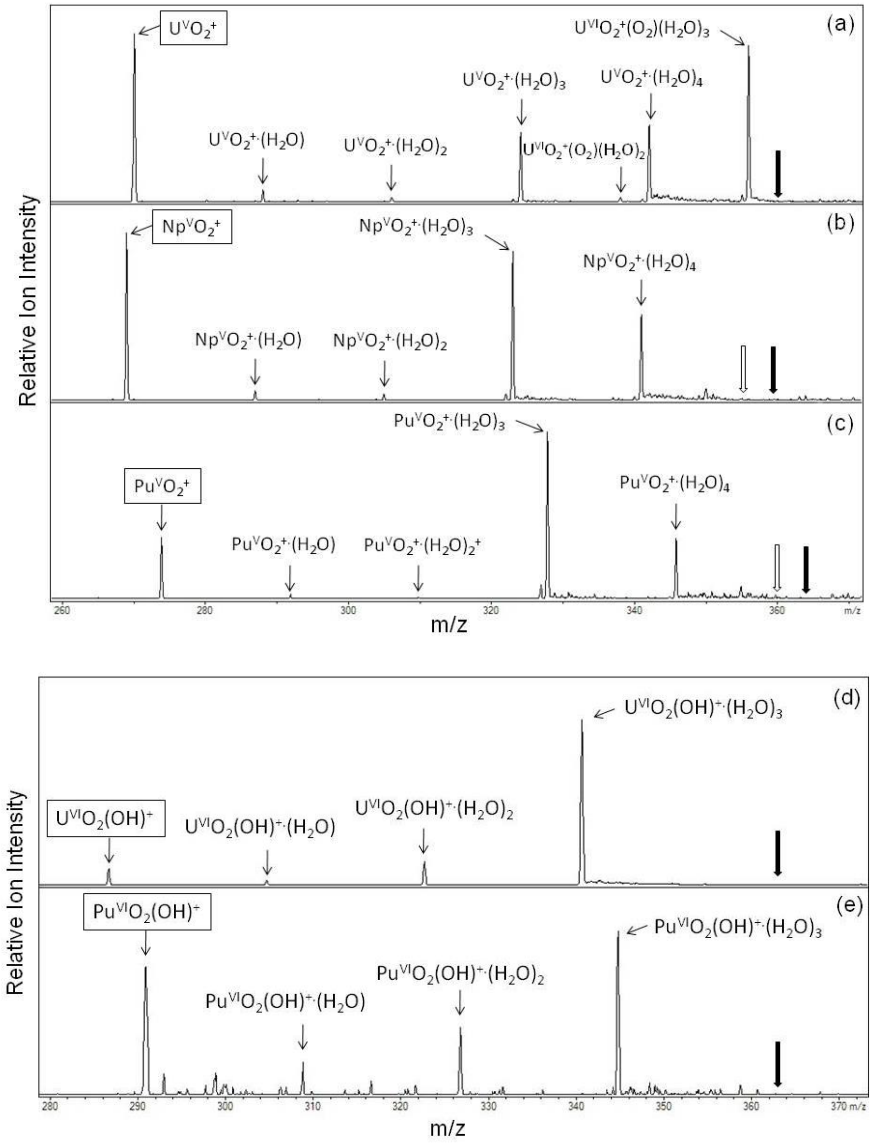

Figure II.2.1. **Top spectra:** Products of isolated (a) $U^{V}O_2^+$, (b) $Np^{V}O_2^+$ and (c) $Pu^{V}O_2^+$ after a reaction time of 10 s. Bold arrows indicate where the non-observed $An^{V}O_2^+\cdot(H_2O)_5$ hydrates would have appeared. The $U^{VI}O_2^+(O_2)(H_2O)_2$ and $U^{VI}O_2^+(O_2)(H_2O)_3$ species are evident in (a); open arrows in (b) and (c) indicate where $NpO_2^+(O_2)(H_2O)_3$ and $PuO_2^+(O_2)(H_2O)_3$ would have appeared. **Bottom spectra:** Products of isolated (d) $UO_2(OH)^+$ and (e) $PuO_2(OH)^+$ after a reaction time of 0.9 s. Bold arrows indicate where the non-observed $AnO_2(OH)^+\cdot(H_2O)_4$ hydrates would have appeared. The several unassigned peaks in (e) reflect the minor intensity of $PuO_2(OH)^+$, which resulted in a low-intensity hydration mass spectrum with significant "noise".

Table II.2.1. Computed bond distances of the ground–state $AnO_2^{+}\cdot(H_2O)_n$, n = 0 –5 structures, and the pentacoordinated $AnO_2^{+}\cdot(H_2O)_5$ isomers.[a]

	An-O_{yl}	**An-O_w**
UO_2^+	1.76	-
NpO_2^+	1.74	-
PuO_2^+	1.73	-
$UO_2^+\cdot(H_2O)$ $NpO_2^+\cdot(H_2O)$	1.77	2.48
$PuO_2^+\cdot(H_2O)$	1.75	2.45
	1.73	2.44
$UO_2^+\cdot(H_2O)_2$	1.79	2.50
$NpO_2^+\cdot(H_2O)_2$	1.76	2.48
$PuO_2^+\cdot(H_2O)_2$	1.75	2.46
$UO_2^+\cdot(H_2O)_3$	1.79	2.50
$NpO_2^+\cdot(H_2O)_3$	1.77	2.50
$PuO_2^+\cdot(H_2O)_3$	1.76	2.49
$UO_2^+\cdot(H_2O)_4$	1.80	2.54
$NpO_2^+\cdot(H_2O)_4$	1.78	2.54
$PuO_2^+\cdot(H_2O)_4$	1.77	2.53
$UO_2^+\cdot(H_2O)_4$*(H_2O)*[b]	1. 80, 1.82	2.52-2.53
$NpO_2^+\cdot(H_2O)_4$*(H_2O)*[b]	1.78, 1.80	2.52-2.53
$PuO_2^+\cdot(H_2O)_4$*(H_2O)*[b]	1.77, 1.78	2.51-2.52
$UO_2^+\cdot(H_2O)_5$	1.80	2.58-2.61
$NpO_2^+\cdot(H_2O)_5$	1.79	2.59-2.60
$PuO_2^+\cdot(H_2O)_5$	1.77	2.58-2.62

[a] In angstroms. Ranges of An-O_w distances are given for the fifth hydrate. [b]Ground-state structures for the fifth–hydrate. These structures are characterized by the presence of two different An-O_{yl} bond distances. Experimental values (in Å) for $NpO_2^{+}\cdot(H_2O)_5$: Np–O_{yl} bond: 1.83[30], 1.83[69]; Np–O_w bond: 2.50, [30] 2.52[69]. Experimental values (in Å) for $PuO_2^{+}\cdot(H_2O)_5$: Pu–O_{yl} bond: 1.81; Pu–O_w bond: 2.47[69].

Table II.2.2. Computed energy (ΔE^0), and Gibbs free energy (ΔG^{298}) changes for the AnO_2^+ and AnO_2OH^+ hydration reactions.[a]

Reaction	UO_2^+	NpO_2^+	PuO_2^+	UO_2OH^+	$NpO_2(OH)^+$	$PuO_2(OH)^+$
n=1						
ΔE^0	-134	-134	-133	-143 [-143][b]	-141	-136
ΔG^{298}	-109	-104	-120	-110	-104	-99
n=2						
ΔE^0	-117	-118	-118	-123 [-124][b]	-123	-118
ΔG^{298}	-81	-82	-82	-83	-88	-83
n=3						
ΔE^0	-108	-106	-104	-93	-94	-87
ΔG^{298}	-72	-70	-68	-54	-56	-49
n=4						
ΔE^0	-83	-79	-74	-55 (-44) [-46] [b]	-54 (-40)	-53 (-31)
ΔG^{298}	-45	-46	-38	-29(-5)	-23 (-2)	-22 (5)
n=5						
ΔE^0	-48 (-37)	-45 (-34)	-44 (-33)	-	-	-
ΔG^{298}	-6 (-7)	-2 (2)	-3 (0)	-	-	-

[a] In $kJ \cdot mol^{-1}$. The reactions correspond to successive hydration reactions: $AnO_2^+ \cdot (H_2O)_{n-1} + H_2O \rightarrow AnO_2^+ \cdot (H_2O)_n$ and $AnO_2OH^+ \cdot (H_2O)_{n-1} + H_2O \rightarrow AnO_2OH^+ \cdot (H_2O)_n$, respectively. Values in parentheses correspond to higher-energy inner-sphere species. [b]In brackets: B3LYP/SDD (U)-aug-cc-pVDZ(O,H).[27]

II.2.4.3 Hydration of $AnO_2(OH)^+$ (An = U, Np, Pu)

The gas-phase hydration behaviors of $UO_2(OH)^+$ and $PuO_2(OH)^+$ were examined, with the key results shown in Figure II.2.1. In contrast to the AnO_2^+ ions, these actinyl hydroxides add only three water molecules with hydration terminating at $AnO_2(OH)^+ \cdot (H_2O)_3$ for both An = U and Pu. Increasing the reaction time resulted in an increase in the abundance of the terminal trihydrate, but not in the appearance of any detectable $AnO_2(OH)^+ \cdot (H_2O)_4$. As discussed above for the AnO_2^+, the interpretation of this result, substantiated by DFT results as discussed below, is that the maximum inner-sphere hydration of the $AnO_2(OH)^+$ is three, and that addition of outer-sphere water molecules is not observed under these conditions. The hydration rates are discussed below. Despite that $NpO_2(OH)^+$ was not observed experimentally, all three $AnO_2(OH)^+$ ions were computationally studied. The most relevant optimized parameters of the ground-state AnO_2OH^+ (An = U, Np and Pu) ions and their hydrates (n = 0–4) are collected in Table II.2.3; the geometrical structures of the $AnO_2(OH)^+(H_2O)_3$*(H_2O)* GS and the higher energy $AnO_2OH^+(H_2O)_4$ isomers are shown in Figure II.2.2. Our calculations indicate that the lowest-energy structure for the

tetrahydrate is obtained when the fourth water molecule is added in the second solvation shell. Several isomers with three water molecules in the inner–shell and the fourth interacting in different coordination motifs in the second shell were found to be practically degenerate in energy with the GS structure; an example of these structures is shown in Fig. S1. The lowest-energy isomer with four water molecules in the inner sphere is higher in energy than the GS by 9 kJ.mol^{-1} for UO_2OH^+, by 22 kJ.mol^{-1} for NpO_2OH^+ and by 18 kJ.mol^{-1} for PuO_2OH^+. The incremental addition of water molecules to the complexes results in essentially no change in the An–O_{yl} axial bonds. The An–OH bond distances are more sensitive to the effect of the addition of water molecules. The increase in the An–OH bond distances in going from the bare AnO_2OH^+ cations to the $AnO_2OH^+\cdot(H_2O)_3$ trihydrates is about 0.06 Å (see Table II.2.3).

The successive hydration energies for the three studied AnO_2OH^+ cations are provided in Table II.2.2, together with the Gibbs free energy changes at 298 K. The energies for addition of the first two water molecules to the $AnO_2(OH)^+$ and AnO_2^+ ions are quite similar. As observed for the actinyl ions, a slight decrease in the magnitude of the hydration energies was found in the actinyl hydroxide cations in going through the series, from U to Pu. Again, the computed Gibbs free energy changes for successive hydrations are notably less favorable than the energy changes, due to the unfavorable entropy for gas-phase association processes. The fourth hydration is exoergic by ~25 kJ.mol^{-1} for the ground–state structure, and practically ergoneutral in the case of the isomer with four inner-sphere water molecules.

Addition of a fourth outer-sphere water to $UO_2(OH)^+$ is computed to be exoergic by -29 kJ.mol^{-1}, yet $UO_2(OH)^+\cdot(H_2O)_4$ is not observed in the experiments. The addition of the fourth inner-sphere water to PuO_2^+ is computed to be exoergic by -38 kJ.mol^{-1} and $PuO_2^+\cdot(H_2O)_4$ is experimentally observed. The free energy difference of -29 kJ.mol versus -38 kJ.mol corresponds to an increase in the “equilibrium constant” by ~40x at 298 K. However, the error in the DFT free energies is sufficiently large—e.g. at least ±5 kJ.mol^{-1}—that the difference could be substantially greater than 9 kJ.mol^{-1}.

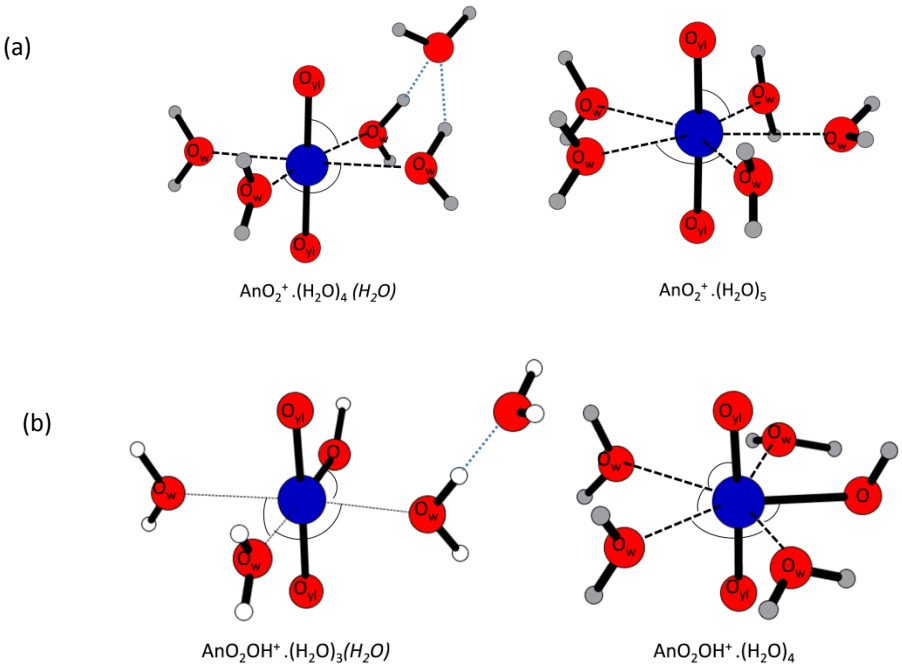

Figure II.2.2. (a) Geometric structures of pentahydrated AnO_2^+ ions. $AnO_2^+\cdot(H_2O)_4$*(H_2O)* is the ground-state structure, whereas $AnO_2^+\cdot(H_2O)_5$ is higher in energy. (b) Lowest-energy optimized structures of tetrahydrated AnO_2OH^+ ions. $AnO_2OH^+\cdot(H_2O)_3$*(H_2O)* is the ground-state structure, whereas $AnO_2OH^+\cdot(H_2O)_4$ is higher in energy. Italics denote water molecules in the second solvation shell. The most relevant geometric parameters are reported in Tables 1 and 3, respectively.

Table II.2.3. Computed bond distances for the ground-state $AnO_2OH^+\cdot(H_2O)_n$, n = 0–4 structures.[a]

	An-O_{yl}	An-OH	An-O_w
UO_2OH^+	1.74	2.01	-
NpO_2OH^+	1.73	2.01	-
PuO_2OH^+	1.72	2.02	-
$UO_2OH^+\cdot(H_2O)$	1.76	2.03	2.44
$NpO_2OH^+\cdot(H_2O)$	1.74	2.02	2.43
$PuO_2OH^+\cdot(H_2O)$	1.73	2.03	2.42
$UO_2OH^+\cdot(H_2O)_2$	1.76	2.05	2.49
$NpO_2OH^+\cdot(H_2O)_2$	1.74	2.04	2.47
$PuO_2OH^+\cdot(H_2O)_2$	1.73	2.05	2.47
$UO_2OH^+\cdot(H_2O)_3$	1.77	2.07	2.50-2.54
$NpO_2OH^+\cdot(H_2O)_3$	1.75	2.07	2.49-2.52
$PuO_2OH^+\cdot(H_2O)_3$	1.73	2.07	2.48-2.53
$UO_2OH^+\cdot(H_2O)_3$*H_2O*[b]	1.78	2.08	2.43-2.55
$NpO_2OH^+\cdot(H_2O)_3$*H_2O*[b]	1.76	2.07	2.42-2.53
$PuO_2OH^+\cdot(H_2O)_3$*H_2O*[b]	1.74	2.08	2.42-2.54
$UO_2OH^+\cdot(H_2O)_4$	1.77	2.13	2.56-2.58
$NpO_2OH^+\cdot(H_2O)_4$	1.75	2.13	2.56-2.57
$PuO_2OH^+\cdot(H_2O)_4$	1.73	2.12	2.54-2.56

[a]In angstroms. Ranges of An-O_w distances are given for the third and fourth hydrate. [b] Ground-state structure for the fourth hydrate.

II.2.4.4 Comparative hydration kinetics: AnO_2^+ versus $AnO_2(OH)^+$

The primary hydration rates corresponding to Equation 2 were measured for the five actinyl ions which could be isolated, $I^+ = UO_2^+$, NpO_2^+, PuO_2^+, $UO_2(OH)^+$ or $PuO_2(OH)^+$.

$$I^+ + H_2O \rightarrow I^+\cdot(H_2O) \qquad (2)$$

As the water pressure in the trap is constant, the kinetics for Eqn. 2 are pseudo-first-order, as given by Equations 3a and 3b.

$$d[I^+]/dt = k[H_2O][I^+] = k'[I^+] \qquad (3a)$$

$$\ln\{[I^+]/[I^+]_0\} = -k't \qquad (3b)$$

The values of k' were obtained from the slope of the log of the actinyl ion decay versus time (an example is shown in Fig. S4). Because the water pressure, as well as the helium pressure, was held constant for all kinetics determinations, the measured rates directly provide comparative kinetics. Rates for uranyl species were measured at ITN as well as at LBNL, to confirm and extend the kinetics comparisons. Measured rates are given in Supporting Information (Table S4). For comparative purposes the following relative rates are normalized to the fastest, that for $UO_2(OH)^+$ in the present work, designated as 100%; the relative rates in italics were determined at ITN (uncertainties are given in parentheses); values from Gresham et al.[3] are in brackets:

$$UO_2(OH)^+ \text{ / } 100;\ \textit{100};\ [63] > PuO_2(OH)^+ \text{ / } 40(18)$$
$$>> PuO_2^+ \text{ / } 5.0(0.9) \approx UO_2^+ \text{ / } 3.9(0.6);\ \textit{3.5(0.5)};\ [100] \approx NpO_2^+ \text{ / } 3.5(0.5)$$

As the rates depend on the extent of third body collisional stabilization, these relative rates will not necessarily be observed under conditions where the pressure of the cooling gas is significantly higher or lower. Given the magnitudes of the assigned uncertainties, differences in the rates between the two $AnO_2(OH)^+$, as well as among the three AnO_2^+, are considered minor. The particularly large uncertainty for $PuO_2(OH)^+$ is attributed to the very low abundance of that reactant ion (see Fig. II.2.1e). As is evident from comparison of the spectra in Figure II.2.1, as well as the measured rates reported above, the $AnO_2(OH)^+$ ions hydrate much more efficiently than do the AnO_2^+ ions, with the rate of hydration of $UO_2(OH)^+$ more than an order of magnitude faster than that of UO_2^+, as determined at both LBNL (26x faster) and ITN (29x faster). In contrast to the present results, Gresham et al.[3] reported that the hydration rate for $UO_2(OH)^+$ is somewhat slower than that for UO_2^+. These previous kinetics results were obtained under similar conditions to those employed here, in an ion trap mass spectrometer with a helium pressure of ~10^{-4} Torr and a water pressure of ~10^{-6} Torr. The origins of the disparity are not obvious but may be related to the adaptive simulated annealing (ASA) methodology employed in the previous work to model kinetics and derive rate constants.[3] The pseudo-first-order kinetics were directly determined in the present work (see Fig. S4); furthermore, comparison of the extent depletion of UO_2^+ after 10 s (Fig. II.2.1a) with that of $UO_2(OH)^+$ after 0.9 s (Fig. II.2.1d), at constant water pressure, clearly reveals that hydration of the latter is much faster. As has been discussed by Böhme and co-workers for association reactions of metal ions with water,[61,62] the comparative kinetics obtained in the present work—i.e., substantially faster hydration for $UO_2(OH)^+$ versus UO_2^+—is attributed to the additional hydroxyl vibrational degrees of freedom in the hot $\{AnO_2(OH)^+\cdot(H_2O)\}^*$ product as compared with $\{AnO_2^+\cdot(H_2O)\}^*$. The ability of nascent hydroxyl hydrates to more effectively

dissipate the hydration energy results in longer-lived association complexes which have a greater opportunity for third-body collisional cooling prior to dissociation.

It was also possible to obtain the following relative sequential hydration rates for $UO_2(OH)^+$ and UO_2^+ at LBNL and/or ITN (ITN values are in italics; uncertainties are in parentheses); values from Gresham et al.[3] are in brackets:

$$UO_2(OH)^+\cdot(H_2O) \text{ / } 100;\ \textit{100};\ [100] > UO_2(OH)^+\cdot(H_2O)_2 \text{ / } 40(18);\ \textit{45(3)};\ [31]$$
$$> UO_2(OH)^+ \text{ / } 20(2);\ \textit{22(2)};\ [27]$$

$$UO_2^+\cdot(H_2O) \text{ / } \textit{100};\ [100] >> UO_2^+ \text{ / } \textit{4.4(0.4)};\ [20]$$

There is good agreement between the LBNL and ITN relative rates for $UO_2(OH)^+\cdot(H_2O)_n$, and also reasonable agreement with those reported by Gresham et al.[3] The water ligand in $UO_2(OH)^+\cdot(H_2O)$ apparently provides additional stabilization of hot product $\{UO_2(OH)^+\cdot(H_2O)_2\}^*$ to enable collisional cooling and enhance hydration efficiency. In accord with evaluations of Böhme and co-workers,[61,62] the decreasing thermodynamic benefit of addition of the third water ligand offsets the additional degrees of freedom in $\{UO_2(OH)^+\cdot(H_2O)_3\}^*$ (see Table II.2.2). The same general rate trend for the corresponding $PuO_2(OH)^+\cdot(H_2O)_n$ (n = 0, 1, 2) is deduced from the similar hydrate abundances in Figs. II.2.1d and II.2.1e.

The above comparative sequential hydration rates obtained for UO_2^+ and $UO_2^+\cdot(H_2O)$ are in qualitative accord with relative rate constants obtained by Gresham et al.[3]. The hydration rate for bare UO_2^+, although thermodynamically the most favorable, is much lower than that for hydration of $UO_2^+\cdot(H_2O)$, reflecting insufficient degrees of freedom for energy dissipation in the stiff bare uranyl ion. Addition of a single water ligand renders hydration of $UO_2^+\cdot(H_2O)$ much more efficient. There is a correspondence between the results for UO_2^+ and $UO_2(OH)^+$, for both of which the monohydrate adds water much more efficiently than does the bare ion, which is attributed to the presence of a single water ligand providing additional vibrational excitation modes for energy dissipation and collisional cooling prior to dissociation.[61,62]

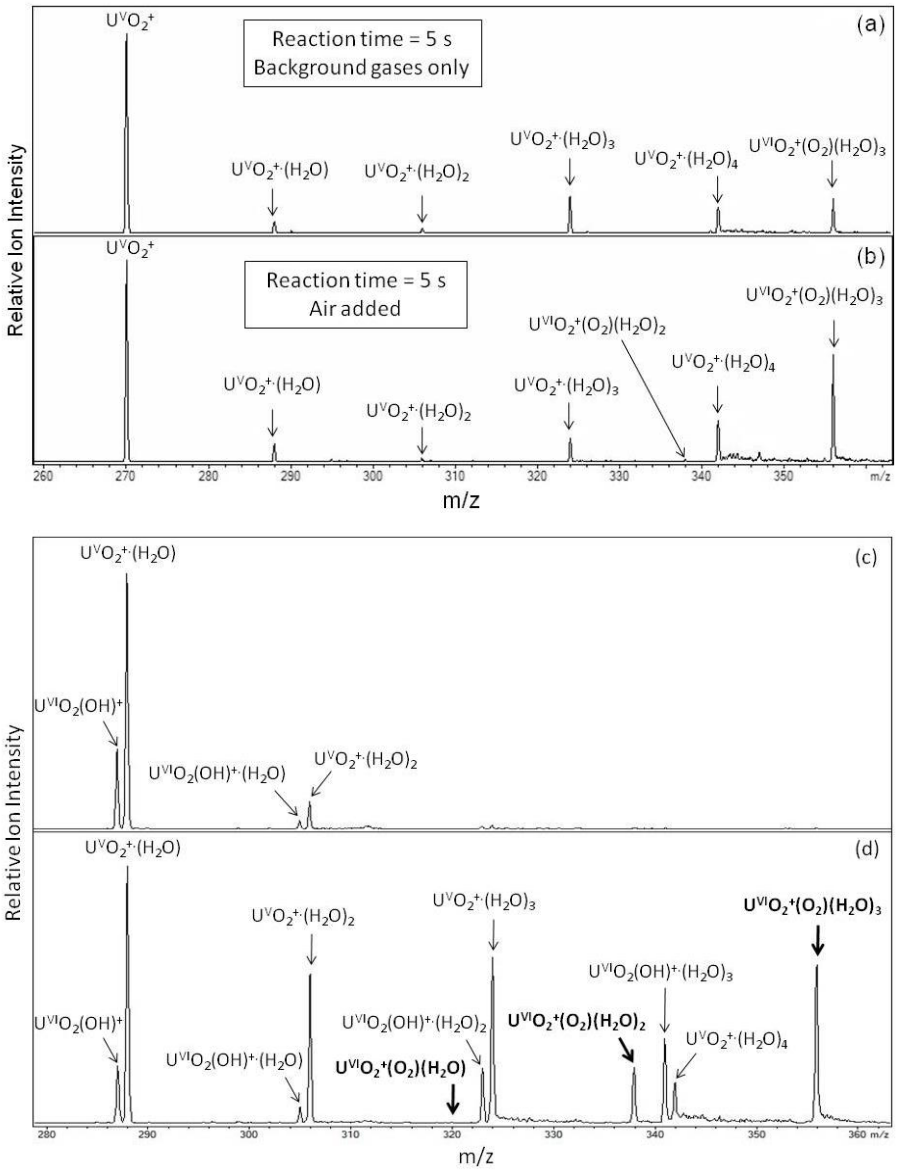

Figure II.2.3. Top spectra: Reaction of isolated UO_2^+ for 5 s: (a) with background gases; (b) after addition of air to the ion trap. The same experiment performed with NpO_2^+ and PuO_2^+ resulted in only the hydrates, no O_2-addition products. **Bottom spectra:** Reaction of isolated $UO_2^+\cdot(H_2O)$ and $UO_2(OH)^+$ with background gases and added air for (c) no applied reaction time; and (d) a reaction time of 0.5 s. The product spectrum (d) shows O_2-addition to $UO_2^+\cdot(H_2O)_2$ and $UO_2^+\cdot(H_2O)_3$, but not to $UO_2^+\cdot(H_2O)$. The appearance of products in spectrum (c) without any applied reaction time reflects an inherent time delay of ~70 ms associated with ion isolation. The "soft ESI" conditions used to enhance the yield of $UO_2^+\cdot(H_2O)$ are described in the Fig. S5.

II.2.4.5 Oxygen addition to $AnO_2{\cdot}(H_2O)_n^+$: uranyl versus neptunyl

A striking result evident in Figure II.2.1a is the appearance of an intense peak corresponding to $UO_2^+(O_2)(H_2O)_3$, and a minor peak corresponding to $UO_2^+(O_2)(H_2O)_2$. No such O_2-addition products were observed in the corresponding spectra for NpO_2^+ or PuO_2^+, as is evident in Figures II.2.1b and II.2.1c. The di-oxygen addition products are attributed to reaction with background O_2 in the ion trap. As confirmation, addition of air into the trap resulted in a substantial increase in the relative intensity of the peak corresponding to $UO_2^+(O_2)(H_2O)_3$, as seen in Figure II.2.3b. Similar addition of air to the trap after isolation of NpO_2^+ and PuO_2^+ did not result in any detectable O_2-addition products. To confirm the minor $UO_2^+(O_2)(H_2O)_2$ product evident in Figures II.2.1a and II.2.3b, the ESI yield of $UO_2^+{\cdot}(H_2O)$ was optimized using the instrumental parameters given in the caption to Figure S5. As is evident in Figure II.2.3d (and Figure S5), both $UO_2^+(O_2)(H_2O)_2$ and $UO_2^+(O_2)(H_2O)_3$ are significant products. It is also apparent from Figure II.2.3d that $UO_2^+(O_2)(H_2O)$ is not produced: O_2-addition evidently occurs only for uranyl(V) dihydrate and trihydrate.

As O_2 addition to other UO_2^+ complexes has been previously reported,[34-36,38] an observation of particular interest in the present study is the difference between uranyl(V) hydrates, which add O_2, versus neptunyl(V) and plutonyl(V) hydrates, which do not. DFT computations were performed to understand the nature of the $UO_2^+(O_2)(H_2O)_n$ products, and why O_2-addition products were not similarly produced for NpO_2^+; these computations were not performed for PuO_2^+ as its behavior is similar to NpO_2. Several initial structures were considered for each of the cations investigated, taking into account two possible O_2-coordination modes, i.e. end-on (η^1) and side-on (η^2). Different possible spin multiplicities (doublet and quartet for $UO_2^+(O_2)(H_2O)_n$; singlet, triplet and quintet for $NpO_2^+(O_2)(H_2O)_n$) were considered for each of the coordination modes.

The geometrical parameters of the lowest-energy structures of the $UO_2(O_2)^+$ cation and its hydrates are shown in Fig. II.2.4; the energy changes together with the free energy changes for the addition of O_2 to the bare and hydrated cations are presented in Table II.2.4 (enthalpy and entropy changes are included as Supporting Information, Table S5). Our computations indicate that O_2 binds to UO_2^+ in a side-on (η^2) configuration for the $UO_2^+(O_2)$ bare cation and its hydrates, in analogy with previous results for other UO_2^+ complexes.[35,36,38] All the $UO_2^+(\eta^2{-}O_2)(H_2O)_n$ structures are in the doublet ground-spin state, and the O–O bond lengths (ca.1.30 Å) are those of a superoxo-complex in which uranium(V) has been oxidized to uranium(VI).[35,38] The di-oxygen binding energies, which include ZPVE and basis sets superposition error corrections, initially rise with the increasing number of water molecules, from 52 kJ.mol^{-1} in the bare cation, $UO_2^+(O_2)$, to 67 kJ.mol^{-1} in $UO_2^+(O_2)(H_2O)$, and to 80 kJ.mol^{-1} in $UO_2^+(O_2)(H_2O)_2$ (Table II.2.4). The presence of a third water molecule results in a slight decrease of the O_2 binding energy, to 74 kJ.mol^{-1}. A similar

trend was observed in a previous theoretical study,[35] in which the O_2 binding modes and energies were analyzed for $UO_2^+(O_2)(acetone)_n$ (n = 0–3). In that work, the strong η^2–O_2 binding to UO_2^+ and its successive solvates were described as two–electron three–atom bonds, in which the increasing number of electron-donor acetone ligands strengthens the interaction energy with di-oxygen; although water is a weaker Lewis base than acetone, a similar effect of increasing uranyl(V)-O_2 binding energy as donor ligands are added is to be expected, and is observed.

The computed free energy of addition of inner-sphere O_2 to $UO_2^+\cdot(H_2O)_3$, -26 kJ.mol^{-1}, which process is observed, is slightly less favorable than that computed for the addition of an outer-sphere H_2O to $UO_2(OH)^+\cdot(H_2O)_3$, -29 kJ.mol^{-1}, which process is not observed. As remarked below, the results suggest that the DFT binding free energies of O_2 to UO_2^+ complexes may be significantly underestimated, by perhaps up to 30 kJ.mol^{-1}. It should also be noted that the relative pressures of O_2 and H_2O in the ion trap are not known, though it is estimated that the pressures should be similar to within an order of magnitude.[3]

The lowest-energy $NpO_2^+(O_2)(H_2O)_n$ isomers are characterized by the presence of a di-oxygen molecule in a η^1 mode (Fig. II.2.5). The O-O bond length is very close to that of the free O_2 molecule (1.206 Å at the B3LYP/SDD level of theory). Our calculations indicate that the open-shell singlet state (antiferromagnetic) computed using the BS approach and the quintet spin state are practically degenerate in energy (within 4 kJ.mol^{-1}), with the singlet state being slightly favored. The di-oxygen binding energies are considerably lower than the corresponding values in the $UO_2^+(\eta^2\text{-}O_2)(H_2O)_n$ ions. The O_2 binding energy in $NpO_2^+(O_2)$ is ca. 24 kJ.mol^{-1}, and this binding energy decreases with the presence of water molecules, which is just the opposite trend observed for the $UO_2^+(\eta^2\text{-}O_2)(H_2O)_n$ superoxo complexes. The computed O_2 binding energies are 19 kJ.mol^{-1} in $NpO_2^+(O_2)(H_2O)$, 16 kJ.mol^{-1} in $NpO_2^+(O_2)(H_2O)_2$, and 4 kJ.mol^{-1} in $NpO_2^+(O_2)(H_2O)_3$; the corresponding free energies for O_2-addition are all positive, from +2 kJ.mol^{-1} for NpO_2^+ to +28 kJ.mol^{-1} for $NpO_2^+\cdot(H_2O)_3$ (Table II.2.4). A summary of NPA charges of all the studied $AnO_2^+(O_2)(H_2O)_n$ ions is included as Supporting Information (Table S6).

In contrast to the uranyl-dioxygen superoxo complexes in which U^V has been oxidized to U^{VI}, the weakly bound neptunyl-dioxygen complexes evidently retain the Np^V oxidation state. The experimental observation of $UO_2^+(O_2)(H_2O)_n$ (n = 2 or 3) complexes, but not $NpO_2^+(O_2)(H_2O)_n$ complexes is essentially a manifestation of the much lower VI/V reduction potential for U as compared with Np,[57] as discussed above. As the VI/V reduction potential for Pu (0.91 V) is substantially greater than that for U (0.06 V), but rather similar to that for Np (1.14 V), the non-observation of $PuO_2^+(O_2)(H_2O)_n$ complexes can also be attributed to the relative inaccessibility of the Pu^{VI} oxidation state.

Addition of O_2 to $UO_2^+\cdot(H_2O)_n$ was only observed for n = 2 or 3, whereas the DFT results (Table II.2.4) reveal that O_2 addition is also thermodynamically favorable for n = 0 or 1. Comparison of the free energies for addition of H_2O and O_2 to $UO_2^+\cdot(H_2O)_n$ (Tables II.2.2 and II.2.4) reveal that H_2O-addition is substantially more exoergic than O_2-addition for n = 0 or 1, in accord with the dominance of hydration. However, as H_2O-addition to $UO_2^+\cdot(H_2O)_n$ remains substantially more exoergic (and exothermic) for n = 2 or 3, it is intriguing that O_2-addition is competitive with H_2O-addition (see Figure II.2.3), and is dominant for n = 3. As remarked below, this and other observations lead to the conclusion that the free energies for addition of O_2 to uranyl(V) hydrates are substantially more favorable than computed.

All the reaction pathways analyzed for UO_2^+ complexes are summarized in Scheme II.2.1.

The species shown in Scheme II.2.1 were isolated and reacted with O_2/H_2O as indicated. Among the species shown there, only $UO_2^+(O_2)(H_2O)$ and $UO_2^+\cdot(H_2O)_4$ could not be isolated, such that it is not known whether H_2O replaces O_2 in the first case, or vice versa in the latter case. However, the reversible reaction shown in the scheme was confirmed. Included in Scheme II.2.1 are the reactions given by Equations 4, 5 and 6; the computed free energies at 298 K are reported here.

$$UO_2^+\cdot(H_2O)_2 + O_2 \xrightarrow{-X} UO_2^+(O_2)(H_2O) + H_2O \qquad \Delta G^{298} = +58 \text{ kJ mol}^{-1} \qquad (4)$$

$$UO_2^+(O_2)(H_2O)_3 + H_2O \xrightarrow{-X} UO_2^+\cdot(H_2O)_4 + O_2 \qquad \Delta G^{298} = -19 \text{ kJ mol}^{-1} \qquad (5)$$

$$UO_2^+(O_2)(H_2O)_2 + H_2O \leftrightarrow UO_2^+\cdot(H_2O)_3 + O_2 \qquad \Delta G^{298} = -35 \text{ kJ mol}^{-1} \qquad (6)$$

The non-occurrence of Eqn. 4 is in accord with the computed free energy. Eqn. 5 is not observed but is computed to be exoergic, albeit by only -19 kJ mol^{-1}; there may be a kinetic barrier to this exchange reaction for a monopositive uranyl ion with a coordination number of five: three monodentate H_2O ligands and one bidentate O_2. The forward reaction given by Eqn. 6 is computed to be exoergic by -35 kJ mol^{-1} and is observed; however the reverse reaction is also observed, which suggests that this exchange reaction is close to thermoneutral (e.g., ΔG in the range of ca. ±10 kJ mol^{-1}). The apparent discrepancy between computed energetic and experimental observations for Eqn. 6 might reflect the greater uncertainties in DFT energies when a change in oxidation state is involved.[63-65] In particular, the DFT computations may somewhat underestimate, by ca. 30 kJ mol^{-1}, the binding free energy of O_2 to $UO_2^+\cdot(H_2O)_2$. This possible error does not substantially affect the overall interpretations of the DFT results.

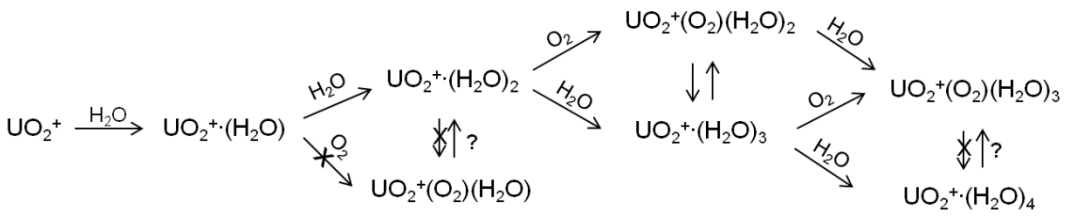

Scheme II.2.1. Reactions of UO_2^+ complexes with H_2O and O_2. Reactions marked with an "X" were not observed; the reaction marked with a "?" could not be studied.

Table II.2.4. Computed energy (ΔE^0) and Gibbs free energy (ΔG^{298}) changes for the O_2 addition reactions.[a]

Reaction	**UO_2^+**	**$UO_2^+\cdot(H_2O)$**	**$UO_2^+\cdot(H_2O)_2$**	**$UO_2^+\cdot(H_2O)_3$**
ΔE^0	-52	-67	-80	-74
ΔG^{298}	-20	-24	-37	-26
Reaction	NpO_2^+	$NpO_2^+\cdot(H_2O)$	$NpO_2^+\cdot(H_2O)_2$	$NpO_2^+\cdot(H_2O)_3$
ΔE^0	-24	-19	-16	-4
ΔG^{298}	2	12	15	28

[a]In kJ mol^{-1}. The reactions correspond to the O_2 addition reactions: $AnO_2^+\cdot(H_2O)_n + O_2 \rightarrow AnO_2^+(O_2)(H_2O)_n$ for An = U, Np (n = 0-3). All reactants and products are in their ground state.

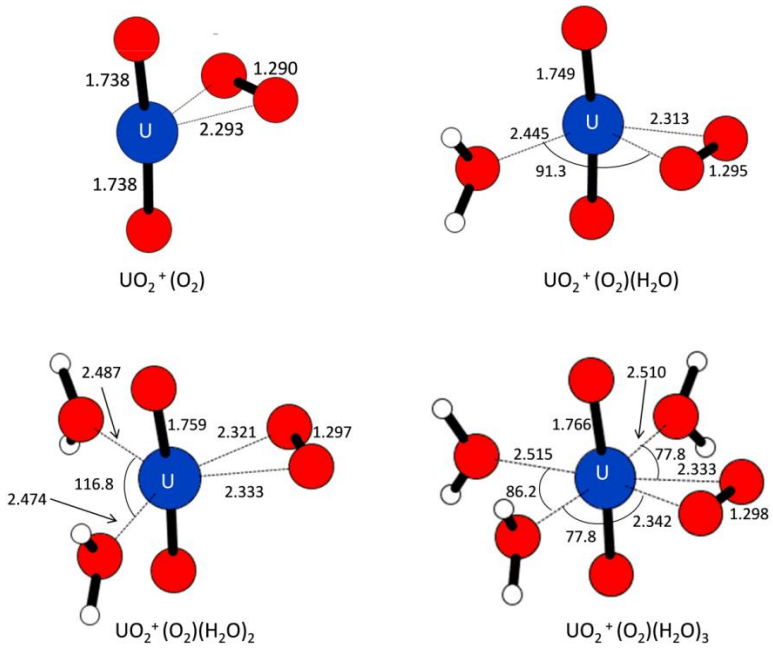

Figure II.2.4. Lowest-energy optimized structures for $UO_2^+(O_2)(H_2O)_n$, n = 0–3. All the species are in the doublet ground spin state.

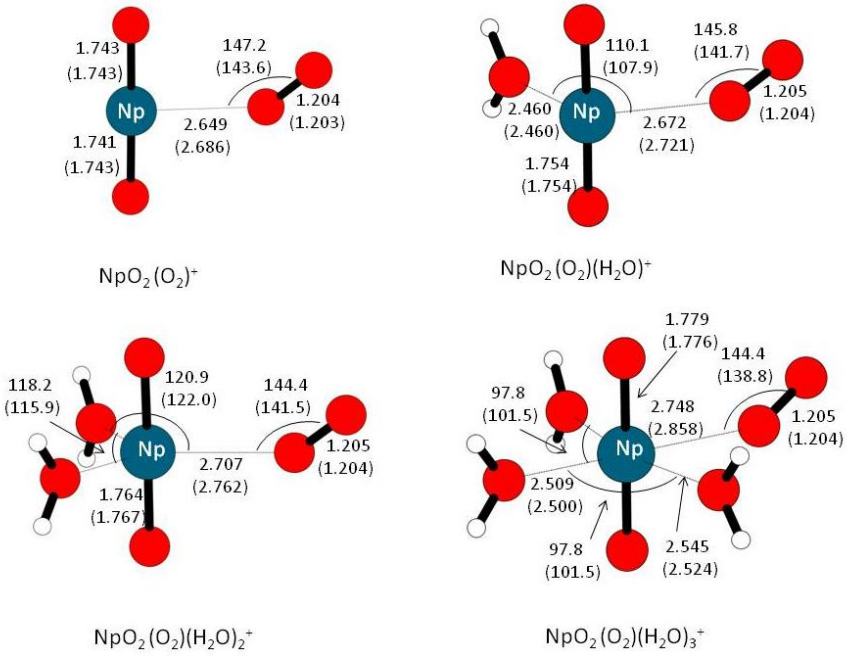

Figure II.2.5. Lowest-energy optimized structures for $NpO_2^+(O_2)(H_2O)_n$, n = 0–3, in the (open-shell) singlet ground spin state and in the quintet spin state (in parenthesis).

II.2.5. Conclusions

The monopositive actinyl ions $An^{V}O_2^+$ (An = U, Np, Pu) and $An^{VI}O_2(OH)^+$ (An = U, Pu) were produced by ESI; the gas-phase addition of water and di-oxygen to these ions was studied by experiment and DFT. The ESI yields of the actinyl(VI) ions, $UO_2(OH)^+$ >> $PuO_2(OH)^+$ > $NpO_2(OH)^+$ (the last was not observed), directly reflect the stabilities of the An^{VI} relative to An^{V}: U >> Pu > Np. Gas-phase hydration of the actinyls terminated at $AnO_2^+\cdot(H_2O)_4$ and at $AnO_2(OH)^+\cdot(H_2O)_3$. DFT computations revealed that the next added water in both cases is outer-sphere for the lowest-energy structures; under our experimental conditions only inner sphere hydrates are observed. The inner-sphere actinyl hydration shell in the gas phase—i.e., the intrinsic elementary hydration—comprises one less water than in solution: $AnO_2^+\cdot(H_2O)_4${gas} versus $AnO_2^+\cdot(H_2O)_5${aqueous}. This disparity is attributed to the "cooperative polarization effect" in solution,[9] whereby water is rendered a more effective electron-donor Lewis base due to electron donation from second-shell water molecules. The comparative hydration rates for the $AnO_2(OH)^+$ ions were more than one order of magnitude greater than for the AnO_2^+ ions, which is attributed to the additional vibrational degrees of freedom in the hydroxides for dissipation of hydration energy to enable stabilization of the nascent hydrate by third-body collisional cooling. The $U^{V}O_2^+\cdot(H_2O)_n$ ions (n = 2 or 3) added O_2 to produce $UO_2^+(O_2)\cdot(H_2O)_n$; DFT revealed these to be superoxides in which uranium has been oxidized, formally $U^{VI}O_2^{2+}(\eta^2\text{-}O_2^-)(H_2O)_n$, with a substantial U-($\eta^2$-$O_2$) binding energy (i.e., >70 kJ.mol^{-1}). Di-oxygen addition was not observed for the corresponding neptunyl or plutonyl hydrates; DFT computations for the neptunyl species revealed that the most stable structures were $NpO_2^+(\eta^1\text{-}O_2)(H_2O)_n$, in which the Np-($\eta^1$-$O_2$) binding energy is small (i.e., <20 kJ.mol^{-1}). The absence of superoxide formation for neptunyl(V) and plutonyl(V) is a manifestation of the relatively large VI/V reduction potentials, 1.16 V for Np and 0.94V for Pu, as compared with the value of 0.09 V for U.[57] The gas-phase results furthermore reveal condensed phase actinide chemistry,[66] including the contrasting prevalence of neptunyl(V)[67] and elusiveness of uranyl(V).[68] Among the aspects of gas-phase chemistry which will be pursued to elucidate and potentially advance condensed phase chemistry are stabilization of neptunyl(VI) and plutonyl(VI) by addition of O_2 to actinyl(V) coordination complexes with more strongly electron-donating ligands than water.

Acknowledgments

Research was supported by the U.S. Department of Energy, Office of Basic Energy Sciences, Heavy Element Chemistry at LBNL, under Contract No. DE-AC02-05CH11231 [D.R., T.H.B., J.K.G.]; by the Università della Calabria [M.C.M]; and by the Fundação para a Ciência e a Tecnologia (acquisition

of the QIT/MS at ITN and support as part of RNEM-Rede Nacional de Espectrometria de Massa, and PhD grant SFRH/BD/70475/2010 to A.F.L.) [A.F.L., J.M.]. M.C.M. is grateful for the opportunity to be a Guest Scientist in the LBNL Chemical Sciences Division. The authors thank Dr. Guoxin Tian for providing the three actinyl stock solutions at LBNL. This research used resources of the National Energy Research Scientific Computing Center (NERSC), which is supported by the Office of Science of the U.S. Department of Energy under Contract No. DE-AC02-05CH11231.

References

(1) Denning, R. G., Electronic-structure and bonding in actinyl ions, *Structure and Bonding* **1992**, 79, 215.

(2) Denning, R. G., Electronic structure and bonding in actinyl ions and their analogs, *Journal of Physical Chemistry A* **2007**, 111, 4125.

(3) Gresham, G. L.; Gianotto, A. K.; Harrington, P. D.; Cao, L. B.; Scott, J. R.; Olson, J. E.; Appelhans, A. D.; Van Stipdonk, M. J.; Groenewold, G. S., Gas-phase hydration of U(IV), U(V), and U(VI) dioxo monocations, *Journal of Physical Chemistry A* **2003**, 107, 8530.

(4) Chien, W.; Anbalagan, V.; Zandler, M.; Van Stipdonk, M.; Hanna, D.; Gresham, G.; Groenewold, G., Intrinsic hydration of monopositive uranyl hydroxide, nitrate, and acetate cations, *Journal of the American Society for Mass Spectrometry* **2004**, 15, 777.

(5) Arnold, P. L.; Love, J. B.; Patel, D., Pentavalent uranyl complexes, *Coordination Chemistry Reviews* **2009**, 253, 1973.

(6) Antonio, M. R.; Soderholm, L.; Williams, C. W.; Blaudeau, J. P.; Bursten, B. E., Neptunium redox speciation, *Radiochimica Acta* **2001**, 89, 17.

(7) Skanthakumar, S.; Antonio, M. R.; Soderholm, L., A comparison of neptunyl(V) and neptunyl(VI) solution coordination: The stability of cation-cation interactions, *Inorganic Chemistry* **2008**, 47, 4591.

(8) Neuefeind, J.; Soderholm, L.; Skanthakumar, S., Experimental coordination environment of uranyl(VI) in aqueous solution, *Journal of Physical Chemistry A* **2004**, 108, 2733.

(9) Bühl, M.; Sieffert, N.; Chaumont, A.; Wipff, G., Water versus acetonitrile coordination to uranyl. Density functional study of cooperative polarization effects in solution, *Inorganic Chemistry* **2011**, 50, 299.

(10) Spencer, S.; Gagliardi, L.; Handy, N. C.; Ioannou, A. G.; Skylaris, C. K.; Willetts, A.; Simper, A. M., Hydration of UO_2^{2+} and PuO_2^{2+}, *Journal of Physical Chemistry A* **1999**, 103, 1831.

(11) Tsushima, S.; Suzuki, A., Hydration numbers of pentavalent and hexavalent uranyl, neptunyl, and plutonyl, *Journal of Molecular Structure: THEOCHEM* **2000**, 529, 21.

(12) Tsushima, S.; Suzuki, A., Abstract of the *Annual Meeting of the Atomic Energy Society of Japan* **1999**, 757.

(13) Hay, P. J.; Martin, R. L.; Schreckenbach, G., Theoretical studies of the properties and solution chemistry of AnO_2^{2+} and AnO_2^{+} aquo complexes for An = U, Np, and Pu, *Journal of Physical Chemistry A* **2000**, 104, 6259.

(14) Tsushima, S.; Yang, T. X.; Suzuki, A., Theoretical gibbs free energy study on $UO_2(H_2O)_n^{2+}$ and its hydrolysis products, *Chemical Physics Letters* **2001**, 334, 365.

(15) Vallet, V.; Wahlgren, U.; Schimmelpfennig, B.; Szabo, Z.; Grenthe, I., The mechanism for water exchange in $[UO_2(H_2O)_5]^{2+}$ and $[UO_2(oxalate)_2(H_2O)]^{2-}$, as studied by quantum chemical methods, *Journal of the American Chemical Society* **2001**, 123, 11999.

(16) Clavaguera-Sarrio, C.; Hoyau, S.; Ismail, N.; Marsden, C. J., Modeling complexes of the uranyl ion $UO_2L_{2n}^{+}$: Binding energies, geometries, and bonding analysis, *Journal of Physical Chemistry A* **2003**, 107, 4515.

(17) Clavaguera-Sarrio, C.; Brenner, V.; Hoyau, S.; Marsden, C. J.; Millie, P.; Dognon, J. P., Modeling of uranyl cation-water clusters, *Journal of Physical Chemistry B* **2003**, 107, 3051.

(18) Moskaleva, L. V.; Krüger, S.; Spörl, A.; Rösch, N., Role of solvation in the reduction of the uranyl dication by water: A density functional study, *Inorganic Chemistry* **2004**, 43, 4080.

(19) Cao, Z. J.; Balasubramanian, K., Theoretical studies of $UO_2(H_2O)_n^{2+}$, $NpO_2(H_2O)_n^{+}$, and $PuO_2(H_2O)_n^{2+}$ complexes (n=4-6) in aqueous solution and gas phase, *The Journal of Chemical Physics* **2005**, 123, 114309.

(20) Shamov, G. A.; Schreckenbach, G., Density functional studies of actinyl aquo complexes studied using small-core effective core potentials and a scalar four-component relativistic method, *Journal of Physical Chemistry A* **2005**, 109, 10961.

(21) Shamov, G. A.; Schreckenbach, G., Density functional studies of actinyl aquo complexes studied using small-core effective core potentials and a scalar four-component relativistic method (vol 109A, PG 10967, 2005), *Journal of Physical Chemistry A* **2006**, 110, 12072.

(22) Gutowski, K. E.; Dixon, D. A., Predicting the energy of the water exchange reaction and free energy of solvation for the uranyl ion in aqueous solution, *Journal of Physical Chemistry A* **2006**, 110, 8840.

(23) Siboulet, B.; Marsden, C. J.; Vitorge, P., A theoretical study of uranyl solvation: Explicit modelling of the second hydration sphere by quantum mechanical methods, *Chemical Physics* **2006**, 326, 289.

(24) Vallet, V.; Macak, P.; Wahlgren, U.; Grenthe, I., Actinide chemistry in solution, quantum chemical methods and models, *Theoretical Chemistry Accounts* **2006**, 115, 145.

(25) Cao, Z. J.; Balasubramanian, K., Theoretical studies of $UO_2(OH)(H_2O)_n^+$, $UO_2(OH)_2(H_2O)_n$, $NpO_2(OH)(H_2O)_n$, and $PuO_2(OH)(H_2O)_n^+$ (n <= 21) complexes in aqueous solution, *Journal of Chemical Physics* **2009**, 131, 164504.

(26) Tsierkezos, N. G.; Roithová, J.; Schröder, D.; Ončák, M.; Slavíček, P., Can electrospray mass spectrometry quantitatively probe speciation? Hydrolysis of uranyl nitrate studied by gas-phase methods, *Inorganic Chemistry* **2009**, 48, 6287.

(27) Ončák, M.; Schröder, D.; Slavíček, P., Theoretical study of the microhydration of mononuclear and dinuclear uranium(VI) species derived from solvolysis of uranyl nitrate in water, *Journal of Computational Chemistry* **2010**, 31, 2294.

(28) Schreckenbach, G.; Shamov, G. A., Theoretical Actinide Molecular Science, *Accounts of Chemical Research* **2010**, 43, 19.

(29) Ramakrishnan, R.; Matveev, A. V.; Rösch, N., Effects of the self-interaction error in Kohn-Sham calculations: A DFT + U case study on penta-aqua uranyl(VI), *Computational and Theoretical Chemistry* **2011**, 963, 337.

(30) Allen, P. G.; Bucher, J. J.; Shuh, D. K.; Edelstein, N. M.; Reich, T., Investigation of aquo and chloro complexes of UO_2^{2+}, NpO_2^+, Np^{4+}, and Pu^{3+} by X-ray absorption fine structure spectroscopy, *Inorganic Chemistry* **1997**, 36, 4676.

(31) Alcock, N. W.; Esperas, S., Crystal and molecular-structure of uranyl diperchlorate heptahydrate, Journal of the Chemical Society, *Dalton Transactions* **1977**, 893.

(32) Aberg, M.; Ferri, D.; Glaser, J.; Grenthe, I., Structure of the hydrated dioxouranium(VI) ion in aqueous-solution - an X-Ray-diffraction and H-1 NMR Study, *Inorganic Chemistry* **1983**, 22, 3986.

(33) Ramakrishnan, R.; Matveev, A. V.; Krüger, S.; Rösch, N., Self-interaction artifacts on structural features of uranyl monohydroxide from Kohn-Sham calculations, *Theoretical Chemistry Accounts* **2011**, 130, 361.

(34) Groenewold, G. S.; Cossel, K. C.; Gresham, G. L.; Gianotto, A. K.; Appelhans, A. D.; Olson, J. E.; Van Stipdonk, M. J.; Chien, W., Binding of molecular O-2 to di- and triligated $[UO_2](+)$, *Journal of the American Chemical Society* **2006**, 128, 3075.

(35) Bryantsev, V. S.; de Jong, W. A.; Cossel, K. C.; Diallo, M. S.; Goddard, W. A.; Groenewold, G. S.; Chien, W.; Van Stipdonk, M. J., Two-electron three-centered bond in side-on (η^2) uranyl(V) superoxo complexes, *Journal of Physical Chemistry A* **2008**, 112, 5777.

(36) Leavitt, C. M.; Bryantsev, V. S.; de Jong, W. A.; Diallo, M. S.; Goddard, W. A.; Groenewold, G. S.; Van Stipdonk, M. J., Addition of H_2O and O_2 to acetone and dimethylsulfoxide ligated uranyl(V) dioxocations, *Journal of Physical Chemistry A* **2009**, 113, 2350.

(37) Bakac, A.; Espenson, J. H., Autoxidation of uranium(V) - Catalysis and inhibition by copper ions, *Inorganic Chemistry* **1995**, 34, 1730.

(38) Ricks, A. M.; Gagliardi, L.; Duncan, M. A., Uranium oxo and superoxo cations revealed using infrared spectroscopy in the gas phase, *Journal of Physical Chemistry Letters* **2011**, 2, 1662.

(39) Gronert, S., Estimation of effective ion temperatures in a quadrupole ion trap, *Journal of the American Society for Mass Spectrometry* **1998**, 9, 845.

(40) Rios, D.; Rutkowski, P. X.; Shuh, D. K.; Bray, T. H.; Gibson, J. K.; Stipdonk, M. J. V., Electron transfer dissociation of dipositive uranyl and plutonyl coordination complexes, *Journal of Mass Spectrometry* **2011**, 46, 1247.

(41) Rutkowski, P. X.; Michelini, M. C.; Bray, T. H.; Russo, N.; Marçalo, J.; Gibson, J. K., Hydration of gas-phase ytterbium ion complexes studied by experiment and theory, *Theoretical Chemistry Accounts* **2011**, 129, 575.

(42) Becke, A. D., Density-Functional Thermochemistry .3. The Role of Exact Exchange, *Journal of Chemical Physics* **1993**, 98, 5648.

(43) Lee, C. T.; Yang, W. T.; Parr, R. G., Development of the colle-salvetti correlation-energy formula into a functional of the electron-density, *Physical Review B* **1988**, 37, 785.

(44) Küchle, W.; Dolg, M.; Stoll, H.; Preuss, H., Energy-adjusted pseudopotentials for the actinides - Parameter sets and test calculations for thorium and thorium Monoxide, *Journal of Chemical Physics* **1994**, 100, 7535.

(45) de Jong, W. A.; Harrison, R. J.; Nichols, J. A.; Dixon, D. A., Fully relativistic correlated benchmark results for uranyl and a critical look at relativistic effective core potentials for uranium, *Theoretical Chemistry Accounts* **2001**, 107, 22.

(46) Krishnan, R.; Binkley, J. S.; Seeger, R.; Pople, J. A., Self-consistent molecular-orbital methods .20. Basis set for correlated wave-functions, *Journal of Chemical Physics* **1980**, 72, 650.

(47) Blaudeau, J. P.; McGrath, M. P.; Curtiss, L. A.; Radom, L., Extension of Gaussian-2 (G2) theory to molecules containing third-row atoms K and Ca, *Journal of Chemical Physics* **1997**, 107, 5016.

(48) Clark, T.; Chandrasekhar, J.; Spitznagel, G. W.; Schleyer, P. V., Efficient diffuse function-augmented basis-sets for anion calculations .3. The 3-21+G Basis set for 1st-row elements, Li-F, *Journal of Computational Chemistry* **1983**, 4, 294.

(49) Frisch, M. J., Gaussian 2009, see Supporting Information for full citation.

(50) Boys, S. F.; Bernardi, F., Calculation of small molecular interactions by differences of separate total energies - some procedures with reduced errors, *Molecular Physics* **1970**, 19, 553.

(51) Norman, J. G.; Ryan, P. B.; Noodleman, L., Electronic-structure of 2-Fe ferredoxin models by X-alpha valence bond theory, *Journal of the American Chemical Society* **1980**, 102, 4279.

(52) Noodleman, L., Valence bond description of anti-ferromagnetic coupling in transition-metal dimers, *Journal of Chemical Physics* **1981**, 74, 5737.

(53) Ciofini, I.; Daul, C. A., DFT calculations of molecular magnetic properties of coordination compounds, *Coordination Chemistry Reviews* **2003**, 238, 187.

(54) Neese, F., Prediction of molecular properties and molecular spectroscopy with density functional theory: From fundamental theory to exchange-coupling, *Coordination Chemistry Reviews* **2009**, 253, 526.

(55) Reed, A. E.; Curtiss, L. A.; Weinhold, F., Intermolecular interactions from a natural bond orbital, donor-acceptor viewpoint, *Chemical Reviews* **1988**, 88, 899.

(56) Rutkowski, P. X.; Rios, D.; Gibson, J. K.; Stipdonk, M. J. V., Gas-phase coordination complexes of $U^{VI}O_2^{2+}$, $Np^{VI}O_2^{2+}$, and $Pu^{VI}O_2^{2+}$ with dimethylformamide, *Journal of the American Society for Mass Spectrometry* **2011**, 22, 2042.

(57) Konings, R. J. M.; Morss, L. R.; Fuger, J. In The chemistry of the actinide and transactinide elements; 3 ed.; Morss, L. R., Edelstein, N. M., Fuger, J., Eds.; Springer Dordrecht, The Netherlands, **2006**; Vol. 4.

(58) Jones, L. H.; Penneman, R. A., Infrared spectra and structure of uranyl and transuranium (V) and (VI) ions in aqueous perchloric acid solution, *Journal of Chemical Physics* **1953**, 21, 542.

(59) Gibson, J. K.; Haire, R. G.; Santos, M.; Marçalo, J.; Pires de Matos, A., Oxidation studies of dipositive actinide ions, An(2+) (An = Th, U, Np, Pu, Am) in the gas phase: Synthesis and characterization of the isolated uranyl, neptunyl, and plutonyl ions UO_2^{2+}(g), NpO_2^{2+} (g), and PuO_2^{2+} (g), *Journal of Physical Chemistry A* **2005**, 109, 2768.

(60) Choppin, G. R.; Rao, L. F., Complexation of pentavalent and hexavalent actinides by fluoride, *Radiochimica Acta* **1984**, 37, 143.

(61) Cheng, P.; Koyanagi, G. K.; Böhme, D. K., Gas-phase reactions of atomic lanthanide cations with D_2O: Room-temperature kinetics and periodicity in reactivity, *Chem Phys Chem* **2006**, 7, 1813.

(62) Cheng, P.; Koyanagi, G. K.; Böhme, D. K., Heavy water reactions with atomic transition-metal and main-group cations: Gas phase room-temperature kinetics and periodicities in reactivity, *Journal of Physical Chemistry A* **2007**, 111, 8561.

(63) Vallet, V.; Schimmelpfennig, B.; Maron, L.; Teichteil, C.; Leininger, T.; Gropen, O.; Grenthe, I.; Wahlgren, U., Reduction of uranyl by hydrogen: an ab initio study, *Chemical Physics* **1999**, 244, 185.

(64) Di Santo, E.; Michelini, M. C.; Russo, N., Activation of ethane C-H and C-C bonds by gas phase Th(+) and U(+): A theoretical study, *Journal of Physical Chemistry A* **2009**, 113, 14699.

(65) Michelini, M. D.; Marçalo, J.; Russo, N.; Gibson, J. K., Gas-phase reactions of uranate ions, UO_2^-, UO_3^-, UO_4^-, and UO_4H^-, with methanol: a convergence of experiment and theory, *Inorganic Chemistry* **2010**, 49, 3836.

(66) Edelstein, N. M.; Fuger, J.; Katz, J. J.; Morss, L. R. In The Chemistry of the Actinide and Transactinide Elements; 3 ed.; Morss, L. R., Edelstein, N. M., Fuger, J., Eds.; Springer: Dordrecht, The Netherlands, **2006**; Vol. 3.

(67) Copping, R.; Mougel, V.; Petit, S.; Den Auwer, C.; Moisy, P.; Mazzanti, M., A versatile precursor for non-aqueous neptunyl(V) chemistry, *Chemical Communications* **2011**, 47, 5497.

(68) Graves, C. R.; Kiplinger, J. L., Pentavalent uranium chemistry-synthetic pursuit of a rare oxidation state, *Chemical Communications* **2009**, 3831.

(69) Combes, J. M.; Chisholmbrause, C. J.; Brown, G. E.; Parks, G. A.; Conradson, S. D.; Eller, P. G.; Triay, I. R.; Hobart, D. E.; Meijer, A., Exafs spectroscopic study of neptunium(V) sorption at the alpha-FeOOH Water Interface, *Environmental Science & Technology* **1992**, 26, 376.

Supporting Information

Table S1. Natural population analysis (NPA) charges on the An and O atoms of the $AnO_2^+.(H_2O)_n$ and $AnO_2OH^+.(H_2O)_n^+$ ground-state (GS) ions and some selected higher energy isomers. [a]

n	UO_2^+	NpO_2^+	PuO_2^+	$UO_2(OH)^+$	$NpO_2(OH)^+$	$PuO_2(OH)^+$
n=0 (GS)						
An	2.29	2.15	2.04	2.21	2.00	1.90
$\mathbf{O_{yl}}$	-0.64	-0.58	-0.52	-0.45	-0.38	-0.32
$\mathbf{O_{OH}}$	-	-	-	-0.85	-0.78	-0.79
$\mathbf{O_w}$	-	-	-	-	-	-
n=1 (GS)						
An	2.17	2.04	1.92	2.02	1.80	1.72
$\mathbf{O_{yl}}$	-0.64	-0.57	-0.51	-0.44	-0.37	-0.31
$\mathbf{O_{OH}}$	-	-	-	-0.83	-0.76	-0.78
$\mathbf{O_w}$	-0.96	-0.95	-0.95	-0.90	-0.90	-0.90
$_{CT}$ [a]	0.11	0.11	0.10	0.17	0.18	0.16
n=2 (GS)						
An	2.04	1.89	1.78	1.84	1.62	1.53
$\mathbf{O_{yl}}$	-0.64	-0.57	-0.52	-0.44	-0.36	-0.31
$\mathbf{O_{OH}}$	-	-	-	-0.82	-0.76	-0.77
$\mathbf{O_w}$	-0.94	-0.93	-0.92	-0.89	-0.88	-0.88
$_{CT}$ [a]	0.23	0.24	0.26	0.34	0.35	0.35
n=3 (GS)						
An	1.85	1.73	1.61	1.65	1.41	1.32
$\mathbf{O_{yl}}$	-0.63	-0.56	-0.51	-0.44	-0.36	-0.31
$\mathbf{O_{OH}}$	-	-	-	-0.81	-0.74	-0.75
$\mathbf{O_w}$	-0.91	-0.91	-0.90	-0.87	-0.86	-0.85
$_{CT}$ [a]	0.41	0.39	0.42	0.53	0.55	0.55
n=4 (GS)						
An	1.70	1.59	1.45	1.64	1.40	1.31
$\mathbf{O_{yl}}$	-0.63	-0.56	-0.51	-0.45	-0.37	-0.31
$\mathbf{O_{OH}}$	-	-	-	-0.81	-0.75	-0.76
$\mathbf{O_w}$	-0.89	-0.90	-0.88	-0.87	-0.86	-0.86
$\mathbf{O_{w(outer\ sphere)}}$	-	-	-	-0.95	-0.95	-0.95
$_{CT}$ [a]	0.56	0.53	0.57	0.57	0.59	0.57
n=4 [b]						
An	-	-	-	1.59	1.36	1.21
$\mathbf{O_{yl}}$	-	-	-	-0.44	-0.36	-0.30
$\mathbf{O_{OH}}$	-	-	-	-0.85	-0.79	-0.79
$\mathbf{O_w}$	-	-	-	-0.86, -0.87	-0.86, -0.87	-0.85, -0.86
$_{CT}$ [a]	-	-	-	0.64	0.65	0.69
n=5 (GS)						
An	1.73	1.61	1.45	-	-	-
$\mathbf{O_{yl}}$	-0.62, -0.70	-0.55, -0.62	-0.49, -0.56	-	-	-
$\mathbf{O_w}$	-0.89,-0.90	-0.89, -0.91	-0.88, -0.89	-	-	-
$\mathbf{O_{w(outer\ sphere)}}$	-0.99	-0.98	-0.98	-	-	-
$_{CT}$ [a]	0.59	0.56	0.61	-	-	-
n=5 [c]						
An	1.64	1.52	1.34	-	-	-
$\mathbf{O_{yl}}$	-0.64	-0.56	-0.51	-	-	-
$\mathbf{O_w}$	-0.88, -0.89	-0.89, -0.90	-0.87, -0.88	-	-	-
$_{CT}$ [a]	0.64	0.60	0.68	-	-	-

[a] CT (Charge transfer): calculated as $[1 - q_{NBO}(An) - 2q_{NBO}(O)]$ for AnO_2^+ and $[1 - q_{NBO}(An) - 2q_{NBO}(O_{yl}) - q\ q_{NBO}(O_{OH}) - q_{NBO}(H)]$ for AnO_2OH^+. [b] Isomer with four inner-sphere water molecules. [c] Isomer with five inner-sphere water molecules.

Table S2. Natural metal charges and orbital populations of UO_2^+, NpO_2^+ and PuO_2^+.[a]

Species	Metal charge	Population			
		5f	6d	7s	7p
UO_2^+	2.29	2.98 (1)	0.91 (0)	0.04 (0)	0.05 (0)
NpO_2^+	2.15	4.15 (2)	0.89 (0)	0.04 (0)	0.05 (0)
PuO_2^+	2.04	5.31 (3)	0.86 (0)	0.03 (0)	0.05 (0)

[a] The formal orbital population for An (V) is given in parentheses.

Table S3. Energy (ΔE^0), enthalpy (ΔH^{298}), entropy (ΔS^{298}), and Gibbs free energy (ΔG^{298}) changes for the AnO_2^+ and AnO_2OH^+ hydration reactions.[a]

Reaction	UO_2^+	NpO_2^+	PuO_2^+	UO_2OH^+	$NpO_2(OH)^+$	$PuO_2(OH)^+$
n=1						
ΔE^0	-134	-134	-133	-143 [-143][b]	-141	-136
ΔH^{298}	-137	-138	-137	-146	-144	-139
ΔS^{298}	-96	-112	-101	-117	-134	-134
ΔG^{298}	-109	-104	-120	-110	-104	-99
n=2						
ΔE^0	-117	-118	-118	-123 [-124][b]	-123	-118
ΔH^{298}	-119	-121	-120	-126	-126	-120
ΔS^{298}	-130	-129	-127	-142	-125	-124
ΔG^{298}	-81	-82	-82	-83	-88	-83
n=3						
ΔE^0	-108	-106	-104	-93	-94	-87
ΔH^{298}	-110	-107	-106	-95	-95	-88
ΔS^{298}	-127	-124	-126	-138	-134	-132
ΔG^{298}	-72	-70	-68	-54	-56	-49
n=4						
ΔE^0	-83	-79	-74	-55	-54	-53
ΔH^{298}	-85	-79	-75	-56	-55	-54
ΔS^{298}	-133	-111	-121	-93	-107	-108
ΔG^{298}	-45	-46	-38	-29	-23	-22
n=4[b]						
ΔE^0	-	-	-	-44 [-46][d]	-40	-31
ΔH^{298}	-	-	-	-45	-41	-36
ΔS^{298}	-	-	-	-136	-132	-143
ΔG^{298}	-	-	-	-5	-2	5
n=5						
ΔE^0	-48	-45	-44	-	-	-
ΔH^{298}	-53	-50	-49	-	-	-
ΔS^{298}	-158	-162	-156	-	-	-
ΔG^{298}	-6	-2	-3	-	-	-
n=5[c]						
ΔE^0	-37	-34	-33	-	-	-
ΔH^{298}	-37	-34	-33	-	-	-
ΔS^{298}	-99	-123	-109	-	-	-
ΔG^{298}	-7	2	0	-	-	-

[a] ΔE^0, ΔH^{298}, and ΔG^{298} are in kJ.mol^{-1}; ΔS^{298} is in J.K^{-1}.mol^{-1}. The reactions correspond to successive hydration reactions: $AnO_2^+\cdot(H_2O)_{n-1} + H_2O \rightarrow AnO_2^+\cdot(H_2O)_n$ and $AnO_2OH^+\cdot(H_2O)_{n-1} + H_2O \rightarrow AnO_2OH^+\cdot(H_2O)_n$, respectively. All reactants and products are in their ground state, with the only exception of n=4[b] and n=5[c], which correspond to the formation of higher-energy isomers containing four and five inner-sphere water molecules, respectively. [d]In brackets: B3LYP/SDD (U)-aug-cc-pVDZ(O,H) taken from Ončák, M. *et al. Journal of Computational Chemistry* 2010, *31*, 2294-2306.

Table S4. Measured pseudo-first-order hydration rates in s^{-1}.[a]

	UO_2^+	UO_2^+ $\cdot(H_2O)$	NpO_2^+	PuO_2^+	$UO_2(OH)^+$	$UO_2(OH)^+$ $\cdot(H_2O)$	$UO_2(OH)^+$ $\cdot(H_2O)_2$	$PuO_2(OH)^+$
Measured	0.096	*3.37*	0.087	0.120	2.59	12.4	4.80	0.66
Value 1	*0.144*				*4.24*	*19.17*	*8.99*	
Measured	0.097	*3.42*	0.087	0.134	2.52	13.7	5.98	1.19
Value 2	*0.141*				*4.63*	*19.26*	*8.29*	
Measured	0.118	*3.49*	0.089	0.148	2.60	12.5	4.51	1.54
Value 3	*0.159*				*4.15*	*19.79*	*8.88*	
Average	0.10(1)	*3.4(1)*	0.09(1)	0.13(2)	2.6(1)	12.9(7)	5.1(8)	1.1(5)[b]
Value	*0.15(1)*				*4.3(3)*	*19.4(4)*	*8.7(4)*	

[a]Values in italics were obtained at ITN; these values are ~60% higher than the corresponding LBNL values, due to a correspondingly higher water pressure in the ITN ion trap. The helium pressures in both traps were essentially the same. Uncertainties in the last digit of the average values are given in parentheses.
[b]The large variation among the three measured values for $PuO_2(OH)^+$ is attributed to very low ion intensity.

Table S5. Energy (ΔE^0), enthalpy (ΔH^{298}), entropy (ΔS^{298}), and Gibbs free energy (ΔG^{298}) changes for the O_2 addition reactions.[a]

Reaction	**UO_2^+**	**$UO_2^+\cdot(H_2O)$**	**$UO_2^+\cdot(H_2O)_2$**	**$UO_2^+\cdot(H_2O)_3$**
ΔE^0	-52	-67	-80	-74
ΔH^{298}	-55	-69	-82	-75
ΔS^{298}	-115	-151	-149	-164
ΔG^{298}	-20	-24	-37	-26
Reaction	NpO_2^+	$NpO_2^+\cdot(H_2O)$	$NpO_2^+\cdot(H_2O)_2$	$NpO_2^+\cdot(H_2O)_3$
ΔE^0	-24	-19	-16	-4
ΔH^{298}	-24	-18	-14	-1
ΔS^{298}	-87	-99	-96	-95
ΔG^{298}	2	12	15	28

[a]ΔE^0, ΔH^{298}, and ΔG^{298} are in $kJ.mol^{-1}$; ΔS^{298} is in $J.K^{-1}.mol^{-1}$. The reactions correspond to the O_2 addition reactions: $AnO_2^+\cdot(H_2O)_n + O_2 \rightarrow AnO_2^+(O_2)(H_2O)_n$ for An = U, Np and n = 0-3. All reactants and products are in their ground state.

Table S6: Natural population analysis (NPA) charges on the An and O atoms of the $UO_2^+(O_2)(H_2O)_n$ GS species and $NpO_2^+(O_2)(H_2O)_n$ quintet spin state for (n = 0-3).

	$UO_2^+(O_2)$	$UO_2^+(O_2)(H_2O)$	$UO_2^+(O_2)(H_2O)_2$	$UO_2^+(O_2)(H_2O)_3$
U	2.12	1.92	1.73	1.53
O_{yl}	-0.45	-0.44	-0.44	-0.43
$O(O_2)$	-0.11	-0.11	-0.11	-0.11
O_w	-	-0.90	-0.88	-0.86
	$NpO_2^+(O_2)$	$NpO_2^+(O_2)(H_2O)$	$NpO_2^+(O_2)(H_2O)_2$	$NpO_2^+(O_2)(H_2O)_3$
Np	2.07	1.93	1.77	1.64
O_{yl}	-0.57	-0.56	-0.55	-0.56
$O(O_2)$	-0.12, 0.19	-0.10, 0.16	-0.07, 0.15	-0.05, 0.11
O_w	-	-0.94	-0.91	-0.91

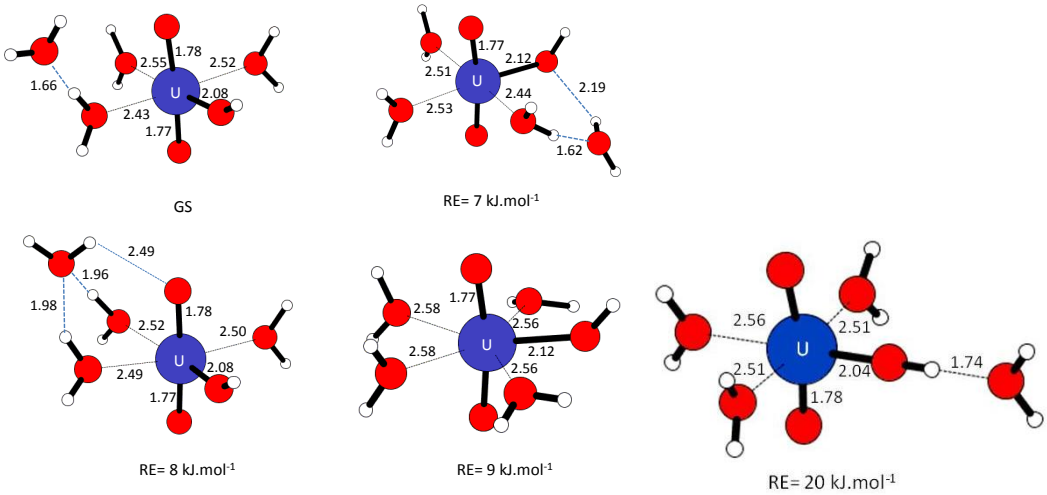

Figure S1: Ground-state and lowest-energy isomers of $UO_2(OH)^+ \cdot (H_2O)_4$. Relative energies (RE) are calculated with respect to the ground-state structure and include ZPVE corrections.

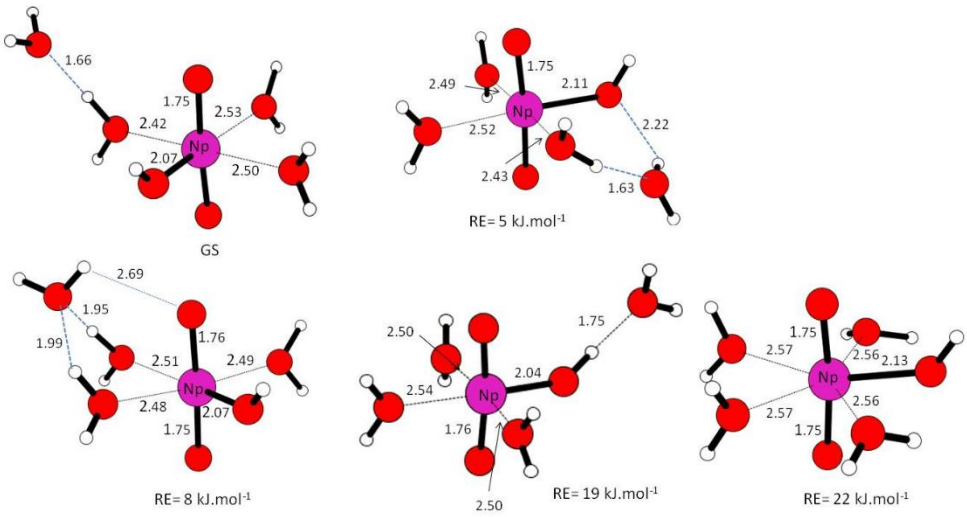

Figure S2: Ground-state and lowest-energy isomers of NpO2(OH)+•(H2O)4. Relative energies (RE) are calculated with respect to the ground-state structure and include ZPVE corrections.

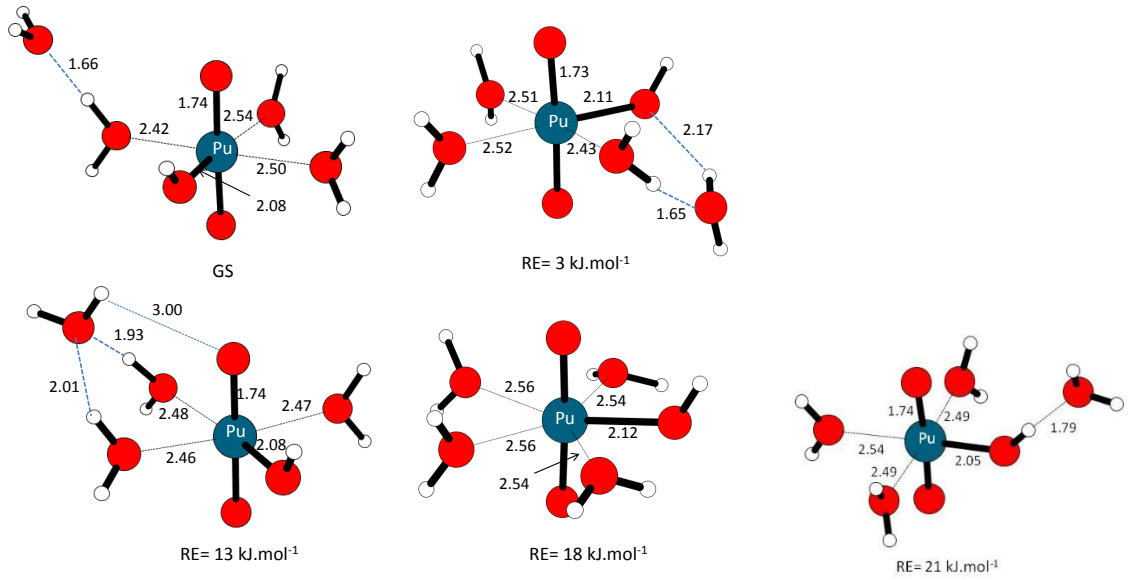

Figure S3: Ground-state and lowest-energy isomers of $PuO_2(OH)^+\cdot(H_2O)_4$. Relative energies (RE) are calculated with respect to the ground-state structure and include ZPVE corrections.

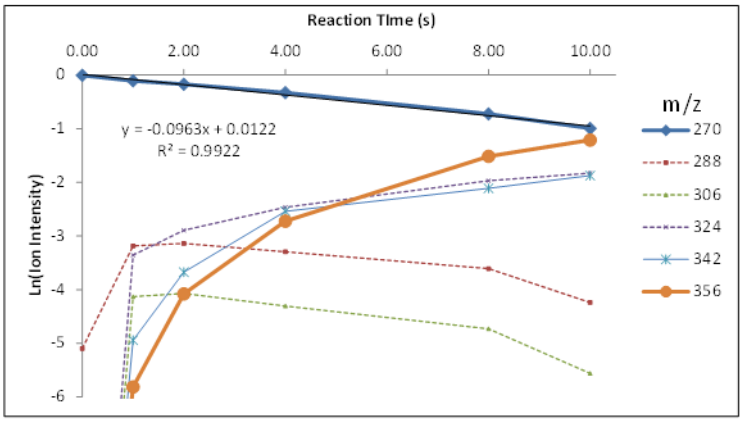

Figure S4: Representative kinetics plot for hydration of UO_2^+ (m/z 270) showing linear logarithmic decay of the reactant ion, and in-growth of the primary hydrate, sequential hydrates and the O_2-addition product. The products are $UO_2^+\cdot(H_2O)$ at m/z 288; $UO_2^+\cdot(H_2O)_2$ at m/z 306; $UO_2^+\cdot(H_2O)_3$ at m/z 324; $UO_2^+\cdot(H_2O)_4$ at m/z 342; and $UO_2^+(O_2)(H_2O)_3$ at m/z 356. The $UO_2^+(O_2)(H_2O)_3$ product ion is included in the hydration rate for UO_2^+ because it was demonstrated that hydration precedes O_2-addition; the minuscule contribution from $UO_2^+(O_2)(H_2O)_2$ is not included. The linear decay gives a pseudo-first-order hydration rate for UO_2^+ of 0.0963 s^{-1}. The terminal reaction time of 10 s corresponds to the longest accessible with the instrument. For $UO_2(OH)^+$, hydration rates were measured to a reaction time of ~1.5 s, when <10% of the reactant remained (see Fig. 4); measured hydration rates for $PuO_2(OH)^+$ were relatively unreliable due to the very small abundance of the reactant ion (see Figs. II.2.1 and II.2.4, and Table S3).

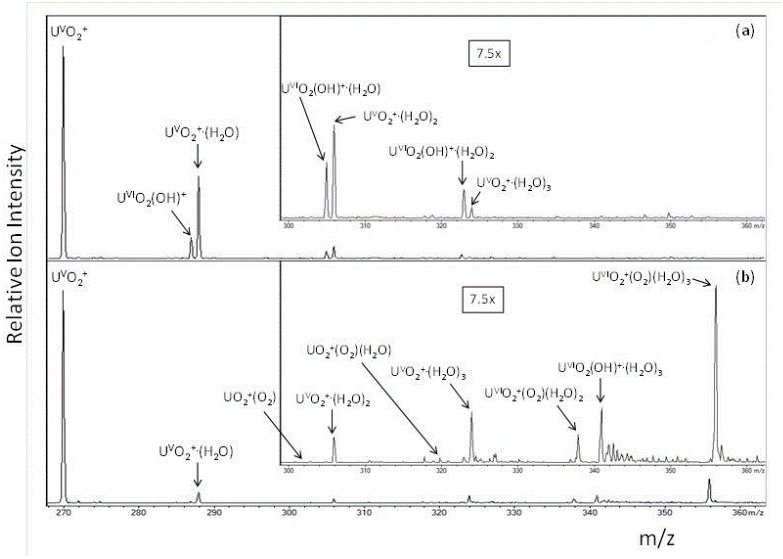

Figure S5: Addition of oxygen to $U^{V}O_2^{+}\cdot(H_2O)_n$ hydrates: (a) no air with no applied reaction time and (b) added air with 1 s reaction time. The ESI conditions were adjusted to obtain substantial $UO_2^{+}\cdot(H_2O)$ in the parent spectrum (a). The absence of $UO_2^{+}(O_2)$ (m/z 322) and only minuscule $UO_2^{+}(O_2)(H_2O)$ (m/z 320) in spectrum (b) establishes that O_2-addition is negligible for bare UO_2 or $UO_2^{+}\cdot(H_2O)$, but is significant for the di- and tri-hydrates. The "soft ESI" instrumental parameters employed to enhance the abundance of $UO_2^{+}\cdot(H_2O)$ in the parent spectrum were as follows: solution flow rate, 60 µl/min; nebulizer gas pressure, 12 psi; capillary voltage and current, -4500 V, 42.7 nA; end plate voltage offset and current, -500 V, 217.5 nA; dry gas flow rate, 5 l/min; dry gas temperature, 100 °C; capillary exit, 300 V; skimmer, 24.9 V; octopole 1 and 2 DC, 9.00 V and 6.00 V; octopole RF amplitude, 270.8 Vpp; lens 1 and 2, -5.0 V and -100.0 V; trap drive, 73.3.

ESI-QIT/MS experimental conditions at ITN

Most spectra were taken with the following instrumental parameters: solution flow rate, 150 µl hr-1; nebulizer gas pressure, 8 psi; capillary voltage, -4000 V; end plate voltage offset, -500 V; dry gas flow rate, 4 l/min; dry gas temperature, 250 oC; capillary exit, 128.5 V; skimmer, 40 V; octopole 1 and 2 DC, 12 V and 1.70 V; octopole RF amplitude, 187.1 Vpp; lens 1 and 2, -5 V and -60 V; trap drive, 216.8.

Solution used for electrospray ionization: 100 µM solution of $U^{VI}O_2(NO_3)_2$ in H_2O/EtOH (1:10); pH ≈ 6.

Complete reference 49

Gaussian 09, Revision A.2, Frisch, M. J.; Trucks, G. W.; Schlegel, H. B.; Scuseria, G. E.; Robb, M. A.; Cheeseman, J. R.; Scalmani, G.; Barone, V.; Mennucci, B.; Petersson, G. A.; Nakatsuji, H.; Caricato, M.; Li, X.; Hratchian, H. P.; Izmaylov, A. F.; Bloino, J.; Zheng, G.; Sonnenberg, J. L.; Hada, M.; Ehara, M.; Toyota, K.; Fukuda, R.; Hasegawa, J.; Ishida, M.; Nakajima, T.; Honda, Y.; Kitao, O.; Nakai, H.; Vreven, T.; Montgomery, Jr., J. A.; Peralta, J. E.; Ogliaro, F.; Bearpark, M.; Heyd, J. J.; Brothers, E.; Kudin, K. N.; Staroverov, V. N.; Kobayashi, R.; Normand, J.; Raghavachari, K.; Rendell, A.; Burant, J. C.; Iyengar, S. S.; Tomasi, J.; Cossi, M.; Rega, N.; Millam, N. J.; Klene, M.; Knox, J. E.; Cross, J. B.; Bakken, V.; Adamo, C.; Jaramillo, J.; Gomperts, R.; Stratmann, R. E.; Yazyev, O.; Austin, A. J.; Cammi, R.; Pomelli, C.; Ochterski, J. W.; Martin, R. L.; Morokuma, K.; Zakrzewski, V. G.; Voth, G. A.; Salvador, P.; Dannenberg, J. J.; Dapprich, S.; Daniels, A. D.; Farkas, Ö.; Foresman, J. B.; Ortiz, J. V.; Cioslowski, J.; Fox, D. J. Gaussian, Inc., Wallingford CT, 2009.

II.3 Gas-phase reactions of molecular oxygen with uranyl(V) anionic complexes – Synthesis and characterization of new superoxides of uranyl(VI)

The content here described is based on the following publication:

***Lucena AF**, Carretas JM, Marçalo J, Michelini MC, Gong Y, Gibson JK, Gas-phase Reactions of Molecular Oxygen with Uranyl(V) Anionic Complexes – Synthesis and Characterization of New Superoxides of Uranyl(VI), **J. Phys. Chem. A, 2015**, 119 (15), 3628–3635, DOI: 10.1021/acs.jpca.5b01445.*

I contributed with the experimental work and data analysis, partially in collaboration with Dr. José M. Carretas and Dr. Yu Gong. Dr. Maria del Carmen Michelini was responsible for the DFT studies.

Abstract

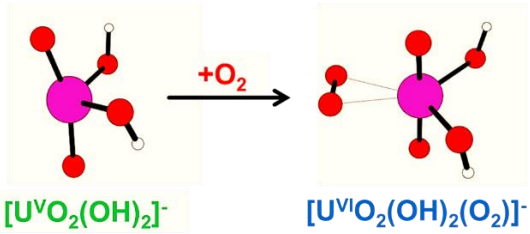

Gas-phase complexes of uranyl(V) ligated to anions X^- (X = F, Cl, Br, I, OH, NO_3, ClO_4, HCO_2, CH_3CO_2, CF_3CO_2, CH_3COS, NCS, N_3), $[UO_2X_2]^-$, were produced by electrospray ionization and reacted with O_2 in a quadrupole ion trap mass spectrometer to form uranyl(VI) anionic complexes, $[UO_2X_2(O_2)]^-$, comprising a superoxo ligand. The comparative rates for the oxidation reactions were measured, ranging from relatively fast $[UO_2(OH)_2]^-$ to slow $[UO_2I_2]^-$. The reaction rates of $[UO_2X_2]^-$ ions containing polyatomic ligands were significantly faster than those containing the monoatomic halogens, which can be attributed to the greater number of vibrational degrees of freedom in the polyatomic ligands to dissipate the energy of the initial O_2-association complexes. The effect of the basicity of the X^- ligands was also apparent in the relative rates for O_2 addition, with a general correlation between increasing ligand basicity and O_2-addition efficiency for polyatomic ligands. Collision-induced dissociation of the superoxo complexes showed in all cases loss of O_2 to form the $[UO_2X_2]^-$ anions, indicating weaker binding of the O_2^- ligand compared to the X^- ligands. Density functional theory computations of the structures and energetics of selected species are in accord with the experimental observations.

II.3.1. Introduction

Transition-metal complexes with dioxygen, generally coordinated as peroxo or superoxo ligand, have major importance in numerous biological, environmental and catalytic processes.[1-3] In actinide condensed-phase chemistry, uranyl(VI) centers generally form η^2-peroxo complexes with dioxygen,[4] but it has been proposed that superoxo complexes are intermediates in the oxidation of uranyl(V) species.[5]

Oxidation of U(V) to U(VI) by association of molecular oxygen to uranyl(V) coordination complexes in the gas phase has been observed by Groenewold et al.,[6] who reported the addition of O_2 to $[UO_2(L)_{2,3}]^+$ complexes to produce $[UO_2(L)_{2,3}(O_2)]^+$, where L are σ-donor neutral ligands such as acetone and water. Such molecular oxygen addition was not observed for uranyl(VI) complexes and it was inferred that the addition to uranyl(V) complexes resulted in superoxo complexes in which uranyl(V) is oxidized to uranyl(VI). This hypothesis was later substantiated by theoretical calculations, which showed that the product complexes had side-on η^2-O_2 superoxo ligands.[7,8] It was also found by Leavitt et al.[8] that the dimethylsulfoxide (dmso) ligand coordinated to uranyl(V) in $[UO_2(L)_{2,3}]^+$ complexes enhanced the addition of O_2 and formation of uranyl(VI) complexes $[UO_2(L)_{2,3}(O_2)]^+$, an effect attributed to an increase of electron density at the uranium center due to the greater charge donation by the more basic dmso ligands.

In a subsequent comparative gas-phase study of actinyl(V) ions,[9] Rios et al. found that $[UO_2(H_2O)_2]^+$ inefficiently added O_2 whereas the addition reaction was more efficient for $[UO_2(H_2O)_3]^+$, consistent with oxidation from uranyl(V) to uranyl(VI) being favored by an additional electron-donating ligand. In contrast to uranyl(V), the analogous neptunyl(V) and plutonyl(V) complexes did not add O_2, a result that could be attributed to the greater reduction potentials of plutonyl(VI) and neptunyl(VI) as compared to uranyl(VI); density functional theory (DFT) computations confirmed that superoxo formation is exothermic for uranyl but not neptunyl.

Elementary superoxo cationic complexes of uranyl(VI), $[UO_2(\eta^2\text{-}O_2)]^+$ and $[UO_2(\eta^2\text{-}O_2)(\eta^1\text{-}O_2)]^+$, have also been produced in a supersonic molecular beam by laser vaporization and characterized by IR spectroscopy and DFT.[10]

Recently, we observed gas-phase O_2-substitution in an anionic uranyl(V) complex, $[UO_2(CH_3SO_2)(SO_2)]^-$, in which the SO_2^- ligand is replaced by O_2 to produce a peroxide complex concomitant with oxidation to uranyl(VI).[11] Formation of $[UO_2(CH_3SO_2)_2(O_2)]^-$ by O_2 addition to the precursor complex $[UO_2(CH_3SO_2)_2]^-$ was also observed, indicating that uranyl(V) coordinated by anionic $CH_3SO_2^-$ ligands can add O_2 to form a superoxo complex.

In the present work we report a systematic study of O_2-addition reactions to anionic uranyl(V)

complexes $[UO_2X_2]^-$ with various X^- ligands, from monoatomic halides to polyatomic ligands with different coordinating atoms, which present varied intrinsic properties such as number of vibrational degrees of freedom and gas-phase basicities. We describe comparative O_2-addition rates and explore the influence of the anionic ligands in the oxygen binding to uranyl(V) metal centers to form uranyl(VI) superoxide complexes, $[UO_2X_2(O_2)]^-$. We also use collision-induced dissociation (CID) experiments to compare the binding of anionic X^- ligands with that of the anionic O_2^- ligand. The experimental studies are supported by DFT calculations that examine structural and energetics features of selected complexes.

II.3.2. Experimental details

II.3.2.1 Instrumental conditions

A Bruker HCT quadrupole ion trap (QIT) mass spectrometer with an electrospray ionization (ESI) source was used. Sample solutions were introduced through a nebulizer with a syringe pump at 150 µL h^{-1}. The spectra were acquired in the negative ion accumulation and detection mode using the following typical instrumental parameters: nebulizing gas (N_2) pressure 8.0 psi; drying gas (N_2) flow rate 4.0 L min^{-1}; drying temperature 250 °C; capillary voltage -4.0 kV; capillary exit voltage -128.5 V; skimmer voltage -40.0 V; trap drive 67.3. The helium buffer gas pressure in the trap was constant at ~10^{-4} Torr. The background water and dioxygen pressure in the ion trap is estimated to be on the order of 10^{-6} Torr. The MS^n capabilities of the QIT were used for isolation of ions with a specific *m/z* and subsequent CID of mass-selected ions, using helium buffer gas as the collision partner, or for introducing an ion/molecule reaction time of up to 10 s. CID is achieved by resonance excitation for ca. 40 ms, with the result that the selected ion undergoes multiple energetic collisions with the He trapping gas. When sufficient energy is imparted to the ion, fragmentation occurs and the CID products are subsequently identified. The helium provides third-body collisions, which remove energy and stabilize product ions after CID, and both thermalize reagent ions and stabilize product ions in ion/molecule reactions. The mass spectrometer has been modified to allow for the introduction of gaseous reagents through a variable leak valve, in a configuration similar to that previously described.[12] This setup was used for introducing in the ion trap either $^{16}O_2$ (Linde, 99.95%) or $^{18}O_2$ (Aldrich, 99% ^{18}O) for specific experiments described below.

II.3.2.2 Sample preparation

Solutions of UO_2^{2+} and X^- were prepared in water with concentrations in the range of 10^{-3}-10^{-4} M. For X = Cl, NO_3, and CH_3CO_2, commercially obtained hydrated UO_2Cl_2, $UO_2(NO_3)_2$, and $UO_2(CH_3CO_2)_2$ salts were used. For X = Br, I, ClO_4, HCO_2, and CF_3CO_2, solutions were prepared by dissolving hydrated UO_3 in the diluted acid HX. For X = CH_3COS, NCS, and N_3, the samples were obtained by adding excess MX (M = Na or K) to solutions of UO_2Cl_2 or $UO_2(ClO_4)_2$. For X = F and OH, see Results and Discussion.

II.3.3. Computational details

DFT computations were performed using the Gaussian09 (revision B.01) package.[13] Full geometry optimizations and frequency calculations were performed using the B3LYP hybrid functional.[14,15] The Stuttgart−Dresden triple-ζ valence basis sets together with the corresponding effective small-core potential (SDD) were used for U,[16,17] and the extended triple-ζ basis sets 6-311G** and 6-311+G(d,p) were used for I and the rest of the atoms, respectively.[18-20] The "ultrafine" option was adopted for numerical integration. All the computed structures are in the doublet spin state. No spin contamination issues were detected. All the computed oxygen addition energies include the zero-point vibrational energy correction (ΔE^0). In addition to the ΔE^0 values, the Gibbs free energy at 298 K is reported for each of the studied reactions (ΔG^{298}). The accuracy of the ΔG^{298} values is necessarily somewhat limited by the use of the harmonic oscillator approximation to treat nuclear motion. It should be remarked that all of the computations were performed for a pressure of 1 atm. In reality, the total pressure under these experimental conditions is approximately 10^{-4} Torr. Furthermore, the "pressures" of the reactants and products, both ions and neutrals, are very low ($\leq 10^{-6}$ Torr) and are unknown. Accordingly, the computed reaction entropies and free energies may deviate from the actual values under these experimental conditions. However, the values for ΔE^0 are not pressure dependent and the key conclusions, which are based on ΔE^0 values, are not affected by the uncertainties in ΔG^{298}. QTAIM analysis[21] was performed on all the computationally studied $[UO_2X_2]^-$ and $[UO_2X_2(O_2)]^-$ complexes. Appropriate wave-function extended files (wfx) were obtained with Gaussian09 and analyzed using the AIMAll package.[22] QTAIM analysis has previously been successfully used to describe the bonding in actinide-containing systems.[23-28] The QTAIM topological properties that characterize the $[UO_2X_2]^-$ and $[UO_2X_2(O_2)]^-$ complexes are included as Supporting Information together with a brief description of the bonding analysis methodology.

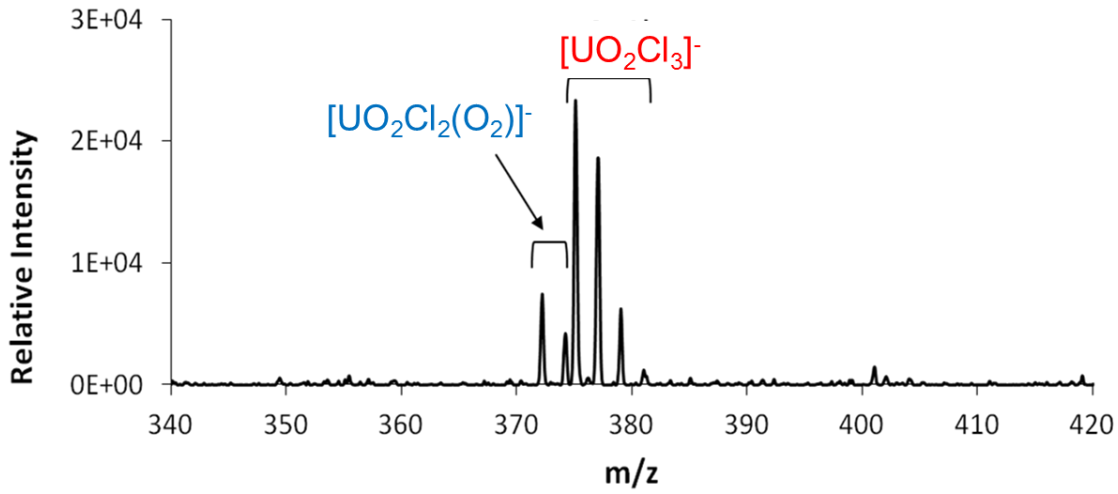

Figure II.3.1. ESI mass spectrum of a 10^{-4} M water solution of UO_2Cl_2.

II.3.4. Results and discussion

II.3.4.1 Synthesis of $[U^VO_2X_2]^-$ complexes

ESI-MS of solutions containing uranyl(VI) and X^- for X = Cl, Br, I, NO_3, ClO_4, HCO_2, CH_3CO_2, CF_3CO_2, CH_3COS, NCS, and N_3, readily produced $[U^{VI}O_2X_3]^-$ ions. $[U^{VI}O_2X_2(O_2)]^-$ ions were also present in the ESI mass spectra with variable abundances, as shown in Fig. II.3.1 for the case of X = Cl.

The formation of these $[U^{VI}O_2X_2(O_2)]^-$ ions by ESI was examined for X = Cl and CH_3CO_2. When ESI mass spectra were obtained with the helium source to the ion trap off, $[U^VO_2X_2]^-$ ions, which were previously absent from the ESI mass spectra, appeared with significant abundance, suggesting that the $[U^{VI}O_2X_2(O_2)]^-$ ions were being formed in the ion trap by gas-phase reaction of $[U^VO_2X_2]^-$ ions with oxygen.

The formation of $[U^VO_2X_2]^-$ complexes was achieved by CID of the $[U^{VI}O_2X_3]^-$ ions in the cases of X = I, CH_3CO_2, CH_3COS, NCS, and N_3. These $[U^{VI}O_2X_3]^-$ ions dissociated exclusively by intact X loss for I, NCS, and N_3. In the case of CH_3CO_2, a 10% CO_2-elimination channel, presumably to form the methyl complex $[U^{VI}O_2(CH_3CO_2)_2(CH_3)]^-$, was also present; Groenewold et al.[29] additionally observed neutral CH_3CO_2 loss from $[U^{VI}O_2(CH_3CO_2)_3]^-$ in infrared multiple photon dissociation (IRMPD) experiments. CID of the CH_3COS complex also resulted in CH_3COSH loss (30%), to yield what can be formally represented as $[UO_2(CH_3COS)(CH_2COS)]^-$, an intriguing species. In the CID mass spectra of the complexes that yielded $[U^VO_2X_2]^-$ ions, formation of $[U^{VI}O_2X_2(O_2)]^-$ was also

observed during the 40 ms period of the CID process (shown for X = NCS in Fig. S1 of the Supporting Information).

The halide complexes of uranyl(VI) with Cl and Br did not yield any CID product ions under our experimental conditions; interestingly, Groenewold et al.[30] observed in IRMPD experiments that $[U^{VI}O_2X_3]^-$ complexes eliminated neutral $[U^{VI}O_2X_2]$ for X = Cl and Br, and eliminated a halogen radical for X = Br and I. In the present experiments, CID of $[U^{VI}O_2X_3]^-$ may similarly result in fragmentation to $[U^{VI}O_2X_2]$ and X^-, with the halide anion unobserved due to the low-mass detection limit imposed by the instrumental parameters. CID of the complexes with X = NO_3 and ClO_4 both yielded the oxo species $[UO_2X_2(O)]^-$ by loss of NO_2 and ClO_3, respectively; these dissociation channels have been previously observed.[31,32] CID of the HCO_2 complex yielded CO (90%) and CO_2 (10%) losses, presumably leading to $[U^{VI}O_2(HCO_2)_2(OH)]^-$ and, remarkably, $[U^{VI}O_2(HCO_2)_2(H)]^-$. CID of the CF_3CO_2 complex led to the formation of $[U^{VI}O_2(CF_3CO_2)_2(F)]^-$ concomitant with neutral CF_2CO_2 loss. Consequently, in the cases of X = Cl, Br, NO_3, ClO_4, HCO_2, CF_3CO_2, and CH_3COS, the formation of the $[U^VO_2X_2]^-$ complexes was achieved by CID of the $[U^{VI}O_2X_2(O_2)]^-$ ions that were present in the ESI mass spectra.

For X = F and OH, $[U^VO_2X_2]^-$ ions were obtained by more elaborate gas-phase procedures involving CID and hydrolysis reactions with background water, as presented in Schemes 1 and 2. In both procedures, sequential isolation and CID of each of the indicated species were performed until the $[U^VO_2X_2]^-$ ions were formed. In the case of the fluoride complex, the experiments involved ESI of a mixture of uranyl(VI) acetate and trifluoroacetate; in the case of the hydroxide complex, a uranyl(VI) acetate solution was used.

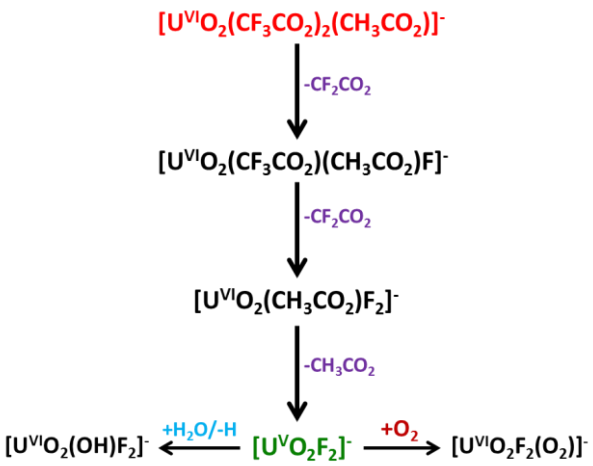

Scheme 1. Gas-phase synthesis of $[U^VO_2F_2]^-$ ions.

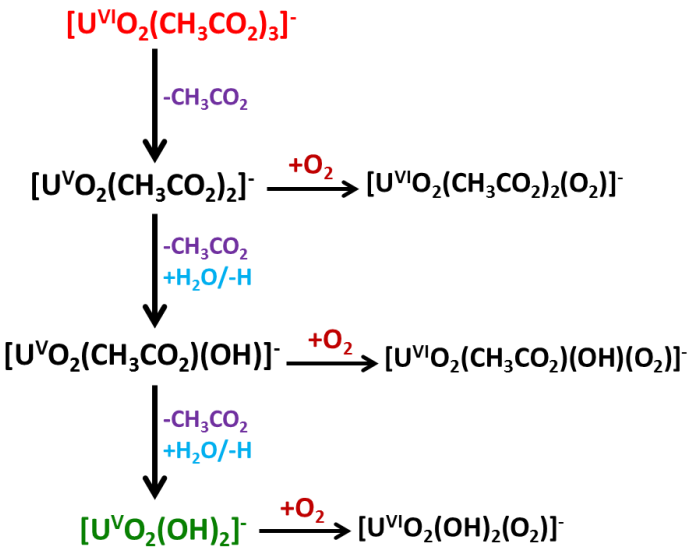

Scheme 2. Gas-phase synthesis of $[U^{V}O_2(OH)_2]^-$ ions.

II.3.4.2 Reactions of $[U^{V}O_2X_2]^-$ complexes with O_2

The gas-phase O_2-addition reactions of the $[U^{V}O_2X_2]^-$ ions (X = F, Cl, Br, I, OH, NO_3, ClO_4, HCO_2, CH_3CO_2, CF_3CO_2, CH_3COS, NCS, and N_3) with the background O_2 present in the QIT to yield $[U^{VI}O_2X_2(O_2)]^-$ ions, were examined in detail. Figure II.3.2 shows spectra obtained at different reaction times for the case of X = Cl. As described above, these reactions were already revealed by the presence of $[U^{VI}O_2X_2(O_2)]^-$ ions in ESI mass spectra and during CID experiments of some of the $[U^{VI}O_2X_3]^-$ ions. No reactions using up to 10 s delay times were observed for isolated uranyl(VI) ions $[U^{VI}O_2X_3]^-$, studied for X = I, CH_3CO_2 and NCS, confirming that the precursor uranyl(VI) complexes were not the origin of the dioxygen complexes.

The measured rates for the O_2 addition are presented in Table II.3. 1. The background oxygen pressure in the trap was nearly constant (to within <10%) as established by the reproducibility of oxygen addition rates measured at different times. Accordingly, the kinetics for O_2 addition is pseudo-first-order as given by Eqs. 1 and 2.

$$d[UO_2X_2^-]/dt = k'[O_2][UO_2X_2^-] = k[UO_2X_2^-] \quad (1)$$

$$\ln\{[UO_2X_2^-]/[UO_2X_2^-]_0\} = -kt \quad (2)$$

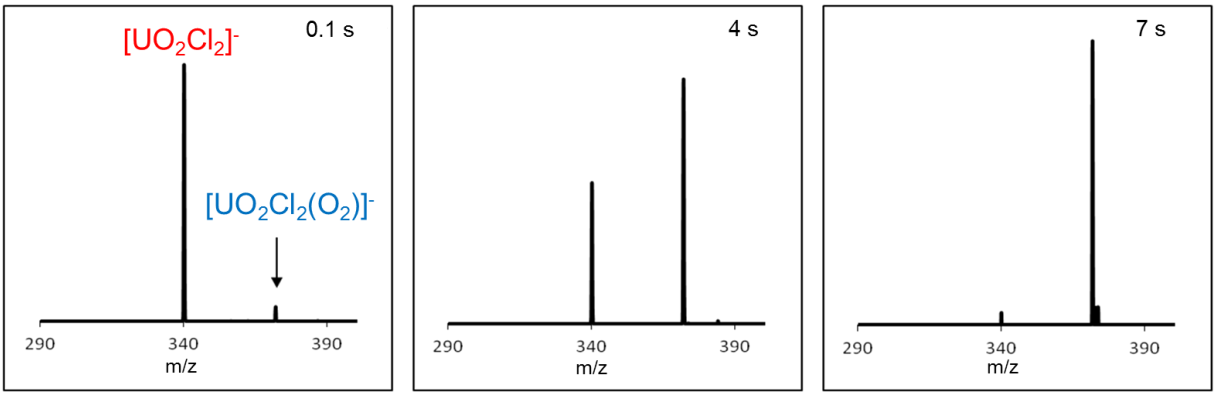

Figure II.3.2. Mass spectra for different reaction times showing O_2-addition to isolated $[UO_2{}^{35}Cl_2]^-$.

Table II.3.1. O_2-addition rates to $[U^VO_2X_2]^-$ complexes.

X	*k* (s^{-1})*
F	2.2 (0.3)
Cl	0.23 (0.05)
Br	0.22 (0.03)
I	0.15 (0.04)
OH	16.3 (1.1)
NO_3	6.3 (0.6)
ClO_4	4.7 (0.2)
HCOO	7.0 (0.6)
CH_3COO	8.7 (0.7)
CF_3COO	6.0 (0.5)
CH_3COS	4.6 (0.4)
NCS	7.0 (0.4)
N_3	8.3 (0.9)

* Averages of at least three measurements with standard deviations in parentheses.

The values of *k* in Table II.3. 1 were obtained from the slope of the log of the $[UO_2X_2]^-$ ion decay versus time, as exemplified for the case of X = CH_3CO_2 in Fig. S2 of the Supporting Information. Because the helium pressure and the background oxygen pressure were essentially constant for all kinetics determinations, the measured rates directly provide comparative kinetics for the different $[UO_2X_2]^-$ ions. Linearity of all the kinetics plots provided evidence for adequate thermalization of the reactant ions through collisions with the helium buffer gas. An additional test of the performance of these kinetics studies involved the introduction of O_2 into the ion trap through the reagent inlet to pressure readings of ca. 2 and 3 times the background pressure reading (with the He closed), and measuring the rate for the case of $[U^VO_2(CH_3CO_2)_2]^-$; this resulted in a significant increase of the rate compared with the experiments without deliberate introduction of O_2, and a ca. 1.5-fold increase in *k* was observed for the two different O_2 pressures used, indicating that the kinetics were well-behaved.

The O_2-addition rates were diverse, ranging from the relatively fast $[UO_2(OH)_2]^-$ (k = 16.3 s^{-1}) to the much slower $[UO_2I_2]^-$ (k = 0.15 s^{-1}), as can be seen in Table II.3. 1. Groenewold, Van Stipdonk, and

co-workers, in their ground-breaking observations of O_2 addition to uranyl(V) ions,[6,8] unveiled key factors that can affect the rates of gas-phase oxygen addition. The number of vibrational degrees of freedom available in the reagent ions is relevant for dissipating the energy of the initial O_2-association complexes, thereby preventing prompt dissociation. Also, a greater basicity of the X^- ligand can favor electron donation from U(V) to the O_2 ligand and contribute to a more effective stabilization of the O_2-association complexes.

In Table II.3.1 it is immediately apparent that the complexes involving the monoatomic halide ligands have considerably lower association rates than the complexes containing polyatomic X^- ligands. Interestingly, the smallest polyatomic ligand, OH^-, is the one that induces a significantly higher rate of O_2 addition. Two effects may be at work here, namely, π-donation from the ligating O atoms in OH^- to the uranium center and steric effects when comparing OH^- with potentially bidentate ligands like NO_3^-, ClO_4^-, HCO_2^-, $CH_3CO_2^-$, $CF_3CO_2^-$, and CH_3COS^-. It should be noted that Groenewold et al.[29] found evidence through IRMPD experiments with $[U^{VI}O_2(CH_3CO_2)_3]^-$ that they contained two bidentate and one monodentate acetate ligands; this indicates that two bidentate acetate ligands may impose a substantial steric impediment for coordination of a third ligand such as O_2 in the equatorial plane of a uranyl complex.

The effect of the basicity of the X^- ligands in the O_2-addition rates also becomes evident if we plot *k* from Table II.3.1 as a function of the gas-phase basicity of the X^- ligand, as measured by the equivalent $\Delta_r G°$ of protonation for all X^- except CH_3COS^-,[33] or gas-phase acidity, ΔG_{acid}, of HX for CH_3COS^-;[34] this plot is presented in Fig. II.3.3.

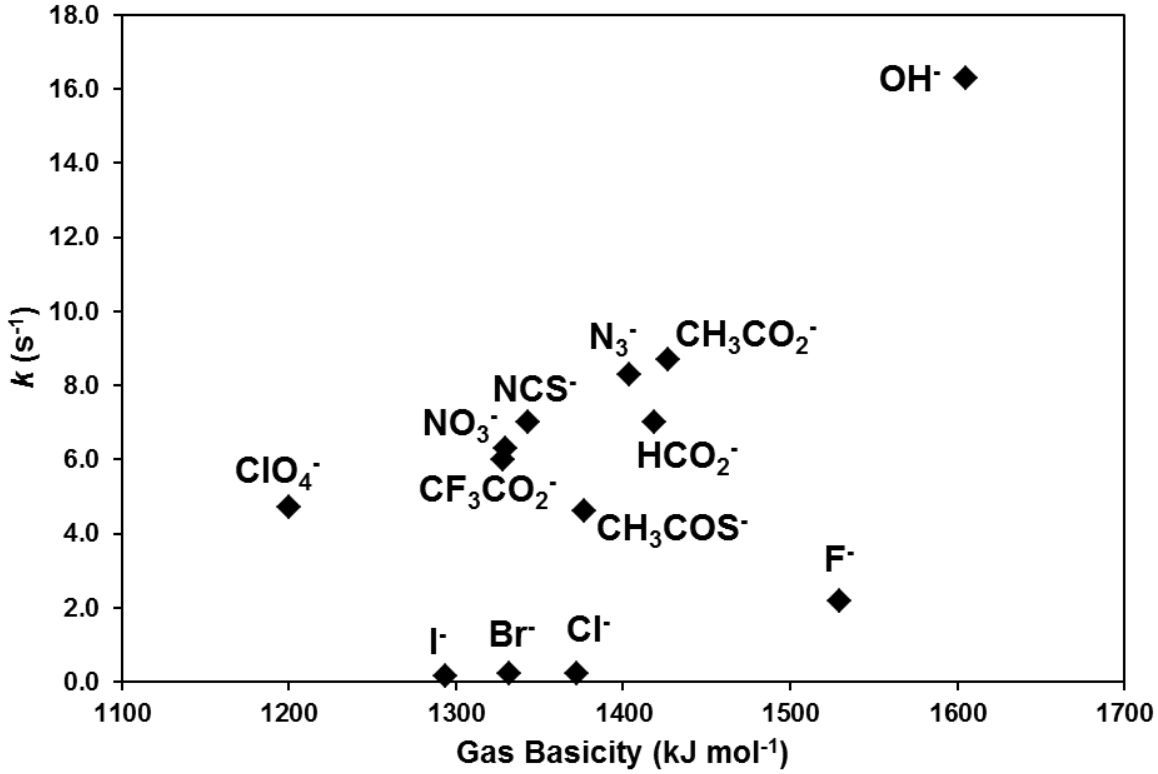

Figure II.3.3. Plot of the rates of O_2 addition to $[UO_2X_2]^-$ ions (*k* from Table II.3. 1) as a function of the gas basicity of X^- (see text for references).

It is apparent from Fig. II.3.3 that the lower rates of O_2-addition to the complexes with monoatomic halide ligands are not a consequence of their basicities. With the exceptions of OH^-, where the previously mentioned effects may be operative in producing a distinctively high rate, and CH_3COS^-, the polyatomic ligands seem to exhibit a fair correlation with the gas basicity. In the case of CH_3COS^-, with the same number of vibrational degrees of freedom as $CH_3CO_2^-$ and $CF_3CO_2^-$, it is not clear how the presence of a coordinating S atom instead of an O atom leads to a lower rate for O_2 addition.

II.3.4.3 Nature and stability of $[U^{VI}O_2X_2(O_2)]^-$ complexes from experiments and computations

A few experiments were performed with $[U^{V}O_2(CH_3CO_2)_2]^-$ ions to probe the nature of the O_2 ligation. If O_2 is coordinated to uranyl(V) as a neutral adduct, varying the He pressure should affect the rate, as changes in the number of collisions with the inert gas can lead to different degrees of stabilization of the initial ion-neutral complex as an adduct species.[35] In contrast, when there is a chemical change subsequent to the formation of the ion-neutral complex, such as the presumed electron transfer from uranyl(V) to oxygen in the present study, no such effect in the rates is expected.[35] When the He pressure down and up was varied within a factor of ca. 4, there was no discernable change in the oxygen addition rates, consistent with the stronger bonding associated with superoxide (rather than adduct) formation. Another experiment involved the introduction of $^{18}O_2$ in the ion trap and examining the exchange reactions of isolated $[UO_2(CH_3CO_2)_2(^{16}O_2)]^-$ ions with $^{18}O_2$ and of $[UO_2(CH_3CO_2)_2(^{18}O_2)]^-$ ions with $^{16}O_2$. No exchange was observed in either case, providing evidence that oxygen is not bonded as a neutral adduct, as exchange should be expected for a weakly bound ligand.[36] These two sets of results indicate that O_2 is bonded as formally O_2^-, as assumed; the superoxide nature of the O_2 ligand in the $[U^{VI}O_2X_2(O_2)]^-$ complexes was confirmed by DFT computations described below.

Other notable observations during the experiments involving $^{18}O_2$ were the absence of exchange between the coordinated O_2 ligand and the oxo ligands of uranyl, as evidenced by CID experiments of $[UO_2(CH_3CO_2)_2(^{18}O_2)]^-$ in which the sole product was $[UO_2(CH_3CO_2)_2]^-$, and the absence of exchange between the coordinated O_2 ligand and the hydroxo ligand in $[UO_2(CH_3CO_2)(OH)(^{18}O_2)]^-$ (see Scheme 2), as indicated by CID resulting only in $^{18}O_2$ loss.

CID of the $[U^{VI}O_2X_2(O_2)]^-$ complexes showed in all cases loss of O_2 to form the $[U^{V}O_2X_2]^-$ anions; these results indicate a weaker binding of the monoanionic O_2^- ligand compared to the studied X^- ligands. A few examples of these CID spectra, for X = NO_3, CH_3CO_2, and NCS, are presented in the Supporting Information. Interestingly, other minor neutral losses were also observed for $[U^{VI}O_2I_2(O_2)]^-$ (I loss), $[U^{VI}O_2(ClO_4)_2(O_2)]^-$ (ClO_3 loss), and $[U^{VI}O_2(NO_3)_2(O_2)]^-$ (NO_2 loss, associated with hydrolysis). In the case of the iodide ligand, weaker binding might be expected, both from experiment and theory.[30,37] This is also apparent from the DFT computations performed in this work and described below. In the case of the ClO_4 and NO_3 complexes, it has been previously reported that the observed neutral losses are facile.[31,32]

DFT computations were performed to elucidate the nature of the $[U^{VI}O_2X_2(O_2)]^-$ complexes; the complexes for X = F, Cl, Br, I, NCS and OH were selected because they were those which formed O_2 association products with relatively low efficiency (halides), intermediate efficiency

(thiocyanate), and high efficiency (hydroxide). To obtain the energetics of the O_2-association reaction, the precursor uranyl(V) complexes were also examined. The geometrical parameters of the ground-state (GS) structures of the precursor and product complexes are presented in Table II.3.2 and Fig. II.3.4; the energy and free energy changes for the addition of O_2 are presented in Table II.3.3. Several initial structures were considered for each of the O_2-complexes investigated, taking into account the two typical O_2-coordination modes, i.e., end-on (η^1) and side-on (η^2). The computations indicate that O_2 binds to uranium in the $[U^VO_2X_2]^-$ complexes in a η^2 configuration, in a similar way to previously studied cationic complexes of uranyl(V).[7,9,10] End-on η^1 isomers were found to be between 53 and 61 kJ mol^{-1} higher in energy than the corresponding GS isomers; details regarding these isomers are reported as Supporting Information (Table S1). As shown in Table II.3.2, in all the GS $[UO_2X_2(O_2)]^-$ complexes the O-O bond lengths of the O_2 ligand (ca. 1.31 Å) are typical of a superoxo ligand,[1] indicating that uranyl(V) has been formally oxidized to uranyl(VI), as had been assumed. Moreover, an analysis of the distribution of the spin density confirms that the unpaired electron is localized on the O_2 moiety in all the $[UO_2X_2(O_2)]^-$ complexes. The computed energies for O_2 addition, presented in Table II.3.3, indicate that this is a favorable process for all the examined $[UO_2X_2]^-$. Notably, the energies are more favorable than the corresponding computed DFT energies in the previously studied cationic uranyl(VI) complexes involving neutral ligands;[7,9] this is in accord with the fact that anionic ligands donate more electron density to the uranium center, therefore favoring electron transfer to O_2 to form the superoxide. Similarly to the empirical correlations with GB of X^-, the computed energies to produce $[UO_2X_2(O_2)]^-$ from $[UO_2X_2]^-$ by addition of O_2 do not correlate with the measured association rates. In particular, the association energy for $[UO_2F_2(O_2)]^-$ is substantially greater than that for $[UO_2(NCS)_2(O_2)]^-$ but the rate for the latter is substantially greater. As discussed above, it is apparent that energetics alone does not establish the association efficiencies and that other factors such as vibrational degrees of freedom come into play.

Table II.3.2. Computed bond distances and angles of the $[UO_2X_2]^-$ and $[UO_2X_2(O_2)]^-$ ground–state structures (X = OH, F, Cl, Br, I, and NCS).[a]

	U-O_{yl}	U-X	U-O	O-O	X-U-X	O_{yl}-U-O_{yl}
$[UO_2(OH)_2]^-$	1.862	2.239	-	-	112.3	160.7
$[UO_2(OH)_2(O_2)]^-$	1.804	2.211	2.459	1.318	108.9	177.7
$[UO_2F_2]^-$	1.865	2.205	-	-	108.2	149.1
$[UO_2F_2(O_2)]^-$	1.795	2.170	2.440	1.316	108.1	175.6
$[UO_2Cl_2]^-$	1.835	2.702	-	-	114.6	152.1
$[UO_2Cl_2(O_2)]^-$	1.777	2.666	2.409	1.312	111.6	175.8
$[UO_2Br_2]^-$	1.830	2.870	-	-	116.4	152.6
$[UO_2Br_2(O_2)]^-$	1.774	2.836	2.402	1.312	113.3	176.1
$[UO_2I_2]^-$	1.822	3.119	-	-	118.7	154.2
$[UO_2I_2(O_2)]^-$	1.771	3.086	2.392	1.311	115.3	176.8
$[UO_2(NCS)_2]^-$	1.829	2.404	-	-	113.9	157.6
$[UO_2(NCS)_2(O_2)]^-$	1.778	2.367	2.405	1.312	110.4	177.3

[a] Distances are in angstroms and angles are in degrees.

Table II.3.3 Computed energy (ΔE^0) and Gibbs free energy (ΔG^{298}) changes for the O_2-addition reactions to $[UO_2X_2]^-$.[a]

Reactant	$[UO_2(OH)_2]^-$	$[UO_2F_2]^-$	$[UO_2Cl_2]^-$	$[UO_2Br_2]^-$	$[UO_2I_2]^-$	$[UO_2(NCS)_2]^-$
ΔE^0	-195	-182	-155	-149	-143	-151
ΔG^{298}	-152	-137	-110	-104	-98	-108

[a] In kJ mol^{-1}. The computed energies correspond to the $[UO_2X_2]^- + O_2 \rightarrow [UO_2X_2(O_2)]^-$ reactions for X = OH, F, Cl, Br, I, and NCS. All reactants and products are in their ground states.

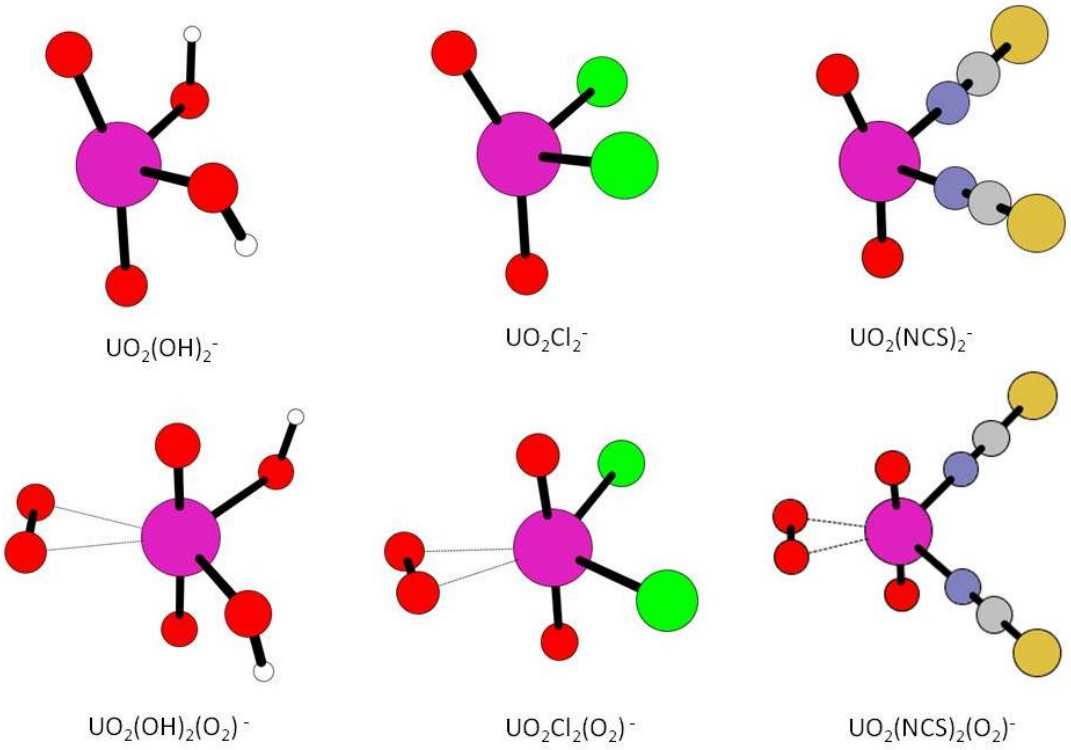

Figure II.3.4. Ground-state structures for $[UO_2X_2]^-$ and $[UO_2X_2(O_2)]^-$, with X = OH, Cl, and NCS.

QTAIM analysis was performed on the $[UO_2X_2]^-$ precursors and on the final O_2-addition complexes, $[UO_2X_2(O_2)]^-$ (X = OH, F, Cl, Br, I, and NCS). The results are provided as Supporting Information (Tables S2 and S3) together with a brief description of the method. A comparison of the topological properties of the initial complexes U-O_{yl} bond shows that the uranyl bond is most weakened by the presence of the F ligand, as shown by the increase in the charge density (ρ) at the U-O_{yl} bond critical point (BCP), ρ_{BCP}, in going from F to I. The results for X = OH are close to those of F, whereas those for X = NCS are close to Br. The increase of the charge density at the U-O_{yl} BCP in going from X = F to I is accompanied by an increase in the absolute value of the total energy density at the BCP, $H_{BCP,}$ which is in all cases negative, and by an increase of the delocalization index, DI(U,O_{yl}). These changes indicate a higher covalent character (i.e. higher sharing of electrons) in the uranyl bond in going from $[UO_2F_2]^-$ to $[UO_2I_2]^-$; which is consistent with the shortening of the U-O_{yl} bond distances in going from $[UO_2F_2]^-$ to $[UO_2I_2]^-$. The values of the U-O_{yl} ρ_{BCP} are in all cases higher than 0.2 au., which is the lower limit of the charge density that is usually used in AIM analysis to consider an interaction as covalent. The strongly polarized character of the U-X bonds is confirmed by the very low values of the ρ_{BCP} (< 0.1 au) and by the very small values of the total energy density,

H_{BCP}. The U-X bonds are therefore better described as ionic. Our results are in agreement with the findings reported by Vallet et al. for uranyl(VI) complexes with Lewis base ligands, including F^- and Cl^-.[27] The highest U-X ρ_{BCP} values are found for X = OH and F, and the lowest for X = I, which indicates that there is a larger charge delocalization between U and F or OH, than between U and the later halogens. This is consistent with the fact that the most weakened U-O_{yl} bond (longer $d_{U\text{-}Oyl}$ and lower charge density at the BCP) is found in $[UO_2F_2]^-$ and $[UO_2(OH)_2]^-$.

In all cases the addition of O_2 increases the charge density on the U-O_{yl} BCP, which is consistent with the shortening of the U-O_{yl} bonds that takes place as a consequence of the O_2-addition and with the hypothesis that dioxygen oxidizes the metal center from U^V to U^{VI}. As a consequence of this oxidation, the U-O_{yl} bonds in the $[UO_2X_2(O_2)]^-$ complexes are generally characterized by more negative H_{BCP} values and higher DI(U,O_{yl}) values, namely, the covalent character of the U-O_{yl} bonds increases. The U-X bonds are also slightly reinforced by the addition of O_2, as evidenced by the shorter bond distances, higher ρ_{BCP}, more negative H_{BCP} and higher DI(U,X). The O_2 bond is more elongated in $[UO_2F_2(O_2)]^-$ as well as in $[UO_2(OH)_2(O_2)]^-$, and closer to that of bare O_2^- than in the rest of the complexes. As a consequence, the O-O BCP charge density increases in going from X = F to I. This is consistent with the fact that the negative atomic charges localized on the O_2 unit is largest in $[UO_2(OH)_2(O_2)]^-$ (0.68 e^-), and systematically decreases in going from $[UO_2F_2(O_2)]^-$ (0.66 e^-) to $[UO_2I_2(O_2)]^-$ (0.48 e^-). The interaction between the uranyl moiety and O_2 is mostly ionic, with values of U-O charge density lower than 0.07 au. and H_{BCP} values that are only slightly negative (Table S3). The number of electrons shared between U and the oxygen atoms of the O_2 unit show a slight increase in going from X = F to X = I, which is consistent with the slight shortening of the U-O bond distance.

II.3.5. Conclusions

Gas-phase anionic uranyl(V) complexes, $[UO_2X_2]^-$, ligated to thirteen different anions X^-, were produced by ESI and reacted with O_2 in a QIT mass spectrometer to form uranyl(VI) superoxo complexes, $[UO_2X_2(O_2)]^-$. The effects of the basicity and number of vibrational degrees of freedom of the X^- ligands on the rates of O_2-addition were revealed, confirming earlier work with cationic complexes of uranyl(V) involving neutral ligands. DFT computations of selected precursor and product uranyl complexes produced energetics data that indicated a stronger binding of the superoxide ligand in the present complexes involving anionic ligands compared with those with neutral ligands. DFT and QTAIM computations on selected complexes confirm the formal

oxidation of U(V) to U(VI) by superoxide formation, and indicate that the charge transfer is more favourable for precursor complexes where the uranyl bond is most weakened by the presence of the ligands, e.g. $[UO_2(OH)_2]^-$ and $[UO_2F_2]^-$. The gas-phase results may indicate that formation of superoxo complexes of uranyl(VI) from reactions of uranyl(V) precursors with O_2 are within reach in condensed phase.

Acknowledgements

This work was supported by Fundação para a Ciência e a Tecnologia/Portugal through PhD grant SFRH/BD/70475/2010 to A.F.L. and RNEM - Rede Nacional de Espectrometria de Massa, by Università della Calabria, and by the U.S. Department of Energy, Office of Science, Office of Basic Energy Sciences, Division of Chemical Sciences, Geosciences and Biosciences at LBNL under Contract Number DE-AC02-05CH11231 (J.K.G.). This research used resources of the National Energy Research Scientific Computing Center (NERSC), which is supported by the Office of Science of the U.S. Department of Energy under Contract No. DE-AC02-05CH11231.

References

(1) Holland, P. L., Metal-dioxygen and metal-dinitrogen complexes: Where are the electrons?, *Dalton Transactions* **2010**, 39, 5415.

(2) Gong, Y.; Zhou, M.; Andrews, L., Spectroscopic and theoretical studies of transition metal oxides and dioxygen complexes, *Chemical Reviews* **2009**, 109, 6765.

(3) Sheng, Y.; Abreu, I. A.; Cabelli, D. E.; Maroney, M. J.; Miller, A. F.; Teixeira, M.; Valentine, J. S., Superoxide dismutases and superoxide reductases, *Chemical Reviews* **2014**, 114, 3854.

(4) Qiu, J.; Burns, P. C., Clusters of actinides with oxide, peroxide, or hydroxide bridges, *Chemical Reviews* **2013**, 113, 1097.

(5) Bakac, A.; Espenson, J. H., Autoxidation of uranium(V), Catalysis and inhibition by copper ions, *Inorganic Chemistry* **1995**, 34, 1730.

(6) Groenewold, G. S.; Cossel, K. C.; Gresham, G. L.; Gianotto, A. K.; Appelhans, A. D.; Olson, J. E.; Van Stipdonk, M. J.; Chien, W., Binding of molecular O_{-2} to di- and triligated $[UO_2](+)$, *Journal of the American Chemical Society* **2006**, 128, 3075.

(7) Bryantsev, V. S.; de Jong, W. A.; Cossel, K. C.; Diallo, M. S.; Goddard, W. A.; Groenewold, G. S.; Chien, W.; Van Stipdonk, M. J., Two-electron three-centered bond in side-on (η^2) Uranyl(V) superoxo complexes, *Journal of Physical Chemistry A* **2008**, 112, 5777.

(8) Leavitt, C. M.; Bryantsev, V. S.; de Jong, W. A.; Diallo, M. S.; Goddard, W. A.; Groenewold, G. S.; Van Stipdonk, M. J., Addition of H_2O and O_2 to acetone and dimethylsulfoxide ligated uranyl(V) dioxocations. *Journal of Physical Chemistry A* **2009**, 113, 2350.

(9) Rios, D.; Michelini, M. C.; Lucena, A. F.; Marçalo, J.; Bray, T. H.; Gibson, J. K., Gas-phase uranyl, neptunyl, and plutonyl: Hydration and oxidation studied by experiment and theory, *Inorganic Chemistry* **2012**, 51, 6603.

(10) Ricks, A. M.; Gagliardi, L.; Duncan, M. A., Uranium oxo and superoxo cations revealed using infrared spectroscopy in the gas phase, *The Journal of Physical Chemistry Letters* **2011**, 2, 1662.

(11) Gong, Y.; Gibson, J. K., Formation and characterization of the uranyl-SO_2 complex, $UO_2(CH_3SO_2)(SO_2)^-$, *Journal of Physical Chemistry A* **2013**, 117, 783.

(12) Rios, D.; Rutkowski, P. X.; Shuh, D. K.; Bray, T. H.; Gibson, J. K.; Van Stipdonk, M. J., Electron transfer dissociation of dipositive uranyl and plutonyl coordination complexes, *Journal of Mass Spectrometry* **2011**, 46, 1247.

(13) Frisch, M. J.; Trucks, G. W.; Schlegel, H. B.; Scuseria, G. E.; Robb, M. A.; Cheeseman, J. R.; Scalmani, G.; Barone, V.; Mennucci, B.; Petersson, G. A.; et al.: Gaussian 09. Gaussian, Inc.: Wallingford, CT, USA, **2009**.

(14) Becke, A. D., Density-functional thermochemistry III. The role of exact exchange, *Journal of Chemical Physics* **1993**, 98, 5648.

(15) Lee, C. T.; Yang, W. T.; Parr, R. G., Development of the colle-salvetti correlation-energy formula into a functional of the electron-density, *Physical Review B* **1988**, 37, 785.

(16) Küchle, W.; Dolg, M.; Stoll, H.; Preuss, H., Energy-adjusted pseudopotentials for the actinides - Parameter sets and test calculations for thorium and thorium monoxide, *Journal of Chemical Physics* **1994**, 100, 7535.

(17) Cao, X. Y.; Dolg, M.; Stoll, H., Valence basis sets for relativistic energy-consistent small-core actinide pseudopotentials, *Journal of Chemical Physics* **2003**, 118, 487.

(18) Krishnan, R.; Binkley, J. S.; Seeger, R.; Pople, J. A., Self-consistent molecular-orbital methods .20. Basis set for correlated wave-functions, *Journal of Chemical Physics* **1980**, 72, 650.

(19) Clark, T.; Chandrasekhar, J.; Spitznagel, G. W.; Schleyer, P. V., Efficient diffuse function-augmented basis-sets for anion calculations III. The 3-21+G basis set for 1st-row elements, Li-F, *Journal of Computational Chemistry* **1983**, 4, 294.

(20) Curtiss, L. A.; McGrath, M. P.; Blaudeau, J.-P.; Davis, N. E.; Binning Jr., R. C.; Radom, L. extension of gaussian-2 theory to molecules containing third-row atoms Ga-Kr, *Journal of Chemical Physics* **1995**, 103 6104.

(21) Bader, R. F. W., Atoms in molecules: A quantum theory; Oxford University Press: Oxford, **1990**.

(22) Keith, T. A.: AIMAll (version 13.05.06), 2013 (aim.tkgristmill.com).

(23) Michelini, M. C.; Russo, N.; Sicilia, E., Gas-phase chemistry of actinides ions: New insights into the reaction of UO^+ and UO^{2+} with water, *Journal of the American Chemical Society* **2007**, 129, 4229.

(24) Petit, L.; Joubert, L.; Maldivi, P.; Adamo, C. A., Comprehensive theoretical view of the bonding in actinide molecular complexes, *Journal of the American Chemical Society* **2006**, 128, 2190.

(25) Tassell, M. J.; Kaltsoyannis, N., Covalency in $AnCp_4$ (An = Th-Cm): A comparison of molecular orbital, natural population and atoms-in-molecules analyses, *Dalton Transactions* **2010**, 39, 6719.

(26) Kaltsoyannis, N., Does covalency increase or decrease across the actinide series? Implications for minor actinide partitioning, *Inorganic Chemistry* **2013**, 52, 3407.

(27) Vallet, V.; Wahlgren, U.; Grenthe, I., Probing the nature of chemical bonding in Uranyl(VI) Complexes with Quantum Chemical Methods, *Journal of Physical Chemistry A* **2012**, 116, 12373.

(28) Gong, Y.; Vallet, V.; Michelini, M. C.; Rios, D.; Gibson, J. K., Activation of gas-phase uranyl: From an oxo to a nitrido complex, *Journal of Physical Chemistry A* **2014**, 118, 325.

(29) Groenewold, G. S.; de Jong, W. A.; Oomens, J.; Van Stipdonk, M. J., Variable denticity in carboxylate binding to the uranyl coordination complexes, *Journal of the American Society for Mass Spectrometry* **2010**, 21, 719.

(30) Groenewold, G. S.; van Stipdonk, M. J.; Oomens, J.; de Jong, W. A.; Gresham, G. L.; McIlwain, M. E., Vibrational spectra of discrete UO_2^{2+} halide complexes in the gas phase, *International Journal of Mass Spectrometry* **2010**, 297, 67.

(31) Pasilis, S.; Somogyi, A.; Herrmann, K.; Pemberton, J. E., Ions generated from uranyl nitrate solutions by electrospray ionization (ESI) and detected with Fourier Transform Ion-Cyclotron Resonance (FT-ICR) Mass Spectrometry, *Journal of the American Society for Mass Spectrometry* **2006**, 17, 230.

(32) Sokalska, M.; Prussakowska, M.; Hoffmann, M.; Gierczyk, B.; Franski, R., Unusual ion UO_4^- formed upon collision induced dissociation of $[UO_2(NO_3)_3]^-$, $[UO_2(ClO_4)_3]^-$, $[UO_2(CH_3COO)_3]^-$ ions, *Journal of the American Society for Mass Spectrometry* **2010**, 21, 1789.

(33) Linstrom, P. J.; Mallard, W. G.: NIST Chemistry WebBook. In NIST standard reference database number 69; National Institute of Standards and Technology: Gaithersburg, MD, **2015**.

(34) Eyet, N.; Bierbaum, V. M., Gas-phase acidities of thiocarboxylic acids, *International Journal Mass Spectrometry* **2007**, 265, 267.

(35) Tonkyn, R.; Ronan, M.; Weisshaar, J. C., Multicollision chemistry of gas-phase transition-metal ions with small alkanes: Rate constants and product branching at 0.75 torr of helium, *Journal of Physical Chemistry* **1988**, 92, 92.

(36) Schwarz, J.; Schwarz, H., Gas-phase generation and structural characterization of the $Fe(CO_2)^+$ cluster, *Organometallics* **1994**, 13, 1518.

(37) Su, J.; Dau, P. D.; Qiu, Y. H.; Liu, H. T.; Xu, C. F.; Huang, D. L.; Wang, L. S.; Li, J., Probing the electronic structure and chemical bonding in tricoordinate uranyl complexes UOX (X = F, Cl, Br, I): Competition between coulomb repulsion and U-X bonding, *Inorganic Chemistry* **2013**, 52, 6617.

Supporting Information

Representative CID mass spectra of $[UO_2X_3]^-$ and $[UO_2X_2(O_2)]^-$ ions. Kinetic plot from the reaction of isolated $[U^VO_2(CH_3CO_2)_2]^-$ with O_2. Quantitative analysis of the electron density using the QTAIM method.

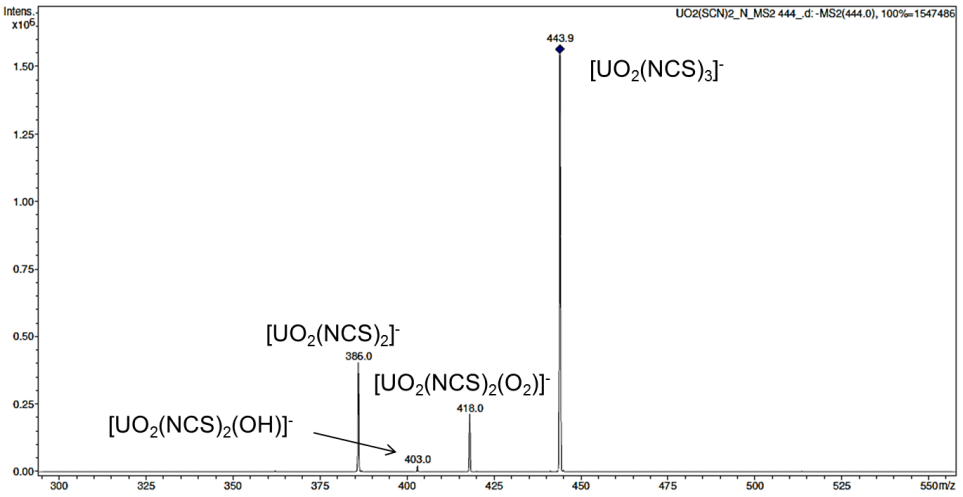

Figure S1. CID mass spectrum of $[UO_2(NCS)_3]^-$.

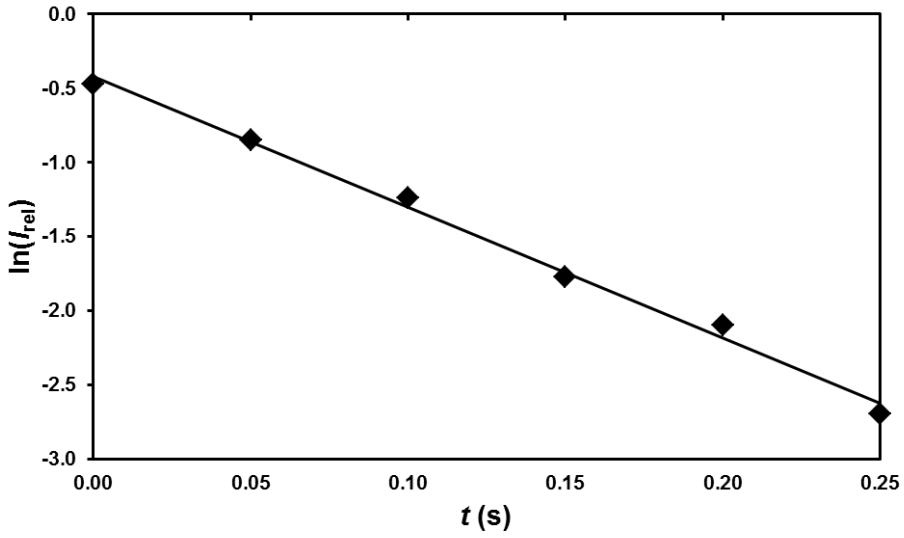

Figure S2. Kinetic plot from the reaction of isolated $[U^VO_2(CH_3CO_2)_2]^-$ with O_2 to form $[U^{VI}O_2(CH_3CO_2)_2(O_2)]^-$ (k = 8.8 s^{-1}; R^2 = 0.9942).

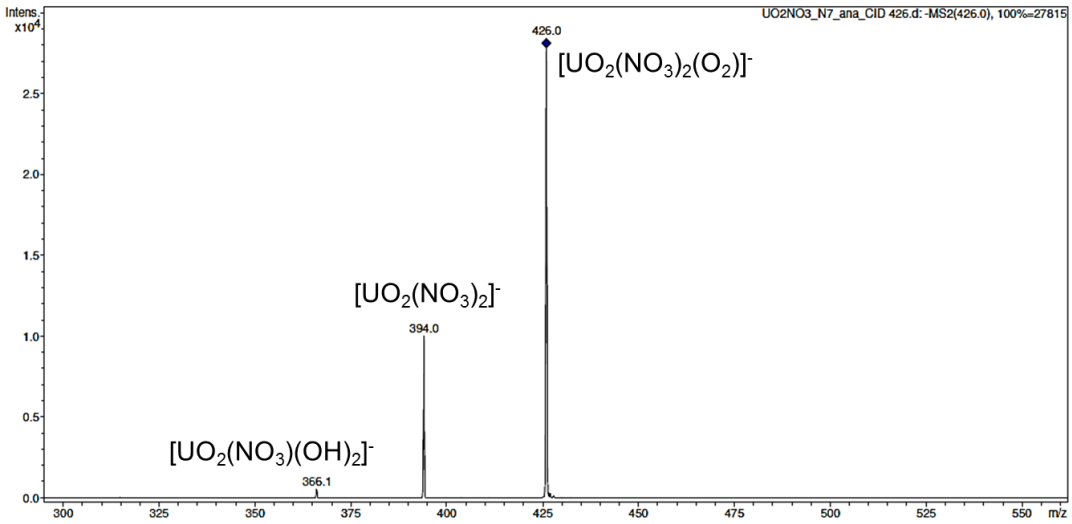

Figure S3. CID mass spectrum of $[UO_2(NO_3)_2(O_2)]^-$.

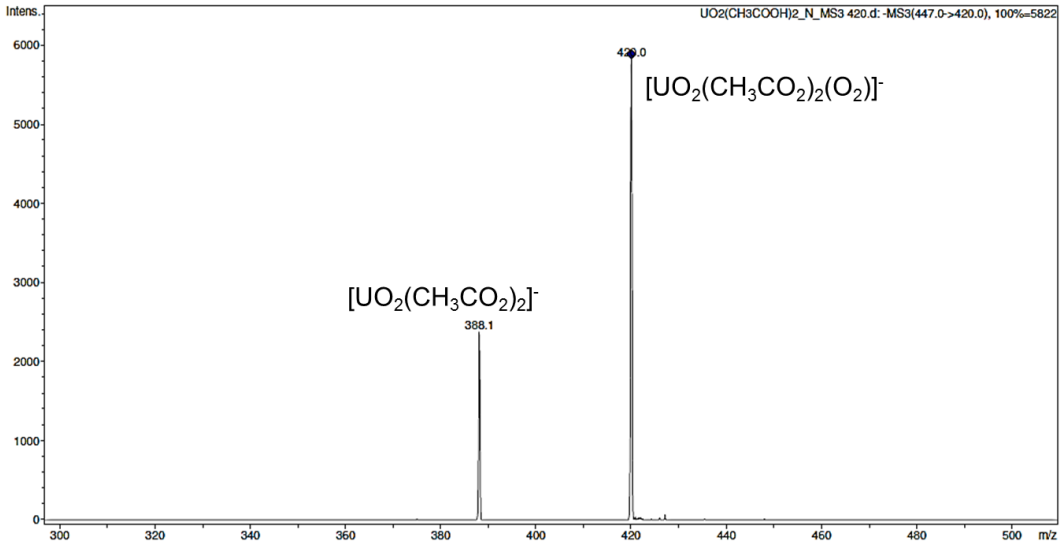

Figure S4. CID mass spectrum of $[UO_2(CH_3CO_2)_2(O_2)]^-$.

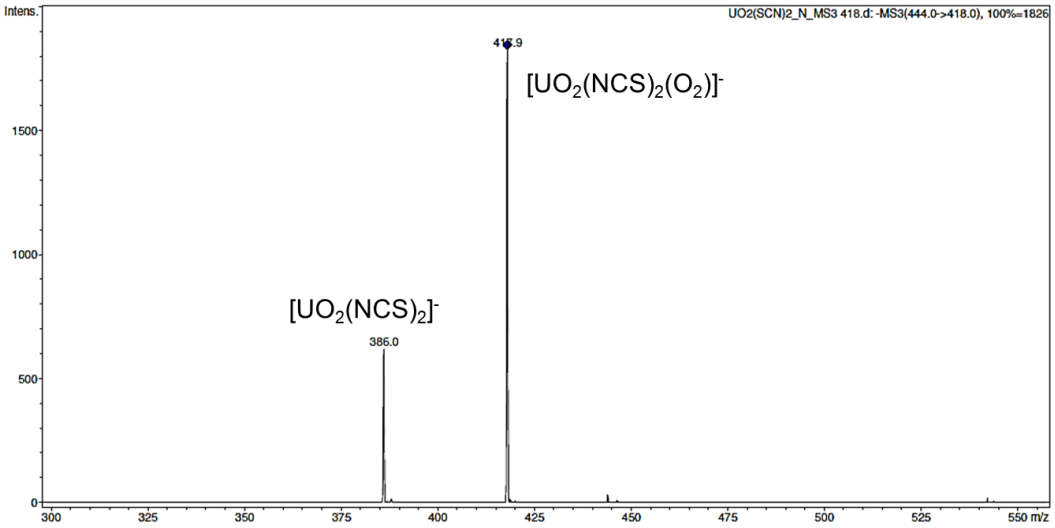

Figure S5. CID mass spectrum of $[UO_2(NCS)_2(O_2)]^-$.

Table S1. Computed bond distances and angles of the $[UO_2X_2(O_2)]^-$ η^1 structures (X = OH, F, Cl, Br, I, and NCS).[a]

	RE	U-O_{yl}	U-O	O-O	U-O-O	O_{yl}-U-O_{yl}
$[UO_2(OH)_2(O_2)]^-$	53	1.801	2.287	1.301	151.2	178.7
$[UO_2F_2(O_2)]^-$	56	1.792	2.267	1.301	149.3	176.4
$[UO_2Cl_2(O_2)]^-$	59	1.776	2.235	1.297	148.8	176.3
$[UO_2Br_2(O_2)]^-$	59	1.773	2.228	1.296	148.2	176.5
$[UO_2I_2(O_2)]^-$	61	1.769	2.217	1.295	148.2	177.2
$[UO_2(NCS)_2(O_2)]^-$	60	1.777	2.228	1.295	149.7	177.9

[a] See Figure S6. Distances are in angstroms and angles are in degrees. RE is the relative energy (in kJ.mol^{-1}) with respect to the η^2 ground-state structures.

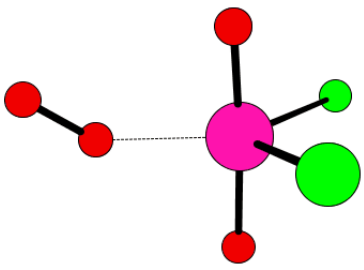

Figure S6. Generic η^1 structure.

QTAIM Analysis

The QTAIM theory is based on the topological analysis of the electron density, $\rho(r)$ [1]. Bonds are defined by a bond path, which is necessary for chemical bonding regardless of its nature. The chemical nature of the bonding may be characterized and classified according to the properties of the Bond Critical Points (BCPs). Topologically, a BCP corresponds to a point in the real space where the gradient of the density, $\nabla\rho_{BCP}$, is zero and where the curvature of ρ_{BCP}, expressed through the three eigenvalues of the diagonalized Hessian of ρ_{BCP}, is positive for an eigenvector linking two atomic centers (λ_3) and negative for the two others (λ_1, λ_2) perpendicular to it. A chemical bond thus results from the competition of the parallel expansion of ρ, which separates charges in their respective atomic basins (λ_3) and the perpendicular contraction of ρ toward a bond path (λ_1, λ_2). The dominant effect is measured by the Laplacian of ρ_{BCP}, $\nabla^2\rho_{BCP}$. Values of ρ_{BCP} greater than 0.2 are typical of covalent bonds, and $\nabla^2\rho_{BCP}$ is generally less than zero for such interactions, reflecting the concentration of electron density along the bond path linking the bonded atoms. In strongly polar bonding there is a significant accumulation of electron density between the nuclei, as in all shared interactions, but the Laplacian can be of either sign. It has been previously reported that in second-row elements and heavier [2-4] the λ_3 term often dominates the Laplacian resulting in a positive overall term. The An-O_{yl} bonds of all the studied cations show in fact positive values of $\nabla^2\rho_{BCP}$ and ρ_{BCP} values higher than 0.2 (Table S3). The energy density (the sum of the kinetic and the potential energy densities) at the BCP, H_{BCP}, is negative for interactions with significant sharing of electrons, its magnitude reflect the covalence of the interaction.[6] The delocalization indexes, DI, between bonded atoms yield a measure of the bond order between them if the electron pairs are equally shared (no appreciable charge transfer). [7]

[1] Bader, R. F. W. Atoms in Molecules: A Quantum Theory; Oxford University Press: Oxford, 1990.

[2] Michelini, M.C.; Russo, N.; Sicilia, E. J. Am. Chem. Soc. 2007, 129, 4229.

[3] Di Santo, E.; Michelini, M.C.; Russo, N. Organometallics 2009, 28, 3716.

[4] Mills, D. P.; Cooper, O. J.; Tuna, F.; McInnes, E. J. L.; Davies, E. S.; McMaster, J.; Moro, F.; Lewis, W.; Blake, A. J.; Liddle, S. T. J. Am. Chem. Soc. 2012, 134, 10047.

[5] Cremer, D.; Kraka, E. Croat. Chem. Acta 1984, 57, 1259.

[6] Cremer, D.; Kraka, E. Angew. Chem. Int. Ed. Engl. 1984, 23,627.

[7] Fradera, X.; Austen, M. A.; Bader, R. F. W. J. Phys. Chem. A 1999, 103, 304.

Table S2. QTAIM atomic charges in $[UO_2X_2]^-$ and $[UO_2X_2(O_2)]^-$ ground-state structures (X = OH, F, Cl, Br, I, and NCS).

	$[UO_2(OH)_2]^-$	**$[UO_2F_2]^-$**	**$[UO_2Cl_2]^-$**	**$[UO_2Br_2]^-$**	**$[UO_2I_2]^-$**	**$[UO_2(NCS)_2]^-$**
U	2.57	2.64	2.56	2.46	2.41	2.61
O_{yl}	-1.07	-1.05	-1.00	-0.99	-0.98	-0.98
X[a]	-1.22	-0.77	-0.75	-0.74	-0.72	-1.39
	$[UO_2(OH)_2(O_2)]^-$	**$[UO_2F_2(O_2)]^-$**	**$[UO_2Cl_2(O_2)]^-$**	**$[UO_2Br_2(O_2)]^-$**	**$[UO_2I_2(O_2)]^-$**	**$[UO_2(NCS)_2(O_2)]^-$**
U	2.86	2.92	2.76	2.72	2.65	2.87
O_{yl}	-0.92	-0.90	-0.87	-0.87	-0.86	-0.86
X[a]	-1.18	-0.73	-0.70	-0.68	-0.66	-1.38
O	-0.34	-0.33	-0.32	-0.31	-0.31	-0.31

[a]For X = OH the value reported is the natural charge on the O atom, for X = SCN the value reported is the charge on the N atom. Bare UO_2^+ = q(U) =2.68, q(O) -0.84; bare UO_2^{2+}: q(U): 3.17, q(O):-0.58.

Table S3. Electron density at the bond critical point (ρ_{BCP}) , Laplacian of electron density ($\nabla^2\rho_{BCP}$), total energy density (H_{BCP}) and delocalization indexes (DI) for $[UO_2X_2]^-$ and $[UO_2X_2(O_2)]^-$ ground-state structures (X = OH, F, Cl, Br, I and NCS).

	$[UO_2(OH)_2]^-$	$[UO_2F_2]^-$	$[UO_2Cl_2]^-$	$[UO_2Br_2]^-$	$[UO_2I_2]^-$	$[UO_2(NCS)_2]^-$
U-O_{yl} bond						
ρ_{BCP}	0.241	0.239	0.258	0.262	0.267	0.263
$\nabla^2\rho_{BCP}$	0.317	0.329	0.306	0.301	0.295	0.294
H_{BCP}	-0.180	-0.178	-0.206	-0.212	-0.220	-0.213
DI(U,O_{yl})	1.786	1.816	1.885	1.900	1.919	1.883
$d_{U\text{-}Oyl}$	1.862	1.865	1.835	1.830	1.822	1.829
U-X bond						
ρ_{BCP}	0.094	0.089	0.057	0.049	0.040	0.067
$\nabla^2\rho_{BCP}$	0.338	0.406	0.137	0.092	0.062	0.223
H_{BCP}	-0.018	-0.090	-0.010	-0.009	-0.007	-0.010
DI(U,X)	0.720	0.634	0.616	0.607	0.602	0.475
$d_{U\text{-}X}$	2.239	2.205	2.702	2.870	3.119	2.404
	$[UO_2(OH)_2(O_2)]^-$	$[UO_2F_2(O_2)]^-$	$[UO_2Cl_2(O_2)]^-$	$[UO_2Br_2(O_2)]^-$	$[UO_2I_2(O_2)]^-$	$[UO_2(NCS)_2(O_2)]^-$
U-O_{yl} bond						
ρ_{BCP}	0.279	0.286	0.295	0.301	0.303	0.298
$\nabla^2\rho_{BCP}$	0.304	0.300	0.323	0.294	0.294	0.296
H_{BCP}	-0.238	-0.249	-0.270	-0.275	-0.279	-0.270
DI(U,O_{yl})	1.883	1.916	1.967	1.978	1.991	1.959
$d_{U\text{-}Oyl}$	1.804	1.795	1.777	1.774	1.771	1.778
U-X bond						
ρ_{BCP}	0.099	0.097	0.062	0.053	0.044	0.073
$\nabla^2\rho_{BCP}$	0.344	0.426	0.142	0.101	0.062	0.238
H_{BCP}	-0.022	-0.012	-0.012	-0.010	-0.008	-0.012
DI(U,X)	0.762	0.677	0.664	0.660	0.666	0.510
$d_{U\text{-}X}$	2.211	2.170	2.666	2.836	3.086	2.367
U-O bond						
ρ_{BCP}	0.057	0.059	0.063	0.065	0.066	0.064
$\nabla^2\rho_{BCP}$	0.207	0.214	0.225	0.228	0.231	0.228
H_{BCP}	-0.003	-0.004	-0.005	-0.005	-0.006	-0.005
DI(U,O)	0.385	0.405	0.436	0.444	0.454	0.443
$d_{U\text{-}O}$	2.459	2.440	2.409	2.402	2.392	2.405
O-O bond						
ρ_{BCP}	0.394	0.397	0.400	0.401	0.402	0.401
$\nabla^2\rho_{BCP}$	-0.198	-0.205	-0.215	-0.217	-0.219	-0.217
H_{BCP}	-0.364	-0.370	-0.377	-0.378	-0.380	-0.378
DI(O,O)	1.760	1.758	1.755	1.754	1.752	1.755
$d_{O\text{-}O}$	1.318	1.316	1.312	1.312	1.311	1.312

[a]In atomic units. Bond distances, d(A,B), in angstroms. With the aim of comparison computed topological properties for bare O_2 ($d_{O\text{-}O}$ = 1.206 Å) are: $_{BCP}$ = 0.539, $\nabla^2\rho_{BCP}$ = -0.765, H_{BCP} =-0.659, DI(O-O) = 2.24; and for bare O_2^- ($d_{O\text{-}O}$ = 1.346 Å) ρ_{BCP} = 0.363, $\nabla^2\rho_{BCP}$ = -0.131, H_{BCP} =-0.310, DI(O-O) = 1.83, respectively. Bare UO_2^+ ($d_{U\text{-}O}$ = 1.760 Å): ρ_{BCP} = 0.314, $\nabla^2\rho_{BCP}$ = 0.234, H_{BCP} =-0.301, DI(O-O) =2.095; bare UO_2^{2+} ($d_{U\text{-}O}$ = 1.698 Å): ρ_{BCP} = 0.368, $\nabla^2\rho_{BCP}$ = 0.283, H_{BCP} =-0.399, DI(O-O) =2.323.

Full reference 13:

Frisch, M. J. et al.; Trucks, G. W.; Schlegel, H. B.; Scuseria, G. E.; Robb, M. A.; Cheeseman, J. R.; Scalmani, G.; Barone, V.; Mennucci, B.; Petersson, G. A.; Nakatsuji, H.; Caricato, M.; Li, X.; Hratchian, H. P.; Izmaylov, A. F.; Bloino, J.; Zheng, G.; Sonnenberg, J. L.; Hada, M.; Ehara, M.; Toyota, K.; Fukuda, R.; Hasegawa, J.; Ishida, M.; Nakajima, T.; Honda, Y.; Kitao, O.; Nakai, H.;

Vreven, T.; Montgomery Jr., J. A.; Peralta, J. E.; Ogliaro, F.; Bearpark, M. J.; Heyd, J.; Brothers, E. N.; Kudin, K. N.; Staroverov, V. N.; Kobayashi, R.; Normand, J.; Raghavachari, K.; Rendell, A. P.; Burant, J. C.; Iyengar, S. S.; Tomasi, J.; Cossi, M.; Rega, N.; Millam, N. J.; Klene, M.; Knox, J. E.; Cross, J. B.; Bakken, V.; Adamo, C.; Jaramillo, J.; Gomperts, R.; Stratmann, R. E.; Yazyev, O.; Austin, A. J.; Cammi, R.; Pomelli, C.; Ochterski, J. W.; Martin, R. L.; Morokuma, K.; Zakrzewski, V. G.; Voth, G. A.; Salvador, P.; Dannenberg, J. J.; Dapprich, S.; Daniels, A. D.; Farkas, Ö.; Foresman, J. B.; Ortiz, J. V.; Cioslowski, J.; Fox, D. J.: *Gaussian 09*. Gaussian, Inc.: Wallingford, CT, USA, 2009.

II.4 Exploring the nature of actinide polysulfide ions

The results presented in this sub-chapter are a continuation of previously reported gas-phase studies of uranium sulfides, with a focus on the formation of several actinide polysulfides. For this research I contributed with all the experimental work, partially in collaboration with Dr. Cláudia C. L. Pereira. The preliminary theoretical calculations were carried out by Dr. Colin Marsden (Université Paul Sabatier Toulouse III). The text below is the first draft of a future manuscript (**Lucena AF**, Pereira CCL, Gibson JK, Marçalo J).

Abstract

Several monopositive (AnS_n^+) and dipositive (AnS_n^{2+}) actinide sulfide species containing up to four sulfur atoms were produced by reaction of An^+ and An^{2+} cations with the sulfur-atom donor COS . Sequential abstraction of two sulfur atoms by Th^{2+} and Np^{2+} resulted in the disulfides ThS_2^{2+} and NpS_2^{2+}, respectively. While in the case of Th a persulfide ligand, S_2^{2-}, may lead to a stable Th(IV) species, for Np it is possible that a thioneptunyl, $S=Np^{2+}=S$, is produced. Preliminary density functional theory computations performed on thorium sulfide species indicated that the ground-state structure for ThS_2^{2+} has a triangular geometry with metrical parameters that may correspond to the presence of a persulfide. An^{2+} ions for An = Pu, Am and Cm showed reduced reactivities and did not yield any sulfide species.

II.4.1. Introduction

Bulk thorium sulfides have been prepared and their stoichiometries, crystal structures, phase systems, and physical properties have been studied in detail in the 1990s.[1-3] In nuclear fuel reprocessing, sulfur is commonly used specially in selective sulfurization and separation of rare earths from uranium oxides.[4] Actinide ions are generally considered hard acceptors while sulfur atoms are soft donors, which has led to important studies on the nature of interactions between these elements and it is a current area of research especially in the development of coordination ligands for actinide separation processes.[4-9] There are few studies published with elementary molecular actinide sulfides. The group of Andrews accomplished the production of the actinide monosulfides ThS and US and the polysulfides ThS_2, US_2 and US_3, by the reaction of sulfur vapour with laser-ablated metal atoms.[10,11] More recently, Pereira *et al* studied in the gas phase by experiment and theory a wide range of actinide monosulfides, AnS, from Ac to Cm. The reactivity of An^+ ions and also actinide oxide ions AnO^+ was evaluated by reactions with CS_2 and COS, as was the reactivity of the produced AnS^+ with oxidants (COS, CO_2, CH_2O and NO).[12] Bond dissociation and ionization energies were measured and compared with theoretical calculations. From this study the authors concluded that the 5f electrons do not substantially participate in actinide–sulfur bonding and that the actinides form extremely strong bonds with both oxygen and sulfur. The same authors reported in 2013 a continuation of the investigation on actinide sulfides in the gas phase, in this case of the formation of uranium polysulfides.[13] Gas-phase U^+ and U^{2+} ions were reacted with COS (which is a facile sulfur-atom donor) to produce several monopositive and dipositive uranium sulfide species containing up to four sulfur atoms. Through sequential abstraction of two sulfur atoms by U^{2+}, the analogue of the uranyl ion (UO_2^{2+}) was produced, that is, the dicationic disulfide US_2^{2+}. The most interesting result of this investigation was that , based on DFT calculations, the ground state structure of US_2^{2+} is not linear as could be expected but instead a triangular isomer, 171 kJ mol $^{-1}$ lower in energy than the linear thiouranyl structure.

In the present work, gas-phase studies of actinide sulfides were performed with a focus on the formation of polysulfides through reactions of An^+ and An^{2+} ions with COS, for An = Th, Pa, Np, Pu, Am, and Cm, to complement the previous studies with uranium.

II.4.2. Experimental section

Gas-phase reactions were studied by Fourier transform ion-cyclotron resonance mass spectrometry (FTICR-MS) in a Extrel/Finnigan FT/MS 2001 - DT spectrometer, equipped with a 3 Tesla superconducting magnet, a Spectra-Physics Quanta-Ray GCR-11 Nd:YAG laser operated at the fundamental wavelength (1064 nm), and a Finnigan Venus Odyssey data system. The $An^{+/2+}$ ions were produced by direct laser desorption/ionization (LDI) of small pieces of alloys that contained ~20% of Th or ~5% of the remaining actinide metals (Pa, Np,Pu, Am, Cm) in a Pt matrix , mounted on the solids probe of the instrument. All ion manipulations and analyses were carried out in the source cell of the dual cell instrument. The COS reagent is a commercial product with >99% purity as confirmed by electron ionization mass spectra. COS was introduced into the spectrometer through a leak valve to pressures of $\sim 1 \times 10^{-7}$ Torr, measured with a Bayard-Alpert type ionization gauge. The gauge readings were corrected for the relative sensitivity of the reagent, calculated according to the procedure of Bartmess and Georgiadis,[14] based on the experimental molecular polarizability.[15] The pressures in the cell were calibrated using standard reactions of methane and acetone ions.[16,17]

The reactant ions $An^{+/2+}$ or sequential product ions were isolated in the cell, and product ion intensities were monitored as a function of the reaction time. Ion selection, namely isolation of the actinide sulfide ions after an initial formation period, was achieved using single-frequency, frequency-sweep, or SWIFT excitation.[18] The background in the spectrometer mainly consisted of water and air, with base pressures of (1-2) x 10^{-8} Torr, that is, one order of magnitude lower than the reagent pressures used. Nevertheless, care was taken to minimize the interference of residual water and oxygen, by using long pumping periods after the solids probe was inserted into the high vacuum chamber but before introducing the neutral reagents. Moreover, all the reactions were compared with those occurring under background conditions.

The reactant ions were thermalized by collisions with argon, which was introduced into the spectrometer through a leak valve to constant pressures in the range of (1-5) x 10^{-6} Torr. Indications that effective thermalization had been achieved came from the reproducibility of the reaction kinetics and product distributions for different collisional cooling periods or collision gas pressures, and from the linearity of the pseudo-first-order kinetics plots. Each reaction was followed until the relative intensity of the reacting ion had reached less than 10% of its initial intensity, except in the particular cases where the reagents were regenerated in subsequent reactions of primary products. Rate constants, *k*, were determined from the pseudo-first-order decay of the relative signals of the reactant ions as a function of time at constant neutral

pressures. Along with the absolute rate constants, *k*, and for comparative purposes, reaction efficiencies are described as k/k_{COL}, where the k_{COL} is the collisional rate constant derived from the modified variational transition state/classical trajectory theory developed by Su and Chesnavich[19]. Collisional rate constants were calculated using the experimental molecular polarizability and dipole moment of the neutral reagent.[15] The main source of uncertainty in the absolute rate constants is the pressure measurement, and errors up to ±50% are usually assigned to them. Relative rate constants for different reactions are estimated to be accurate to ±20%, while typical precisions for replicate measurements of the same reaction are ±10%. The detection limit for most reactions was $k \leq 0.01 \times 10^{-9}$ cm^3 molecule^{-1} s^{-1}, due to interfering reactions with background O_2 and/or H_2O. In collision-induced dissociation (CID), selected ions are excited and undergo energetic collisions with neutral gas atoms, primarily argon, which has been added to the cell.

II.4.3. Results and discussion

Gas-phase reactions of monopositive and dipositive actinide cations, $An^{+/2+}$ (An = Th, Pa, Np, Pu, Am, Cm), with COS were examined or re-examined, with a focus on the formation of polysulfides. The reactions of An^+, AnO^+, and AnS^+ (An = Th, Pa, U, Np, Pu, Am, Cm) with COS were described previously and the formation of AnS_2^+ was observed for An = Th, Pa, U, and Np.[12] Previous experiments by Gibson have shown that AnS_2^+ species can also be obtained using thiols as reagents, at least for the cases of U, Np, Pu and Am.[20] Recently, a detailed study of the reactions of monopositive and dipositive uranium cations with COS was reported, with focus on the formation of US_2^{2+}, potentially the thio-uranyl ion; the formation of polysulfides US_n^+ and US_n^{2+} for n = 3 and 4 was also reported.[12,13] As in the case of uranium, carbonyl sulfide was chosen because it is a thermodynamically favorable sulfur-atom donor, with the following bond dissociation energies: D(OC−S) = 308 ± 1 kJ mol^{-1} and D(O−CS) = 672 ± 2 kJ mol^{-1} (see supporting information, Table S1).[12,21] For the case of the An^{2+} ions, an important selection criterion was also the rather high ionization energy of COS [IE(COS) = 11.18 eV or 1078 kJ mol^{-1}][21], which could disfavor electron-transfer pathways.

The observed reactions are summarized in Schemes II.4.1, II.4.2, II.4.3 and II.4.4. In Tables II.4.1 and II.4.2 are the product distributions obtained for the reactions of the mono- and dications, respectively, with indication of the respective thermodynamic constraints (in the Supporting

Information are the main reactions and energy relationships for the sequential reactions of $An^{+/2+}$ ions with COS from which the thermodynamic constraints were derived); the previously reported results are also indicated for comparison. In Table II.4.3, the rate constants and efficiencies for the studied reactions are summarized together with the previously reported results. Figure II.4.1 shows a representative mass spectrum obtained in the study of the reactions of Th^{2+} and subsequent products with COS.

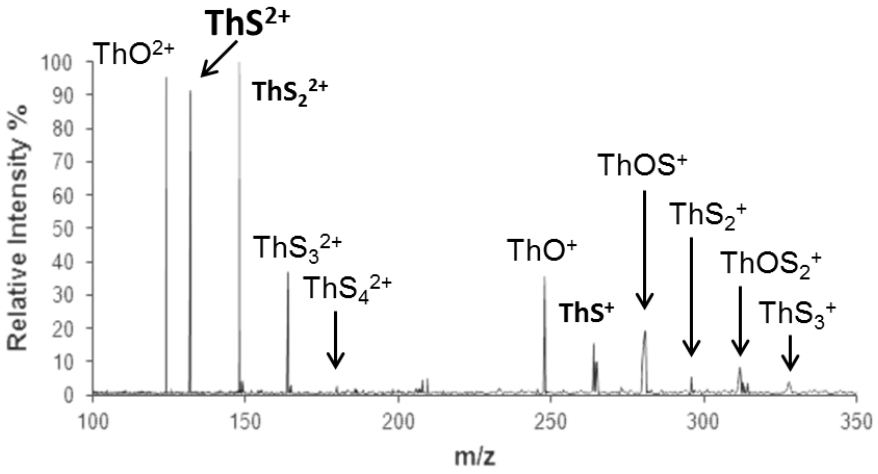

Figure II.4.1 Mass spectrum from the reaction ThS^{2+} + COS (t=0.3 s, P_{COS}=2.0x10^{-7} Torr; P_{Ar}~2x10^{-6} Torr).

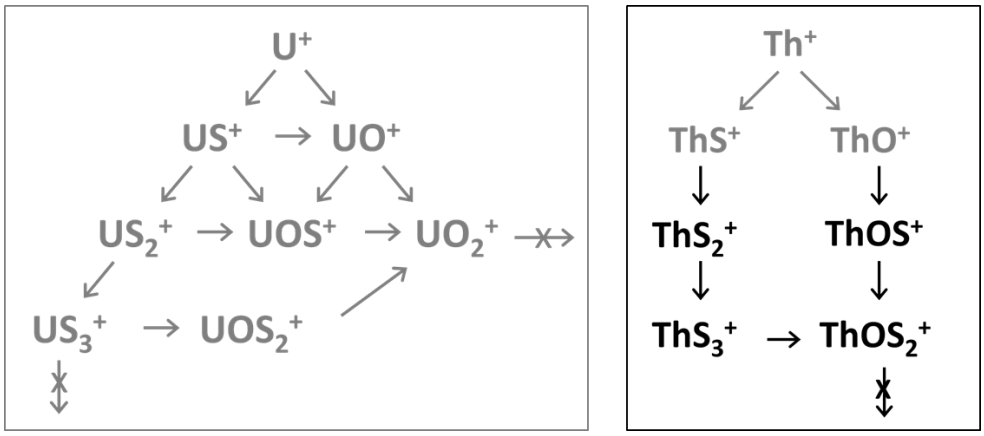

Scheme II.4.1 Reaction Pathways for the Primary and Sequential Reactions of U^+ (left),[12,13] and Th^+ (right) with COS (in grey the previously reported reactions from reference 12).

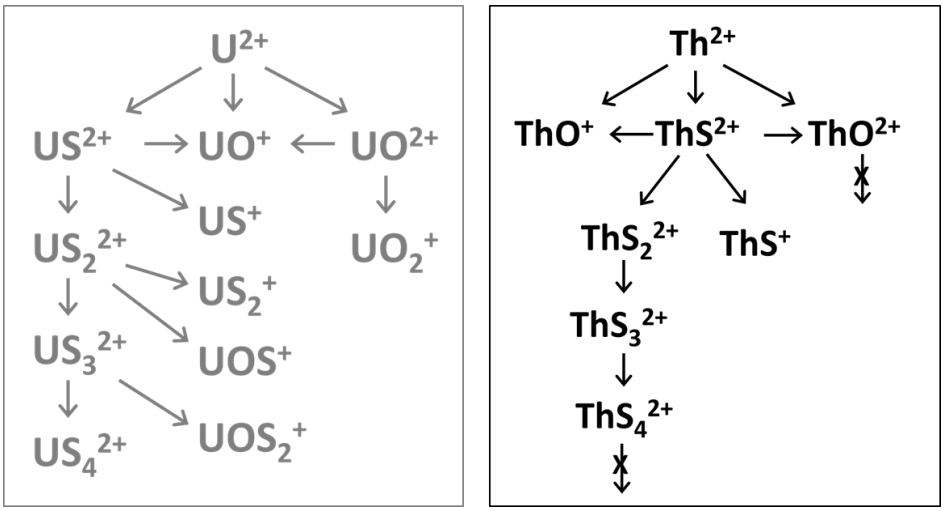

Scheme II.4.2 Reaction Pathways for the Primary and Sequential Reactions of U^{2+} (left),[12,13] and Th^{2+} (right) with COS (in grey the previously reported reactions from reference 12).

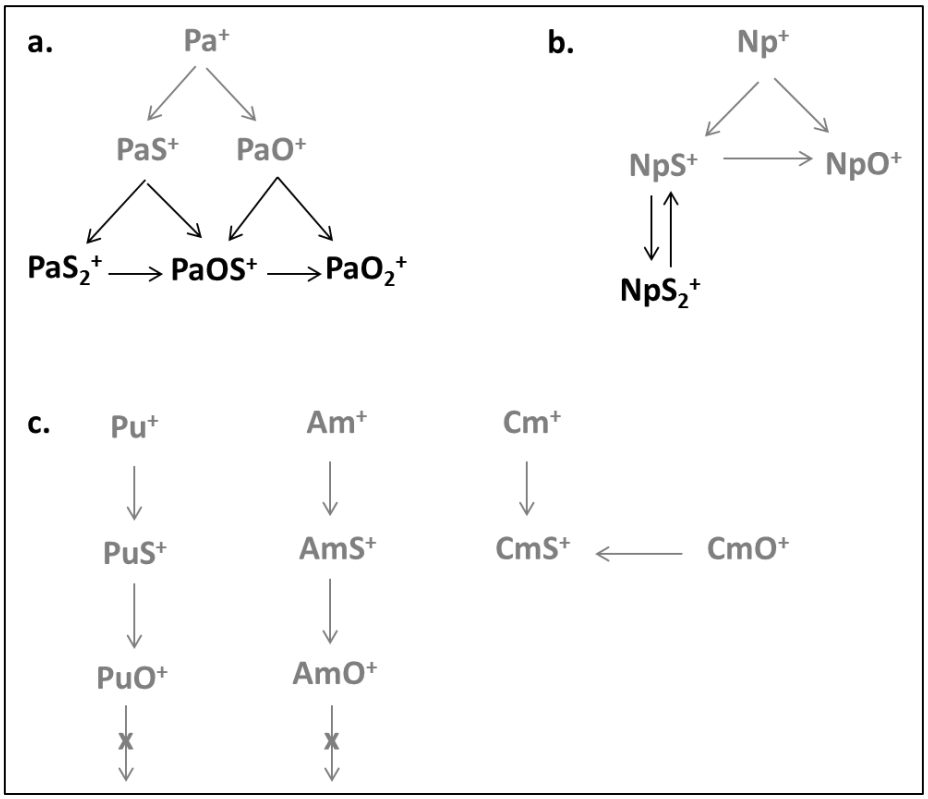

Scheme II.4.3 Reaction pathways for the primary and sequential reactions of An^{+} with COS, from reference 12 (in grey) and this work.

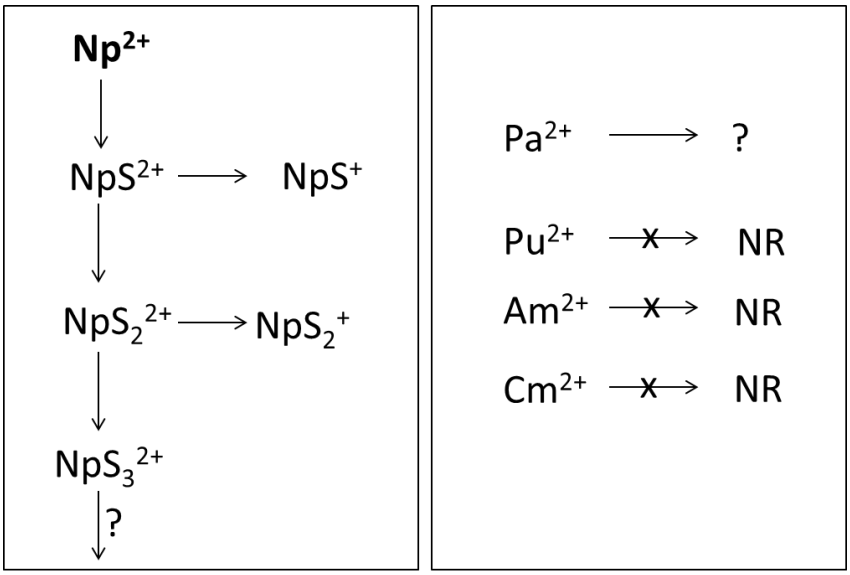

Scheme II.4.4 Reaction pathways for the primary and sequential reactions of An^{2+} (An = Pa, Np, Pu, Am, Cm) with COS. NpS_3^{2+} and Pa^{2+} could not be studied due to poor signal intensity.

Table II.4.1 Reaction products and thermodynamic constraints for the sequential reactions of the actinide monocations with COS. In grey are the previously reported results for comparison.[12,13]*

Reactant ion	Products	Thermodynamic constraints (kJ mol^{-1})**	Reactant ion	Products	Thermodynamic constraints (kJ mol^{-1})**
U^+	UO^+ (60%) US^+ (40%)	$D[U^+\text{-}O] \geq 672$ $D[U^+\text{-}S] \geq 308$ $D[U^+\text{-}S] = 500\pm60$	**Th^+**	ThO^+ (60%) ThS^+ (40%)	$D[Th^+\text{-}O] = 843\pm25$ $D[Th^+\text{-}S] = 570\pm75$
US^+	UO^+ (45%) UOS^+ (10%) US_2^+ (45%)	$D[U^+\text{-}S] \leq 560$ $D[U^+\text{-}S] = 500\pm60$ $D[SU^+\text{-}O] \geq 672$ $D[SU^+\text{-}S] \geq 308$	**ThS^+**	ThS_2^+ (100%)	$D[STh^+\text{-}S] \geq 308$
UO^+	UOS^+ (85%) UO_2^+ (15%)	$D[OU^+\text{-}S] \geq 308$ $D[OU^+\text{-}O] \geq 672$	**ThO^+**	$ThOS^+$ (100%)	$D[OTh^+\text{-}S] \geq 308$
US_2^+	UOS^+ (85%) US_3^+ (15%)	$D[SU^+\text{-}S] \leq D[SU^+\text{-}O] - 227$ $D[S_2U^+\text{-}S] \geq 308$	**ThS_2^+**	ThS_3^+ (100%)	$D[S_2Th^+\text{-}S] \geq 308$
US_3^+	UOS_2^+ (100%)	$D[S_2U^+\text{-}S] \leq D[S_2U^+\text{-}O] - 227$	**ThS_3^+**	$ThOS_2^+$ (100%)	$D[S_2Th^+\text{-}S] \leq D[S_2Th^+\text{-}O] - 231$
UOS^+	UO_2^+ (100%)	$D[OU^+\text{-}S] \leq 528$	**$ThOS^+$**	$ThOS_2^+$ (100%)	$D[OTh^+\text{-}S] \leq D[OTh^+\text{-}O]$ (462) + $D[SC\text{-}S]$ (441) – $D[SC\text{-}O]$ (672)
UOS_2^+	UO_2^+ (100%)	$D[OSU^+\text{-}S] + D[OU^+\text{-}S] \leq 528$ $D[OSU^+\text{-}S] + D[OU^+\text{-}S] \leq 511$			
Pa^+	PaS^+ (40%) PaO^+ (60%)	$D[Pa^+\text{-}S] = 525 \pm 86$ $D[Pa^+\text{-}O] = 800 \pm 50$	**Np^+**	NpS^+ (40%) NpO^+ (60%)	$D[Np^+\text{-}S] = 491 \pm 52$ $D[Np^+\text{-}O] = 760\pm10$
PaS^+	PaS_2^+ (55%) $PaOS^+$ (45%)	$D[SPa^+\text{-}S] \geq 308$ $D[SPa^+\text{-}O] \geq 672$	**NpO^+**	NR	
PaO^+	$PaOS^+$ (60%) PaO_2^+ (40%)	$D[OPa^+\text{-}S] \geq 308$ $D[OPa^+\text{-}O] \geq 672$	**NpS^+**	NpS_2^+ (40%) NpO^+ (60%)	$D[SNp^+\text{-}S] \geq 308$ $D[Np^+\text{-}S] \leq 529$
$PaOS^+$	PaO_2^+ (100%)	$D[OPa^+\text{-}S] \leq 553$	**NpS_2^+**	NpS^+ (100%)	$D[SNp^+\text{-}S] \leq 608$
PaS_2^+	$PaOS^+$ (100%)	$D[SPa^+\text{-}S] \leq D[SPa^+\text{-}O]$ -231			

* A dash (-) indicates that the reaction was not studied; NR indicates that any reaction is below the detection limit (see Experimental section and refences 12,13). ** See Supplementary Information, Tables S1 and S2.

Table II.4.2 Reaction products and thermodynamic constraints for the sequential reactions of the actinide dications with COS. In grey are the previously reported results for comparison.[13] *

Reactant ion	Products	Thermodynamic constraints (kJ mol^{-1})**	Reactant ion	Products	Thermodynamic constraints (kJ mol^{-1})**
U^{2+}	US^{2+} (60%) UO^{2+} (30%) UO^{+} (10%)	$D[U^{2+}\text{-}S] \geq 308$ $D[U^{2+}\text{-}O] \geq 672$ $D[U^{+}\text{-}O] \geq 604$	**Th^{2+}**	ThS^{2+} (25%) ThO^{2+} (60%) ThO^{+} (15%)	$D[Th^{2+}\text{-}S] \geq 308$ $D[Th^{2+}\text{-}O] \geq 672$ $D[Th^{+}\text{-}O] = 843$
US^{2+}	US_2^{2+} (60%) US^{+} (20%) UO^{+} (20%)	$D[SU^{2+}\text{-}S] \geq 308$ $IE[US^{+}] \geq 1078$ $D[U^{2+}\text{-}S] \leq 742$	**ThS^{2+}**	ThS_2^{2+} (85%) ThS^{+} (15%)	$D[STh^{2+}\text{-}S] \geq 308$ $IE[ThS^{+}] \geq 646$ $D[Th^{+}\text{-}S] = 570$
UO^{2+}	UO^{+} (80%) UO_2^{+} (20%)	$IE[UO^{+}] \geq 1078$ $D[OU^{+}\text{-}O] \geq 508$	**ThO^{2+}**	NR	-
US_2^{2+}	US_3^{2+} (45%) US_2^{+} (15%) UOS^{+} (40%)	$D[S_2U^{2+}\text{-}S] \geq 308$ $IE[US^{2+}] \geq 1078$ $D[SU^{+}\text{-}S] \leq D[SU^{+}\text{-}O] + IE[US^{2+}] - 1199$ $D[SU^{2+}\text{-}S] \leq D[SU^{+}\text{-}O] + IE[US^{+}] - 1199$	**ThS_2^{2+}**	ThS_3^{2+}	$D[S_2Th^{2+}\text{-}S] \geq 308$
US_3^{2+}	US_4^{2+} (75%) UOS_2^{+} (25%)	$D[S_3U^{2+}\text{-}S] \geq 308$ $D[S_2U^{+}\text{-}S] \leq D[S_2U^{+}\text{-}O] + IE[US_3^{+}] -1199$ $D[S_2U^{2+}\text{-}S] \leq D[S_2U^{+}\text{-}O] + IE[US^{2+}] - 1199$	**ThS_3^{2+}**	ThS_4^{2+}	$D[S_3Th^{2+}\text{-}S] \geq 308$
Np^{2+}	NpS^{2+} (100%)	$D[Np^{2+}\text{-}S] \geq 308$	**Pu^{2+}**	NR	-
NpS^{2+}	NpS_2^{2+} (45%) NpS+ (55%)	$D[SNp^{2+}\text{-}S] \geq 308$	**Am^{2+}**	NR	-
NpS_2^{2+}	NpS_3^{2+} (45%) NpS_2^{+} (55%)	$D[S_2Np^{2+}\text{-}S] \geq 308$	**Cm^{2+}**	NR	-
NpS_3^{2+}	***	-			

* A dash (-) indicates that the reaction was not studied; NR indicates that any reaction is below the detection limit (see Experimental section and references 12,13). ** See Supplementary Information, Tables S1 and S2. *** Could not be studied due to poor signal.

Table II.4.3 Summary of the rate constants and efficiencies for the reactions of actinide mono- and dications with COS. In grey are the previously reported results used for comparison.[12,13] *

	Th		***Pa***		***U***		***Np***		***Pu***		***Am***		***Cm***	
	k_{ABS}	k/k_{COL}	k_{ABS}	k/k_{COL}	k_{ABS}	k/k_{COL}	k_{ABS}	k/k_{COL}	k_{ABS}	k/k_{COL}	k_{ABS}	k/k_{COL}	k_{ABS}	k/k_{COL}
***An*$^{+}$**	0.84	0.87	0.80	0.83	0.90	0.92	0.81	0.83	0.24	0.25	0.021	0.022	0.40	0.42
***AnO*$^{+}$**	0.65	0.67	0.85	0.88	0.50	0.51	0.00	0.00	0.00	0.00	0.00	0.00	0.22	0.23
***AnS*$^{+}$**	0.59	0.62	0.33	0.35	0.22	0.23	0.13	0.13	0.18	0.19	0.13	0.14	0.00	0.00
***AnOS*$^{+}$**	0.31	0.32	0.26	0.27	0.15	0.16	-	-	-	-	-	-	-	-
***AnS*$_2^{+}$**	0.14	0.15	0.28	0.30	0.14	0.15	0.15	0.15	-	-	-	-	-	-
***AnOS*$_2^{+}$**	-	-	-	-	0.23	0.25	-	-	-	-	-	-	-	-
***AnS*$_3^{+}$**	0.30	0.32	-	-	0.083	0.087	-	-	-	-	-	-	-	-
***An*$^{2+}$**	1.75	0.90	-	-	1.45	0.75	0.85	0.44	0.00	0.00	0.00	0.00	0.00	0.00
***AnO*$^{2+}$**	0.00	0.00	-	-	0.074	0.039	-	-	-	-	-	-	-	-
***AnS*$^{2+}$**	1.29	0.67	-	-	1.50	0.79	1.78	0.92	-	-	-	-	-	-
***AnS*$_2^{2+}$**	0.81	0.42	-	-	0.69	0.36	0.34	0.35	-	-	-	-	-	-
***AnS*$_3^{2+}$**	0.48	0.25	-	-	0.67	0.36	-	-	-	-	-	-	-	-

* A dash (-) indicates that the reaction was not studied; a value of 0.00 indicates that the *k* is below the detection limit (see Experimental section and references 12,13).

II.4.3.1 Synthesis of singly-charged actinide polysulfides

In the previously reported study of the reactivity of An^+, AnO^+, and AnS^+ (An = Th, Pa, U, Np, Pu, Am, Cm) with COS,[12] the formation of AnS_2^+ was observed for An = Th, Pa, U, and Np, and not for An = Pu, Am, and Cm; oxo-sulfides $AnOS^+$ were also obtained in the cases of An = Th, Pa, and U (Schemes II.4.1 and II.4.3).

In the case of U,[13] as can be seen in Scheme II.4.1, the US_2^+ ion reacted with COS to form US_3^+ and UOS^+ ions, and these reacted further to produce UOS_2^+ and UO_2^+ ions, respectively; UOS_2^+ also formed UO_2^+ by reaction with another COS molecule.

The reactivity of the remaining AnS_2^+ ions (An = Th, Pa, and Np), as summarized in Schemes II.4.1 and II.4.3, presented different outcomes: ThS_3^+ was the only product observed in the case of Th, PaS_2^+ led only to $PaOS^+$, and NpS_2^+ intriguingly yielded NpS^+; interestingly, the reactivity of US_2^+ was intermediate between that of ThS_2^+ and PaS_2^+.

II.4.3.2 Synthesis of doubly-charged actinide polysulfides

The formation of doubly-charged uranium disulfide and other polysulfides was previously reported,[13] as summarized in Scheme II.4.2.

US_2^{2+}, US_3^{2+} and US_4^{2+} were obtained by sequential reactions with COS starting with U^{2+} ions that efficiently formed US^{2+}. As indicated in Schemes II.4.2 and II.4.4, Th^{2+} and Np^{2+} also produced AnS^{2+} ions that subsequently reacted with COS to form AnS_2^{2+} and further polysulfides, namely ThS_3^{2+}, ThS_4^{2+} and NpS_3^{2+}. Pu^{2+}, Am^{2+} and Cm^{2+} ions were unreactive with COS, therefore precluding the formation of polysulfides. The reaction of Pa^{2+} could not be studied due to the poor signal obtained from the existing Pa-Pt alloy samples.

In the reaction of An^{2+} species with COS, Th^{2+} yielded only 25% of the correspondent sulfide, ThS^{2+} (and 60% of ThO^{2+} and 15% of ThO^+) while U^{2+} yielded 60% of US^{2+} (and 30% of UO^{2+} and 10% of UO^+), and Np^{2+} originated 100% of NpS^{2+}. Apparently, the formation of the dicationic thorium oxide overcomes the sulfide formation in the reaction of Th^{2+} with COS while the contrary is observed for U^{2+}. The reaction efficiencies for these species follow the order: Th^{2+} (0.90) > U^{2+} (0.75) > Np^{2+} (0.44), with Th^{2+} being the most reactive with COS. This reactivity trend has been observed before in the reactions of An^{2+} cations with other neutrals, namely oxidants and hydrocarbons.[22]

II.4.3.3 Structural aspects of actinide polysulfides

In the previous study of uranium polysulfides,[13] DFT computations of the structures of several experimentally observed species were reported. These indicated that the GS of the US_2^{2+} ion has a triangular structure, with the linear isomer, "thiouranyl", computed to be 171 kJ mol^{-1} higher than the GS (Fig. II.4.2 (a) and (b)), and bent isomers also much higher in energy. In the case of US_2^{+}, the triangular and linear isomers were computed to be essentially degenerate in energy (Fig. II.4.2 (c)). The computed GS structures of US_3^{2+} and US_4^{2+} are presented in Fig. II.4.3.

Preliminary DFT (TZP/B3LYP) computations of several Th polysulfide and oxo-sulfide species, most of them observed experimentally, were performed and the GS structures are presented in Figs. II.4.4 and II.4.5, respectively.

For the produced ThS_2^{2+} ion, and comparing with uranium, the scenario is different as Th can achieve a maximum oxidation state of +4 while U can go up to +6. Therefore, while the formation of a thioactinyl could be expected for uranium (although apparently not formed), in the case of Th a persulfide ligand, S_2^{2-}, may lead to a stable Th(IV) species. In fact, and as can be seen in Fig. II.4.4, the ground-state structure for ThS_2^{2+} has a triangular geometry with metrical parameters that may correspond to the presence of a persulfide. Pereira *et al.*[13] computed [B3LYP/6-311+G(2d)] the S−S bond distance for the free S_2 molecule as 1.923 Å, that for the free $S_2^{\bullet-}$ radical anion as 2.043 Å, and that for the free S_2^{2-} anion as 2.208 Å. The computed bond distances for ThS_2^{2+} were S-S 2.181 Å and Th-S 2.470 Å, while for the case of US_2^{2+} the computed bond lengths were S-S 2.042 Å and U-S 2.613 Å,[13] which are indicative of the presence of a persulfide ligand in ThS_2^{2+}, formally corresponding to a Th(IV) species, and, intriguingly, of a supersulfide ligand in US_2^{2+}, formally corresponding to a U(III) species.

The GS structures for neutral ThS_2 and monocationic ThS_2^{+} were also computed, showing bent structures (Fig. II.4.4). For neutral, monocationic and dicationic ThOS (Figure II.4.5), the same pattern is observed, with a triangular isomer for the (non-observed) $ThOS^{2+}$ ion as the lower energy structure and bent structures for the other 2 isomers.

Thorium chemistry shows resemblance to the Group 4 d-transition elements Zr and Hf. Recently, Lourenço et al. reported a gas-phase study of the reactivity of Hf^{2+} ions towards several oxidants.[23] HfO_2^{2+} ions were produced in sequential reactions with N_2O and DFT computations indicated the formation of a triangular structure and the presence of a peroxide ligand.

The GS structures of other Th polysulfides and oxo-sulfides, namely for the experimentally observed ThS_3^{+}, $ThOS_2^{+}$, ThS_3^{2+} and ThS_4^{2+}, were also computed and are shown in Figs. II.4.4 and II.4.5. The structures of ThS_3^{2+} and ThS_4^{2+} present overall similarities with the structures

computed for the analogous uranium polysulfides, as can be seen in Fig. II.4.3.[13] It seems that the presence of the sulfur atoms and the facile formation of S-S bonds in polysulfides can be on the origin of the preferred GS structures.

It was not possible to compute the structure for the neptunyl disulfide dication NpS_2^{2+} (and other Np polysulfides) due to the complexity of the system at the DFT level. It is conceivable that a thioneptunyl, $S=Np^{2+}=S$, is produced, however, similarity to the uranyl disulfide, US_2^{2+}, with a metallacycle geometry as GS structure can also be expected.

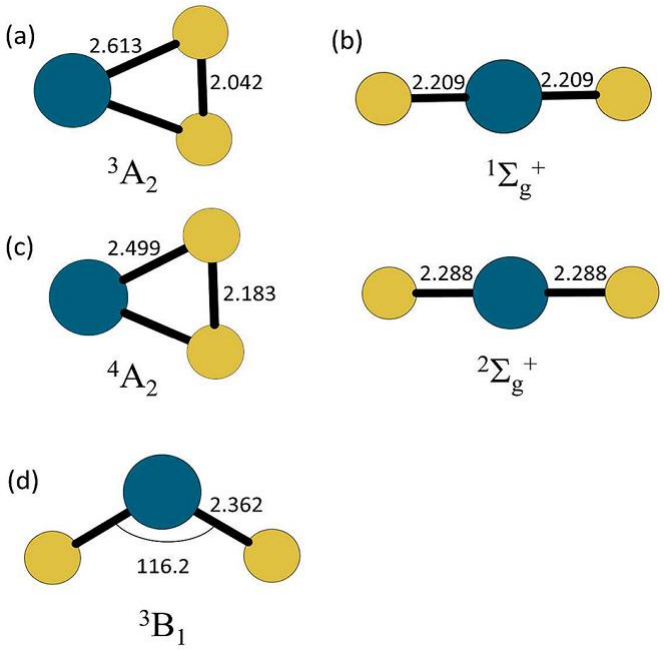

Figure II.4.2 Computed structures of (a) GS US_2^{2+}, (b) US_2^{2+} thiouranyl isomer (171 kJ mol^{-1} above the GS), (c) GS US_2^{+} (the two isomers shown are essentially degenerate in energy, to within 1 kJ mol^{-1}, at the B3LYP/SDD level of theory), and (d) GS US_2. Bond distances are in angstroms and angles are in degrees.[13]

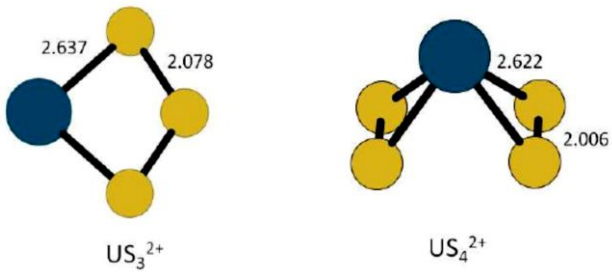

Figure II.4.3 Computed GS structures of US_3^{2+} and US_4^{2+}.[13]

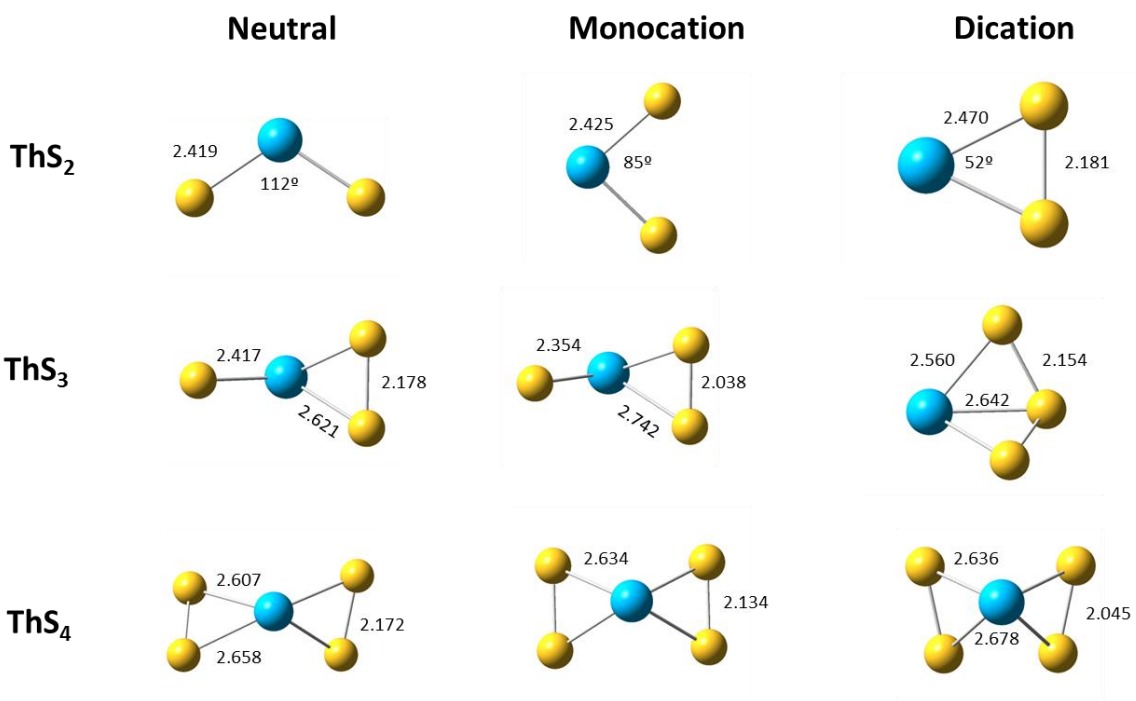

Figure II.4.4 Computed DFT (TZP/B3LYP) ground state structures of ThS_2, ThS_3 and ThS_4 neutral, monocation and dication. Bond distances are in angstroms and angles are in degrees. $ThS_3^{0/+/2+}$ species have C_s symmetries; ThS_4 has C_2 symmetry; ThS_4^{+} has C_{2v} symmetry; ThS_4^{2+} has C_s symmetry.

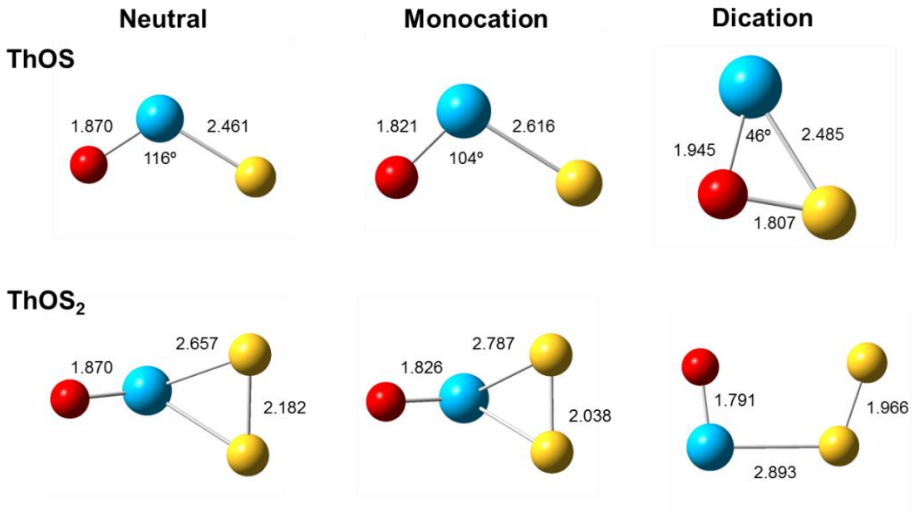

Figure II.4.5 Computed DFT (TZP/B3LYP) ground state structures of ThOS, $ThOS_2$ neutral, monocation and dication. Bond distances are in angstroms and angles are in degrees. $ThOS_2^{0/+}$ species have C_s symmetries; $ThOS_2^{2+}$ is planar, with O-Th-S = 96° and Th-S-S = 110°.

CID experiments were performed on several actinide sulfide ions produced in these studies and are summarized in Tables II.4.4 and II.4.5, which include previously reported results obtained with uranium sulfide ions,[13] for comparison. In favorable cases, CID experiments may give structural information on the examined ions.

Table II.4.4 CID products for singly charged thorium, protactinium and neptunium sulfide ions. In grey are the published uranium results[13] for comparison.

Precursor ion	CID products	Precursor ion	CID products	Precursor ion	CID products	Precursor ion	CID products
ThS^+	$Th^+ + S$			**US^+**	$U^+ + S$		
ThS_2^+	$ThS^+ + S$	**PaS_2^+**	$PaS^+ + S$	**US_2^+**	$US^+ + S$	**NpS_2^+**	$NpS^+ + S^+$
ThS_3^+	$ThS^+ + S_2$			**US_3^+**	$US^+ + S_2$		
$ThOS^+$	$ThO^+ + S$	**$PaOS^+$**	$PaO^+ + S$	**UOS^+**	$UO^+ + S$		
$ThOS_2^+$	$ThO^+ + S_2$			**UOS_2^+**	$UO^+ + S_2$		

Table II.4.5 CID products for doubly charged thorium and neptunium sulfide ions. In grey are the published uranium results[13] for comparison.

Precursor ion	CID products	Precursor ion	CID products	Precursor ion	CID products
ThS^{2+}	$Th^{2+} + S$	**US^{2+}**	$U^{2+} + S$	**NpS^{2+}**	$Np^{2+} + S$
ThS_2^{2+}	$ThS^{2+} + S$ $ThS^+ + S^+$	**US_2^{2+}**	$US^+ + S^+$	**NpS_2^{2+}**	$Np^+ + S^+$ $NpS^+ + S^+$ $Np^{2+} + S_2$
ThS_3^{2+}	$ThS^+ + S_2^+$	**US_3^{2+}**	$US^+ + S_2^+$		
ThS_4^{2+}	$ThS_2^+ + S_2^+$	**US_4^{2+}**	$US_2^+ + S_2^+$		

CID of the $AnOS^+$ (An = Th, Pa, U) and $AnOS_2^+$ (An = Th, U) species yielded actinide oxides AnO^+ with S or S_2 elimination, respectively. In the case of Th and referring to the computed structures of Fig. II.4.5, S elimination from $ThOS^+$ is in agreement with an oxo-sulfide structure and with the Th-S bond being weaker than the Th-O bond, and the elimination of S_2 from $ThOS_2^+$ also appears to be in agreement with the computed structure.

CID of the AnS_2^+ (An = Th, Pa, U, Np) and AnS_3^+ (An = Th, U) ions resulted in eliminations of S and S_2, respectively. As in the case of the oxo-sulfide ions, the fragmentations are in agreement with the computed structures for Th (Fig. II.4.4), disulfide for ThS_2^+ and sulfide-supersulfide for ThS_3^+. CID of the doubly-charged species showed mainly fragmentation channels involving charge separation. The available preliminary DFT studies of the Th sulfides did not provide the energetics for the possible dissociation channels and the discussion of the observed

fragmentations is necessarily incomplete. Only for ThS_4^{2+} does the elimination of S_2^+ appear to be in agreement with the computed structure; for ThS_3^{2+} and ThS_2^{2+} it is not clear why the observed fragmentations are preferred. In the case of uranium, the DFT studies included the computation of the energetics of dissociation, which allowed a more detailed discussion, but in a few cases the observed fragmentations could not be explained.[13]

II.4.4. Conclusions

Gas-phase synthesis of several actinide polysulfide ions was successfully accomplished by reacting $An^{+/2+}$ ions with COS. Th^+, like previously reported U^+, sequentially abstracted three sulfur atoms from COS to yield ThS_3^+. PaS_2^+ reacted sequentially to form $PaOS^+$ and very stable PaO_2^+, while NpS_2^+ intriguingly formed NpS^+; AnS^+ for An = Pu, Am and Cm failed to produce AnS_2^+ species.

An^{2+} ions for An = Th and Np sequentially abstracted up to four sulfur atoms from COS to produce AnS_n^{2+} ions, n = 2, 3, 4 for Th and n = 2, 3 for Np; the products obtained for Th parallel those previously reported for the case of U. The other An^{2+} studied, Pu, Am and Cm, did not yield monosulfides and, consequently, polysulfides.

Previously, DFT computations had shown that the GS structure of US_2^{2+} is a triangular isomer, with the linear structure 171 kJ mol^{-1} higher in energy, indicating that the uranyl disulfide dication is not a *thiouranyl*. In relation to the other disulfide dications obtained experimentally in this study, the geometry of NpS_2^{2+} could be analogous to that of US_2^{2+} although formation of the *thioneptunyl* cannot be excluded; however, computations for the Np species were not possible to achieve due to the complexity of the system. The synthesized ThS_2^{2+} ion cannot be considered analogous to the NpS_2^{2+} or US_2^{2+} since Th is tetravalent and, thus, a *thiothoranyl* is not achievable. In fact, preliminary DFT computations showed that the GS structure is of the metallacycle type, like in the case of uranium, with the computed metrical parameters indicating the formation of a Th(IV) *persulfide* species; interestingly, the previously reported metrical parameters for the triangular GS structure of US_2^{2+} indicate the formation of a U(III) *supersulfide* species.

Acknowledgments

This work was supported by Fundação para a Ciência e a Tecnologia (FCT) (PhD grant SFRH/BD/70475/2010 to A.F.L. and Ciência 2007 Programme) and also by the U.S. Department of Energy, Office of Basic Energy Sciences, Heavy Element Chemistry, at LBNL under Contract DE-AC02-05CH11231 (J.K.G.). The OCS was a generous gift from Dr. João M. A. Frazão at ISEL, Lisbon, Portugal. The authors gratefully acknowledge Dr. Colin Marsden for the preliminary DFT computations of the thorium sulfide species.

References

(1) Fitzmaurice, J. C.; Parkin, I. P., Self-propagating routes to uranium and thorium pnictides and chalcogenides, *New Journal of Chemistry* **1994**, 18, 825.

(2) Kohlmann, H.; Beck, H. P., Pseudo-symmetry in the crystal structure of An(2)X(5) compounds (An = Th, U, Np; X = S, Se), *Zeitschrift Fur Kristallographie* **1999**, 214, 341.

(3) Narducci, A. A.; Ibers, J. A., Ternary and quaternary uranium and thorium chalcogenides, *Chemistry of Materials* **1998**, 10, 2811.

(4) Sato, N.; Shinohara, G.; Kirishima, A.; Tochiyama, O., Sulfurization of rare-earth oxides with CS_2, *Journal of Alloys and Compounds* **2008**, 451, 669.

(5) Ingram, K. I. M.; Tassell, M. J.; Gaunt, A. J.; Kaltsoyannis, N., Covalency in the f element-chalcogen bond. Computational studies of $M[N(EPR_2)_2]_3$ (M = La, Ce, Pr, Pm, Eu, U, Np, Pu, Am, Cm; E = O, S, Se, Te; R = H, (i)Pr, Ph), *Inorganic Chemistry* **2008**, 47, 7824.

(6) Gaunt, A. J.; Reilly, S. D.; Enriquez, A. E.; Scott, B. L.; Ibers, J. A.; Sekar, P.; Ingram, K. I. M.; Kaltsoyannis, N.; Neu, M. P., Experimental and theoretical comparison of actinide and lanthanide bonding in $M[N(EPR_2)_2]_3$ complexes (M = U, Pu, La, Ce; E = S, Se, Te; R = Ph, iPr, H), *Inorganic Chemistry* **2008**, 47, 29.

(7) Dam, H. H.; Reinhoudt, D. N.; Verboom, W., Multicoordinate ligands for actinide/lanthanide separations, *Chemical Society Reviews* **2007**, 36, 367.

(8) Gaunt, A. J.; Scott, B. L.; Neu, M. P., U(IV) chalcogenolates synthesized via oxidation of uranium metal by dichalcogenides, *Inorganic Chemistry* **2006**, 45, 7401.

(9) Gutowski, K. E.; Bridges, N. J.; Rogers, R. D., The Chemistry of the Actinide and Transactinide Elements, vol.4, chapter 22, Springer, **2006**.

(10) Liang, B.; Andrews, L., Matrix infrared spectra and quasirelativistic DFT studies of ThS and ThS_2, *Journal of Physical Chemistry A* **2002**, 106, 4038.

(11) Liang, B. Y.; Andrews, L.; Ismail, N.; Marsden, C. J., The first infrared spectra and quasirelativistic DFT studies of the US, US_2, and US_3 molecules, *Inorganic Chemistry* **2002**, 41, 2811.

(12) Pereira, C. C. L.; Marsden, C. J.; Marçalo, J.; Gibson, J. K., Actinide sulfides in the gas phase: experimental and theoretical studies of the thermochemistry of AnS (An = Ac, Th, Pa, U, Np, Pu, Am and Cm), *Physical Chemistry Chemical Physics* **2011**, 13, 12940.

(13) Pereira, C. C. L.; Michelini, M. C.; Marçalo, J.; Gong, Y.; Gibson, J. K., Synthesis and properties of uranium sulfide cations. An evaluation of the stability of thiouranyl, $\{S=U=S\}^{2+}$, *Inorganic Chemistry* **2013**, 52, 14162.

(14) Bartmess, J. E.; Georgiadis, R. M., Empirical-methods for determination of ionization gauge relative sensitivities for different gases, *Vacuum* **1983**, 33, 149.

(15) R., L. D. CRC Handbook of Chemistry and Physics; 88th Edition ed.; CRC Press, Boca Raton, FL, **2007**.

(16) Bruce, J. E.; Eyler, J. R., Probing trapped ion energies via ion-molecule reaction-kinetics - Fourier transform ion-cyclotron resonance mass spectrometry, *Journal of the American Society for Mass Spectrometry* **1992**, 3, 727.

(17) Yi, L.; Ridge, D. P.; Munson, B., Association reactions of trimethylsilyl ions, *Organic Mass Spectrometry* **1991**, 26, 550.

(18) Guan, S. H.; Marshall, A. G., Stored waveform inverse Fourier transform (SWIFT) ion excitation in trapped-ion mass spectometry: Theory and applications, *International Journal of Mass Spectrometry and Ion Processes* **1996**, 157, 5.

(19) Su, T.; Chesnavich, W. J., Parametrization o the ion-polar molecule collision rate-constant by trajectory calculations, *Journal of Chemical Physics* **1982**, 76, 5183.

(20) Gibson, J. K., Gas-phase transuranium chemistry: Reactions of actinide ions with alcohols and thiols, *Journal of Mass Spectrometry* **1999**, 34, 1166.

(21) Lias, S. G.; Bartmess, J. E.; Liebman, J. F.; Holmes, J. L.; Levin, R. D.; Mallard, W. G., Gas-Phase ion and neutral thermochemistry, *Journal of Physical and Chemical Reference Data* **1988**, 17, 1.

(22) Heaven, M.C., ; Gibson, J.K; Marçalo, J. In The Chemistry of the Actinide and Transactinide Elements; Morss, L. R., Edelstein, N. M., Fuger, J., Eds.; Springer, vol.6, **2010**.

(23) Lourenço, C.; Michelini, M. C.; Marçalo, J.; Gibson, J. K.; Oliveira, M. C., Gas-phase reaction studies of dipositive hafnium and hafnium oxide ions: Generation of the peroxide HfO_2^{2+}, *Journal of Physical Chemistry A* **2012**, 116, 12399.

(24) Marçalo, J.; Gibson, J. K., Gas-phase energetics of actinide oxides: An assessment of neutral and cationic monoxides and dioxides from thorium to curium, *Journal of Physical Chemistry A* **2009**, 113, 12599.

Supporting Information

Main reactions and energy relationships for the sequential reactions of $An^{+/2+}$ ions with COS:

$An^+ + COS \rightarrow AnO^+ + CS$ **An = Th, Pa, U, Np** **(1a)**

$D[An^+\text{-}O] \geq D[SC\text{-}O]$

$An^+ + COS \rightarrow AnS^+ + CO$ **An = Th, Pa, U, Np, Pu, Am, Cm** **(1b)**

$D[An^+\text{-}S] \geq D[OC\text{-}S]$

$AnO^+ + COS \rightarrow AnOS^+ + CO$ **An = Th, Pa, U** **(2a)**

$D[OAn^+\text{-}S] \geq D[OC\text{-}S]$

$AnO^+ + COS \rightarrow AnO_2^+ + CS$ **An = Pa, U** **(2b)**

$D[OAn^+\text{-}O] \geq D[SC\text{-}O]$

$AnO^+ + COS \rightarrow AnS^+ + CO_2$ **An = Cm** **(2c)**

$D[An^+\text{-}S] \geq D[An^+\text{-}O] + D[OC\text{–}S] - D[OC\text{–}O]$

$AnS^+ + COS \rightarrow AnS_2^+ + CS$ **An = Th, Pa, U, Np** **(3a)**

$D[SAn^+\text{-}S] \geq D[OC\text{-}S]$

$AnS^+ + COS \rightarrow AnOS^+ + CS$ **An = Pa, U** **(3b)**

$D[SAn^+\text{-}O] \geq D[SC\text{-}O]$

$AnS^+ + COS \rightarrow AnO^+ + CS_2$ **An = U, Np, Pu, Am** **(3c)**

$D[An^+\text{-}S] \leq D[An^+\text{-}O] + D[SC\text{–}S] - D[SC\text{–}O]$

$AnOS^+ + COS \rightarrow AnOS_2^+ + CO$ **An = Th** **(4a)**

$D[OSAn^+\text{-}S] \geq D[OC\text{-}S]$

$AnOS^+ + COS \rightarrow AnO_2^+ + CS_2$ **An = Pa, U** **(4b)**

$D[OAn^+\text{-}S] \leq D[OAn^+\text{-}O] + D[SC\text{-}S] - D[SC\text{-}O]$

$AnS_2^+ + COS \rightarrow AnS_3^+ + CO$ **An = Th, U** **(5a)**

$D[S_2An^+\text{-}S] \geq D[OC\text{-}S]$

$AnS_2^+ + COS \rightarrow AnOS^+ + CS_2$ **An = Pa, U** **(5b)**

$D[SAn^+\text{-}S] \leq D[SAn^+\text{-}O] + D[SC\text{-}S] - D[SC\text{-}O]$

$AnS_2^+ + COS \rightarrow AnS^+ + CO, S_2$ **An = Np** **(5c)**

$D[SAn^+\text{-}S] \leq D[An^+\text{-}S] + D[S\text{-}S] - D[OC\text{-}S]$

$AnS_3^+ + COS \rightarrow AnOS_2^+ + CS_2$ **An = Th, U** **(6)**

$D[S_2An^+\text{-}S] \leq D[S_2An^+\text{-}O] + D[SC\text{-}S] - D[SC\text{-}O]$

$An^{2+} + COS \rightarrow AnS^{2+} + CO$ **An = Th, U, Np** **(7a)**

$D[An^{2+}\text{-}S] \geq D[OC\text{-}S]$

$An^{2+} + COS \rightarrow AnO^{2+} + CS$ **An = Th, U** **(7b)**

$D[An^{2+}\text{-}O] \geq D[SC\text{-}O]$

$An^{2+} + COS \rightarrow AnO^+ + CS^+$ **An = Th, U** **(7c)**

$D[An^+\text{-}O] \geq D[SC\text{-}O] + IE[CS] - IE[An^+]$

$AnO^{2+} + COS \rightarrow AnO^+ + COS^+$ **An = U** **(8a)**

$IE[AnO^+] \geq IE[COS]$

$AnO^{2+} + COS \rightarrow AnO_2^+ + CS^+$ **An = U** **(8b)**

$D[OAn^+\text{-}O] \geq D[SC\text{-}O] - IE[AnO^+] + IE[CS]$

$AnS^{2+} + COS \rightarrow AnS_2^{2+} + CO$ **An = Th, U, Np** **(9a)**

$D[SAn^{2+}\text{-}S] \geq D[OC\text{-}S]$

$AnS^{2+} + COS \rightarrow AnS^+ + COS^+$ **An = Th, U, Np** **(9b)**

$IE[AnS^+] \geq IE[COS]$

$AnS^{2+} + COS \rightarrow AnO^+ + CS_2^+$ **An = Th, U** **(9c)**

$D[An^{2+}\text{-}S] \leq D[An^{2+}\text{-}O] + D[SC\text{-}S] - D[SC\text{-}O] + IE[An^+] - IE[CS_2]$

$AnS^{2+} + COS \rightarrow AnO^{2+} + CS_2$ **An = Th** **(9d)**

$D[An^{2+}\text{-}S] \leq D[An^{2+}\text{-}O] + D[SC\text{–}S] - D[SC\text{–}O]$

$AnS_2^{2+} + COS \rightarrow AnS_3^{2+} + CO$ **An = Th, U, Np** **(10a)**

$D[S_2An^{2+}\text{-}S] \geq D[OC\text{-}S]$

$AnS_2^{2+} + COS \rightarrow AnS_2^+ + COS^+$ **An = U, Np** **(10b)**

$IE[AnS_2^+] \geq IE[COS]$

$AnS_2^{2+} + COS \rightarrow AnOS^+ + CS_2^+$ **An = U** **(10c)**

$D[SAn^{2+}\text{-}S] \leq D[SAn^+\text{-}O] + IE[AnS^+] + D[SC\text{-}S] - D[SC\text{-}O] - IE[CS_2]$

$AnS_3^{2+} + COS \rightarrow AnS_4^{2+} + CO$ **An = Th, U** **(11a)**

$D[S_3An^{2+}\text{-}S] \geq D[OC\text{-}S]$

$AnS_3^{2+} + COS \rightarrow AnSO_2^+ + CS_2^+$ **An = U** **(11b)**

$D[S_2An^{2+}\text{-}S] \leq D[S_2An^+\text{-}O] + IE[AnS_2^+] + D[SC\text{-}S] - D[SC\text{-}O] - IE[CS_2]$

Table S1. Reference supplemental bond and ionization energies (in *kJ mol^{-1}*).[12,21,24]

D[S-S]	425±1
D[OC-S]	308±1
D[SC-O]	672±2
D[SC-S]	441±2
IE[S]	999±0
IE[S_2]	613±0
IE[CS]	1093±1
IE[CS_2]	972±0
IE[COS]	1078±1

Table S2. Reference values for the dissociation and ionization energies of AnS, AnO and AnO_2 neutrals and ions (in *kJ mol^{-1}*).[12,24]

An	*D[An$^+$-S]*	*D[An-S]*	*IE[AnS]*	*D[An$^+$-O]*	*D[OAn$^+$-O]*	*D[An^{2+}-O]*
Th	570±75	608±77	646±19	843±25	462±36	829±80
Pa	525±86	545±91	589±29	800±50	780±36	781±30
U	500±60	510±63	608±19	774±13	741±14	706±45
Np	491±52	494±55	608±19	760±10	610±22	524±26
Pu	420±23	446±30	608±19	651±19	509±38	439±49
Am	334±27	375±33	618±19	560±28	410±56	367±13
Cm	455±16	504±25	627±19	670±38	202±60	342±12

Chapter III

Lanthanide and actinide cluster fragmentation and chemistry

III.1. Metal ion charge densities from fission of bimetallic clusters: the charge density of uranyl

III.2. Synthesis and hydrolysis of gas-phase lanthanide and actinide oxide nitrate complexes

III.1 Dissociation of gas-phase bimetallic clusters as a probe of charge densities: The effective charge of uranyl

The content here described is based on the publication:

***Lucena AF**, Carretas JM, Marçalo J, Michelini MC, Rutkowski P X, Gibson JK, Dissociation of Gas-Phase Bimetallic Clusters as a Probe of Charge Densities: The Effective Charge of Uranyl, **J. Phys. Chem. A**, **2014**, 118 (11), 2159–2166, DOI: 10.1021/jp500946y.*

I contributed with the experiments performed at C2TN-IST, namely, collision-induced dissociation of anion clusters of composition $MM'A_{(m+n+1)}^-$, where the metals (M) used were rare earths, lanthanides and uranium, and the anions (A) used were NO_3^- and Cl^-, with collaboration from Dr. José M. Carretas. Dr. Philip X Rutkowski performed additional experiments at LBNL for confirmation. The theoretical computations were carried out by Dr. Maria del Carmen Michelini.

Abstract

A method for evaluating relative charge densities of metal cations in gas-phase clusters is presented. Collision induced dissociation (CID) and/or density functional theory computations were performed on anion clusters of composition $MM'A_{(m+n+1)}^-$, where the two metal ions have formal charge states M^{m+} and M'^{n+}, and A is an anion, NO_3^-, Cl^- or F^- in this work. Results for alkaline earth and lanthanide metal ions reveal that cluster CID generally preferentially produces $MA_{(m+1)}^-$ and neutral $M'A_n$ if the charge density of M is greater than that of M': the metal ion with the higher charge density takes the extra anion. Computed dissociation energies corroborate that dissociation occurs via the lowest energy process. CID of clusters in which one of the two metal ions is uranyl, UO_2^{2+}, show that the effective charge density of uranyl is greater than that of alkaline earths and comparable to that of the late trivalent lanthanides; this is in accord with previous solution results for uranyl, from which an effective charge of 3.2+ was derived.

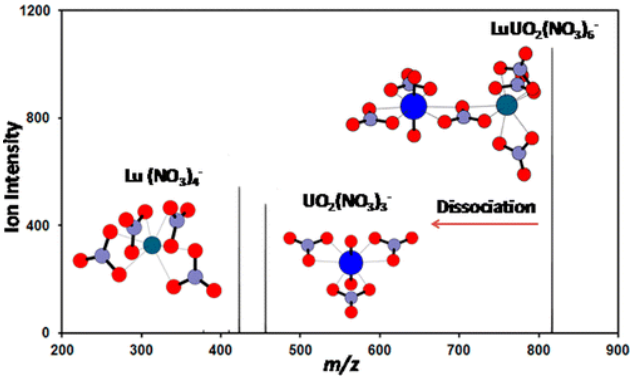

III.1.1. Introduction

The surface charge density of a metal ion, σ may be defined as by Eqn. 1, where q is the metal ion charge and r_i is its ionic radius.

$$\sigma = q/4\pi r_i^2 \qquad (1)$$

As has been noted elsewhere,[1] it is the surface charge density rather than the volume charge density, $\rho = Z/(4/3)\pi r_i^3$, that should be considered in evaluating interactions between ions in most chemical environments. A nearly idealized value for σ is in MHe^{n+} with minimal electrostatic or chemical interactions to perturb the charge and radius of M^{n+}.[2] However, realistic chemical environments induce substantial deviations from such idealized σ, largely due to lowering of q to an effective charge, q_{eff}, as a result of charge transfer from coordinating atoms or ions to the metal center: $\sigma_{eff} = q_{eff}/4\pi r_i^2$. This latter relationship further suffers from the necessity to assign r_i, for which empirical values are defined as "effective ionic radii" by creating relative scales that can be useful but are somewhat arbitrary. A widely used set of self-consistent "relative ionic radii" is based on Shannon's assignment of radius of 1.40 Å to O_2^{2-}, but Shannon also provided "crystal radii" using an anchor value for O_2^{2-} of 1.26 Å.[3] The utility of these two sets of radii depending on the environment of the ion illustrate that there is no fixed physical value corresponding to an ionic radius. The conundrum of defining metal ion radii, and charge densities, is analogous to assigning standard redox potentials based on the definition of the H^+/H_2 reduction potential as zero.[4]

The difficulty in assigning metal ion charges is exemplified by aqueous lanthanide (Ln) solutions, where the charge of the Ln^{3+} ion is reduced to some indeterminate charge below 3+ due to charge transfer from coordinating H_2O molecules.[1] In solid complexes and compounds, reductions in q below formal charge states result in lower Madelung contributions to lattice energy.[5] Physically meaningful charge densities can be defined in solids from X-ray diffraction experiments,[6] an example being that of uranium in solid $Cs_2(UO_2)Cl_4$.[7] Examples of the role of charge density in chemistry include transport properties of f-element ions dissolved in water,[8] RNA stability when complexed by divalent metal cations,[9] metal ion activation of *S*-Adenosylmethionine Decarboxylase,[10] and lanthanide chloride complex stability.[11] A recent example of the chemical effects of relative charge densities is the differences between U^{VI}-Se and Np^{VI}-Se bonding with a diselenophosphinate ligand due to the higher charge density of Np^{VI}, which is a manifestation of the smaller radius of neptunium.[12]

The uranyl ion, UO_2^{2+}, presents the challenge of establishing the effective charge and/or charge density of an oxo-ligated metal cation. There is general consensus that in bare uranyl the charge on uranium, $q[U/UO_2^{2+}]$, is close to 3+.[13-18] In solution, $q[U/UO_2^{2+}]$ should be reduced below 3+ due to charge donation from solvent molecules. An experimental value in aqueous solution of 3.2+ has been

reported,[14] but this is as an "effective cationic charge" with reference to the formal charges of other metal cations in solution and should not be considered as the actual charge, $q[U/UO_2^{2+}]$.

Given the role of charge density in the chemistry of metal ions, it is desirable to develop additional approaches to systematically probe this property, and its variation in different chemical environments. We report a method to evaluate the relative charge densities of two metal ions, M^{m+} and M'^{n+}, where *m+* and *n+* are the formal charge states of the two metal ions. Relative charge densities of the constituent metal ions are evaluated in gas-phase anion dimers of the general composition $MM'A_{(m+n+1)}^-$, where A is an anion, specifically NO_3^-, Cl^- or F^- in the present work. It is demonstrated that collision induced dissociation (CID) of $MM'A_{(m+n+1)}^-$ results in two dissociation channels, to $[MA_{m+1}^- + M'A_n]$ and $[MA_m + M'A_{n+1}^-]$, and that for most studied complexes the first channel dominates if $\sigma_{eff}[M] > \sigma_{eff}[M']$ whereas the second dominates if $\sigma_{eff}[M] < \sigma_{eff}[M']$. Dissociation energetics computed at the DFT level are in accord with the observations. Dissociation of complexes comprising uranyl as one of the constituent metal ions provides an evaluation of the effective charge density of U in UO_2^{2+}. Limitations and precautions associated with the approach are noted.

III.1.2. Experimental details

Solid $M(NO_3)_2$, $Ln(NO_3)_3$, MCl_3, and $LnCl_3$ salts (M = Mg, Ca, Sr, Ba; Ln = La, Pr, Eu, Tb, Ho, Tm, Lu) were obtained from commercial vendors and used without further purification. The uranyl nitrate and uranyl chloride salts were prepared at Centro de Ciências e Tecnologias Nucleares. Solutions containing two salts at a concentration of 1 mM each were prepared by dissolution in methanol; the solid salts were likely partially hydrated and no special effort was made to maintain anhydrous conditions during the experiments.

Experiments were performed using a Bruker HCT Quadrupole Ion Trap Mass Spectrometer (QIT/MS), which is a non-linear spherical high-capacity ion trap that incorporates sequential MS^n capabilities, enabling CID of mass-selected ions. The instrument has a storage and detection range of 50-3000 m/z, with a resolution of ~0.25 *m/z*. Mass spectra were obtained using the negative ion accumulation and detection mode. Solutions were injected into an electrospray needle via a syringe pump and were nebulized by nitrogen gas upon exiting the needle, resulting in the creation of smaller droplets. Anion microdroplets were further desolvated in the transfer capillary by dry heated nitrogen, which also supplied the nebulizing gas. The ultimately produced anions passed through an ion-focusing skimmer and into two focusing octopoles during transfer into the ion trap. Mass spectra were acquired using the following typical instrumental parameters: Solution flow rate, 2.5 µl/min; Nebulizer gas pressure, 8 psi; Dry gas flow rate, 4 L/min; Dry gas temperature, 250 °C; Capillary voltage, 4 kV; Capillary exit voltage, -129 V; Skimmer voltage, -40 V; Octopole 1 and 2 DC voltages, -12 V and -1.7 V; Octopole RF

amplitude, 187 Vpp; Lens 1 and 2 voltages, 5 V and 60 V; Trap drive, 67.3. Helium present at ~10^{-4} Torr as the buffer gas in the trap served to collisionally cool the trapped ions. The helium provides third-body collisions which remove energy and stabilize hot product ions after CID.

The $MM'A_{(m+n+1)}^-$ ion of interest is isolated by applying RF voltages that result in the ejection of all other ions from the ion trap. The isolated cluster anion is then subjected to CID using the MS^n capabilities of the instrument. CID is by resonance excitation for ca. 40 ms, with the result that the ion undergoes multiple energetic collisions with the He trapping gas. When sufficient energy is imparted to the cluster, fragmentation occurs. The CID fragmentation products are identified by mass selective ejection from the ion trap after the excitation period. In the case of the studied $MM'A_{(m+n+1)}^-$ clusters the only significant fragmentation processes yield $[MA_{(m+1)}^- + M'A_n]$ or $[MA_m + M'A_{(n+1)}^-]$. Increasing the CID excitation voltage, or CID duration, results in a greater degree of dissociation, but the relative fragmentation yields are essentially unchanged; the observed CID distributions evidently represent a canonical ensemble from near threshold up to significantly higher energies.

III.1.3. Computational details

DFT computations were performed using the Gaussian09 (revision B.01) package.[19] Full geometry optimizations and frequency calculations were performed using the B3LYP hybrid functional.[20, 21] The Stuttgart-Dresden triple–ζ valence basis sets together with the corresponding effective small-core potential (SDD)[22, 23] were used for La, Lu and U and the Pople triple–ζ basis sets, 6-311+G(d), for the rest of the atoms.[24-26] The "ultrafine" option was adopted for numerical integration. All the computed species are closed shell. Natural population analysis (NPA) was performed using NBO 3.1 as implemented in Gaussian09.[27]

III.1.4. Results and discussion

Shannon's ionic radii provide values of σ_{ideal} according to Eqn. 1 for metal ions given in Table III.1 1, where Z is defined as the formal metal ion charge state.[3] The assignment of this value as an ideal surface charge density reflects the considerations discussed above, whereby in real environments the actual charge on the metal ion can exhibit substantial deviations from the formal charge and the assignment of an ionic radius is essentially indeterminate. These values for ρ_{ideal} nonetheless provide a useful set of comparative charge densities. We here evaluate factors, specifically the corresponding effective charge and charge density, q_{eff} and σ_{eff}, which determine product distributions in fragmentation of gas-phase bimetallic clusters induced by CID.[28] Computed dissociation energetics are employed to validate the CID observations and enable extrapolation to systems that may not be experimentally accessible.

Representative ESI mass spectra are shown in Supporting Information (Figures S1- S8), prior to isolation of the cluster ion of interest. Abundant $MM'(NO_3)_{(m+n+1)}^-$ clusters are produced for two metals with the same formal charge, i.e., two alkaline earth metals or two lanthanide metals. In contrast, $CaLu(NO_3)_6^-$ is produced in relatively low abundance, with clusters containing up to four Ca atoms appearing in greater abundances. The yields of $Ca(UO_2)(NO_3)_5^-$, $La(UO_2)(NO_3)_6^-$ and $Lu(UO_2)(NO_3)_6^-$ were minor. Nonetheless, there were adequate abundances of all $MM'(NO_3)_{(m+n+1)}^-$ of interest to isolate for CID, albeit with increase in background noise for CID of low intensity clusters. ESI of the chloride solutions similarly produced adequate $MM'Cl_x^-$ clusters for isolation and CID. It was not possible to prepare fluoride clusters but DFT computations were performed on some to predict their dissociation behaviors.

ESI mass spectra cannot generally be employed to reliably evaluate solution speciation, due to electrochemical and other chemically disruptive processes that occur during ESI. However, the predominance of $UO_2(NO_3)_3^-$ over $Ca(NO_3)_3^-$ from the mixed UO_2^{2+}/Ca^{2+} solution (Fig. S6) suggests a greater affinity of UO_2^{2+} for the nitrate anion, which is consistent with the conclusion below that the effective charge density of UO_2^{2+} is substantially greater than that of Ca^{2+}.

Table III.1.1. Metal ionic radii and idealized surface charge densities.

M^{n+}	r_i [a]	σ_{ideal} [b]
Mg^{2+}	0.72	0.31
Ca^{2+}	1.00	0.16
Sr^{2+}	1.18	0.11
Ba^{2+}	1.35	0.09
La^{3+}	1.03	0.23
Ce^{3+}	1.01	0.23
Pr^{3+}	0.99	0.24
Nd^{3+}	0.98	0.25
Eu^{3+}	0.95	0.26
Tb^{3+}	0.92	0.28
Ho^{3+}	0.90	0.29
Tm^{3+}	0.88	0.31
Yb^{3+}	0.87	0.32
Lu^{3+}	0.86	0.32
U^{3+}	1.03	0.23

[a]Ionic radii (Å) from Shannon for coordination number 6.[3] The corresponding ionic radii for O^{2-}, Cl^- and F^- are 1.40 Å, 1.81 Å and 1.33 Å, respectively.

[b]Idealized surface charge density, $\sigma_{ideal} = Z/4\pi r_i^2$ in units of e/Å^2, where Z is the formal metal ion charge, +2 or +3.

III.1.4.1 Nitrate Clusters

Fragmentation occurs according to Equation 2a or 2b, where M and M' are different metal ions and A is an anion.

$$MM'A_{(m+n+1)}^- \rightarrow MA_{m+1}^- + M'A_n \qquad (2a)$$

$$MM'A_{(m+n+1)}^- \rightarrow MA_m + M'A_{n+1}^- \qquad (2b)$$

The number of anions A in the selected anion cluster is such that cluster has a net charge of -1. Representative CID spectra are shown in Figures III.1.1-III.1.3.

Specific examples are Equations 3 and 4, where the observed dissociation distributions are in brackets.

$$CaBa(NO_3)_5^- \rightarrow Ca(NO_3)_3^- + Ba(NO_3)_2 \qquad (3a) \quad [95\%]$$

$$CaBa(NO_3)_5^- \rightarrow Ba(NO_3)_3^- + Ca(NO_3)_2 \qquad (3b) \quad [5\%]$$

$$CaLa(NO_3)_6^- \rightarrow La(NO_3)_4^- + Ca(NO_3)_2 \qquad (4a) \quad [100\%]$$

$$CaLa(NO_3)_6^- \rightarrow Ca(NO_3)_3^- + La(NO_3)_3 \qquad (4b) \quad [<1\%]$$

These examples illustrate a general observation: the metal cation with the higher σ_{eff} takes the extra anion upon dissociation. As remarked above, the ideal charge densities in Table III.1 1 are not physically valid. However, for two metal ions in similar ionic chemical environments, such as in bimetallic nitrate clusters, it is anticipated that σ_{ideal} should correlate with the *relative* effective charge densities, σ_{eff}. Since $\sigma_{ideal}[Ca^{2+}]$ = 0.16 e/Å^2, $\sigma_{ideal}[Ba^{2+}]$ = 0.09 e/Å^2, and $\sigma_{ideal}[La^{3+}]$ = 0.23 e/Å^2 it is predicted that Equations 3a and 4a should dominate, as observed.

The CID cluster fragmentation results, for both nitrates and chlorides, are compiled in Table III.1 2.

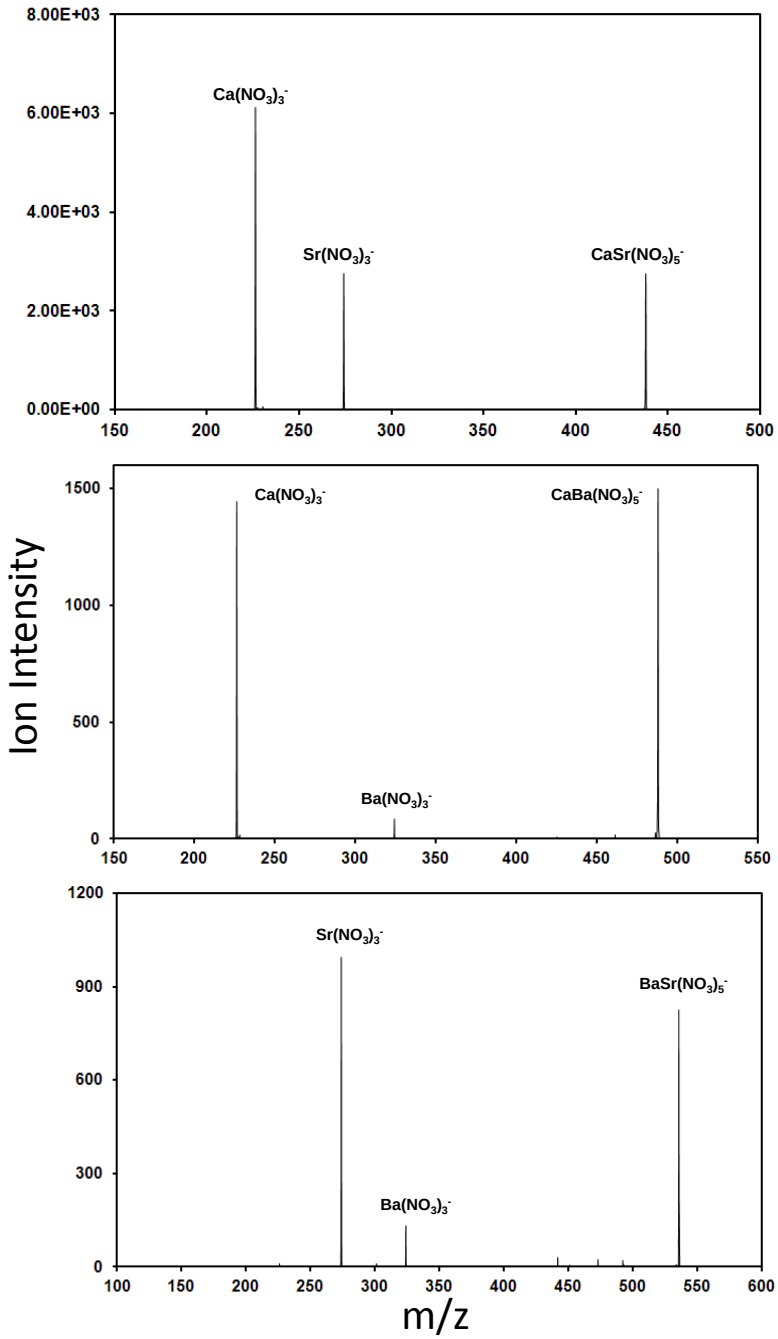

Figure III.1.1. CID mass spectra for isolated $CaSr(NO_3)_5^-$, $CaBa(NO_3)_5^-$ and $BaSr(NO_3)_5^-$. The ion intensity scale is not absolute but is consistent between spectra. For abundant ions such as $CaSr(NO)_3^-$ the CID spectra are exhibit only the two dissociation products; for lower abundance ions such as $BaSr(NO_3)_5^-$ additional minor unassigned peaks are apparent.

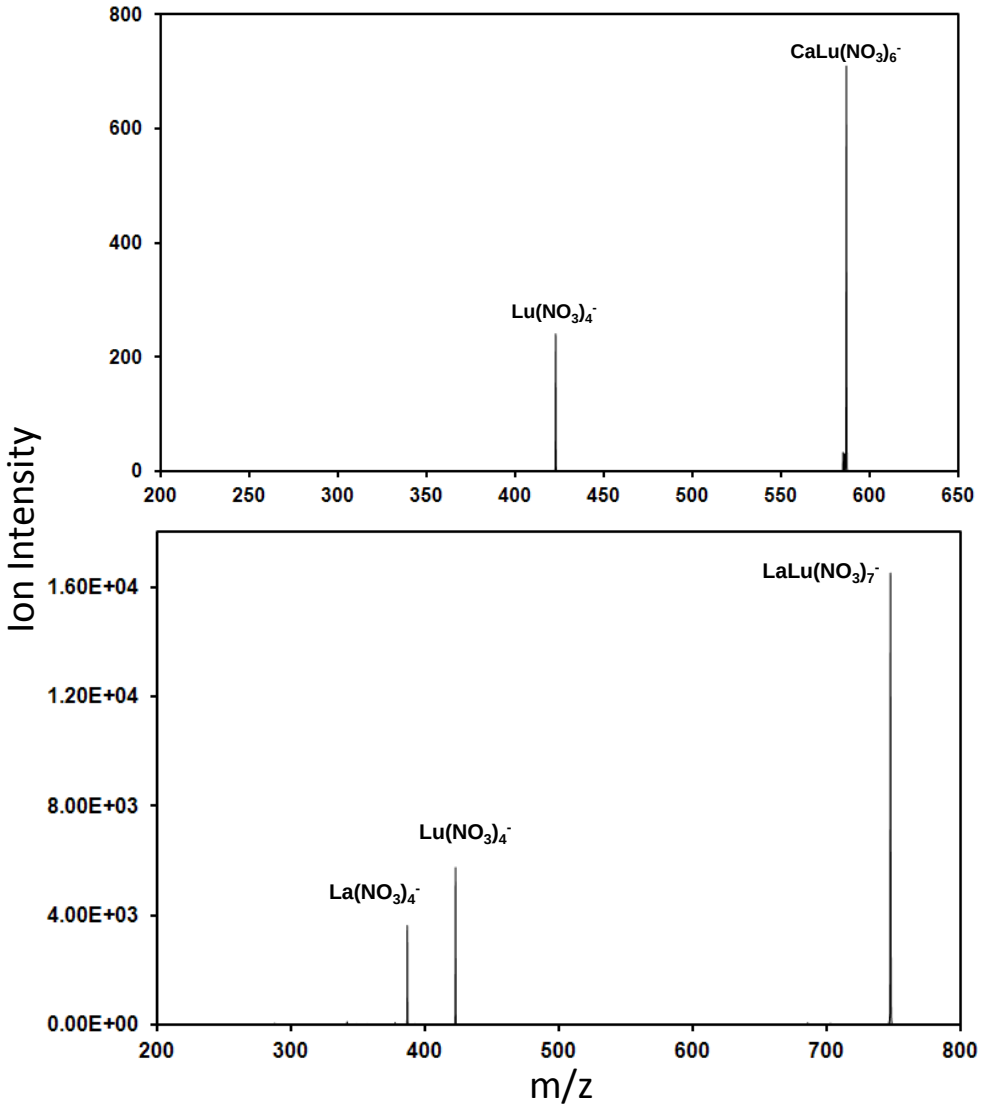

Figure III.1.2. CID mass spectra for isolated $CaLu(NO_3)_6^-$ and $LaLu(NO_3)_7^-$.

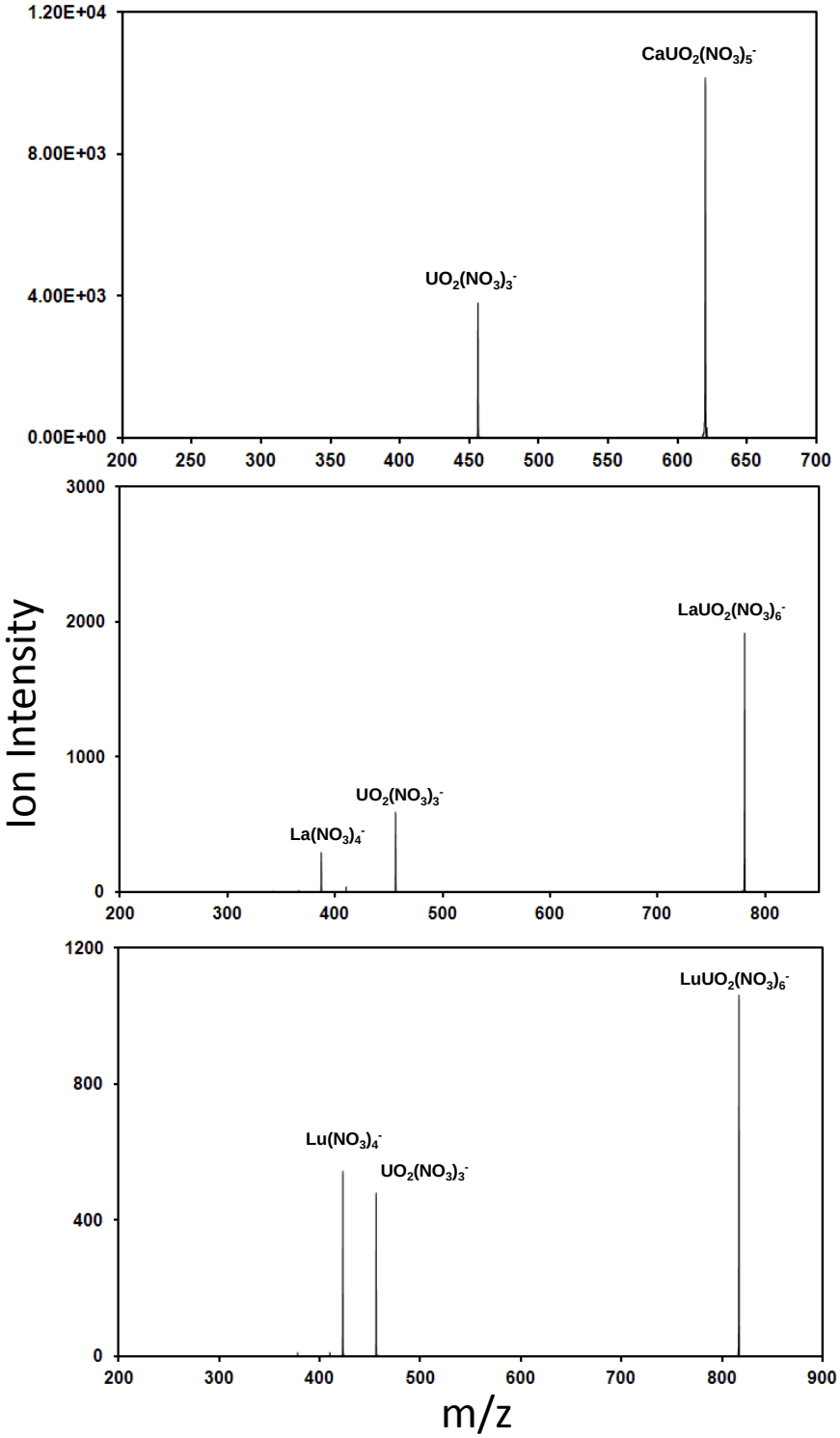

Figure III.1.3. CID mass spectra for isolated $Ca(UO_2)(NO_3)_5^-$, $La(UO_2)(NO_3)_6^-$ and $Lu(UO_2)(NO_3)_6^-$.

Table III.1.2. Product distributions for CID fragmentation of bimetallic anion clusters.

Cluster	CID Anion Product Distribution[a]
$MgCa(NO_3)_5^-$	**75% $Ca(NO_3)_3^-$** / 25% $Mg(NO_3)_3^-$
$CaSr(NO_3)_5^-$	**70% $Ca(NO_3)_3^-$** / 30% $Sr(NO_3)_3^-$
$CaBa(NO_3)_5^-$	**95% $Ca(NO_3)_3^-$** / 5% $Ba(NO_3)_3^-$
$SrBa(NO_3)_5^-$	**90% $Sr(NO_3)_3^-$** / 10% $Ba(NO_3)_3^-$
$LaLu(NO_3)_7^-$	**60% $Lu(NO)_4^-$** / 40% $La(NO_3)_4^-$
$CaLn(NO_3)_6^-$ [b]	**100% $Ln(NO_3)_4^-$**
$M(UO_2)(NO_3)_5^-$ [c]	**100% $(UO_2)(NO_3)_3^-$**
$La(UO_2)(NO_3)_6^-$	**70% $(UO_2)(NO_3)_3^-$** / 30% $La(NO_3)_4^-$
$Ce(UO_2)(NO_3)_6^-$	**80% $(UO_2)(NO_3)_3^-$** / 20% $Ce(NO_3)_4^-$
$Pr(UO_2)(NO_3)_6^-$	**60% $(UO_2)(NO_3)_3^-$** / 40% $Pr(NO_3)_4^-$
$Nd(UO_2)(NO_3)_6^-$	**55% $(UO_2)(NO_3)_3^-$** / 45% $Nd(NO_3)_4^-$
$Eu(UO_2)(NO_3)_6^-$	**60% $(UO_2)(NO_3)_3^-$** / 40% $Eu(NO_3)_4^-$
$Tb(UO_2)(NO_3)_6^-$	**55% $Tb(NO_3)_4^-$** / 45% $(UO_2)(NO_3)_3^-$
$Ho(UO_2)(NO_3)_6^-$	**60% $Ho(NO_3)_4^-$** / 40% $(UO_2)(NO_3)_3^-$
$Tm(UO_2)(NO_3)_6^-$	**55% $(UO_2)(NO_3)_3^-$** / 45% $Tm(NO_3)_4^-$
$Yb(UO_2)(NO_3)_6^-$	**60% $(UO_2)(NO_3)_3^-$** / 40% $Yb(NO_3)_4^-$
$Lu(UO_2)(NO_3)_6^-$	**60% $Lu(NO_3)_4^-$** / 40% $(UO_2)(NO_3)_3^-$
$LaLuCl_7^-$	**95% $LuCl_4^-$** / 5% $LaCl_3$
$CaLnCl_6^-$ [d]	**100% $LnCl_4^-$**
$Ca(UO_2)Cl_5^-$	**100% $(UO_2)Cl_3^-$**
$La(UO_2)Cl_5^-$	**85% $LaCl_4^-$** / 15% $(UO_2)Cl_3^-$
$Pr(UO_2)Cl_6^-$	**85% $PrCl_4^-$** / 15% $(UO_2)Cl_3^-$
$Eu(UO_2)Cl_6^-$	**95% $EuCl_4^-$** / 5% $(UO_2)Cl_3^-$
$Tb(UO_2)Cl_6^-$	**100% $TbCl_4^-$**
$Ho(UO_2)Cl_6^-$	**100% $HoCl_4^-$**
$Lu(UO_2)Cl_6^-$	**100% $LuCl_4^-$**

[a]Product distributions are based on at least three replicate CID experiments, with the yields accurate to within 5%. For reported yields of 100%, the alternative channel was unobserved to within <1%.
[b]Ln = La, Pr, Eu, Tb, Ho, Tm, Lu
[c]M = Ca, Sr, Ba
[d]Ln = La, Pr, Eu, Tb, Ho

From the results for $CaSr(NO_3)_5^-$, $CaBa(NO_3)_5^-$, $SrBa(NO_3)_5^-$ and $LaLu(NO_3)_7^-$ it is apparent that dissociation identifies the metal cation with the higher charge density for ions having the same formal charge, 2+ or 3+. The important exception of $MgCa(NO_3)_5^-$ is discussed below. The results for $CaLn(NO_3)_6^-$ (Ln = La, Pr, Eu, Tb, Ho, Tm, Lu) reveal complete discrimination, with all Ln^{3+} exclusively taking the additional anion. When the formal charges of the two metal ions are the same, 2+ or 3+, the metal ion with the higher ideal charge density preferentially takes the extra anion. For all studied clusters it was found that when the formal charges are different, 2+ or 3+, the higher charge M^{3+} takes the extra anion. This consistent discrimination between M^{2+} and M^{3+} offers a means to evaluate the effective charge of a coordinated metal, such as uranium in UO_2^{2+}.

It is apparent from the results in Table III.1.2 that fragmentation of $M(UO_2)(NO_3)_5^-$ (M = Ca, Sr, Ba) yields exclusively $(UO_2)(NO_3)_3^-$ and neutral $M(NO_3)_2$. In taking the extra anion, the UO_2^{2+} ion behaves like Ln^{3+}, indicating that dipositive uranyl exhibits similarity to tripositive lanthanide ions. Dissociation of $Ln(UO_2)(NO_3)_6^-$ results in both $Ln(NO_3)_4^-$ and $(UO_2)(NO_3)_3^-$, further demonstrating that q_{eff} for uranium is comparable to that of the Ln^{3+} ions. For $La(UO_2)(NO_3)_6^-$ and $Ce(UO_2)(NO_3)_6^-$, $(UO_2)(NO_3)_3^-$ predominates over $Ln(NO_3)_4^-$, indicating a somewhat higher σ_{eff} for U. Beyond Ce the distribution between $Ln(NO_3)_4^-$ and $(UO_2)(NO_3)_3^-$ is roughly comparable, indicating similar σ_{eff} for U and the later Ln^{3+}. As noted in Table III.1.1, the ionic radius of U^{3+} is nearly the same as that of La^{3+} so that their charge densities are similar; the CID results suggest that the effective charge density of uranyl is slightly greater than that of La^{3+} and thus also U^{3+}. These results are in accord with the estimate for UO_2^{2+} by Choppin and Rao that $Z_{eff}[U] \approx 3.2$.[14] An alternative experimental value of $Z_{eff}[U] \approx 2.5$ is lower, possibly due to charge donation from coordinating water molecules.[15] It should be noted that $Z_{eff}[U] \approx 3.2$ is in accord with relative hydrolysis strengths: $U^{4+} > UO_2^{2+} > U^{3+} > UO_2^{2+}$.[29]

Computed cluster fragmentation energetics are compiled in Table III.1.3. For $CaLa(NO_3)_6^-$, $CaLu(NO_3)_6^-$, $Ca(UO_2)(NO_3)_6^-$ and $La(UO_2)(NO_3)_6^-$ the observed lower energy dissociation is that observed. For the case of $Lu(UO_2)(NO_3)_6^-$ the two pathways are essentially degenerate to within the accuracy of the computations, with the prediction that the $(UO_2)(NO_3)_3^-$ pathway should be favored by only 2 $kJ.mol^{-1}$. The experimental observation was that the $Lu(NO_3)_4^-$ pathway is slightly favored, by 60% versus 40% $(UO_2)((NO_3)_3^-$. The conclusion is that effective charge densities of Lu^{3+} and UO_2^{2+} in $Lu(UO_2)(NO_3)_6^-$ are roughly comparable. The computed fragmentation energetics for $MgCa(NO_3)_5^-$ are in accord with the CID results—$Ca(NO_3)_3^-$ is lower energy and dominant—but in apparent discord with the general hypothesis that the ion with the higher charge density, presumably Mg^{2+} (Table III.1.1) takes the extra anion; this anomaly is discussed below.

Table III.1.3. Computed fragmentation energies.

Parent Anion	Fragmentation Products	Δ*E* (kJ mol^{-1})
$MgCa(NO_3)_5^-$	$Mg(NO_3)_2$ + **$Ca(NO_3)_3^-$**	175
	$Mg(NO_3)_3^-$ + $Ca(NO_3)_2$	183
$MgLa(NO_3)_6^-$	$Mg(NO_3)_2$ + **$La(NO_3)_4^-$**	157
	$Mg(NO_3)_3^-$ + $La(NO_3)_3$	174
$MgLu(NO_3)_6^-$	$Mg(NO_3)_2$ + **$Lu(NO_3)_4^-$**	147
	$Mg(NO_3)_3^-$ + $Lu(NO_3)_3$	175
$CaLa(NO_3)_6^-$	$Ca(NO_3)_2$ + **$La(NO_3)_4^-$**	173
	$Ca(NO_3)_3^-$ + $La(NO_3)_3$	182
$CaLu(NO_3)_6^-$	$Ca(NO_3)_2$ + **$Lu(NO_3)_4^-$**	163
	$Ca(NO_3)_3^-$ + $Lu(NO_3)_3$	183
$Ca(UO_2)(NO_3)_5^-$	$Ca(NO_3)_2$ + **$(UO_2)(NO_3)_3^-$**	145
	$Ca(NO_3)_3^-$ + $(UO_2)(NO_3)_2$	167
$La(UO_2)(NO_3)_6^-$	$La(NO_3)_3$ + **$(UO_2)(NO_3)_3^-$**	133
	$La(NO_3)_4^-$ + $(UO_2)(NO_3)_2$	145
$Lu(UO_2)(NO_3)_6^-$	$Lu(NO_3)_3$ + **$(UO_2)(NO_3)_3^-$**	137
	$Lu(NO_3)_4^-$ + $(UO_2)(NO_3)_2$	139
$La(UO_2)Cl_6^-$	**$LaCl_4^-$** + $(UO_2)Cl_2$	178
	$LaCl_3$ + $(UO_2)Cl_3^-$	190
$Lu(UO_2)Cl_6^-$	**$LuCl_4^-$** + $(UO_2)Cl_2$	161
	$LuCl_3$ + $(UO_2)Cl_3^-$	206
$MgCaF_5^-$	**MgF_3^-** + CaF_2	307
	MgF_2 + CaF_3^-	328
$LaMgF_6^-$	MgF_2 + **LaF_4^-**	251
	MgF_3^- + LaF_3	273
$LuMgF_6^-$	MgF_2 + **LuF_4^-**	228
	MgF_3^- + LuF_3	317
$La(UO_2)F_6^-$	LaF_3 + **$(UO_2)F_3^-$**	210
	LaF_4^- + $(UO_2)F_2$	235
$Lu(UO_2)F_6^-$	**LuF_4^-** + $(UO_2)F_2$	218
	LuF_3 + $(UO_2)F_3^-$	259

The computed structures of ground-state $CaLa(NO_3)_6^-$, $Ca(UO_2)(NO_3)_5^-$, $Lu(UO_2)(NO_3)_6^-$ and $MgCa(NO_3)_5^-$ are shown in Figure III.1.4. The optimized structures of all the ground state species together with some relevant higher energy isomers are reported as Supporting Information (Figures S9 to S13). Whereas $Ca(UO_2)(NO_3)_5^-$ and $Lu(UO_2)(NO_3)_6^-$ have a single bridging NO_3 with bidentate bonding to both metal centers, there are three bridging NO_3 moieties in $CaLa(NO_3)_6^-$ and $CaMg(NO_3)_5^-$ with varying denticity. A key feature of all of the structures is that the minimum number of nitrate anions are associated with both metal centers such that the two alternative fragmentation channels should not require substantial rearrangement and should be essentially barrierless, with the resulting prediction that fragmentation energetics should determine the product distributions.

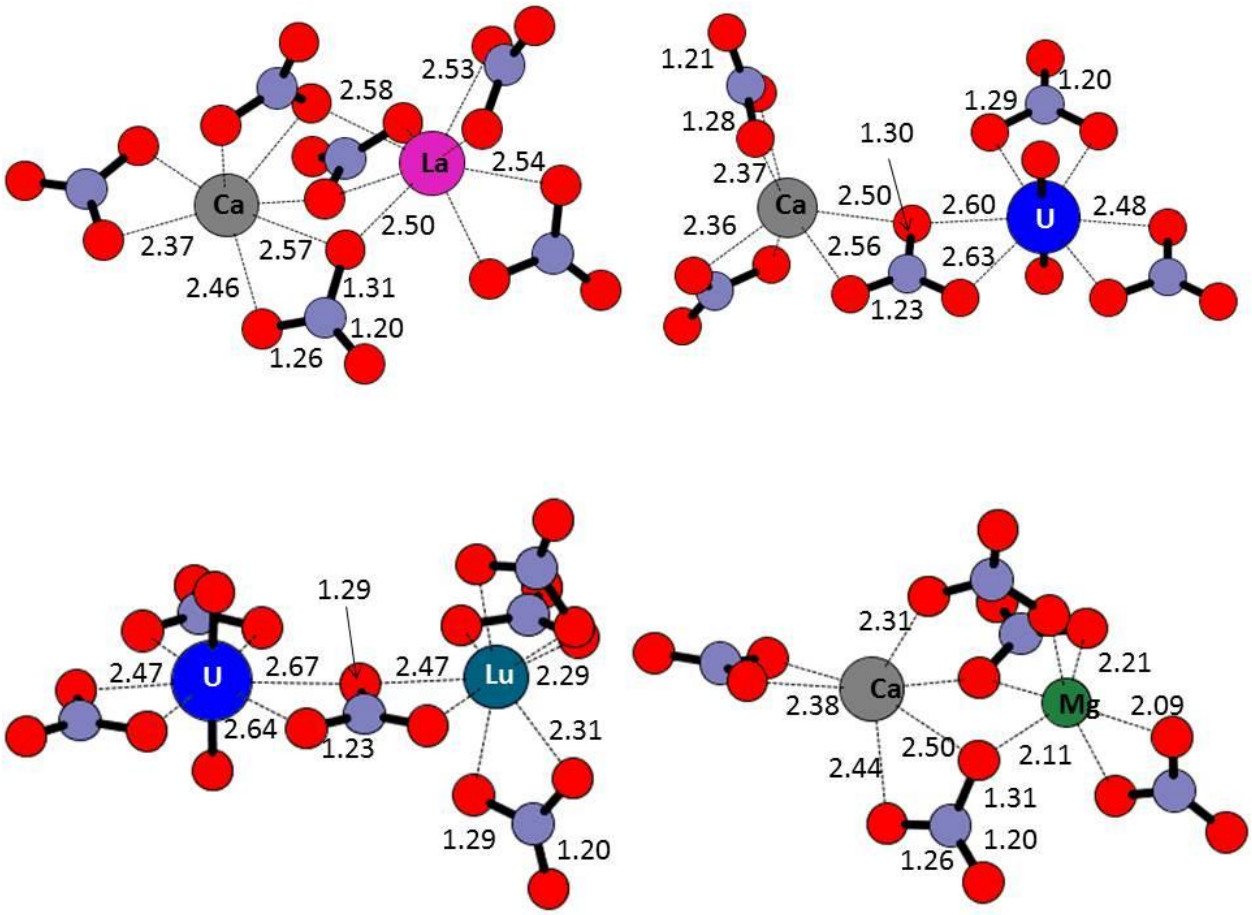

Figure III.1.4. Computed ground state structures of $CaLa(NO_3)_6^-$, $Ca(UO_2)(NO_3)_5^-$, $Lu(UO_2)(NO_3)_6^-$ and $MgCa(NO_3)_5^-$. The structure of $CaLu(NO_3)_6^-$ is similar to that of $CaLa(NO_3)_6^-$; the structure of $La(UO_2)(NO_3)_6^-$ is similar to that of $Lu(UO_2)(NO_3)_6^-$ (Figure S9, supporting information).

III.1.4.2 Chloride Clusters

The effect of the Pearson anion "hardness" on σ_{eff} and Z_{eff} was evaluated using complexes containing the "softer" chloride anion in $MM'Cl_{(m+n+1)}^-$ complexes.[30, 31] The CID results are included in Table III.1.2. The predominance of $LuCl_4^-$ from $LaLuCl_7^-$ is substantially greater than that of $Lu(NO_3)_4^-$ from $LaLu(NO_3)_7^-$, revealing a substantial influence due to the nature of the anion. Another significant difference from the nitrate clusters is the greater predominance of $LnCl_4^-$ from all of the $Ln(UO_2)Cl_6^-$ clusters. These results suggest that, compared with nitrate, the softer chloride ligand, with the potential for enhanced covalent bonding, binds more strongly to lanthanide ions than to uranyl.[32]

The CID results are in accord with the computations for $La(UO_2)Cl_6^-$ and $Lu(UO_2)Cl_6^-$ (Table III.1.3); for both the $LnCl_4^-$ is the favored anion fragmentation product. A particularly notable result is that whereas the energetics for the two dissociation pathways for $Lu(UO_2)(NO_3)_6^-$ were essentially

degenerate, in the case of $Lu(UO_2)Cl_6^-$ the $LuCl_4^-$ channel is substantially favored, by 45 kJ.mol. This result suggests stronger bonding in $LuCl_4^-$ versus $UO_2Cl_3^-$. The lowest energy structures of $La(UO_2)Cl_6^-$ and $Lu(UO_2)Cl_6^-$, shown in Fig. III.1.5, have two bridging chloride atoms such that fragmentation to either of the anion products does not require rearrangement and should be barrierless, with the product distributions determined by energetics rather than kinetics. An interesting feature of the ground state structures is the higher coordination number of the La metal center through the bonding interaction with one of the uranyl oxo-atoms, and effect not apparent in the ground state structure for the smaller complex with smaller Lu^{3+}. Higher-energy isomers of $La(UO_2)Cl_6^-$ and $Lu(UO_2)Cl_6^-$ are included as Supporting Information (Figure S14 and S15).

Despite the apparent effects of non-ionic bonding upon substituting chloride for nitrate, it should be emphasized that the key result is that $CaLnCl_6^-$ and $Ca(UO_2)Cl_5^-$ yield exclusively the anions $LnCl_4^-$ and $(UO_2)Cl_3^-$, respectively. The chloride results substantiate the core conclusion from dissociation of nitrate dimers that dipositive uranyl behaves in a similar manner to tripositive lanthanides.

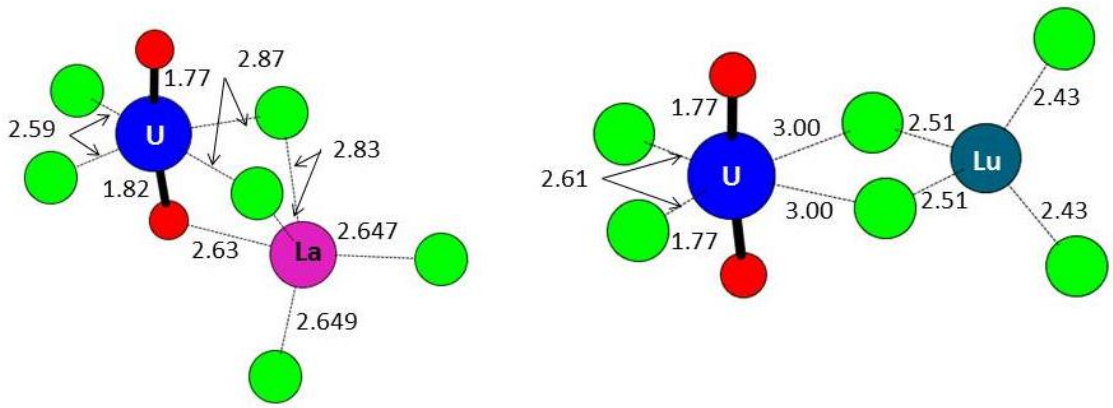

Figure III.1.5. Computed ground state structures of $La(UO_2)Cl_6^-$ and $Lu(UO_2)Cl_6^-$.

III.1.4.3 Fluoride Clusters

In view of potential effects of covalency on the energetics of dissociation of $MM'A_{(m+n+1)}^-$ clusters, it is desirable to employ the harder F^- anion to evaluate relative charge densities. From an experimental perspective the low solubilities of many metal fluorides largely precludes producing adequate abundances of $MM'F_{(m+n+1)}^-$ clusters for CID; from a computational perspective there is no such hindrance to studying fluoride clusters.

Computed energies for fragmentation of selected bimetallic fluoride clusters are included in Table III.1.3. In contrast to the anomalous case of $MgCa(NO_3)_5^-$ discussed below, the computed energies for

$MgCaF_5^-$ indicate that the favored anion product is MgF_3^-, in accord with the smaller ionic radius and higher charge density of Mg^{2+} (Table III.1.1).

The computed energetics for fragmentation of $La(UO_2)F_6^-$ and $Lu(UO_2)F_6^-$ are in essential accord with the nitrate and chloride results. The computed energetics predict that the favored anion fragmentation products should be $(UO_2)F_3^-$ from $La(UO_2)F_6^-$, and LuF_4^- from $Lu(UO_2)F_6^-$. This result is in agreement with the conclusion that the effective charge of uranyl is intermediate between those of La^{3+} and Lu^{3+}.

III.1.4.4 Magnesium Anomalies

The results for $MgCa(NO_3)_5^-$, $MgLa(NO_3)_6$, $MgLu(NO_3)_6$, $LaMgF_6^-$ and $LuMgF_6^-$ do not appear to be in accord with the general observation that the metal ion with the higher charge density takes the extra anion upon fragmentation. Referring to Table III.1.1, the charge density of Mg^{2+} should be substantially greater than that of Ca^{2+} and La^{3+}, and nearly the same as that of Lu^{3+}. However, the CID and DFT results for $MgCa(NO_3)_5^-$, and the DFT results for $MgLa(NO_3)_6$, $MgLu(NO_3)_6$, $LaMgF_6^-$ and $LuMgF_6^-$, indicate that the energetically preferred fragmentations are to $Ca(NO_3)_3^-$, $La(NO_3)_4^-$, $Lu(NO_3)_4^-$, LaF_4^- and LuF_4^-, respectively. The case of $LuMgF_6^-$ is representative: although the ideal charge densities of Mg^{2+} and Lu^{3+} are nearly the same, fragmentation to LuF_4^- is substantially favored over that to MgF_3^- by about 90 kJ mol^{-1}.

The origins of the evidently anomalous behavior of magnesium clusters are likely related to the particularly small ionic radius of Mg^{2+}, 0.72 Å. An effect of a smaller radius cation is to enhance the relative stability of products with fewer anion ligands; anion ligands exhibit greater repulsive interactions with one another when coordinated to smaller cations. The result of this steric effect would be to destabilize $Mg(NO_3)_3^-$ relative to $Mg(NO_3)_2$ as a result of increased nitrate-nitrate Coulombic repulsion.[34] The DFT result that the energetically lower energy dissociation of $MgCaF_5^-$ is to MgF_3^-, not CaF_3^-, suggests that the repulsive effect is diminished for the smaller fluoride anion. As is evident in the computed structures for $CaMgF_5^-$ and $MgLaF_6^-$ in Figure III.1.6, the fluoride anion is sufficiently small that the structures accommodate three bridging fluorides. Another possible contribution to the $MgCa(NO_3)_5^-$ anomalies is the difference in charge transfer from the ligands to the different metals. A comparison between the Mg and Ca partial NPA atomic charges in $MgCa(NO_3)_5^-$ shows an increased charge transfer in the case of Mg (Table S1), resulting in a partial Mg charge of +1.35 compared to the +1.55 charge of Ca. The same trend is observed in the fragmentation monomers (Table S2). In contrast to the nitrates, in $MgCaF_5^-$ and its fragmentation monomers, the partial atomic charges on Mg and Ca are similar (Tables S1 and S3). Although the origins of the deviant dissociation energetics of magnesium complexes are not fully understood, these results underscore

the necessity for caution in interpreting the results of such fragmentations solely in the context of charge density, particularly for systems in which anion-anion repulsive interactions become increasingly significant.

A result that does appear to generally pertain for the studied metal ions, including Mg^{2+}, is that the extra anion is carried by the metal ion with the higher formal charge. The key interpretation that the effective charge of uranyl is close to that of the later trivalent lanthanides is not put in doubt by the evidently anomalous results for magnesium clusters.

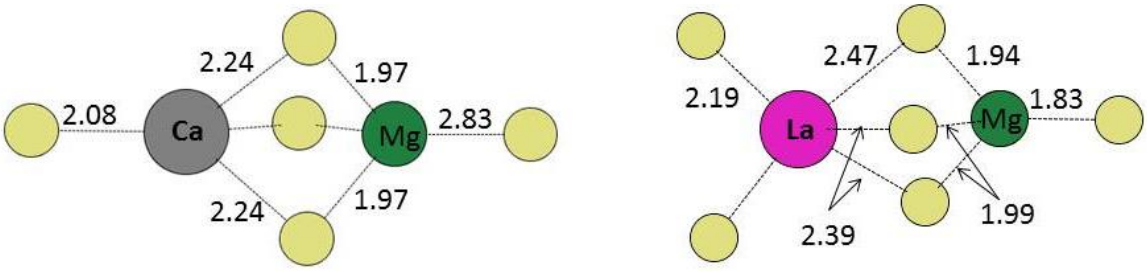

Figure III.1.6. Computed ground state structures of $CaMgF_5^-$ and $MgLaF_6^-$. The structure of $MgLuF_6^-$ is similar to that of $MgLaF_6^-$ (Figure S17, supporting information).

III.1.5. Conclusions

It has been demonstrated that for clusters of the general composition $MM'A_{(m+n+1)}^-$ fragmentation provides information about the relative charge densities of the constituent metal ions, M^{m+} and M'^{n+}. Both experimental CID and computational DFT results indicate that the dominant anionic product of cluster fragmentation is generally MA_y^- if the charge density of M is greater than that of M'. The relationship was evaluated for alkaline earth and lanthanide cations, and nitrate, chloride and fluoride anions. This charge density effect is attributed to the more favorable electrostatic interaction between the anions and the metal ion with higher charge density. The approach was employed to demonstrate that the effective charge density of uranyl, UO_2^{2+}, is comparable to that of tripositive lanthanide ions, Ln^{3+}. The assignment of the effective charge of U in uranyl as ca. 3+ is in accord with results from solution chemistry, as well as previous computations. Differences in fragmentation behaviors of nitrate and chloride clusters indicate a role of covalent bonding and suggest that the more ionic fluoride anion should be most useful for evaluating effective charges of cations using this approach. Clusters containing Mg^{2+} provided some results inconsistent with the general hypothesis that the cation with the higher charge density takes the extra anion upon fragmentation. In particular, dissociation of $MgCa(NO_3)_5^-$ preferentially yields $Ca(NO)_3^-$, a result attributed to destabilizing nitrate-nitrate repulsion when coordinated to the smaller Mg^{2+} cation.

Acknowledgements

This work was supported by Fundação para a Ciência e a Tecnologia/Portugal ("Ciência 2007" Programme; PhD grant SFRH/BD/70475/2010 to A.F.L.), by Università della Calabria, and by the U.S. Department of Energy, Office of Science, Office of Basic Energy Sciences, Division of Chemical Sciences, Geosciences and Biosciences at LBNL under Contract Number DE-AC02-05CH11231 (J.K.G.). This research used resources of the National Energy Research Scientific Computing Center (NERSC), which is supported by the Office of Science of the U.S. Department of Energy under Contract No. DE-AC02-05CH11231.

References

(1) Kuta, J.; Clark, A. E., Trends in aqueous hydration across the 4f period assessed by reliable computational methods, *Inorganic Chemistry* **2010**, 49, 7808.

(2) Wright, T. G.; Breckenridge, W. H., Radii of atomic ions determined from diatomic ion-He bond lengths, *Journal of Physical Chemistry A* **2010**, 114, 3182.

(3) Shannon, R. D., Revised effective ionic-radii and systematic studies of interatomic distances in halides and chalcogenides, *Acta Crystallographica A* **1976**, 32, 751.

(4) Halliwell, H. F.; Nyburg, S. C., Enthalpy of hydration of proton, *Transactions of the Faraday Society* **1963**, 59, 1126.

(5) Glasser, L., Solid-state energetics and electrostatics: Madelung constants and madelung energies, *Inorganic Chemistry* **2012**, 51, 2420.

(6) Coppens, P., Experimental charge-densities in chemistry - What is next, *Journal of Physical Chemistry-Us* **1989**, 93, 7979.

(7) Zhurov, V. V.; Zhurova, E. A.; Stash, A. I.; Pinkerton, A. A., Characterization of bonding in cesium uranyl chloride: Topological analysis of the experimental charge density, *Journal of Physical Chemistry A* **2011**, 115, 13016.

(8) Mauerhofer, E.; Zhernosekov, K.; Rosch, F., Limiting transport properties of lanthanide and actinide ions in pure water, *Radiochimica Acta* **2003**, 91, 473.

(9) Koculi, E.; Hyeon, C.; Thirumalai, D.; Woodson, S. A., Charge density of divalent metal cations determines RNA stability, *Journal of the American Chemical Society* **2007**, 129, 2676.

(10) Lu, Z. C. J.; Markham, G. D., Metal ion activation of S-adenosylmethionine decarboxylase reflects cation charge density, *Biochemistry-Us* **2007**, 46, 8172.

(11) Fernandez-Ramirez, E.; Jimenez-Reyes, M.; Solache-Rios, M. J., Effects of ionic strength and charge density on the stability of chloride complexes of trivalent lanthanides, *Journal of Chemical and Engineering Data* **2008**, 53, 1756.

(12) Jones, M. B.; Gaunt, A. J.; Gordon, J. C.; Kaltsoyannis, N.; Neu, M. P.; Scott, B. L., Uncovering f-element bonding differences and electronic structure in a series of 1:3 and 1:4 complexes with a diselenophosphinate ligand, *Chemical Science* **2013**, 4, 1189.

(13) Connick, R. E.; Hugus, Z. Z., The participation of f-orbitals in bonding in uranium and the transuranium elements, *Journal of the American Chemical Society* **1952**, 74, 6012.

(14) Choppin, G. R.; Rao, L. F., Complexation of pentavalent and hexavalent actinides by fluoride, *Radiochimica Acta* **1984**, 37, 143.

(15) Neuefeind, J.; Soderholm, L.; Skanthakumar, S., Experimental coordination environment of uranyl(VI) in aqueous solution, *The Journal of Physical Chemistry A* **2004**, 108, 2733.

(16) de Jong, W. A.; Visscher, L.; Nieuwpoort, W. C., On the bonding and the electric field gradient of the uranyl ion, *Journal of Molecular Structure - Theochem* **1999**, 458, 41.

(17) Michelini, M. C.; Russo, N.; Sicilia, E., Gas-phase chemistry of actinides ions: New insights into the reaction of UO^+ and UO_2^+ with water, *Journal of the American Chemical Society* **2007**, 129, 4229.

(18) Denning, R. G.; Green, J. C.; Hutchings, T. E.; Dallera, C.; Tagliaferri, A.; Giarda, K.; Brookes, N. B.; Braicovich, L., Covalency in the uranyl ion: A polarized x-ray spectroscopic study, *Journal of Chemical Physics* **2002**, 117, 8008.

(19) Frisch, M. J. Gaussian **2009** (revision B01). See Supporting Information for full citation.

(20) Becke, A. D., Density-functional thermochemistry .3. The role of exact exchange, *Journal of Chemical Physics* **1993**, 98, 5648.

(21) Lee, C. T.; Yang, W. T.; Parr, R. G., Development of the Colle-Salvetti correlation-energy formula into a functional of the electron-density, *Physical Reviews B* **1988**, 37, 785.

(22) Küchle, W.; Dolg, M.; Stoll, H.; Preuss, H., Energy-adjusted pseudopotentials for the actinides - Parameter sets and test calculations for thorium and thorium monoxide, *Journal of Chemical Physics* **1994**, 100, 7535.

(23) Cao, X. Y.; Dolg, M.; Stoll, H., Valence basis sets for relativistic energy-consistent small-core actinide pseudopotentials, *Journal of Chemical Physics* **2003**, 118, 487.

(24) Krishnan, R.; Binkley, J. S.; Seeger, R.; Pople, J. A., Self-consistent molecular-orbital methods .20. Basis set for correlated Wave-functions, *Journal of Chemical Physics* **1980**, 72, 650.

(25) Blaudeau, J. P.; McGrath, M. P.; Curtiss, L. A.; Radom, L., Extension of Gaussian-2 (G2) theory to molecules containing third-row atoms K and Ca, *Journal of Chemical Physics* **1997**, 107, 5016.

(26) Clark, T.; Chandrasekhar, J.; Spitznagel, G. W.; Schleyer, P. V., Efficient diffuse function-augmented basis-sets for anion calculations .3. The 3-21+G basis set for 1st-row elements, Li-F, *Journal of Computational Chemistry* **1983**, 4, 294.

(27) Glendening, E. D.; Reed, A. E.; Carpenter, J. E.; Weinhol, F. NBO Version 3.1.

(28) Ince, M. P.; Perera, B. A.; Van Stipdonk, M. J., Production, dissociation, and gas phase stability of sodium fluoride cluster ions studied using electrospray ionization ion trap mass spectrometry, *International Journal of Mass Spectrometry* **2001**, 207, 41.

(29) Choppin, G. R., Solution chemistry of the actinides, *Radiochimica Acta* **1983**, 32, 43.

(30) Pearson, R. G., Hard and soft acids and bases, *Journal of the American Chemical Society* **1963**, 85, 3533.

(31) Pearson, R. G., Hard and soft acids and bases - the evolution of a chemical concept, *Coordination Chemical Reviews* **1990**, 100, 403.

(32) Choppin, G. R., Covalency in f-element bonds, *Journal of Alloys and Compounds* **2002**, 344, 55.

(33) Adamo, C.; Maldivi, P., A theoretical study of bonding in lanthanide trihalides by density functional methods, *Journal of Physical Chemistry A* **1998**, 102, 6812.

(34) Prestianni, A.; Joubert, L.; Chagnes, A.; Cote, G.; Adamo, C., A density functional theory study of uranium(VI) nitrate monoamide complexes, *Physical Chemistry Chemical Physics* **2011**, 13, 19371.

Supporting Information

Table S1. Computed NPA metal charges: nitrate, fluoride and chloride dimers.[a]

Species	Mg	Ca	U	La	Lu
$MgCa(NO_3)_5^-$	1.35 (6)	1.55 (6)	-	-	-
$CaLa(NO_3)_6^-$	-	1.50 (7)	-	1.71 (8)	-
$CaLu(NO_3)_6^-$	-	1.52 (7)	-	-	1.61 (8)
$Ca(UO_2)(NO_3)_5^-$	-	1.55 (6)	1.42 (8)	-	-
$La(UO_2)(NO_3)_6^-$	-	-	1.43 (8)	1.77 (8)	-
$Lu(UO_2)(NO_3)_6^-$	-	-	1.44 (8)	-	1.68 (8)
$MgCaF_5^-$	1.62 (4)	1.69 (4)	-	-	-
$MgLaF_6^-$	1.64 (4)	-	-	2.11 (5)	-
$MgLuF_6^-$	1.65 (4)	-	-	2.12 (5)	-
$La(UO_2)F_6^-$	-	-	1.67 (6)	2.15 (5)	-
$Lu(UO_2)F_6^-$	-	-	1.73 (6)	-	2.16 (4)
$La(UO_2)Cl_6^-$	-	-	0.95 (6)	1.35 (5)	-
$Lu(UO_2)Cl_6^-$	-	-	1.15 (6)	-	1.16 (4)
$MgLa(NO_3)_6^-$	1.36 (6)	-	-	1.71 (8)	-
$MgLu(NO_3)_6^-$	1.37 (6)	-	-	-	1.62 (8)

[a]Metal coordination number in parentheses.

Table S2. Computed NPA metal charges of nitrate products.[a]

Species	Mg	Ca	U	La	Lu
$Mg(NO_3)_2^-$	1.54 (4)	-	-	-	-
$Mg(NO_3)_3^-$	1.35 (6)	-	-	-	-
$Ca(NO_3)_2^-$	-	1.68 (4)	-	-	-
$Ca(NO_3)_3^-$	-	1.53 (6)	-	-	-
$UO_2(NO_3)_2^-$	-	-	1.76 (6)	-	-
$UO_2(NO_3)_3^-$	-	-	1.38 (8)	-	-
$La(NO_3)_3^-$	-	-	-	2.04 (6)	-
$La(NO_3)_4^-$	-	-	-	1.73 (8)	-
$Lu(NO_3)_3^-$	-	-	-	-	1.97 (6)
$Lu(NO_3)_4^-$	-	-	-	-	1.65 (8)
UO_2^{2+}	-	-	2.81 (2)	-	-

[a] Metal coordination number in parentheses.

Table S3. Computed NPA metal charges of fluoride products.[a]

Species	Mg	Ca	U	La	Lu
MgF_2	1.75 (2)	-	-	-	-
MgF_3^-	1.67 (3)	-	-	-	-
CaF_2	-	1.74 (2)	-	-	-
CaF_3^-	-	1.69 (3)	-	-	-
UO_2F_2	-	-	1.97 (4)	-	-
$UO_2F_3^-$	-	-	1.76 (5)	-	-
LaF_3	-	-	-	2.23 (3)	-
LaF_4^-	-	-	-	2.13 (4)	-
LuF_3	-	-	-	-	2.26 (3)
LuF_4^-		-	-	-	2.10 (4)

[a] Metal coordination number in parentheses.

Table S4. Computed NPA metal charges of chloride products [a]

Species	U	La	Lu
UO_2Cl_2	1.49 (4)	-	-
$UO_2Cl_3^-$	1.24 (5)	-	-
$LaCl_3$	-	1.64 (3)	-
$LaCl_4^-$	-	1.34 (4)	-
$LuCl_3$	-	-	1.52 (3)
$LuCl_4^-$	-	-	1.13 (4)

[a] Metal coordination number in parentheses.

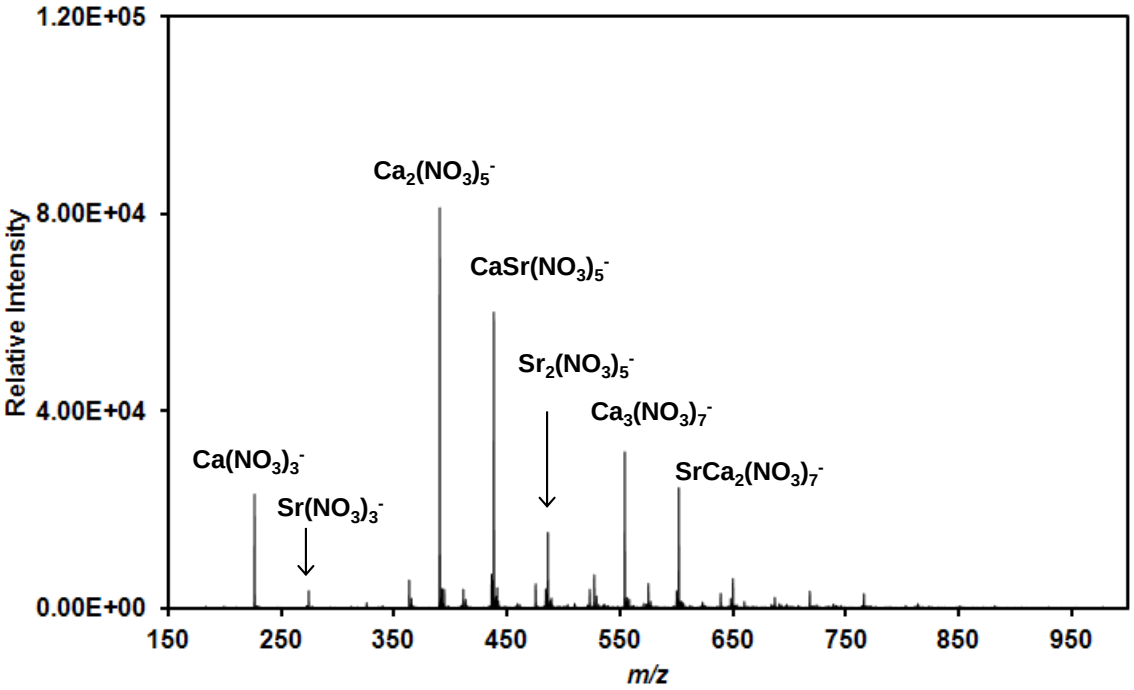

Figure S1. ESI mass spectrum for a mixed Ca^{2+}/Sr^{2+} nitrate solution.

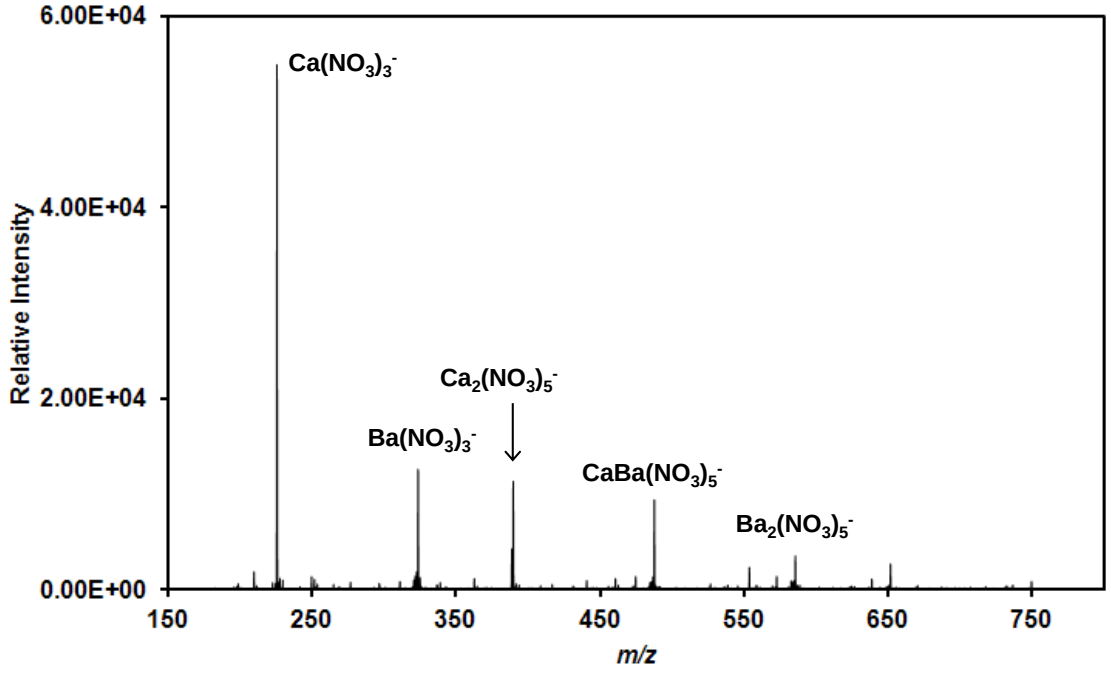

Figure S2. ESI mass spectrum for a mixed Ca^{2+}/Ba^{2+} nitrate solution.

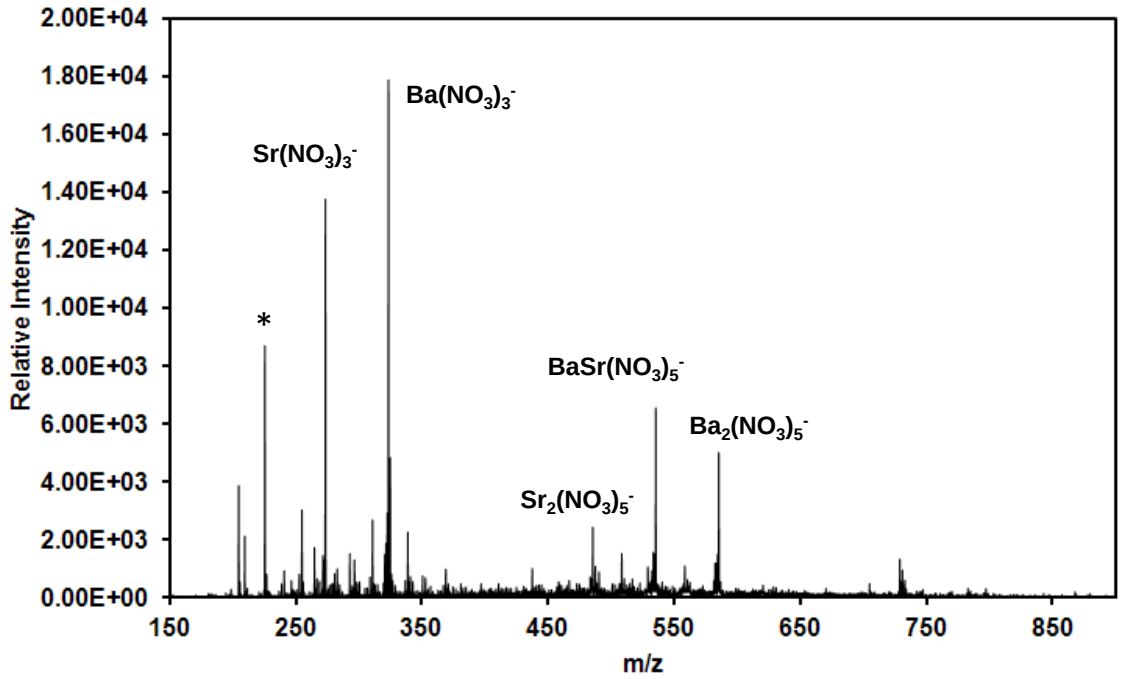

Figure S3. ESI mass spectrum for a mixed Sr^{2+}/Ba^{2+} nitrate solution. The asterisked peak is attributed to $(CF_3COO)_2H^-$ from residual trifluoracetic acid in the ESI system.

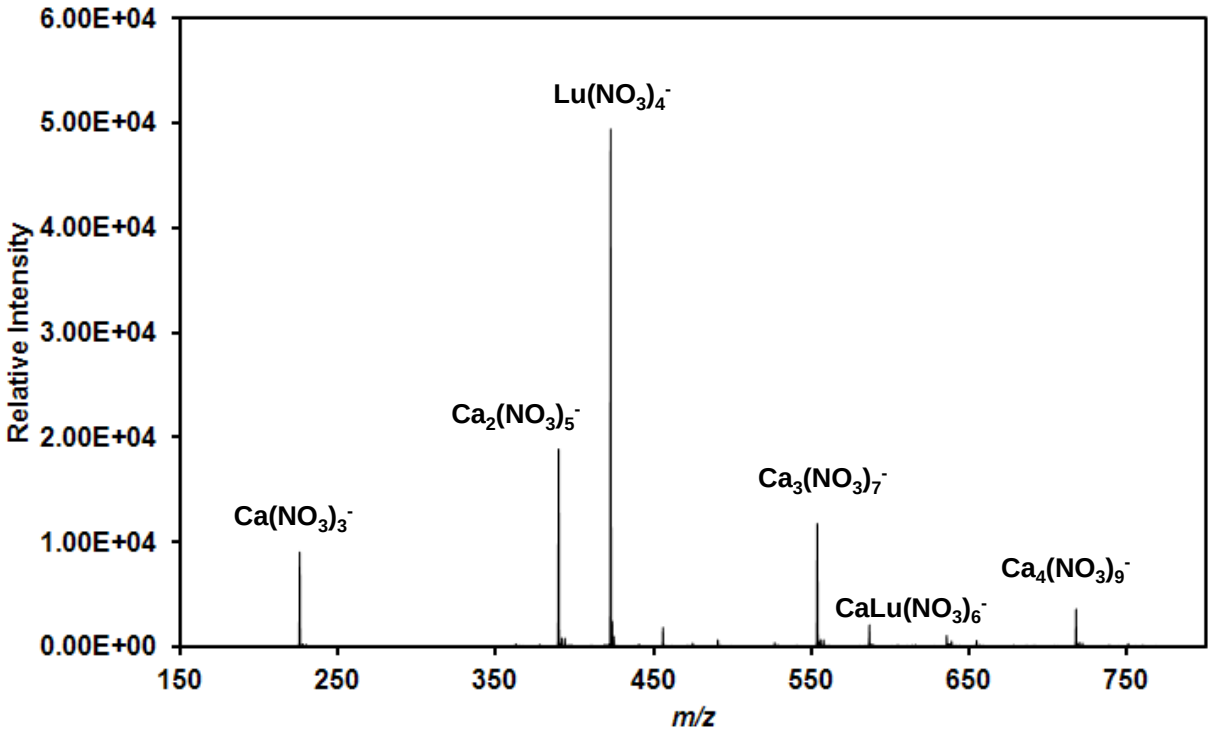

Figure S4. ESI mass spectrum for a mixed Ca^{2+}/Lu^{3+} nitrate solution.

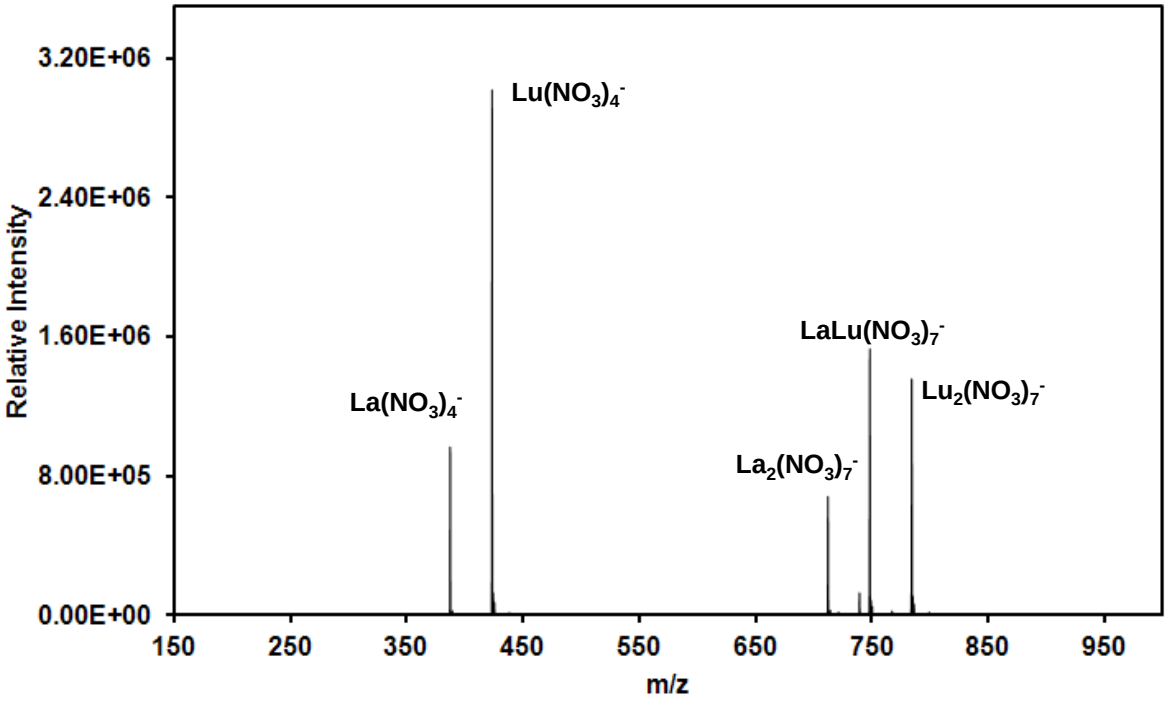

Figure S5. ESI mass spectrum for a mixed La^{3+}/Lu^{3+} nitrate solution.

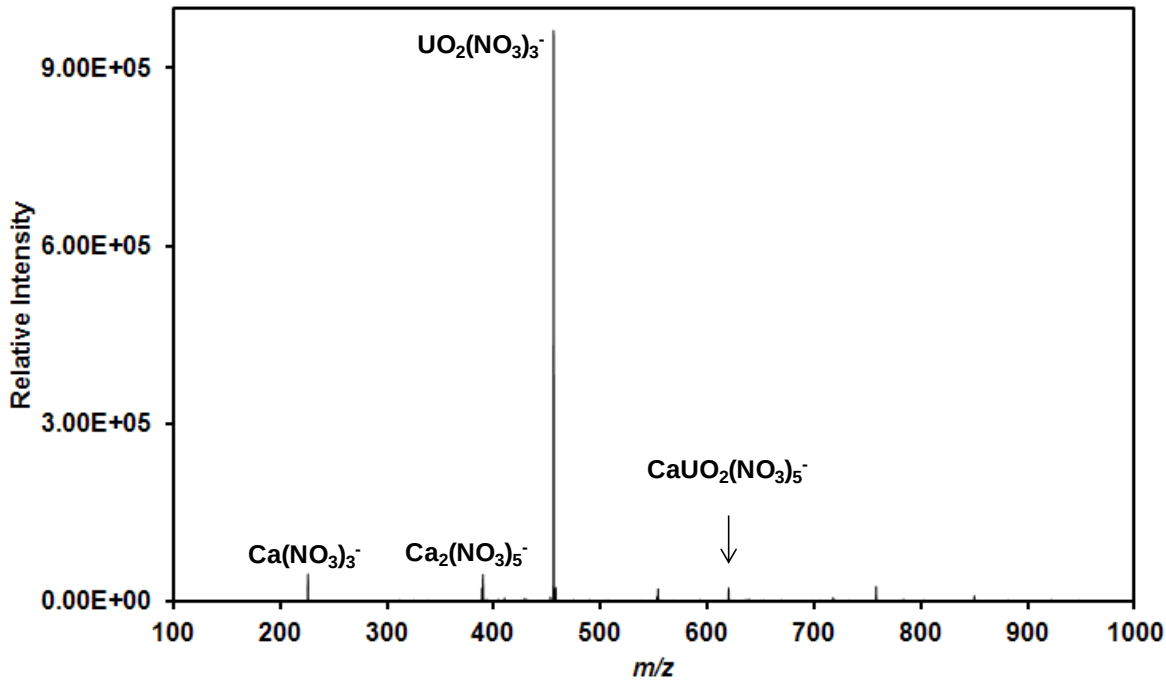

Figure S6. ESI mass spectrum for a mixed Ca^{2+}/UO_2^{2+} nitrate solution.

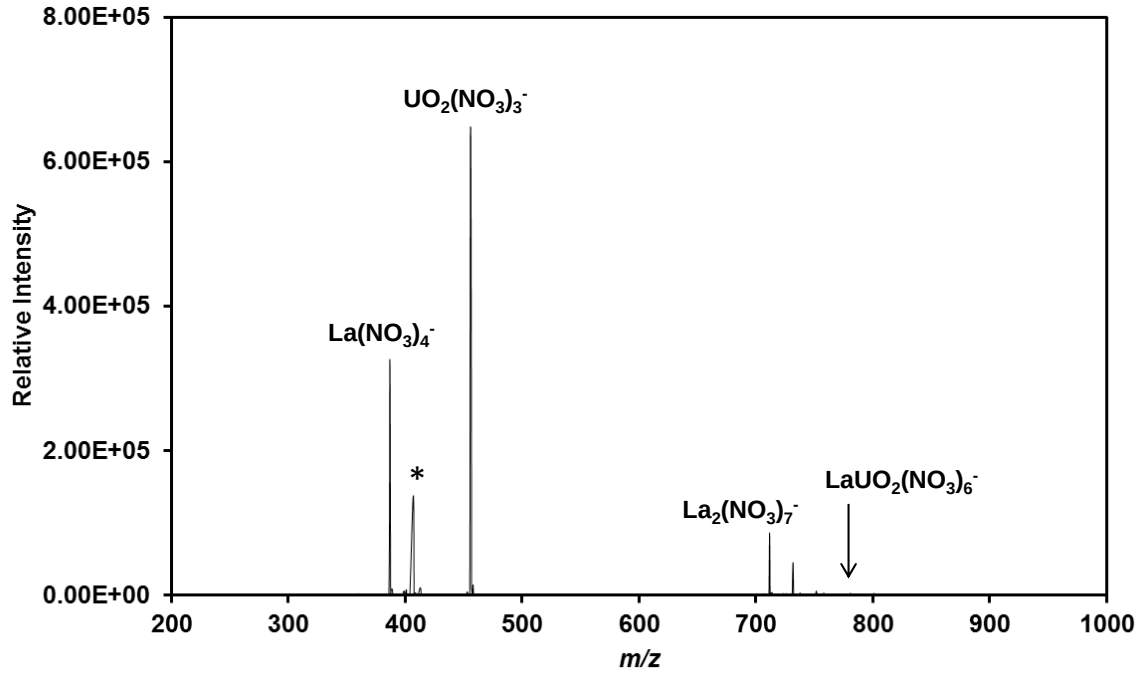

Figure S7. ESI mass spectrum for a mixed La^{3+}/UO_2^{2+} nitrate solution. The asterisked peak is assigned to $Tb(NO_3)_4^-$ due to residual terbium in the ESI system.

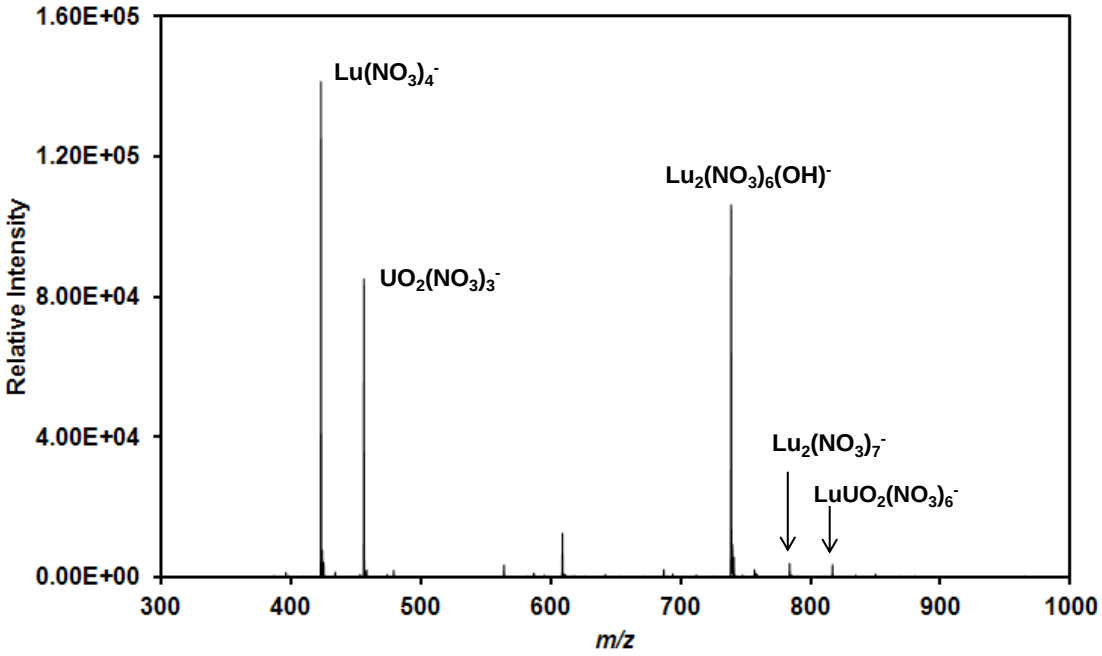

Figure S8. ESI mass spectrum for a mixed Lu^{3+}/UO_2^{2+} nitrate solution.

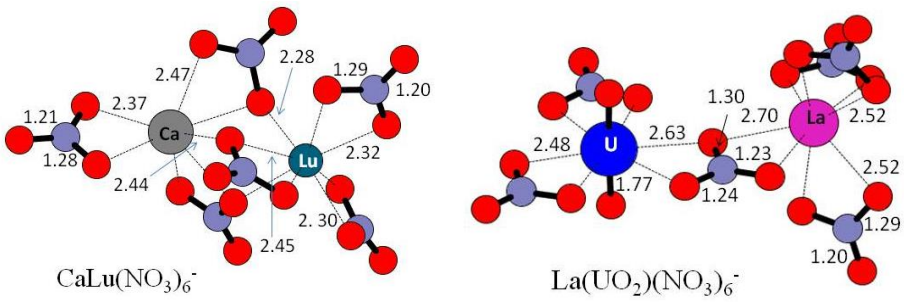

Figure S9. Computed ground state structures of $CaLu(NO_3)_6^-$ and $La(UO_2)(NO_3)_6^-$; bond distances are in angstroms.

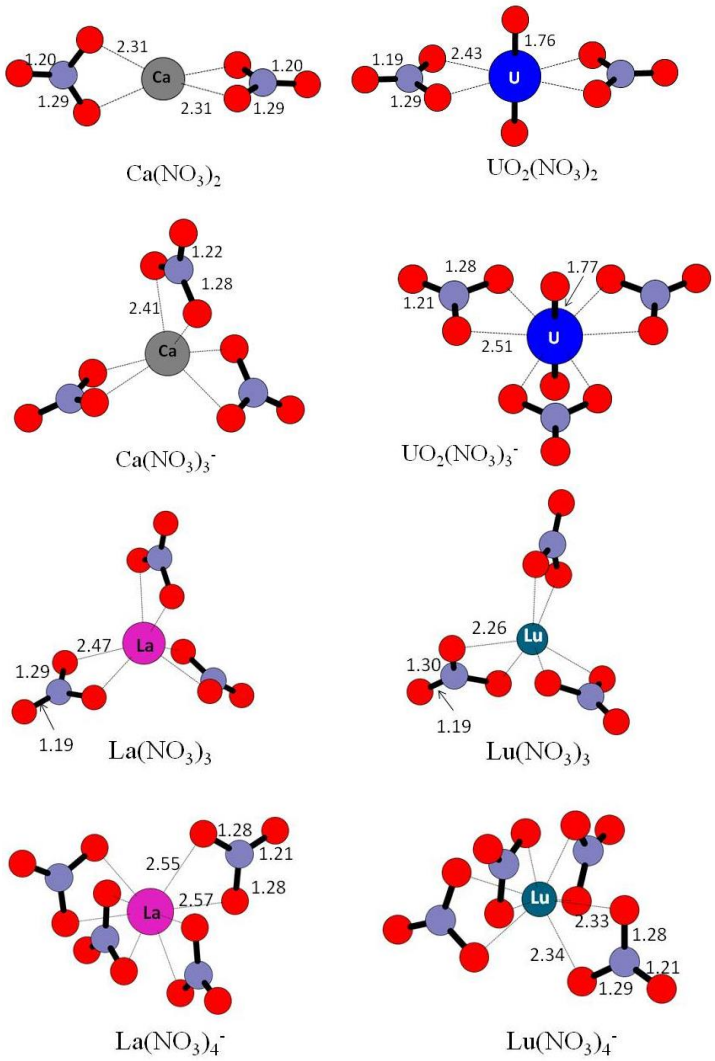

Figure S10. Computed $Ca(UO_2)(NO_3)_5^-$, $La(UO_2)(NO_3)_6^-$, and $Lu(UO_2)(NO_3)_6^-$ fragmentation products; bond distances are in angstroms.

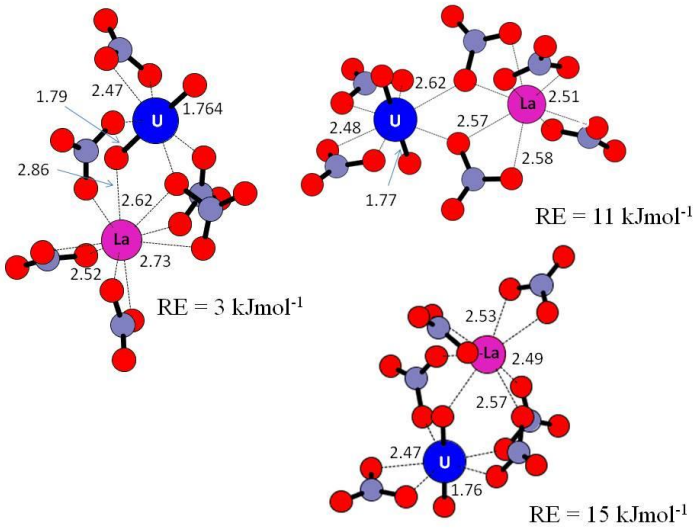

Figure S11. Computed $La(UO_2)(NO_3)_6^-$ higher energy isomers; bond distances are in angstroms. RE is the relative energy with respect to the ground state isomer reported in Figure S9.

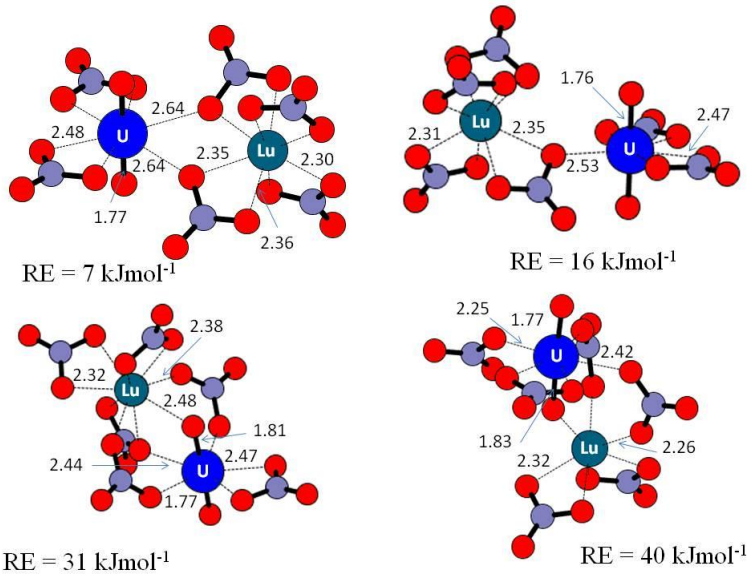

Figure S12. Computed $Lu(UO_2)(NO_3)_6^-$ higher energy isomers; bond distances are in angstroms. RE is the relative energy with respect to the ground state isomer reported in Figure 4.

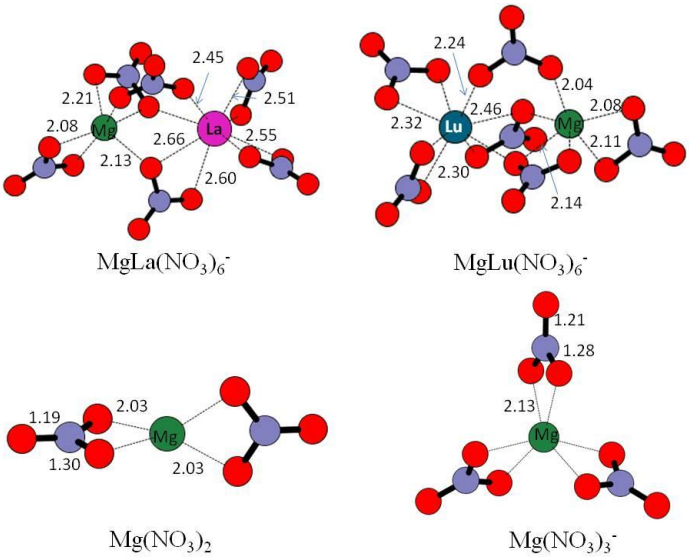

Figure S13. Computed ground state $MgLa(NO_3)_6^-$, $MgLu(NO_3)_6^-$, $Mg(NO_3)_2$ and $Mg(NO_3)_3^-$; bond distances are in angstroms.

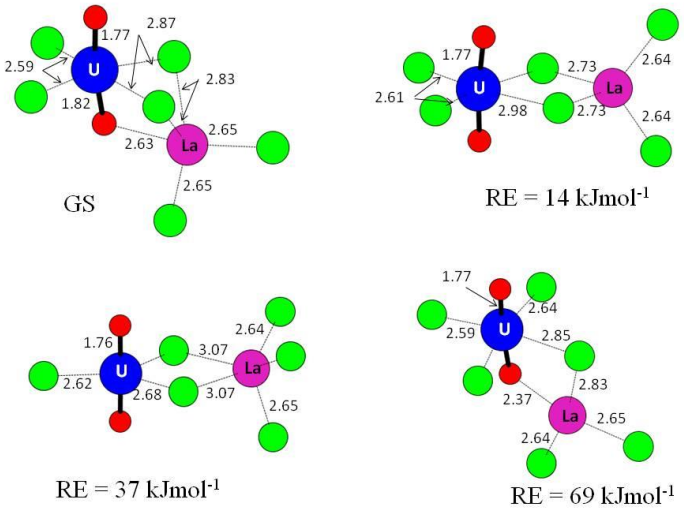

Figure S14. Computed $La(UO_2)Cl_6^-$ ground state (GS) and higher energy isomers; bond distances are in angstroms. RE is the relative energy with respect to the GS isomer.

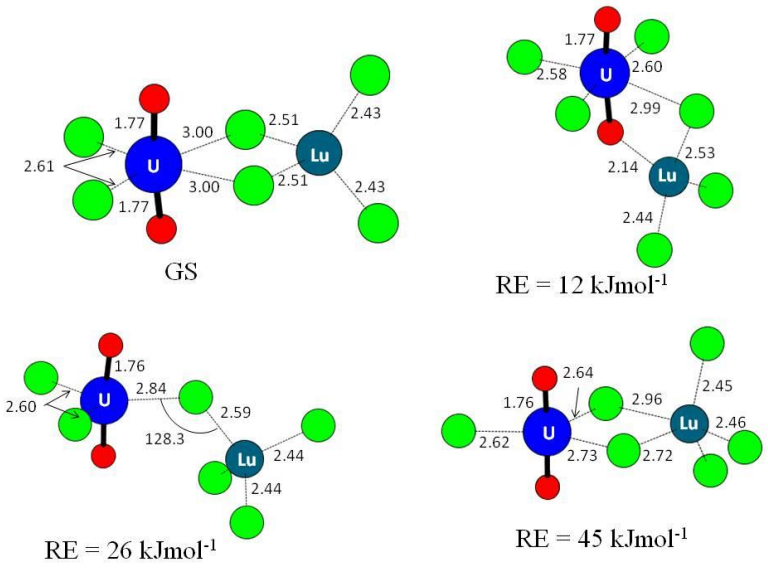

Figure S15. Computed $Lu(UO_2)Cl_6^-$ ground state (GS) and higher energy isomers; bond distances are in angstroms and bond angles are in degrees. RE is the relative energy with respect to the GS isomer.

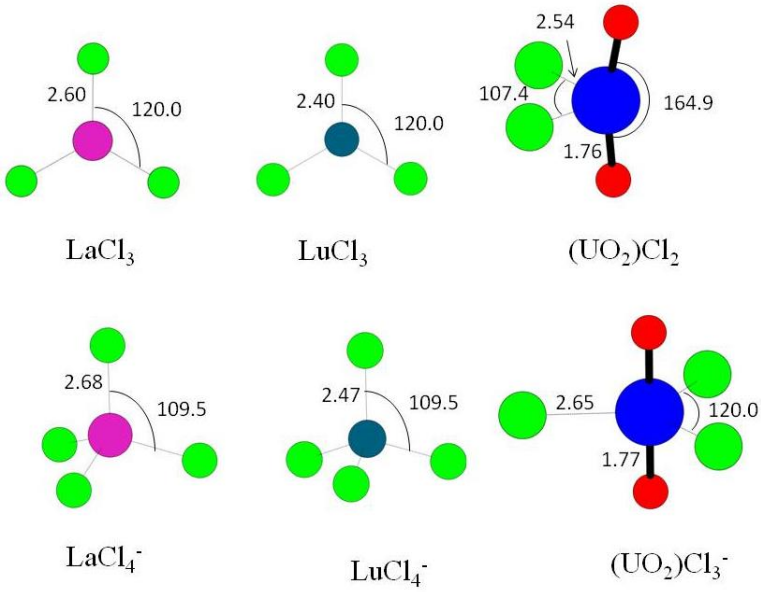

Figure S16. Computed ground state $La(UO_2)Cl_6^-$ and $Lu(UO_2)Cl_6^-$ possible fragmentation products; bond distances are in angstroms and bond angles are in degrees.

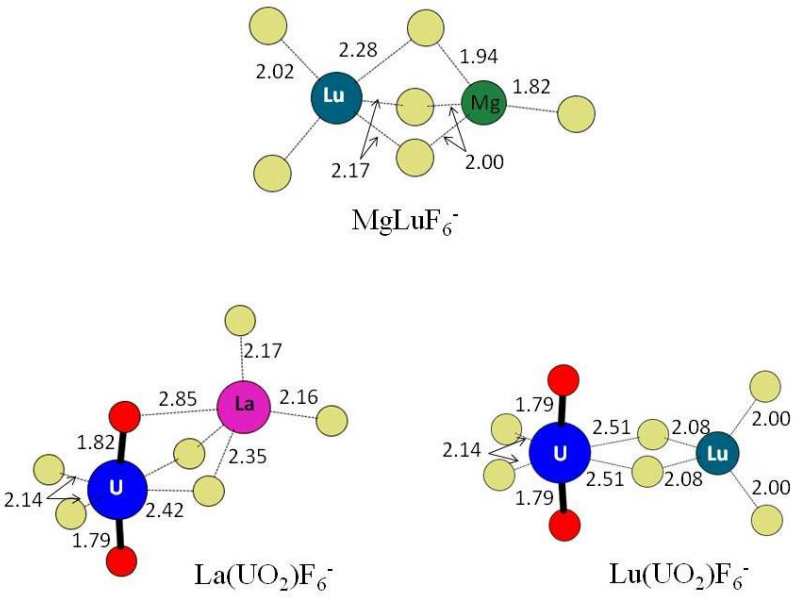

Figure S17. Computed ground state $MgLuF_6^-$, $La(UO_2)F_6^-$ and $Lu(UO_2)F_6^-$; bond distances are in angstroms.

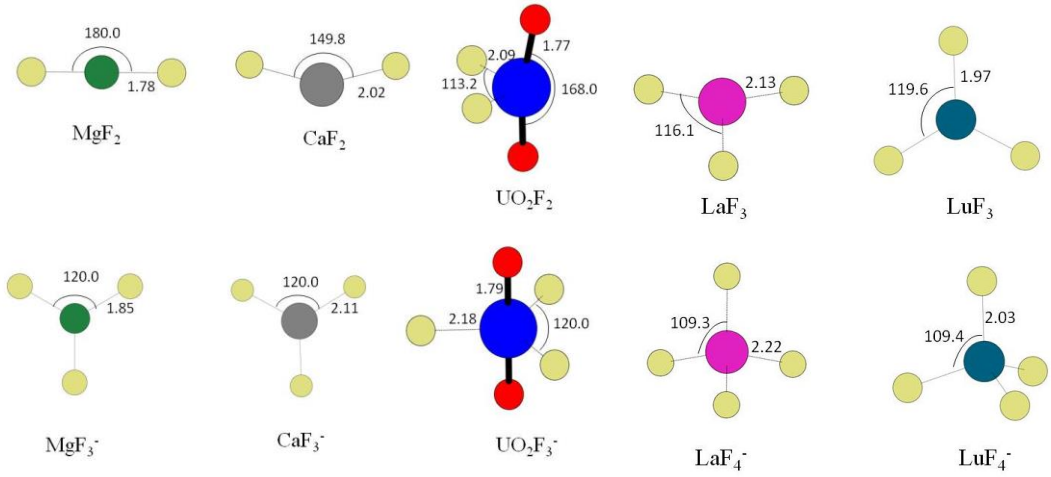

Figure S18. Computed ground state $MgCaF_5^-$, $MgLa_6^-$ and $MgLuF_6^-$ possible fragmentation products; bond distances are in angstroms, bond angles in degrees.

Full citation reference 14.
Gaussian 09, Revision B.01, Frisch, M. J.; Trucks, G. W.; Schlegel, H. B.; Scuseria, G. E.; Robb, M. A.; Cheeseman, J. R.; Scalmani, G.; Barone, V.; Mennucci, B.; Petersson, G. A.; Nakatsuji, H.; Caricato, M.; Li, X.; Hratchian, H. P.; Izmaylov, A. F.; Bloino, J.; Zheng, G.; Sonnenberg, J. L.; Hada, M.; Ehara, M.; Toyota, K.; Fukuda, R.; Hasegawa, J.; Ishida, M.; Nakajima, T.; Honda, Y.; Kitao, O.; Nakai, H.; Vreven, T.; Montgomery, Jr., J. A.; Peralta, J. E.; Ogliaro, F.; Bearpark, M.; Heyd, J. J.; Brothers, E.; Kudin, K. N.; Staroverov, V. N.; Kobayashi, R.; Normand, J.; Raghavachari, K.; Rendell, A.; Burant, J. C.; Iyengar, S. S.; Tomasi, J.; Cossi, M.; Rega, N.; Millam, N. J.; Klene, M.; Knox, J. E.; Cross, J. B.; Bakken, V.; Adamo, C.; Jaramillo, J.; Gomperts, R.; Stratmann, R. E.; Yazyev, O.; Austin, A. J.; Cammi, R.; Pomelli, C.; Ochterski, J. W.; Martin, R. L.; Morokuma, K.; Zakrzewski, V. G.; Voth, G. A.; Salvador, P.; Dannenberg, J. J.; Dapprich, S.; Daniels, A. D.; Farkas, Ö.; Foresman, J. B.; Ortiz, J. V.; Cioslowski, J.; Fox, D. J. Gaussian, Inc., Wallingford CT, 2009.

III.2 Synthesis and hydrolysis of gas-phase lanthanide and actinide oxide nitrate complexes

This sub-chapter is divided in 2 sections:

III.2. A - The content described is based on the following publication:
***Lucena AF**, Lourenço C, Michelini MC, Rutkowski PX, Carretas JN, Zorz N, Berthon L, Dias A, Oliveira MC, Gibson JK, Marçalo J, Synthesis and Hydrolysis of Gas-Phase Lanthanide and Actinide Oxide Nitrate Complexes: A Correspondence to Trivalent Metal Ion Redox Potentials and Ionization Energies, **Phys. Chem. Chem. Phys., 2015**, 17, 9942-9950, DOI: 10.1039/C5CP00515A.*

III.2. B – The content describes other results not yet published about the formation, dissociation and hydrolysis of other gas-phase lanthanide and actinide oxide nitrate complexes. The experimental work was done in the same conditions of those described in section III.2. A. Only the results and a brief conclusion are shown, as the introduction presented in section III.2. A already gives the state of the art on the subject.

In this research, I contributed with all the experimental work performed at C2TN-IST (PT), CQE-IST (PT), and CEA (FR). Ms. Célia Lourenço and Dr. José M. Carretas contributed with experimental work at C2TN-IST and Ms. Célia Lourenço also at CEA. Dr. Philip X. Rutkowski contributed with experimental work at LBNL (US). Dr. Maria C. Michelini was responsible for all the computational work here described. Ms. Ana Dias and Dr. M. Conceição Oliveira were in charge of the ESI-MS at CQE-IST, and Ms. Nicole Zorz and Dr. Laurence Berthon of the ESI-MS at CEA.

III.2 A - Synthesis and hydrolysis of gas-phase lanthanide and actinide oxide nitrate complexes: a correspondence to trivalent metal ion redox potentials and ionization energies

Abstract

Several lanthanide and actinide tetranitrate ions, $M^{III}(NO_3)_4^-$, were produced by electrospray ionization and subjected to collision induced dissociation in quadrupole ion trap mass spectrometers. The nature of the $MO(NO_3)_3^-$ products that result from NO_2 elimination was evaluated by measuring the relative hydrolysis rates under thermalized conditions. Based on the experimental results it is inferred that the hydrolysis rates relate to the intrinsic stability of the M^{IV} oxidation states, which correlate with both the solution IV/III reduction potentials and the fourth ionization energies. Density functional theory computations of the energetics of hydrolysis and atoms-in-molecules bonding analysis of representative oxide and hydroxide nitrates substantiate the interpretations. The results allow differentiation between those $MO(NO_3)_3^-$ that comprise an O^{2-} ligand with oxidation to M^{IV} and those that comprise a radical O^- ligand with retention of the M^{III} oxidation state. In the particular cases of $MO(NO_3)_3^-$ for M = Pr, Nd and Tb it is proposed that the oxidation states are intermediate between M(III) and M(IV).

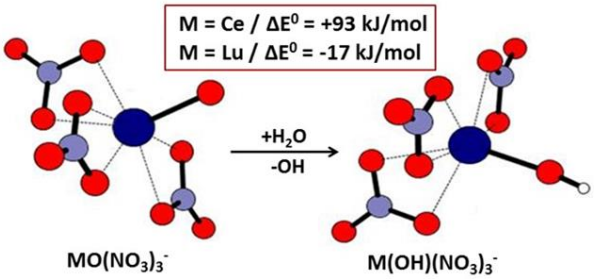

III.2.1. Introduction

Thermal decomposition of metal nitrates to produce solid oxides is enabled by the susceptibility of NO_3 towards dissociation into NO_2 and O (ΔH^0_{289K} = 211 kJ mol^{-1}),[1] a process that becomes favorable at high temperature when the NO_2 concentration in the vapor phase is low. Among the first reports of the thermal dissociation of solid metal nitrates was that by Butkow and Tschassowenny in 1936.[2] Several binary and ternary metal oxides have since been synthesized by nitrate decomposition,[3-10] including catalytic materials.[11-13], thin films,[14-16] and nanoparticles.[17, 18] Of particular relevance to the present work are reports of the decomposition of lanthanide nitrates.[19-22] Dill and Meyer reported the partial decomposition of lanthanide nitrates, $Ln(NO_3)_3$, to produce novel oxide nitrate solids, $LnO(NO_3)$.[23]

Decomposition of solid nitrates is a useful synthetic approach to novel materials. To understand fundamental aspects of the decomposition processes it is informative to study the fragmentation of elementary gas-phase species. Studies of the fragmentation of gas-phase metal nitrate anion complexes, $M(NO_3)_x^-$, have revealed the capability to induce changes in oxidation state: reduction by NO_3 elimination to produce $M(NO_3)_{x-1}^-$, or oxidation by NO_2 elimination to produce $MO(NO_3)_{x-1}^-$. Houk and co-workers employed electrospray ionization (ESI) of metal nitrate solutions to produce a variety of gas-phase metal nitrate anion complexes with metals having more than one stable oxidation state (e.g. Cu^{II}/Cu^{I} and Fe^{III}/Fe^{II}) exhibiting both in the nitrate clusters.[24] This same group subsequently studied the fragmentation of these complexes by collision induced dissociation (CID).[25] The CID behavior of group I and II nitrates was rather straightforward, with loss of NO_3^- to produce $M^{I}(NO_3)$ for alkali metals, or $M^{II}(NO_3)_2$ for alkaline earth metals, results that reflect the inability to oxidize these metals. CID of Cu^{II} and Fe^{III} nitrate complexes resulted in NO_3 elimination concomitant with reduction to Cu^{I} and Fe^{II}. Several transition metal nitrate complexes eliminated NO_2 to produce $MO(NO_3)_{x-1}^-$.[25] For metal ions with prohibitively high ionization energies to achieve oxidation, such as Fe^{3+} (IE[Fe^{3+}] = 54.8 eV[26]), it was reasonably concluded that the oxidation state is not increased in the oxide products.[25] In cases such as $MnO(NO_3)_2^-$ it is feasible that the elimination of NO_2 results in an increase in the oxidation state from Mn^{II} to Mn^{III} because IE[Mn^{2+}] = 33.7 eV is much lower.[26]

Frański et al. recently reported on CID of transition metal nitrate anion clusters and concluded that elimination of NO_2 could result in extensive oxidation of the metals.[27] Among the oxidation states assigned were Mn(VII) in MnO_4^-, Cr(VI) in $CrO_3(NO_3)^-$, Fe(VI) in $FeO_3(NO_3)^-$, and Co(V) in CoO_3^-. There was no direct evidence for these assignments; the structures of the gas-phase oxides were assumed to comprise only M=O bonds in which formal charge state is O^{2-}. In gas-phase metal complexes that have multiple ligating oxygen atoms it is well established that peroxo (O_2^{2-}) and superoxo (O_2^-) are

stable ligands, such as in $[U^{VI}O_2(O_2)]^+$.[28] Li et al. have computed that the ground state of plutonium tetroxide is not $Pu^{VIII}O_4$ but is rather the superoxide $Pu^{V}O_2(O_2^-)$ in which Pu is remarkably not even in its readily accessible hexavalent oxidation state as it would be in the peroxide $Pu^{VI}O_2(O_2^{2-})$.[29] It is apparent that the assumption that all oxygen atoms in metal oxide clusters can be considered as O^{2-} is not well founded. This issue was addressed by Groenewold et al., who concluded that NO_2 loss from $U^{VI}O_2(NO_3)_3^-$ induced by infrared multiphoton dissociation (IRMPD) produced $U^{VI}O_2(NO_3)_2(O)^-$ in which the additional oxygen ligand is an O^- radical.[30] In that same work, IRMPD of $Eu(NO_3)_4^-$ resulted in NO_3 loss and NO_2 loss (as well as additional channels). The $Eu(NO_3)_3^-$ product almost certainly comprises the stable Eu(II) oxidation state but the nature of the oxygen ligand and the europium oxidation state in $EuO(NO_3)_3^-$ is not obvious. The variable nature of the oxygen ligand in metal oxide nitrates such as this is further addressed in the present work. In an IRMPD study of $M^{II}(NO_3)_3^-$, where M is an alkaline earth metal, the observed dissociation channel was NO_3^- elimination to produce neutral $M^{II}(NO_3)_2$ in which the divalent oxidation state is retained.[31] CID of cobalt and nickel nitrate cation clusters studied by Schröder et al. resulted in the loss of NO_2 to result in oxide species with reasonable modest oxidation states.[32] In other work, Schröder et al. prepared (phenanthroline)$Cu^{III}O^+$ by CID-induced NO_2-elimination from (phenanthroline)$Cu^{II}(NO_3)^+$.[33]

In the work reported here several $M^{III}(NO_3)_4^-$ were produced by ESI and subjected to low-energy CID in quadrupole ion trap mass spectrometers (QIT-MS). The nature of the $MO(NO_3)_3^-$ products that result from NO_2 elimination was experimentally evaluated by their hydrolysis to produce $M^{III}(OH)(NO_3)_3^-$. Density functional theory (DFT) computations of the structure and bonding of representative nitrate precursors, oxide and hydroxide nitrates, as well as the energetics of hydrolysis provide insights into the experimental results and allow differentiation between those $MO(NO_3)_3^-$ that comprise an O^{2-} ligand with oxidation to M^{IV}, and those that comprise an O^- ligand with retention of the M^{III} oxidation state.

III.2.2. Experimental approach

The ^{242}Pu, ^{241}Am and ^{248}Cm isotopes used in this work are alpha-emitting radionuclides with half-lives of $4x10^5$ y, 433 y and $3x10^5$ y, respectively. Special safety precautions must be followed when handling these isotopes. The experiments reported here with these radionuclides were performed in special radiological containment glove boxes.

The QIT-MS experiments were performed using four instruments, each equipped with ESI interfaces with MS^n CID capabilities: a Bruker HCT at Centro de Ciências e Tecnologias Nucleares, Instituto Superior Técnico, Portugal (C2TN), a Varian 500-MS IT at Centro de Química Estrutural, Instituto

Superior Técnico, Portugal (CQE), a Bruker Esquire-LC at CEA-Marcoule, France (CEA), and an Agilent 6340 at Lawrence Berkeley National Laboratory, USA (LBNL). The instruments at C2TN and CQE allowed comparison of results for widely divergent background water pressures. The instruments at CEA and LBNL enabled the study of highly radioactive actinides Pu, Am and Cm.

Solutions of $Ln^{III}(NO_3)_3(H_2O)_x$ and An(III) were prepared in water, ethanol or isopropanol with most concentrations in the range 10^{-3} to 10^{-4} M; the concentration of Cm(III) was less than 10^{-5} M. $Am(NO_3)_3$ solutions of 10^{-4} M in ethanol and in water were prepared from the stock solution of $1.5x10^{-3}$ M $Am(NO_3)_3$ with a HNO_3 concentration of 0.1 M. Pu-242 and Cm-248 nitrate stock solutions were diluted to prepare $1.8x10^{-4}$ M and $5x10^{-6}$ M solutions, respectively, for ESI.

All four instruments were operated in the negative ion accumulation and detection mode. The metal nitrate solutions were directly injected into the capillaries in the ESI sources using syringe pumps with flow rates in the range of 60 - 600 µL h^{-1}.

For the Bruker HCT at C2TN, sample solutions were introduced with a flow rate of 150 µL h^{-1}. The spectra were acquired using the following typical instrumental parameters: capillary voltage 4000 V, nebulizer gas (N_2) pressure 8.0 psi, drying gas (N2) at 250 °C with flow rate 4.0 L.min^{-1}, capillary exit voltage -128.5 V, skimmer voltage -40.0 V, trap drive 67.3 V.

For the Varian 500-MS IT at CQE-IST spectra were acquired using the following instrumental parameters: solution flow rate 600 µL h^{-1}, capillary voltage -20 V, needle -4500 V, spray shield -600 V, radiofrequency (RF) load 90%, nebulizer gas (N_2) pressure 35 psi, drying gas (N_2) pressure 10 psi at 350 ºC.

The Bruker Esquire-LC at CEA was installed in a radiological-containment glove box.[34] A syringe infusion pump delivered the sample at 90 µL h^{-1} to the electrospray source. The experimental conditions were the following: drying gas (N_2) 5 L min^{-1} at 250ºC, nebulizer gas (N_2) pressure 5 psi, ion spray voltage 4000 V, capillary exit offset -60 V, skimmer (1) -60 V, skimmer (2) -10 V, trap drive 50 V.

The Agilent 6340 QIT/MS (LBNL), which is essentially the same as the Bruker HCT, was operated also with the source region of the QIT/MS inside of a radiological-containment glove box, as previously described.[35] Spectra were typically acquired using the following approximate instrumental parameters: solution flow rate 60 µL h^{-1}, nebulizer gas (N_2) 15 psi, capillary voltage 4500 V and current 15 nA, dry gas (N_2 from a boil-off of a liquid nitrogen Dewar) flow rate 5 L min^{-1} at 325 ^{o}C, capillary exit -160 V, skimmer -50 V, trap drive 140 V. As has been discussed elsewhere,[36] the background water pressure in this ion trap is estimated as ~10^{-6} Torr.

The buffer gas used in the four ion traps was helium (constant pressure of ~$1x10^{-4}$ mbar). Ion-molecule reactions can occur in the ion trap by applying a variable reaction delay time of up to 10 s at the trap

temperature of ~300 K.[37] Collision induced dissociation (CID) experiments are performed by isolation of the ions of interest and ejection of all the other ions, which allows time-dependent hydration reaction studies with the background water in the traps under thermal conditions. Because the CID and other instrumental conditions were not identical for all four instruments, comparisons between CID product yields are necessarily somewhat qualitative. Relative hydration rates were measured under low-energy thermal conditions such that they can be directly compared, with differences in rates attributable to different background water pressures in the ion traps.

Pseudo-first order reaction rates, k, for thermal (ca. 300 K) hydrolysis of trapped ions in the QITs were obtained by isolating the ion of interest and allowing it to react with background water for variable times. Plots of the logarithmic decay of the ratio of the reactant ion intensity to the total ion intensity as a function of time provide the hydrolysis reaction rates. The hydrolysis rates were different for the four QITs due to different water pressures, by up to a factor of 100 times, in the ion traps. As described below, by obtaining rates for the same hydrolysis reaction in all four QITs (for $ScO(NO_3)_3^-$) it was possible to establish the following relative water pressures (arbitrarily normalized to 100 for the C2TN trap): C2TN/100; LBNL/62; CEA/8.6; CQE/1.3. As remarked above, the C2TN and LBNL instruments are essentially identical; the lower water pressure in the LBNL trap might be due to the use of high-purity N_2 evaporated from liquid nitrogen, rather than from a nitrogen generator.

III.2.3. Computational methods

DFT computations of the structure of representative nitrate precursors, oxide nitrates and hydroxide nitrates were performed using the Gaussian09 (revision B.01) package.[38] Full geometry optimizations and frequency calculations were performed using the B3LYP hybrid functional.[39, 40] The Stuttgart-Dresden triple–ζ valence basis sets together with the corresponding effective small-core potential (SDD) were used for the lanthanide and transition metal (Sc, Y) atoms [41, 42] and the Pople triple–ζ basis sets, 6-311++G(d,p), for the rest of the atoms.[43-45] The "ultrafine" pruned grid was adopted for the numerical integration option in all computations. Geometry optimizations were performed without symmetry restrictions. Computation of open-shell systems were performed using spin-unrestricted methods. The broken-symmetry (BS) approach[46-49] was used to study the open-shell $CeO(NO_3)_3^-$ (singlet spin state) and the antiferromagnetically coupled $PrO(NO_3)_4^-$ (doublet spin state). All the computed reaction energies include the zero-point vibrational energy correction (ΔE^0). In addition to the ΔE^0 values, the Gibbs free energy at 298 K is reported for each of the studied reactions (ΔG^{298}). The accuracy of the ΔG^{298} values is necessarily somewhat limited by the use of the harmonic oscillator approximation to treat nuclear motion. It should be remarked that all of the computations were

performed for a pressure of 1 atm. In reality, the total pressure under these experimental conditions is approximately 10^{-4} Torr. Furthermore, the "pressures" of the reactants and products, both ions and neutrals, are very low (≤ 10^{-6} Torr) and are unknown. Accordingly, the computed reaction entropies and free energies may deviate from the actual values under these experimental conditions. However, the values for ΔE^0 are not pressure dependent and the key conclusions, which are based on ΔE^0 values, are not affected by the uncertainties in ΔG^{298}. QTAIM analysis[50] was performed on all the studied $MO(NO_3)_4^-$ and $M(OH)(NO_3)_3^-$ complexes to analyze and compare the characteristics of the M-O bonds. Appropriate wave-function extended files (wfx) were obtained with Gaussian09 and analyzed using the AIMAll package.[51] The electron density (ρ_{BCP}), the Laplacian of electron density ($\nabla^2\rho_{BCP}$) and total energy density (H_{BCP}) of the M-OH and M-O (oxide) bond critical point of the $M(OH)(NO_3)_3^-$ and $MO(NO_3)_3^-$ complexes (M = La, Ce, Pr, Lu, Al, Sc, and Y) are included as Supporting Information (Table S1).

III.2.4. Results and discussion

The first experimental component of this work was a study of the fragmentation behavior of $M^{III}(NO_3)_4^-$ complexes, with an emphasis on how the product distributions relate to the intrinsic stability of the M(IV) oxidation states. The second part involved studying the kinetics of hydrolysis of fragmentation products to produce M(III) hydroxides. The experimental observations are evaluated in comparison with computed structures of the products, and the computed energetics of the fragmentation and hydrolysis processes.

III.2.4.1 Fragmentation of $M(NO_3)_4^-$

The key CID results for the $M(NO_3)_4^-$ complexes are in Table III.2.1. The dominant products were $MO(NO_3)_3^-$ and $M(OH)(NO_3)_3^-$ (representative CID mass spectra are in Supporting Information). For several of the $M(NO_3)_4^-$ an additional minor (<10%) product was $MO_2(NO_3)_3^-$ via elimination of NO, but the nature of these species and other secondary products (see SI) are not considered in detail here, except to mention that the $MO_2(NO_3)_3^-$ may be superoxides comprising an O_2^- ligand, such that the stable M(III) oxidation state is retained. In the distinctive cases of $Eu(NO_3)_4^-$ and $Yb(NO_3)_4^-$, a very minor (≤5%) CID channel was ligand loss to produce $M(NO_3)_3^-$ in which the metal has been reduced from a formal M(III) to a M(II) oxidation state. Previous work has demonstrated that CID of gas-phase complexes parallels solution redox chemistry, with metal complexes having higher reduction potentials being more prone to reduction upon CID.[52] The observed reduction of Eu(III) and Yb(III) to the divalent state by ligand loss is consistent that these two are the studied M(III) with the highest

III/II reduction potentials.[53]

The dominant CID process is given by Equation (1). The appearance of substantial hydroxide suggests that Equation (2) occurs efficiently under CID conditions as a secondary reaction. The efficiency of Equation (2) depends on both the background water pressure in the ion trap and the nature of the reactant ion. An alternative source of $M(OH)(NO_3)_3^-$ is direct hydrolysis of the nitrate, Equation (3).

$$M(NO_3)_4^- \rightarrow MO(NO_3)_3^- + NO_2 \quad (1)$$

$$MO(NO_3)_3^- + H_2O \rightarrow M(OH)(NO_3)_3^- + OH \quad (2)$$

$$M(NO_3)_4^- + H_2O \rightarrow M(OH)(NO_3)_3^- + HNO_3 \quad (3)$$

Structures of representative $M(NO_3)_4^-$, $MO(NO_3)_3^-$ and $M(OH)(NO_3)_3^-$ shown in Figure III.2.1, with key M-O bond distances given in Table III.2.2, are discussed below. Computed energetics for Equations (1), (2) and (3) are in Table III.2.3. Equation (3) can be excluded as a significant pathway based on the following considerations. Equation (3) involves no change in oxidation state and corresponds to the replacement of a nitrate ligand by a hydroxide ligand concomitant with consumption of H_2O and elimination of HNO_3. Although there may be minor variations in the kinetics and thermodynamics associated with such a process across the lanthanide series, there is no basis to expect the observed substantial differences in hydroxide yields, particularly for adjacent lanthanides. For example, the result that under essentially the same conditions substantial $La^{III}(OH)(NO_3)_3^-$ is produced whereas no $Ce^{III}(OH)(NO_3)_3^-$ is produced (Table III.2.1) indicates that Equation (3) is not a significant source of the $M^{III}(OH)(NO_3)_3^-$ products. This interpretation is substantiated by the computed energetics for Equation (3) (Table III.2.3), which indicate that both ΔE^0 and ΔG^{298} are essentially the same for M = La, Ce, Pr and Lu.

Table III.2.1. Product yields for CID of $M(NO_3)_4^-$.[a]

	$MO(NO_3)_3^-$	$M(OH)(NO_3)_3^-$
La	5 /*45*	85 / *50*
Ce	100 / *100*	0 / *0*
Pr	100 / *100*	0 / *0*
Nd	100 / *100*	0 / *0*
Sm	<3 / *55*	95 / *40*
Eu[b]	0 / *45*	95 / *45*
Gd	10 / *50*	90 / *50*
Tb	100 / *100*	0 / *0*
Dy	10 / *55*	85 / *45*
Ho	10 / *60*	90 / *40*
Er	5 / *60*	90 / *40*
Tm	10 / *60*	90 / *40*
Yb[b]	<3 / *60*	95 / *35*
Lu	10 / *50*	80 / *50*
Sc	55 / *100* / 70[c]	45 / *0* / 25[c]
Y	10 / *55*	90 / *40*
Al	100	0
Pu	95[c]	0[c]
Am	100[d]	0[d]
Cm	100[c]	0[c]

[a]Intensities of product ions, rounded to 5% to reflect reproducibility. Where two values are given, that in regular font (left) is from CT2N and that in italics (right) is from CQE. A value of <3% indicates detection in the range of 1-2%; 0% indicates not detected to <1%. Small (<10%) yields of $MO_2(NO_3)_3^-$ were observed, except for M = Ce, Pr, Eu, Al and Cm.

[b]$M(NO_3)_3^-$ was produced at ~5% yield for M = Eu and at ~1% yield for M = Yb.

[c]From LBNL.

[d]From CEA

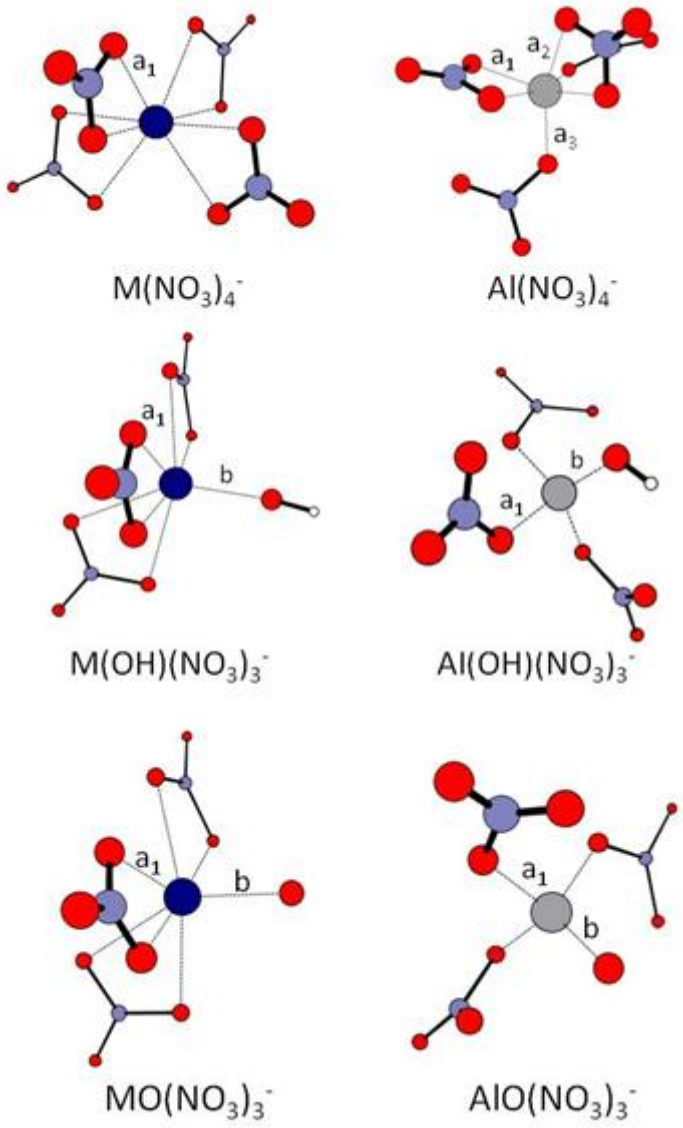

Figure III.2.1. Geometrical structures of ground state $Al(NO_3)_4^-$, $Al(OH)(NO_3)_3^-$, $AlO(NO_3)_3^-$ ions, and of ground state $M(NO_3)_4^-$, $M(OH)(NO_3)_3^-$, $MO(NO_3)_3^-$ ions for M = La, Ce, Pr, Sc, Y and Lu. Selected geometrical parameters are reported in Table III.2.2.

Table III.2.2. Selected optimized M-O bond distances[a]

M	$M(NO_3)_4^-$ a_1, a_2, a_3	$M(OH)(NO_3)_3^-$ a_1; b	$MO(NO_3)_3^-$ a_1; b
La	2.56 [8]	2.60 [6]; 2.15	2.59 [6]; 2.26
Ce	2.54 [8]	2.58 [6]; 2.13	2.55 [6]; 1.80
Pr	2.52 [8]	2.56 [6]; 2.06	2.54 [6]; 1.85
Lu	2.34 [8]	2.37 [6]; 2.00	2.36 [6]; 2.09
Al[b]	1.95 [2], 2.03 [2]; 1.85 [2]	1.84 [3]; 1.72	1.84 [3]; 1.77
Sc	2.23 [8]	2.26 [6]; 1.89	2.25 [6] ; 1.96
Y	2.40 [8]	2.43 [6]; 2.05	2.42 [6] ; 2.16

[a]In Angstroms (see Figure III.2.1); values of a_1, a_2 and a_3 are averaged values over the number of nearly equivalent (to within ~0.01 Å) coordinating oxygen atoms in the NO_3 ligands, with the number of M-O interactions indicated in brackets.
[b]$Al(NO_3)_4^-$ presents three sets of a values, a_1 and a_2 for the two bidentate nitrates, and the shorter a_3 distance for the two monodentat nitrates (see Figure III.2.1). Al-O distances of >2.8 Å for $Al(OH)(NO_3)_3^-$ and $AlO(NO_3)_3^-$ are not reported.

Table III.2.3. Computed energetics (kJ.mol^{-1}) for formation of $MO(NO_3)_3^-$ by elimination of NO_2 from $M(NO_3)_4^-$ (Eqn. 1), for hydrolysis of $MO(NO_3)_3^-$ to form $M(OH)(NO_3)_3^-$ (Eqn. 2), and for hydrolysis of $M(NO_3)_4^-$ to form $M(OH)(NO_3)_3^-$ (Eqn. 3).

	Equation 1		**Equation 2**		**Equation 3**	
	ΔE^0	ΔG^{298}	ΔE^0	ΔG^{298}	ΔE^0	ΔG^{298}
La	287	235	-17	-12	96	86
Ce	177	137	93	88	95	85
Pr	261	216	10	6	96	85
Lu	282	229	-13	-10	95	83
Sc	262	207	-7	-5	80	66
Y	289	236	-16	-12	98	88
Al	223	164	-10	-7	38	21

The results in Table III.2.1 were acquired using four different QITs with widely disparate background water pressures. The CID results for $Ln(NO_3)_4^-$ are reported for the C2TN and CEA ion traps; the water pressure is ca. 100 times lower in the latter (see below). It is apparent that the yields of $Ln(OH)(NO_3)_3^-$ by Eqn. 2 are substantially greater in the C2TN ion trap. A typical CID duration is ca. 40 ms, which is sufficient time for significant hydrolysis. Among the lanthanide nitrates, $LnO(NO_3)_3^-$ was the sole product only in the cases of Ln = Ce, Pr, Nd, Tb (Table III.2.1). As is evident in Table III.2.4, these are the four Ln with the lowest fourth ionization energies (IE4) and also the lowest IV/III reduction potentials. The IV/III reduction potentials are related to IE4 and are only estimates except for the case

of Ce(IV/III).[53] Whereas reduction potentials are most pertinent in solution, ionization energies are most relevant in gas phase where solvation does not play a role. Accordingly, the remainder of the discussion will focus on comparative ionization energies, specifically IE4, with the understanding that there is a correlation to IV/III reduction potentials. The correlation between oxide IE4 and abundance suggests that the stability of the $LnO(NO_3)_3^-$ ions are directly related to the stability of Ln^{4+}, and that the four $LnO(NO_3)_3^-$ produced exclusively upon CID can be considered as nitrate-coordinated lanthanide monoxides in which the oxidation state is Ln(IV) or intermediate between Ln(III) and Ln(IV). The computational results below confirm that the oxidation state is Ce(IV) in $CeO(NO_3)_3^-$. For CID of the other ten $Ln(NO_3)_4^-$ there is a significant amount of $Ln(OH)(NO_3)_3^-$. According to our computations and bonding analysis (see below), the lanthanide atoms in $LnO(NO_3)_3^-$ and $Ln(OH)(NO_3)_3^-$ (Ln = La, Lu) are Ln^{3+} coordinated by a radical oxygen or a hydroxide and three nitrate anion ligands. As there is no change in oxidation state, the yields of the $Ln(OH)(NO_3)_3^-$ are similar for different Ln, 80-95% at C2TN and 35-50% at CQE, with no correlation of the hydroxide yields with IE4.

Table III.2.4. Selected properties of metal ions.

	IE[M^{3+}→M^{4+}] (eV)[a]	Δ*E*[IV/III] (V)[b]	r[M^{3+}] (Å)[c]
La	50.0	-	1.06
Ce	36.8	+1.7	1.03
Pr	39.0	+3.7	1.01
Nd	40.4	+4.9	1.00
Sm	41.4	+5.5	0.96
Eu	42.7	+6.6	0.95
Gd	44.0	+7.9	0.94
Tb	39.8	+3.3	0.92
Dy	41.5	+4.9	0.91
Ho	42.5	+5.9	0.89
Er	42.7	+6.0	0.88
Tm	42.7	+6.0	0.87
Yb	43.6	+6.9	0.86
Lu	45.3	+8.5	0.85
Sc	73.5	-	0.73
Y	60.6	-	0.89
Al	120.0	-	0.53
Pu	34.6	+1.1	1.00
Am	36.2	+2.6	1.01
Cm	36.8	+3.0	0.98

[a]Fourth ionization energies from ref.[26]; values for Pu, Am and Cm are estimates from ref.[54]

[b]IV/III reduction potentials. Values for Ln(IV/III) are from ref.[53]; all except the value for Ce are estimates. Values for An(IV/III) are from ref.[55]. Values not provided are predicted to be >>10 V.

[c]Effective ionic radii from Shannon and Prewitt for CN6.[56]

Three actinide nitrates were subjected to CID for comparison with the lanthanides. CID of $An(NO_3)_4^-$ for An = Pu, Am and Cm resulted in $AnO(NO_3)_3^-$, with no detected $An(OH)(NO_3)_3^-$. As seen in Table III.2.4, IE4 of Pu, Am and Cm are less than or equal to IE4[Ce], suggesting that the three $AnO(NO_3)_3^-$ comprise An(IV).

To elucidate the role of ionic radii on hydrolysis, CID of $M(NO_3)_4^-$ for M = Sc, Y and Al was studied, with the results in Table III.2.1. Based on the very high IE4 values of these metals (Table III.2.4) it can be confidently predicted that these are M(III) oxides and from the Ln results that hydrolysis should be prevalent as in the case of $Y(NO_3)_4^-$. For $Sc(NO_3)_4^-$, the yield of $ScO(NO_3)_3^-$ is higher, 100% at CQE, than would be predicted from the high IE4 for Sc. For $Al(NO_3)_4^-$, only $AlO(NO_3)_3^-$ was produced, with no evidence for hydrolysis, which is remarkable in view of the very high Al IE4 of 120 eV. As is seen in Table III.2.4, the ionic radius of Y^{3+} is comparable to those of the late Ln^{3+} whereas that of Sc^{3+} is 0.12 Å smaller than that of Lu^{3+} and that of Al^{3+} is 0.33 smaller than that of Lu^{3+}. It is inferred that $MO(NO_3)_3^-$ having M^{3+} with sufficiently small radii are resistant to hydrolysis under CID conditions regardless of the magnitude of IE4.

III.2.4.2 Hydrolysis of $MO(NO_3)_3^-$

To study hydrolysis under thermal conditions for comparison with the CID results, rates for Eqn. 2 were measured for $MO(NO_3)_3^-$, with the results compiled in Table III.2.5 for the four different QIT mass spectrometers. The measured pseudo-first order rates for Eqn. 3 were obtained from the decay of the reactant according to Eqn. (4).

$$-d[MO(NO_3)_3^-]/dt \equiv \text{rate} = k_M[H_2O] \qquad (4)$$

Table III.2.5. Hydrolysis rates for $MO(NO_3)_3^-$.[a]

	k **(s^{-1})**
La	*7.0*
Ce	NR / *NR*
Pr	NR[b] / *NR*
Nd	0.012 / *NR*
Sm	*5.3*
Eu	*5.0*
Gd	*5.6*
Tb	0.006 / *NR*
Dy	*5.3*
Ho	*5.5*
Er	*5.3*
Tm	*5.7*
Yb	*4.7*
Lu	*5.5*
Sc	10.4 / *0.13* / 0.89[c] / 6.4[d]
Y	*6.5*
Al	0.15
Pu	NR[c]
Am	NR[b]
Cm	NR[c]

[a] Unless otherwise noted the values in regular font were obtained at C2TN and those in italics at CQE; the results for Pu and Cm were obtained at LBNL, and those for Am at CEA. NR means no reaction for the 10 s maximum reaction time. Most of the Ln and Y hydrolyzed too rapidly in the C2TN instrument to allow isolation and rate determinations.

[b]Increasing the water pressure in the C2TN trap by a factor of ca. 5x resulted in minuscule but detectable hydration. Normalization to the usual background pressure in the trap results in an estimated rate of 0.0001 s^{-1}, ca 60x slower than the rate for $TbO(NO_3)_3^-$.

[c]Measured at CEA.

[d]Measured at LBNL.

An example of data for $ScO(NO_3)_3^-$ used to obtain hydrolysis rates is shown in Fig. III.2.2 with the corresponding kinetics plot in Fig. III.2.3. Hydrolysis rates were measured for $ScO(NO_3)_3^-$ in all four QITs (Table III.2.5). Because the rate constant, k_{Sc}, is invariant, the relative rates provide the relative water pressure, $[H_2O]$, in the traps (normalized to 100 at C2TN): C2TN/100; LBNL/62; CEA/8.6; CQE/1.3. The invariance of the water pressures in each trap, to within ca. 10%, was confirmed by establishing that the measured rates did not vary significantly when measured at different times. It has been estimated that the water pressure in the LBNL ion trap is ca. 10^{-6} Torr; the pressure in the CT2N trap is roughly comparable, that in the CEA trap significantly lower, and that in CQE trap is even lower.

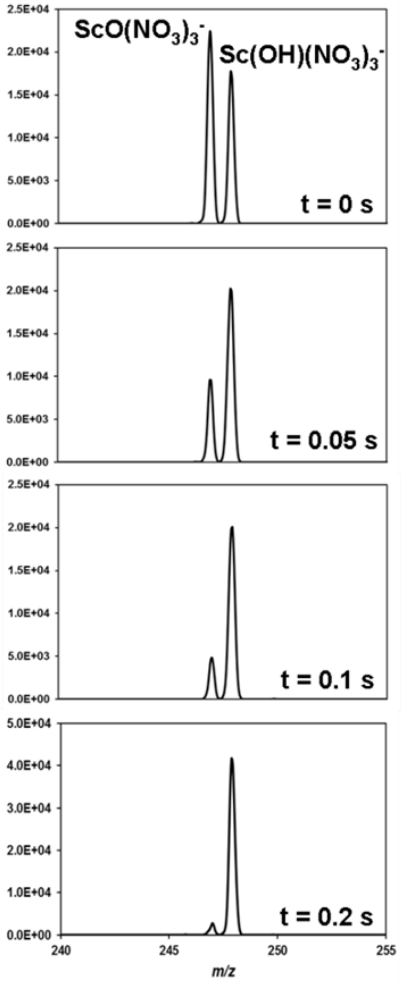

Figure III.2.2. Hydrolysis of $ScO(NO_3)_3^-$ as observed at C2TN. The indicated time is the delay between isolation of $ScO(NO_3)_3^-$ and detection of the residual reactant and hydrolysis product; the appearance of substantial product for t = 0 s is a result of the ca. 0.04 s time for isolation.

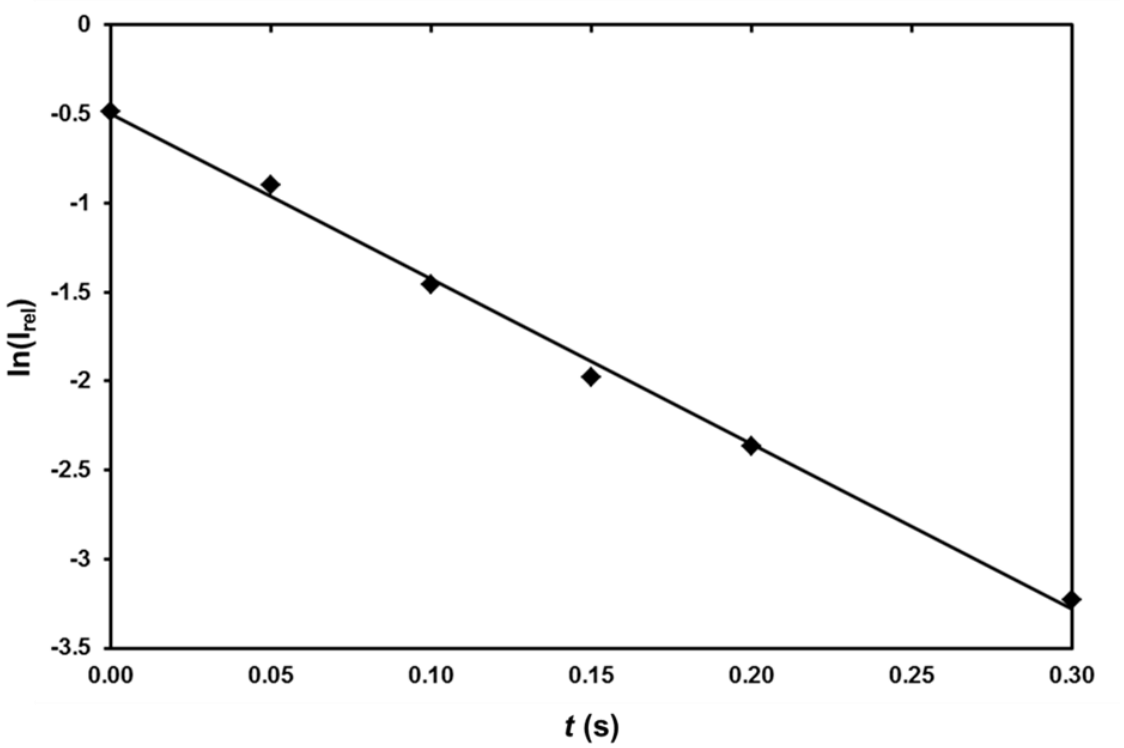

Figure III.2.3. Kinetic plot from the reaction of isolated $ScO(NO_3)_3^-$ with H_2O to form $Sc(OH)(NO_3)_3^-$ from results obtained at C2TN (R^2 = 0.9967).

The predicted resistance of tetranitrates, $M(NO_3)_4^-$, towards spontaneous hydrolysis according to Eqn. 3 was confirmed for M = La, Tb, Eu, Ho, Lu, Sc, Y, Al and Pu. The $M(NO_3)_4^-$ were isolated in either the C2TN or LBNL traps, which have the highest water pressures, with a 10 s reaction time applied: there was no indication of any $M(OH)(NO_3)_3^-$ products.

All of the $LnO(NO_3)_3^-$, as well as $ScO(NO_3)_3^-$ could be isolated in the CQE ion trap for determination of hydrolysis rates. For Ln = Ce, Pr, Nd and Tb, no hydrolysis was observed after isolation for the maximum accessible reaction time of 10 s. For all other Ln, the hydrolysis rates were similar, in the narrow range of 5 - 7 s^{-1}. The rate for $ScO(NO_3)_3^-$, 0.13 s^{-1}, was notably slower. The $MO(NO_3)_3^-$ complexes could be isolated and hydrolysis rates obtained in the C2TN trap for M = Ce, Pr, Nd, Tb, Sc, and Al. There was no detectable hydrolysis for M = Ce and Pr after the maximum reaction time of 10 s. By increasing the water pressure by a factor of five, very inefficient hydrolysis of $PrO(NO_3)_3^-$ (but not $CeO(NO_3)_3^-$) could be detected, as noted in Table III.2.5; this very inefficient process could be attributed to a small population of non-thermalized ions. The measured rates for Nd and Tb, 0.012 s^{-1} and 0.006 s^{-1}, respectively were much slower than for M = Sc (10.4 s^{-1}) and Al (0.15 s^{-1}). The results that $CeO(NO_3)_3^-$ and $PrO(NO_3)_3^-$ do not spontaneously hydrolyze is consistent with the computed energetics for Eqn. 2 in Table III.2.3. The computations predict that $MO(NO_3)_3^-$ for M = La, Lu, Sc, and

Al should spontaneously hydrolyze, as experimentally observed, with the slower rates for the latter two attributed to the small ionic radii of Sc^{3+} and Al^{3+}. The computed exothermicities for those $MO(NO_3)_3^-$ that do hydrolyze differ by 10 $kJ.mol^{-1}$ or less; for oxides that can be considered as $Ln^{III}O(NO_3)_3^-$, the oxidation state of the metal does not change upon hydrolysis and similar rates are thus expected.

III.2.4.3 Computed structures and bonding analysis of the nitrate complexes

For M = La, Ce, Pr, Lu, Sc and Y, the computed ground state structures of $M(NO_3)_4^-$, $MO(NO_3)_3^-$and $M(OH)(NO_3)_3^-$ are shown in Figure III.2.1 with the M-O distances given in Table III.2.2. In the $Ln(NO_3)_4^-$ the four nitrates exhibit bidentate coordination with the Ln-O bond lengths contracting from La to Lu in accord with the lanthanide contraction. The Ln-O distances decrease by 0.22 Å from $La(NO_3)_4^-$ to $Lu(NO_3)_4^-$ (Table III.2.2); the ionic radii decrease by 0.21 Å from La^{3+} to Lu^{3+} (Table III.2.4). The $Ln(OH)(NO_3)_3^-$ (Fig. III.2.1) have three bidentate nitrate ligands and one hydroxide ligand, with the decrease in Ln-OH bond distances from La to Lu of 0.15 Å again in accord with the lanthanide contraction. It is apparent that the $Ln(NO_3)_4^-$ and $Ln(OH)(NO_3)_3^-$ are Ln(III) complexes, which was verified by QTAIM bond analysis. La and Lu hydroxides are in their singlet ground spin state, whereas in $Ce(OH)(NO_3)_4^-$ (doublet spin state) and $Pr(OH)(NO_3)_4^-$ (triplet spin state) the spin density is localized on the metal atoms. The topological properties concerning the M-OH bonds of the $Ln(OH)(NO_3)_4^-$ complexes are summarized in Table S1 (Supporting Information). All hydroxides show electron densities at the M-OH bond critical points (ρ_{BCP}) that are close to 0.10 au., the Laplacian of the electron density at the BCPs, $\nabla^2\rho_{BCP,}$ are positive, and the total electronic energy densities (H_{BCP}) values are very small and negative (between -0.0064 and -0.0237 au.). M-OH topological properties are comparable with the corresponding M-O (nitrates) ρ_{BCP} values, indicating a similar type of interaction. The delocalization indexes (DI) indicate that in all cases the number of electrons shared by the metal and oxygen atoms is very low (< 0.75e). In all cases the metal electronic configuration of the $M(OH)(NO_3)_4^-$ ions is consistent with the Ln(III) oxidation state, and the bonding topologies characteristic of closed-shell interactions (i.e. ionic bonds).

The nature of the $LnO(NO_3)_3^-$ complexes is quite more intriguing in view of the variable IE4 and stabilities of the Ln(IV) oxidation states. The structures of the $LnO(NO_3)_3^-$ are similar, with three bidentate nitrates and one Ln-O linkage. The decrease in the Ln-O nitrate distance, 0.23 Å from La to Lu, is again indicative of ionic bonding to the metal centers. The clear distinction between the structures of the $LnO(NO_3)_3^-$ is that the Ln-O (oxide) distance does not whatsoever correspond to the lanthanide contraction. For $CeO(NO_3)_3^-$ (singlet spin state) the Ce-O distance is 0.33 Å shorter than

the Ce-OH distance in $Ce(OH)(NO_3)_3^-$, indicating significant double bond character and a Ce(IV) oxidation state in the oxide complex. This was corroborated by QTAIM bcp properties; the Ce-O ρ_{BCP} (0.2563 a.u.) and H_{BCP} (-0.2060 a.u.) values indicate the presence of a Ce-O covalent bond. The triplet state $CeO(NO_3)_4^-$ and the open-shell singlet $CeO(NO_3)_4^-$ isomer, which have electronic configurations consistent with a Ce(III) ($4f^1$) metal center interacting with a radical oxygen, were found to be more than 100 kJ.mol^{-1} higher in energy. In contrast, the Ln-O distances in $LaO(NO_3)_3^-$ and $LuO(NO_3)_3^-$ are both ~0.1 Å *longer* than the La-OH distance in $La(OH)(NO_3)_3^-$, clearly indicating that these are not Ln=O double bonds, this in accord with the very high IE4 for La and Lu. The $LaO(NO_3)_3^-$ and $LuO(NO_3)_3^-$ M-O (oxide) topological properties are characteristic of ionic bonds (Table S1). $LaO(NO_3)_3^-$ and $LuO(NO_3)_3^-$ are in their doublet ground spin state, and the spin density is localized on the (oxide) oxygen atoms, confirming that the metal electronic configuration is consistent with a Ln(III) central cation interacting with a radical oxygen. The oxidation states of all of the other $LnO(NO_3)_3^-$ that hydrolyze with similarly high efficiencies are apparently Ln(III) such that hydrolysis proceeds efficiently. The $PrO(NO_3)_3^-$ doublet ground state structure obtained at the level of theory used here (DFT) has a mixed electronic configuration, with a spin density corresponding to 1.5 electrons localized on the metal center, 0.5 electrons of opposite spin localized on the oxygen atom, and a Pr-O oxide bond distance of 1.85 Å. The quartet spin state $Pr^{III}O(NO_3)_3^-$ isomer that comprises two electrons localized on the metal atom ferromagnetically coupled with a radical oxygen atom was found to be 25 kJ.mol^{-1} higher in energy (d_{Pr-O} = 2.22 Å), whereas the antiferromagnetically coupled doublet spin state isomer is 19 kJ.mol^{-1} higher in energy (d_{Pr-O} =2.19 Å) than the GS isomer. The characteristics of the electronic configuration of the $PrO(NO_3)_3^-$ ground state and the presence of low-energy isomers suggest that an accurate description of this species could only be obtained using multireference methodologies, and support the hypothesis of $PrO(NO_3)_3^-$ having a mixed Ln(IV)/Ln(III) character. Based on the very slow hydrolysis rates for $NdO(NO_3)_3^-$ and $TbO(NO_3)_3^-$ it is inferred that these are not Ln(III) complexes. The IE4 of Nd and Tb are intermediate between IE4[Ce] and IE4 for those Ln for which the oxidation state in $LnO(NO_3)_3^-$ is III. We conclude that $NdO(NO_3)_3^-$ and $TbO(NO_3)_3^-$, like $PrO(NO_3)_3^-$, likely exhibit oxidation states intermediate between Ln(III) and Ln(IV). As remarked above, based on comparison with of IE4 for Ce with IE4 for An = Pu, Am and Cm, it is inferred that the oxidation states are An(IV) in the $AnO(NO_3)_3^-$ complexes, in accord with the absence of hydrolysis.

The computed structures of $M(NO_3)_4^-$, $M(OH)(NO_3)_3^-$ and $MO(NO_3)_3^-$ for M = Sc and Y are similar to those for M = Ln, with the M-O bond distances paralleling the M^{3+} radii (Figure III.2.1, Tables III.2.2 and III.2.3). The structures of the Al complexes are different from the others, as seen in Figure III.2.1, evidently a result of steric crowding due to the much smaller radius of Al^{3+}. In contrast to the other

$M(NO_3)_4^-$ with three bidentate nitrate ligands, in the case of $Al(NO_3)_4^-$ there are two bidentate and two monodentate nitrates, with the three Al-O distances as given in Table III.2.2. In both $Al(OH)(NO_3)_3^-$ and $AlO(NO_3)_3^-$ all three nitrates are monodentate with short Al-O distances. The characteristics of the $MO(NO_3)_3^-$ ions (M = Al, Sc, and Y) are similar to those of $LnO(NO_3)_3^-$ ions for which the oxidation state IV is inaccessible, i.e. the M-O distances are longer than the M-OH distances and the spin density is localized on the oxide oxygen atom. In particular, the topological properties of the $MO(NO_3)_3^-$ oxides (M = Al, Sc, and Y) are similar to those of $LaO(NO_3)_3^-$, and $LuO(NO_3)_3^-$ (Table S1).

III.2.5. Conclusions

Tetranitrate ions, $M^{III}(NO_3)_4^-$, were produced by ESI and subjected to low-energy CID in QIT mass spectrometers. The dominant CID products for M = Ce, Pr, Nd, Tb, Pu, Am and Cm are the metal oxide ions, $MO(NO_3)_3^-$. The main CID product for the rest of the lanthanide ions are $M(OH)(NO_3)_3^-$, which are produced in a secondary reaction by hydrolysis of initially formed $MO(NO_3)_3^-$. DFT results confirm that in the case of Ce the most stable $CeO(NO_3)_3^-$ complex contains a Ce-O covalent bond and a metal electronic configuration consistent with a Ce(IV) oxidation state. In contrast, the $LaO(NO_3)_3^-$ and $LuO(NO_3)_3^-$ anion complexes contain metal centers in the Ln(III) oxidation state interacting electrostatically with O^- radical ions. The measured hydrolysis rates for $MO(NO_3)_3^-$ shows that the ions more resistant to hydrolysis are those containing metals with the relatively low IE4 (and IV/III reduction potentials), i.e. the lanthanides Ce, Pr, Tb and Nd, and the actinides Pu, Am and Cm. For $PrO(NO_3)_3^-$ the computations suggest that the oxidation state is intermediate Pr(IV/III). Based on the hydrolysis kinetics, and the IE4 values, we conclude that Nd and Tb, like Pr, are likely intermediate Ln(IV/III) oxidation states, whereas Pu, Am and Cm are likely in the An(IV) oxidation states. Among the $LnO(NO_3)_3^-$ the oxidation state is Ln(IV) only for Ce. Slow hydrolysis for $AlO(NO_3)_3^-$despite favorable energetics reveals a kinetic hindrance for association of water when the ionic radius of the metal ion is small. The computed energetics of the hydrolysis reactions are in agreement with the experimental results. Besides its relevance for a better comprehension of the gas-phase behavior of lanthanides and actinides, this study may be of use for the interpretation of mass spectra of ligated lanthanide, actinide, and other metal complexes.

Acknowledgements

This work was supported by Fundação para a Ciência e a Tecnologia (PhD grant SFRH/BD/70475/2010 to A.F.L.; RNEM - Rede Nacional de Espectrometria de Massa: C2TN-IST and CQE-IST Nodes; projects PTDC/QUI-QUI/108977/2008 and PEst-OE/QUI/UI0100/2011); European Commission (projects

ACSEPT - FP7-Euratom/CP-2007-211267 and ACTINET-I3-FP7-III-232631/JRP17). The work of MCM was supported by Università della Calabria. The work of PXR and JKG was fully supported by the U.S. Department of Energy, Office of Basic Energy Sciences, Heavy Element Chemistry, at LBNL under Contract No. DE-AC02-05CH11231. This research used resources of the National Energy Research Scientific Computing Center (NERSC), which is supported by the Office of Science of the U.S. Department of Energy under Contract No. DE-AC02-05CH11231. The work at the CEA was supported by the DISN/RSTB/RBPCH (Basic Research for Physical Chemistry) Program.

References

(1) NIST Chemistry WebBook, NIST Standard Reference Database Number 69, ed. Linstrom, P. J. and Mallard W. G.; National Institute of Standards and Technology: Gaithersburg, MD, **2014**.

(2) Butkow, K.; Tschassowenny, W., Spectroscopic analysis of the thermal dissociation of $NaNO_2$, $HgNO_3$ and $Ba(NO_3)_2$, *Acta physicochimica URSS* **1936**, *5*, 645.

(3) Wendlandt, W. W., The Thermal properties of inorganic compounds. I. Some mercury(I) and (II) compounds., *Thermochimica Acta* **1974**, *10*, 101.

(4) Mu, J.; Perlmutter, D. D., Thermal-decomposition of metal nitrates and their hydrates, *Thermochimica Acta* **1982**, *56*, 253.

(5) Markov, L.; Petrov, K., Nickel cobalt oxide spinels prepared by thermal-decomposition of nickel(Ii) cobalt(Ii) hydroxide nitrates, *Reactivity of Solids* **1986**, *1*, 319.

(6) Van Driessche, I.; Mouton, R.; Hoste, S., Rapid formation of the $Bi_{2-x}Pb_xSr_xCa_2Cu_3O_y$ high T-c-phase, using spray-dried nitrate precursor powders, *Materials Research Bulletin* **1996**, *31*, 979.

(7) Dash, S.; Kamruddin, M.; Bera, S.; Ajikumar, P. K.; Tyagi, A. K.; Narasimhan, S. V.; Raj, B., Temperature programmed decomposition of uranyl nitrate hexahydrate, *Journal of Nuclear Materials* **1999**, *264*, 271.

(8) Ullal, C. K.; Balasubramaniam, K. R.; Gandhi, A. S.; Jayaram, V., Non-equilibrium phase synthesis in Al_2O_3-Y_2O_3 by spray pyrolysis of nitrate precursors, *Acta Materialia* **2001**, *49*, 2691.

(9) Ehrhardt, C.; Gjikaj, M.; Brockner, W., Thermal decomposition of cobalt nitrato compounds: Preparation of anhydrous cobalt(II)nitrate and its characterisation by Infrared and Raman spectra, *Thermochimica Acta* **2005**, *432*, 36.

(10) Brockner, W.; Ehrhardt, C.; Gjikaj, M., Thermal decomposition of nickel nitrate hexahydrate, $Ni(NO_3)_2.6H_2O$ in comparison to $Co(NO_3)_2.6H_2O$ and $Ca(NO_3)_2.4H_2O$, *Thermochimica Acta* **2007**, *456*, 64.

(11) Karita, R.; Kusaba, H.; Sasaki, K.; Teraoka, Y., Superiority of nitrate decomposition method for synthesis of K_2NiF_4-type La_xSr_2-$xMnO_4$ catalysts, *Catalysis Today* **2007**, *126*, 471.

(12) Sietsma, J. R. A.; Friedrich, H.; Broersma, A.; Versluijs-Helder, M.; van Dillen, A. J.; de Jongh, P. E.; de Jong, K. P., How nitric oxide affects the decomposition of supported nickel nitrate to arrive at highly dispersed catalysts, *Journal of Catalysis* **2008**, *260*, 227.

(13) Marceau, E.; Che, M.; Cejka, J.; Zukal, A., Nickel(II) nitrate vs. acetate: Influence of the precursor on the structure and reducibility of Ni/MCM-41 and Ni/Al-MCM-41 catalysts, *Chemcatchem* **2010**, *2*, 413.

(14) Colombo, D. G.; Gilmer, D. C.; Young, V. G.; Campbell, S. A.; Gladfelter, W. L., Anhydrous metal nitrates as volatile single source precursors for the CVD of metal oxide film, *Chemical Vapor Deposition* **1998**, *4*, 220.

(15) Wu, Z. B.; Okuya, M.; Kaneko, S., Spray pyrolysis deposition of zinc ferrite films from metal nitrates solutions, *Thin Solid Films* **2001**, *385*, 109.

(16) Wang, W. N.; Itoh, Y.; Lenggoro, I. W.; Okuyama, K., Nickel and nickel oxide nanoparticles prepared from nickel nitrate hexahydrate by a low pressure spray pyrolysis, *Materials Science and Engineering: B* **2004**, *111*, 69.

(17) Sietsma, J. R. A.; Meeldijk, J. D.; den Breejen, J. P.; Versluijs-Helder, M.; van Dillen, A. J.; de Jongh, P. E.; de Jong, K. P., The preparation of supported NiO and Co_3O_4 nanoparticles by the nitric oxide controlled thermal decomposition of nitrates, *Angewandte Chemie International Edition* **2007**, *46*, 4547.

(18) Strobel, R.; Pratsinis, S. E., Effect of solvent composition on oxide morphology during flame spray pyrolysis of metal nitrates, *Physical Chemistry Chemical Physics* **2011**, *13*, 9246.

(19) Wendlandt, W. W.; Bear, J. L., Thermal Decomposition of the Heavier Rare-Earth Metal Nitrate Hydrates - Thermobalance and differential thermal analysis studies, *Journal of Inorganic and Nuclear Chemistry* **1960**, *12*, 276.

(20) Kumar, M. D. S.; Srinivasan, T. M.; Subramanian, C.; Ramasamy, P., Synthesis of lanthanum aluminate by thermal decomposition of hydrated nitrates, *Ceramics International* **1997**, *23*, 419.

(21) Nibha; Kapoor, I. P. S.; Singh, G.; Frohlich, R., Preparation, X-ray crystallography and thermolysis of lanthanide metal nitrate complexes with 2,2 '-bipyridine, Part-88, *Journal of Molecular Structure* **2013**, *1034*, 296.

(22) Nibha; Baranwal, B. P.; Singh, G.; Daniliuc, C. G., Synthesis, characterization and thermolysis of lanthanide metal nitrate complexes with 1, 10-phenanthroline, Part-95, *Journal of Rare Earths* **2014**, *32*, 545.

(23) Dill, S.; Meyer, H. J., Synthesis and studies of lanthanide oxide nitrates $LnONO_3$ (Ln = Pr, Nd, and Sm-Yb), *Zeitschrift für Naturforschung B* **2006**, *61*, 11.

(24) Mollah, S.; Pris, A. D.; Johnson, S. K.; Gwizdala, A. B.; Houk, R. S., Identification of metal cations, metal complexes, and anions by electrospray mass spectrometry in the negative ion mode, *Analytical Chemistry* **2000**, *72*, 985.

(25) Li, F. M.; Byers, M. A.; Houk, R. S., Tandem mass spectrometry of metal nitrate negative ions produced by electrospray ionization, *Journal of the American Society for Mass Spectrometry* **2003**, *14*, 671.

(26) Lide, D. R. *CRC Handbook of Chemistry and Physica*; 84 ed.; CRC Press: Boca Raton, Florida, **2003**.

(27) Franski, R.; Sobieszczuk, K.; Gierczyk, B., Mass spectrometric decomposition of $[M_n^+(NO3^-)_{(n+1)}]^-$ anions originating from metal nitrates $M(NO3)_n$, *International Journal of Mass Spectrometry* **2014**, *369*, 98.

(28) Ricks, A. M.; Gagliardi, L.; Duncan, M. A., Uranium oxo and superoxo cations revealed using infrared spectroscopy in the gas phase, *Journal of Physical Chemistry Letters* **2011**, *2*, 1662.

(29) Huang, W.; Xu, W. H.; Su, J.; Schwarz, W. H. E.; Li, J., Oxidation states, geometries, and electronic structures of plutonium tetroxide PuO_4 isomers: Is octavalent Pu viable?, *Inorganic Chemistry* **2013**, *52*, 14237.

(30) Groenewold, G. S.; Oomens, J.; de Jong, W. A.; Gresham, G. L.; McIlwain, M. E.; Van Stipdonk, M. J., Vibrational spectroscopy of anionic nitrate complexes of UO_2^{2+} and Eu^{3+} isolated in the gas phase, *Physical Chemistry Chemical Physics* **2008**, *10*, 1192.

(31) Oomens, J.; Myers, L.; Dain, R.; Leavitt, C.; Pham, V.; Gresham, G.; Groenewold, G.; Van Stipdonk, M., Infrared multiple-photon photodissociation of gas-phase group II metal-nitrate anions, *International Journal of Mass Spectrometry* **2008**, *273*, 24.

(32) Schröder, D.; de Jong, K. P.; Roithová, J., Gas-Phase Model Studies Relevant to the Decomposition of Transition-Metal Nitrates $M(NO3)_2$ (M =Co, Ni) into metal-oxo species, *European Journal of Inorganic Chemistry* **2009**, 2121.

(33) Schröder, D.; Holthausen, M. C.; Schwarz, H., Radical-like activation of alkanes by the ligated copper oxide cation (Phenanthroline)CuO, *Journal of Physical Chemistry B* **2004**, *108*, 14407.

(34) Berthon, L.; Zorz, N.; Gannaz, B.; Lagrave, S.; Retegan, T.; Fermvik, A.; Ekberg, C., Use of electrospray ionization mass spectrometry for the characterization of actinide complexes in solution, *IOP Conference Series: Materials Science and Engineering* **2010**, *9*, 012059.

(35) Rios, D.; Rutkowski, P. X.; Shuh, D. K.; Bray, T. H.; Gibson, J. K.; Van Stipdonk, M. J., Electron transfer dissociation of dipositive uranyl and plutonyl coordination complexes, *Journal of Mass Spectrometry* **2011**, *46*, 1247.

(36) Rutkowski, P. X.; Michelini, M. C.; Bray, T. H.; Russo, N.; Marçalo, J.; Gibson, J. K., Hydration of gas-phase ytterbium ion complexes studied by experiment and theory, *Theoretical Chemistry Accounts* **2011**, *129*, 575.

(37) Gronert, S., Estimation of effective ion temperatures in a quadrupole ion trap, *Journal of the American Society for Mass Spectrometry* **1998**, *9*, 845.

(38) Frisch, M. J. Gaussian **2009** (revision B01). See Supporting Information for full citation.

(39) Becke, A. D., Density-functional thermochemistry .3. The role of exact exchange, *Journal of Chemical Physics* **1993**, *98*, 5648.

(40) Lee, C. T.; Yang, W. T.; Parr, R. G., Development of the Colle-Salvetti correlation-energy formula into a functional of the electron-density, *Physical Review B* **1988**, *37*, 785.

(41) Küchle, W.; Dolg, M.; Stoll, H.; Preuss, H., Energy-adjusted pseudopotentials for the actinides - Parameter sets and test calculations for thorium and thorium monoxide, *Journal of Chemical Physics* **1994**, *100*, 7535.

(42) Cao, X. Y.; Dolg, M.; Stoll, H., Valence basis sets for relativistic energy-consistent small-core actinide pseudopotentials, *Journal of Chemical Physics* **2003**, *118*, 487.

(43) Krishnan, R.; Binkley, J. S.; Seeger, R.; Pople, J. A., Self-consistent molecular-orbital methods .20. Basis set for correlated wave-functions, *Journal of Chemical Physics* **1980**, *72*, 650.

(44) Blaudeau, J. P.; McGrath, M. P.; Curtiss, L. A.; Radom, L., Extension of Gaussian-2 (G2) theory to molecules containing third-row atoms K and Ca, *Journal of Chemical Physics* **1997**, *107*, 5016.

(45) Clark, T.; Chandrasekhar, J.; Spitznagel, G. W.; Schleyer, P. V., Efficient diffuse function-augmented basis-sets for anion calculations .3. The 3-21+G basis set for 1st-row elements, Li-F, *Journal of Computational Chemistry* **1983**, *4*, 294.

(46) Norman, J. G.; Ryan, P. B.; Noodleman, L., Electronic-structure of 2-Fe ferredoxin models by X-alpha valence bond theory, *Journal of the American Chemical Society* **1980**, *102*, 4279.

(47) Noodleman, L., Valence bond description of anti-ferromagnetic coupling in transition-metal dimers, *Journal of Chemical Physics* **1981**, *74*, 5737.

(48) Ciofini, I.; Daul, C. A., DFT calculations of molecular magnetic properties of coordination compounds, *Coordination Chemistry Reviews* **2003**, *238*, 187.

(49) Neese, F., Prediction of molecular properties and molecular spectroscopy with density functional theory: From fundamental theory to exchange-coupling, *Coordination Chemistry Reviews* **2009**, *253*, 526.

(50) Bader, R. F. W. *Atoms in Molecules: A Quantum Theory*; Oxford University Press: Oxford, **1990**.

(51) Keith, T. A., AIMALL (version 13.05.06), **2013**, aim.tkgristmill.com.

(52) Gong, Y.; Hu, H. S.; Rao, L. F.; Li, J.; Gibson, J. K., Experimental and theoretical studies on the fragmentation of gas-phase uranyl-, neptunyl-, and plutonyl-diglycolamide complexes, *Journal of Physical Chemistry A* **2013**, *117*, 10544.

(53) Bratsch, S. G.; Lagowski, J. J., Lanthanide thermodynamic predictions .7. Thermodynamics of 2+, 3+, and 4+ aquo ions and standard electrode-potentials at 298.15-K, *Journal of Physical Chemistry* **1985**, *89*, 3317.

(54) Bratsch, S. G.; Lagowski, J. J., Actinide thermodynamic predictions. Thermodynamics of compounds and aquo ions of the 2+, 3+, and 4+ oxidation states and standard electrode-potentials at 298.15 K, *Journal of Physical Chemistry* **1986**, *90*, 307.

(55) Konings, R. J. M.; Morss, L. R.; Fuger, J. In *The Chemistry of the Actinide and Transactinide Elements*; Morss, L. R., Edelstein, N. M., Fuger, J., Eds.; Springer: Dordrecht, The Netherlands, **2006**; Vol. 4, p 2113.

(56) Shannon, R. D.; Prewitt, C. T., Effective ionic radii in oxides and fluorides, *Acta Crystallographica Section B* **1969**, *B 25*, 925.

Supporting information

Complete Reference 38:

Gaussian 09, Revision B.01, Frisch, M. J.; Trucks, G. W.; Schlegel, H. B.; Scuseria, G. E.; Robb, M. A.; Cheeseman, J. R.; Scalmani, G.; Barone, V.; Mennucci, B.; Petersson, G. A.; Nakatsuji, H.; Caricato, M.; Li, X.; Hratchian, H. P.; Izmaylov, A. F.; Bloino, J.; Zheng, G.; Sonnenberg, J. L.; Hada, M.; Ehara, M.; Toyota, K.; Fukuda, R.; Hasegawa, J.; Ishida, M.; Nakajima, T.; Honda, Y.; Kitao, O.; Nakai, H.; Vreven, T.; Montgomery, J. A., Jr.; Peralta, J. E.; Ogliaro, F.; Bearpark, M.; Heyd, J. J.; Brothers, E.; Kudin, K. N.; Staroverov, V. N.; Kobayashi, R.; Normand, J.; Raghavachari, K.; Rendell, A.; Burant, J. C.; Iyengar, S. S.; Tomasi, J.; Cossi, M.; Rega, N.; Millam, M. J.; Klene, M.; Knox, J. E.; Cross, J. B.; Bakken, V.; Adamo, C.; Jaramillo, J.; Gomperts, R.; Stratmann, R. E.; Yazyev, O.; Austin, A. J.; Cammi, R.; Pomelli, C.; Ochterski, J. W.; Martin, R. L.; Morokuma, K.; Zakrzewski, V. G.; Voth, G. A.; Salvador, P.; Dannenberg, J. J.; Dapprich, S.; Daniels, A. D.; Farkas, Ö.; Foresman, J. B.; Ortiz, J. V.; Cioslowski, J.; Fox, D. J. Gaussian, Inc., Wallingford CT, 2009.

Table S1. Electron density (ρ_{BCP}), Laplacian of electron density ($\nabla^2\rho_{BCP}$), and total energy density (H_{BCP}) for the M-OH BCP of $M(OH)(NO_3)_3^-$ and the M-O BCP of $MO(NO_3)_3^-$ complexes; M = La, Ce, Pr, Lu, Al, Sc, and Y.[a, b,c]

$M(OH)(NO_3)_3^-$	La (1)	Ce (2)	Pr (3)	Lu (1)	Al (1)	Sc (1)	Y (1)
ρ_{BCP}	0.0930 [0.0938]	0.0942 [0.0958]	0.0956	0.1065	0.0994 [0.1068]	0.1105	0.0865
$\nabla^2\rho_{BCP}$	0.3712 [0.3770]	0.4005 [0.4041]	0.4169	0.5714	0.8060 [0.7642]	0.6360	0.4777
H_{BCP}	-0.0191 [-0.0193]	-0.0172 [-0.0191]	-0.0176	-0.0237	0.0013 [-0.0014]	-0.0104	-0.0064
DI(M,O)	0.715 [0.709]	0.733 [0.725]	0.736	0.618	0.341 [0.330]	0.680	0.595
$d_{M\text{-}OH}$[d]	2.15	2.13	2.12	2.00	1.72	1.89	2.05
$MO(NO_3)_3^-$	La (2)	Ce (1)	Pr (2)[e]	Lu (2)	Al (2)	Sc (2)	Y (2)
ρ_{BCP}	0.0893 [0.0900]	0.2563 [0.2576]	0.2223	0.1001	0.0926 [0.0993]	0.1059	0.0806
$\nabla^2\rho_{BCP}$	0.2526 [0.2532]	0.2645 [0.2380]	0.3241	0.4089	0.6813 [0.6443]	0.4775	0.3360
H_{BCP}	-0.0199 [-0.0210]	-0.2060 [-0.2126]	-0.1519	-0.0242	-0.0011 [-0.0015]	-0.0127	-0.0073
DI(M,O)	0.693 [0.682]	1.946 [1.920]	1.779	0.598	0.343 [0.329]	0.671	0.585
$d_{M\text{-}O}$[d]	2.26	1.80	1.85	2.09	1.77	1.96	2.16

[a]In atomic units. [b] Spin multiplicity in parentheses. [c]With the aim of analyzing the basis sets effect on AIM properties, single point B3LYP/SDD(Ln):6-311++(2df,2dp) (rest of the atoms) were performed on the B3LYP/SDD(An):6-311++(d,p) optimized geometries, on selected cases. The AIM properties at this level of theory are reported in square brackets. [d]Metal-oxygen bond lengths in angstroms. [e] The antiferromagnetically coupled doublet spin state isomer (19 kJ.mol^{-1} higher in energy, $d_{Pr\text{-}O}$ = 2.19Å) has topological characteristics similar to those of $LaO(NO_3)_3^-$ and $LuO(NO_3)_3^-$ oxides.

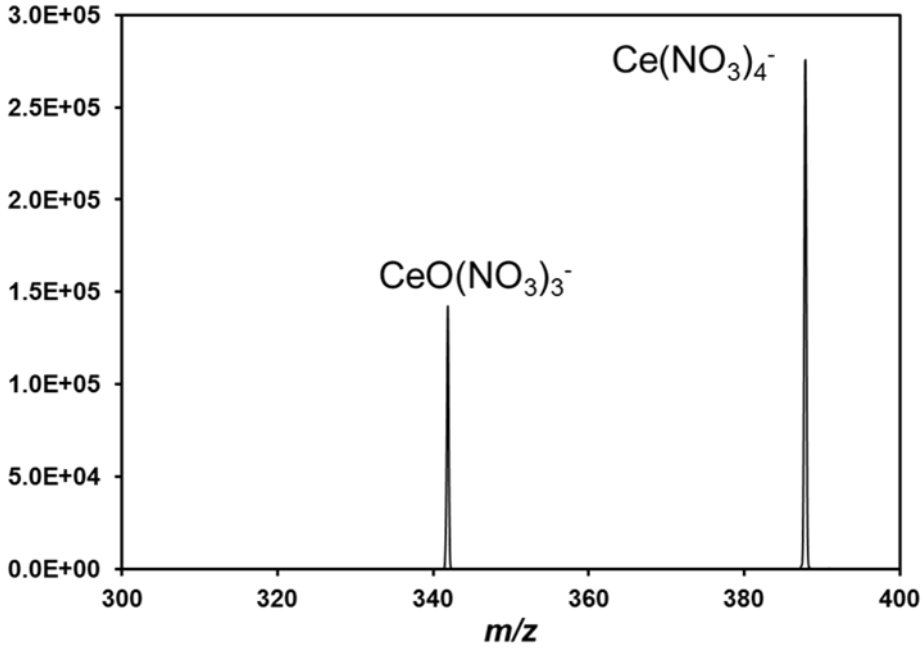

Figure S1. CID mass spectrum of $Ce(NO_3)_4^-$ (C2TN-IST).

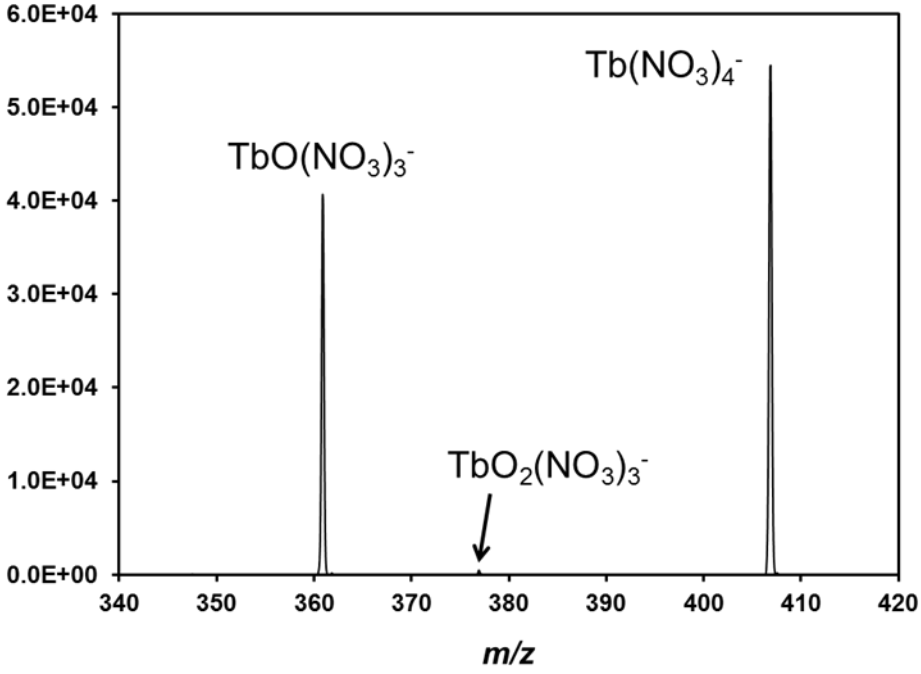

Figure S2. CID mass spectrum of $Tb(NO_3)_4^-$ (C2TN-IST).

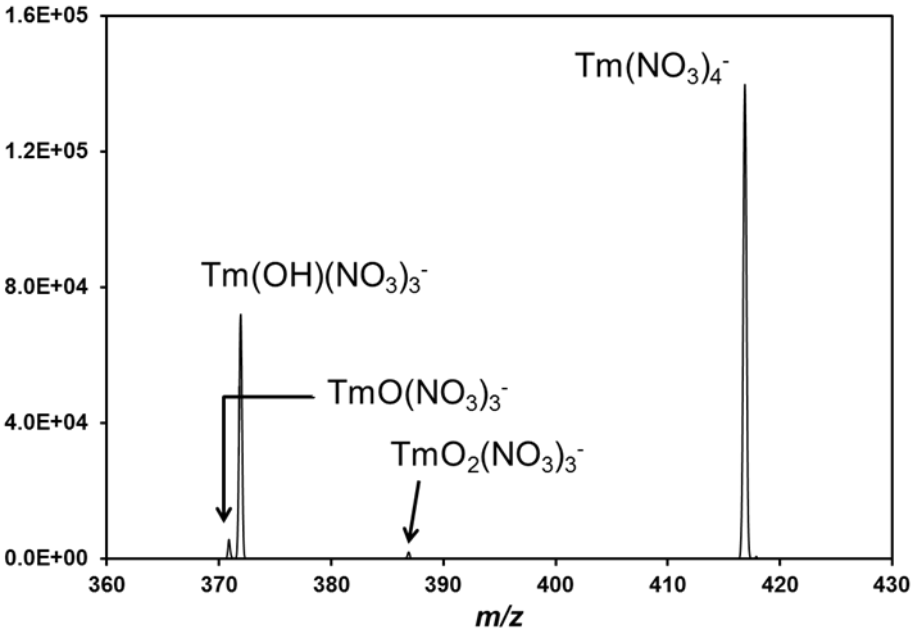

Figure S3. CID mass spectrum of $Tm(NO_3)_4^-$ (C2TN-IST).

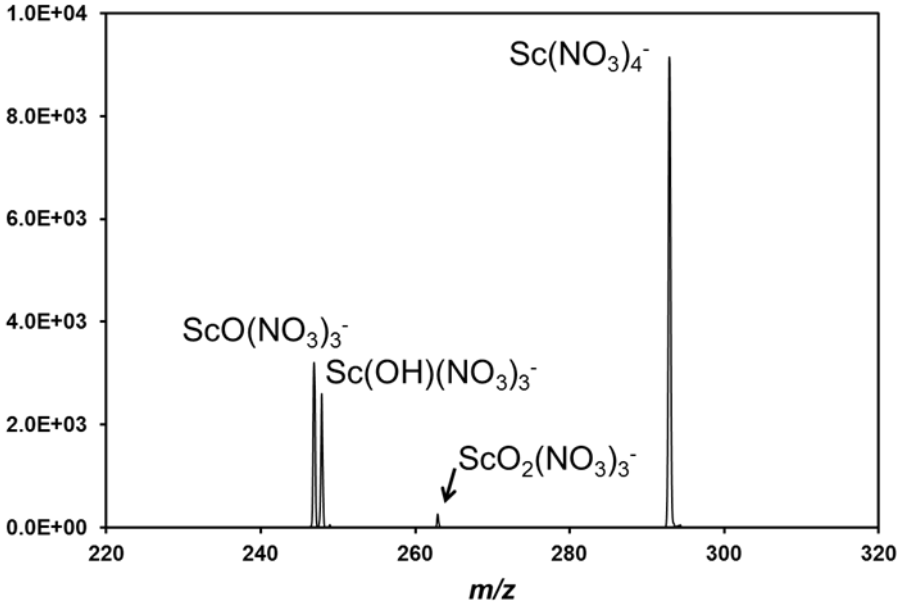

Figure S4. CID mass spectrum of $Sc(NO_3)_4^-$ (C2TN-IST).

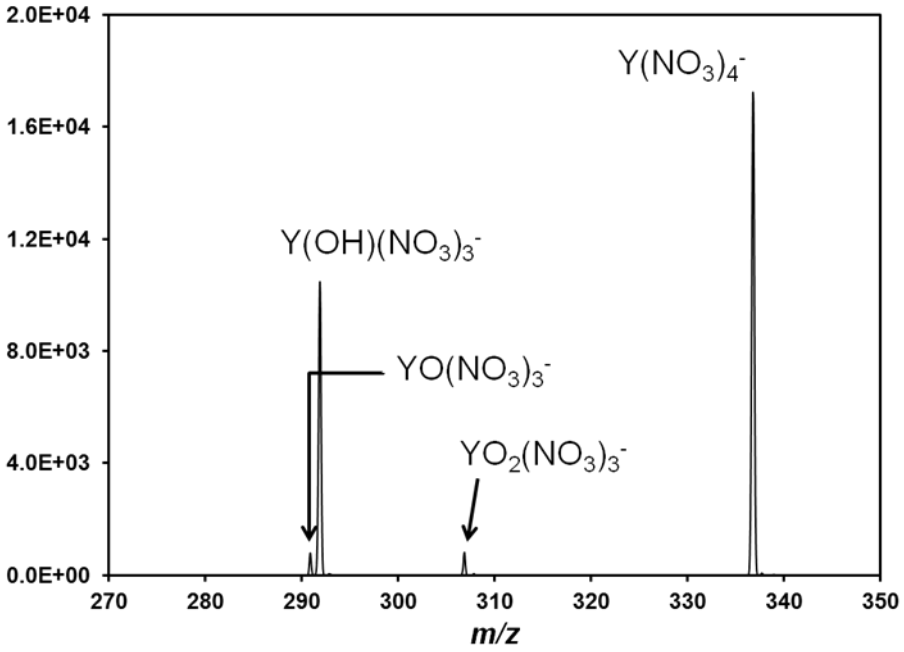

Figure S5. CID mass spectrum of $Y(NO_3)_4^-$ (C2TN-IST).

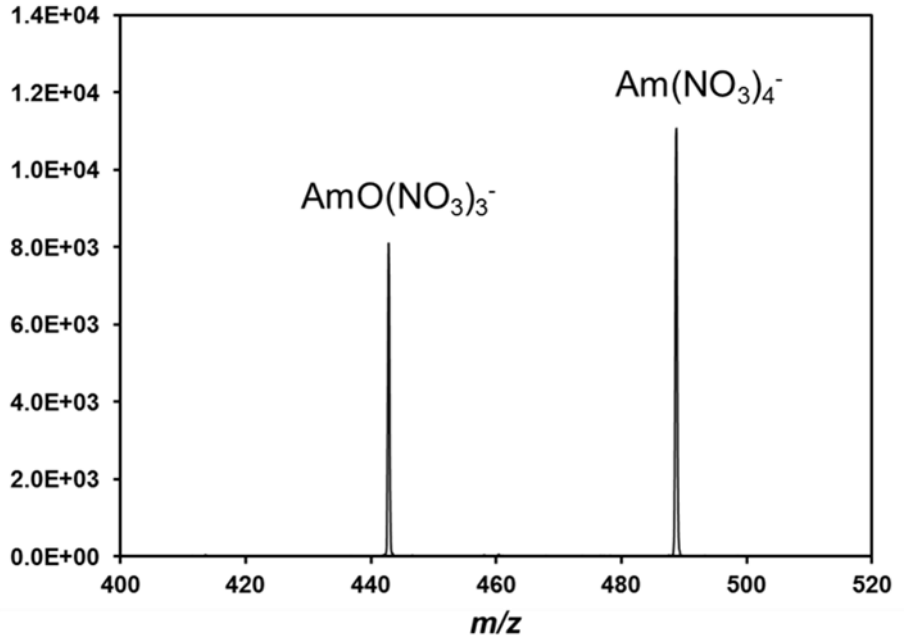

Figure S6. CID mass spectrum of $Am(NO_3)_4^-$ (CEA).

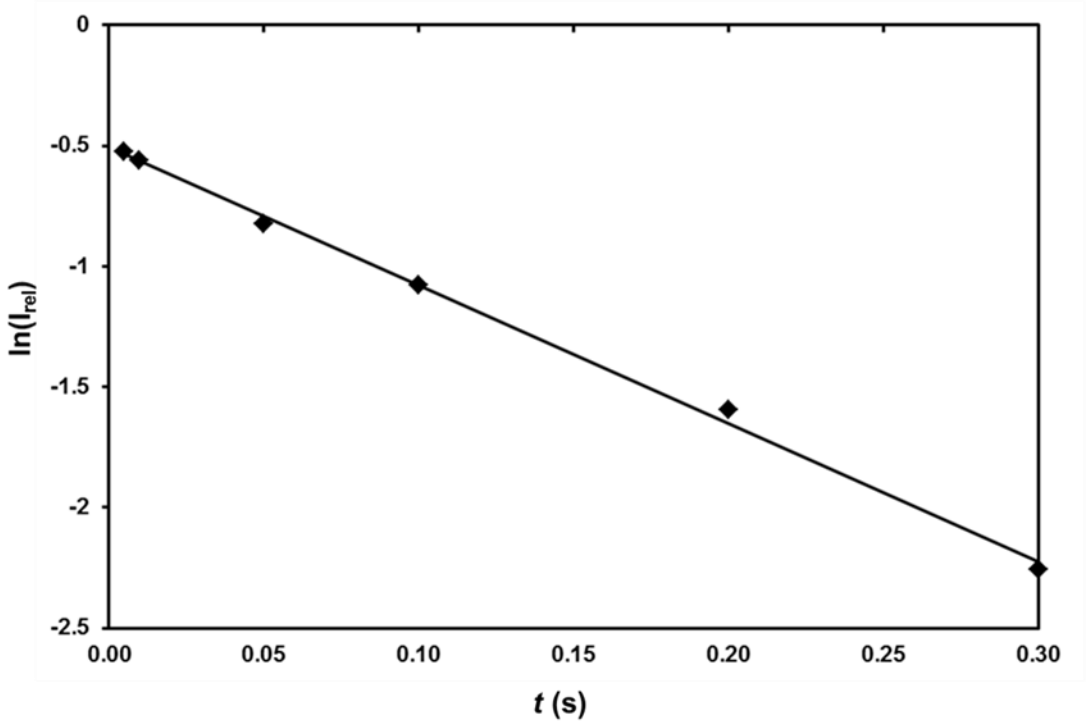

Figure S7. Kinetic plot from the reaction of isolated $HoO(NO_3)_3^-$ with H_2O to form $Ho(OH)(NO_3)_3^-$, obtained at CQE-IST ($R^2 = 0.9977$).

III.2 B - Synthesis and hydrolysis of other gas-phase lanthanide and actinide oxide nitrate complexes

III.2.1. Results and discussion

III.2.1.1 Fragmentation of $MO(NO_3)_3^-$ ions

CID experiments with several $MO(NO_3)_3^-$ ions were performed and the results are presented in Table III.2.B1 and summarized in Eq. 1 and 2. Schemes 1-5 present an overall picture of the CID and hydration/hydrolysis pathways of the studied metal nitrate anions.

$$MO(NO_3)_3^- \rightarrow MO_2(NO_3)_2^- + NO_2 \quad (1)$$

$$MO_2(NO_3)_2^- + H_2O \rightarrow MO_2(H_2O)(NO_3)_2^- \text{ or } M(OOH)(OH)(NO_3)_2^- \quad (2)$$

Table III.2.B1 Collision induced dissociation of $MO(NO_3)_3^-$ ions.*

M	Product ion	
	$MO_2(NO_3)_2^-$	**$M(O_2)(H_2O)(NO_3)_2^-$** or **$M(OOH)(OH)(NO_3)_2^-$**
La	0 *97*	100 *3*
Ce	100 *100*	0 *0*
Pr	100 *100*	0 *0*
Tb	0 *86*	100 *14*
Ho	0 *59*	100 *41*
Lu	0 *48*	100 *52*
Sc	100 *100*	0 *0*
Y	0 *87*	100 *13*
Pu	100	0
Am	100	0
Cm	100	0

*The relative intensity of the observed product ions is in %; the results in regular font were obtained at C2TN-IST and the ones in italic at CQE-IST; the results for Pu and Cm were obtained at LBNL, and those for Am at CEA.

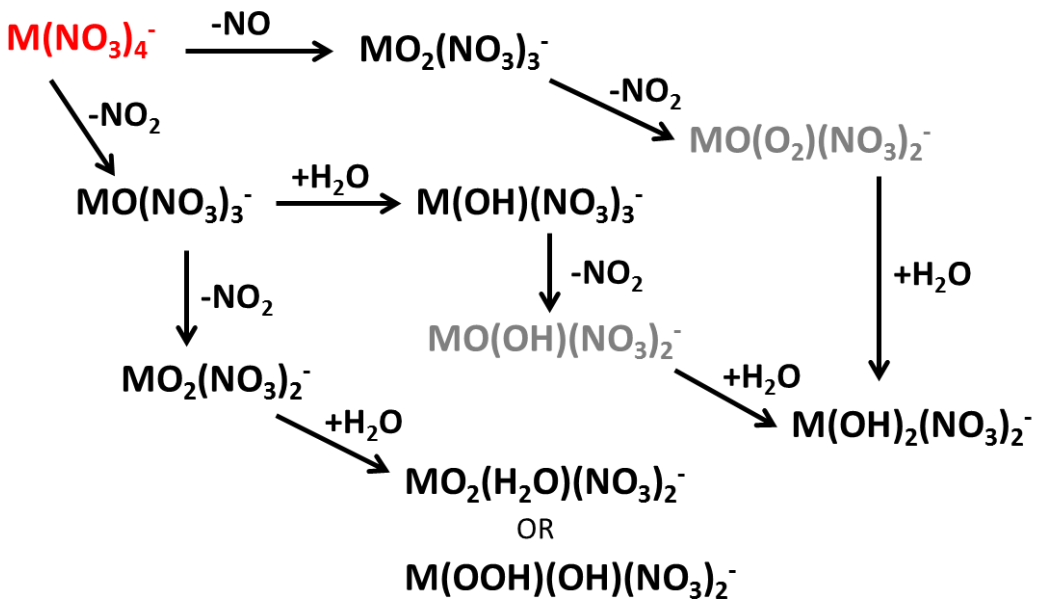

Scheme 1. CID and hydration/hydrolysis pathways for the trivalent rare earth nitrate anions except scandium (C2TN-IST; species observed in the ESI mass spectra in red; species not observed in the CID mass spectra in grey).

As in the case of CID of the tetranitrate anions, elimination of NO_2 appears to be main pathway. In the experiments of Houk and co-workers,[1] double elimination of NO_2 was also observed to produce $MO_2(NO_3)_{n-2}^-$ ions from $M(NO_3)_n^-$. In the present experiments, depending on the water pressure in the ion traps and, therefore, especially in the one at C2TN-IST, fast hydration or hydrolysis occurred for some of the metal ions. It appears again that the metals with more stable +4 oxidation states survive hydration or hydrolysis, namely Ce, Pr, Pu, Am, and Cm. The case of Sc is intriguing but as before steric effects may be determining the non-occurrence of hydration or hydrolysis (Scheme 2).

In Table II.2.1, $MO(NO_3)_3^-$ ions also appear as minor CID products for those metals that preferentially form $M(OH)(NO_3)_3^-$ in the QIT of C2TN-IST, namely, La, Sm, Gd, Dy, Ho, Er, Tm, Yb, Lu, and Y. If very fast hydrolysis is occurring for the $MO(NO_3)_3^-$ ions, it seems odd that a fraction survives the process to be still apparent in the CID spectra. It is possible to envisage at least one isomer of the oxo-trinitrate complex, a superoxo-nitrito-dinitrate complex $M(O_2)(NO_2)(NO_3)_2^-$, in which the +3 oxidation state of the metal ion is retained and hydrolysis could be not favorable. This would be the case of the La, Ho, Lu, and Y ions in Table III.2.B1. The suggested formulation would still allow the CID process to yield $MO_2(NO_3)_2^-$ ions, followed by fast hydration or hydrolysis.

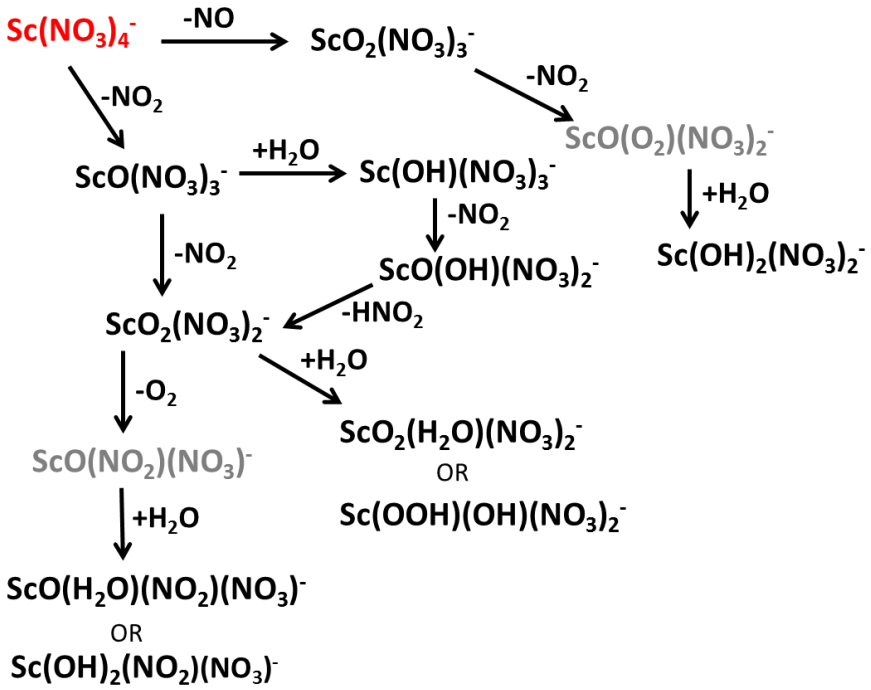

Scheme 2. CID and hydration/hydrolysis pathways for scandium nitrate anions (C2TN-IST; species observed in the ESI mass spectra in red; species not observed in the CID mass spectra in grey).

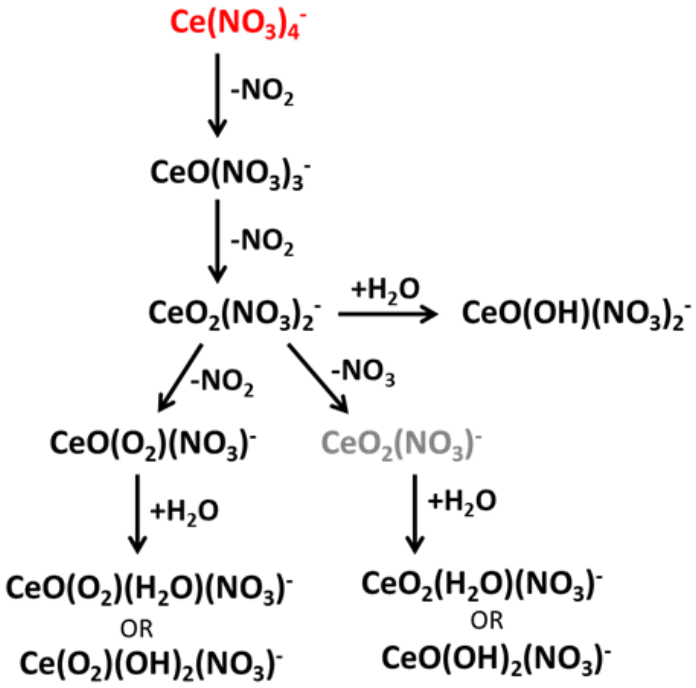

Scheme 3. CID and hydration/hydrolysis pathways for cerium nitrate anions (C2TN-IST; species observed in the ESI mass spectra in red; species not observed in the CID mass spectra in grey).

III.2.1.2 Fragmentation and hydrolysis of $MO_2(NO_3)_2^-$ ions

In the $MO_2(NO_3)_2^-$ CID products of $MO(NO_3)_3^-$ ions, the O_2 ligand could be a peroxide, O_2^{2-}, with the metals in a stable +3 oxidation state. A superoxide ligand, O_2^-, would leave the metal in $MO_2(NO_3)_2^-$ ions in an unstable +2 oxidation state. In either case, hydrolysis could be favorable. As the $MO_2(NO_3)_2^-$ ions seem to be more stable for Ce, Pr, and the actinides, a dioxo ion with one O^{2-} and one O^- could also be formed, with the metals in the +4 oxidation state. In the case of Pu and Am, with higher oxidation states available, it is also conceivable that a dioxo complex with two O^{2-} is formed, corresponding to a +5 oxidation state of the metal. The possible hydration product, $MO_2(H_2O)(NO_3)_2^-$, would have the same implications as the $MO_2(NO_3)_2^-$ precursor ion regarding oxidation state. An hydrolysis product like $M(OOH)(OH)(NO_3)_2^-$ could set the product ions in a +3 oxidation sate.

CID of $MO_2(NO_3)_2^-$ ions (Schemes 1-5) and their reactions with H_2O were examined for the cases of Ce, Pr, and Sc at C2TN-IST, Pu at LBNL, and Am at CEA; $CmO_2(NO_3)_2^-$ ions could not be isolated for further study. For these metals, reaction with water had not been observed during CID of the $MO(NO_3)_3^-$ ions (Table III.2.B1). Remarkably, for Pu, Am, and Pr, no reaction with H_2O was observed, while $CeO(OH)(NO_3)_2^-$ ions very slowly formed (k = 0.061 s^{-1}) in the case of Ce (Scheme 3). The reaction product found in the case of Ce seems to be a manifestation of the stability of the +4 oxidation state and probably comprises an O^{2-} ligand. In the case of Pu and Am, the absence of reaction with water could be an indication that the $AnO_2(NO_3)_2^-$ ions are in fact dioxo species. In the case of Sc, an undeniably trivalent metal, slow formation (k = 0.29 s^{-1}) of the hydration or hydrolysis product as in Eq. 1 was obtained.

CID of $MO_2(NO_3)_2^-$ ions, in the examined cases of Pu, Am, Ce, and Sc, showed the formation of different species which we tentatively assign as: $Pu^{VI}O_2(OH)_2(NO_3)^-$ (100%) from NO_2 loss and fast hydration/hydrolysis; $Am^{V}O_2(OH)(NO_3)^-$ (100%) from NO_2 loss and fast hydrolysis; $Sc^{III}O(H_2O)(NO_2)(NO_3)^-$ or $Sc^{III}(OH)_2(NO_2)(NO_3)^-$ from O_2 loss and fast hydration/hydrolysis; $Ce^{IV}O(O_2)(NO_3)^-$ (15%), $Ce^{IV}O(O_2)(H_2O)(NO_3)^-$ or $Ce^{IV}(O_2)(OH)_2(NO_3)^-$ (25%), and $Ce^{IV}O_2(H_2O)(NO_3)^-$ or $Ce^{IV}O(OH)_2(NO_3)^-$ (60%), from NO_2 loss, NO_2 loss plus fast hydration/hydrolysis, and NO_3 loss plus fast hydration/hydrolysis, respectively. Interestingly, Pu and Ce form species with identical compositions but most probably corresponding to different ligations of the oxygen atoms. A noticeable difference is found between the products formed for Pu and Am, probably corresponding to +6 and +5 oxidation states, respectively, in agreement with the relative stabilities in solution.[2] The loss of O_2 observed in the case of Sc could be an indication that the O_2 ligand in the precursor ion is peroxide.

III.2.1.3 Fragmentation and hydrolysis of other rare earth nitrate anions

CID and reactivity with water were also examined for other metal nitrate anions. $Eu(NO_3)_3^-$, formed in CID of $Eu(NO_3)_4^-$ and the only divalent metal species observed in the present experiments, did not react with water in the C2TN-IST ion trap, revealing the high stability of Eu(II) species in the gas phase. Nevertheless, CID of $Eu(NO_3)_3^-$ yielded as sole product $Eu(OH)_2(NO_3)_2^-$, a Eu(III) species that most probably resulted from NO_2 loss to yield $EuO(NO_3)_2^-$ ions that underwent very fast water addition and hydrolysis.

The $MO_2(NO_3)_3^-$ ions, also formed in the initial CID of $M(NO_3)_4^-$ by loss of NO (see previous section), did not react with water in the C2TN-IST ion trap, as examined for the cases of La, Tb, Ho, Er, Lu, Sc, and Y. CID of these $MO_2(NO_3)_3^-$ ions, as studied for the same metals, led to the formation of $M(OH)_2(NO_3)_2^-$ ions that could result from NO_2 loss followed by very fast hydrolysis, as hypothesized in Eq. 3 and 4 below.

$$MO_2(NO_3)_3^- \rightarrow MO(O_2)(NO_3)_2^- + NO_2 \quad (3)$$

$$MO(O_2)(NO_3)_2^- + H_2O \rightarrow M(OH)_2(NO_3)_2^- + O_2 \quad (4)$$

$M(OH)(NO_3)_3^-$ ions formed during CID of the initial $M(NO_3)_4^-$ ions (see previous section) did not react with H_2O in the C2TN-IST ion trap, as examined for M = La, Ho, Lu, and Y. This is not an unexpected result as the metal ions are in the +3 oxidation state and bonded to stable ligands; as indicated before, $M(NO_3)_4^-$ ions did not react with water. CID of the $M(OH)(NO_3)_3^-$ ions, also examined for M = La, Ho, Lu, and Y, yielded $M(OH)_2(NO_3)_2^-$ ions by apparent sequential NO_2 loss and fast hydrolysis. CID experiments with the Sc analogue remarkably produced $ScO(OH)(NO_3)_2^-$ (70%) and $ScO_2(NO_3)_2^-$ (30%), corresponding to loss of NO_2 and HNO_2, respectively; as in other cases, hydrolysis of species involving the small Sc^{3+} ion seems to be kinetically hindered.

III.2.1.4 Fragmentation and hydrolysis of other actinide nitrate anions

While the (mostly) trivalent rare earth metals yielded exclusively $M(NO_3)_4^-$ by ESI, two of the actinides referenced so far, Pu and Am, presented a more diverse ESI behavior (Cm formed only $M(NO_3)_4^-$).

Americium. In aqueous solutions, Am may exhibit the III to VI oxidation states,[2] and the ESI mass spectrum of Am nitrate from a water/ethanol solution, besides $Am^{III}(NO_3)_4^-$, showed the presence of $Am^{IV}O(NO_3)_3^-$ and $Am^{V}O_2(NO_3)_2^-$. The CID and hydrolysis of $An^{III}(NO_3)_4^-$, $An^{IV}O(NO_3)_3^-$, and

$An^{V}O_2(NO_3)_2^-$ ions, for An = Pu and Am, were described in the previous sections (CID in Scheme 4); no differences were found between analogous ions formed by ESI and CID.

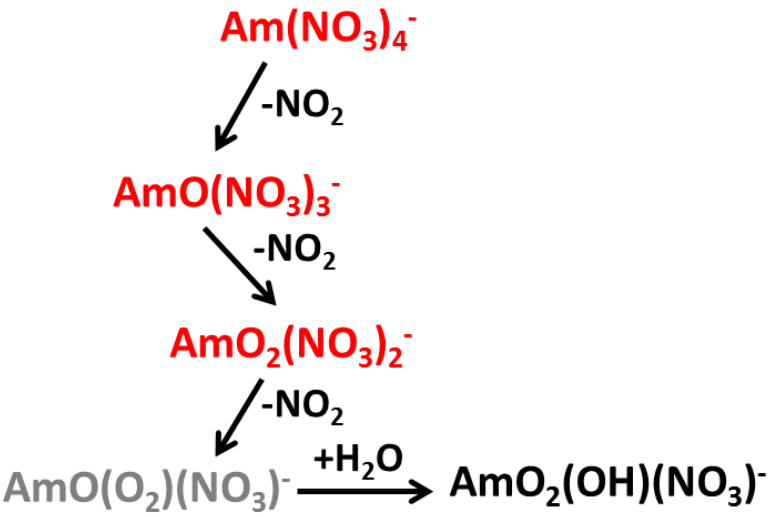

Scheme 4. CID and hydration/hydrolysis pathways for americium nitrate anions (CEA; species observed in the ESI mass spectra in red; species not observed in the CID mass spectra in grey).

Plutonium. The solution chemistry of Pu is complex and five oxidation states (III to VII) may be present simultaneously in water, with the more common oxidation states being III to VI.[3] The ESI mass spectrum of Pu nitrate from a water/isopropanol solution, besides $Pu^{III}(NO_3)_4^-$, showed the presence of $Pu^{IV}(NO_3)_5^-$, $Pu^{V}O_2(NO_3)_2^-$, and $Pu^{VI}O_2(NO_3)_3^-$, that is, the other stable oxidation states. CID of $Pu^{IV}(NO_3)_5^-$ (Scheme 5), examined at LBNL, showed the sole formation of $PuO_2(NO_3)_3^-$ by loss of N_2O_4 or $2NO_2$. This unusual fragmentation, as compared with the ones previously described that typically involved single NO_2 loss, indicates that the product is probably the stable dioxo ion $Pu^{VI}O_2(NO_3)_3^-$. CID of $PuO_2(NO_3)_3^-$ produced major $PuO_3(NO_3)_2^-$ by NO_2 loss and minor $PuO_2(NO_3)_2^-$ by NO_3 loss. Although Pu(VII) may be accessible,[3-9] other structures for $PuO_3(NO_3)_2^-$ with lower Pu oxidation states can be envisioned; $PuO_2(NO_3)_2^-$ was described in the previous section. CID of $PuO_3(NO_3)_2^-$ yielded $PuO_2(O_2)(NO_3)^-$ as major product by NO_2 loss; this ion could correspond to a dioxo-peroxide that would leave Pu in the +6 oxidation state. Minor CID products were $PuO(NO_3)_2^-$, a Pu^{III} species, and previously observed $PuO_2(NO_3)_2^-$. Recently, Maurice et al.[10] have reported a gas-phase study based on experimental and theoretical details on the possibility of the formation of a heptavalent species of plutonium nitrates. CID of $Pu^{VI}O_2(NO_3)_3^-$ resulted in NO_2 elimination to yield $PuO_3(NO_3)_2^-$, in which the oxidation state of plutonium could be VII, a known oxidation state in condensed phase but not yet in the gas phase. Nevertheless, DFT calculations confirmed that

the nature of these species is essentially a plutonyl(VI) core, $Pu^{VI}O_2^{2+}$, coordinated in the equatorial plane by two nitrate ligands and one radical oxygen atom.

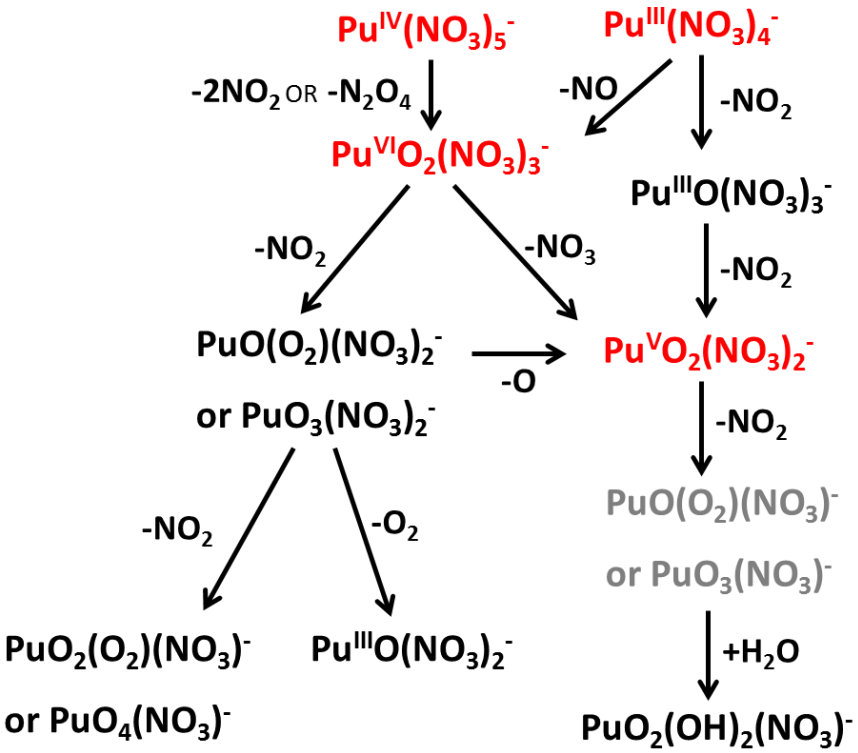

Scheme 5. CID and hydration/hydrolysis pathways for plutonium nitrate anions (LBNL; species observed in the ESI mass spectra in red; species not observed in the CID mass spectra in grey). In agreement with the recently published results by Maurice et al.[10]

Thorium. CID of $Th^{IV}(NO_3)_5^-$ (Scheme 6), easily produced by ESI of an ethanol solution of Th nitrate, was examined at C2TN-IST for comparison with $Pu^{IV}(NO_3)_5^-$. Different products were observed: major $Th(OH)(NO_3)_4^-$ and $Th(OH)_2(NO_3)_3^-$, corresponding to NO_2 and $2NO_2$ or N_2O_4 losses to form $ThO(NO_3)_4^-$ and $ThO_2(NO_3)_3^-$, respectively, followed by fast hydration/hydrolysis; and minor $ThO_2(NO_3)_4^-$, which corresponds to NO loss. Unlike Pu, Th species apparently tend to retain the +4 oxidation state, leading to fast hydrolysis processes in the QIT of C2TN-IST. Similarly to the case of the trivalent rare earth ions, for which the $MO(NO_3)_3^-$ formed by CID of $M^{III}(NO_3)_4^-$ rapidly hydrolyzed to yield $M^{III}(OH)(NO_3)_3^-$, CID of $Th^{IV}(NO_3)_5^-$ generated $Th(OH)(NO_3)_4^-$ by sequential CID and hydrolysis. Interestingly, hydrolysis of $ThO_2(NO_3)_3^-$, presumably the peroxide so that Th retains the +4 oxidation state, led to $Th(OH)_2(NO_3)_3^-$, while the seemingly equivalent $MO_2(NO_3)_2^-$ ions, described before (see Table II.2.B1), did not produce $M(OH)_2(NO_3)_2^-$ ions. CID of $Th(OH)(NO_3)_4^-$ also yielded $Th(OH)_2(NO_3)_3^-$, again by fast sequential NO_2 loss and hydrolysis. CID of the $ThO_2(NO_3)_4^-$ ions formed as minor products in CID of $Th^{IV}(NO_3)_5^-$, and probably involving a superoxide ligand to

maintain the +4 oxidation state of Th, led to $ThO_2(NO_3)_3^-$, presumably the peroxide, and $Th(OH)_2(NO_3)_3^-$, its hydrolysis product. CID of the $ThO_2(NO_3)_3^-$ ions produced $ThO_2(OH)_2(NO_3)_2^-$, apparently by sequential NO_2 loss and hydration/hydrolysis, with the +4 oxidation state of Th being retained if the O_2 ligand is now superoxide. Noticeably, $ThO_2(NO_3)_4^-$ ions could also be produced directly by ESI when a thorium nitrate solution in water was used.

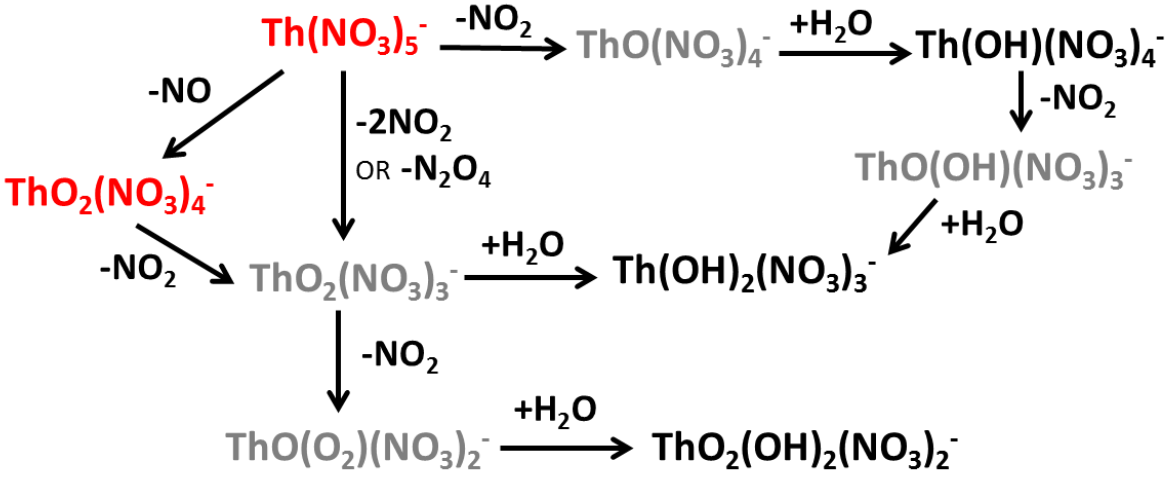

Scheme 6. CID and hydration/hydrolysis pathways for thorium nitrate anions (C2TN-IST; species observed in the ESI mass spectra in red; species not observed in the CID mass spectra in grey).

Uranium. CID of $U^{VI}O_2(NO_3)_3^-$ (Scheme 7), readily produced by ESI of an ethanol solution of uranyl nitrate, was also examined at C2TN-IST for comparison with $PuO_2(NO_3)_3^-$; the observation of single formation of $UO_3(NO_3)_2^-$ by NO_2 loss seems to confirm $PuO_2(NO_3)_3^-$ as a Pu(VI) species. Interestingly, CID of $UO_3(NO_3)_2^-$ led to $UO_2(OH)_2(NO_3)^-$ from NO_2 loss plus fast hydrolysis, while, as described above, $PuO_2(O_2)(NO_3)^-$ was stable to hydrolysis during the CID experiment; minor NO_3 loss was also observed, leading to $UO_3(NO_3)^-$ that could correspond to a U(VI) trioxo-nitrate species. Several of these uranyl nitrate anions have been previously identified by Pasilis et al. using ESI-FTICR-MS and involving CID experiments and reactions with D_2O.[11]

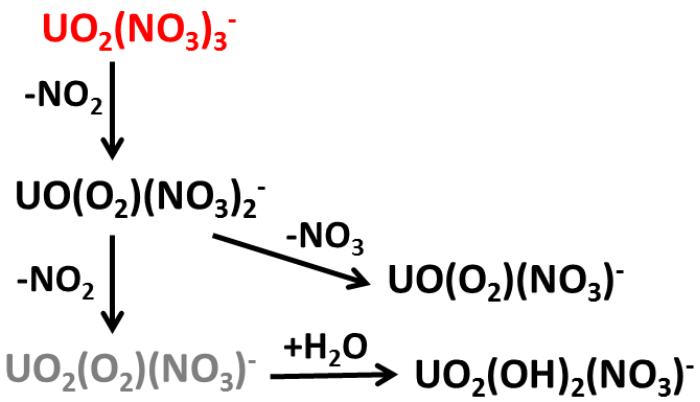

Scheme 7. CID and hydration/hydrolysis pathways for uranium nitrate anions (C2TN-IST; species observed in the ESI mass spectra in red; species not observed in the CID mass spectra in grey).

III.2.2. Conclusions

As observed in the previous section, CID experiments performed in QIT mass spectrometers with different metal nitrate anions, comprising all the lanthanides (except Pm), scandium, yttrium, aluminium, and the actinides Th, U, Pu, Am, and Cm, showed the formation of an array of oxo, peroxo, and superoxo species that mostly reflected the stability of different oxidation states for the several metals examined. A key finding was that hydrolysis, resulting from gas-phase reactions of the CID products with the background water in the QITs, was a fast process that revealed redox stabilities of the metal ions. Special attention was given to the relative stabilities of the III/IV oxidation states, as the mostly trivalent rare earth metals were investigated (Chapter III.2. A).

In this section, other results were obtained from the CID and hydrolysis of other metal nitrate anions, containing different types of oxygen ligands, and formed in successive CID processes. Concerning the CID of the $MO(NO_3)_3^-$ species, it was observed that as in the CID of the tetranitrate ions, fast hydration or hydrolysis occurred for some of the metal ions. The metals with more stable +4 oxidation states were resistant to hydration or hydrolysis, namely Ce, Pr, Pu, Am, and Cm. The case of Sc is still intriguing but as before steric effects may be determining the non-occurrence of hydration or hydrolysis.

CID of $MO_2(NO_3)_3^-$ ions, as studied for the same metals, led to the formation of $M(OH)_2(NO_3)_2^-$ ions that could result from NO_2 loss followed by very fast hydrolysis.

The $M(OH)(NO_3)_3^-$ ions formed during CID of the initial $M(NO_3)_4^-$ ions (see previous section) did not react with H_2O in the C2TN-IST ion trap, as examined for M = La, Ho, Lu, and Y which is an expected result as the metal ions are in the +3 oxidation state and bonded to stable ligands. CID of these $M(OH)(NO_3)_3^-$ ions also examined for M = La, Ho, Lu, and Y, yielded $M(OH)_2(NO_3)_2^-$ ions by apparent

sequential NO_2 loss and fast hydrolysis. CID with the Sc analogue produced $ScO(OH)(NO_3)_2^-$ (70%) and $ScO_2(NO_3)_2^-$ (30%), corresponding to loss of NO_2 and HNO_2, respectively. As in other cases, hydrolysis of species involving the small Sc^{3+} ion seems to be kinetically hindered.

In CID and hydrolysis of actinide nitrate ions, like Pu and Am, a more diverse ESI behavior was observed. The ESI-MS of the Am nitrate solution, besides $Am^{III}(NO_3)_4^-$, showed also the presence of $Am^{IV}O(NO_3)_3^-$ and $Am^{V}O_2(NO_3)_2^-$, while ESI of the Pu nitrate solution led to the formation of other stable species such as $Pu^{III}(NO_3)_4^-$, $Pu^{IV}(NO_3)_5^-$, $Pu^{V}O_2(NO_3)_2^-$, and $Pu^{VI}O_2(NO_3)_3^-$. U and Th nitrate solutions were tested for comparison with the Pu nitrate solutions. The single formation of $UO_3(NO_3)_2^-$ by NO_2 loss seems to confirm $PuO_2(NO_3)_3^-$ as a Pu(VI) species. However, $PuO_2(O_2)(NO_3)^-$ showed to be resistant to hydrolysis while $UO_3(NO_3)_2^-$ led to $UO_2(OH)_2(NO_3)^-$ from NO_2 loss plus fast hydrolysis reaction. On the other hand, Th species apparently tend to retain the +4 oxidation state, while Pu species do not, which led to fast hydrolysis processes.

References

(1) Li, F. M.; Byers, M. A.; Houk, R. S., Tandem mass spectrometry of metal nitrate negative ions produced by electrospray ionization, *Journal of the American Society for Mass Spectrometry* **2003**, 14, 671.

(2) Morss, L.R., Comparative thermochemical and oxidation reduction properties of lanthanides and actinides, in Handbook on the Physics and Chemistry of Rare Earths, volume 18 - Lanthanides/Actinides: Chemistry, Gschneidner, K. A.; Eyring, J. L.; Choppin, G. R.; Lander, G. H., Eds.; Elsevier, **1994**, chap. 122, p. 239.

(3) Spitsyn, V. I.; Gel'man, A. D.; Krot, N. N.; Mefodiye, M. P.; Zakharov, F. A.; Komkov, Y. A.; Shilov, V. P.; Smirnova, I. V., Heptavalent state of neptunium and plutonium, *Journal of Inorganic and Nuclear Chemistry* **1969**, 31, 2733−2745.

(4) Keller, C.; Seiffert, H., Heptavalent plutonium, *Angewandte Chemie International Edition in English* **1969**, 8, 279−280.

(5) Tananaev, I. G.; Nikonov, M. V.; Myasoedov, B. F.; Clark, D. L., Plutonium in higher oxidation states in alkaline media, *Journal of Alloys and Compounds* **2007**, 444, 668−672.

(6) Domanov, V. P.; Lobanov, Y. V., Refinement of data on the volatility of octavalent plutonium in the form of tetraoxide PuO_4, *Radiochemistry* **2009**, 51, 14−17.

(7) Nikonov, M. V.; Kiselev, Y. M.; Tananaev, I. G.; Myasoedov, B. F., Plutonium volatility in ozonization of alkaline solutions of Pu(VI) hydroxo complexes, *Doklady Chemistry* **2011**, 437, 69−71.

(8) Huang, W.; Xu, W. H.; Su, J.; Schwarz, W. H. E.; Li, Oxidation states, geometries, and electronic structures of plutonium tetroxide PuO_4 isomers: Is octavalent Pu viable?, *Journal of inorganic chemistry* **2013**, 52, 14237−14245.

(9) Zaitsevskii, A. V.; Titov, A. V.; Mal'kov, S. S.; Tananaev, I. G.; Kiselev, Y. M., On the existence of oxide molecules of plutonium in highest oxidation states, *Doklady Chemistry* **2013**, 448, 1−3.

(10) Maurice R., Renault E., Gong Y., Rutkowski P. X, Gibson J.K., Synthesis and structures of plutonyl nitrate complexes: Is plutonium heptavalent in $PuO_3(NO_3)_2^-$? *Inorganic chemistry* **2015**, 54, 2367−2373.

(11) Pasilis, S.; Somogyi, A.; Herrmann, K.; Pemberton, J. E., Ions generated from uranyl nitrate solutions by electrospray ionization (ESI) and detected with Fourier transform ion-cyclotron resonance (FT-ICR) mass spectrometry, *Journal of the American Society for Mass Spectrometry* **2006**, 17, 230.

Chapter IV. Coordination of actinyl ions with amino acids in the gas phase

This chapter includes preliminary results on the coordination chemistry of actinyl ions with amino acids in the gas phase, which are presented as a first draft of a manuscript (**Lucena AF**, Maria L, Gong Y, Gibson JK, Marçalo J). This project was carried out experimentally by me at C2TN-IST, in collaboration with Dr. Leonor Maria, and at LBNL, in collaboration with Dr. Yu Gong.

Abstract

Gas-phase experiments were conducted in an attempt to probe the basic interactions of actinides with molecules of biological relevance, namely amino acids (aas). The amino acids chosen in this study were those that are more prone to bind to metal ions, that is, L-cysteine (Cys), L-histidine (His) and L-aspartic acid (Asp); glycine (Gly) was also included in the study as the more simple aa. Potential coordinating groups include the thiolate of Cys, the imidazole of His and the carboxylates of Asp. The effects of the presence of these different binding sites were examined. The relative gas-phase affinities these amino acids towards actinyl ions, $AnO_2^{+/2+}$ (uranyl, neptunyl and plutonyl), were studied, with a focus on uranyl. The few existent theoretical calculations on actinyl-aa coordination were useful for elucidation on the most favorable structures of some of the species formed by ESI-MS and CID. Of key interest were the differences observed between the binding of two amino acids to a given actinyl, as well as the binding of a given amino acid to the 3 actinyls. The observed competition between two different aas to the actinyl ion was an important asset of this investigation. The ability to explore variations across the actinide series, for An = U, Np, Pu, as well as disparities observed in the CID of species with different oxidation states and complexes produced, was also accomplished. Furthermore, hydration and hydrolysis of selected species were investigated, which provided also insights into the stabilities of the An-aa species formed.

IV.1. Introduction

The extensive use of nuclear technology is associated with the possibility of contamination by the actinides, which may induce both radiological and chemical toxicity.[1-3] The bio-coordination chemistry of the actinides has, in recent years, focused on the development of sequestering and decorporation agents with significant success.[4-6] Prior to decorporation, the actinides can interact with biomolecules and compete for the biological sites of essential metallic ions, exerting adverse effects on and altering the functions of enzymes, proteins or nucleic acids.[7-9] The molecular mechanisms of biological action of the actinides are poorly understood, even in the more common case of uranium, although it is clear that they are highly dependent on their interactions with biomolecules.[10-13]

Gas-phase studies based on mass spectrometry techniques can provide intrinsic physical and chemical properties of elementary species. This type of study provides an opportunity to probe the relationships between molecular structure, electronic structure, reactivity and energetics. Additionally, the information obtained can be compared directly with the results from theoretical studies.

For some years now, MS is being employed, with significant results, in the investigation of metal ion interactions with molecules of biological relevance at a fundamental level, with emphasis on energetics and structure, accompanied by select spectroscopic experiments and theoretical studies, and naturally focused on alkali, alkaline earth, and a few key transition metals.[14-22]

However, such approaches have not been used to date to examine the interactions of the actinides with simple biomolecules, not even for ubiquitous uranyl, and only a few theoretical studies have recently appeared addressing this topic.[23-25] An important advantage of MS studies is that the more radioactive actinides are also amenable to investigation.

The interactions of actinides with simple biomolecules (amino acids, small peptides, nucleic acid building blocks) are poorly understood, especially in the case of coordination to actinyl ions ($AnO_2^{+/2+}$).

Amino acids and peptides have different functional groups, such as carboxyl (e.g. aspartic acid, CH_2COO-), hydroxyl, amino (or amido) groups that can form complexes with actinides. Most of these amino acids exist also in the zwitterionic form (Figure IV.1).

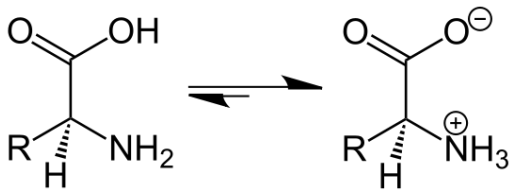

Figure IV.1 Representation of an amino acid which contains both acidic (carboxylic acid fragment) and basic (amine fragment) centres. The isomer on the right is the zwitterionic form.[26]

All functional groups are both Lewis and Brønsted acids/bases and the mode of coordination is therefore pH dependent. Potentiometric data have showed that the protonation of the amino group prevents chelate formation at lower pH (2–4) and the amino acids are then coordinated only via the carboxylate oxygens and in the case of uranium(VI) most of the reported results point towards a bidentate coordination.[27] At higher pH the amine nitrogen is deprotonated and chelates are formed with N, O coordination. In cysteine (R-CH_2SH) the thiol group is not involved in the complex formation, only the amino acid moiety is coordinated, reflecting the "hard" acceptor character of the uranyl ion and the preference of nitrogen over sulfur donors.[28] Reported results of ligand proton complex formation for simple α-amino acids showed a decrease as the donor group changes from -NH_2 to -OH to -SH. This is in accord with the order of decreasing basicity of the ligand. However the possibility of a steric effect should also be considered.[29]

Likewise, there is little or no evidence for the coordination of aliphatic hydroxyl group, either in serine (R-CH2OH) or in threonine (R-$CH(CH_3)OH$).[28] In the case of aspartic acid (RCH_2COO-), the ^{13}C NMR chemical shift changes of the ligand upon coordination with uranium(VI) have showed a chelate formation by the coordination of the carboxylate oxygens instead of the amino group.[30] Conversely, studies with thorium(IV) complexes with aspartic acid indicated a tridentate coordination via both carboxylates and the amino group.[31]

Nevertheless, several factors affect the stability of the complexes and can influence interactions with metal dications, e.g. the size of the chelate ring, the steric and inductive effects of the substituent at the α-carbon, the gas phase acidity, the proton affinity and the side chain functionality .[32] Recently, Bohme et al. reported gas-phase studies of bond activation in complexes of Pb^{2+} and other transition-metal dications (Fe^{2+}, Co^{2+}, Ni^{2+}, Cu^{2+}, Zn^{2+}) with several deprotonated amino acids.[33,34] The authors used electrospray ionization mass spectrometry for producing 1:1 complexes of deprotonated aa and atomic transition metal dications in the gas phase. The observed dissociation products and measured onset energies for dissociation in the presence and absence of Pb^{2+} and the other dications provided insights into bond activation. Deprotonated glycine appeared to be substantially activated by Pb^{2+}.[33,34]

Determination of thermodynamic equilibrium constants provides a quantitative measurement of the affinity of a particular ligand for actinide ions.[1,3] Stability constants of actinides with selected ligands are given as examples in Table IV.1.[35]

Table IV.1 Stability constants of some biological and chemically relevant actinide complexes.[35]

Actinides	Thorium	Uranium	Neptunium		Plutonium	Americium	Curium
Chemical form	Th(IV)	U(VI)	Np(IV)	Np(V)	Pu(IV)	Am(III)	Cm(III)
$\log K_1$ ($I = 0$)							
Glycine (L^-)	10.5	8.0		3.3 ($I = 0.1$)		4.1 ($I = 1$)	
Cysteine (L^{2-})	9.2	6.7				4.2 ($I = 1$)	
Aspartate (L^{2-})	11.0	9.3		2.6 ($I = 1$)		6.1	
Glutamate (L^{2-})	10.8	9.2		2.7 ($I = 1$)		5.6 ($I = 1$)	
Lactate (L^-)	5.7	2.9	2.1	2.1		2.4 ($I = 1$)	
Citrate (L^{3-})	13.7	9.0	16.3	3.7	15.3 ($I = 0.5$)	8.6	

Glycine (Gly) is the simplest amino acid, very common in the biosphere and usually exists in zwitterionic form. Several experimental investigations of uranyl-glycine have been reported.[36-40] For instance, X-ray structural studies of solid uranyl-glycine complexes showed that the carboxylate rather than the amino group binds to oxophilic uranium. Other studies proved that glycine does rarely act as a chelating ligand with its CO_2^- and NH_2 ends forming a 5-membered ring.[41] Usually, mono- or bidentate carboxylate coordination by the R-CO_2^- ligand is observed in the crystals, forming a four membered ring in the latter case. Often, monodentate coordination of the zwitterionic Gly is assumed. In basic solution, chelation by $NH_2CH_2CO_2^-$ has also been suggested.[24,36-39] Potentiometric and calorimetric studies have showed that at lower pH only the carboxylate end of a dipeptide (GlycylGlycine) is coordinated to uranium(VI).[42] However, the results on the structure of the chelates formed at higher pH are contradictory and it can be questioned if the nitrogen or the oxygen of the peptide group is involved in the ring formation beside the carboxylate end.[32]

Another study on the complex behavior of U(VI) with the amino acids L-glycine and L-cysteine in aqueous solution was investigated by time resolved laser-induced fluorescence spectroscopy and UV–Vis spectroscopy, in which properties of the formed uranyl complexes were determined in comparison to the free uranyl cation.[43] It was observed the formation of several protonated uranyl-amino acid complexes with metal:ligand in ratios of 1:1 (glycine and cysteine system) and 1:2 complexes (glycine system) at low pH values. The results showed a change of the complexation behavior of amino acids towards the uranyl cation and the spectroscopic properties of the system dependent on the presence of the functional groups (–COOH/–COO-, –SH/–S-, NH_2/NH_3^+). At relative high uranium concentration a 1:1 species in the U(VI)/cysteine system with a metal

coordination through the deprotonated carboxyl group and –S or $–NH_2$ group was detected.[43] In the 1980s, Ramanujam[44] and Bismondo[45] have shown that glycine acts as monodentate ligand through the carboxylate group, while the amino moiety is not involved in the metal coordination. Contrary to this, Lagrange[46] and Cerfola[47] favored the formation of a chelate complex between the uranyl cation and the amino acid. IR spectroscopic measurements carried out by Lagrange suggest the dissociation of a proton from the NH_3^+ during the interaction with UO_2^{2+}.[46] Szabo and Grenthe[36] demonstrated the formation of uranyl-glycine complexes in the form of a zwitterion without deprotonation at low pH and of a chelate with deprotonation at higher pH values.

Solution interactions between the uranyl ion and histidine have also been reported.[13] The imidazole side chain of histidine can interact with UO_2^{2+} by an inner-sphere imine–uranium bonding arrangement, or an outer-sphere H-bonding imidazolium–oxo interaction (Figure IV.2).[12,48] Both imine to uranyl and oxo-H-bonding are commonly found in small molecule X-ray data, but oxo-H-bonding as a ‘‘coordination motif” has been less studied and only seen in biological metal transport studies.[49] Prior solution studies suggest the possibility of N–imino coordination from the imidazole side chain of this amino acid. Bidentate coordination appears to be assumed in a specific study on uranyl–histidine binding constants using an extraction technique[50,51] but direct experimental evidence for this mode of coordination in solution or some other arrangement is lacking. Still, there is some evidence that imidazole coordinates to uranyl in the gas-phase in collision-induced dissociation (CID) experiments.[10,13]

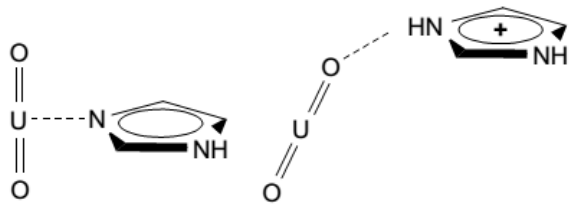

Figure IV.2 Solid state interactions between uranyl and imidazole or imidazolium: direct coordination and H-bonding to oxo ligands.[13]

IV.2 Experimental conditions

IV.2.1 Sample preparation

At C2TN-IST, uranyl-aa solutions were prepared from 1-4 vol. 1 mM aa in H_2O plus 1 vol. 1 mM $UO_2X_2•(H2O)_n$ (X = NO_3, Cl) in H_2O and using 2-5 vol. EtOH as the spray solvent. The pH of the solutions were in the range 6-7. For cysteine, pH was a bit more acidic, 5-6. Also, cysteine solutions needed to be freshly prepared with deoxygenated water as cystine is easily formed through oxidation of two cysteine molecules that covalently link via a disulfide bond. Excess aa was necessary to yield positive ion spectra (except for histidine).

At LBNL, the mixtures $AnO_2(ClO_4)_2$:aa (An = U, Np, Pu) were prepared with 1:10 ratios, using MeOH as the spray solvent. The sprayed solutions had concentrations of ca. 10^{-4} M in actinyl. The isotopes ^{238}U, ^{237}Np, ^{242}Pu used in this work are alpha-emitting radionuclides with half-lives of $4x10^9$ y, $4x10^5$ y, and $3x10^5$ y, respectively. Therefore, special safety precautions were taken when handling these isotopes, meaning that all experiments were performed in special radiological containment glove boxes. The stock solutions used were $PuO_2(ClO_4)_2$ [Pu(VI)] 0.8 mM, $NpO_2(ClO_4)_2$ [Np(VI)] 27 mM and Gly 14 mM. All the solutions were prepared in water. The mixture $AnO_2(ClO_4)_2$:Gly was prepared with a stoichimetry of 1:10 and a concentration of 200 µM using MeOH as the spray solvent.

For the competitive CID experiments, mixtures of 2 different amino acids were prepared with a 1:1 stoichiometry and mixed with uranyl(VI) chloride in H_2O/EtOH. The sprayed solution had a uranyl concentration of 10^{-4} M. The concentration of aa was 4 times the concentration of uranyl to promote complexation. Uranyl(VI) nitrate was also tested but mixed species of uranyl with 2 distinct aa and NO_3^- were not detected in the ESI-MS.

IV.2.2 Instrumental conditions

Bruker HCT (C2TN-IST, PT) and Agilent 6340 (LBNL, CA, USA) QIT/MS instruments, equipped with ESI sources, were used; these two instruments have similar configurations. The Agilent 6340 QIT/MS was operated with the source region inside of a radiological-containment glove box, as previously described.[52] Mass spectra were recorded in the negative and positive ion accumulation and detection modes. Sample solutions were introduced through a nebulizer with a syringe pump at 150 µL h^{-1} at C2TN-IST and 60 µL h^{-1} at LBNL. The spectra were acquired using the following instrumental parameters for both instruments: nebulizer gas pressure, 15 psi; capillary voltage, -4500 V; dry gas flow rate, 5 $l.min^{-1}$; dry gas temperature, 325 °C; capillary exit, 141.7 V. High-

purity nitrogen gas was used for nebulization and drying in the ion transfer capillary. At LBNL, the N_2 was supplied from the boil-off of a liquid nitrogen Dewar; at C2TN-IST a nitrogen generator was used. The background water pressure in the ion trap is estimated as ~$1x10^{-6}$ Torr;[53] the relative water pressure in the two ion traps has been determined: C2TN-IST 100, LBNL 62 (see Chapter III.2). The helium buffer gas pressure in the trap is constant at ~$1x10^{-4}$ Torr.

Ion-molecule reactions can occur in the ion trap by applying a variable reaction delay time of up to 10 s at the trap. Collision induced dissociation experiments are performed by isolation of the ions of interest and ejection of all the other ions, which allows time-dependent hydration reaction studies with the background water in the traps under thermal conditions. Pseudo-first order reaction rates, k, of trapped ions in the QITs were obtained by isolating the ion of interest and allowing it to react with background water/oxygen for variable times. Plots of the logarithmic decay of the ratio of the reactant ion intensity to the total ion intensity as a function of time provide the hydrolysis reaction rates.

IV.3. Results and discussion

IV.3.1 Dissociation of protonated and deprotonated amino acids

The physical properties of the aas used in this study, Gly, Cys, His, and Asp, are outlined in Table IV.2.

The amino acids chosen for this study provided good protonated and deprotonated amino acid signals to measure dissociation profiles, in the positive and negative mode, respectively. Primary dissociation channels and respective equations for the 4 aas are summarized in Table IV.3. All the aaH^+ with side-chain exhibit primarily loss of HCOOH. These dissociations require C-αC bond scission and intramolecular proton transfer from the amino to the carboxyl group, as has been observed previously.[54] The role of side-chains is very prominent in the dissociations of these ions. The presence of heteroatoms (S, N, or O) and functional groups (imidazole, carboxylic, thiol) can lead to bond scission at the carbon-heteroatom bond or detachment of the functional group. It is the case of the dissociation of $(Asp-H)^-$, with loss of carbon dioxide with detachment of side-chain functional group (carboxyl). In the case of cysteine, which contains an S-atom in the side-chain, the deprotonated amino acid, $(Cys-H)^-$, should dissociate by C-S bond scission and lead to the formation of SH^- but no fragments were observed due to the cutoff lower than 30 *m/z*. The SH group of cysteine can be easily oxidized to yield cystine (Cis) in which two Cys moieties are attached to each other by a disulfide bond. CID of the deprotonated Cis yielded fragments of decarboxylation, water loss, neutral Cys and doubly

deprotonated Cys. CID of the deprotonated histidine showed loss of H_2O, NH_3 and HCOOH, in agreement with the experiments done by Bohme and co-workers.[34]

Table IV.2 Physical properties of selected amino acids Gly, Cys, His and Asp.[55]

Glycine (Gly)	***L*-Cysteine (Cys)**	***L*-Histidine (His)**	***L*-Aspartic acid (Asp)**
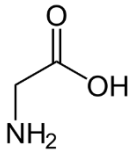	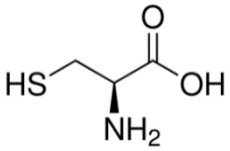	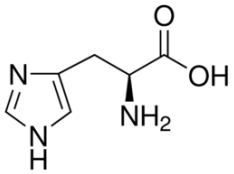	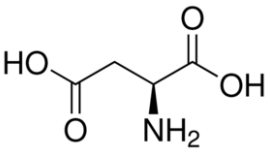

Amino acid (aa)	**Mol. form.**	M_r	t_m/°C	pK_a	pK_b	pK_c	pI	S/g kg^{-1}	**Proton affinity (kJ mol^{-1})**	**Gas basicity (kJ mol^{-1})**
Gly	$C_2H_5NO_2$	75.07	290	2.34	9.58	-	5.97	239	886.5	852.2
Asp	$C_4H_7NO_4$	133.10	270	1.95	9.66	3.71	2.77	5.04	908.9	875.0
Cys	$C_3H_7NO_2S$	121.16	240	1.91	10.28	8.14	5.07	v.s.	903.2	869.3
His	$C_6H_9N_3O_2$	155.15	287	1.70	9.09	6.04	7.59	43.5	988.0	950.2

Table IV.3 Primary dissociation channels for the protonated and deprotonated amino acid ions studied. Dissociation channels are expressed either as a loss of a neutral molecule from the parent ion or as the product ion.

Ion	Primary dissociation channel	Equation
$(GlyH)^+$, *m/z* 76	-CO	$(GlyH)^+ \rightarrow CH_6NO^+$ (*m/z* 48) + CO
$(AspH)^+$, *m/z* 134	$-H_2O$ (M); -HCOOH	$(AspH)^+ \rightarrow C_4H_7NO_2^+$ (*m/z* 116) + H_2O
		$(AspH)^+ \rightarrow C_3H_6NO_2^+$ (*m/z* 88) + HCOOH
$(HisH)^+$, *m/z* 156	-HCOOH (M), $-(CO_2+NH_3)$	$(HisH)^+ \rightarrow C_5H_8N_3^+$ (*m/z* 110) + HCOOH
$(CysH)^+$, *m/z* 122	$-NH_3$ (M), $-H_2O$, -HCOOH	$(CysH)^+ \rightarrow C_3H_5O_2S^+$ (*m/z* 105) + NH_3
		$(CysH)^+ \rightarrow C_3H_6NOS^+$ (*m/z* 104) + H_2O
		$(CysH)^+ \rightarrow C_2H_6NS^+$ (*m/z* 80) + HCOOH
$(Gly\text{-}H)^-$, *m/z* 74	*	
$(Asp\text{-}H)^-$, *m/z* 132	$-CO_2$, $-NH_3$, $-H_2O$	$(Asp\text{-}H)^- \rightarrow C_3H_6NO_2^-$ (*m/z* 88) + CO_2
		$(Asp\text{-}H)^- \rightarrow C_4H_3O_4^-$ (*m/z* 115) + NH_3
$(His\text{-}H)^-$, *m/z* 154	$-H_2O$, $-NH_3$, -HCOOH	$(His\text{-}H)^- \rightarrow C_6H_6N_3O^-$ (*m/z* 136) + H_2O
		$(His\text{-}H)^- \rightarrow C_6H_5N_2O_2^-$ (*m/z* 137) + NH_3
		$(His\text{-}H)^- \rightarrow C_5H_6N_3^-$ (*m/z* 110) + HCOOH
$(Cys\text{-}H)^-$, *m/z* 119	*	
$(Cis\text{-}H)^-$, *m/z* 239	$-H_2O$, $-CO_2$, -(Cys-2H), -Cys	$(Cis\text{-}H)^- \rightarrow C_6H_{10}N_2O_3S_2^-$ (*m/z* 221) + H_2O
		$(Cis\text{-}H)^- \rightarrow C_5H_{12}N_2O_2S_2^-$ (*m/z* 195) + CO_2
		$(Cis\text{-}H)^- \rightarrow C_3H_4NO_2S^-$ (*m/z* 118) + Cys
		$(Cis\text{-}H)^- \rightarrow C_3H_2NO_2S^-$ (*m/z* 116) + Cys-2H

M = major dissociation observed in the CID.
*no observed species in the CID.

IV.3.2 ESI-MS of actinyl complexes with glycine

The ESI of mixtures of glycine (Gly) and uranyl chloride or uranyl nitrate in ethanol/water and actinyl perchlorate in methanol solutions generated monopositive and mononegative complexes containing the $U^{VI}O_2^{2+}$ with 1 to 3 Gly ligands and the $An^{V}O_2^{+}$ (An = U, Np, Pu) with 1 or 2 Gly ligands. The positive U(VI) complexes formed included $[U^{VI}O_2(Gly\text{-}H)(Gly)_2]^+$, $[U^{VI}O_2Cl(Gly)_2]^+$ and $[U^{VI}O_2(NO_3)(Gly)_2]^+$, and in the negative ion mode the complexes $[UO_2(X)_n(Gly\text{-}H)_{3-n}]^-$ (X = Cl^-, NO_3^-, n = 0, 1, 2) were formed. Actinyl(V) species $[AnO_2(Gly)_n]^+$ and $[AnO_2(Gly\text{-}H)_2]^-$ (n = 1, 2; An = U, Np, Pu) were also observed.

IV.3.2.1 Dissociation of uranyl(VI) complexes with neutral and deprotonated glycine (positive mode)

$U^{VI}O_2^{2+}$ complexes $[UO_2(X)(Gly)_2]^+$ (X = $(Gly\text{-}H)^-$, Cl^-, NO_3^-) were produced in the positive ion mode. In Scheme IV.1 are represented the dissociations pathways (CID) for the complexes of $[UO_2(X)(Gly)_2]^+$. In Figure IV.3A is the CID spectrum of the isolated $[UO_2(Gly\text{-}H)(Gly)_2]^+$. The CID of these species (Table IV.4) clearly reveals that the uranyl species exhibit loss of Gly or HX, with rapid hydrolysis with the background water to produce $[UO_2(Gly)_2(OH)]^+$, occurring during the collision-induced dissociation experiment. The loss of one neutral glycine reduces the coordination around the equatorial plane and the hydroxyl group completes a coordination number five in the equatorial plane for UO_2^{2+}, considering that the glycine is bidentate by the two oxygen atoms of the carboxylate function, which is also suggested previously by reported DFT calculations.[24] The CID spectrum of $[UO_2(X)(Gly)_2]^+$ also includes the presence of the ion $[UO_2(Gly)(OH)(NH_2CH_3)]^+$. This species could be produced through two dissociation channels: a) loss of CO_2 (through cleavage of the C-αC bond or also known as backbone dissociation of Gly) of the species $[UO_2(Gly)_2(OH)]^+$ or b) loss of CO_2 and rapid reaction with the background water from the supposed intermediary $[UO_2(Gly)(Gly\text{-}H)]^+$. The hydrolysis rate of this intermediary was estimated from the CID of the precursor (Eq. 1):

$$[UO_2(Gly\text{-}H)(Gly)]^+ + H_2O \dashrightarrow [UO_2(Gly)_2(OH)]^+ \quad k > 73\ s^{-1} \quad (1)$$

CID of the species $[UO_2(Gly)(OH)(NH_2CH_3)]^+$ (MS^3) generates loss of NH_2CH_3, loss of CO_2 and loss of neutral Gly, yielding $[UO_2(Gly)(OH)]^+$, $[UO_2(OH)(NH_2CH_3)_2]^+$ and $[UO_2(OH)(NH_2CH_3)]^+$, respectively.

These species hydrate easily in the QIT. The species uranyl-glycine-hydroxide also decarboxylates (MS^4) yielding the species $[UO_2(OH)(NH_2CH_3)]^+$ which quickly reacts with the background water to form the species $[UO_2(OH)(NH_2CH_3)(H_2O)]^+$ and $[UO_2(OH)(NH_2CH_3)(H_2O)_2]^+$, and dissociates ($MS^4$) by loss of NH_2CH_3 yielding the species uranyl hydroxide $[UO_2(OH)]^+$. This species is already known to add a maximum of 3 water molecules according to previous reported experiments.[56]

IV.3.2.2 Dissociation of uranyl(VI) complexes with deprotonated glycine (negative mode)

In the negative ion mode, the complexes $[UO_2(X)_n(Gly\text{-}H)_{3-n}]^-$ (X = Cl^-, NO_3^-, n = 0, 1, 2) were formed upon the electrospray. In Figure IV.3B is the CID spectrum of the isolated $[UO_2(Gly\text{-}H)_3]^-$. In Table IV.5 the fragments obtained from the CID of the $[UO_2(X)_n(Gly\text{-}H)_{3-n}]^-$ species are shown. The complexes $[UO_2(Gly\text{-}H)_3]^-$ and $[UO_2(X)(Gly\text{-}H)_2]^-$ sequentially eliminate one deprotonated glycine and quickly react with the background water (see Scheme IV.2). The formation of uranyl(V) species by loss of deprotonated glycine is evidenced by the presence of O_2-addition products formed by reaction with background O_2, as it was observed in other experiments for several uranyl(V) species,[57-60] particularly $[UO_2X_2]^-$ species (see Chapter II.3). CID of the $[UO_2(X)_n(Gly\text{-}H)_{3-n}]^-$ species showed as well a decarboxylation pathway, presumably leading to a methylamide ligand that undergoes subsequent hydrolysis.

The species $[UO_2(X)_2(Gly\text{-}H)]^-$ exhibit somewhat different CID profiles compared to the other $[UO_2(X)_n(Gly\text{-}H)_{3-n}]^-$ species (n= 0, 1; see Table IV.5), although loss of CO_2 is a major pathway for either species. There are also a few differences between the uranyl nitrate- and uranyl chloride-glycine mixed species for n = 2. The CID of $[UO_2(NO_3)_2(Gly\text{-}H)]^-$ does not yield ligand loss with water addition [-(Gly-H)+H_2O-H] whereas $[UO_2(Cl)_2(Gly\text{-}H)]^-$ does and it is the major fragment in the spectrum (50%). It is clear that oxygen addition occurs more easily than the hydration process for the uranyl nitrate-Glycine species. Also, in the CID of the uranyl chloride-Glycine species, ligand loss (-Gly-H) is a minor fragment (5%) and oxygen addition was not observed, in agreement with the results obtained in the study of O_2-addition to $[U^VO_2X_2]^-$ complexes where for X = Cl a very low rate of addition was obtained (see Chapter II.3).

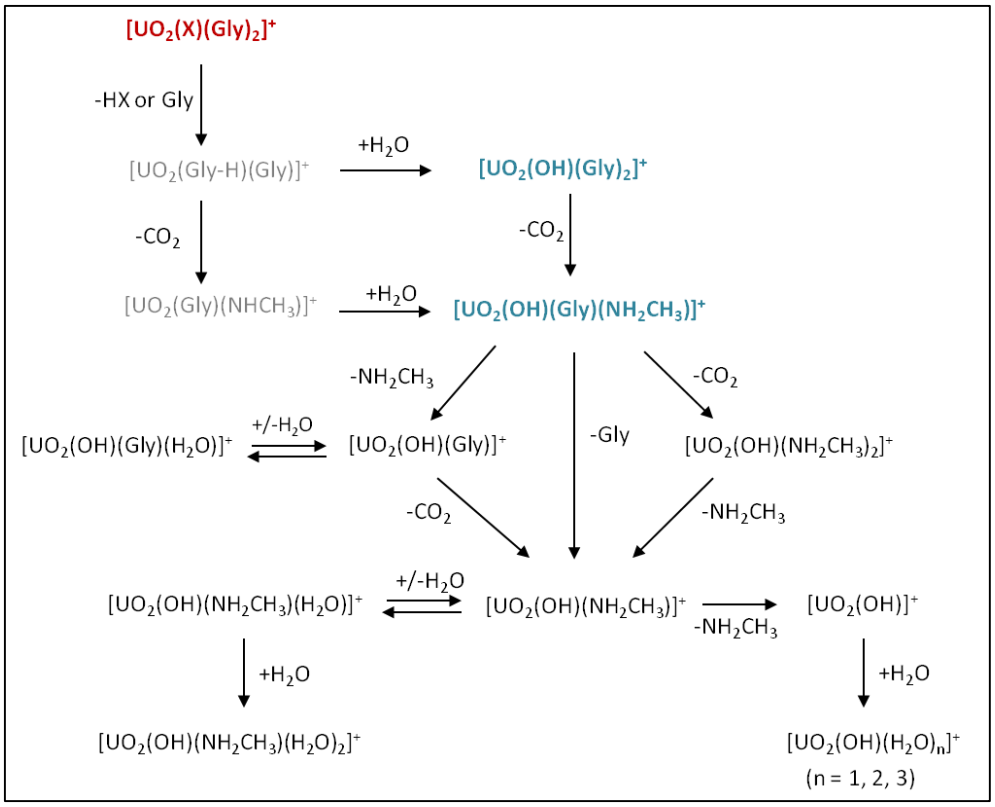

Scheme IV.1 Suggested CID and hydration/hydrolysis pathways of $[UO_2(X)(Gly)_2]^+$ (X = $(Gly\text{-}H)^-$, Cl^-, NO_3^-). The species in blue are the main products obtained in the first CID experiment (MS^2) and the species in grey are supposed intermediates.

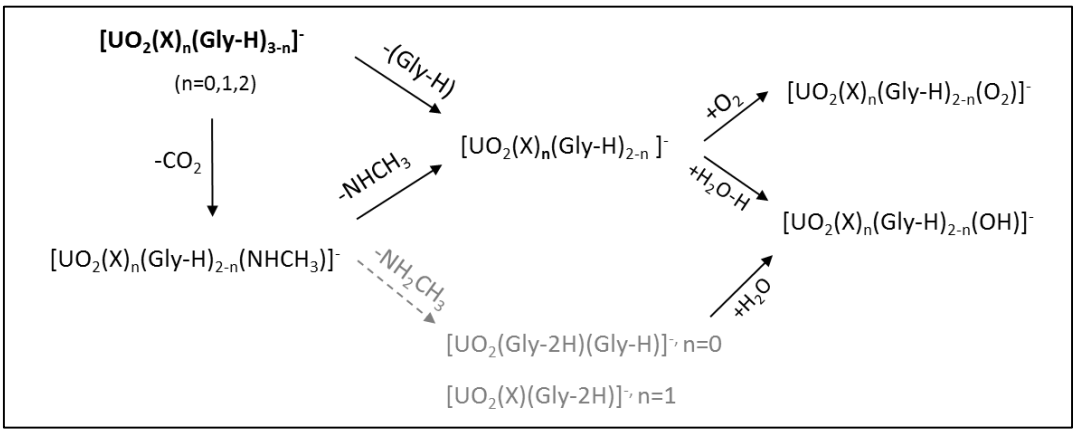

Scheme IV.2 Suggested CID and hydration/hydrolysis/oxidation pathways of $[UO_2(X)_n(Gly)_{3-n}]^-$ (X = Cl^-, NO_3^-; n = 0, 1, 2). The species in grey are supposed intermediates.

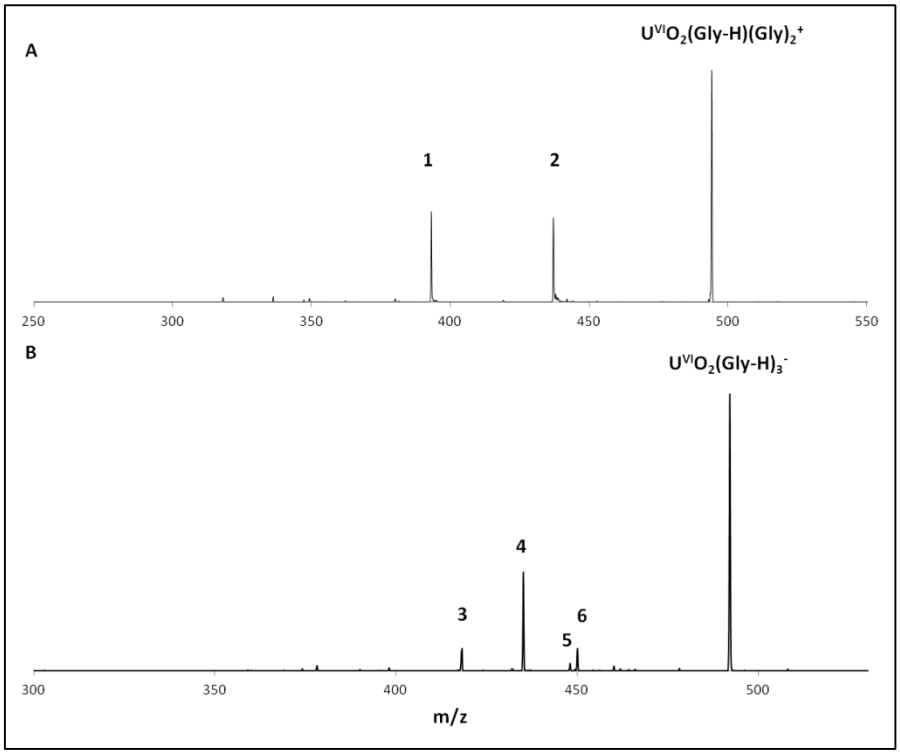

Figure IV.3 CID spectra of A. $UO_2(Gly\text{-}H)(Gly)_2^+$ and B. $UO_2(Gly\text{-}H)_3^-$. The observed CID fragments were: 1. $UO_2(Gly)(OH)(NH_2CH_3)^+$, 2. $UO_2(Gly)_2(OH)^+$, 3. $UO_2(Gly\text{-}H)_2^-$, 4. $UO_2(Gly\text{-}H)_2(OH)^-$, 5. $UO_2(Gly\text{-}H)_2(NHCH_3)^-$, 6. $UO_2(O_2)(Gly\text{-}H)_2^-$.

Table IV.4 CID of $[UO_2(X)(Gly)_2]^+$. (X = $(Gly\text{-}H)^-$, NO_3^-, Cl^-). Fragments are represented in percentage (%) of relative intensity.

Fragment	$[UO_2(Gly\text{-}H)(Gly)_2]^+$	$[UO_2(NO_3)(Gly)_2]^+$	$[UO_2(Cl)(Gly)_2]^+$
$[M\text{-}HX]^+$	3	0	0
$[M\text{-}HX+H_2O]^+$	53	50	50
$[M\text{-}HX+H_2O\text{-}CO_2]^+$	44	50	50

Table IV.5 CID of $[UO_2(X)_n(Gly\text{-}H)_{3-n}]^-$ species (X = NO_3^-, Cl^-; n = 0, 1, 2). Fragments are represented in percentage (%) of relative intensity.

	$[UO_2(Gly\text{-}H)_3]^-$	$[UO_2(X)(Gly\text{-}H)_2]^-$		$[UO_2(X)_2(Gly\text{-}H)]^-$	
		X= NO_3^-	X= Cl^-	X= NO_3^-	X= Cl^-
$[M\text{-}CO_2]^-$	5	2	2	45	45
$[M\text{-}(Gly\text{-}H)]^-$	15	18	10	30	5
$[M\text{-}(Gly\text{-}H)+O_2]^-$	15	15	8	25	0
$[M\text{-}(Gly\text{-}H)+H_2O\text{-}H]^-$	65	65	80	0	50

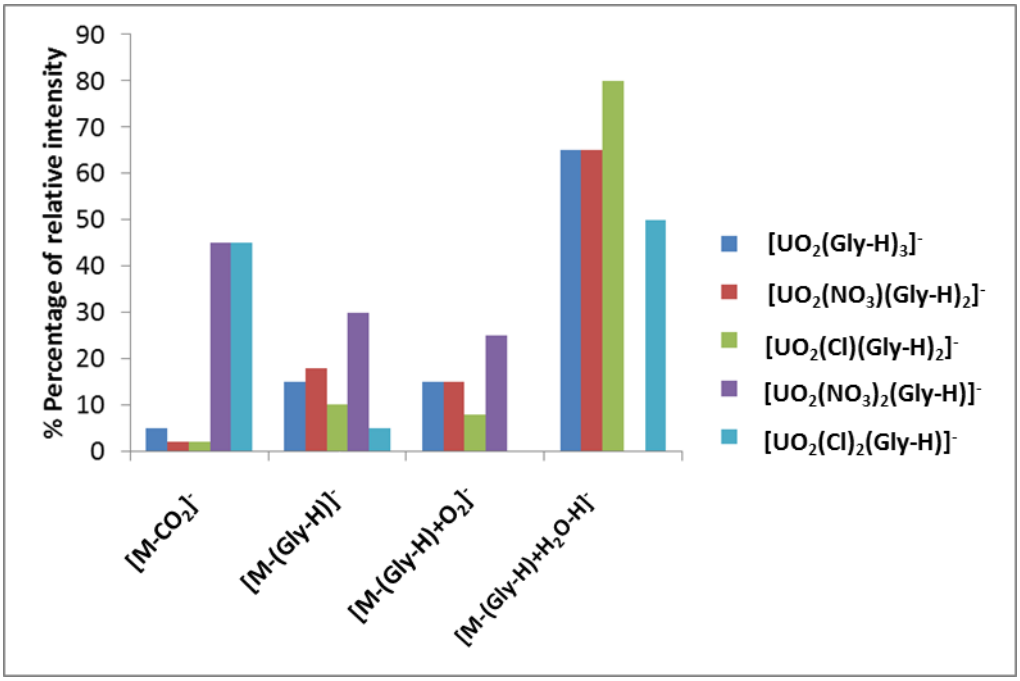

Figure IV.4 CID of $[UO_2(X)_n(Gly\text{-}H)_{3-n}]^-$ (X = NO_3^-, Cl^-; n = 0, 1, 2) represented in percentage of relative intensity.

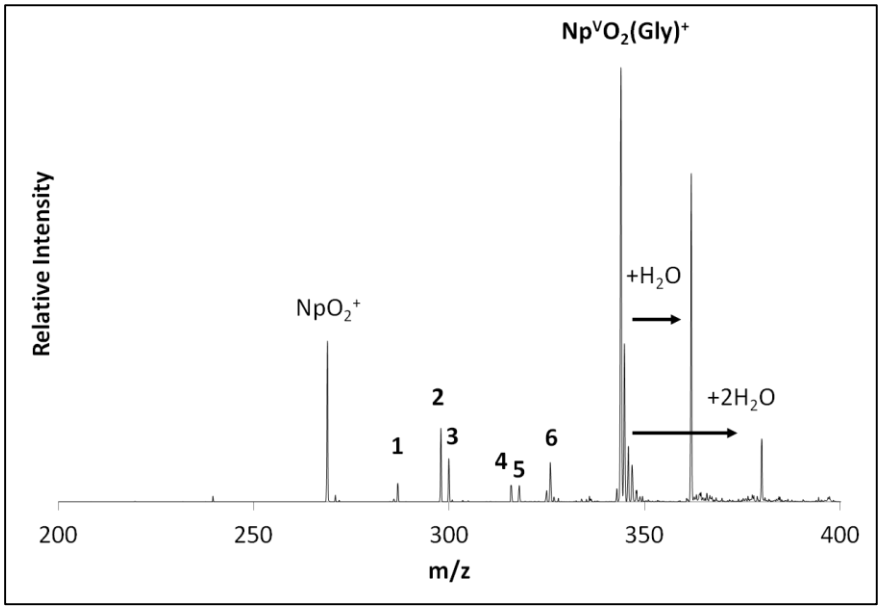

Figure IV.5 CID spectrum of $[NpO_2(Gly)]^+$. 1. $[M\text{-}Gly+H_2O]^+$; 2. $[M–HCOOH]^+$; 3. $[M\text{-}CO_2]^+$; 4. $[M–CO]^+$; 5. $[M\text{-}CO_2+H_2O]^+$; 6. $[M\text{-}H_2O]^+$.

IV.3.2.3 Dissociation of actinyl(V) complexes with neutral and deprotonated glycine

Actinyl(V) species $[AnO_2(Gly)_n]^+$ and $[AnO_2(Gly\text{-}H)_2]^-$ (n = 1, 2; An = U, Np, Pu) were generated by ESI in the gas phase in the positive and negative mode, respectively. These species hydrate easily with the background water present in the QIT. In Figure IV.5 a spectrum of the CID of $[NpO_2(Gly)]^+$ is presented , where, besides several fragments, the addition of one and two water molecules is observed.

The CID of the An(V)-glycine species is summarized in Table IV.6 and in Figure IV.6. Loss of the neutral glycine ligand is predominant in the CID spectra of the $[AnO_2(Gly)]^+$ and $[AnO_2(Gly)_2]^+$ complexes, while in the negative mode, loss of glycine plus water addition is preferred for the anionic complexes $[AnO_2(Gly\text{-}H)_2]^-$. CID of $[AnO_2(Gly)_2]^+$ yields 60% loss of Gly and 35% loss of Gly with water addition $[M–Gly+H_2O]^+$ and 5% of $[M–Gly+2H_2O]$. The $[AnO_2(Gly)]^+$ species hydrate much faster than $[AnO_2(Gly)_2]^+$, however, the rates are not available since the reactions exhibited indecipherable kinetics.

In the negative mode, CID of $[PuO_2(Gly\text{-}H)_2]^-$ yielded 100% of $M–Gly+H_2O$ while $[UO_2(Gly\text{-}H)_2]^-$ yielded also minor fragments of H_2O and CO_2 loss. It was not possible to isolate and fragment $[NpO_2(Gly\text{-}H)_2]^-$.

Table IV.6 CID of $[AnO_2(Gly)_n]^+$ and $[AnO_2(Gly\text{-}H)_2]^-$ complexes (n = 1, 2; An = U, Np, Pu). Product species are represented in % of relative intensity.

	$[AnO_2(Gly)]^+$			$[AnO_2(Gly)_2]^+$			$[AnO_2(Gly\text{-}H)_2]^-$		
	U	**Np**	**Pu**	**U**	**Np**	**Pu**	**U**	**Np**	**Pu**
[M-H_2O]	20	25	17	*	0	0	3	*	0
[M-HCOOH]	20	20	11	*	0	0	0	*	0
[M-CO_2]	0	7	10	*	0	0	15	*	0
[M-CO_2+H_2O]	10	5	5	*	0	0	0	*	0
[M-CO]	0	5	5	*	0	0	0	*	0
[M-Gly]	50	33	48	*	60	62	0	*	0
[M-Gly+H_2O]	0	5	4	*	35	35	62	*	100
[M-Gly+2H_2O]	0	0	0	*	5	3	0	*	0
Others	0	0	0	*	0	0	20	*	0

* It was not possible to isolate and perform CID on $UO_2(Gly)_2^+$ and $NpO_2(Gly\text{-}H)_2^-$.

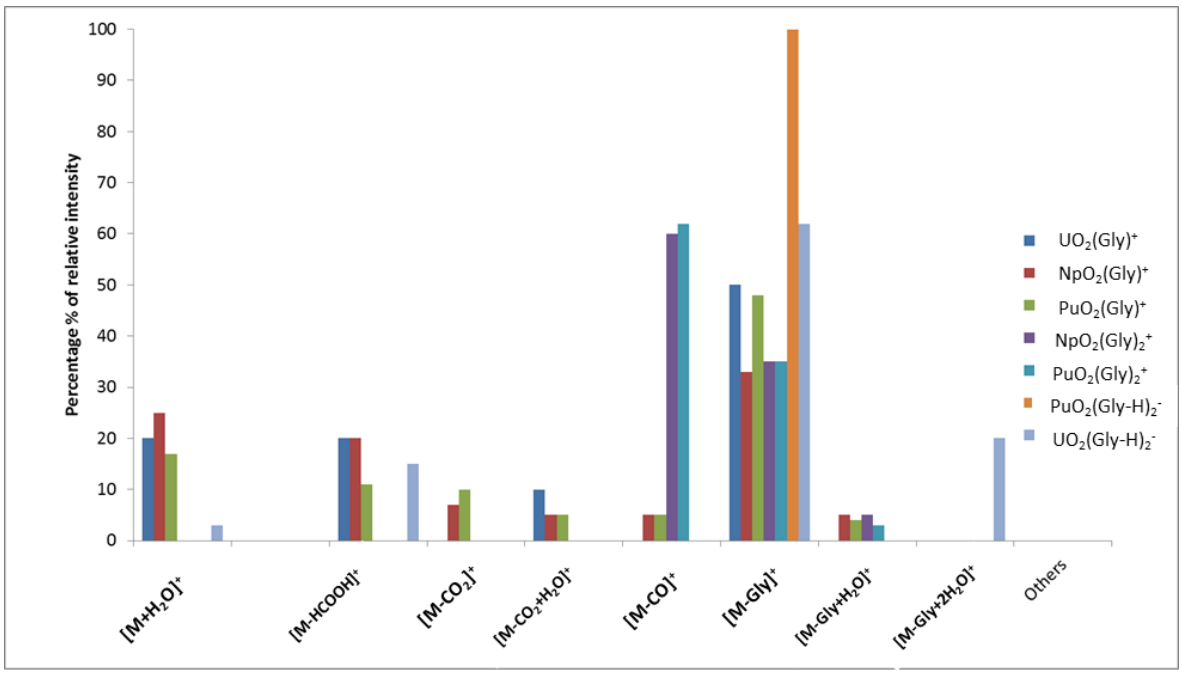

Figure IV.6 CID of $[AnO_2(Gly)_n]^+$ and $[AnO_2(Gly\text{-}H)_2]^-$ complexes (n = 1, 2; An = U, Np, Pu); product species in percentage of relative intensity.

IV.3.3 ESI-MS of actinyl complexes with cysteine, histidine and aspartic acid

The ESI of mixtures of aa (aa = Cys, His and Asp) and uranyl chloride or uranyl nitrate in methanol/water solutions generated monopositive and mononegative complexes containing the $U^{VI}O_2^{2+}$ ion with 1 to 3 aa ligands (see Supporting Information, Figure S1 and S2) and the $An^{V}O_2^{+}$ (An = U, Np, Pu) with 1 to 2 aa ligands (Table IV.7). The complexes generated for the oxidation state VI of uranyl include the cations $[U^{VI}O_2(aa\text{-}H)(aa)_2]^+$ and $[U^{VI}O_2(X)(aa)_2]^+$, and the anions $[AnO_2(aa\text{-}H)_3]^-$, $[UO_2(X)(aa\text{-}H)_2]^-$ and $[UO_2(X)_2(aa\text{-}H)]^-$, X = NO_3^-, Cl^-. The complexes formed with the oxidation state V were $[AnO_2(aa)_n]^+$, n = 1-2, in the positive mode and $[AnO_2(aa\text{-}H)_2]^-$ in the negative mode.

Table IV.7 Species generated by ESI-MS of mixtures of aa with uranyl/actinyl solutions. X = NO_3-, Cl-; aa = His, Asp, Cys; An = U, Pu, Np.

	Cations	**Anions**
An(VI)	$[UO_2(aa\text{-}H)(aa)_2]^+$	$[AnO_2(aa\text{-}H)_3]^-$, An = U, Pu
	$[UO_2(X)(aa)_2]^+$	$[UO_2(X)(aa\text{-}H)_2]^-$
		$[UO_2(X)_2(aa\text{-}H)]^-$
An(V)	$[AnO_2(aa)]^+$	$[AnO_2(aa\text{-}H)_2]^-$
	$[AnO_2(aa)_2]^+$	

IV.3.3.1 Dissociation in the positive mode

CID of $[UO_2(aa\text{-}H)(aa)_2]^+$ complexes

The CID of $[UO_2(aa\text{-}H)(aa)_2]^+$ complexes with the aa His and Asp is shown in Scheme IV.3. With His, there is 100% aa loss forming the species $[UO_2(His\text{-}H)(His)]^+$ while for Asp the loss of aa is 80% followed by water addition yielding the species $[UO_2(OH)(Asp)_2]^+$ with a relative abundance of 20% (Table IV.8). At LBNL it was observed the intriguing formation of less percentage of the aa loss (98% for his and 51% for asp) and more of the $-aa+H_2O$ loss (2% for his and 49% for asp); the opposite was expected since, as seen before (chapter III.2A), the water pressure in the C2TN QIT is higher than at LBNL (C2TN/100; LBNL/62; CEA/8.6; CQE/1.3).

$[UO_2(Cys\text{-}H)(Cys)_2]^+$ species is discussed below separately since it showed peculiar dissociation pathways.

Kinetics of the water addition to the species $[UO_2(aa\text{-}H)(aa)]^+$ is presented in Table IV.9. No reaction with the background water was observed for $[UO_2(His\text{-}H)(His)]^+$ and this is in agreement with the CID of the species $[UO_2(His\text{-}H)(His)_2]^+$.

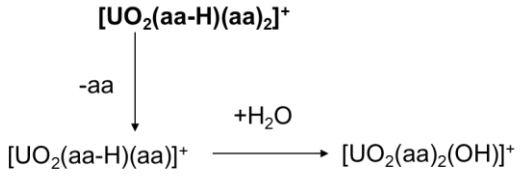

Scheme IV.3 CID of $[UO_2(aa\text{-}H)(aa)_2]^+$, aa = His, Asp.

Table IV.8 CID patterns of the species $[UO_2(aa\text{-}H)(aa)_2]^+$, aa = His, Cys, Asp. The values in parentheses were obtained at LBNL.

	$[M\text{-}aa]^+$	**$[M\text{-}aa+H_2O]^+$**
$[UO_2(His\text{-}H)(His)_2]^+$	100 (98)	0 (2)
$[UO_2(Asp\text{-}H)(Asp)_2]^+$	80 (51)	20 (49)
	$[M\text{-}Cys+H_2O]^+$	**$[M\text{-}NH_3]^+$**
$[UO_2(Cys\text{-}H)(Cys)_2]^+$	30	70

Table IV.9 Hydrolysis rates of the species $[UO_2(aa\text{-}H)(aa)]^+$.

	Eq.	***k* (s^{-1})**
$[UO_2(His\text{-}H)(His)]^+ + H_2O$ --> $[UO_2(OH)(His)_2]^+$	(2)	NR[a]
$[UO_2(Asp\text{-}H)(Asp)]^+ + H_2O$ --> $[UO_2(OH)(Asp)_2]^+$ [a]	(3)	3.6; 5.6[b]
$[UO_2(Cys\text{-}H)(Cys)]^+ + H_2O$ --> $[UO_2(OH)(Cys)_2]^+$	(4)	>30[b]

[a]NR means that it was not observed any reaction product within 10s of reaction.

[b]Estimated from the CID spectrum.

The particular case of UO_2^{2+}-Cys complexes

CID of the uranyl-Cys species is quite different from the other two aa and rather complex probably due to the structural differences of the side chain. CID of the species $[UO_2(Cys\text{-}H)(Cys)_2]^+$ yields a major fragment (70%), $[UO_2(Cys)(Cys\text{-}H)(Cys\&)]^+$ (Cys& = HOOCCHCHSH), by loss of NH_3, and 30% of $[UO_2(OH)(Cys)_2]^+$ by ligand loss and consecutive water addition (Scheme IV.4 and Figure IV.7 top). When higher energy is applied in the CID, it is also observed the formation of the species $[UO_2(Cys^*)(Cys\text{-}H)]^+$, (Cys*= $HOOCCHNH_2CH_2SSH$), which can come from two dissociation channels: a) loss of Cys plus loss of a sulfur atom (-89 = 121-32 = -$HOOCCHNH_2CH_3$, or –Cys-S), or b) loss of NH_3 plus loss of $HOOCCHCH_2$. The neutral species Cys* and Cys& as well as the loss of the neutral -$HOOCCHCH_2$ and –Cys-S fragments may have the suggested structures represented in Figure IV.9. Computations of possible structures formed upon CID of these uranyl-Cys species would be necessary to confirm these suggested structures and complement this study.

Other minor fragments are seen in the CID but from secondary fragmentations. It is the case of the species $[UO_2(Cys\text{-}H)(Cys\&)(H_2O)]^+$ (or $[UO_2(Cys)(Cys\&)(OH)]^+$), which can be formed by two channels: a) loss of -Cys + H_2O from the species $[UO_2(Cys)(Cys\text{-}H)(Cys\&)]^+$, or b) from the species $[UO_2(Cys)(Cys\text{-}H)]^+$, through loss of $–NH_3$ + H_2O. The species $[UO_2(Cys\text{-}H)(Cys\&)]^+$ is a minor intermediary species formed by both channels. In addition, the shape of the $[UO_2(Cys\text{-}H)(Cys\&)(H_2O)]^+$ peak in the CID mass spectrum indicates that its origin is most certainly a product of a gas-phase reaction (Figure IV.7). Also, reaction in the gas phase of the species $[UO_2(Cys)(Cys\text{-}H)]^+$ yields $[UO_2(OH)(Cys)_2]^+$ through water addition ($k > 30\ s^{-1}$). This reaction is common and was observed also with Asp (Table IV.9). The species $[UO_2(Cys\text{-}H)(Cys)]^+$ hydrates nearly 8 times faster than $[UO_2(Asp\text{-}H)(Asp)]^+$ (Table IV.9).

CID of Ca^{2+}-Cys species versus UO_2^{2+}-Cys species

To complement and understand the rather complex dissociations of these uranyl(VI)-Cys species, CID of analogous Ca^{2+}-Cys species was also done. Salpin and co-workers have reported recently[61] a very interesting gas-phase study of $[Ca(Cys)]^{2+}$ species by ESI-MS complemented with DFT theory. The dissociation of this species was dominated by loss of ammonia, a Coulomb explosion yielding NH_4^+ and $[CaC_3H_3O_2S]^+$, and the loss of H_2S. The authors concluded that that the structures in which the metal dication interacts with the carboxylate group of the zwitterionic form of Cys are at the origin of the different reaction pathways.

CID of the $[Ca(Cys\text{-}H)(Cys)_2]^+$ species is represented in Scheme IV.5. The dissociation resulted in analogous fragments to the uranyl-Cys CID formed species (Figure IV.8): $[M–NH_3]^+$, $[M\text{-}Cys]^+$ and $[M\text{-}Cys+H_2O]^+$ from reaction with the background water in the QIT. The last two species are present in majority in the CID spectrum (Figure IV.8).

The product ion $[Ca(Cys\text{-}H)(Cys\&)(H_2O)]^+$ (*m/z* = 282) is analogous to the fragment $[UO_2(Cys\text{-}H)(Cys\&)(H_2O)]^+$ and is also present in the CID spectrum but with much less abundance than for the uranyl species. These fragments are reaction products with the background water of the intermediary precursors $[Ca(Cys\text{-}H)(Cys\&)]^+$ and $[UO_2(Cys\text{-}H)(Cys\&)]^+$, respectively. The species $[Ca(Cys\text{-}H)(Cys)]^+$ is much more abundant in the mass spectrum than $[UO_2(Cys\text{-}H)(Cys)]^+$, which indicates a much faster hydration reaction for the uranyl species (evident in the lower energy CID spectrum of the precursor ion $[UO_2(Cys\text{-}H)(Cys)_2]^+$ on Figure IV.7). The fact that the Ca(II) species hydrate much slower than the uranyl species is in agreement with their charge density (see Chapter III.1). CID of the species $[UO_2(Cys\text{-}H)(Cys\&)]^+$ was not possible to perform due to the very low intensity in the mass spectrum and fast reaction with background water as described previously. In the case of the species $[Ca(Cys\text{-}H)(Cys\&)]^+$ the CID was possible since the hydration is much slower. The product of the fragmentation is $[Ca(Cys^*)]^+$ by loss of $HOOCCHCH_2$, which also hydrates to form the species $[Ca(Cys^*)(OH)_n]^+$ or $[Ca(Cys^*\text{-}H)(H_2O)_n]^+$, n=1,2. Another important consideration to take in account is the much more abundant fragmentation by loss of NH_3 in the uranyl species CID than in the calcium species, which determines all the subsequent reactions.

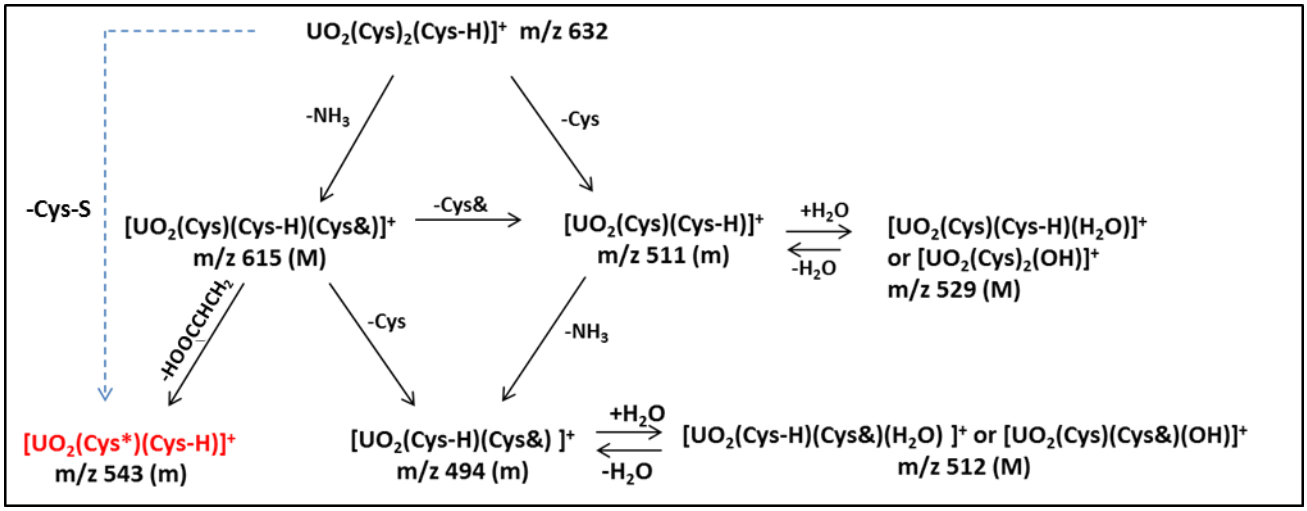

Scheme IV.4 Suggested CID pathway for $[UO_2(Cys\text{-}H)(Cys)_2]^+$. Cys*= $HOOCCHNH_2CH_2SSH$; Cys& = HOOCCHCHSH; Cys-S = $HOOCCHNH_2CH_3$. The arrow in blue indicates a non confirmed step; species with Cys* are indicated in red.

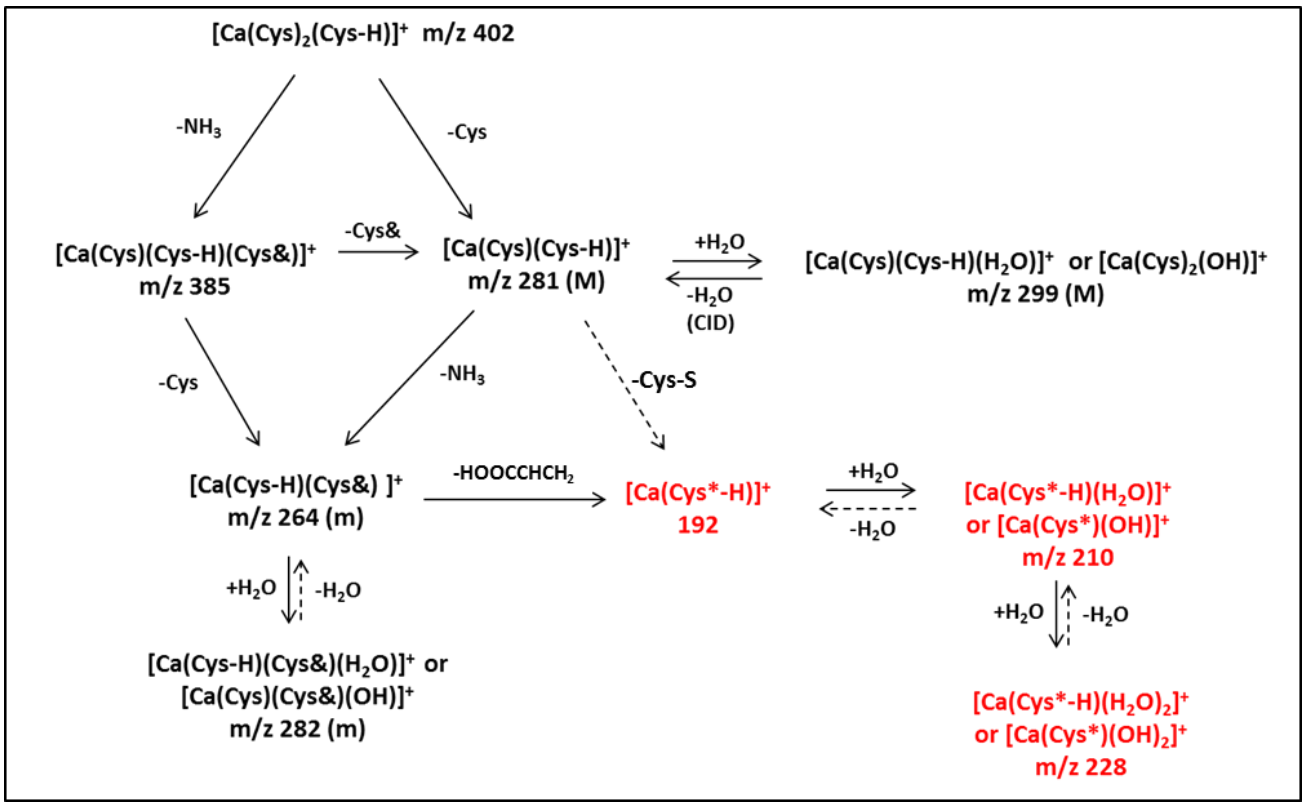

Scheme IV.5 Suggested CID pathway for $[Ca(Cys\text{-}H)(Cys)_2]^+$. Cys*= $HOOCCHNH_2CH_2SSH$, Cys& = HOOCCHCHSH; Cys-S = $HOOCCHNH_2CH_3$. Species with Cys* are indicated in red.

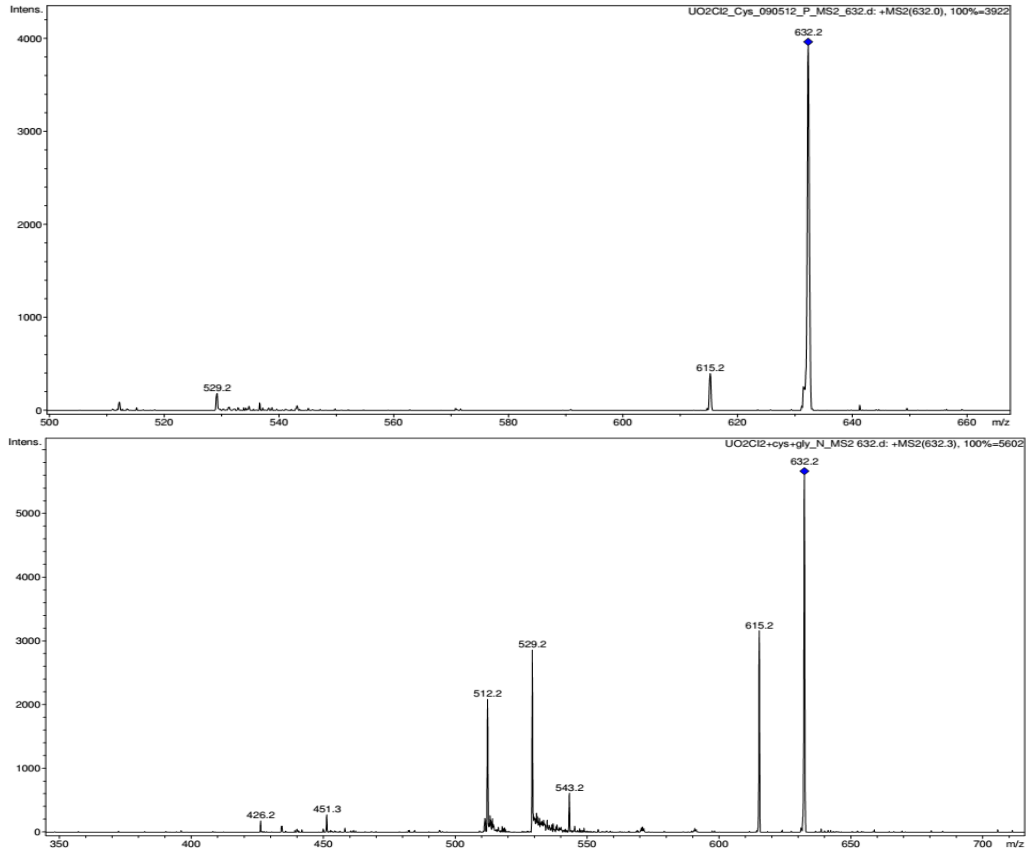

Figure IV.7 CID mass spectrum of $[UO_2(Cys\text{-}H)(Cys)_2]^+$ with lower (top) and higher (bottom) energy of fragmentation.

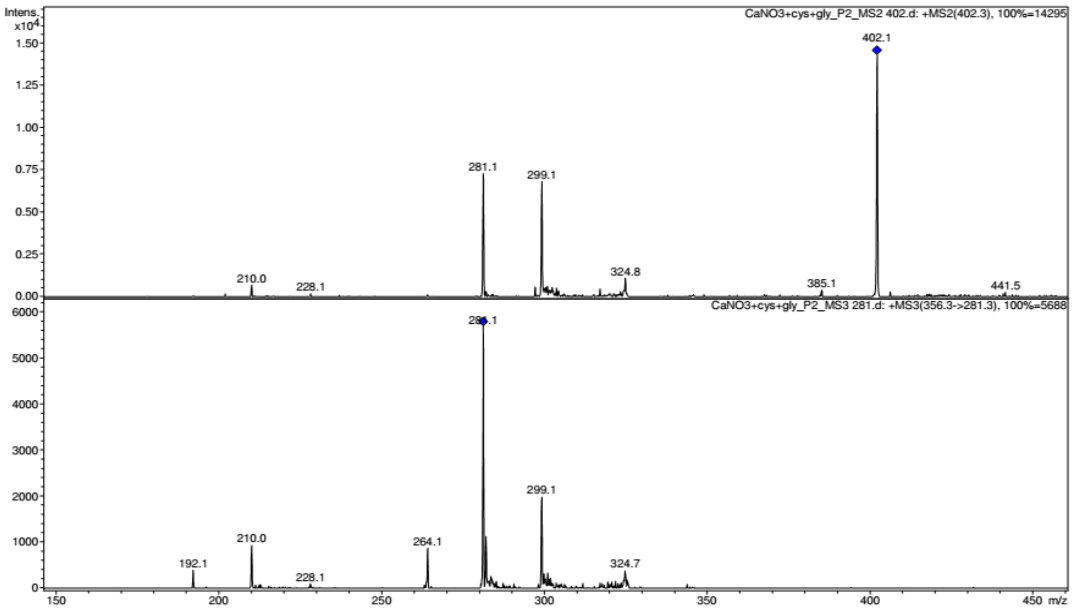

Figure IV.8 CID spectra of $[Ca(Cys\text{-}H)(Cys)_2]^+$ (top) and $[Ca(Cys\text{-}H)(Cys)]^+$ (bottom).

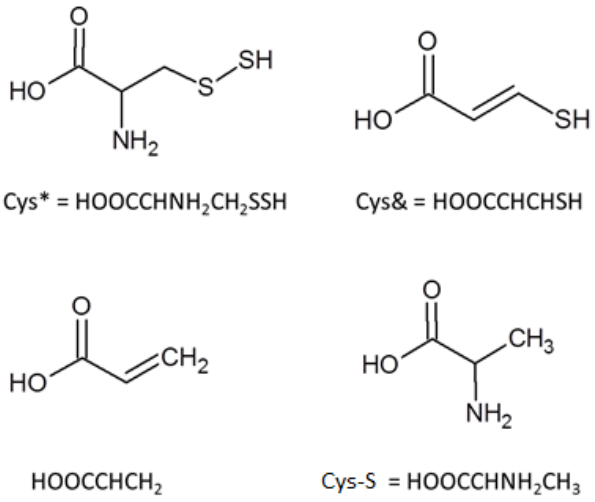

Figure IV.9 Suggested structures for the neutrals Cys*and Cys& and the observed fragments –$HOOCCHCH_2$ and –Cys-S.

CID of $[UO_2(X)(aa)_2]^+$ complexes

CID of $[UO_2(X)(aa)_2]^+$ species where X = NO_3^-, Cl^- were examined. The CID pattern is outlined in Scheme IV.6. In Table IV.10 is represented in relative percentage the obtained fragments. For aa = His, both $[UO_2(NO_3)(His)_2]^+$ and $[UO_2(Cl)(His)_2]^+$ yielded 100% of $[UO_2(His)(His\text{-}H)]^+$ by loss of HX. Again, there is no reaction with the background water, as it was observed before with other uranyl-histidine species. At LBNL, $[UO_2(ClO_4)(His)_2]^+$ species were also studied and the CID yielded 100% of $[UO_2(His\text{-}H)(His)]^+$ by loss of $HClO_4$.

For aa = Asp and Cys, -HX+H_2O was the major fragment observed from the dissociation of the species $[UO_2(X)(aa)_2]^+$, yielding $[UO_2(OH)(aa)_2]^+$. However, the loss of –HX was observed only in CID of $[UO_2(Cl)(Asp)_2]^+$ (40%) and in very small percentage, 1%, for $[UO_2(X)(Cys)_2]^+$. The CID of the uranyl nitrate -Cys species yields more fragments due to the side chain effect, as discussed above.

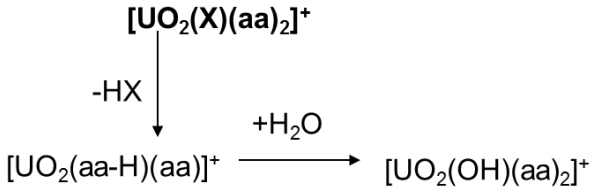

Scheme IV.6 CID pathway of $[UO_2(X)(aa)_2]^+$, X = NO_3^-, Cl^-.

Table IV.10 CID fragments of $[UO_2(X)(aa)_2]^+$, X = NO_3^-, Cl^-; aa = His, Cys, Asp in relative percentage (%).[a]

	$[UO_2(NO_3)(His)_2]^+$	$[UO_2(NO_3)(Cys)_2]^+$	$[UO_2(NO_3)(Asp)_2]^+$
$[M-HNO_3]^+$	100	1	0
$[M-HNO_3+H_2O]^+$	0	47	100
$[M-NH_3]^+$	-	21	-
Others	-	32[b]	0
	$[UO_2(Cl)(His)_2]^+$	$[UO_2(Cl)(Cys)_2]^+$	$[UO_2(Cl)(Asp)_2]^+$
$[M-HCl]^+$	100	1	40
$[M-HCl+H_2O]^+$	0	60	60
$[M-NH_3]^+$	-	0	-
Others	-	39[b]	0

[a]0% indicates not detected to <1%. A dash (-) indicates it is not applicable.
[b]corresponds to the fragment $[UO_2(Cys-H)(Cys\&)(H_2O)]^+$ or $[UO_2(Cys)(Cys\&)(OH)]^+$. See the fragmentation of UO_2^{2+}-Cys species above.

CID of $[AnO_2(aa)_n]^+$ complexes

The dissociation of An(V) complex species, namely $[AnO_2(aa)_n]^+$, n=1-2; An = Np, Pu; aa = His, Asp, were studied at LBNL. The fragments and their relative intensity for $[AnO_2(aa)]^+$ are outlined in Table IV.11 and for $[AnO_2(aa)_2]^+$ in Table IV.12. The CID of all species resulted in many fragments and the most abundant reacted with background water (Eq. 5).

$$AnO_2(aa)_y^+ + H_2O \longrightarrow AnO_2(aa)_y(H_2O)_n^+,\ y= 1\text{-}2\ n=1\text{-}3 \quad (5)$$

CID of $[NpO_2(His)]^+$ and $[PuO_2(His)]^+$ yielded water loss as major fragments, 40% and 50% respectively, while CID of $[NpO_2(Asp)]^+$ lead to loss of CO as major fragment (67%). On the other hand, when neptunyl is coordinated by two aa, $[NpO_2(aa)_2]^+$, water loss becomes the main product with either Cys, Asp or His, and the same is observed in the CID of $[PuO_2(Asp)_2]^+$. CID of $[PuO_2(His)_2]^+$ yielded 100% of decarboxylation followed by water addition, $[M-CO_2+H_2O]$. Contrarily to His and Asp, CID of $[NpO_2(Cys)_2]^+$ yielded also 3% of $[NpO_2(Cys)(Cys-CO)]^+$, 2% of $[NpO_2(Cys-H_2O)_2]^+$ and 3% $[NpO_2(Cys-OH)]^+$ by loss of M-CO, M-2H_2O and M-(Cys-OH), respectively. $[PuO_2(Cys)_2]^+$ species were formed in the electrospray but due to low signal intensity, CID studies were not possible.

In summary, water loss and decarboxylation/or loss of CO of either Cys, His or Asp are dominant in the CID of An(V) species. Np(V) and Pu(V) are responsible for bond activation of the C-αC bond in all three aa.

Table IV.11 CID fragments of $[AnO_2(aa)]^+$ in relative percentage %.

	$[NpO_2(His)]^+$	$[NpO_2(Asp)]^+$	$[PuO_2(His)]^+$	$[PuO_2(Asp)]^+$
$[M-H_2O]^+$	40	-	50	5
$[M-HCOOH]^+$	27	33	11	15
$[M-CO_2]^+$	23	-	26	-
$[M-CO_2+H_2O]^+$	5	-	10	-
$[M-CO]^+$	5	67	3	15
$[M-aa]^+$	-	-	-	10
$[M-aa+H_2O]^+$	-	-	-	-
Others	-	-	-	55

Table IV.12 CID fragments of the species $[AnO_2(aa)_2]^+$ in relative percentage %.

	$[NpO_2(His)_2]^+$	$[NpO_2(Asp)_2]^+$	$[NpO_2(Cys)_2]^+$	$[PuO_2(His)_2]^+$	$[PuO_2(Asp)_2]^+$
$[M-H_2O]^+$	57	45	60	0	55
$[M-CO]^+$	-	-	3	-	-
$[M-CO_2-H_2O]^+$	31	-	-	100	-
$[M-CO_2]^+$	8	21	-	-	-
$[M-aa]^+$	1	-	6	-	-
$[M-aa+H_2O]^+$	3	-	20	-	15
$[M-aa+2H_2O]^+$	-	-	6	-	-
$[M-HCOOH]^+$	0	34	-	-	30
Others	-	-	5	-	-

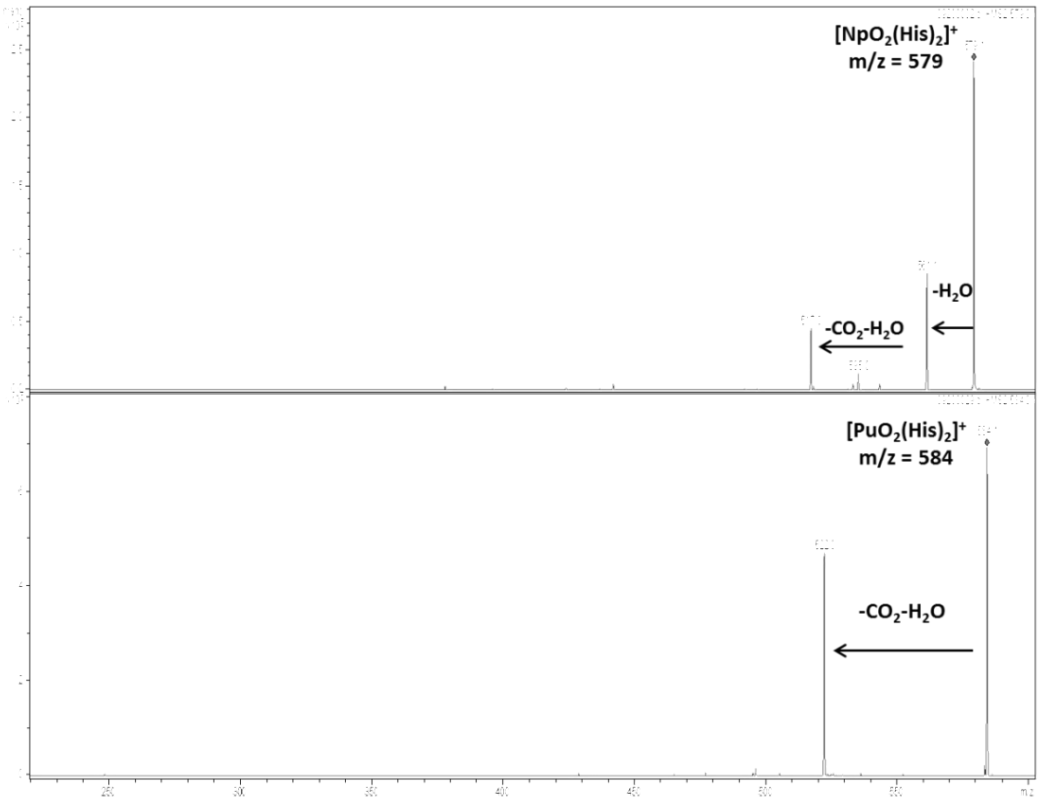

Figure IV.10 CID spectra of the species $[NpO_2(His)_2]^+$ (top) and $[PuO_2(His)_2]^+$ (bottom).

IV.3.3.2 Dissociation in the negative mode

CID of $[An^{VI}O_2(aa\text{-}H)_3]^-$ and $[An^{V}O_2(aa\text{-}H)_2]^-$ complexes

CID of $[AnO_2(aa\text{-}H)_3]^-$ (An = U, Pu) and $[AnO_2(aa\text{-}H)_2]^-$ (An = Np, Pu) complex species was evaluated. Pathways for $[UO_2(aa\text{-}H)_3]^-$, aa = His, Cys, Asp, are shown in Scheme IV.7. Relative intensities of the observed fragments are represented in Table IV.13 for the An(VI) species and in Table IV.14 for the An(V) species.

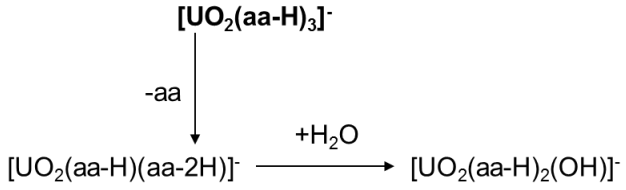

Scheme IV.7 CID pathways of the $[UO_2(aa\text{-}H)_3]^-$ Species.

CID of $[UO_2(Cys\text{-}H)_3]^-$, $[UO_2(Asp\text{-}H)_3]^-$ and $[PuO_2(Asp\text{-}H)_3]^-$ yielded 100% of $[AnO_2(aa\text{-}H)(aa\text{-}2H)]^-$ (An = U, Pu) by aa loss while CID of $[UO_2(His\text{-}H)_3]^-$ yielded 30% of $[UO_2(His\text{-}H)(His\text{-}2H)]^-$ and 70% of $[UO_2(OH)(His\text{-}H)_2]^-$, and CID of $[PuO_2(His\text{-}H)_3]^-$ yielded 100% of $[Pu^{V}O_2(His\text{-}H)_2]^-$ by reduction through loss of a aa-H ligand (Figure IV.11).

In relation to the An(V) species, CID of $[NpO_2(His\text{-}H)_2]^-$ and $[PuO_2(His\text{-}H)_2]^-$ yielded fragments of aa loss and aa loss with consecutive hydration/hydolysis but with different percentages of relative intensity.

Also, loss of (CO_2, H_2O) was observed in the CID of the plutonyl V species with higher loss percentage (20%) in the CID of $[PuO_2(Asp\text{-}H)_2]^-$. Apparently, with PuO_2^+ there is bond activation by loss of CO_2 of the aa ligands. The major fragment in the CID of this species was by water loss while for His the major fragment was ligand loss with 60% abundance. CID of $[NpO_2(Asp\text{-}H)_2]^-$ was not possible to perform due to low signal intensity. It was also possible to form the species $[NpO_2(Cys\text{-}H)_2]^-$ in the ESI-MS. CID yielded $[Np^{V}O_2(Cys\text{-}2H)]^-$ by loss of Cys and $[Np^{VI}O_3(Cys\text{-}2H)]^-$ by loss of Cys and hydrolysis; loss of water and loss of (H_2O, CO_2) were also observed.

CID and hydrolysis (Table IV.15) of the species $[UO_2(aa\text{-}H)(aa\text{-}2H)]^-$ were also possible to perform in the QIT with quite good overall intensity of the fragments. CID yielded the U(VI) species $[UO_2(OH)(aa\text{-}2H)]^-$ by major loss of aa + H_2O for Asp and His. The species $[UO_2(aa\text{-}H)(aa\text{-}2H)]^-$ (Eq. 6) hydrolyze in the order His>Cys~Asp, where no reaction was observed for the species with Asp. This result indicates the strength of the doubly-deprotonated ligand (Asp-2H) to the uranyl ion and also the mode of coordination, probably bidentate by the deprotonated carboxylate ends of

Asp. In relation to Eqs. 7 and 8, the same trend is observed in the hydrolysis reactions of the species $[UO_2(NO_3)(aa\text{-}2H)]^-$ and $[UO_2(Cl)(aa\text{-}2H)]^-$.

Table IV.13 CID fragments of the species $[UO_2(aa\text{-}H)_3]^-$and $[PuO_2(aa\text{-}H)_3]^-$ and relative intensity in percentage %. * values were obtained at LBNL.

	$[M\text{-}aa]^-$	**$[M\text{-}aa+H_2O]^-$**	**$[M\text{-}aa\text{-}H]^-$**
$[UO_2(His\text{-}H)_3]^-$	30 (30)	70 (70)	0
$[UO_2(Cys\text{-}H)_3]^-$	100	0	0
$[UO_2(Asp\text{-}H)_3]^-$	100 (100)	0 (0)	0
***$[PuO_2(His\text{-}H)_3]^-$**	0	0	100
***$[PuO_2(Asp\text{-}H)_3]^-$**	100	0	0

Table IV.14 CID fragments of the species $[PuO_2(aa\text{-}H)_2]^-$ and $[NpO_2(aa\text{-}H)_2]^-$ and relative intensity in percentage %.

	$[M\text{-}aa]^-$	**$[M\text{-}aa+H_2O]^-$**	**$[M\text{-}H_2O]^-$**	**$[M\text{-}CO_2\text{-}H_2O]^-$**	**others**
$[PuO_2(His\text{-}H)_2]^-$	60	30	5	5	-
$[PuO_2(Asp\text{-}H)_2]^-$	0	0	80	20	-
$[NpO_2(His\text{-}H)_2]^-$	28	50	22	0	-
$[NpO_2(Asp\text{-}H)_2]^-$	*	*	*	*	-
$[NpO_2(Cys\text{-}H)_2]^-$	-	-	60	10	30

*Low intensity of the signal; not possible to perform CID.
(-) A dash indicates that those fragments are not present in the CID.

Table IV.15 Hydrolysis rates of the species $[UO_2(aa\text{-}H)(aa\text{-}2H)]^-$ and $[UO_2(X)(aa\text{-}2H)]^-$; aa=Cys, His, Asp; $X=NO_3^-$, Cl^-; k (s^{-1}); NR no reaction (10 s); * from CID of the precursor.

	Equation	**His**	**Asp**	**Cys**
$[UO_2(aa\text{-}H)(aa\text{-}2H)]^- + H_2O$ --> $[UO_2(aa\text{-}H)_2(OH)]^-$	(6)	10.7	NR	<0.06
$[UO_2(NO_3)(aa\text{-}2H)]^{-\cdot} + H_2O$ --> $[UO_2(NO_3)(aa\text{-}H)(OH)]^-$	(7)	9.9	NR	3.8
$[UO_2Cl(aa\text{-}2H)]^- + H_2O$ --> $[UO_2Cl(aa\text{-}H)(OH)]^-$	(8)	66-73*	1.3	35.9

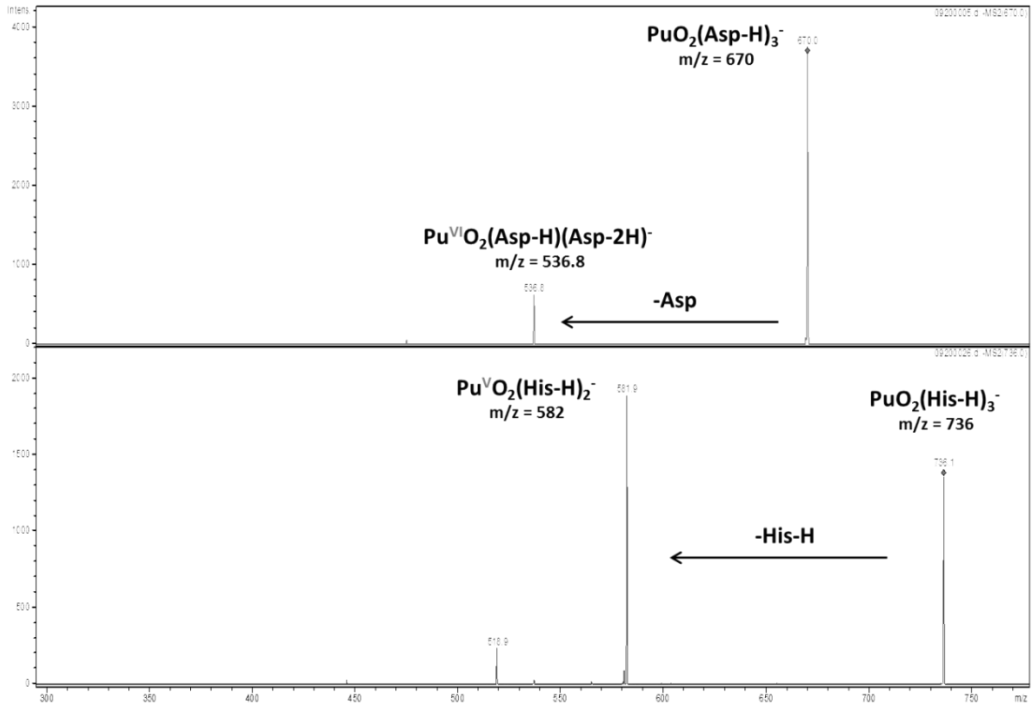

Figure IV.11 CID spectra of the species $[PuO_2(Asp\text{-}H)_3]^-$ (top) and $[PuO_2(His\text{-}H)_3]^-$ (bottom).

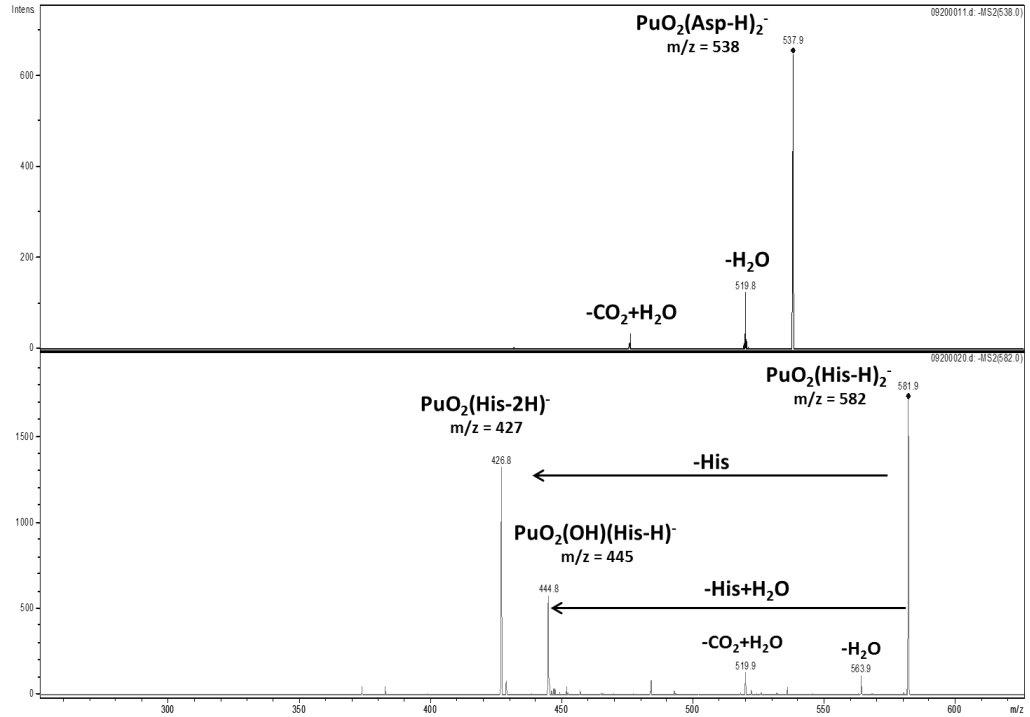

Figure IV.12 CID spectra of the species $[PuO_2(Asp\text{-}H)_2]^-$ (top) and $[PuO_2(His\text{-}H)_2]^-$ (bottom).

CID of $[UO_2(X)(aa\text{-}H)_2]^-$ and $[UO_2(X)_2(aa\text{-}H)]^-$ species

CID of uranyl nitrate or uranyl chloride species coordinated to 1 or 2 deprotonated aa were studied in the QIT (Figure IV.13 and Table IV.16). CID of $[UO_2(NO_3)(Cys\text{-}H)_2]^-$ and $[UO_2(NO_3)(Asp\text{-}H)_2]^-$ yielded aa loss as the major fragmentation while for $[UO_2(NO_3)(His\text{-}H)_2]^-$ loss of HNO_3 was preferred. For the species coordinated to only one deprotonated aa and 2 nitrates, the opposite was observed: for $[UO_2(NO_3)_2(Cys\text{-}H)]^-$ and $[UO_2(NO_3)_2(Asp\text{-}H)]^-$ loss of HNO_3 is dominant in the CID spectra.

The chloride species follow the same trend but with loss of HCl dominating the CID spectra: since the Cl ligand is weaker in strength than the nitrate. CID of $[UO_2(Cl)(His\text{-}H)_2]^-$ resulted in a combined loss of HCl and water addition (55%) and only a small fragment of loss of HCl is seen (15%), while CID of $[UO_2(Cl)(Cys\text{-}H)_2]^-$ and $[UO_2(Cl)(Asp\text{-}H)_2]^-$ yielded preferentially loss of HCl (>80%). Also CID of the species $[UO_2(Cl)_2(aa\text{-}H)]^-$, aa = Cys, Asp, yielded fragments of loss of HCl followed by water addition (65%), and with aa = His, CID yielded 90% of loss of HCl forming $[UO_2(Cl)(aa\text{-}2H)]^-$ for aa = Cys, Asp and $[UO_2(Cl)(OH)(His\text{-}H)]^-$.

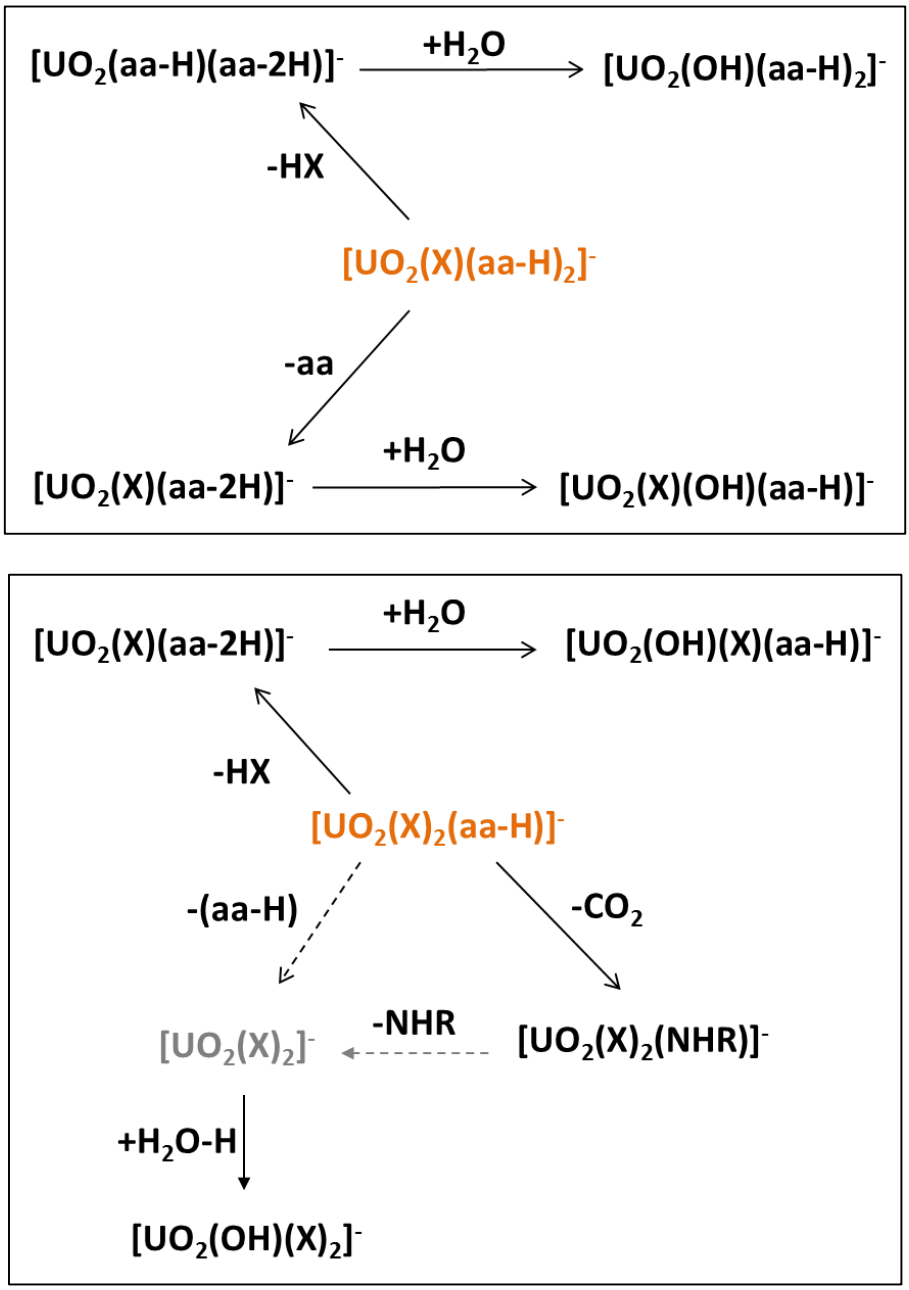

Figure IV.13 CID pathways of $[UO_2(X)(aa\text{-}H)_2]^-$ top figure and $[UO_2(X)_2(aa\text{-}H)]^-$ bottom figure. X = NO_3-,Cl-; aa = His, Cys, Asp. In grey are supposed intermediaries. The loss of CO_2 is minor (see Table IV.15).

Table IV.16 CID of $[UO_2(X)(aa\text{-}H)_2]^-$ and $[UO_2(X)_2(aa\text{-}H)]^-$and relative intensity of products (%) . X = NO_3-,Cl-; aa = His, Cys, Asp. Y= -(aa-H)+H_2O-H. Values in () were obtained at LBNL for comparison.

	$[M\text{-}HX]^-$	$[M\text{-}HX+H_2O]^-$	$[M\text{-}aa]^-$	$[M\text{-}aa+H_2O]^-$	$[M\text{-}Y]^-$	$[M\text{-}CO_2]^-$
$[UO_2(NO_3)(His\text{-}H)_2]^-$	50 (8)	30 (15)	5 (55)	15 (22)	-	0
$[UO_2(NO_3)(Cys\text{-}H)_2]^-$	5	0	80	15	-	0
$[UO_2(NO_3)(Asp\text{-}H)_2]^-$	15 (18)	0	85 (82)	0	-	0
$[UO_2(Cl)(His\text{-}H)_2]^-$	15	55	5	25	-	0
$[UO_2(Cl)(Cys\text{-}H)_2]^-$	85	0	5	10	-	0
$[UO_2(Cl)(Asp\text{-}H)_2]^-$	100	0	0	0	-	0
$[UO_2(NO_3)_2(His\text{-}H)]^-$	45	45	-	-	10	0
$[UO_2(NO_3)_2(Cys\text{-}H)]^-$	85	15	-	-	0	0
$[UO_2(NO_3)_2(Asp\text{-}H)]^-$	100	0	-	-	0	0
$[UO_2(Cl)_2(His\text{-}H)]^-$	5	65	-	-	25	5
$[UO_2(Cl)_2(Cys\text{-}H)]^-$	30	65	-	-	5	0
$[UO_2(Cl)_2(Asp\text{-}H)]^-$	90	5	-	-	5	0

IV.3.4 Competitive CID: formation and dissociation pathways of actinyl-mixed amino acid complexes

Competitive CID of uranyl mixed aa species was studied with the aim of determining the relative affinity and gas-phase stability of the formed species.

Uranyl complexes with neutral and deprotonated aspartic acid, histidine, cysteine and glycine were produced by ESI of solutions of uranyl chloride (UO_2Cl_2) and mixtures of two amino acids in a 1:1 ratio with a final concentration of 10^{-4}M in H_2O/EtOH spray solution. The concentration of the aa was approximately 4 times the concentration of $[UO_2Cl_2]$ to ensure complexation. Uranyl nitrate was not used for this study since it didn't yield as many mixed-species as with the uranyl chloride. The following species were formed: $[UO_2(aa^1)_2(aa^2\text{-}H)]^+$ or $[UO_2(aa^1)(aa^1\text{-}H)(aa^2)]^+$, $[UO_2(aa^2)_2(aa^1\text{-}H)]^+$ or $[UO_2(aa^2)(aa^2\text{-}H)(aa^1)]^+$, $[UO_2Cl(aa^1)(aa^2)]^+$, $[UO_2Cl(aa^1\text{-}H)(aa^2\text{-}H)]^-$, and $[UO_2(aa^1\text{-}H)_2(aa^2\text{-}H)]^-$ and $[UO_2(aa^2\text{-}H)_2(aa^1\text{-}H)]^-$. Plutonyl mixed complexes $[PuO_2(His)_2(Asp\text{-}H)]^+$ or $[PuO_2(His\text{-}H)(His)(Asp)]^+$ and $[PuO_2(His)(Asp)(Asp\text{-}H)]^+$ or $[PuO_2(His\text{-}H)(Asp)_2]^+$ were also possible to obtain by ESI-MS in the positive mode. CID of these species were analyzed and compared to the uranyl mixed species. Computational studies would be necessary in order to obtain data on the most favorable species as many are the possibilities in both positive and negative modes.

IV.3.4.1 Positive mode

CID of the mixed-aa species $[UO_2(aa^1)_2(aa^2\text{-}H)]^+$ (or $[UO_2(aa^1)(aa^1\text{-}H)(aa^2)]^+$) showed primarily loss of a neutral aa, followed by reaction with the background water in the QIT for some of the products. In the positive mode (Table IV.17), CID of $[UO_2(His\text{-}H)(His)(Asp)]^+$ (or $[UO_2(His)_2(Asp\text{-}H)]^+$) and $[UO_2(His\text{-}H)(His)(Cys)]^+$ (or $[UO_2(His)_2(Cys\text{-}H)]^+$) showed 100% loss of a neutral Asp or Cys, respectively, yielding the species $[UO_2(His)(His\text{-}H)]^+$ (Figure IV.14 **a** and IV.14 **b**), while CID of $[UO_2(Cys)_2(Asp\text{-}H)]^+$ (or $[UO_2(Cys\text{-}H)(Cys)(Asp)]^+$) yielded 44% loss of neutral Cys and 44% loss of Cys plus rapid reaction with background H_2O.

CID of $[UO_2(Asp)_2(His\text{-}H)]^+$ (or $[UO_2(His)(Asp)(Asp\text{-}H)]^+$) (Figure IV.14 **c**) yielded more of the $[M\text{-}aa+H_2O]^+$ species than loss of the neutral aa, while the opposite occurred for $[UO_2(Asp)_2(Cys\text{-}H)]^+$ (or $[UO_2(Cys)(Asp)(Asp\text{-}H)]^+$). CID of mixed species with Cys yielded also small percentages of NH_3 loss, a common fragmentation previously observed for the protonated aa, due to the SH side chain influence. However, the percentage of NH_3 loss is higher in the CID of the Uranyl-Cys-Gly mixed species, with 30% loss in the CID of the species with 2 coordinated Cys, $[UO_2(Cys)_2(Gly\text{-}H)]^+$ (or

$[UO_2(Cys\text{-}H)(Cys)(Gly)]^+$), and 20% loss in the CID of the species with 2 coordinated Gly, $[UO_2(Gly)_2(Cys\text{-}H)]^+$ (or $[UO_2(Cys)(Gly)(Gly\text{-}H)]^+$). In the CID of the species $[UO_2(aa)_2(Cys\text{-}H)]^+$, aa = His or Asp, loss of NH_3 was not observed.

Comparatively to CID of $[UO_2(His\text{-}H)(His)(Asp)]^+$ (or $[UO_2(His)_2(Asp\text{-}H)]^+$), which yielded 100% loss of neutral Asp, CID of the plutonyl mixed species $[PuO_2(His\text{-}H)(His)(Asp)]^+$ (or $[PuO_2(His)_2(Asp\text{-}H)]^+$) yielded only 20% of the $[M–Asp]^+$ fragment and 2% of $[M–Asp+H_2O]^+$ but the main fragment was $[M–Asp\text{-}CO_2]^+$ with 78% of relative intensity in the spectrum yielding the species $[PuO_2(His)(His\text{-}CO_2)]^+$. This result indicates that, as seen before, with plutonyl, there is preference for bond activation in the His ligand through decarboxylation instead of the aa loss as seen in the uranyl species (Table IV.18). Hydrolysis rates of some $[UO_2(aa^1\text{-}H)(aa^2)]^+$ species originated from the dissociation of $[UO_2(aa^1\text{-}H)(aa^2)_2]^+$ are presented in Table IV.19.

Table IV.17 Competitive CID of positive mixed ligand species in relative percentage of intensity.*

	[M-His]$^+$	[M-His+H_2O]$^+$	[M-Asp]$^+$	[M-Asp+H_2O]$^+$	[M-NH_3]$^+$
[UO_2(His-H)(His)(Asp)]$^+$	0	0	100 (100)	0	-
or [UO_2(His)$_2$(Asp-H)]$^+$					
[UO_2 (Asp)$_2$(His-H)]$^+$or	0	0	30	70	-
[UO_2(His)(Asp)(Asp-H)]$^+$					
	[M-His]$^+$	**[M-His+H_2O]$^+$**	**[M-Cys]$^+$**	**[M-Cys+H_2O]$^+$**	**[M-NH_3]$^+$**
[UO_2(Cys)$_2$(His-H)]$^+$ or	0	0	10	80	10
[UO_2(His)(Cys)(Cys-H)]$^+$					
[UO_2(His-H)(His)(Cys)]$^+$ or	0	0	100	0	0
[UO_2(His)$_2$(Cys-H)]$^+$					
	[M-His]$^+$	**[M-His+H_2O]$^+$**	**[M-Gly]$^+$**	**[M-Gly+H_2O]$^+$**	**[M-NH_3]$^+$**
[UO_2(His-H)(His)(Gly)]$^+$ or	10	0	90	0	-
[UO_2(His)$_2$(Gly-H)]$^+$					
[UO_2(His)(Gly)(Gly-H)]$^+$ or	0	0	5	95	-
[UO_2(His-H)(Gly)$_2$]$^+$					
	[M-Cys]$^+$	**[M-Cys+H_2O]$^+$**	**[M-Asp]$^+$**	**[M-Asp+H_2O]$^+$**	**[M-NH_3]$^+$**
[UO_2(Cys)$_2$(Asp-H)]$^+$ or	44	44	1	1	10
[UO_2(Cys-H)(Cys)(Asp)]$^+$					
[UO_2(Cys)(Asp)(Asp-H)]$^+$	65	25	5	5	0
or [UO_2(Asp)$_2$(Cys-H)]$^+$					
	[M-Asp]$^+$	**[M-Asp+H_2O]$^+$**	**[M-Gly]$^+$**	**[M-Gly+H_2O]$^+$**	**[M-NH_3]$^+$**
[UO_2(Asp)$_2$(Gly-H)]$^+$ or	10	5	55	30	-
[UO_2(Asp-H)(Asp)(Gly)]$^+$					
[UO_2(Gly)$_2$(Asp-H)]$^+$or	0	0	50	50	-
[UO_2(Asp)(Gly)(Gly-H)]$^+$					
	[M-Cys-H]$^+$	**[M-Cys+H_2O]$^+$**	**[M-Gly-H]$^+$**	**[M-Gly+H_2O]$^+$**	**[M-NH_3]$^+$**
[UO_2(Cys)$_2$(Gly-H)]$^+$ or	5	25	15	25	30
[UO_2(Cys-H)(Cys)(Gly)]$^+$					
[UO_2(Gly)$_2$(Cys-H)]$^+$ or	0	0	15	65	20
[UO_2(Cys)(Gly)(Gly-H)]$^+$					

*Two possibilities for each species are given; in grey are the less likely species to be formed.

Table IV.18 Competitive CID of the positive plutonyl mixed ligand species in relative percentage of intensity.**

	$[M\text{-}His]^+$	$[M\text{-}His+H_2O]^+$	$[M\text{-}Asp]^+$	$[M\text{-}Asp+H_2O]^+$	$[M\text{-}Asp\text{-}CO_2]^+$
$[PuO_2(His\text{-}H)(His)(Asp)]^+$ or $[PuO_2(His)_2(Asp\text{-}H)]^+$	0	0	20	2	78
***$[PuO_2(Asp)_2(His\text{-}H)]^+$ or *$[PuO_2(His)(Asp)(Asp\text{-}H)]^+$**	-	-	-	-	-

*Not a very good yield of the species in the PS. Unable to perform CID due to very low signal intensity.
** In grey are the less likely species to be formed.

Table IV.19 Hydrolysis rates of uranyl mixed-aa species.

Reaction	Equation	k (s^{-1})
$[UO_2(Asp\text{-}H)(His)]^+$ or $[UO_2(Asp)(His\text{-}H)]^+ + H_2O$ --> $[UO_2(OH)(Asp)(His)]^+$	(9)	>30*
$[UO_2(Asp\text{-}H)(Cys)]^+$ or $[UO_2(Asp)(Cys\text{-}H)]^+ + H_2O$ --> $[UO_2(OH)(Asp)(Cys)]^+$	(10)	>17*
$[UO_2(Asp\text{-}H)(Gly)]^+$ or $[UO_2(Asp)(Gly\text{-}H)]^+ + H_2O$ --> $[UO_2(OH)(Asp)(Gly)]^+$	(11)	>17*
$[UO_2(Cys\text{-}H)(His)]^+$ or $[UO_2(Cys)(His\text{-}H)]^+ + H_2O$ --> $[UO_2(OH)(Cys)(His)]^+$	(12)	>58*
$[UO_2(Gly\text{-}H)(Cys)]^+$ or $[UO_2(Gly)(Cys\text{-}H)]^+ + H_2O$ --> $[UO_2(OH)(Gly)(Cys)]^+$	(13)	#
$[UO_2(Gly\text{-}H)(His)]^+$ or $[UO_2(Gly)(His\text{-}H)]^+ + H_2O$ --> $[UO_2(OH)(Gly)(His)]^+$	(14)	#

* Calculated from the CID spectrum of the precursor.
#very fast reaction, not possible to measure the rate. The intensity of the precursor was very low.

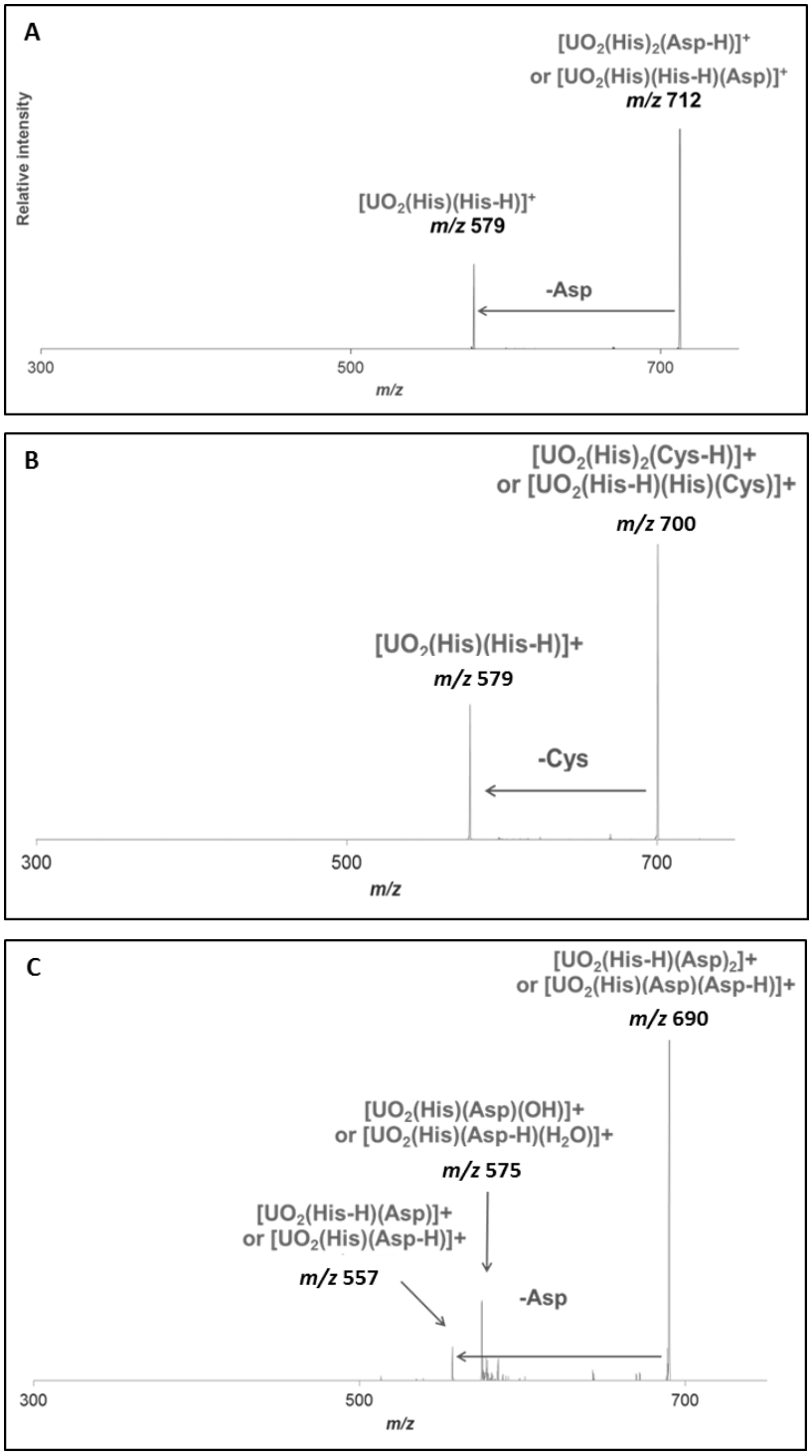

Figure IV.14 Competitive CID spectra of positive uranyl mixed-aa species.

IV.3.4.2 Negative mode

In the negative mode (Table IV.20), CID of $[UO_2Cl(aa^1\text{-}H)(aa^2\text{-}H)]^-$ complexes resulted mostly in loss of HCl, while in CID of the $[UO_2(His\text{-}H)_2(aa^2\text{-}H)]^-$ species (aa^2 = Asp or Cys) preferential loss of the neutral amino acid was observed (Fig. IV.15 A and IV.15 B) in the order His~Cys>Asp, indicating particularly strong coordination of doubly-deprotonated Asp to UO_2^{2+} (Table IV.20), a result indicated also by the hydrolysis reactions of the species $[UO_2(aa\text{-}H)(aa\text{-}2H)]^-$ (Table IV.21). CID of the $[AnO_2(Asp\text{-}H)_2(His\text{-}H)]^-$ (An= U, Pu) species yielded 50% of loss of each neutral aa (Fig. IV.15 C) while CID of $[UO_2(Asp\text{-}H)_2(Cys\text{-}H)]^-$ yielded 90% loss of neutral Cys and only 10% loss of neutral Asp.

CID of the species $[UO_2(aa\text{-}H)_2(Gly\text{-}H)]^-$ and $[UO_2(aa\text{-}H)(Gly\text{-}H)_2]^-$, aa = Cys, His, Asp, yielded essentially loss of neutral Gly and/or -Gly loss + H_2O. This shows that the coordination between uranyl and Gly is not as strong as with the other aa, mainly due to its size and lack of side chain.

CID of the species $[AnO_2(His\text{-}H)_2(Asp\text{-}H)]^-$ (An = U, Pu) yielded 100% loss of His in the case of uranyl and 82% for the plutonyl species (Figure IV.16) forming the species $[AnO_2(His\text{-}H)(Asp\text{-}2H)]^-$. The latter yielded also 18% loss of CO_2 and H_2O. Again, plutonyl(VI) is accountable for bond activation through decarboxylation in either His or Asp.

Table IV.20 Competitive CID for the negative mixed ligand species in relative percentage of intensity. Values in () and plutonyl species were obtained at LBNL.

	$[M\text{-}His]^-$	$[M\text{-}His+H_2O]^-$	$[M\text{-}Asp]^-$	$[M\text{-}Asp+H_2O]^-$	$[M\text{-}HCl]^-$	$[M\text{-}HCl+H_2O]^-$	$[M\text{-}CO_2\text{-}H_2O]^-$
$[UO_2Cl(His\text{-}H)(Asp\text{-}H)]^-$	0	0	0	0	100	0	
$[UO_2(His\text{-}H)_2(Asp\text{-}H)]^-$	100 (100)	0	0	0	0	0	0
$[UO_2(His\text{-}H)(Asp\text{-}H)_2]^-$	50 (50)	0	50 (50)	0	0	0	0
$[PuO_2(His\text{-}H)_2(Asp\text{-}H)]^-$	82	0	0	0	0	0	18
$[PuO_2(His\text{-}H)(Asp\text{-}H)_2]^-$	50	0	50	0	0	0	0
	$[M\text{-}His]^-$	$[M\text{-}His+H_2O]^-$	$[M\text{-}Cys]^-$	$[M\text{-}Cys+H_2O]^-$	$[M\text{-}HCl]^-$	$[M\text{-}HCl+H_2O]^-$	$[M\text{-}CO_2\text{-}H_2O]^-$
$[UO_2Cl(His\text{-}H)(Cys\text{-}H)]$-	0	0	0	0	100	0	0
$[UO_2(His\text{-}H)_2(Cys\text{-}H)]$-	86	2	5	7			0
$[UO_2(His\text{-}H)(Cys\text{-}H)_2]$-	9	4	84	3			0
	$[M\text{-}Cys]^-$	$[M\text{-}Cys+H_2O]^-$	$[M\text{-}Asp]^-$	$[M\text{-}Asp+H_2O]^-$	$[M\text{-}HCl]^-$	$[M\text{-}HCl+H_2O]^-$	$[M\text{-}CO_2\text{-}H_2O]^-$
$[UO_2Cl(Cys\text{-}H)(Asp\text{-}H)]^-$	5	0	0	0	95	0	0
$[UO_2(Cys\text{-}H)_2(Asp\text{-}H)]^-$	50	0	0	50	-	-	0
$[UO_2(Cys\text{-}H)(Asp\text{-}H)_2]^-$	90	0	10	0	-	-	0
	$[M\text{-}His]^-$	$[M\text{-}His+H_2O]^-$	$[M\text{-}Gly]^-$	$[M\text{-}Gly+H_2O]^-$	$[M\text{-}HCl]^-$	$[M\text{-}HCl+H_2O]^-$	$[M\text{-}CO_2\text{-}H_2O]^-$
$[UO_2Cl(His\text{-}H)(Gly\text{-}H)]^-$	0	0	5	50	20	25	0
$[UO_2(His\text{-}H)_2(Gly\text{-}H)]^-$	20	10	5	65	-	-	0
$[UO_2(His\text{-}H)(Gly\text{-}H)_2]^-$	10	0	40	50	-	-	0
	$[M\text{-}Asp]^-$	$[M\text{-}Asp+H_2O]^-$	$[M\text{-}Gly]^-$	$[M\text{-}Gly+H_2O]^-$	$[M\text{-}HCl]^-$	$[M\text{-}HCl+H_2O]^-$	$[M\text{-}CO_2\text{-}H_2O]^-$
$[UO_2Cl(Asp\text{-}H)(Gly\text{-}H)]^-$	0	0	15	0	85	0	0
$[UO_2(Asp\text{-}H)_2(Gly\text{-}H)]^-$	0	0	100	0	-	-	0
$[UO_2(Asp\text{-}H)(Gly\text{-}H)_2]^-$	0	0	100	0	-	-	0
	$[M\text{-}Cys]^-$	$[M\text{-}Cys+H_2O]^-$	$[M\text{-}Gly]^-$	$[M\text{-}Gly+H_2O]^-$	$[M\text{-}HCl]^-$	$[M\text{-}HCl+H_2O]^-$	$[M\text{-}CO_2\text{-}H_2O]^-$
$[UO_2Cl(Cys\text{-}H)(Gly\text{-}H)]^-$	0	0	20	39	40	1	0
$[UO_2(Cys\text{-}H)_2(Gly\text{-}H)]^-$	0	0	100	0	-	-	0
$[UO_2(Cys\text{-}H)(Gly\text{-}H)_2]^-$	0	0	85	15	-	-	0

Table IV.21 Hydrolysis rates of the mixed uranyl-aa species $[UO_2(aa^1\text{-}H)(aa^2\text{-}2H)]^-$, aa = Gly, Cys, Asp.

	Equation	k (s^{-1})
$[UO_2(Cys\text{-}H)(Asp\text{-}2H)]^-$ or $[UO_2(Cys\text{-}2H)(Asp\text{-}H)]^- + H_2O$ --> $[UO_2(OH)(Cys\text{-}H)(Asp\text{-}H)]^-$	(24)	NR
$[UO_2(Cys\text{-}H)(His\text{-}2H)]^-$ or $[UO_2(Cys\text{-}2H)(His\text{-}H)]^- + H_2O$ --> $[UO_2(OH)(Cys\text{-}H)(His\text{-}H)]^-$	(25)	#
$[UO_2(His\text{-}H)(Asp\text{-}2H)]^-$ or $[UO_2(His\text{-}2H)(Asp\text{-}H)]^- + H_2O$ --> $[UO_2(OH)(His\text{-}H)(Asp\text{-}H)]^-$	(26)	&
$[UO_2(Gly\text{-}H)(Asp\text{-}2H)]^-$ or $[UO_2(Gly\text{-}2H)(Asp\text{-}H)]^- + H_2O$ --> $[UO_2(OH)(Gly\text{-}H)(Asp\text{-}H)]^-$	(27)	&
$[UO_2(Cys\text{-}H)(Gly\text{-}2H)]^-$ or $[UO_2(Cys\text{-}2H)(Gly\text{-}H)]^- + H_2O$ --> $[UO_2(OH)(Cys\text{-}H)(Gly\text{-}H)]^-$	(28)	>4.1 $
$[UO_2(His\text{-}H)(Gly\text{-}2H)]^-$ or $[UO_2(His\text{-}2H)(Gly\text{-}H)]^- + H_2O$ --> $[UO_2(OH)(His\text{-}H)(Gly\text{-}H)]^-$	(29)	10-20 $

NR = no reaction (10 s);

variable, max. 10% product;

& 0% $+H_2O$ in CID spectrum of precursor;

$ from CID spectrum of precursor.

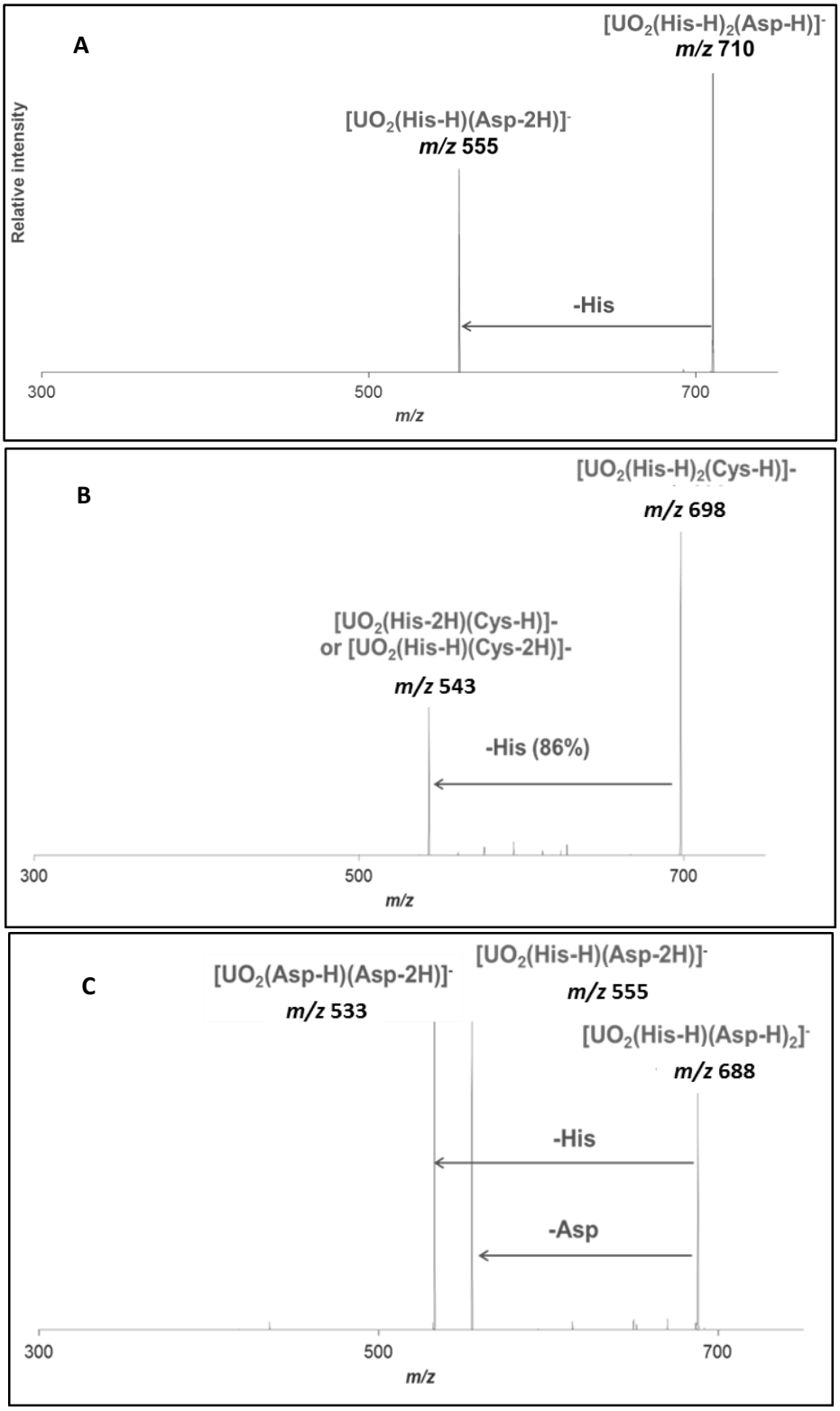

Figure IV.15 CID of positive uranyl mixed ligands: A. $[UO_2(His\text{-}H)_2(Asp\text{-}H)]^-$ B. $[UO_2(His\text{-}H)_2(Cys\text{-}H)]^-$ C. $[UO_2(His\text{-}H)(Asp\text{-}H)_2]^-$.

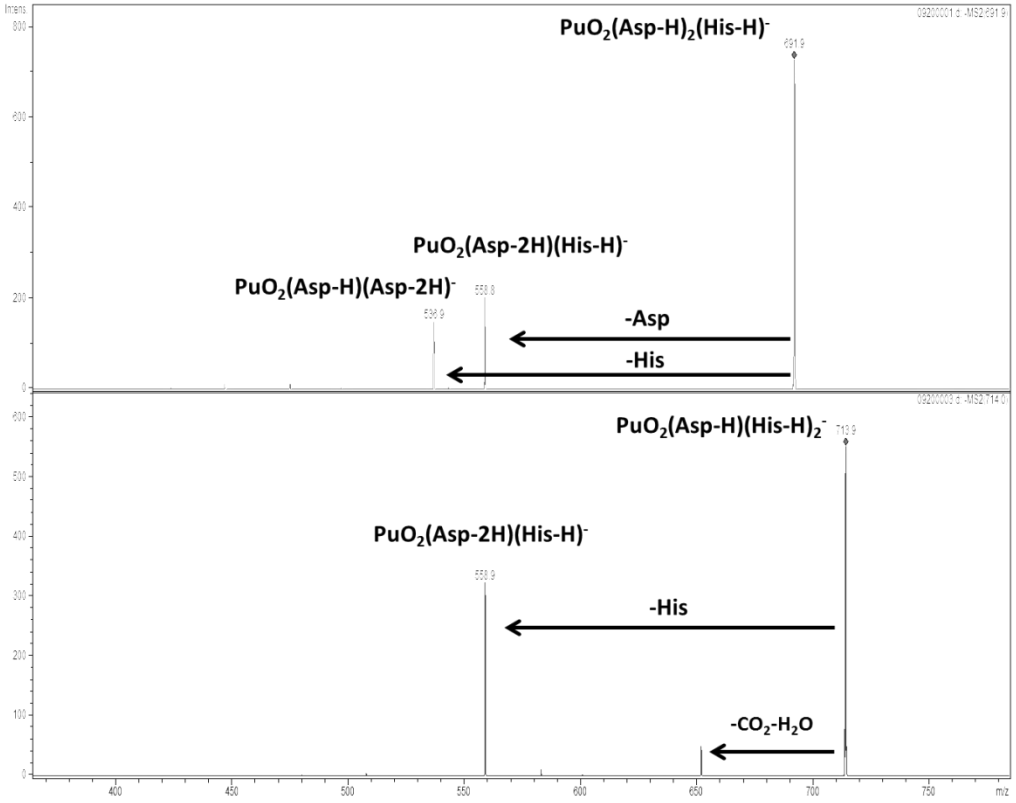

Figure IV.16 CID spectra of Pu(VI) mixed species in the negative mode.

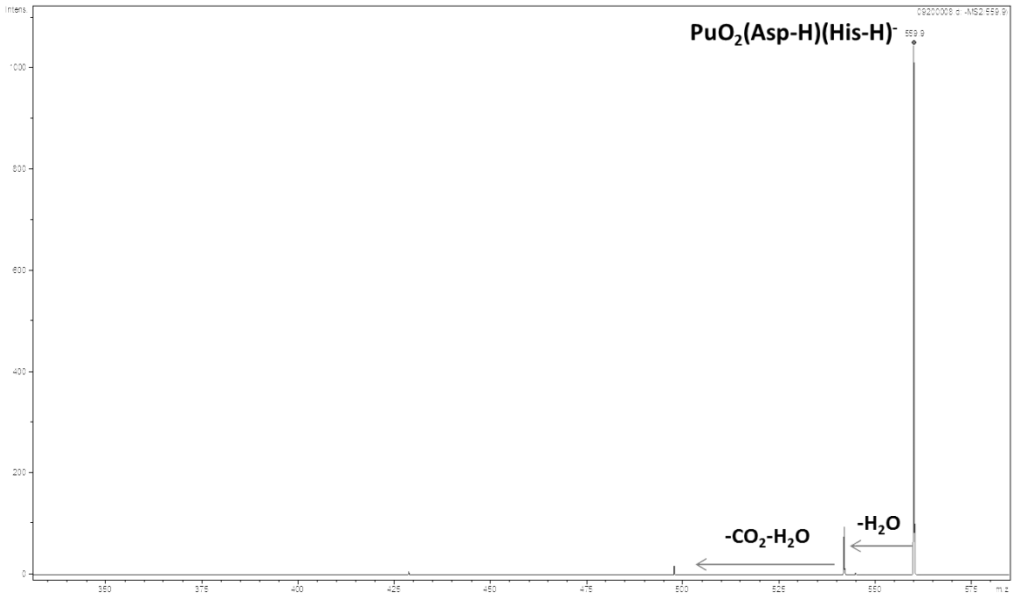

Figure IV.17 CID spectrum of Pu(V) mixed species in the negative mode.

IV.4. Conclusions

ESI-MS has proven to be an efficient method for producing several complexes of neutral, protonated and deprotonated amino acids with actinyl cations, $AnO_2^{+/2+}$, in the gas phase. From these studies, information about the coordination of the amino acids to the actinyls and their relative affinities could be obtained based on dissociation patterns and hydrolysis reactions of the complexes.

It was observed, as expected, that UO_2Cl_2 yields more aa-substituted species than $UO_2(NO_3)_2$. Chloride ions are weaker in ligand strength than nitrate ions and, therefore, there is more substitution. For that reason, for some studies the uranyl chloride was preferentially used, especially in the preparation of mixed aa complexes for competitive dissociations. In relation to the aa used to form complexes with the actinyls, actinyl-Gly complexes demonstrated to be clearly different from the other aa-actinyl complexes more probably due to the lack of side-chain and its smaller size. Backbone dissociation with bond activation via loss of CO_2 by the uranyl dication is observed only with Gly. Actinyl(V) ions, PuO_2^+ and NpO_2^+, activated also the C-αC bonds of Gly, His, Cys and Asp.

Dissociation of uranyl(VI) complexes with neutral and deprotonated glycine in the positive mode revealed that the uranyl species exhibit loss of neutral Gly or HX (X = Cl^-, NO_3^-, $(Gly\text{-}H)^-$), with rapid hydrolysis with the background water occurring during the dissociation process. The loss of one neutral glycine reduces the coordination around the equatorial plane and the hydroxyl group completes a coordination number five in the equatorial plane for UO_2^{2+}, considering that the glycine is bidentate by the two oxygen atoms of the carboxylate function, which is also suggested previously by reported DFT calculations. Decarboxylation occurs also in the CID of the subsequent fragmented species which leads to cleavage of the C-αC of Gly promoted by the uranyl(VI).

In the negative mode, dissociation of uranyl(VI) complexes with deprotonated glycine, complexes $[UO_2(X)_n(Gly\text{-}H)_{3-n}]^-$ (X = Cl^-, NO_3^-, n = 0, 1, 2), yielded mostly fragments of sequentially elimination of one deprotonated glycine and fast reaction with the background water (-(-Gly-H)+H_2O-H). U(V) species are very reactive and tend to form U(VI) species, either by hydrolysis or by oxygen addition as is the case of the $[UO_2(X)_n(Gly\text{-}H)_{2-n}]^-$ species. Decarboxylation is most evident in the dissociation of the species $[UO_2(X)_2(Gly\text{-}H)]^-$, which leads to the bond activation by the uranyl dication in the fragmentation process.

The dissociation of actinyl complexes with cysteine, histidine and aspartic acid led to the formation of several interesting species, in both ionization modes. Complexes of uranyl(VI) with 1 to 3 aa ligands and actinyl(V) (for U, Np, Pu) with 1 to 2 aa ligands were produced and CID of all these species was examined in detail.

For the protonated species, CID of the uranyl-Cys complexes showed interesting differences from the other aa, with major loss of NH_3 which is probably due to the structural differences in the side chain of this aa. Loss of the neutral aa was a minor fragment in the dissociation pathway of these species. Cations of uranyl(VI)-aa with Cl^- or NO_3^- were also observed in the ESI spectra. CID of these complexes yielded mostly fragments of HX loss. This is expected as uranyl-X bonds are probably weaker than uranyl-aa bonds. In the dissociation of the actinyl(V)-aa species, water loss and decarboxylation or loss of CO from Cys, His or Asp are dominant in the CID. Np(V) and Pu(V) are responsible for bond activation of the C-αC bond in all three aa.

In relation to the formed anionic species, the ESI spectra indicate that the formation of uranyl-aa complexes (and of more aa-substituted species) increases in the order Gly<Cys<Asp≤His.

An important observation is that the species $[UO_2(aa\text{-}H)(aa\text{-}2H)]^-$ formed through major loss of aa from CID of $[UO_2(aa\text{-}H)_3]^-$, hydrate in the order His>Cys~Asp (no reaction was observed for the species with Asp). This result reveals the strength of the doubly-deprotonated ligand (Asp-2H) to the uranyl ion and also a hint on the mode of coordination, probably bidentate by the deprotonated carboxylate. The strength/stability of the anionic (aa-H) follows the order Asp>Cys>His>Gly.

Competitive CID of uranyl species with mixed aa was also an asset. These species were meticulously analyzed with the aim of determining the relative affinity and gas-phase stability of the formed species. Hydrolysis reactions confirmed the conclusion on the strength/stability of the di-anionic (aa-2H), which, as mentioned above, follows the order Asp>His>Cys (Gly doesn't yield (aa-2H)).

In the positive mode, CID and respective hydrolysis suggest that the strength of the (neutral aa)-UO_2^{2+} interaction follows the order His>Asp>Cys which happens to be the same trend as the gas basicity of these amino acids (Taable IV.1.2). In the negative mode, CID of the $[UO_2(aa^1\text{-}H)_2(aa^2\text{-}H)]^-$ species showed preferential loss of the neutral amino acid in the order His~Cys>Asp, indicating particularly strong coordination of doubly-deprotonated Asp to UO_2^{2+}.

To complement and to unravel some remaining aspects of the experimental data, computed structures of the species $[UO_2(aa\text{-}H)_3]^-$, $[UO_2(aa\text{-}H)(aa\text{-}2H)]^-$ and $[UO_2(aa\text{-}H)(aa)_2]^+$ could be very

useful. An important issue is whether the neutral aa in these complexes is present or not as zwitterion. Also, the energetics of the preferred fragmentation of the cations and anions of the aa-mixed complexes would complement the observed data.

References

(1) Ansoborlo, E.; Prat, O.; Moisy, P.; Den Auwer, C.; Guilbaud, P.; Carriere, M.; Gouget, B.; Duffield, J.; Doizi, D.; Vercouter, T.; Moulin, C.; Moulin, V., Actinide speciation in relation to biological processes, *Biochimie* **2006**, *88*, 1605.

(2) Bresson, C.; Ansoborlo, E.; Vidaud, C., Radionuclide speciation: A key point in the field of nuclear toxicology studies, *Journal of Analytical Atomic Spectrometry* **2011**, *26*, 593.

(3) Durbin, P., Actinides in animals and man, In *The Chemistry of the Actinide and Transactinide Elements*; Morss, L. R., Edelstein, N. M., Fuger, J., Eds.; Springer: **2006**; Vol. 5, p 3339.

(4) Gorden, A. E. V.; Xu, J. D.; Raymond, K. N.; Durbin, P., Rational design of sequestering agents for plutonium and other actinides, *Chemical Reviews* **2003**, *103*, 4207.

(5) Durbin, P. W., Lauriston S. Taylor Lecture: The quest for therapeutic actinide chelators *Health Physics* **2008**, *95*, 465.

(6) Ni, C.; Shuh, D. K.; Raymond, K. N., Uranyl sequestration: synthesis and structural characterization of uranyl complexes with a tetradentate methylterephthalamide ligand, *Chemical Communications* **2011**, *47*, 6392.

(7) Pible, O.; Vidaud, C.; Plantevin, S.; Pellequer, J.-L.; Quemeneur, E., Predicting the disruption by UO_2^{2+} of a protein-ligand interaction, *Protein Science* **2010**, *19*, 2219.

(8) Heintze, E.; Aguilera, C.; Davis, M.; Fricker, A.; Li, Q.; Martinez, J.; Gage, M. J., Toxicity of depleted uranium complexes is independent of p53 activity, *Journal of Inorganic Biochemistry* **2011**, *105*, 142.

(9) Hartsock, W. J.; Cohen, J. D.; Segal, D. J., Uranyl acetate as a direct inhibitor of DNA-binding proteins, *Chemical Research in Toxicology* **2007**, *20*, 784.

(10) Huang, H.; Chaudhary, S.; Van Horn, J. D., Uranyl-peptide interactions in carbonate solution with DAHK and derivatives, *Inorganic Chemistry* **2005**, *44*, 813.

(11) Pible, O.; Guilbaud, P.; Pellequer, J. L.; Vidaud, C.; Quemeneur, E., Structural insights into protein-uranyl interaction: towards an in silico detection method, *Biochimie* **2006**, *88*, 1631.

(12) Van Horn, J. D.; Huang, H., Uranium(VI) bio-coordination chemistry from biochemical, solution and protein structural data, *Coordination Chemistry Reviews* **2006**, *250*, 765.

(13) Xie, W.; Badawi, A.; Huang, H.; Van Horn, J. D., Solution interactions between the uranyl cation UO22+ and histidine, N-acetyl-histidine, tyrosine, and N-acetyl-tyrosine, *Journal of Inorganic Biochemistry* **2009**, *103*, 58.

(14) Rodgers, M. T.; Armentrout, P. B., A thermodynamic "vocabulary" for metal ion interactions in biological systems, *Accounts of Chemical Research* **2004**, *37*, 989.

(15) Bush, M. F.; Oomens, J.; Saykally, R. J.; Williams, E. R., Effects of alkaline earth metal ion complexation on amino acid zwitterion stability: Results from infrared action spectroscopy, *Journal of the American Chemical Society* **2008**, *130*, 6463.

(16) Ye, S. J.; Armentrout, P. B., Absolute thermodynamic measurements of alkali metal cation interactions with a simple dipeptide and tripeptide, *Journal of Physical Chemistry A* **2008**, *112*, 3587.

(17) Ruan, C.; Rodgers, M. T., Modeling Metal Cation-Phosphate Interactions in Nucleic Acids: Activated Dissociation of Mg^+, Al^+, Cu^+, and Zn^+ Complexes of Triethyl Phosphate, *Journal of the American Chemical Society* **2009**, *131*, 10918.

(18) Citir, M.; Stennett, E. M. S.; Oomens, J.; Steill, J. D.; Rodgers, M. T.; Armentrout, P. B., Infrared multiple photon dissociation spectroscopy of cationized cysteine: Effects of metal cation size on gas-phase conformation, *International Journal of Mass Spectrometry* **2010**, *297*, 9.

(19) Prell, J. S.; Flick, T. G.; Oomens, J.; Berden, G.; Williams, E. R., Coordination of Trivalent Metal Cations to Peptides: Results from IRMPD Spectroscopy and Theory, *Journal of Physical Chemistry A* **2010**, *114*, 854.

(20) Ye, S. J.; Armentrout, P. B., Guided ion beam and theoretical studies of sequential bond energies of water to sodium cysteine cation, *Physical Chemistry Chemical Physics* **2010**, *12*, 13419.

(21) Dunbar, R. C.; Steill, J. D.; Oomens, J., Chirality-induced conformational preferences in peptide-metal ion binding revealed by IR spectroscopy, *Journal of the American Chemical Society* **2011**, *133*, 1212.

(22) Polfer, N. C., Infrared multiple photon dissociation spectroscopy of trapped ions, *Chemical Society Reviews* **2011**, *40*, 2211.

(23) Benavides-Garcia, M. G.; Balasubramanian, K., structural insights into the binding of uranyl with human serum protein apotransferrin structure and spectra of protein-uranyl interactions, *Chemical Research in Toxicology* **2009**, *22*, 1613.

(24) Su, J.; Zhang, K.; Schwarz, W. H. E.; Li, J., Uranyl-glycine-water complexes in solution: Comprehensive computational modeling of coordination geometries, stabilization energies, and luminescence properties, *Inorganic Chemistry* **2011**, *50*, 2082.

(25) Watson, L. A.; Hay, B. P., Role of the uranyl oxo group as a hydrogen bond acceptor, *Inorganic Chemistry* **2011**, *50*, 2599.

(26) Zwitterion, Wikipedia, https://en.wikipedia.org/.

(27) Bismondo, A.; Casellato, U.; Sitran, S.; Graziani, R., Preparation and characterization of some uranyl complexes of amino-acids - The crystal structure of UO_2 (gamma-aminobutanoic acid)$_3$(NO_3)$_2$, *Inorganica Chimica Acta-f-Block Elements Articles and Letters* **1985**, *110*, 205.

(28) Raghavan, A.; Santappa, M., Complexes of uranyl ion with amino and marcapto acids, *Journal of Inorganic & Nuclear Chemistry* **1973**, *35*, 3363.

(29) Nourmand, M.; Meissami, N., Complex-formation between uranium(VI) and thorium(IV) ions with some alpha-amino acids, *Journal of the Chemical Society-Dalton Transactions* **1983**, 1529.

(30) Wieczorek, H.; Kozlowski, H., NMR and spectroscopic studies on uranyl-ion interaction with aspartic acid and asparagine, *Inorganic & Nuclear Chemistry Letters* **1980**, *16*, 401.

(31) Khalil, M. M.; Taha, M., Equilibrium studies of binary and ternary complexes involving tricine and some selected alpha-amino acids, *Monatshefte Fur Chemie* **2004**, *135*, 385.

(32) Szabo, Z.; Toraishi, T.; Vallet, V.; Grenthe, I., Solution coordination chemistry of actinides: Thermodynamics, structure and reaction mechanisms, *Coordination Chemistry Reviews* **2006**, *250*, 784.

(33) Banu, L.; Blagojevic, V.; Bohme, D. K., Dissociation of deprotonated glycine complexes with Pb^{2+} and five transition-metal dications (Fe^{2+}, Co^{2+}, Ni^{2+}, Cu^{2+}, Zn^{2+}): The importance of metal bond activation, *International Journal of Mass Spectrometry* **2012**, *330*, 168.

(34) Banu, L.; Blagojevic, V.; Bohme, D. K., Bond activation in complexes of Pb(II) with 15 deprotonated amino acids: correlation with gas-phase acidity, *International Journal of Mass Spectrometry* **2012**, *316*, 23.

(35) Ansoborlo, E.; Amekraz, B.; Moulin, C.; Moulin, V.; Taran, F.; Bailly, T.; Burgada, R.; Henge-Napoli, M.-H.; Jeanson, A.; Den Auwer, C.; Bonin, L.; Moisy, P., Review of actinide decorporation with chelating agents, *Comptes Rendus Chimie* **2007**, *10*, 1010.

(36) Szabo, Z.; Grenthe, I., Potentiometric and multinuclear NMR study of the binary and ternary uranium(VI)-L-fluoride systems, where L is alpha-hydroxycarboxylate or glycine, *Inorganic Chemistry* **2000**, *39*, 5036.

(37) Jiang, J.; Renshaw, J. C.; Sarsfield, M. J.; Livens, F. R.; Collison, D.; Charnock, J. M.; Eccles, H., Solution chemistry of uranyl ion with iminodiacetate and oxydiacetate: A combined NMR/EXAFS and potentiometry/calorimetry study, *Inorganic Chemistry* **2003**, *42*, 1233.

(38) Moll, H.; Geipel, G.; Reich, T.; Bernhard, G.; Fanghanel, T.; Grenthe, I., Uranyl(VI) complexes with alpha-substituted carboxylic acids in aqueous solution, *Radiochimica Acta* **2003**, *91*, 11.

(39) Rao, L. F.; Garnov, A. Y.; Jiang, J.; Di Bernardo, P.; Zanonato, P.; Bismondo, A., Complexation of uranium(VI) and samarium(III) with oxydiacetic acid: Temperature effect and coordination modes, *Inorganic Chemistry* **2003**, *42*, 3685.

(40) Gharib, F.; Mojtabaei, R., Complex formation of dioxouranium(VI) ion with some aliphatic peptides, *Russian Journal of Inorganic Chemistry* **2005**, *50*, 1536.

(41) Keramidas, A. D.; Rikkou, M. P.; Drouza, C.; Raptopoulou, C. P.; Terzis, A.; Pashalidis, I., Investigation on uranyl interaction with bioactive ligands. Synthesis and structural studies of the uranyl complexes with glycine and N-(2-mercaptopropionyl)glycine, *Radiochimica Acta* **2002**, *90*, 549.

(42) Bismondo, A.; Rizzo, L., Thermodinamics of the complex-formation between uranyl(VI) and some polypeptides in aqueous solution *Thermochimica Acta* **1992**, *196*, 131.

(43) Guenther, A.; Geipel, G.; Bernhard, G., Complex formation of uranium(VI) with the amino acids L-glycine and L-cysteine: A fluorescence emission and UV-Vis absorption study, *Polyhedron* **2007**, *26*, 59.

(44) Ramanujam, V. V.; Rengaraj, K.; Sivasankar, B., Studies on uranyl complexes, *Bulletin of the Chemical Society of Japan* **1979**, *52*, 2713.

(45) Bismondo, A.; Rizzo, L.; Tomat, G.; Curto, D.; Dibernardo, P.; Cassol, A., Thermodynamic properties of actinide complexes - uranyl(VI)-glycine and thorium(IV)-glycine systems, *Inorganica Chimica Acta-Articles* **1983**, *74*, 21.

(46) Lagrange, P.; Schneider, M.; Zare, K.; Lagrange, J., Determination and comparison of stability-constants of uranium(VI) and vanadium(V) glycine complexes, *Polyhedron* **1994**, *13*, 861.

(47) Cefola, M.; Celiano, A. V.; Taylor, R. C.; Gentile, P. S., Coordination compounds, 3 chelalate compounds of uranyl ion with hydroxy, mercapto and amino acids, *Journal of Physical Chemistry* **1962**, *66*, 790.

(48) Levdikov, V. M.; Blagova, E. V.; Brannigan, J. A.; Cladiere, L.; Antson, A. A.; Isupov, M. N.; Seror, S. J.; Wilkinson, A. J., The crystal structure of YloQ, a circularly permuted GTPase essential for Bacillus subtilis viability, *Journal of Molecular Biology* **2004**, *340*, 767.

(49) Prudden, A. R.; Lien, N. R.; Telford, J. R., An outer-sphere ligand for uranyl carbonate, *Chemical Communications* **2004**, 172.

(50) Gianguzza, A.; Pettignano, A.; Sammartano, S., Interaction of the dioxouranium(VI) ion with aspartate and glutamate in NaCl(aq) at different ionic strengths, *Journal of Chemical and Engineering Data* **2005**, *50*, 1576.

(51) Vidaud, C.; Gourion-Arsiquaud, S.; Rollin-Genetet, F.; Torne-Celer, C.; Plantevin, S.; Pible, O.; Berthomieu, C.; Quemeneur, E., Structural consequences of binding of UO_2^{2+} to apotransferrin: Can this protein account for entry of uranium into human cells?, *Biochemistry* **2007**, *46*, 2215.

(52) Rios, D.; Rutkowski, P. X.; Shuh, D. K.; Bray, T. H.; Gibson, J. K.; Van Stipdonk, M. J., Electron transfer dissociation of dipositive uranyl and plutonyl coordination complexes, *Journal of Mass Spectrometry* **2011**, *46*, 1247.

(53) Rutkowski, P. X.; Michelini, M. C.; Bray, T. H.; Russo, N.; Marçalo, J.; Gibson, J. K., Hydration of gas-phase ytterbium ion complexes studied by experiment and theory, *Theoretical Chemistry Accounts* **2011**, *129*, 575.

(54) Eckersley, M.; Bowie, J. H.; Hayes, R. N., Collision-induced dissociation of deprotonated alpha-amino-acids - The occurence of specific proton transfers preceding fragmentation, *International Journal of Mass Spectrometry and Ion Processes* **1989**, *93*, 199.

(55) Lide, D. R.; CRC Handbook of Chemistry and Physics, 89th ed. **2009**.

(56) Rios, D.; Michelini, M. C.; Lucena, A. F.; Marçalo, J.; Bray, T. H.; Gibson, J. K., Gas-phase uranyl, neptunyl, and plutonyl: Hydration and oxidation studied by experiment and theory, *Inorganic Chemistry* **2012**, *51*, 6603.

(57) Groenewold, G. S.; Cossel, K. C.; Gresham, G. L.; Gianotto, A. K.; Appelhans, A. D.; Olson, J. E.; Van Stipdonk, M. J.; Chien, W., Binding of molecular O-2 to di- and triligated UO_2^+, *Journal of the American Chemical Society* **2006**, *128*, 3075.

(58) Bryantsev, V. S.; de Jong, W. A.; Cossel, K. C.; Diallo, M. S.; Goddard, W. A.; Groenewold, G. S.; Chien, W.; Van Stipdonk, M. J., Two-electron three-centered bond in side-on (η^2) uranyl(V) superoxo complexes, *Journal of Physical Chemistry A* **2008**, *112*, 5777.

(59) Leavitt, C. M.; Bryantsev, V. S.; de Jong, W. A.; Diallo, M. S.; Goddard, W. A., III; Groenewold, G. S.; Van Stipdonk, M. J., Addition of H_2O and O_2 to acetone and dimethylsulfoxide ligated uranyl(V) dioxocations, *Journal of Physical Chemistry A* **2009**, *113*, 2350.

(60) Gong, Y.; Zhou, M.; Andrews, L., Spectroscopic and theoretical studies of transition metal oxides and dioxygen complexes, *Chemical Reviews* **2009**, *109*, 6765.

(61) Hurtado, M.; Monte, M.; Lamsabhi, A. M.; Yanez, M.; Mo, O.; Salpin, J.-Y., Modeling interactions between an amino acid and a metal dication: Cysteine-calcium(II) reactions in the gas phase, *Chempluschem* **2013**, *78*, 1124.

Supporting Information

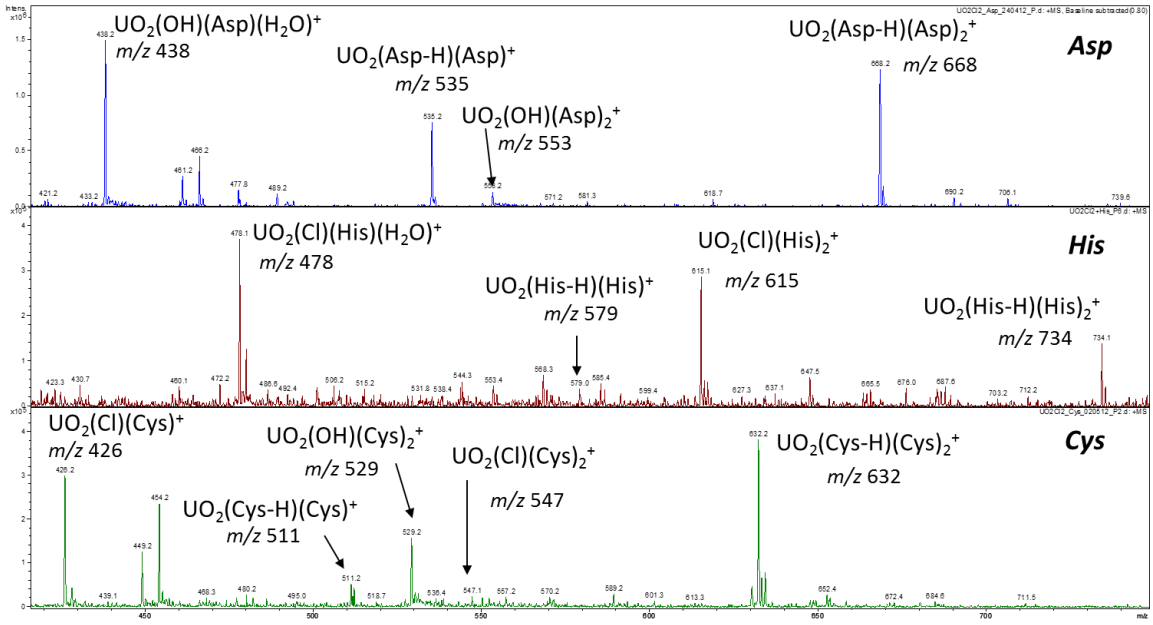

Figure S1. ESI-MS spectra of uranyl chloride + amino acid solution (1:4) in the positive mode.

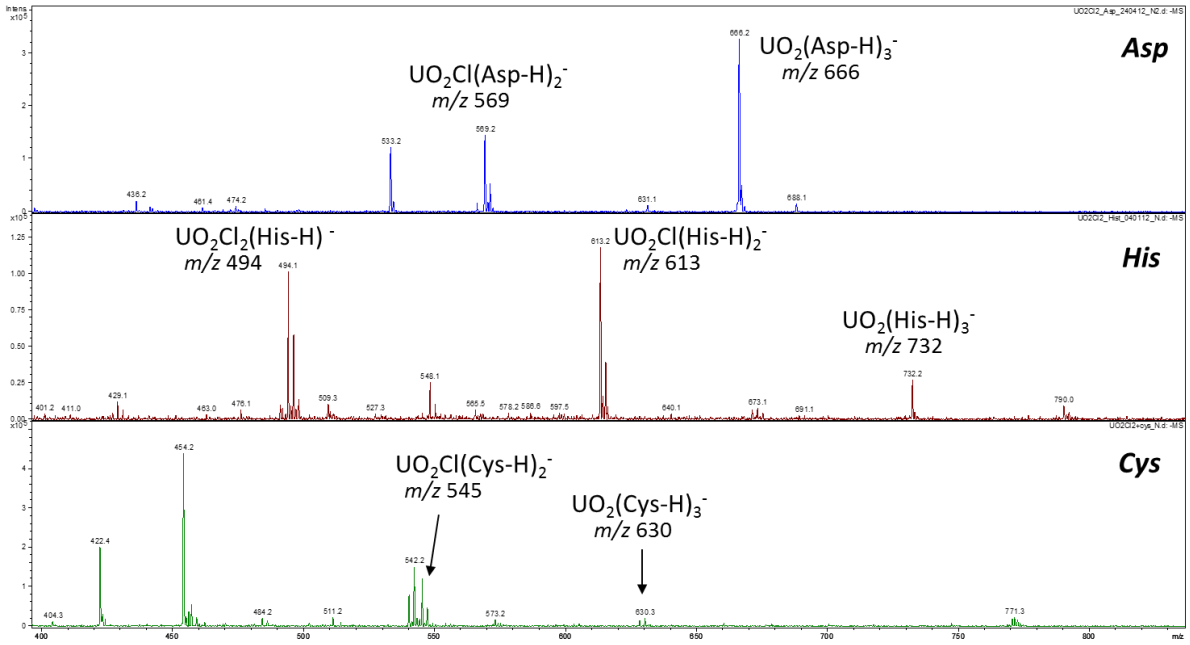

Figure S2. ESI-MS spectra of uranyl chloride + amino acid solution (1:4) in the negative mode.

Chapter V.
General conclusions and final remarks

Chapter V. General conclusions and final remarks

Several fundamental aspects of gas-phase *f*-element chemistry, more specifically actinide ion chemistry, were extensively explored in the work described in this thesis. The use of mass spectrometry beyond its most common use in analytical chemistry allowed exploring several properties of these elements. Two distinct ionization modes were chosen to carry out this investigation: soft ionization, ESI, and a stronger ionization mode, laser ionization (LI), which enabled the access to different reactant actinide ions. Collision induced dissociation (CID) was employed in most of the studies: it allows manipulation of the level of fragmentation according to the energy applied, leading to the formation of several fragments and thus giving access to structural information through characteristic fragmentation patterns. LI was chosen because it easily allows ion generation at an atomic level through laser irradiation of the sample surface, which was useful in the study of oxo-exchange reactions of actinyl ions, $AnO_2^{+/2+}$, with water and methanol (Chapter II.1) and synthesis of actinide sulfide ions, $AnS_n^{+/2+}$ (Chapter II.4). In both cases, actinide ions ($An^{+/2+}$) were generated from solid alloys of platinum containing a few atom percent of the actinide. ESI-MS was employed for the work in the remaining chapters, where the properties of actinyl ions, with a focus on the uranyl ion, UO_2^{2+}, were explored. The main aspects examined in this work were reactions with the background water and molecular oxygen present in the ion trap (QIT) (Chapters II.2 and II.3), exchange reactions (Chapter II.1), synthesis of new species (Chapter II.4), redox stabilities (Chapter III.2), fundamental properties such as charge density (Chapter III.1) and coordination of biologically relevant ligands – amino acids (aa) with actinyl ions (Chapter IV). Theoretical computations were a fundamental help in this work to complement and confirm the experimental observations and also to increase the understanding of the role of the 5*f* orbitals, the electronic structure, most favorable configurations and geometries, bond distances, energetics and several other important properties of most of the studied species formed either through gas-phase reactions or by CID processes.

Oxo-exchange reactions of the actinyls UO_2^+, NpO_2^+ and PuO_2^+ with H_2O, were previously studied by ESI-MS but due to the impossibility to obtain exact reaction efficiencies and measure absolute rate constants, the same study was continued and complemented by FTICR-MS (***Chapter II.1***), a technique which provided more information on intrinsic factors through ion/molecule reactions. It was confirmed that exchange with water is much faster for the uranyl dication UO_2^{2+} than with UO_2^+ by at least 100 times, validating the previous prediction. Oxo-exchange with methanol was

also evaluated and it was observed that UO_2^+ and UO_2^{2+} exchange more efficiently with methanol than with water. Another important conclusion taken from these results deals with the covalency of these species, since it seems that there is greater covalency of the actinyl bonds upon proceeding across the actinyl series, with a resulting decreasing efficiency of oxo-exchange from UO_2^+ to PuO_2^+.

As a follow-up study on the exploration of fundamental aspects in actinyl chemistry, ***Chapter II.2*** comprised important reactions of water and molecular oxygen with actinyl ions, $An^{V}O_2^+$ (An = U, Np, Pu) and $An^{VI}O_2(OH)^+$ (An = U, Pu). These were studied experimentally and complemented with density functional theory (DFT) computations. The ESI mass spectra of the uranyl solution distinctively yielded more of the uranyl hydroxide (VI) species than the uranyl (V), an observation that clearly reflects the stabilities of the An^{VI} relative to An^{V}: U >> Pu > Np. Furthermore, the hydration study of actinyls(V) showed that in the gas phase there is addition of one less water molecule than in solution, which can be attributed to a cooperative polarization effect that occurs in solution. It was seen that $AnO_2(OH)^+$ ions hydrate much faster (by more than an order of magnitude) than the AnO_2^+ ions, which can be attributed to the fact that the additional vibrational degrees of freedom in the hydroxides for dissipation of hydration energy enable stabilization of the nascent hydrate by third-body collisional cooling. In relation to O_2 addition, uranyl(V) hydrate ions add molecular oxygen and oxidize to the oxidation state VI. This was confirmed by the DFT calculations, which revealed that these di-oxygen ligands are superoxides, η^2-O_2^-. Oxygen addition was not observed for neptunyl(V) and plutonyl(V) hydrates. These results are in agreement with the VI/V reduction potentials, which is substantially smaller for U (0.09) than for Np (1.16 V) or Pu (0.94 V).

Still under the scope of oxygen addition reactions to uranyl ions, in ***Chapter II.3*** this reaction was also studied for anionic uranyl(V) complexes, $[UO_2X_2]^-$, containing 13 different anions X^-. Uranyl(VI) superoxo complexes, $[UO_2X_2(O_2)]^-$, were formed in agreement with the observation for the uranyl(V) cations. The gas-phase basicity and number of vibrational degrees of freedom of the X^- ligands determined the rates of O_2 addition. DFT and QTAIM computations confirmed superoxide formation and indicated that the charge transfer is more favorable for precursor complexes where the uranyl bond is most weakened by the presence of the ligands, e.g. $[UO_2(OH)_2]^-$ and $[UO_2F_2]^-$.

It was also possible to accomplish the synthesis of new actinide species, namely, actinide polysulfides, $AnS_n^{+/2+}$, by reacting $An^{+/2+}$ ions, for An = Th, Pa, Np, Pu, Am, and Cm, with the neutral sulfur-donating reagent COS (***Chapter II.4***), complementing previous studies with uranium. Sequential abstraction of two sulfur atoms by Th^{2+} and Np^{2+} resulted in the disulfides ThS_2^{2+} and NpS_2^{2+}, respectively. Preliminary DFT computations performed on the thorium species indicated

that the ground-state structure has a triangular geometry with geometrical parameters that may correspond to the presence of a persulfide ligand. For the previously reported US_2^{2+}, DFT also predicted a triangular geometry as the GS structure but with geometrical parameters that point to the presence of a supersulfide ligand. DFT computations were not available for the case of Np, and it is uncertain whether NpS_2^{2+} is a thioneptunyl, $S{=}Np^{2+}{=}S$, or has a triangular geometry similar to US_2^{2+}. An^{2+} ions for An = Pu, Am and Cm showed reduced reactivities and did not yield any sulfide species. Mono- and dicationic tri- and tetrasulfides, ThS_3^+, ThS_3^{2+}, ThS_4^{2+} and NpS_3^{2+}, were also synthesized.

In Chapter III, several interesting results were reported on the subject of lanthanide and actinide cluster fragmentations, where relative charge densities of the constituent metal ions could be unveiled (***Chapter III.1***), and in the fragmentation and hydrolysis of lanthanide and actinide tetranitrate anions, which revealed III/IV redox stabilities in the gas phase (***Chapter III.2***). In the first sub-chapter, CID of mixed anionic dimers comprising alkaline earth (+2), lanthanide (+3), and the uranyl ion, UO_2^{2+}, and nitrate or chloride as the anions, demonstrated that the effective charge density of uranyl is comparable to that of the tripositive lanthanide ions, Ln^{3+}. The assignment of the effective charge of U in uranyl as ca. 3+ was shown to be in agreement with the results from solution chemistry, as well as with DFT computational studies. Differences in the fragmentation behaviors of nitrate and chloride clusters indicated a role of covalent bonding and the DFT computations suggested that the more ionic fluoride anion should be most useful for evaluating effective charges of cations using this approach.

In the second sub-chapter (***Chapter III.2***), trinitrate oxide metal ions $MO(NO_3)_3^-$ (M = Ce, Pr, Nd, Tb, Pu, Am and Cm) and the hydroxides $M(OH)(NO_3)_3^-$ (M = remaining lanthanides) were obtained by CID of the tetranitrate ions $M^{III}(NO_3)_4^-$. The trinitrate hydroxide was formed by hydrolysis of the oxide in a secondary reaction with the background water. The measured hydrolysis rates for $MO(NO_3)_3^-$ showed that Ce, Pr, Nd, Tb, Pu, Am and Cm are more resistant to hydrolysis as they have relatively low fourth ionization energies (and IV/III reduction potentials). DFT computations indicated that in the $MO(NO_3)_3^-$ complex Ce forms a Ce=O covalent bond and has an electronic configuration consistent with an oxidation state IV, while Pr may have an intermediate IV/III oxidation state. The experimental results are consistent with the actinides Pu, Am and Cm being in the oxidation state IV, whereas Nd and Tb may be similar to Pr.

Finally, the last chapter – ***Chapter IV*** – describes work developed with the aim of exploring the interactions between selected amino acids and actinyl ions, a subject previously not examined in gas-phase actinide ion chemistry. Many species were formed from the ESI of the electrosprayed

actinyl solutions containing glycine (the simplest aa) and 3 aa with different side-chains: cysteine, histidine and aspartic acid. Dissociation patterns of the formed cations and anions were carefully analyzed and many similarities and/or disparities were observed. Also, gas-phase reactions, namely hydration/hydrolysis and oxygen addition from the background gases occurred in the QIT. In summary, actinyl-Gly and actinyl-Cys complexes demonstrated very different CID profiles in comparison with the other actinyl-aa complexes, probably due to the lack of the side-chain in the case of Gly and the influence of the –SH of the side chain in the case of Cys. Backbone dissociation with bond activation via loss of CO_2 by the uranyl dication was observed only with Gly. The actinyl (V) ions PuO_2^+ and NpO_2^+ proved to be also capable of C-αC bond scission of Gly, His, Cys and Asp. In the dissociation of uranyl (VI) cations with glycine, the loss of neutral Gly followed by hydrolysis was the major CID pathway. This led to reduction of the coordination around the equatorial plane by loss of Gly; the hydroxyl group then completes a coordination number five in the equatorial plane for UO_2^{2+}, considering that Gly could coordinate as bidentate by the two oxygen atoms of the carboxylate function, which was also suggested by previously reported DFT computations. For the protonated species of the uranyl-Cys complexes, the CID showed interesting differences from the other amino acids, with a major loss of NH_3, probably due to the structural differences in the side chain of this aa. In the dissociation of the actinyl (V)-aa species, water loss and decarboxylation and/or loss of CO of Cys, His or Asp was dominant in the CID. For anionic species, the formation of uranyl-aa complexes increased in the order Gly<Cys<Asp≤His. Furthermore, the hydration/hydrolysis rates of the formed species $[UO_2(aa\text{-}H)(aa\text{-}2H)]^-$, obtained from the major loss of the aa from $[UO_2(aa\text{-}H)_3]^-$, followed the order His>Cys~Asp, which indicates that the (Asp-2H) ligand is strongly ligated to the uranyl ion. Also, it was possible to get a trend of strength/stability of the anionic (aa-H), in the order Asp>Cys>His>Gly. Competition between uranyl species with mixed amino acids was also examined in the QIT, which allowed establishing gas-phase affinity trends. For the anions, the CID of the $[UO_2(aa^1\text{-}H)_2(aa^2\text{-}H)]^-$ species showed preferential loss of the neutral amino acid in the order His~Cys>Asp, indicating, a particularly strong coordination of doubly-deprotonated Asp to UO_2^{2+}, a fact mentioned above based on the hydrolysis rates obtained for the anions $[UO_2(aa\text{-}H)(aa\text{-}2H)]^-$. For the cations, the trend of strength of the (neutral aa)-UO_2^{2+} interaction followed the order His>Asp>Cys, in agreement with the gas basicities of these amino acids.

In summary, the present thesis has hopefully contributed to the expansion of the current scientific knowledge on the gas-phase ion chemistry of *f* elements. However, further studies could be important to continue and complement this vast subject. As for instance, under the scope of the oxo-exchange studies, other An species such as different AnO^+, and PaO_2^+ and AmO_2^+, among

others, could improve understanding the role of covalency in these species; also, cluster dissociation could be used to unravel other important properties in the gas phase related to charge density as for example ionic size; in relation to the coordination studies of actinyls with relevant biomolecules, nucleobases, nucleosides and nucleotides could also be considered to complement the preliminary studies with the amino acids.